Author:
Kershaw, James A

Title:
Stylasterid coral geochemistry

a novel approach for oceanographic reconstruction

Stylasterid coral geochemistry: a novel approach for oceanographic reconstruction

James Alex Kershaw

A dissertation submitted to the University of Bristol in accordance with the requirements for award of the degree of Doctor of Philosophy in the Faculty of Science

School of Earth Sciences

November 2023

Word count: 71978

Abstract

The carbonate skeletons of azooxanthellate coral groups are important archives of past subsurface ocean conditions. Previous work has focused on anthozoan coral groups, while hydrozoan corals, such as the Stylasteridae, remain largely unexplored. Stylasterids are widely distributed in the modern ocean, and build hard carbonate skeletons from either aragonite or high-Mg calcite. Recent work has shown that the skeletal geochemistry of stylasterid skeletons correlates with seawater temperature, while the boron isotopic composition of stylasterid skeletons ($\delta^{11}B$) may reflect seawater pH. However, the palaeoceanographic utility of stylasterids is currently limited by a paucity of data.

In this thesis, I develop new calibrations between stylasterid inorganic skeletal geochemistry and seawater conditions, and investigate the application of U-series and radiocarbon dating techniques to stylasterid skeletons. I show that stylasterid Ba/Ca is a novel proxy for the dissolved concentration of Ba in seawater, and that stylasterid $\delta^{11}B$ is a robust archive of seawater pH. Application of U-series dating techniques to stylasterids is complicated by their low skeletal [U]. Conversely, coherent radiocarbon growth chronologies are generated for large, live-collected stylasterids, which grow over decadal to centennial timescales. With robust proxies for seawater temperature, $[Ba]_{SW}$ and pH now established, large, live-collected stylasterids represent important archives of recent variations in subsurface ocean conditions.

The decadal-centennial timescale of stylasterid growth underscores the importance of protecting these corals and the ecosystems they support from destruction or damage. More broadly, the geochemical data presented also provides insights into stylasterid biomineralisation. Aragonitic stylasterid $\delta^{11}B$ is in equilibrium with the borate anion in seawater, including when ambient seawater is undersaturated with respect to aragonite. This finding is consistent with stylasterids employing reduced levels of pH upregulation during calcification, compared to scleractinian corals. The implications of these findings for the future vulnerability of stylasterids in a changing ocean is, as yet, uncertain.

Acknowledgements

"Prep well and make some good decisions. Keep your fingers crossed and maybe you'll get lucky"

Russell D. Day

Author's declaration

I declare that the work in this dissertation was carried out in accordance with the requirements of the University's *Regulations and Code of Practice for Research Degree Programmes* and that it has not been submitted for any other academic award. Except where indicated by specific reference in the text, the work is the candidate's own work. Work done in collaboration with, or with the assistance of, others, is indicated as such. Any views expressed in the dissertation are those of the author.

SIGNED: James Alex Kershaw

DATE: 10/11/2023

Table of Contents

List of figures

List of tables

Chapter 1: Introduction

1. Motivation

1.1 Climate change and the ocean

Anthropogenic activities – primarily the burning of fossil fuels - are releasing CO_2 into the atmosphere at a geologically-unprecedented rate (Zeebe et al., 2016). In 2022 - the last full year of observations at the time of writing this thesis – global surface atmospheric $[CO_2]$ averaged 417 ppm, 50 % above pre-industrial levels and the highest in over 4 million years (Lan et al., 2023). Global average surface temperatures have responded accordingly, and in 2022 were 0.86 ^{o}C higher than the 20th century average (NOAA, 2023).

The implications of anthropogenically-induced climate change for ecosystems and civilisations depend critically on the interactions between multiple components of the Earth system, including the atmosphere, cryosphere, terrestrial biosphere and the ocean. The global ocean plays a particularly important role in the wider earth system, and is intricately linked to Earth's climatic state on decadal to millennial timescales, partly as a result of the large-scale, thermohaline ocean circulation (Figure 1; e.g. Broecker, 1991; Rahmstorf, 2002; Talley, 2013). As a result of this circulation, the global ocean stores large amounts of heat, carbon and nutrients, distributes these around the planet, and exchanges them with the atmosphere to provide a critical link to the global climatic state (e.g. Macdonald and Wunsch, 1996; Ganachaud and Wunsch, 2000; Rahmstorf, 2002; Bigg et al., 2003; Reid et al., 2009). For example, the ocean holds a significant and climatically-relevant reservoir of dissolved CO_2 (e.g. Falkowski et al., 2000; Sigman and Boyle, 2000; Rae et al., 2018; DeVries, 2022), while the poleward transport of warm, equatorial surface waters in the Atlantic supplies heat which heavily influences the climate of northern Europe (e.g. Ganachaud and Wunsch, 2000; Figure 1).

As a direct result of anthropogenic climate change, the global ocean is undergoing significant changes (e.g. IPCC, 2019). The ocean has taken up some 26 % of anthropogenic CO_2 emissions since 1850 (Friedlingstein et al., 2022), and has accounted for the majority (> 90 %) of the resulting increase in global thermal energy (Levitus et al., 2012; IPCC, 2019). As a result, global surface ocean pH has decreased, surface marine heatwaves have become more common, stratification in the upper 200 m of the ocean has increased, and associated changes in ocean mixing, circulation and productivity have led to a decrease in upper-ocean (< 1000 m) oxygen levels (IPCC, 2019).

These changes in ocean conditions are having a substantial impact on marine ecosystems globally (e.g. Doney et al., 2012; IPCC, 2019). It is estimated that the ocean hosts ~ 15 % of described species (Reaka-Kudla, 1997), and their vulnerability to future changes in ocean conditions will have important implications for the human communities which rely on them (e.g. Doney et al., 2012; Mora et al., 2013; Thurber et al., 2014; IPCC, 2019). There is also increasing concern that anthropogenic emissions are affecting the oceanic processes which regulate Earth's climatic state. For instance, some authors have argued for a recent, unprecedented slowdown in the rate of the Atlantic Meridional Overturning

Circulation (AMOC), with potentially large implications for northern hemisphere climate (Caesar et al., 2018; Caesar et al., 2021; although see Kilbourne et al., 2022).
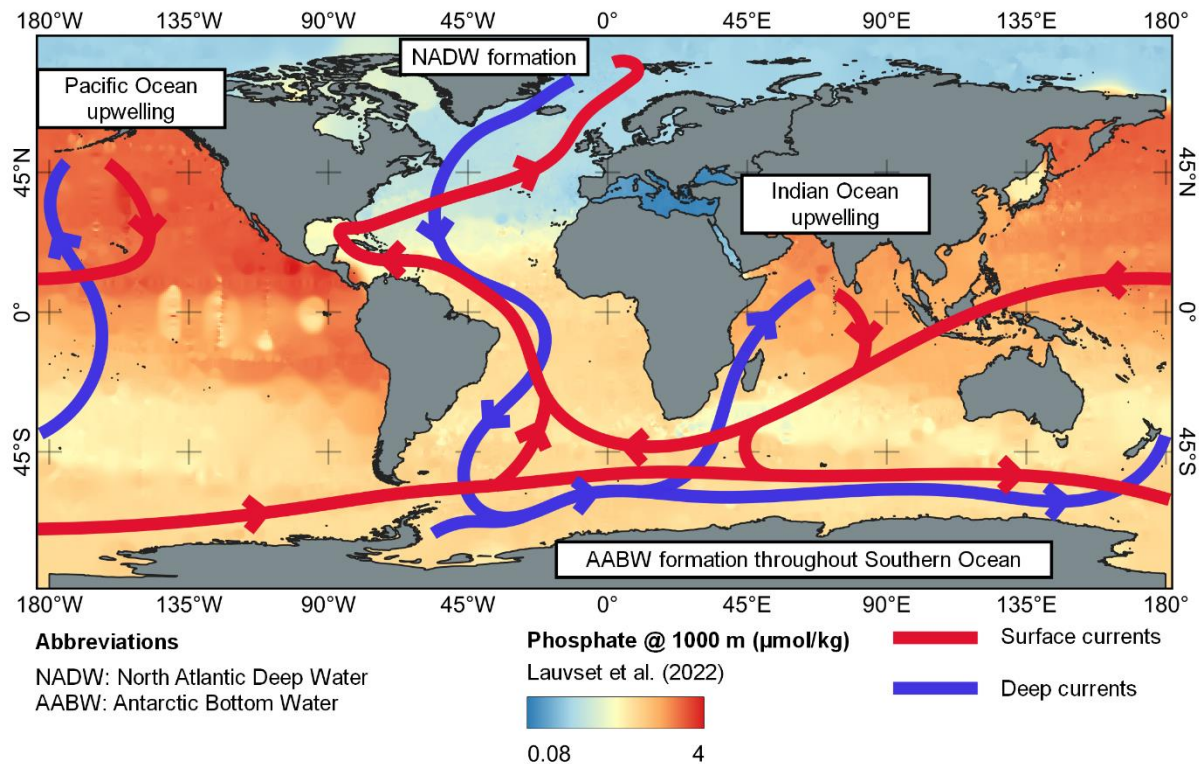
Figure 1. Simplified overview of the global overturning circulation, adapted from IPCC (2001). Background colours show dissolved phosphate concentration at 1000 m water depth, taken from the GLODAP bottle database (Lauvset et al., 2022).

Measuring the magnitude and rate of ongoing changes in ocean conditions since substantial emissions began (i.e. ~ the last 250 years) is thus important when predicting the response of the wider Earth system to anthropogenic greenhouse gas emissions over a range of timescales (e.g. Sarmiento et al., 1998; Reid et al., 2009). Additionally, comparing current changes to those which have occurred in Earth's historical and geological past allows us to place modern trends in proper historical and geological context, and provides valuable information on past "natural experiments" which can help elucidate the links between Earth's ocean and climate. For example, the increase in atmospheric CO_2 concentration across the last glacial to interglacial transition has been widely attributed to the release of CO_2 from the deep ocean, providing powerful evidence for the importance of the ocean in regulating global climate (e.g. Marchitto et al., 2007; Anderson et al., 2009; Skinner et al., 2010; Rae et al., 2018).

The direct observational record of the oceans is limited in both its spatial and temporal coverage. Systematic observations of surface ocean pH, for instance, cover only the last few decades, and are limited to a small number of locations (e.g. the Hawaii Ocean Time-series (HOT) began in 1989 (Karl and Lukas, 1996)). Therefore, alternative approaches are required to constrain the longer-term (i.e. > 50 year)

evolution of oceanic conditions. The field of palaeoceanography is concerned with the development and application of these approaches.

1.2   Palaeoceanographic proxies

In the absence of a direct observational record, palaeoceanographic reconstructions rely on proxy measurements, which can be conceptualised as an indirect measurement of a quantity, Y, which itself has a known and quantifiable relation to some other quantity of interest, X:

$$Y = f(X) \qquad (1)$$

A number of geological and biological materials have been developed as archives of climatic and oceanographic conditions, including ice cores, sediment cores, and the shells and skeletons of marine organisms including foraminifera, diatoms, bivalves and corals (e.g. Dansgaard et al., 1982; Druffel, 1997; Wefer et al., 1999; Henderson, 2002; Calvert and Pederson, 2007; Kucera, 2007; Swann and Leng, 2009; Robinson et al., 2014). Because these archives can be preserved for many hundreds, thousands or even millions of years, the information they store can provide crucial windows into conditions in Earth's past.

The development of robust palaeoceanographic archives requires a number of criteria to be met. Firstly, the archive must be formed at some time in Earth's past, and this date must be determined accurately and precisely. Secondly, environmental conditions at that time (i.e. the X term in equation 1) must influence some measurable property of that archive (the Y term in equation 1), and we must be able to determine the function (the f term in equation 1) linking X and Y. Finally, the signature Y must be preserved without significant alteration from the time of formation until it's measurement in the modern day.

In this thesis, I focus on the palaeoceanographic archive potential of azooxanthellate (i.e. without photosymbionts) corals, whose occurrence at depths below the influence of daily and seasonal fluctuations in surface ocean conditions means they are well-placed to provide constraint on important, sub-surface processes including ocean circulation and deep-ocean carbon storage (e.g. Robinson et al., 2014; Rae et al., 2018; Chen et al., 2020; Stewart et al., 2021).

1.3   Azooxanthellate coral resilience

In addition to the need to understand the past evolution of Earth's ocean and climate, there is also a pressing need to develop our understanding of the vulnerability of marine ecosystems - including azooxanthellate corals - to ongoing changes in ocean conditions (e.g. Levin and Le Bris, 2015). As carbonate-forming and respiring organisms, ocean acidification and deoxygenation due to climate change (see section 1.1) are expected to have a negative impact on azooxanthellate coral ecosystems, while changing circulation and primary productivity patterns may also affect their food supply (e.g. Feely et al., 2004; Guinotte et al., 2006; Davies and Guinotte, 2011; Thiagarajan et al., 2013; Bostock et al., 2015). Further, azooxanthellate corals are directly threatened by anthropogenic activities including bottom trawling (e.g. Hall-Spencer et al., 2002; Roberts and Hirshfield, 2004; Roberts et al., 2006). Associated

changes in azooxanthellate coral health, abundance and/or distribution will have broader implications for deep-marine ecosystems, owing to the importance of azooxanthellate corals as engineers of deep-marine habitats (e.g. Roberts et al., 2006; Hoarau et al., 2021; section 2).

1.4 This thesis

The two broad themes outlined in sections 1.2 and 1.3 motivate the lines of inquiry addressed by this thesis: (i) the development of tools for reconstructing ocean conditions in Earth's past, and (ii) understanding the vulnerability of carbonate marine ecosystems to changes in ocean conditions. Specifically, I present novel measurements of the inorganic, skeletal geochemistry of an important, but understudied, group of azooxanthellate coral: the Stylasteridae (herein referred to as the stylasterids). In the following sections, I introduce the stylasterids, before detailing how the inorganic chemical composition of their skeletons can provide insights into palaeoceanography and ecosystem resilience.

2. Introducing the stylasterids

The stylasterids are one of seven coral taxa currently recognised (Cairns, 2007). The meaning of the term "coral" is somewhat ambiguous (Cairns, 2007), but it may be defined as a polyphyletic grouping of cnidarian animals – both anthozoan and hydrozoan - which either produce calcium carbonate secretions or have a proteinaceous axis (Cairns, 2007). The phylogenetic relationships between stylasterids and other common azooxanthellate coral groups referred to in this thesis (specifically, the Scleractinia and bamboo corals (part of the Octocorallia)) are summarised in Figure 2.

Phylum	Class	Subclass	Order	Family
			Scleractinia	
		Hexacorallia	Zoanthidea	
			Antipatharia	
	Anthozoa	Octocorallia		
Cnidaria	Hydrozoa	Hydroidolina	Anthoathecata	**Stylasteridae**
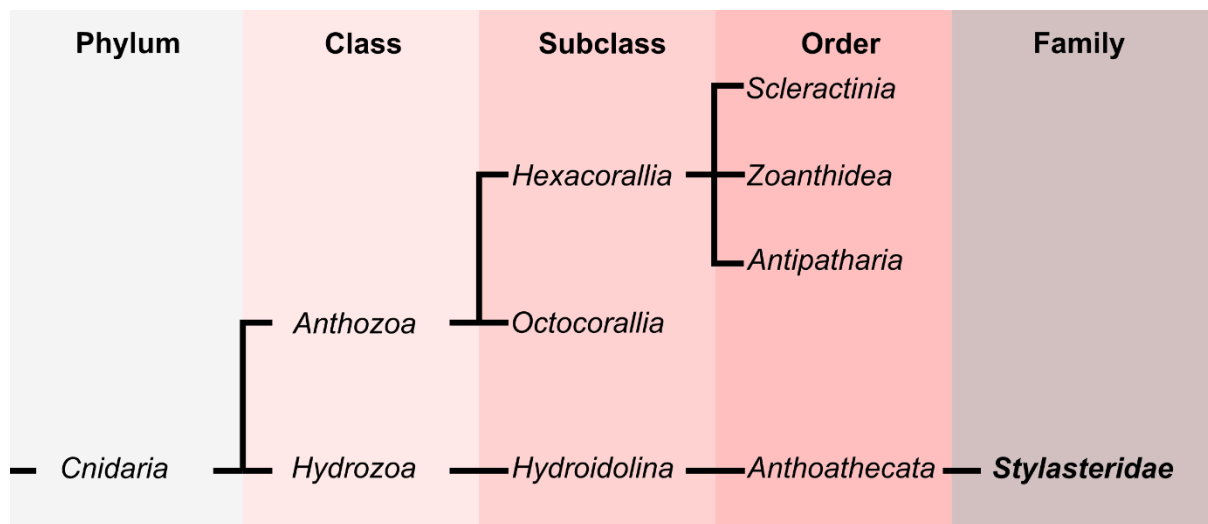
Figure 2. Simplified cnidarian phylogeny, showing the relationship of the stylasterids to the Scleractinia and Octocorallia (including the bamboo corals). Figure follows relationships in Cairns (2007).

Consisting at last count of 247 living species and 21 species known exclusively from the fossil record, the stylasterids are a family of entirely azooxanthellate, hydrozoan coral (Cairns, 2011). Their azooxanthellate nature means their occurrence is not limited by the availability of light, and stylasterids have been found across a wide range of water depths (0 – 2789 m in Cairns, 2011). More generally, stylasterids are globally

distributed in the modern ocean (Cairns, 2011; Figure 3). Their widespread distribution is reflected in the range of samples analysed in this thesis, which includes those collected from the shallow waters of the Great Barrier Reef, to those from the depths of the Southern and north Pacific oceans (Figure 3).
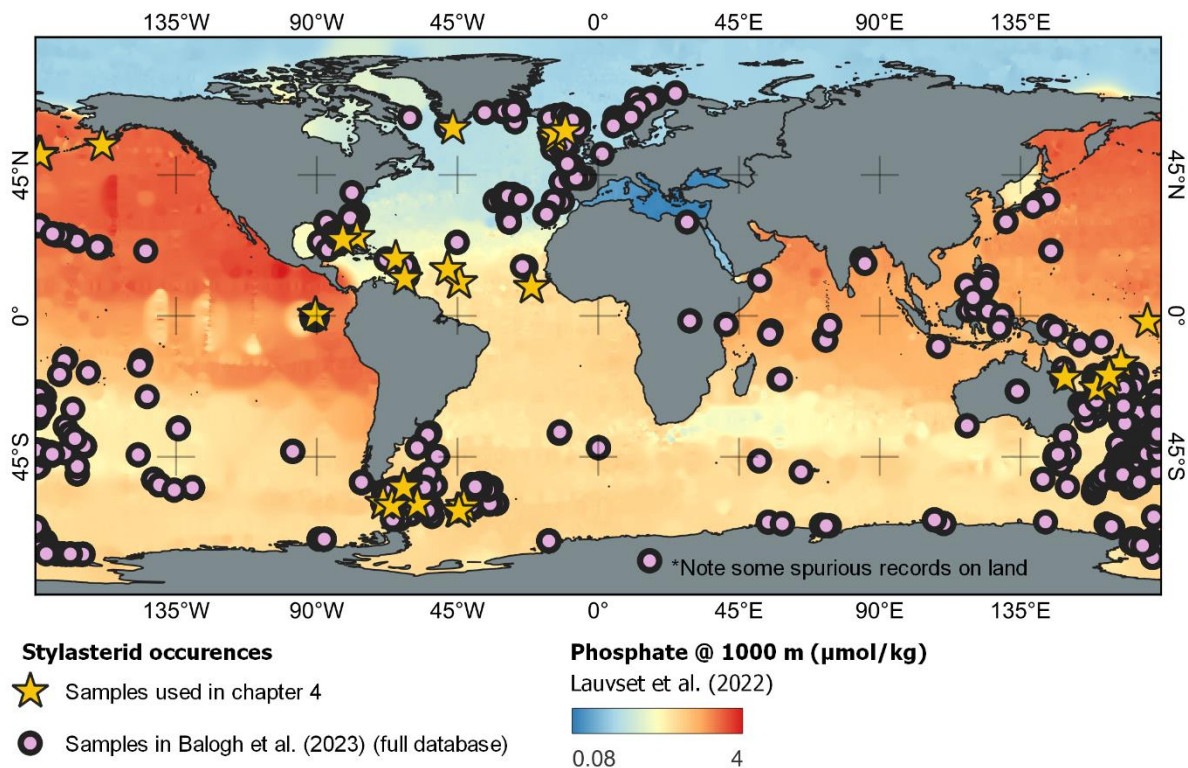
Figure 3. Distribution of stylasterid corals in the database compiled by Balogh et al. (2023), overlain on dissolved phosphate concentration at 1000 m depth from the GLODAP bottle database (Lauvset et al., 2022). Also shown are samples used in chapter 4 of this thesis (includes samples in Stewart et al., 2022), which show that stylasterids are found in a wider range of locations (e.g. in the north Pacific). Note the full database in Balogh et al. (2023) is used, rather than the pruned database, which results in some spurious records (e.g. those on land; see Balogh et al. (2023) for details). All samples in chapter 3 of this thesis are included in chapter 4, while samples in chapter 5 of this thesis are from sites close to those in chapter 4. The distribution of chapter 4 samples therefore represents the geographic range covered by samples measured in this thesis.

The vast majority of stylasterid species form hard, continuous, carbonate skeletons, which confers upon them a wider importance to marine ecosystems. Stylasterids are recognised as a foundational taxon, whose skeletal structures provide valuable habitats for fish and marine invertebrates (e.g. Hoarau et al., 2021). They therefore form a crucial component of shallow and deep-marine ecosystems (e.g. Bax and Cairns, 2014).

The gross morphology of the stylasterid skeleton formed the basis for initial attempts to constrain the phylogenetic relationships between stylasterid species (Cairns, 1984; Cairns, 1987). More recently, molecular analyses have been applied to this pursuit (e.g. Lindner et al., 2008; Lindner et al., 2014; Puce et al., 2016; Maggioni et al., 2022). Gross skeletal morphology remains a primary tool for stylasterid

identification (e.g. Cairns, 1991), and stylasterids exhibit a wide range skeletal forms (e.g. Figure 4). Skeletal elements are often related to the 3 types of stylasterid polyp: the gastrozooids, dactylozooids and gonophores. These are responsible for defence, obtaining food and reproduction, respectively (see glossary in Cairns, 2011). Gastrozooids and dactylozooids are associated with surface pores termed gastropores and dactylopores, respectively, while gonophores are housed within skeletal elements termed ampullae (Figure 4; Cairns, 2011). Further, these skeletal elements may be spatially coordinated. For example, some stylasterid taxa display cyclosystems - rings of dactylopores surrounding a central gastropore – which are a key element whose characteristics (e.g. number of dactylopores, presence of lids, irregular gaps between dactylopores (termed diastemas)) can be used in stylasterid identification (Figure 4; e.g. Cairns, 1991).

The small number of taxonomic experts and reliance on skeletal morphology means that the accurate identification of stylasterid specimens is challenging (see chapter 2, supplementary information). More broadly, the uncertainties associated with stylasterid identification are echoed in our wider understanding of this coral taxon. For example, while some published studies have addressed the stable oxygen and carbon isotopic composition of stylasterid skeletons (Weber and Woodhead, 1972; Wisshak et al., 2009; Black and Andrus, 2012; Samperiz et al., 2020; Stewart et al., 2020), only two studies have explored the concentration and/or isotopic composition of trace elements in stylasterid coral skeletons (Stewart et al., 2020; Stewart et al., 2022). Similarly, our current understanding of stylasterid skeletal growth rates is also derived from a small number of published datasets (Chong and Stratford, 2002; Miller et al., 2004; Wisshak et al., 2009; King et al., 2018).

This uncertainty motivates the work documented in this thesis, in which I address the paucity of stylasterid inorganic geochemical data, targeting two main objectives. The first and primary focus of this work is developing the use of stylasterids as palaeoceanographic archives. However, the geochemical data generated in this pursuit can also provide insights into stylasterid biomineralisation mechanisms and growth rates, with implications for their resilience. Each of these objectives is introduced in the following sections.
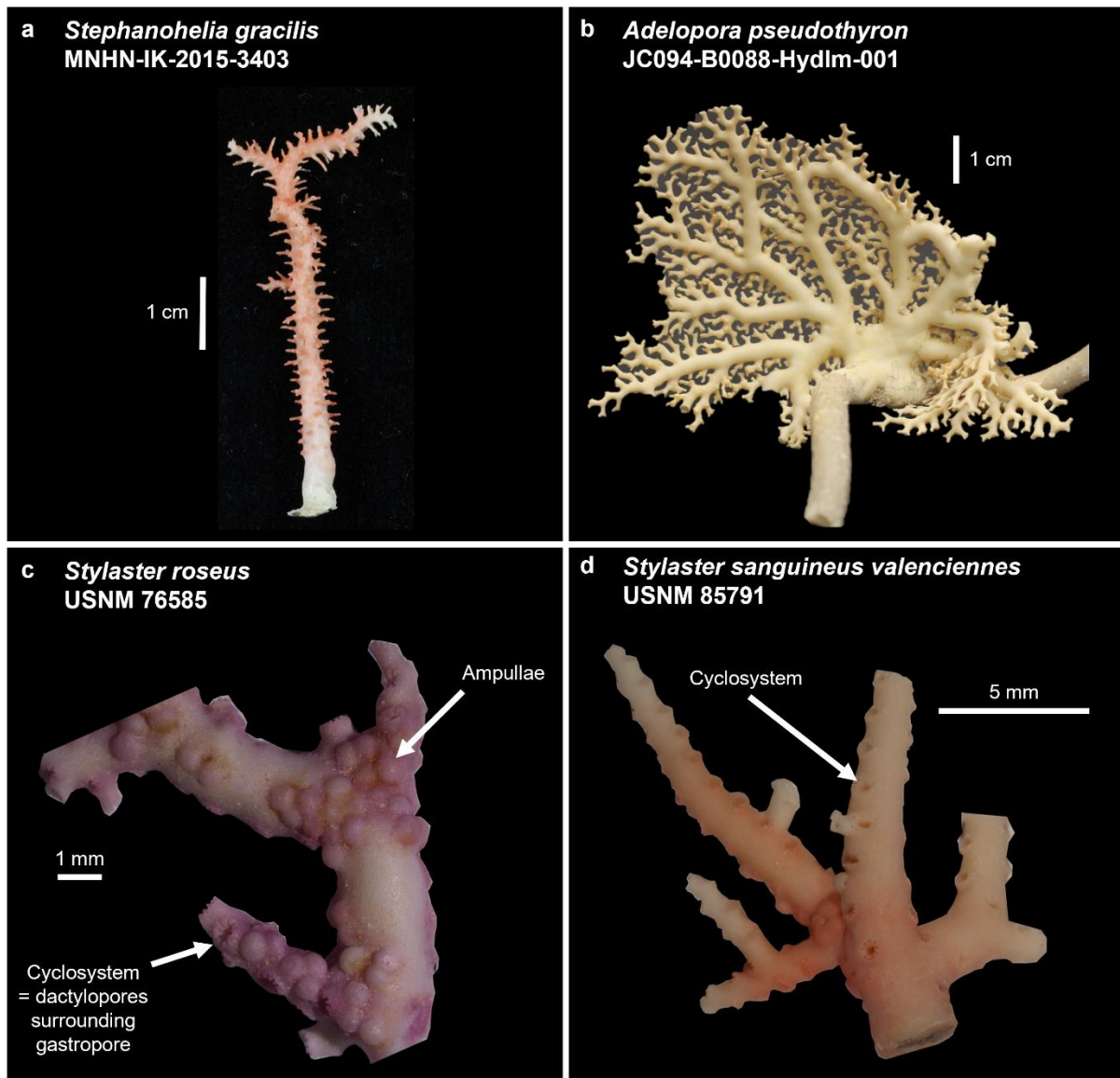
Figure 4. Examples of stylasterid specimens used in this study. Key skeletal features discussed in the text (section 2) are labelled in panels c and d. Samples in panels a, c and d were identified by taxonomic experts, sample in panel b identified by J. Kershaw.

3. Stylasterids in palaeoceanography

Firstly, this thesis addresses two of the aspects of proxy development alluded to in section 1.2: a) determining the function linking measurable quantities (i.e. aspects of stylasterid coral geochemistry) to ocean conditions (chapters 3 and 4) and b) determining the age and/or growth chronologies of preserved stylasterid coral skeletons (chapter 5). Previous work developing stylasterids as palaeoceanographic archives is limited at the time of writing to 5 published papers (Wisshak et al., 2009; King et al., 2018; Samperiz et al., 2020; Stewart et al., 2020; Stewart et al., 2022), and significantly more work has been carried out on anthozoan azooxanthellate coral taxa. Summarising the use of anthozoan coral taxa in palaeoceanography provides a valuable baseline against which hydrozoan stylasterid corals can be compared.

3.1 Anthozoan corals as palaeoceanographic archives

3.1.1 Calibrating coral geochemistry to modern conditions

Fundamental to the development of anthozoan coral groups as palaeoceanographic archives has been calibrating their skeletal geochemistry to modern ocean conditions (i.e. the development of equation 1). Various aspects of scleractinian and bamboo coral skeletal geochemistry have been shown to covary with a range of ocean conditions (Robinson et al., 2014). For example, scleractinian skeletal Li/Mg records seawater temperature (e.g. Case et al., 2010; Raddatz et al., 2013; Montagna et al., 2014; Cuny-Guirriec et al., 2019; Stewart et al., 2020; Figure 5), while the radiocarbon content of scleractinian and bamboo coral skeletons records that of seawater, and may thus be applied as a record of changes in ocean ventilation (e.g. Adkins et al., 1998; Frank et al., 2004; Farmer et al., 2015b; Chen et al., 2020; Chen et al., 2023; Beisel et al., 2023).

In this thesis, I focus on two further proxy systems which have been successfully applied to anthozoan coral skeletons to constrain past variations in ocean carbon storage, circulation and primary productivity. These are the concentration of barium and isotopic composition of boron in coral skeletons. While the details of these proxies are presented in the introductions to their respective chapters (3 and 4), it is worth introducing them briefly here.

Firstly, the dissolved concentration of barium in seawater (herein, $[Ba]_{SW}$) is the subject of chapter 3. $[Ba]_{SW}$ is controlled by several climatically relevant processes. The formation of barite (barium sulphate) associated with aggregated organic matter removes dissolved Ba from the shallow ocean (e.g. Dehairs et al., 1980), resulting in a link between $[Ba]_{SW}$ at shallow depths and regional primary productivity (e.g. Horner et al., 2015; Bates et al., 2017). In turn, these shallow waters sink in high-latitude regions to form the major deep-water masses which fill the interior ocean basins (Figure 1). Deep ocean $[Ba]_{SW}$ is thus in part controlled by conservative mixing of these water masses (Horner et al., 2015; Bates et al., 2017). Previous work has shown that the Ba/Ca ratio of azooxanthellate scleractinian and bamboo coral skeletons is linearly related to $[Ba]_{SW}$ (e.g. Anagnostou et al., 2011; LaVigne et al., 2011; Hemsing et al., 2018; Spooner et al., 2018; Figure 5). This proxy has in turn been applied to the reconstruction of past changes in $[Ba]_{SW}$. For example, azooxanthellate scleractinian Ba/Ca ratios have recently been used to link changes in ocean circulation and productivity across the last deglaciation to coeval changes in Earth climate (Stewart et al., 2021).

Secondly, chapter 4 of this thesis focuses on reconstructing changes in subsurface ocean pH, which is a fundamental target of palaeoceanographic studies. On recent (decadal to centennial) timescales, reconstructing ocean pH allows us to extend the record of anthropogenically-induced ocean acidification, while on longer (i.e. millennial) timescales, ocean pH is dominantly a function of climatically-relevant parameters including biological productivity, carbon remineralisation, ocean circulation patterns and ocean-atmosphere gas exchange (e.g. Feely et al., 2004; Lauvset et al., 2020). The most commonly applied carbonate proxy for ocean pH is the boron isotopic composition ($\delta^{11}B$) of marine biogenic carbonates

(e.g. Hemming and Hanson, 1992; review in Foster and Rae, 2016). A full description of the δ11B-pH proxy is given in chapter 4. Here, it is sufficient to note that azooxanthellate bamboo and scleractinian coral skeletal δ11B is related to the δ11B of borate anion in seawater (δ11B$_{borate}$), which in turn depends on subsurface ocean pH (e.g. Anagnostou et al., 2012; McCulloch et al., 2012; Farmer et al., 2015a; Figure 5). Previous work has used these relationships to infer, for example, changes in ocean carbon storage and/or circulation across the last 20,000 years of Earth history (e.g. Rae et al., 2018; Stewart et al., 2021).
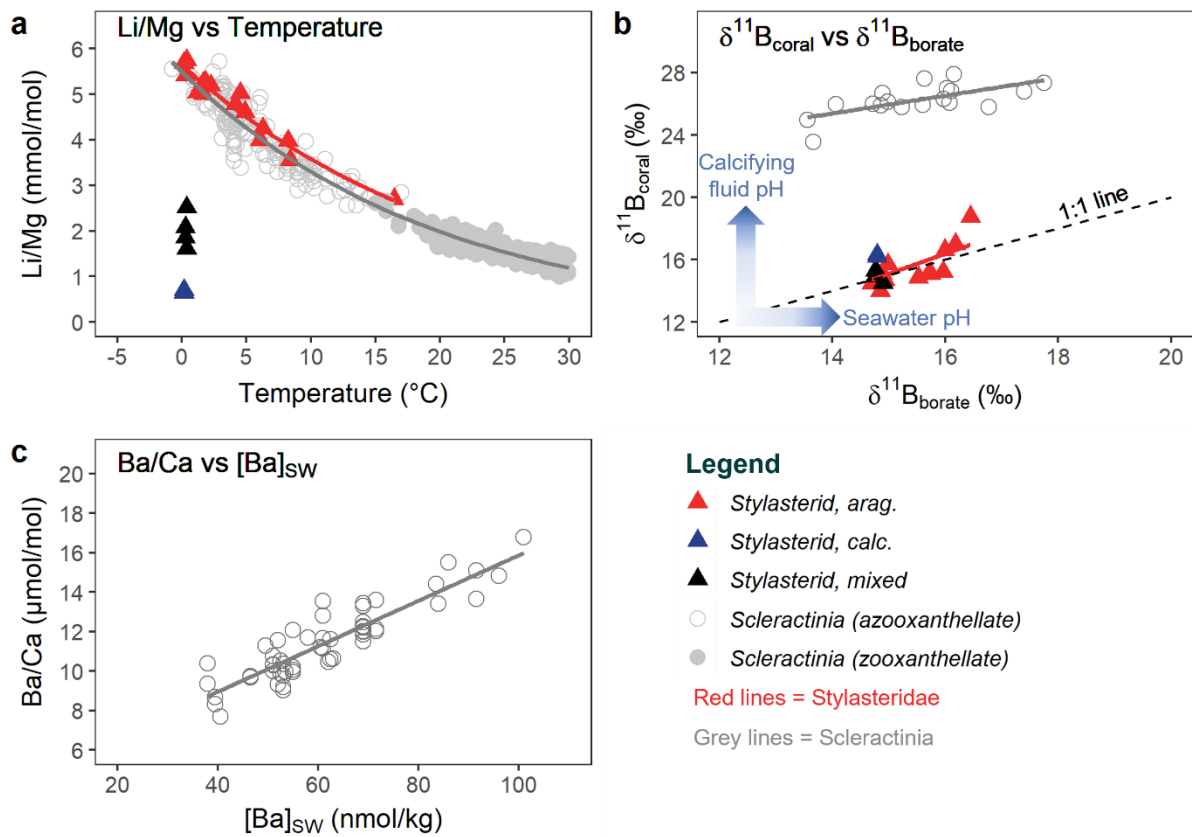
Figure 5. Previously published calibrations between stylasterid and scleractinian coral geochemistry and seawater temperature (a; Stewart et al., 2020), δ11B$_{borate}$ (b; Anagnostou et al., 2012; McCulloch et al., 2012; Stewart et al., 2016; Rae et al., 2018) and [Ba]$_{SW}$ (c; Spooner et al., 2018). Illustrative least squares regression lines shown for Scleractinia (solid grey) and aragonitic stylasterids (red). In panel b, black dashed line represents the 1:1 δ11B$_{borate}$:δ11B$_{coral}$ line, while arrows show theoretical direction of increasing seawater (x-axis) and coral calcifying fluid (y-axis) pH.

3.1.2 Radiometric dating anthozoan coral skeletons

A key advantage of using anthozoan azooxanthellate corals as palaeoceanographic archives is our ability to absolutely date their skeletons with a high degree of accuracy and precision. Such temporal constraint is vital to the application of the calibrations discussed in section 3.1.1, and has generally relied on radiometric techniques which take advantage of the U-series, radiocarbon and/or ^{210}Pb decay series. In chapter 5 of this thesis, I focus on dating stylasterid coral skeletons by U-series and radiocarbon techniques, the details of which are outlined at the start of that chapter. Importantly, azooxanthellate

scleractinian corals have high skeletal uranium concentrations and low initial skeletal Th concentrations, making them ideally suited to dating by U-series methods. These methods can provide high-precision ages on individual corals, which in turn can be combined to generate longer-term, centennial to millennial scale oceanographic records (e.g. Cheng et al., 2000; Robinson et al., 2014; Chen et al., 2015; Rae et al., 2018). For high-Mg calcitic bamboo corals, their lower skeletal U concentration means that U-series dating techniques are potentially unsuitable (Sinclair et al., 2011). Instead, growth chronologies can be constructed for individual corals using radiocarbon or ^{210}Pb dating, with the timescale of coral growth meaning individual specimens have the potential to provide palaeoceanographic constraint on centennial timescales (e.g. Andrews et al., 2009; Hill et al., 2011; Farmer et al., 2015b; Liu et al., 2023).

3.1.3 Caveats and constraints

Anthozoan corals have been widely applied in palaeoceanographic studies, with often multi-proxy approaches used to constrain the coevolution of Earth's ocean and climate over centennial to millennial timescales (e.g. Rae et al., 2018; Chen et al., 2020; Thresher and Fallon, 2021; Stewart et al., 2021; Chen et al., 2023). Despite this, no proxy archive is without limitations, and azooxanthellate corals are no different. Most importantly, there is significant evidence to suggest that the geochemical composition of both bamboo and scleractinian coral skeletons is influenced by their biomineralisation process (e.g. Gaetani and Cohen, 2006; Sinclair et al., 2006; Gagnon et al., 2007; Robinson et al., 2014; Farmer et al., 2015a; Stewart et al., 2016; Flöter et al., 2019). These effects have been conceptualised under the umbrella term "vital effects" and can be used to provide valuable constraint on coral calcification mechanisms, as discussed in more detail in section 4.1.

Here, it is sufficient to note that these effects can obscure the relationships between coral skeletal geochemistry and environmental conditions, potentially complicating the application and interpretation of anthozoan coral palaeoceanographic proxies. As an example, while both azooxanthellate scleractinian and bamboo coral δ^{11}B have been proposed (and used) as an archive of seawater pH, both coral taxa exhibit δ^{11}B values which deviate from equilibrium with the borate anion in seawater. Scleractinian coral δ^{11}B, for instance, is significantly heavier (i.e. enriched in ^{11}B) than would be expected if these corals derived their boron isotopic signature directly from unmodified seawater (Anagnostou et al., 2012; McCulloch et al., 2012; Figure 5), while bamboo corals exhibit more subtle elevations in δ^{11}B at lower ambient seawater pH (Farmer et al., 2015a). In both coral taxa, these elevations have been proposed as the signature of pH upregulation during the coral calcification process (see section 4.1; Figure 5). While the empirical δ^{11}B-pH calibrations proposed for each taxon are robust, the signature of pH upregulation can complicate interpretation of changes in ocean pH through time. For example, the azooxanthellate scleractinian coral δ^{11}B-pH relationship varies between genera, thus requiring application of genus-specific normalisations (e.g. McCulloch et al., 2012; Stewart et al., 2021), while scleractinian coral δ^{11}B can also vary significantly within the skeleton of individual corals themselves, requiring careful consideration of sampling techniques (e.g. Stewart et al., 2016).

Consideration of the caveats associated with using anthozoan coral groups as palaeoceanographic archives is a primary motivation for the work carried out in this thesis. In the following section, I introduce recent work which has demonstrated that various aspects of stylasterid coral geochemistry are impacted to a lesser degree by calcification-related processes, and thus that this coral taxon may more faithfully record true variations in palaeoenvironmental conditions.

3.2   Stylasterids in palaeoceanography: this thesis

Although anthozoan corals have been widely developed as palaeoceanographic archives, as outlined in detail above, very few studies have addressed the palaeoceanographic utility of the stylasterids. This is somewhat surprising, given their abundance in oceanographically important regions such as the Southern and Pacific Oceans (e.g. Cairns, 1992). Despite this, the small amount of work which has been carried out hints at the great promise of stylasterids as archives of past ocean conditions.

Stylasterid skeletal Li/Mg and stable oxygen isotope ratios, firstly, correlate strongly with seawater temperature, and both show less evidence for the influence of complicating vital effects than in azooxanthellate scleractinian corals (Samperiz et al., 2020; Stewart et al., 2020). Preliminary work has also raised the possibility that stylasterid $\delta^{11}B$ could be a novel and advantageous archive of past ocean pH (Stewart et al., 2022). Although yet to be calibrated across a wide range of ocean conditions, an initial dataset has revealed that, unlike scleractinian corals, stylasterid $\delta^{11}B$ is not impacted by the signature of pH upregulation (Stewart et al., 2022; Figure 5; see discussion in section 4.2). Further, the radiocarbon content of stylasterid skeletons records ambient seawater $\Delta^{14}C$, and may be used to reconstruct changes in ocean circulation and ventilation (King et al., 2018). This work also demonstrated that stylasterid skeletons grow on centennial timescales, raising the possibility that large, live-collected specimens could provide high-resolution archives of recent (i.e. last 200 year) variations in ocean conditions (King et al., 2018). Thus, while the development of stylasterid geochemistry in palaeoceanography is still ongoing, early indications are positive and suggest that this group of coral has potential in this regard.

In this thesis, I build on this initial work, focusing on three key outstanding questions, which are summarised in Table 1.

Firstly, various aspects of stylasterid geochemistry remain entirely unstudied. In particular, the success of anthozoan coral Ba/Ca as an archive of past $[Ba]_{SW}$ (and thus ocean circulation and primary productivity; see section 3.1.1) provides strong motivation for the exploration of this proxy in the stylasterids. Chapter 3 is thus devoted to the development of a novel stylasterid Ba/Ca vs $[Ba]_{SW}$ proxy.

Secondly, the tantalising prospect that stylasterid $\delta^{11}B$ could represent a reliable pH proxy minimally affected by the influence of pH upregulation (Stewart et al., 2022) motivates the exploration of stylasterid $\delta^{11}B$ across a wider range of pH. This work is the focus of chapter 4.

Finally, the application of promising stylasterid geochemical proxies requires developing tools for chronological constraint. Thus far, no work has addressed the application of U-series techniques to stylasterids. This evidence gap is addressed in chapter 5, along with further development of radiocarbon-based growth chronologies for larger stylasterid specimens, building on previous work (King et al., 2018).

Chapter	Measurement	Palaeoceanographic use	Previous stylasterid publication(s)	Knowledge gaps	This thesis
3	Ba/Ca	Proxy for $[Ba]_{SW}$	None	No existing stylasterid data	Relationship between stylasterid Ba/Ca and $[Ba]_{SW}$
4	$\delta^{11}B$	Proxy for seawater pH	Stewart et al., 2022	Calibrated over small pH range	Extends calibration across wider pH range
5	U-series	Dating	None	No existing stylasterid data	First application of U-series techniques to stylasterids
5	$\Delta^{14}C$	Dating and proxy for seawater $\Delta^{14}C$	King et al., 2018	Data limited to small number of specimens in the Southern Ocean	^{14}C growth chronologies from Pacific and Atlantic stylasterid specimens. Application of developed proxies to those growth chronologies

Table 1. Summary of the palaeoceanographic topics addressed in this thesis.

4. Stylasterid coral biomineralisation

Although not the focus of this thesis, as alluded to in section 3.1.3, the inorganic geochemistry of coral skeletons can also inform on coral biomineralisation mechanisms and thus their resilience in a changing ocean. Again, most previous work in this regard has focused on anthozoan coral taxa, and in particular the Scleractinia. This taxon thus provides a natural comparison against which to assess stylasterid coral biomineralisation.

4.1 Geochemical signatures of azooxanthellate scleractinian coral biomineralisation

It is widely accepted that scleractinian corals calcify from a seawater-derived, (partially) isolated calcifying fluid, and that they modify the composition of this fluid via the Ca-ATPase pump to increase pH and therefore promote carbonate formation (e.g. Al-Horani et al., 2003). As alluded to in section 3.1.1, the

signature of pH upregulation is recorded in the $\delta^{11}B$ of azooxanthellate scleractinian skeletons (Anagnostou et al., 2012; McCulloch et al., 2012; Figure 5).

The geochemical variability found in the skeletons of individual azooxanthellate scleractinian corals has also been used to constrain their calcification process. For instance, substantial variations in scleractinian skeletal $\delta^{11}B$ and element/Ca ratios (e.g. Mg/Ca, Sr/Ca, U/Ca and Ba/Ca) have been attributed to variations in factors including (but not limited to) pH upregulation, growth rates, and degrees of calcifying fluid isolation (e.g. Gaetani and Cohen, 2006; Sinclair et al., 2006; Blamart et al., 2007; Gagnon et al., 2007; Stewart et al., 2016; Jurikova et al., 2019; Fietzke and Wall, 2022).

The ability to isolate their calcifying fluid from external seawater and upregulate its pH may in turn explain how azooxanthellate scleractinian corals can exist in waters undersaturated with respect to aragonite (e.g. McCulloch et al., 2012; Bostock et al., 2015; Wall et al., 2015), and is often cited as a form of resilience to ocean acidification (e.g. McCulloch et al., 2012). However, other authors have highlighted the increasing energetic burden associated with pH upregulation in an acidifying ocean (e.g. Gagnon et al., 2021).

The skeletal inorganic geochemistry of scleractinian corals has thus provided valuable insights into their calcification mechanism, with implications for their resilience in an acidifying, warming and deoxygenating ocean. It follows that equivalent measurements on stylasterid corals have the potential to provide similar insights.

4.2   Stylasterid coral biomineralisation: this thesis

The limited available inorganic geochemical evidence has already provided important and intriguing evidence regarding stylasterid calcification. Importantly, despite also building carbonate skeletons, it seems that stylasterids employ a markedly different mode of calcification to azooxanthellate scleractinian corals.

Firstly, stylasterids can build their skeletons from either dominantly aragonite, dominantly high-Mg calcite, or a mixture of both polymorphs (Cairns and Macintyre, 1992; Samperiz et al., 2020). This is in direct contrast to other coral groups: scleractinian corals, for instance, are almost all entirely aragonitic, with only one recorded instance of a species showing evidence for the use of both aragonite and high-Mg calcite (*Paraconotrochus antarcticus*; Stolarski et al., 2021). In addition to suggesting fundamental differences between the calcification strategies of these two coral groups, variability in stylasterid mineralogy has potentially important implications for their vulnerability to ocean acidification. The proportion of Mg in stylasterid high-Mg calcite (Mg/Ca ~ 80 mmol/mol; Stewart et al., 2020) is relatively low compared with other biogenic high-Mg calcites (e.g. coralline algae, Mg/Ca ~ 100 to 180 mmol/mol; Hetzinger et al., 2009). At these concentrations of Mg, high-Mg calcite has an equivalent or slightly lower solubility than aragonite (Ries, 2011). Stylasterid taxa which build their skeletons from high-Mg calcite may therefore be more resilient to ocean acidification than those which use dominantly aragonite.

Secondly, stylasterid inorganic geochemical signatures also suggest strong differences in biomineralisation to scleractinian corals. Stylasterid oxygen and carbon stable isotopic ratios ($\delta^{18}O$ and $\delta^{13}C$) are closer to equilibrium with seawater than the same ratios in scleractinian corals (Samperiz et al., 2020). It has also been shown that bulk stylasterid $\delta^{11}B$ values are in equilibrium with $\delta^{11}B_{borate}$ (Stewart et al., 2022; Figure 5). Taken together, this stable isotopic evidence suggests that stylasterids employ far less pH upregulation than scleractinian corals (Stewart et al., 2022).

In turn, this raises fundamental questions regarding how stylasterids build their skeletons, given they have been reported from waters undersaturated with respect to aragonite (e.g. Auscavitch et al., 2020; Stewart et al., 2022). Additional controls on the boron isotopic composition of coral carbonate could decouple stylasterid calcifying fluid pH from their skeletal $\delta^{11}B$, meaning some degree of pH upregulation cannot be discounted (Gagnon et al., 2021; Stewart et al., 2022). Alternatively, a number of studies have provided evidence for the direct involvement of organic molecules in coral calcification (e.g. Cuif and Dauphin, 2005; Tambutté et al., 2007; Drake et al., 2013; Mass et al., 2013; Von Euw et al., 2017; see reviews in Tambutté et al., 2011; Falini et al., 2015). In some cases, these studies have suggested that the presence of these organic molecules alone is sufficient to begin the process of calcification (e.g. Von Euw et al., 2017). It is thus possible that stylasterids employ a more organically-mediated calcification strategy, with a reduced reliance on pH upregulation (Stewart et al., 2022).

The mechanism by which stylasterids build their skeletons is important to predicting their future resilience in a changing ocean. An inability to upregulate calcifying fluid pH may make stylasterids less resilient to ocean acidification (e.g. following McCulloch et al., 2012). Alternatively, it is possible that, by not relying on pH upregulation and instead employing an organically-mediated calcification strategy, stylasterid calcification has a lower energetic burden, which may in fact increase their resilience (e.g. Von Euw et al., 2017; Stewart et al., 2022).

Overall, a number of questions regarding the stylasterid calcification mechanism remain unanswered, and their resilience in a changing ocean is uncertain (Stewart et al., 2022). The inorganic geochemical data presented here can begin to provide insight into these questions. In particular, to develop stylasterid $\delta^{11}B$ as an archive of seawater pH (chapter 4), I analyse a number of stylasterid individuals from particularly acidic, low pH waters, which represent an ideal opportunity to study stylasterid calcification in a particularly extreme environment. Where possible, this thesis therefore includes discussion of stylasterid biomineralisation. Specific themes addressed include the comparison of stylasterid and scleractinian inorganic geochemistry (chapters 3 and 4), the interpretation of stylasterid skeletal $\delta^{11}B$ across a wide range of environments (chapter 4), and the construction of radiocarbon-based growth chronologies (chapter 5). The latter permits discussion of the timescales of ecosystem recovery, following disturbances by activities such as bottom trawling.

5.   Thesis structure

In summary, this thesis addresses key gaps in our current understanding of the inorganic geochemistry of stylasterid coral skeletons, to explore the palaeoceanographic potential of these corals and assess their resilience to future changes in ocean conditions. The thesis is structured in 5 main chapters:

Chapter 2 outlines the analytical methods employed in this thesis. Many of these methods are shared between chapters, and are therefore addressed in detail here. Other, chapter-specific aspects of the methodology are summarised in each chapter separately.

Chapter 3 develops stylasterid Ba/Ca as an archive of past $[Ba]_{SW}$, as well as providing comparative discussion of stylasterid and scleractinian coral geochemistry, and the possible biomineralisation-related origins of those differences.

Chapter 4 develops a stylasterid $\delta^{11}B$ vs pH proxy, and provides additional constraint on their biomineralisation mechanism. In particular, this chapter focuses on analyses of stylasterids from a wide range of ocean conditions, permitting a comprehensive assessment of their calcification process.

Chapter 5 explores the radiometric dating of stylasterid coral skeletons, including both U-series and radiocarbon-based approaches. In addition to applying the proxies developed by previous work and in chapters 3 and 4 of this thesis, this chapter also provides novel constraint on the growth rates of stylasterid skeletons.

Chapter 6 provides a summary of the main conclusions of this thesis, as well as perspectives on future work.

6. References

Adkins, J.F., Cheng, H., Boyle, E.A., Druffel, E.R.M., Edwards, R.L., 1998. Deep-Sea Coral Evidence for Rapid Change in Ventilation of the Deep North Atlantic 15,400 Years Ago. Science 280, 725–728. https://doi.org/10.1126/science.280.5364.725

Al-Horani, F.A., Al-Moghrabi, S.M., de Beer, D., 2003. Microsensor study of photosynthesis and calcification in the scleractinian coral, *Galaxea fascicularis*: active internal carbon cycle. Journal of Experimental Marine Biology and Ecology 288, 1–15. https://doi.org/10.1016/S0022-0981(02)00578-6

Anagnostou, E., Huang, K.-F., You, C.-F., Sikes, E.L., Sherrell, R.M., 2012. Evaluation of boron isotope ratio as a pH proxy in the deep sea coral *Desmophyllum dianthus*: Evidence of physiological pH adjustment. Earth and Planetary Science Letters 349–350, 251–260. https://doi.org/10.1016/j.epsl.2012.07.006

Anagnostou, E., Sherrell, R.M., Gagnon, A., LaVigne, M., Field, M.P., McDonough, W.F., 2011. Seawater nutrient and carbonate ion concentrations recorded as P/Ca, Ba/Ca, and U/Ca in the deep-sea coral *Desmophyllum dianthus*. Geochimica et Cosmochimica Acta 75, 2529–2543. https://doi.org/10.1016/j.gca.2011.02.019

Anderson, R.F., Ali, S., Bradtmiller, L.I., Nielsen, S.H.H., Fleisher, M.Q., Anderson, B.E., Burckle, L.H., 2009. Wind-Driven Upwelling in the Southern Ocean and the Deglacial Rise in Atmospheric CO_2. Science 323, 1443–1448. https://doi.org/10.1126/science.1167441

Andrews, A.H., Stone, R.P., Lundstrom, C.C., DeVogelaere, A.P., 2009. Growth rate and age determination of bamboo corals from the northeastern Pacific Ocean using refined ^{210}Pb dating. Mar. Ecol. Prog. Ser. 397, 173–185. https://doi.org/10.3354/meps08193

Auscavitch, S.R., Lunden, J.J., Barkman, A., Quattrini, A.M., Demopoulos, A.W.J., Cordes, E.E., 2020. Distribution of deep-water scleractinian and stylasterid corals across abiotic environmental gradients on three seamounts in the Anegada Passage. PeerJ 8, e9523. https://doi.org/10.7717/peerj.9523

Balogh, V., Fragkopoulou, E., Serrão, E.A., Assis, J., 2023. A dataset of cold-water coral distribution records. Data in Brief 48, 109223. https://doi.org/10.1016/j.dib.2023.109223

Bates, S.L., Hendry, K.R., Pryer, H.V., Kinsley, C.W., Pyle, K.M., Woodward, E.M.S., Horner, T.J., 2017. Barium isotopes reveal role of ocean circulation on barium cycling in the Atlantic. Geochimica et Cosmochimica Acta 204, 286–299. https://doi.org/10.1016/j.gca.2017.01.043

Bax, N.N., and Cairns, S.D., 2014. Stylasteridae (Cnidaria; Hydrozoa), in: Biogeographic Atlas of the Southern Ocean, eds C. de Broyer, P. K. Koubbi, H. J. Griffiths, B. Raymond, C. d'Udekem d'Acoz, A. Van de Putte, et al. (Cambridge: Scientific Committee on Antarctic Research), 107–212.

Beisel, E., Frank, N., Robinson, L.F., Lausecker, M., Friedrich, R., Therre, S., Schröder-Ritzrau, A., Butzin, M., 2023. Climate Induced Thermocline Aging and Ventilation in the Eastern Atlantic Over the

Last 32,000 Years. Paleoceanog and Paleoclimatol 38, e2023PA004662.
https://doi.org/10.1029/2023PA004662

Bigg, G.R., Jickells, T.D., Liss, P.S., Osborn, T.J., 2003. The role of the oceans in climate. Int. J. Climatol. 23, 1127–1159. https://doi.org/10.1002/joc.926

Black, H., Andrus, C.F.T., 2012. Taphonomy and Diagenesis on the Deep-Sea Hydrocoral *Stylaster erubescens* Fossils from the Charleston Bump. Univ Alabama McNair J 12, 19–40.

Blamart, D., Rollion-Bard, C., Meibom, A., Cuif, J.-P., Juillet-Leclerc, A., Dauphin, Y., 2007. Correlation of boron isotopic composition with ultrastructure in the deep-sea coral *Lophelia pertusa*: Implications for biomineralization and paleo-pH. Geochem. Geophys. Geosyst. 8, Q12001.
https://doi.org/10.1029/2007GC001686

Bostock, H.C., Tracey, D.M., Currie, K.I., Dunbar, G.B., Handler, M.R., Mikaloff Fletcher, S.E., Smith, A.M., Williams, M.J.M., 2015. The carbonate mineralogy and distribution of habitat-forming deep-sea corals in the southwest pacific region. Deep Sea Research Part I: Oceanographic Research Papers 100, 88–104. https://doi.org/10.1016/j.dsr.2015.02.008

Broecker, W.S., 1991. The great ocean conveyor. Oceanography 4, 79–89.

Caesar, L., McCarthy, G.D., Thornalley, D.J.R., Cahill, N., Rahmstorf, S., 2021. Current Atlantic Meridional Overturning Circulation weakest in last millennium. Nat. Geosci. 14, 118–120.
https://doi.org/10.1038/s41561-021-00699-z

Caesar, L., Rahmstorf, S., Robinson, A., Feulner, G., Saba, V., 2018. Observed fingerprint of a weakening Atlantic Ocean overturning circulation. Nature 556, 191–196. https://doi.org/10.1038/s41586-018-0006-5

Cairns, S.D., 1984. A generic revision of the Stylasteridae (Coelenterata: Hydrozoa). Part 2. Phylogenetic analysis. Bulletin of Marine Science 35, 38–53.

Cairns, S. D., 1987. Evolutionary trends in the Stylasteridae (Cnidaria, Hydrozoa), in: Modern Trends in the Systematics, Ecology, and Evolution of Hydroids and Hydromedudae, edited by Bouillon, J., 257–274. Clarendon Press: Oxford.

Cairns, S.D., 1991. A generic revision of the Stylasteridae (Coelenterata: Hydrozoa) Part 3 Keys to the genera. Bulletin of Marine Science 49, 538–545.

Cairns, S.D., Macintyre, I.G., 1992. Phylogenetic Implications of Calcium Carbonate Mineralogy in the Stylasteridae (Cnidaria: Hydrozoa). PALAIOS 7, 96. https://doi.org/10.2307/3514799

Cairns, S.D., 1992. Worldwide distribution of the Stylasteridae (Cnidaria: Hydrozoa). Sci. Mar. 56, 125–130.

Cairns, S.D., 2007. Deep-water corals: an overview with special reference to diversity and distribution of deep-water scleractinian corals. Bulletin of Marine Science 81, 311–322.

Cairns, S.D., 2011. Global Diversity of the Stylasteridae (Cnidaria: Hydrozoa: Athecatae). PLoS ONE 6, e21670. https://doi.org/10.1371/journal.pone.0021670

Calvert, S.E., Pedersen, T.F., 2007. Chapter Fourteen Elemental Proxies for Palaeoclimatic and Palaeoceanographic Variability in Marine Sediments: Interpretation and Application, in: Developments in Marine Geology. Elsevier, pp. 567–644. https://doi.org/10.1016/S1572-5480(07)01019-6

Case, D.H., Robinson, L.F., Auro, M.E., Gagnon, A.C., 2010. Environmental and biological controls on Mg and Li in deep-sea scleractinian corals. Earth and Planetary Science Letters 300, 215–225. https://doi.org/10.1016/j.epsl.2010.09.029

Chen, T., Robinson, L.F., Burke, A., Claxton, L., Hain, M.P., Li, T., Rae, J.W.B., Stewart, J., Knowles, T.D.J., Fornari, D.J., Harpp, K.S., 2020. Persistently well-ventilated intermediate-depth ocean through the last deglaciation. Nat. Geosci. 13, 733–738. https://doi.org/10.1038/s41561-020-0638-6

Chen, T., Robinson, L.F., Burke, A., Southon, J., Spooner, P., Morris, P.J., Ng, H.C., 2015. Synchronous centennial abrupt events in the ocean and atmosphere during the last deglaciation. Science 349, 1537–1541. https://doi.org/10.1126/science.aac6159

Chen, T., Robinson, L.F., Li, T., Burke, A., Zhang, X., Stewart, J.A., White, N.J., Knowles, T.D.J., 2023. Radiocarbon evidence for the stability of polar ocean overturning during the Holocene. Nat. Geosci. 16, 631–636. https://doi.org/10.1038/s41561-023-01214-2

Cheng, H., Adkins, J., Edwards, R.L., Boyle, E.A., 2000. U-Th dating of deep-sea corals. Geochimica et Cosmochimica Acta 64, 2401–2416. https://doi.org/10.1016/S0016-7037(99)00422-6

Chong, A.K., Stratford, P., 2002. Underwater digital stereo-observation technique for red hydrocoral study. Photogrammetric Engineering & Remote Sensing 68, 745–751.

Cuif, J.-P., Dauphin, Y., 2005. The two-step mode of growth in the scleractinian coral skeletons from the micrometre to the overall scale. Journal of Structural Biology 150, 319–331. https://doi.org/10.1016/j.jsb.2005.03.004

Cuny-Guirriec, K., Douville, E., Reynaud, S., Allemand, D., Bordier, L., Canesi, M., Mazzoli, C., Taviani, M., Canese, S., McCulloch, M., Trotter, J., Rico-Esenaro, S.D., Sanchez-Cabeza, J.-A., Ruiz-Fernández, A.C., Carricart-Ganivet, J.P., Scott, P.M., Sadekov, A., Montagna, P., 2019. Coral Li/Mg thermometry: Caveats and constraints. Chemical Geology 523, 162–178. https://doi.org/10.1016/j.chemgeo.2019.03.038

Dansgaard, W., Clausen, H.B., Gundestrup, N., Hammer, C.U., Johnsen, S.F., Kristinsdottir, P.M., Reeh, N., 1982. A New Greenland Deep Ice Core. Science 218, 1273–1277. https://doi.org/10.1126/science.218.4579.1273

Davies, A.J., Guinotte, J.M., 2011. Global Habitat Suitability for Framework-Forming Cold-Water Corals. PLoS ONE 6, e18483. https://doi.org/10.1371/journal.pone.0018483

Dehairs, F., Chesselet, R., Jedwab, J., 1980. Discrete suspended particles of barite and the barium cycle in the open ocean. Earth and Planetary Science Letters 49, 528–550. https://doi.org/10.1016/0012-821X(80)90094-1

DeVries, T., 2022. The Ocean Carbon Cycle. Annu. Rev. Environ. Resour. 47, 317–341. https://doi.org/10.1146/annurev-environ-120920-111307

Doney, S.C., Ruckelshaus, M., Emmett Duffy, J., Barry, J.P., Chan, F., English, C.A., Galindo, H.M., Grebmeier, J.M., Hollowed, A.B., Knowlton, N., Polovina, J., Rabalais, N.N., Sydeman, W.J., Talley, L.D., 2012. Climate Change Impacts on Marine Ecosystems. Annu. Rev. Mar. Sci. 4, 11–37. https://doi.org/10.1146/annurev-marine-041911-111611

Drake, J.L., Mass, T., Haramaty, L., Zelzion, E., Bhattacharya, D., Falkowski, P.G., 2013. Proteomic analysis of skeletal organic matrix from the stony coral *Stylophora pistillata*. Proc. Natl. Acad. Sci. U.S.A. 110, 3788–3793. https://doi.org/10.1073/pnas.1301419110

Druffel, E.R.M., 1997. Geochemistry of corals: Proxies of past ocean chemistry, ocean circulation, and climate. Proc. Natl. Acad. Sci. U.S.A. 94, 8354–8361. https://doi.org/10.1073/pnas.94.16.8354

Falini, G., Fermani, S., Goffredo, S., 2015. Coral biomineralization: A focus on intra-skeletal organic matrix and calcification. Seminars in Cell & Developmental Biology 46, 17–26. https://doi.org/10.1016/j.semcdb.2015.09.005

Falkowski, P., Scholes, R.J., Boyle, E., Canadell, J., Canfield, D., Elser, J., Gruber, N., Hibbard, K., Högberg, P., Linder, S., Mackenzie, F.T., Moore Iii, B., Pedersen, T., Rosenthal, Y., Seitzinger, S., Smetacek, V., Steffen, W., 2000. The Global Carbon Cycle: A Test of Our Knowledge of Earth as a System. Science 290, 291–296. https://doi.org/10.1126/science.290.5490.291

Farmer, J.R., Hönisch, B., Robinson, L.F., Hill, T.M., 2015a. Effects of seawater-pH and biomineralization on the boron isotopic composition of deep-sea bamboo corals. Geochimica et Cosmochimica Acta 155, 86–106. https://doi.org/10.1016/j.gca.2015.01.018

Farmer, J.R., Robinson, L.F., Hönisch, B., 2015b. Growth rate determinations from radiocarbon in bamboo corals (genus *Keratoisis*). Deep Sea Research Part I: Oceanographic Research Papers 105, 26–40. https://doi.org/10.1016/j.dsr.2015.08.004

Feely, R.A., Sabine, C.L., Lee, K., Berelson, W., Kleypas, J., Fabry, V.J., Millero, F.J., 2004. Impact of Anthropogenic CO_2 on the $CaCO_3$ System in the Oceans. Science 305, 362–366. https://doi.org/10.1126/science.1097329

Fietzke, J., Wall, M., 2022. Distinct fine-scale variations in calcification control revealed by high-resolution 2D boron laser images in the cold-water coral *Lophelia pertusa*. Sci. Adv. 8, eabj4172. https://doi.org/10.1126/sciadv.abj4172

Flöter, S., Fietzke, J., Gutjahr, M., Farmer, J., Hönisch, B., Nehrke, G., Eisenhauer, A., 2019. The influence of skeletal micro-structures on potential proxy records in a bamboo coral. Geochimica et Cosmochimica Acta 248, 43–60. https://doi.org/10.1016/j.gca.2018.12.027

Foster, G.L., Rae, J.W.B., 2016. Reconstructing Ocean pH with Boron Isotopes in Foraminifera. Annu. Rev. Earth Planet. Sci. 44, 207–237. https://doi.org/10.1146/annurev-earth-060115-012226

Frank, N., Paterne, M., Ayliffe, L., Van Weering, T., Henriet, J.-P., Blamart, D., 2004. Eastern North Atlantic deep-sea corals: tracing upper intermediate water $\Delta^{14}C$ during the Holocene. Earth and Planetary Science Letters 219, 297–309. https://doi.org/10.1016/S0012-821X(03)00721-0

Friedlingstein, P., O'Sullivan, M., Jones, M.W., Andrew, R.M., Gregor, L., Hauck, J., Le Quéré, C., Luijkx, I.T., Olsen, A., Peters, G.P., Peters, W., Pongratz, J., Schwingshackl, C., Sitch, S., Canadell, J.G., Ciais, P., Jackson, R.B., Alin, S.R., Alkama, R., Arneth, A., Arora, V.K., Bates, N.R., Becker, M., Bellouin, N., Bittig, H.C., Bopp, L., Chevallier, F., Chini, L.P., Cronin, M., Evans, W., Falk, S., Feely, R.A., Gasser, T., Gehlen, M., Gkritzalis, T., Gloege, L., Grassi, G., Gruber, N., Gürses, Ö., Harris, I., Hefner, M., Houghton, R.A., Hurtt, G.C., Iida, Y., Ilyina, T., Jain, A.K., Jersild, A., Kadono, K., Kato, E., Kennedy, D., Klein Goldewijk, K., Knauer, J., Korsbakken, J.I., Landschützer, P., Lefèvre, N., Lindsay, K., Liu, J., Liu, Z., Marland, G., Mayot, N., McGrath, M.J., Metzl, N., Monacci, N.M., Munro, D.R., Nakaoka, S.-I., Niwa, Y., O'Brien, K., Ono, T., Palmer, P.I., Pan, N., Pierrot, D., Pocock, K., Poulter, B., Resplandy, L., Robertson, E., Rödenbeck, C., Rodriguez, C., Rosan, T.M., Schwinger, J., Séférian, R., Shutler, J.D., Skjelvan, I., Steinhoff, T., Sun, Q., Sutton, A.J., Sweeney, C., Takao, S., Tanhua, T., Tans, P.P., Tian, X., Tian, H., Tilbrook, B., Tsujino, H., Tubiello, F., Van Der Werf, G.R., Walker, A.P., Wanninkhof, R., Whitehead, C., Willstrand Wranne, A., Wright, R., Yuan, W., Yue, C., Yue, X., Zaehle, S., Zeng, J., Zheng, B., 2022. Global Carbon Budget 2022. Earth Syst. Sci. Data 14, 4811–4900. https://doi.org/10.5194/essd-14-4811-2022

Gaetani, G.A., Cohen, A.L., 2006. Element partitioning during precipitation of aragonite from seawater: A framework for understanding paleoproxies. Geochimica et Cosmochimica Acta 70, 4617–4634. https://doi.org/10.1016/j.gca.2006.07.008

Gagnon, A.C., Adkins, J.F., Fernandez, D.P., Robinson, L.F., 2007. Sr/Ca and Mg/Ca vital effects correlated with skeletal architecture in a scleractinian deep-sea coral and the role of Rayleigh fractionation. Earth and Planetary Science Letters 261, 280–295. https://doi.org/10.1016/j.epsl.2007.07.013

Gagnon, A.C., Gothmann, A.M., Branson, O., Rae, J.W.B., Stewart, J.A., 2021. Controls on boron isotopes in a cold-water coral and the cost of resilience to ocean acidification. Earth and Planetary Science Letters 554, 116662. https://doi.org/10.1016/j.epsl.2020.116662

Ganachaud, A., Wunsch, C., 2000. Improved estimates of global ocean circulation, heat transport and mixing from hydrographic data. Nature 408, 453–457. https://doi.org/10.1038/35044048

Guinotte, J.M., Orr, J., Cairns, S., Freiwald, A., Morgan, L., George, R., 2006. Will human-induced changes in seawater chemistry alter the distribution of deep-sea scleractinian corals? Frontiers in Ecology and the Environment 4, 141–146. https://doi.org/10.1890/1540-9295(2006)004[0141:WHCISC]2.0.CO;2

Hall–Spencer, J., Allain, V., Fosså, J.H., 2002. Trawling damage to Northeast Atlantic ancient coral reefs. Proc. R. Soc. Lond. B 269, 507–511. https://doi.org/10.1098/rspb.2001.1910

Hemming, N.G., Hanson, G.N., 1992. Boron isotopic composition and concentration in modern marine carbonates. Geochimica et Cosmochimica Acta 56, 537–543. https://doi.org/10.1016/0016-7037(92)90151-8

Hemsing, F., Hsieh, Y.-T., Bridgestock, L., Spooner, P.T., Robinson, L.F., Frank, N., Henderson, G.M., 2018. Barium isotopes in cold-water corals. Earth and Planetary Science Letters 491, 183–192. https://doi.org/10.1016/j.epsl.2018.03.040

Henderson, G.M., 2002. New oceanic proxies for paleoclimate. Earth and Planetary Science Letters 203, 1–13. https://doi.org/10.1016/S0012-821X(02)00809-9

Hetzinger, S., Halfar, J., Kronz, A., Steneck, R.S., Adey, W., Lebednik, P.A., Schone, B.R., 2009. HIGH-RESOLUTION MG/CA RATIOS IN A CORALLINE RED ALGA AS A PROXY FOR BERING SEA TEMPERATURE VARIATIONS FROM 1902 TO 1967. PALAIOS 24, 406–412. https://doi.org/10.2110/palo.2008.p08-116r

Hill, T.M., Spero, H.J., Guilderson, T., LaVigne, M., Clague, D., Macalello, S., Jang, N., 2011. Temperature and vital effect controls on bamboo coral (*Isididae*) isotope geochemistry: A test of the "lines method." Geochem. Geophys. Geosyst. 12. https://doi.org/10.1029/2010GC003443

Hoarau, L., Rouzé, H., Boissin, É., Gravier-Bonnet, N., Plantard, P., Loisil, C., Bigot, L., Chabanet, P., Labarrère, P., Penin, L., Adjeroud, M., Mulochau, T., 2021. Unexplored Refugia with High Cover of Scleractinian *Leptoseris* spp. and Hydrocorals *Stylaster flabelliformis* at Lower Mesophotic Depths (75–100 m)

on Lava Flows at Reunion Island (Southwestern Indian Ocean). Diversity 13, 141. https://doi.org/10.3390/d13040141

Horner, T.J., Kinsley, C.W., Nielsen, S.G., 2015. Barium-isotopic fractionation in seawater mediated by barite cycling and oceanic circulation. Earth and Planetary Science Letters 430, 511–522. https://doi.org/10.1016/j.epsl.2015.07.027

Intergovernmental Panel On Climate Change (IPCC), 2001. Climate Change 2001: Synthesis Report. A Contribution of Working Groups I, II, and III to the Third Assessment Report of the Integovernmental Panel on Climate Change [Watson, R.T. and the Core Writing Team (eds.)]. Cambridge University Press, Cambridge, United Kingdom, and New York, NY, USA, 398 pp.

Intergovernmental Panel On Climate Change (IPCC), 2019. The Ocean and Cryosphere in a Changing Climate: Special Report of the Intergovernmental Panel on Climate Change, 1st ed. Cambridge University Press. https://doi.org/10.1017/9781009157964

Jurikova, H., Liebetrau, V., Raddatz, J., Fietzke, J., Trotter, J., Rocholl, A., Krause, S., McCulloch, M., Rüggeberg, A., Eisenhauer, A., 2019. Boron isotope composition of the cold-water coral *Lophelia pertusa* along the Norwegian margin: Zooming into a potential pH-proxy by combining bulk and high-resolution approaches. Chemical Geology 513, 143–152. https://doi.org/10.1016/j.chemgeo.2019.01.005

Karl, D.M., Lukas, R., 1996. The Hawaii Ocean Time-series (HOT) program: Background, rationale and field implementation. Deep Sea Research Part II: Topical Studies in Oceanography 43, 129–156. https://doi.org/10.1016/0967-0645(96)00005-7

Kilbourne, K.H., Wanamaker, A.D., Moffa-Sanchez, P., Reynolds, D.J., Amrhein, D.E., Butler, P.G., Gebbie, G., Goes, M., Jansen, M.F., Little, C.M., Mette, M., Moreno-Chamarro, E., Ortega, P., Otto-Bliesner, B.L., Rossby, T., Scourse, J., Whitney, N.M., 2022. Atlantic circulation change still uncertain. Nat. Geosci. 15, 165–167. https://doi.org/10.1038/s41561-022-00896-4

King, T.M., Rosenheim, B.E., Post, A.L., Gabris, T., Burt, T., Domack, E.W., 2018. Large-Scale Intrusion of Circumpolar Deep Water on Antarctic Margin Recorded by Stylasterid Corals. Paleoceanography and Paleoclimatology 33, 1306–1321. https://doi.org/10.1029/2018PA003439

Kucera, M., 2007. Chapter Six Planktonic Foraminifera as Tracers of Past Oceanic Environments, in: Developments in Marine Geology. Elsevier, pp. 213–262. https://doi.org/10.1016/S1572-5480(07)01011-1

Lan, X., Tans, P., Thoning, K., NOAA Global Monitoring Laboratory, 2023. Trends in globally-averaged CO_2 determined from NOAA Global Monitoring Laboratory measurements. Version 2023-08. https://doi.org/10.15138/9N0H-ZH07

Lauvset, S.K., Carter, B.R., Pèrez, F.F., Jiang, L. -Q., Feely, R.A., Velo, A., Olsen, A., 2020. Processes Driving Global Interior Ocean pH Distribution. Global Biogeochem. Cycles 34. https://doi.org/10.1029/2019GB006229

Lauvset, S.K., Lange, N., Tanhua, T., Bittig, H.C., Olsen, A., Kozyr, A., Alin, S., Álvarez, M., Azetsu-Scott, K., Barbero, L., Becker, S., Brown, P.J., Carter, B.R., Da Cunha, L.C., Feely, R.A., Hoppema, M., Humphreys, M.P., Ishii, M., Jeansson, E., Jiang, L.-Q., Jones, S.D., Lo Monaco, C., Murata, A., Müller, J.D., Pérez, F.F., Pfeil, B., Schirnick, C., Steinfeldt, R., Suzuki, T., Tilbrook, B., Ulfsbo, A., Velo, A., Woosley, R.J., Key, R.M., 2022. GLODAPv2.2022: the latest version of the global interior ocean biogeochemical data product. Earth Syst. Sci. Data 14, 5543–5572. https://doi.org/10.5194/essd-14-5543-2022

LaVigne, M., Hill, T.M., Spero, H.J., Guilderson, T.P., 2011. Bamboo coral Ba/Ca: Calibration of a new deep ocean refractory nutrient proxy. Earth and Planetary Science Letters 312, 506–515. https://doi.org/10.1016/j.epsl.2011.10.013

Levin, L.A., Le Bris, N., 2015. The deep ocean under climate change. Science 350, 766–768. https://doi.org/10.1126/science.aad0126

Levitus, S., Antonov, J.I., Boyer, T.P., Baranova, O.K., Garcia, H.E., Locarnini, R.A., Mishonov, A.V., Reagan, J.R., Seidov, D., Yarosh, E.S., Zweng, M.M., 2012. World ocean heat content and thermosteric sea level change (0-2000 m), 1955-2010. Geophys. Res. Lett. 39, L10603. https://doi.org/10.1029/2012GL051106

Lindner, A., Cairns, S.D., Cunningham, C.W., 2008. From Offshore to Onshore: Multiple Origins of Shallow-Water Corals from Deep-Sea Ancestors. PLoS ONE 3, e2429. https://doi.org/10.1371/journal.pone.0002429

Lindner, A., Cairns, S.D., Zibrowius, H., 2014. *Leptohelia flexibilis* gen. nov. *et* sp. nov., a remarkable deep-sea stylasterid (Cnidaria: Hydrozoa: Stylasteridae) from the southwest Pacific. Zootaxa 3900, 581. https://doi.org/10.11646/zootaxa.3900.4.8

Liu, Q., Robinson, L.F., Hendy, E., Prokopenko, M.G., Stewart, J.A., Knowles, T.D.J., Li, T., Samperiz, A., 2023. Reinterpreting radiocarbon records in bamboo corals – New insights from the tropical North Atlantic. Geochimica et Cosmochimica Acta 348, 296–308. https://doi.org/10.1016/j.gca.2023.03.019

Macdonald, A.M., Wunsch, C., 1996. An estimate of global ocean circulation and heat fluxes. Nature 382, 436–439. https://doi.org/10.1038/382436a0

Maggioni, D., Terraneo, T.I., Chimienti, G., Marchese, F., Pica, D., Cairns, S.D., Eweida, A.A., Rodrigue, M., Purkis, S.J., Benzoni, F., 2022. The First Deep-Sea Stylasterid (Hydrozoa, Stylasteridae) of the Red Sea. Diversity 14, 241. https://doi.org/10.3390/d14040241

Marchitto, T.M., Lehman, S.J., Ortiz, J.D., Flückiger, J., Van Geen, A., 2007. Marine Radiocarbon Evidence for the Mechanism of Deglacial Atmospheric CO_2 Rise. Science 316, 1456–1459. https://doi.org/10.1126/science.1138679

Mass, T., Drake, J.L., Haramaty, L., Kim, J.D., Zelzion, E., Bhattacharya, D., Falkowski, P.G., 2013. Cloning and Characterization of Four Novel Coral Acid-Rich Proteins that Precipitate Carbonates In Vitro. Current Biology 23, 1126–1131. https://doi.org/10.1016/j.cub.2013.05.007

McCulloch, M., Trotter, J., Montagna, P., Falter, J., Dunbar, R., Freiwald, A., Försterra, G., López Correa, M., Maier, C., Rüggeberg, A., Taviani, M., 2012. Resilience of cold-water scleractinian corals to ocean acidification: Boron isotopic systematics of pH and saturation state up-regulation. Geochimica et Cosmochimica Acta 87, 21–34. https://doi.org/10.1016/j.gca.2012.03.027

Miller, K.J., Mundy, C.N., Chadderton, W.L., 2004. Ecological and genetic evidence of the vulnerability of shallow-water populations of the stylasterid hydrocoral *Errina novaezelandiae* in New Zealand's fiords. Aquatic Conserv: Mar. Freshw. Ecosyst. 14, 75–94. https://doi.org/10.1002/aqc.597

Montagna, P., McCulloch, M., Douville, E., López Correa, M., Trotter, J., Rodolfo-Metalpa, R., Dissard, D., Ferrier-Pagès, C., Frank, N., Freiwald, A., Goldstein, S., Mazzoli, C., Reynaud, S., Rüggeberg, A., Russo, S., Taviani, M., 2014. Li/Mg systematics in scleractinian corals: Calibration of the thermometer. Geochimica et Cosmochimica Acta 132, 288–310. https://doi.org/10.1016/j.gca.2014.02.005

Mora, C., Wei, C.-L., Rollo, A., Amaro, T., Baco, A.R., Billett, D., Bopp, L., Chen, Q., Collier, M., Danovaro, R., Gooday, A.J., Grupe, B.M., Halloran, P.R., Ingels, J., Jones, D.O.B., Levin, L.A., Nakano, H., Norling, K., Ramirez-Llodra, E., Rex, M., Ruhl, H.A., Smith, C.R., Sweetman, A.K., Thurber, A.R., Tjiputra, J.F., Usseglio, P., Watling, L., Wu, T., Yasuhara, M., 2013. Biotic and Human Vulnerability to Projected Changes in Ocean Biogeochemistry over the 21st Century. PLoS Biol 11, e1001682. https://doi.org/10.1371/journal.pbio.1001682

NOAA National Centers for Environmental Information, Monthly Global Climate Report for Annual 2022, published online January 2023, retrieved on August 17, 2023 from https://www.ncei.noaa.gov/access/monitoring/monthly-report/global/202213/supplemental/page-3.

Puce, S., Pica, D., Schiaparelli, S., Negrisolo, E., 2016. Integration of Morphological Data into Molecular Phylogenetic Analysis: Toward the Identikit of the Stylasterid Ancestor. PLoS ONE 11, e0161423. https://doi.org/10.1371/journal.pone.0161423

Raddatz, J., Liebetrau, V., Rüggeberg, A., Hathorne, E., Krabbenhöft, A., Eisenhauer, A., Böhm, F., Vollstaedt, H., Fietzke, J., López Correa, M., Freiwald, A., Dullo, W.-Chr., 2013. Stable Sr-isotope, Sr/Ca, Mg/Ca, Li/Ca and Mg/Li ratios in the scleractinian cold-water coral *Lophelia pertusa*. Chemical Geology 352, 143–152. https://doi.org/10.1016/j.chemgeo.2013.06.013

Rae, J.W.B., Burke, A., Robinson, L.F., Adkins, J.F., Chen, T., Cole, C., Greenop, R., Li, T., Littley, E.F.M., Nita, D.C., Stewart, J.A., Taylor, B.J., 2018. CO_2 storage and release in the deep Southern Ocean on millennial to centennial timescales. Nature 562, 569–573. https://doi.org/10.1038/s41586-018-0614-0

Rahmstorf, S., 2002. Ocean circulation and climate during the past 120,000 years. Nature 419, 207–214. https://doi.org/10.1038/nature01090

Reaka-Kudla, M.L., 1997. The global biodiversity of coral reefs: a comparison with rain forests, in: M. L. Reaka-Kudla, D. E. Wilson, & E. O. Wilson (Eds.), Biodiversity II: Understanding and Protecting Our Biological Resources, pp. 83–108. Joseph Henry/National Academy Press, Washington, D.C.

Reid, P.C., Fischer, A.C., Lewis-Brown, E., Meredith, M.P., Sparrow, M., Andersson, A.J., Antia, A., Bates, N.R., Bathmann, U., Beaugrand, G., Brix, H., Dye, S., Edwards, M., Furevik, T., Gangstø, R., Hátún, H., Hopcroft, R.R., Kendall, M., Kasten, S., Keeling, R., Le Quéré, C., Mackenzie, F.T., Malin, G., Mauritzen, C., Ólafsson, J., Paull, C., Rignot, E., Shimada, K., Vogt, M., Wallace, C., Wang, Z., Washington, R., 2009. Chapter 1 Impacts of the Oceans on Climate Change, in: Advances in Marine Biology. Elsevier, pp. 1–150. https://doi.org/10.1016/S0065-2881(09)56001-4

Ries, J.B., 2011. Skeletal mineralogy in a high-CO_2 world. Journal of Experimental Marine Biology and Ecology 403, 54–64. https://doi.org/10.1016/j.jembe.2011.04.006

Roberts, J.M., Wheeler, A.J., Freiwald, A., 2006. Reefs of the Deep: The Biology and Geology of Cold-Water Coral Ecosystems. Science 312, 543–547. https://doi.org/10.1126/science.1119861

Roberts, S., Hirshfield, M., 2004. Deep-sea corals: out of sight, but no longer out of mind. Frontiers in Ecology and the Environment 2, 123–130. https://doi.org/10.1890/1540-9295(2004)002[0123:DCOOSB]2.0.CO;2

Robinson, L.F., Adkins, J.F., Frank, N., Gagnon, A.C., Prouty, N.G., Brendan Roark, E., De Flierdt, T.V., 2014. The geochemistry of deep-sea coral skeletons: A review of vital effects and applications for palaeoceanography. Deep Sea Research Part II: Topical Studies in Oceanography 99, 184–198. https://doi.org/10.1016/j.dsr2.2013.06.005

Samperiz, A., Robinson, L.F., Stewart, J.A., Strawson, I., Leng, M.J., Rosenheim, B.E., Ciscato, E.R., Hendry, K.R., Santodomingo, N., 2020. Stylasterid corals: A new paleotemperature archive. Earth and Planetary Science Letters 545, 116407. https://doi.org/10.1016/j.epsl.2020.116407

Sarmiento, J.L., Hughes, T.M.C., Stouffer, R.J., Manabe, S., 1998. Simulated response of the ocean carbon cycle to anthropogenic climate warming. Nature 393, 245–249. https://doi.org/10.1038/30455

Sigman, D.M., Boyle, E.A., 2000. Glacial/interglacial variations in atmospheric carbon dioxide. Nature 407, 859–869. https://doi.org/10.1038/35038000

Sinclair, D.J., Williams, B., Allard, G., Ghaleb, B., Fallon, S., Ross, S.W., Risk, M., 2011. Reproducibility of trace element profiles in a specimen of the deep-water bamboo coral *Keratoisis* sp. Geochimica et Cosmochimica Acta 75, 5101–5121. https://doi.org/10.1016/j.gca.2011.05.012

Sinclair, D.J., Williams, B., Risk, M., 2006. A biological origin for climate signals in corals—Trace element "vital effects" are ubiquitous in Scleractinian coral skeletons. Geophys. Res. Lett. 33, L17707. https://doi.org/10.1029/2006GL027183

Skinner, L.C., Fallon, S., Waelbroeck, C., Michel, E., Barker, S., 2010. Ventilation of the Deep Southern Ocean and Deglacial CO_2 Rise. Science 328, 1147–1151. https://doi.org/10.1126/science.1183627

Spooner, P.T., Robinson, L.F., Hemsing, F., Morris, P., Stewart, J.A., 2018. Extended calibration of cold-water coral Ba/Ca using multiple genera and co-located measurements of dissolved barium concentration. Chemical Geology 499, 100–110. https://doi.org/10.1016/j.chemgeo.2018.09.012

Stewart, J.A., Anagnostou, E., Foster, G.L., 2016. An improved boron isotope pH proxy calibration for the deep-sea coral *Desmophyllum dianthus* through sub-sampling of fibrous aragonite. Chemical Geology 447, 148–160. https://doi.org/10.1016/j.chemgeo.2016.10.029

Stewart, J.A., Li, T., Spooner, P.T., Burke, A., Chen, T., Roberts, J., Rae, J.W.B., Peck, V., Kender, S., Liu, Q., Robinson, L.F., 2021. Productivity and Dissolved Oxygen Controls on the Southern Ocean Deep-Sea Benthos During the Antarctic Cold Reversal. Paleoceanography and Paleoclimatology, 36, e2021PA004288. https://doi.org/10.1029/2021PA004288

Stewart, J.A., Robinson, L.F., Day, R.D., Strawson, I., Burke, A., Rae, J.W.B., Spooner, P.T., Samperiz, A., Etnoyer, P.J., Williams, B., Paytan, A., Leng, M.J., Häussermann, V., Wickes, L.N., Bratt, R., Pryer, H., 2020. Refining trace metal temperature proxies in cold-water scleractinian and stylasterid corals. Earth and Planetary Science Letters 545, 116412. https://doi.org/10.1016/j.epsl.2020.116412

Stewart, J.A., Strawson, I., Kershaw, J., Robinson, L.F., 2022. Stylasterid corals build aragonite skeletons in undersaturated water despite low pH at the site of calcification. Sci Rep 12, 13105. https://doi.org/10.1038/s41598-022-16787-y

Stolarski, J., Coronado, I., Murphy, J.G., Kitahara, M.V., Janiszewska, K., Mazur, M., Gothmann, A.M., Bouvier, A.-S., Marin-Carbonne, J., Taylor, M.L., Quattrini, A.M., McFadden, C.S., Higgins, J.A., Robinson, L.F., Meibom, A., 2021. A modern scleractinian coral with a two-component calcite–aragonite skeleton. Proc. Natl. Acad. Sci. U.S.A. 118, e2013316117. https://doi.org/10.1073/pnas.2013316117

Swann, G.E.A., Leng, M.J., 2009. A review of diatom $\delta^{18}O$ in palaeoceanography. Quaternary Science Reviews 28, 384–398. https://doi.org/10.1016/j.quascirev.2008.11.002

Talley, L., 2013. Closure of the Global Overturning Circulation Through the Indian, Pacific, and Southern Oceans: Schematics and Transports. Oceanography 26, 80–97. https://doi.org/10.5670/oceanog.2013.07

Tambutté, E., Allemand, D., Zoccola, D., Meibom, A., Lotto, S., Caminiti, N., Tambutté, S., 2007. Observations of the tissue-skeleton interface in the scleractinian coral *Stylophora pistillata*. Coral Reefs 26, 517–529. https://doi.org/10.1007/s00338-007-0263-5

Tambutté, S., Holcomb, M., Ferrier-Pagès, C., Reynaud, S., Tambutté, É., Zoccola, D., Allemand, D., 2011. Coral biomineralization: From the gene to the environment. Journal of Experimental Marine Biology and Ecology 408, 58–78. https://doi.org/10.1016/j.jembe.2011.07.026

Thiagarajan, N., Gerlach, D., Roberts, M.L., Burke, A., McNichol, A., Jenkins, W.J., Subhas, A.V., Thresher, R.E., Adkins, J.F., 2013. Movement of deep-sea coral populations on climatic timescales. Paleoceanography 28, 227–236. https://doi.org/10.1002/palo.20023

Thresher, R.E., Fallon, S.J., 2021. Apparent Periodic and Long-Term Changes in AAIW and UCDW Properties at Fixed Depths in the Southwest Pacific, With Indications of a Regime Shift in the 1930s. Geophysical Research Letters 48, e2020GL092329. https://doi.org/10.1029/2020GL092329

Thurber, A.R., Sweetman, A.K., Narayanaswamy, B.E., Jones, D.O.B., Ingels, J., Hansman, R.L., 2014. Ecosystem function and services provided by the deep sea. Biogeosciences 11, 3941–3963. https://doi.org/10.5194/bg-11-3941-2014

Von Euw, S., Zhang, Q., Manichev, V., Murali, N., Gross, J., Feldman, L.C., Gustafsson, T., Flach, C., Mendelsohn, R., Falkowski, P.G., 2017. Biological control of aragonite formation in stony corals. Science 356, 933–938. https://doi.org/10.1126/science.aam6371

Wall, M., Ragazzola, F., Foster, L.C., Form, A., Schmidt, D.N., 2015. pH up-regulation as a potential mechanism for the cold-water coral *Lophelia pertusa* to sustain growth in aragonite undersaturated conditions. Biogeosciences 12, 6869–6880. https://doi.org/10.5194/bg-12-6869-2015

Weber, J.N., Woodhead, P.M.J., 1972. Stable isotope ratio variations in non-scleractinian coelenterate carbonates as a function of temperature. Mar. Biol. 15, 293–297. https://doi.org/10.1007/BF00401388

Wefer, G., Berger, W.H., Bijma, J., Fischer, G., 1999. Clues to Ocean History: a Brief Overview of Proxies, in: Fischer, Gerhard, Wefer, Gerold (Eds.), Use of Proxies in Paleoceanography. Springer Berlin Heidelberg, Berlin, Heidelberg, pp. 1–68. https://doi.org/10.1007/978-3-642-58646-0_1

Wisshak, M., López Correa, M., Zibrowius, H., Jakobsen, J., Freiwald, A., 2009. Skeletal reorganisation affects geochemical signals, exemplified in the stylasterid hydrocoral *Errina dabneyi* (Azores Archipelago). Mar. Ecol. Prog. Ser. 397, 197–208. https://doi.org/10.3354/meps08165

Zeebe, R.E., Ridgwell, A., Zachos, J.C., 2016. Anthropogenic carbon release rate unprecedented during the past 66 million years. Nature Geosci 9, 325–329. https://doi.org/10.1038/ngeo2681

Chapter 2: Analytical methods

Contributions and acknowledgements

1. Introduction

This thesis presents an examination of the inorganic, geochemical composition of stylasterid coral skeletons. The new data comprise element/Ca ratios, stable boron isotopic ratios, and U-series and radiocarbon measurements, all of which were generated by mass spectrometry techniques.

Owing to the similarity of the laboratory and analytical procedures employed across this thesis, I here provide an overview of these techniques, to avoid replication of methods in each individual chapter. Additionally, a vast amount of time and effort was spent on method development and trouble-shooting, and while the results of many of these experiments and experiences do not contribute directly to the data presented in this thesis, they are worthy of discussion in their own right.

Analytical procedures aside, the contextual relevance of each type of measurement and other study-specific aspects of the methodology are presented separately in each of chapters 3, 4 and 5, including information on sample selection, mineralogical determination, hydrographic data pairing and the statistical methods and calculations used. One aspect of the methodology which will not be covered elsewhere is the identification of stylasterid specimens, which is instead summarised in the supplementary information of this chapter (section 8.1).

The rest of this chapter documents the common laboratory and analytical methods associated with the mass spectrometry techniques employed during this thesis, addressing in turn the different measurements made.

2. Equipment cleaning and preparation

The determination of precise and accurate trace elemental and isotopic ratios requires high levels of lab cleanliness. Many of the elements of interest here are present in the natural environment, introducing the possibility of sample contamination during preparation. For example, boron is enriched in products including cosmetics and washing powders (e.g. Eisenhut et al., 1996), while Th is highly particle-reactive, meaning any contaminant particulate phase could remove Th from dissolved sample solutions. This section therefore provides a brief overview of the steps taken during this thesis to minimise sample contamination.

Firstly, the procedures used onboard the cruises and in the museums which collected and provided the specimens used in this thesis were screened to minimise the risk of sample contamination. For radiocarbon measurements, specific efforts were made to ensure that samples had not been exposed to materials enriched in ^{14}C (e.g. equipment used in carbon isotope tracer experiments). Further, museum specimens preserved in formalin were avoided, primarily because formalin preparations are commonly buffered using borax, a Na-borate salt with a negative $\delta^{11}B$ signature that contrasts greatly with the sample boron isotope ratios in this study (e.g. Kasemann et al., 2004). Once in Bristol, all samples were stored dry in closed containers in the Bristol coral collection.

All sample handling after initial collection and cutting was carried out in the same clean laboratory in the Bristol Isotope Group, fitted with boron-free membrane air filters. The time that samples were exposed to air was minimised, since air exposure is known to cause contamination of various elements, in particular boron (Foster et al., 2006). For element/Ca ratios and boron isotopic measurements, no stage of the sample preparation was carried out in high airflow (extracted) fume hoods, aside from addition of HF to samples immediately prior to boron isotopic measurements (see section 4).

Analysis type	Step	Equipment	Cleaning procedure*
All	Sample cleaning	1.5 mL plastic** tubes	Rinse × 3 with Milli-Q
All	Sample cleaning	Plastic pipette tips	3 M HCl (TM***), 1 week
El/Ca ratios, δ^{11}B	Sample dissolution	1.5 mL plastic tubes	3 M HCl (TM) overnight @ 80 °C & 1.5 M HNO$_3$ (distilled****) overnight
U-series	Sample dissolution	Teflon vials	7 M HNO$_3$ (TM) in Teflon jar & 6 M HCl (TM) in Teflon jar & 7 M HNO$_3$ (distilled) inside vials, all overnight @ 80 °C
El/Ca ratios, δ^{11}B, U-series	Sample dissolution	Plastic pipette tips	3 M HCl (distilled) overnight @ 80 °C & 0.3 M HNO$_3$ (distilled), 2 hours @ 80 °C
El/Ca ratios, U-series	Sample dilution	Plastic pipette tips	3 M HCl (TM), 1 week
δ^{11}B	Column chemistry and sample dilution	Plastic pipette tips	3 M HCl (distilled) overnight @ 80 °C & 0.3 M HNO$_3$ (distilled), 2 hours @ 80 °C
El/Ca ratios, δ^{11}B, U-series	Solution (e.g. standard) preparation	Plastic pipette tips	3 M HCl (distilled) overnight @ 80 °C & 0.3 M HNO$_3$ (distilled), 2 hours @ 80 °C
δ^{11}B	Sample collection during column chemistry, sample measurement	Teflon vials	7 M HNO$_3$ (TM) inside vials, 2 hours @ 80 °C & 7 M HNO$_3$ (TM) in Teflon jars, overnight @ 80 °C & 0.75 M HNO$_3$ (distilled) in Teflon jars, overnight @ 80 °C & 1.5 M HNO$_3$ (distilled) inside vials immediately prior to use, 2 hours @ 80 °C
El/Ca ratios	Sample measurement	2 mL plastic vials	3 M HCl (TM) overnight @ 80 °C & 1.5 M HNO$_3$ (distilled) overnight
U-series	Sample measurement	1.5 mL plastic vials	3 M HCl (TM), 1 week

*All steps involving acids were followed by 3 rinses with Milli-Q.

**All plastic vials and pipette tips were composed of Polypropylene.

***TM refers to trace metal grade specification of acid cleanliness (undistilled).

****Acid distillations were performed in-house.

Table 1. Summary of cleaning procedures for vials and pipette tips used during geochemical analyses.

Pipette tips and vials used in sample preparation, dissolution, storage and measurement require proper cleaning prior to use. Cleaning procedures adopted here vary for each type of equipment and analysis, and become increasingly stringent from sample preparation through to measurement. The procedures adopted are summarised in Table 1.

3. Element/Ca ratios

The primary technique applied to all coral samples in this thesis was determination of the concentrations of various elements in the coral skeleton, expressed as element/Ca ratios (chapters 3, 4 and 5). Treatment of samples from the period immediately after collection until prior to analysis varied between research cruises, museum collections, and aims of the chapter in question, and the reader is referred to specific chapters for this information. Here, I focus on the common sample preparation and analytical procedures employed in making these measurements. It is worth noting that for chapter 4 of this thesis, boron isotopic measurements (section 4) were paired with measured element/Ca ratios. To ensure these different analyses were truly paired for each sample, the same powders and dissolved solutions were measured, as summarised in Figure 1. Where additional analyses were carried out (^{14}C and U-series dating), the relationships between measured aliquots were more complex, and the reader is referred to chapter 5 for details.
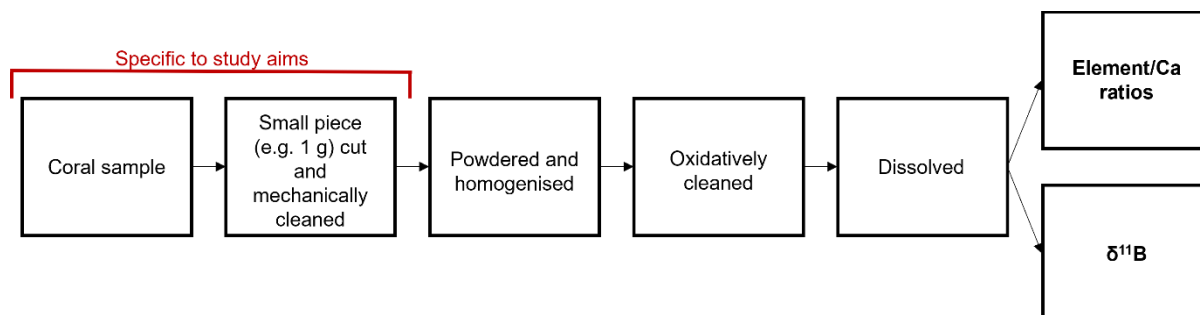
Figure 1. Flowchart showing the relationship between element/Ca ratio and δ^{11}B measurements made in this thesis. Where ^{14}C and U-series dating measurements were made, the relationship between measured sample aliquots is summarised in chapter 5.

3.1 Sample preparation

In all cases, samples of finely crushed carbonate were obtained for analysis of elemental (and boron isotopic) compositions. These carbonate samples were cleaned using standard oxidative cleaning techniques, adapted for paired elemental and boron isotopic analysis (adapted from Boyle, 1981; Boyle and Keigwin, 1985; Barker et al., 2003; Ni et al., 2007). Procedures are documented in detail in Table 2. Briefly, approximately 5 mg of each sample (or less, if samples were small) was treated with 250 - 500 μL (dependent on sample size) of a warm (80 $^{\circ}$C) oxidising solution consisting of 1 % H_2O_2 buffered by 0.1 M NH_4OH, to remove organic matter.

After rinsing 3 times with Milli-Q, samples were transferred to an acid-cleaned 1.5 mL plastic vial and subjected to a weak acid leach (0.0005 M HNO_3), to remove any contaminant phases which had re-adsorbed onto sample surfaces (Boyle and Keigwin, 1985). Samples were rinsed a further 2 times with Milli-Q, before dissolution in the minimum required volume of distilled 0.5 M HNO_3. The minimum amount of acid was used to in turn minimise the amount of buffer required for boron isotopic analysis (see section 4.1). Immediately after dissolution, samples were centrifuged to separate the dissolved sample from any remaining dissolution-resistant phases (e.g. organic matter, silicates). The dissolved phase was then transferred to a clean 1.5 mL plastic vial, tightly sealed and refrigerated until analysis.

It is notable that the reductive cleaning steps designed by Boyle and Keigwin (1985) were not used here. These steps were designed to remove Fe-Mn oxy-hydroxides, which can contain significant amounts of elements including Fe, Mn, Cd and Ba (Boyle, 1981; chapter 3). However, this step can lead to partial carbonate dissolution, which can itself significantly alter ratios including Mg/Ca (Barker et al., 2003). Given that most coral samples were collected alive or in pristine condition, the effects of Fe-Mn oxyhydroxides were considered to be minimal. Furthermore, the large size of coral samples generally allows for the vast majority of coatings on sub-fossil samples to be removed by physical cleaning, in contrast to foraminifera for which reductive cleaning techniques were originally designed. Therefore, I chose not to employ reductive cleaning steps, and instead monitored for the possible effects of Fe-Mn oxy-hydroxides using Fe/Ca and Mn/Ca ratios (e.g. see chapter 3 and chapter 5).

Step	Description
	Sample cleaning
1	Weigh ~ 5 mg of sample into vial
2	Oxidative mixture* (250 to 500 μL) in water bath at 80 ⁰C for 5 minutes. Ultrasonicate for 10 seconds. Repeat a further 2 or 3 times (depending on amount of CO_2 released)
3	Remove supernatant
4	Milli-Q rinse (fill vials and lids) × 3
5	Transfer to clean, acid-leached vial
6	Add 250 to 500 μL 0.0005 M HNO_3, leave for 30 seconds
7	Ultrasonicate (10 seconds) and fill vial with Milli-Q to quench reaction
8	Remove supernatant
9	Milli-Q rinse (fill vials and lids) × 2
	Sample dissolution
1	Add 50 μL Milli-Q to slow initial reaction
2	Dissolve by stepwise (100 to 200 μL) addition of distilled 0.5 M HNO_3
3	Centrifuge sample
4	Transfer dissolved phase to clean plastic vial for storage

*Oxidative mixture: 30 × dilution of 30 % H_2O_2 in 0.1 M NH_4OH

Table 2. Summary of oxidative sample cleaning and dissolution procedures applied for measurement of element/Ca and boron isotopic ratios.

3.2 Analytical techniques

Coral element/Ca ratios were measured at the University of Bristol using a Thermo-Element ICP-MS. Equipment and relevant instrument parameters are summarised in Table 3. Initially, small aliquots (20 µL) of each sample were diluted (20 x dilution factor), and intensities of ^{43}Ca measured against a standard of known concentration. A further aliquot of each sample was then taken and diluted accordingly (total volume > 0.5 mL) to derive a solution with [Ca] of 4 mM, matched with the chosen bracketing standard. This process of concentration matching is important to minimise matrix effects, which are known to vary with solution [Ca] and can affect element/Ca ratios (e.g. Yu et al., 2005).

Intensities of various elements were then measured for samples, blanks (0.5 M HNO_3) and a well-characterised bracketing standard, Bristol Multi-Element 1 (BME1; introduced in 0.5 M HNO_3). Prewash and wash solutions (0.5 M HNO_3 + 0.3 M HF; see below) were used to clean the introduction system after each sample and bracketing standard. Intensities of all elements measured on samples and bracketing standards were corrected for background by subtracting the average of blanks before and after each sample. In general, measured blank intensities were << 1 % for all elements, except for B and Li.

Considering B, firstly, it is well-established that the volatilisation of boric acid in the spray chamber causes a boron memory effect, coating the inside of the spray chamber and thus contributing to boron measured in the subsequent sample (Al-Ammar et al., 1999). Various solutions have been proposed to reduce the boron memory effect (e.g. Al-Ammar et al., 2000; Misra et al., 2014; Rae et al., 2018; see section 4.2.2 for detailed discussion). Here, we add HF to the prewash and wash to form 0.5 M HNO_3, 0.3 M HF solutions (following Rae et al., 2018; Zeebe and Rae, 2020). Li blanks were also found to be high after cone cleaning, which may result from the increased size of the ^{7}N beam, the high-mass end of which overlaps and interferes with the ^{7}Li peak. By conditioning the cones for 30 to 60 minutes before starting each sequence, Li blanks could be reduced to acceptable levels (always < 2 % of sample intensities, generally falling to < 1 % over the course of the sequence). This conditioning was achieved by aspirating Ca-rich solutions (e.g. the BME bracketing standard), and could be done as part of the [Ca] checks outlined above. Finally, for elements with low concentrations in coral skeletons compared with background (e.g. Cu, Sn), measurements were only considered significantly different from the background (i.e. above the limit of detection) if they were > 5 standard deviations larger than the average background intensity for that analytical session.

Blank corrected intensities were then ratioed to ^{43}Ca, and sample element/Ca ratios derived by normalisation to BME1. ^{7}Li, ^{11}B, ^{26}Mg, ^{27}Al, ^{55}Mn, ^{60}Ni, ^{63}Cu, ^{66}Zn, ^{86}Sr, ^{111}Cd, ^{118}Sn, ^{138}Ba, ^{146}Nd and ^{238}U were measured in low resolution, while intensities of ^{23}Na, ^{56}Fe and ^{59}Co were measured in medium resolution. ^{43}Ca was measured in both low and medium resolution, with the appropriate resolution used to ratio each respective element. Target resolution (R) in medium resolution was ~ 4000 (where R = (molar mass of target peak) / (difference in molar mass between target and next resolvable peak)), and was tuned using the ArO gas peak.

Equipment/Condition	Type/comment
Nebuliser	PFA microflow 50 µL/min
Spray Chamber	PFA HF-resistant barrel
Injector	ESI Sapphire
Sampler cone	Pt - standard
Skimmer cone	Pt – H
Tuning	Sensitivity tuned using Li, In and U
	Parameters typically tuned for sensitivity: torch position (x, y, z), sample gas, focus, x-deflection, y-deflection, shape
	Parameters tuned for peak shape (medium resolution): focus quad (other lenses made only a small difference)
Oxide production	< 5 %, assessed using counts of UO compared to counts of U
Runs	40 in low resolution, 24 in medium resolution
Passes	1 (both low and medium resolution)
Detection mode	All elements in analog, except for Li, B, Cu, Zn, Cd, Sn, Nd, U, which were in counting
Resolution	All elements in low resolution, except for Na, Fe and Co which were measured in medium resolution. Ca was measured in both low and medium resolution, and the appropriate (i.e. matching) resolution used to ratio each respective element.
Take-up time	60 to 90 s (variable dependent on sample gas)
Wash time	100 to 120 s

Table 3. Equipment and instrument settings used during measurement of element/Ca ratios.

Analytical reproducibility was assessed using repeat measurements of reference materials NIST RM 8301 (Coral) (Stewart et al., 2020) and JCp-1 (Hathorne et al., 2013). Long-term reproducibility for all element/Ca ratios presented here (Li/Ca, B/Ca, Na/Ca, Mg/Ca, Sr/Ca, Ba/Ca, U/Ca) was better than 2 % (RSD; 2 σ) for both reference materials (Table 4).

Analytical accuracy was assessed by comparison to interlaboratory consensus values published for NIST RM 8301 (Coral), which is known to be more homogeneous and reproducible than JCp-1 (Stewart et al., 2020). Long-term average values for all elements of interest differed from published values by < 3.5 %. All element/Ca ratios were adjusted by appropriate correction factors, to facilitate direct comparison with previous work. Correction factors were used to the nearest percent, reflecting uncertainty in both the literature and laboratory mean values. Long-term average values, reproducibility and correction factors are summarised in Table 4 and Figure 2. Finally, accuracy and reproducibility of ratios including Fe/Ca was found to be worse than for other elements, in agreement with previous work (e.g. Stewart et al., 2020; Table 4). These values were not corrected for interlaboratory offsets, and are used as guides for monitoring sample contamination only.
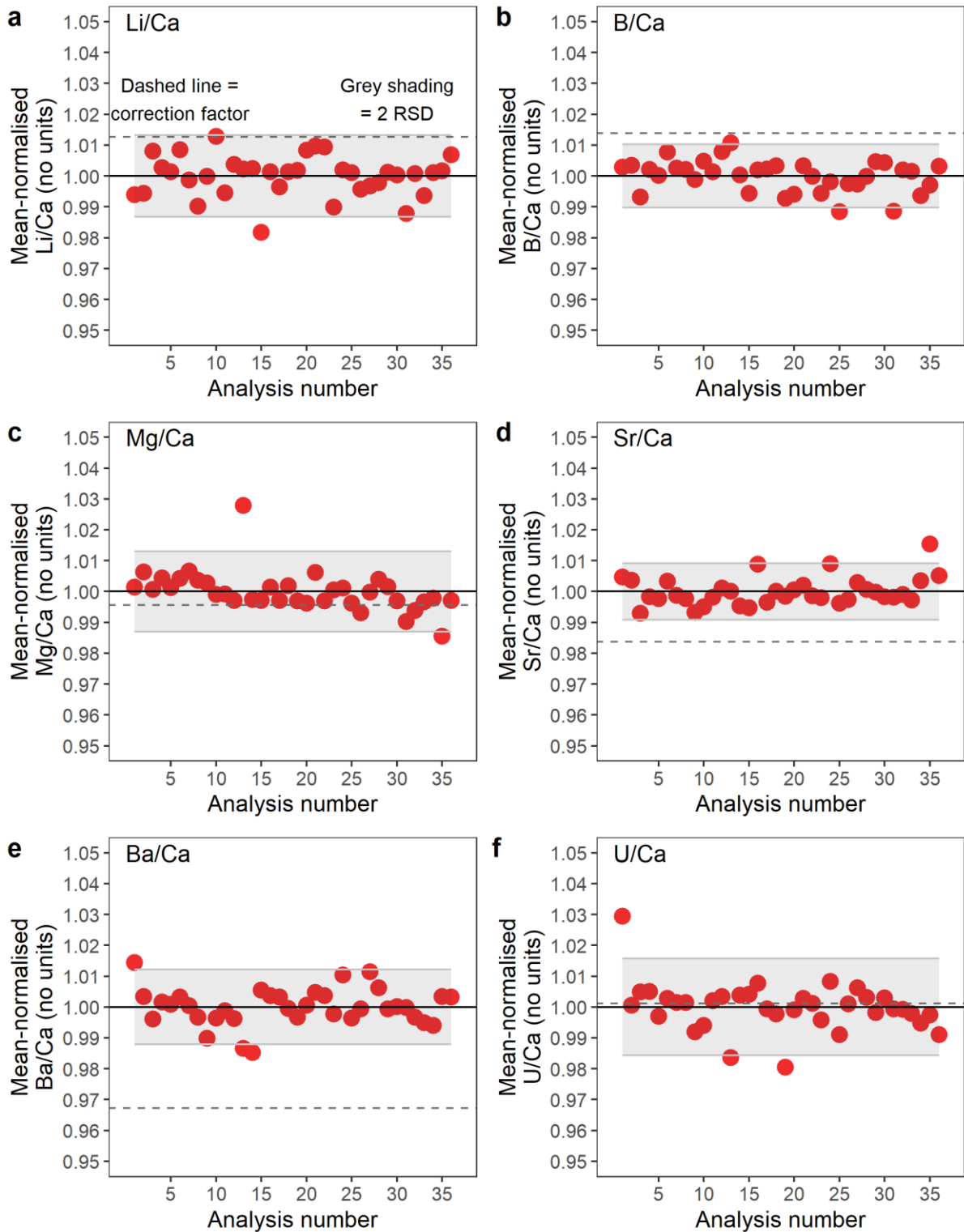
Figure 2. Mean-normalised Li/Ca, B/Ca, Mg/Ca, Sr/Ca, Ba/Ca and U/Ca measurements for NIST RM 8301 (Coral). Analysis period ran from February 2020 (n = 1) to January 2023 (n = 36). Grey shaded region shows analytical reproducibility (RSD; 2 σ). Dashed horizontal lines show interlaboratory consensus values (Stewart et al., 2020) normalised to mean values from this study, and therefore represent the correction factors applied in this study. In practise, correction factors were rounded to the nearest 1 %.

Reference material	Ratio	n	Mean (mmol/mol)	RSD (2 σ)	Literature value (mmol/mol)	Correction factor
8301c (Stewart et al., 2020)	Li/Ca	36	0.00533	1.3	0.00540	1.01
	B/Ca	36	0.521	1.0	0.528	1.01
	Mg/Ca	36	4.13	1.3	4.11	1.00
	Sr/Ca	36	8.24	0.9	8.10	0.98
	Ba/Ca	36	0.00612	1.2	0.00592	0.97
	U/Ca	36	0.000828	1.6	0.000829	1.00
	Na/Ca	34	20.1	0.9	20.0	1.00
	Fe/Ca	34	0.0106	3.8	0.0154	Not used
	Mn/Ca	36	0.00248	1.1	0.00259	Not used
JCp-1 (Hathorne et al., 2013)	Li/Ca	34	0.00615	1.2	0.006185	Not used
	B/Ca	36	0.456	1.3	0.4596	Not used
	Mg/Ca	36	4.23	1.2	4.199	Not used
	Sr/Ca	36	8.88	0.8	8.838	Not used
	Ba/Ca	36	7.50	1.8	7.465	Not used
	U/Ca	36	0.00120	1.4	0.00192	Not used
	Na/Ca	34	20.0	2.0	-	Not used
	Fe/Ca	33	0.013	15	-	Not used
	Mn/Ca	36	0.0012	15	-	Not used

Table 4. Reference material reproducibility and accuracy during this study. NIST RM 8301 (Coral) was used to assess accuracy, with samples corrected to be in line with interlaboratory consensus values (Stewart et al., 2020). Reference material JCp-1 (Hathorne et al., 2013) was also used to assess reproducibility.

4. Boron isotopic analysis

The boron isotopic composition (i.e. $\delta^{11}B$) of a subset of coral samples was measured on the same dissolved solutions as element/Ca ratios (chapters 4 and 5; see Figure 1). Initial cleaning and dissolution of samples for boron isotopic analysis thus follows the procedures outlined in section 3.1. The following sections outline the boron-specific procedures which follow sample dissolution.

4.1 Column chemistry

Measurement of the boron isotopic composition of marine carbonates requires separating boron from the carbonate matrix. To this end, a small aliquot of each dissolved sample was passed through microcolumns containing an Amberlite IRA 743 boron-specific anionic exchange resin (Lemarchand et al., 2002). The adherence of boron to this resin is highly pH dependent, with boron having a higher affinity for the resin at higher pH. This allows boron to be separated from the carbonate matrix using careful combination of solutions with varying pH (Lemarchand et al., 2002). The full column procedure is outlined in Table 5, and follows Foster (2008).

Briefly, columns were cleaned at the start of each session using repeated rinses of 0.5 M HNO$_3$ followed by Milli-Q, to remove any boron accumulated during storage. During this procedure, the resin was disturbed using a clean pipette tip, to remove any channels or air bubbles formed during the previous column batch which could reduce column efficacy. Small amounts of each sample were then buffered with an appropriate amount of a buffer solution, which comprised 2 M Na acetate and 0.05 M acetic acid, and was itself passed through columns to remove any boron (see Table 5). The amount of sample used was varied based on B/Ca ratios to ensure the final boron isotope sample had a [B] close to 50 ppb (sample volumes varied from 10 to 80 µL). Meanwhile, the volume of buffer solution added to each sample was varied to ensure sufficient buffering of the acidic sample solution while using the minimum amount of buffer (Foster, 2008). In practise, buffer:sample volume ratios were between 3:1 and 1:1.

Samples were then loaded onto columns by stepwise addition of small volumes (typically 3 additions of 40 µL). Stepwise sample addition is thought to result in greater removal of boron from the sample than passing the entire sample through the column in one application, owing to the greater reaction time between resin and the sample (e.g. Lemarchand et al., 2002). The carbonate sample matrix was then washed from the resin by repeated addition of Milli-Q, added as drops around the rim of each column. Droplets descended onto the column resin after drumming on the lab bench or gently tapping column holders.

Samples were then collected in acid-cleaned Teflon beakers (see Table 1) using 550 µL of distilled 0.5 M HNO$_3$, again added stepwise in small amounts (55 to 110 µL). Column elution tails were also collected in 150 µL of 0.5 M HNO$_3$. Finally, columns were cleaned at the end of each analytical session using repeated rinses of 0.5 M HNO$_3$ and Milli-Q, before storage in Milli-Q. Column resin can be reused multiple times (Foster, 2008) and was replaced 3 times over the course of the thesis period, at times when columns had stopped dripping freely.

Step	Description	Reagent	Volume	Timing
1	Column cleaning	0.5 M HNO$_3$	Fill column	Allow to drip completely
2	Column cleaning	0.5 M HNO$_3$	1 mL	Allow to drip completely
3	Column cleaning	Milli-Q	1 mL	Allow to drip completely
4	Column cleaning	Milli-Q	1 mL	Allow to drip completely
5a	Load buffered samples	Sample + Na-acetate buffer	Sample added stepwise in small (e.g. 10 to 40 µL) amounts	2 to 4 minutes between each stepwise addition
5b	Na-acetate buffer cleaning	Uncleaned Na-acetate buffer	Two stacked columns, Na-acetate passed through both and collected	Allow to drip completely
6	Remove carbonate matrix	Milli-Q	10 × 160 µL, added in drops around column rim	5 - 10 minutes between each rinse
7	Collect sample	0.5 M HNO$_3$	550 µL (4 × 55 µL + 3 × 110 µL)	5 to 10 minutes between each rinse. Third step (first 110 µL application) left for 20 minutes.
8	Collect column tails	0.5 M HNO$_3$	1 × 150 µL	Allow to drip completely
9	Column cleaning	0.5 M HNO$_3$	Fill column	Allow to drip completely
10	Column cleaning	0.5 M HNO$_3$	1 mL	Allow to drip completely
11	Column cleaning	Milli-Q	1 mL	Allow to drip completely
12	Column cleaning	Milli-Q	1 mL	Allow to drip completely

Table 5. Summary of column chemistry procedures for separating boron from the carbonate matrix. Note that after step 5b, the columns used to clean the Na-acetate buffer are cleaned (skip to step 9 onwards).

4.2 Analytical techniques

Boron isotope values were measured on the separated boron fraction using a Thermo Neptune Multi-Collector ICP-MS at the University of Bristol, following techniques in Foster (2008). The analytical set up is summarised in Table 6. Prior to sample analysis, a number of tests were performed, to check column elution tails, carbonate matrix removal, sample [B] and procedural blanks. These checks are outlined first, before sample analysis techniques are detailed in section 4.2.2.

Equipment/Condition	Type/comment
Nebuliser	PFA microflow 50 μL/min
Spray Chamber	PFA HF-resistant barrel
Injector	ESI Sapphire
Sampler cone	Ni - standard
Skimmer cone	Ni – X
Cup configuration	^{11}B measured on cup H3, ^{10}B on cup L3
Amplifiers used	Either $2 \times 10^{12}\ \Omega$ or $2 \times 10^{13}\ \Omega$
RF power	1200 W
Tuning	Sensitivity tuned using ^{11}B
	Parameters typically tuned for sensitivity: torch position (x, y, z), sample gas and the focus, x-deflection, y-deflection and shape lenses
	Parameters tuned for peak shape: shape lens, focus quad
Cycles per measurement	30
Integration time per cycle	4 s
Resolution	Low
Take-up time	60 to 80 s (variable dependent on sample gas)
Wash time	120 s

Table 6. Equipment and instrument settings used during boron isotopic analysis.

4.2.1 Column quality control

Firstly, the efficacy of column chemistry procedures was checked using four distinct measurements, which were carried out prior to analysis of sample boron isotopic compositions.

It is well-established that boron isotopes are fractionated during elution of samples from the column resin, with ^{11}B preferentially removed at the start of the elution and ^{10}B at the end (Lemarchand et al., 2002). It is therefore important that all the boron which adheres to the resin during sample loading is removed during sample collection (step 7 in Table 5). To test ensure that all B was collected, the concentration of boron remaining on each column after sample collection (the so-called elution tail, step 8 in Table 5) was measured for all samples, and compared to the amount of boron in the collected sample. The amount of boron present in elution tails for samples measured as part of this thesis averaged 0.1 % of the total boron collected in samples, and was at most 0.6 %. Therefore, incomplete recovery of boron during column chemistry is unlikely to affect the boron isotopic values presented here.

Secondly, incomplete removal of the carbonate matrix during column chemistry (step 6 in Table 5) can lead to the sample and bracketing standards having different matrices, and thus potentially differing mass fractionation behaviour during measurement (Foster, 2008; Guerrot et al., 2011). To check whether carbonate matrix removal was complete, ^{23}Na intensities were measured on small aliquots of each sample (10 μL sample diluted in 140 μL distilled HNO_3). Although there is no hard limit for acceptable ^{23}Na

intensities, measured intensities of $^{23}Na > 0.3$ V (i.e. around 4 × greater than background levels) were considered problematic and were generally measured separately from other samples (Figure 3).

Testing for ^{23}Na intensities also revealed the importance of thoroughly cleaning the equipment used during analysis. At the start of the analytical period, multiple column batches appeared to suffer from ^{23}Na intensities exceeding acceptable limits, with ^{23}Na intensities in diluted aliquots exceeding 1 V (Figure 3). These issues continued after replacement of the column resin and all reagents used in the column process. Eventually, I measured the intensity of ^{23}Na in an undiluted sample immediately following column chemistry, by placing the autosampler probe directly into the Teflon collection vial. The intensity of ^{23}Na measured was indistinguishable from background, however, after pipetting a small aliquot of this sample into another vial, the intensity of ^{23}Na measured increased significantly.
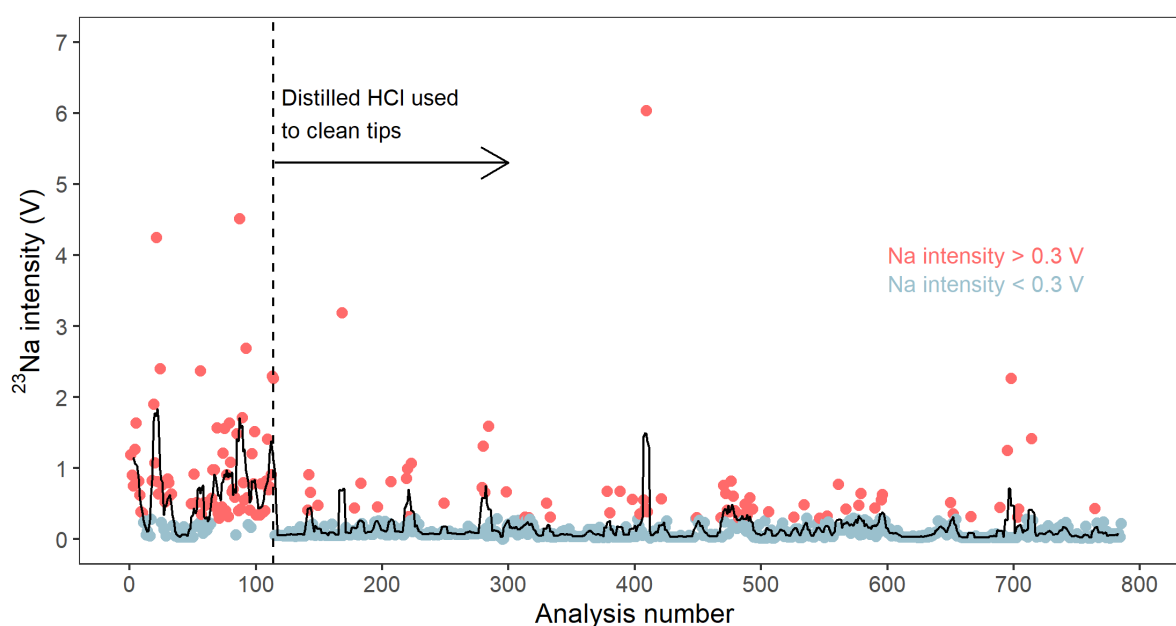
Figure 3. Na intensities (10^{11} Ω amplifier) measured on sample aliquots from the period October 2019 (left) to February 2023 (right). Plot includes data from all samples measured at the Bristol Isotope Group during this period, comprising samples from this thesis and measurements made by Dr Joseph Stewart, Maoyu Wang and Elliot Robson. Dashed vertical line shows time at which pipette cleaning procedure was changed. Solid black line shows the 5-point, centred, rolling mean.

The origin of elevated ^{23}Na intensities therefore appeared to be contamination by pipette tips, which at that time were cleaned using cold, 3 M trace metal grade HCl for a period of 1 week (see Table 1; "Pipette tips for sample cleaning"). I therefore switched to using pipette tips cleaned overnight at 80 °C in distilled 3 M HCl, followed by 2 hours at 80 °C in 0.3 M distilled HNO$_3$ (Table 1). This change in approach is clearly visible in measured ^{23}Na intensities over the course of the thesis period (Figure 3). Data from all but 5 measured samples (representing 3 corals) presented here had ^{23}Na intensities ≤ 0.3 V. For 2 of the 3 corals whose subsamples were measured with high Na intensities, sample replicate δ^{11}B values (i.e.

different cut pieces of the same coral) agree to within 0.12 ‰, indicating these data are likely robust and justifying their inclusion here.

The concentration of boron in collected sample fractions was measured as part of the same sequence used for checking ^{23}Na intensities. Intensities of ^{11}B in samples were measured against a standard of known concentration to derive sample [B]. Samples were then diluted if required to be close to the target concentration for the analytical run (25 ppb or 50 ppb).

Finally, procedural blanks were also monitored for every batch of columns used in this thesis, and were typically small (mean = 47 pg; n = 20; Figure 4). The size of the procedural blank showed a subtle decrease over the course of the analysis period, correlating with column batch number (a proxy for time) at a 90 % significance level ($r = 0.4$, $p = 0.06$; Figure 4). The origin of this decrease is uncertain. Conversely, procedural blank δ^{11}B showed no visual systematic change over time and was not significantly correlated with column batch number ($r = 0.2$, $p > 0.3$; Figure 4). Implied blank corrections using the long-term average procedural blank δ^{11}B (— 8 ± 31 ‰; 2 σ) were ≤ 0.12 ‰ for all samples aside from one replicate of calcitic sample Erfe04ac (implied correction + 0.28 ‰). The correction for this sample was larger owing to its small [B] (resulting both from its calcitic mineralogy and small sample size), rather than high [B] in the respective procedural blank. Owing to the small magnitude of - and large uncertainty in – implied blank corrections, I chose not to correct sample δ^{11}B for this effect.
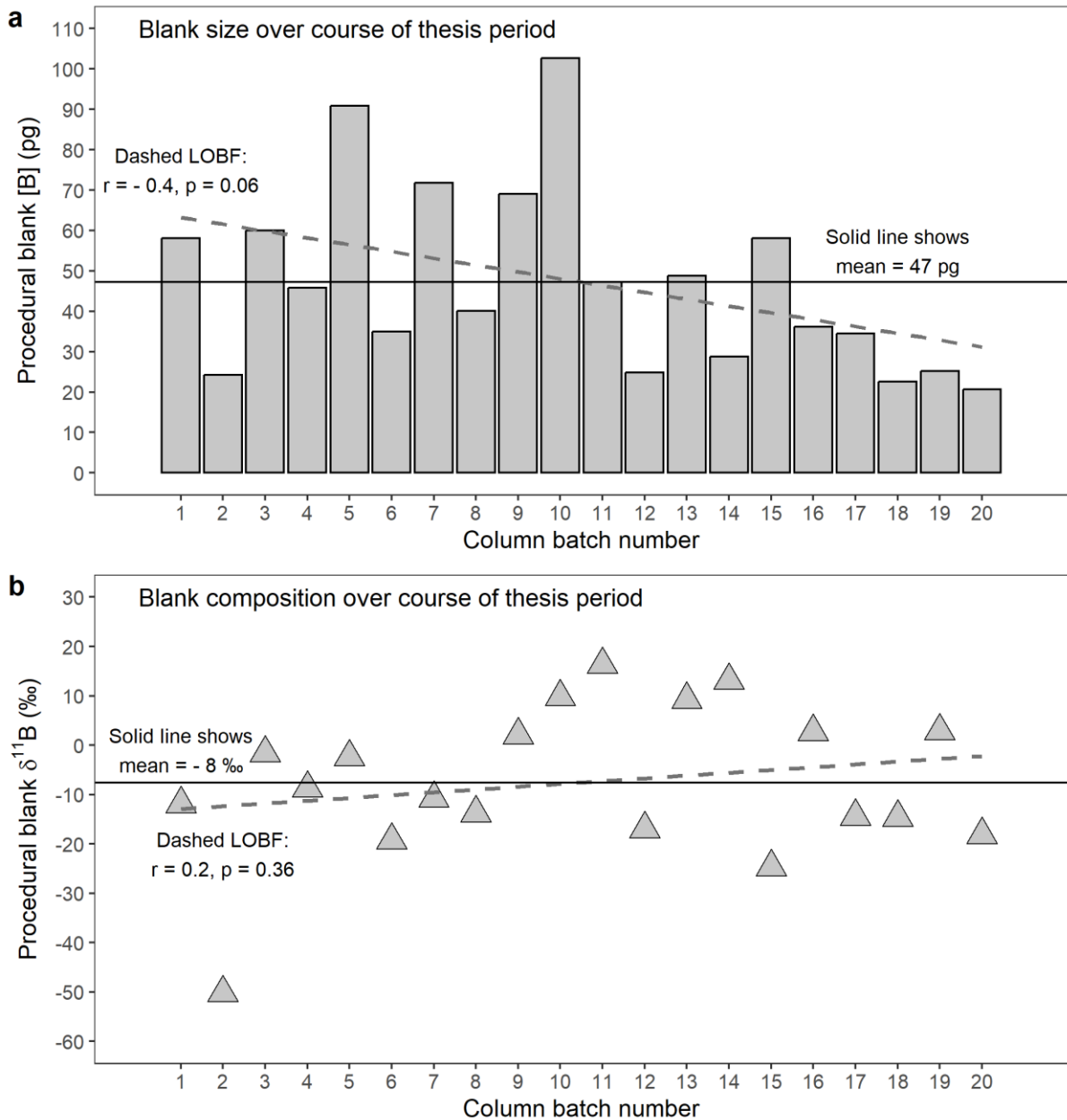
Figure 4. a) [B] and b) δ^{11}B, measured in procedural blanks associated with samples presented in this thesis. Solid lines show mean values, dashed lines show representative linear fits of the correlations with column batch number (Pearson r and p values indicated in each plot).

4.2.2 Sample analysis

Once quality control was complete, sample δ^{11}B was measured and reported relative to NIST SRM 951 (Foster, 2008; Rae et al., 2018), given by the equation:

$$\delta^{11}B_{sample}\ (‰) = \frac{\left(\frac{^{11}B}{^{10}B}\right)_{sample} - \left(\frac{^{11}B}{^{10}B}\right)_{NIST951}}{\left(\frac{^{11}B}{^{10}B}\right)_{NIST951}} \times 1000 \qquad (1)$$

Samples, standards, blanks and wash solutions were introduced in mixed 0.5 M HNO_3 and 0.3 M HF, and the prewash solution in a slightly higher [HF] (0.5 M HNO_3 and 0.9 M HF), to prevent excessive build-up of boron in the introductory system (following Rae et al., 2018; Zeebe and Rae, 2020). This so-called boron memory effect is well-established, and results from volatilisation of boric acid in the spray chamber, coating the inside of the spray chamber and contributing to measured boron in later samples (Al-Ammar et al., 1999). A number of solutions have been proposed to this problem, including introducing samples with a small amount of ammonia gas (Al-Ammar et al., 2000; Foster, 2008) and introducing samples in 0.3 M HF (Misra et al., 2014). The option chosen here is to introduce samples in mixed 0.5 M HNO_3 and 0.3 M HF, with the HF added after column chemistry immediately prior to sample analysis (Rae et al., 2018). The rationale behind introducing samples in an HF matrix is that boron will form fluoroboric acid ($HBF_4.H_2O$), which is highly water soluble and has a boiling point > 100 °C, meaning it will not be volatile under normal measurement conditions (Misra et al., 2014). Using HF only at the final step of sample preparation is preferred because this reduces the use of HF in the laboratory.

Intensities of ^{11}B and ^{10}B in blanks, bracketing standards and samples were measured simultaneously on Faraday cups H3 and L3, respectively, with the signal amplified by either two 10^{12} Ω amplifiers or – later in the analysis period – two 10^{13} Ω amplifiers. In practise, the choice of amplifiers used made no difference to the quality (i.e. precision and accuracy) of sample measurements, except at very low [B] (see section 4.2.4). Measurements were carried out using 30 cycles, with a 4 s integration time and a 2 minute wash cycle between each measurement (Table 6). Intensities of both isotopes measured on samples and standards were corrected for background using blanks measured every three samples. Background corrections were always < 1 %. Each sample was bracketed by measurements of NIST SRM 951, and $\delta^{11}B$ values derived by normalisation to this standard (Foster, 2008). This procedure corrects for variable instrumental mass fractionation, which changes both between and - to a lesser extent – during analytical sessions (e.g. Foster, 2008; Guerrot et al., 2011; see section 4.2.3; Figure 6).

Analytical reproducibility and accuracy were assessed using repeat measurements of two reference materials: boric acid standard BAM ERM-AE121 (Vogl and Rosner, 2012) and NIST RM 8301 (Coral) (Stewart et al., 2020) (Figure 5). BAM ERM-AE121 was used to monitor instrument performance, and repeat measurements yielded an average value of 19.61 ‰ ± 0.15 (n = 36; 2 σ; measurement period October 2019 to February 2023). This long-term value is in excellent agreement with the current interlaboratory consensus value of 19.64 ‰ ± 0.17 (Stewart et al., 2020; revised from Vogl and Rosner, 2012; Figure 5). The reproducibility and accuracy of BAM ERM-AE121 measurements was consistent over the course of the analysis period. Samples were measured in two main periods: a semi-continuous period from October 2019 to August 2021, followed by a second continuous period from June 2022 to February 2023. The average BAM ERM-AE121 values from these two periods are indistinguishable and have similar reproducibility, indicating consistent instrument performance over the course of the thesis period (Figure 5; 2019 to 2021: 19.62 ± 0.12 (2 σ) ‰, 2022 to 2023: 19.58 ± 0.11 (2 σ) ‰).

Repeat measurements of NIST RM 8301 (Coral) were used to monitor performance of the entire analytical procedure (column chemistry through to sample measurement). It is worth noting that the reproducibility estimate derived from repeat measurements of NIST RM 8301 (Coral) does not account for variability introduced by sample collection, cutting, cleaning and dissolution techniques. These yielded an average value of 24.18 ± 0.29 ‰ (n = 34; 2 σ; measurement period October 2019 to February 2023), in good agreement with both the interlaboratory consensus value (24.17 ‰; Stewart et al., 2020; Figure 5) and the value reported for the previously published stylasterid dataset used in this compilation (24.27 ± 0.16 ‰; Stewart et al., 2022).

Unlike BAM ERM-AE121, the reproducibility of NIST RM 8301 (Coral) improved over the course of the analysis period. In the period from October 2019 to August 2021, the average value was significantly higher and more variable than that from the period encompassing June 2022 to February 2023 (Figure 5; 2019 to 2021: 24.27 ± 0.33 (2 σ) ‰, 2022 to 2023: 24.11 ± 0.16 (2 σ) ‰). The cause of this difference is unclear, as outlined in the following discussion.

Firstly, as outlined in more detail in section 4.2.3, a number of air leaks in the instrument were fixed in the period between August 2021 and June 2022. If these repairs were the cause of improved NIST RM 8301 (Coral) reproducibility, one would expect to see a similar improvement for the BAM ERM-AE121 reference material. However, BAM ERM-AE121 exhibits similar reproducibility across both periods, in turn suggesting that improved instrumental performance is not the root cause of improved NIST RM 8301 (Coral) reproducibility.

Improvements in reproducibility also cannot be explained by changes in the size and/or composition of procedural blank contributions. As shown in Supplementary figure 1, the difference in reproducibility between the two time periods identified remains robust after correcting each NIST RM 8301 (Coral) for its respective procedural blank (i.e. the size and composition of the blank specific to the relevant column batch; Supplementary figure 1).

The shift in reproducibility also does not correlate with either replenishment of the column resin or any change in matrix-removal efficacy (assessed by the Na-screening procedure outlined in section 4.2.1). Instead, it is notable that the step change in NIST RM 8301 (Coral) reproducibility aligns with a change in the column chemistry procedure, and specifically the proportion of NIST RM 8301 (Coral) stock solution to Na-acetate buffer loaded onto the columns. For the 2019 to 2021 period, 3 µL of NIST RM 8301 (Coral) was loaded onto columns, mixed with 60 µL buffer (1:20 standard:buffer ratio). However, for the period 2022 to 2023, 3 µL NIST RM 8301 (Coral) was mixed with 45 µL buffer (1:15 standard:buffer ratio). This observation could suggest that the boron column chemistry procedure is sensitive to the ratio of solution:buffer, and that over-buffering may lead to variable boron isotopic fractionation. This may be consistent with the observed pH and ionic strength controls on the boron partition coefficient of the Amberlite IRA 743 resin (Lemarchand et al., 2002), or with larger volumes of liquid passing through columns more quickly, resulting in variable boron recovery (e.g. Stewart et al., 2020). However, the

change in buffer:sample ratio is small, and it thus seems unlikely that this is the origin of the variable NIST RM 8301 (Coral) reproducibility observed.

The origin of the change in NIST RM 8301 (Coral) reproducibility is unclear. Fortunately, the difference between NIST RM 8301 (Coral) values measured in each period is small, and both values are accurate to within 0.1 ‰ of the interlaboratory consensus value (Figure 5). When coupled with consistently good instrument performance (assessed by BAM ERM-AE121), our low procedural blanks and effective matrix removal screening (section 4.2.1), we have high confidence in our measurements of coral sample $\delta^{11}B$. The question remains as to which measurement period is most representative of our coral samples, and thus which reproducibility to use as the analytical error. Given the robust difference between the two periods, I choose to assign each sample the appropriate reproducibility for the period it was measured in (see values in Figure 5).
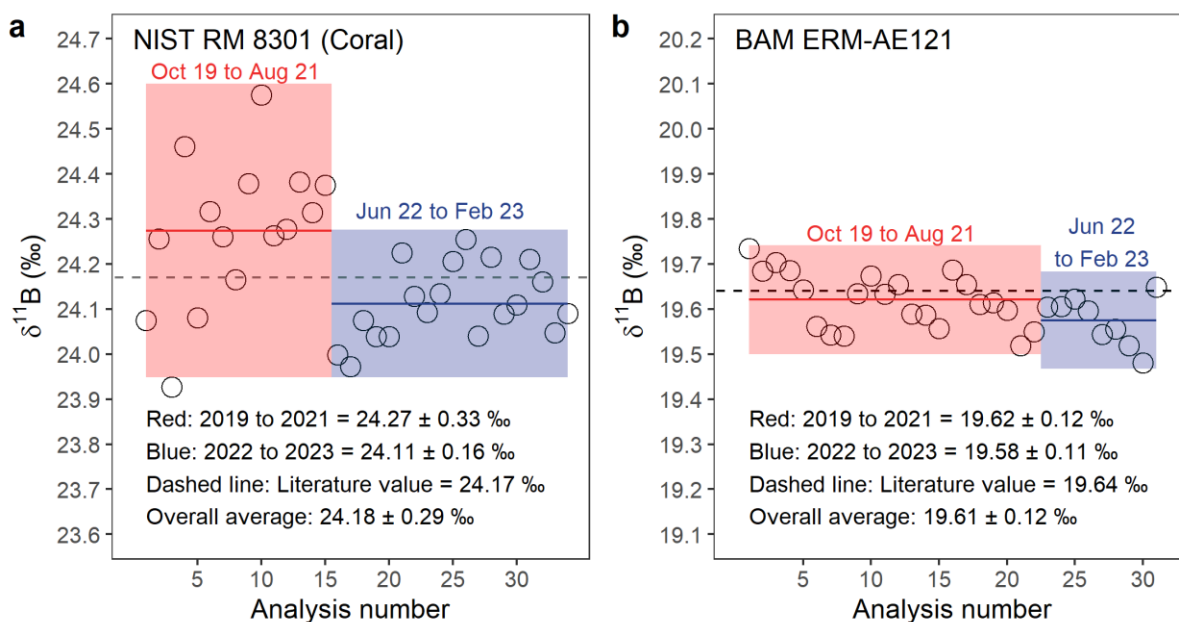
Figure 5. Reproducibility of boron isotopic standards a) NIST RM 8301 (Coral) (Stewart et al., 2020) and b) BAM ERM-AE121 (Vogl and Rosner, 2012). Red and blue shading represents two semi-continuous analysis periods from October 2019 to August 2021 (red) and June 2022 to February 2023 (blue). Solid lines are the long-term laboratory averages for each period, shading indicates precision ($\pm 2\sigma$). Dashed lines show current interlaboratory consensus values, both taken from Stewart et al. (2020).

4.2.3 Ratio stability during analytical sessions

As alluded to in section 4.2.2, boron isotopic mass fractionation (i.e. the measured $^{11}B/^{10}B$ ratio of a given solution) can vary significantly between instruments, laboratories and over time, necessitating the use of a bracketing standard (NIST SRM 951) against which sample $\delta^{11}B$ values are reported. However, obtaining $\delta^{11}B$ values in this manner requires minimal variation in instrumental mass fractionation over the time period of analysis (i.e. for a single sample, the measurements of blanks, the sample itself and bracketing

standard NIST SRM 951) (Foster, 2008). For the analytical setup employed here, this equates to requiring mass fractionation stability over the course of ~ 60 minutes.

Factors affecting the stability of instrumental mass fractionation include the sample gas flow rate (Foster, 2008), time between switching the plasma on and analysis (Guerrot et al., 2011) and, through experience, the torch z position and RF power used (in practise, the torch z position, RF power and sample gas flow rate all interact). Further, the most stable $^{11}B/^{10}B$ ratio generally does not occur at the range of conditions which also lead to maximum instrument sensitivity (Foster, 2008; Figure 6). Therefore, prior to each analytical session, the instrument was tuned for the most stable sample gas flow rate, by increasing the sample gas in small steps (0.01 L/min) and measuring the $^{11}B/^{10}B$ ratio (Figure 6). The sample gas flow rate used for the analytical session was chosen to optimise ratio stability, and the blank-corrected $^{11}B/^{10}B$ of NIST SRM 951 monitored over the course of every analytical session. In general, two stability plateaus were identified during each sample gas test (Figure 6). Through experience, it was found that the plateau at higher sample gas flow rates gave better within-run stability than the plateau at lower flow rates.

Stability for all samples presented in this thesis was generally good, however over the course of the thesis period, significant problems with ratio stability were encountered (Figure 6). The root cause of these problems was never fully identified, and was likely a combination of multiple factors. After identifying and fixing leaks in the torch, introductory system tubing (i.e. sample gas, waste line) and internal instrumental tubing, stability was improved markedly (Figure 6).
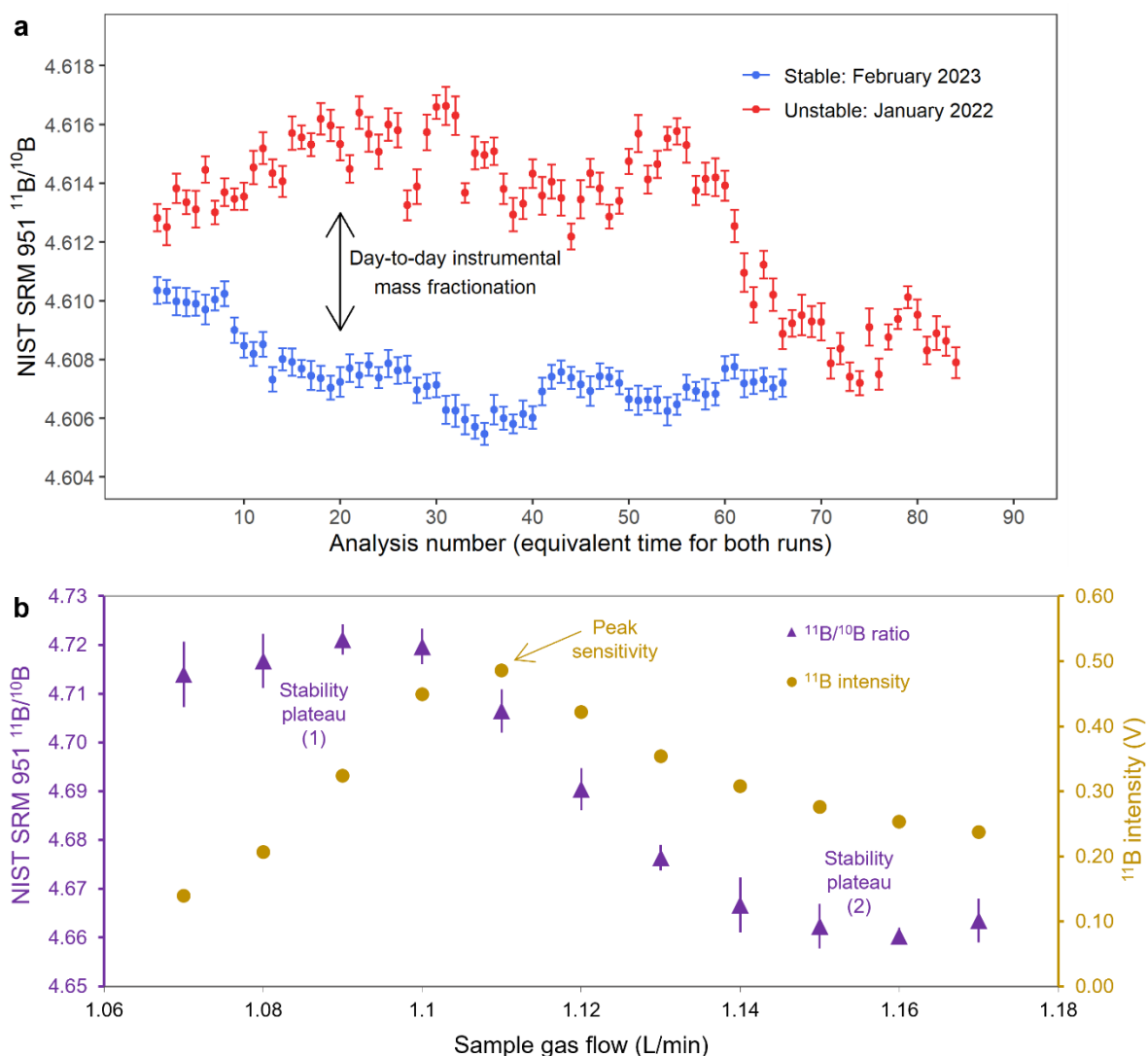
Figure 6. Effects of introduction system air flows on instrumental mass fractionation and $^{11}B/^{10}B$ ratio stability. A) Blank-corrected NIST SRM 951 $^{11}B/^{10}B$ ratios from a stable (blue) and unstable (red) analytical session. Analysis numbers for each session are directly comparable in terms of time from start of session. Error bars are ± 2 SE on the 30 measured cycles. B) NIST SRM 951 $^{11}B/^{10}B$ ratios (red triangles) and ^{11}B intensity (blue circles) as a function of sample gas flow rate.

4.2.4 Effect of amplifier choice on measurement precision and techniques

Boron isotope measurements presented in this thesis were initially made using $10^{12}\,\Omega$ amplifiers attached to both cups (H3 and L3). However, in early 2021, the Bristol Isotope Group replaced these with newly purchased $10^{13}\,\Omega$ amplifiers. Unfortunately, the nature of the straight swap of these amplifiers meant I could not do a like-for-like comparative test. However, a number of $10^{11}\,\Omega$ amplifiers remained fitted to the Neptune, permitting comparison of 10^{11} and $10^{13}\,\Omega$ amplifier performance.

I therefore measured NIST SRM 951 bracketed against itself (i.e. theoretical $\delta^{11}B = 0$ ‰) at concentrations ranging from 1 ppm to 50 ppb, using three separate amplifier configurations (Table 7):

using 10^{13} Ω amplifiers to measure both ^{11}B (cup H3) and ^{10}B (cup L3),

using 10^{11} Ω amplifiers to measure both ^{11}B and ^{10}B, and

using a 10^{11} Ω amplifier to measure ^{11}B and a 10^{13} Ω amplifier to measure ^{10}B.

Concentration	H3: 10^{13} Ω & L3: 10^{13} Ω			H3: 10^{11} Ω & L3: 10^{13} Ω			H3: 10^{11} Ω & L3: 10^{11} Ω		
	$\delta^{11}B$ NIST SRM 951 (‰)	± 2SE (‰)	n	$\delta^{11}B$ NIST SRM 951 (‰)	± 2SE (‰)	n	$\delta^{11}B$ NIST SRM 951 (‰)	± 2SE (‰)	n
1 ppb	0.30	0.19	5	0.28	0.40	6	0.82	1.30	6
5 ppb	-0.02	0.13	6	0.16	0.11	6	0.19	0.34	6
10 ppb	-0.04	0.10	6	0.07	0.09	6	-0.07	0.20	6
15 ppb	0.02	0.08	6	0.04	0.09	6	0.12	0.11	6
25 ppb	0.06	0.03	6	0.04	0.09	6	-0.08	0.12	6
50 ppb	-	-	-	-0.01	0.05	6	-0.05	0.05	6

Table 7. Reproducibility of NIST SRM 951 $\delta^{11}B$ measurements as a function of [B], using different amplifier combinations.

Each concentration was measured 5 or 6 times in each configuration, and the standard error (± 2SE) used to assess analytical performance. All measurements were made in the same analytical session (i.e. without turning the plasma off), to minimise run-to-run variability in instrument performance. Finally, the maximum potential difference measurable on 10^{13} Ω amplifiers is 0.05 V (or 0.5 V on the Neptune display, which displays voltages as though they are measured across 10^{11} Ω resistors), and therefore NIST SRM 951 was not measured at 50 ppb as intensities for ^{11}B this exceeded that limit.

The performance of all three amplifier combinations was largely equivalent at [B] = 15, 25 and 50 ppb (Table 7). It was only at low [B] (i.e. < 10 ppb) that the advantages of using 10^{13} Ω amplifiers became clear, with vastly improved measurement precision. The average sample [B] measured in this thesis was 48 ppb, meaning that the advantages of changing to 10^{13} Ω amplifiers were, in general, minimal. However, some samples were measured at lower [B], with the lowest presented here measured at 9 ppb. 5 repeat measurements of NIST RM 8301 (Coral) at [B] between 5 and 8 ppb yielded a mean average $\delta^{11}B$ of 24.03 ± 0.50 ‰ (n = 5; 2 σ). This is within error of both the robust interlaboratory consensus value (Stewart et al., 2020) and the long-term average value derived from measurements at 50 ppb [B] from this thesis (section 4.2.2), suggesting that the small number of low [B] measurements presented here are robust.

Notably, initial problems were found when using 10^{13} Ω amplifiers during the paired checks for the [B] in each sample and removal of the carbonate matrix by monitoring ^{23}Na intensity (see section 4.2.1). When 10^{12} Ω amplifiers were used, ^{11}B was initially measured on cup H3, before the beam was moved to measure ^{23}Na on the centre cup. However, when using the 10^{13} Ω amplifiers, it was observed that during this beam switch, a transient pulse of signal would appear on cup H3, which measured multiple volts (normalised to 10^{11} Ω resistors) in intensity. This pulse of signal was likely due to a major ion (e.g. related to H_2O) with mass between ^{11}B and ^{23}Na being passed over cup H3 during the beam movement, and was only seen on 10^{13} Ω amplifiers due to their faster response time. In turn, this signal would take multiple minutes to decay (since it far exceeded the 0.5 V intensity limit for 10^{13} Ω amplifiers) potentially impacting on the next measurements of [B]. To address this, we therefore switched to measuring both ^{11}B and ^{23}Na intensities using a 10^{11} Ω amplifier on the centre cup. An alternative solution would be to write the ^{23}Na and ^{11}B intensity measurements as separate method files and sequence lines, as the switch between methods/sequence lines results in a shut down of the extraction voltage during beam switching. Conversely, the extraction voltage is not switched off when the two measurements are made in a single method, as was the case for our chosen method.

4.2.5 The importance of torch box extraction for blank control

Finally, as outlined in section 4.2.2, controlling boron background levels requires careful consideration. However, to the best of my knowledge, the importance of effectively extracting air from the instrument torch box to control boron background levels has never been demonstrated. During one analytical session in early 2020, the boron background levels increased quickly and plateaued at an unusually high level (52eviati. 1.8 % of sample intensity; samples at 50 ppb; Figure 7). It was observed that the blank could be reduced after prolonged periods in the wash solution, suggesting that this build-up was not due to contamination of the solutions or introductory system being used. Instead, it was observed that opening the doors of the torch box reduced the background levels slightly, and further that ventilating the torch box by pointing a desk fan into the torch box very quickly reduced background boron intensity to acceptable levels (Figure 7). I then confirmed that the air extraction which normally ventilates the torch box (arrow A in Figure 7) was indeed broken, and fixing this returned the background to normal levels. Therefore, ventilation of the torch box is key to controlling boron background levels, and intriguingly suggests that volatilised boron accumulates in the torch box. While the desk fan approach proved a useful demonstration of this effect, I do not recommend it for every-day Neptune operation as plasma conditions are extremely unstable under this turbulent air flow.
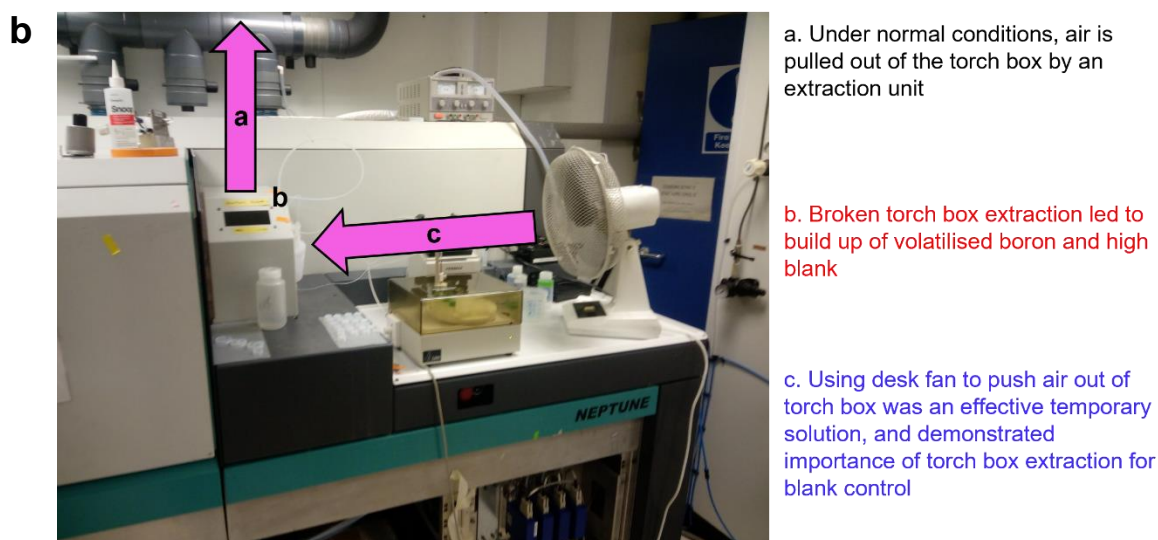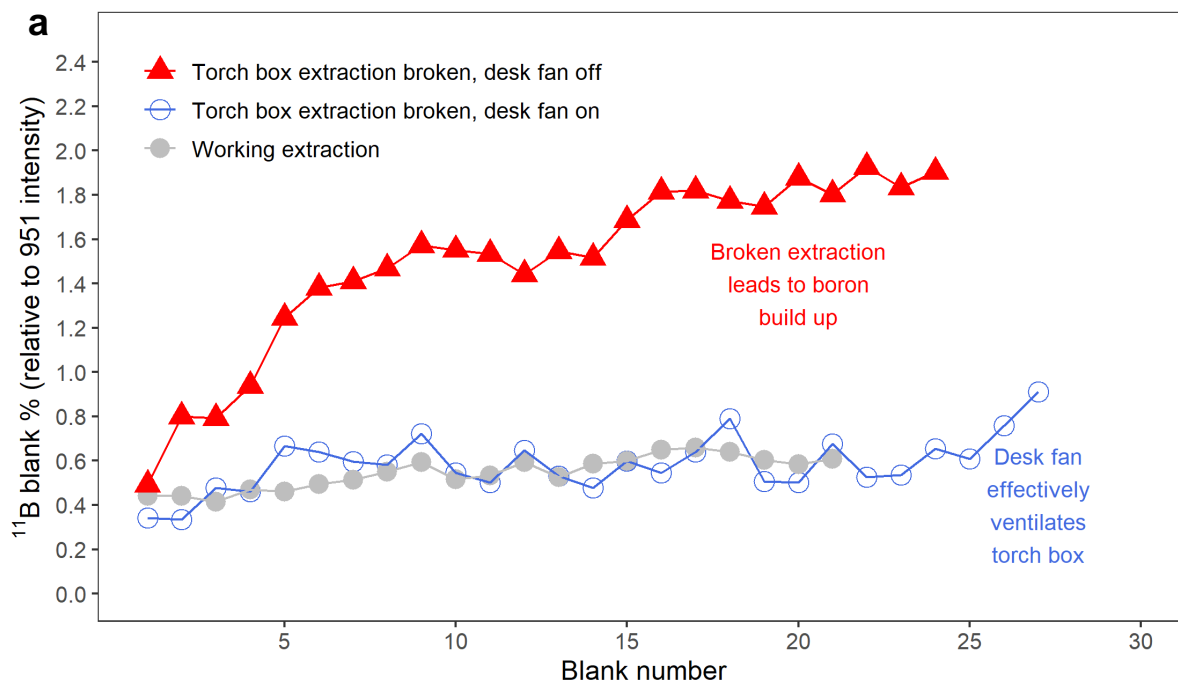
Figure 7. a) Graph showing the effects of various methods of torch box ventilation on boron background intensities. Background levels are shown as % ^{11}B intensities relative to NIST SRM 951 measured at [B] = 50 ppb. Blank numbers are directly comparable representations of time for each run. B. Labelled photo of set up showing "working" torch box extraction (arrow a) and the desk fan trial (arrow c) used in this study.

5. U-series dating methods

A number of coral samples were dated by U-series isotope dilution methods in chapter 5 of this thesis. The following methods describe the chemical sample cleaning, sample dissolution, separation of U and Th fractions and analytical methods applied, which were common to all samples (with the exception of cleaning procedures, see chapter 5). The statistical methods associated with the calculation of U-series ages and $\delta^{234}U$ ratios are briefly introduced, with more detailed discussion provided in chapter 5.

5.1   Sample cleaning and separation of U and Th fractions

Approximately 150 mg of each sample was obtained, and in most cases cleaned using established oxidative and reductive techniques (Cheng et al., 2000a; Shen and Boyle, 1988; Adkins et al., 2002; see chapter 5 for exceptions). The full cleaning procedure is outlined in Table 8. Separation and purification of the U and Th in coral skeletons followed established procedures which have been described elsewhere (e.g. Edwards et al., 1987; Burke and Robinson, 2012; Chen et al., 2015). The full procedure is summarised in Table 9, and can be broken down into the following constituent steps. First, cleaned samples were dissolved in 7.5 M HNO_3, and spiked gravimetrically with a $^{236}U – ^{229}Th$ mixed spike, the $^{236}U/^{229}Th$ ratio of which is known to within $\pm$ 4.1 ‰ (2 σ) (Burke and Robinson, 2012; spike addition step in Table 9). After drying the sample down and redissolving in 2 M HCl, U and Th were removed from the carbonate matrix by co-precipitation with Fe hydroxides (Chen et al., 1986; Edwards et al., 1987; Fe coprecipitation step in Table 9). Finally, samples were redissolved in 7.5 M HNO_3, the U and Th fractions separated by anion-exchange column chemistry (Edwards et al., 1987; Burke and Robinson, 2012; Chen et al., 2015; column chemistry step in Table 9), before dissolution in 1.2 M HNO_3 (+ 0.08 M HF, for the Th fraction) ready for analysis (measurement step in Table 9).

	Step	Time	Repeats
1	Milli-Q rinse with ultrasonication	20 minutes	1
2	Oxidising solution* with ultrasonication	20 minutes	1
3	Milli-Q		3
4	Milli-Q with ultrasonication	1 minute	2
5	Perchloric solution** with ultrasonication	1 minute	1
6	Milli-Q		3
7	Milli-Q with ultrasonication	1 minute	2
8	Milli-Q rinse with ultrasonication	20 minutes	1
9	Oxidising solution with ultrasonication	20 minutes	1
10	Milli-Q		3
11	Milli-Q with ultrasonication	1 minute	2
12	Methanol with ultrasonication	20 minutes	1
13	Milli-Q		2
14	Milli-Q with ultrasonication	1 minute	2
15	Perchloric solution with ultrasonication	1 minute	1
16	Milli-Q		3
17	Milli-Q with ultrasonication	1 minute	2
18	Milli-Q	1 minute	3
19	Methanol with ultrasonication	20 minutes	1
20	Milli-Q		2
21	Milli-Q with ultrasonication	1 minute	1
22	0.2 % HNO_3 with ultrasonication	1 minute	1

	Step	Time	Repeats
23	Milli-Q		2
24	Milli-Q with ultrasonication	1 minute	1
25	Oxidising solution with ultrasonication	20 minutes	1
26	Milli-Q		2
27	Milli-Q with ultrasonication	1 minute	2
28	Reducing solution*** with ultrasonication	20 minutes	1
29	Milli-Q		2
30	Milli-Q with ultrasonication	1 minute	2
31	Oxidising solution with ultrasonication	20 minutes	1
32	Milli-Q		2
33	Milli-Q with ultrasonication	1 minute	2
34	0.2 % HNO_3 with ultrasonication	1 minute	1
35	Milli-Q		2
36	Milli-Q with ultrasonication	1 minute	2
37	EDTA solution**** with ultrasonication	20 minutes	1
38	Milli-Q with ultrasonication	1 minute	2
39	Transfer to acid-cleaned plastic vial		
40	0.2 % HNO_3 with ultrasonication	20 minutes	1
41	Milli-Q		2

*Oxidising solution = 1:1 mixture of 30 % H_2O_2 and 1 M NaOH

**Perchloric solution = 1:1 mixture of 30 % H_2O_2 and 1 % $HClO_4$

***Reducing solution = 3.5 % hydrazine in 1:1 mixture of NH_4OH and citric acid (30 g powder in 250 mL solution)

****EDTA solution = 1:1 mixture of 2 M NaOH and EDTA solution (3.7 g powder in 55 mL Milli-Q)

Table 8. Chemical cleaning procedures for U-series and radiocarbon dating. Method includes oxidative (white shading) and reductive (grey shading) steps.

Step		Procedure
Spike addition	1	Weigh sample in clean Teflon beaker
	2	Dissolve in 7.5 M HNO_3 (2 mL)
	3	Add 1 drop of ^{236}U-^{229}Th spike per 100 mg coral sample (1 drop ~ 0.0025 g)
	4	Dry down
Fe coprecipitation	1	Dissolve sample in 2 M HCl (15 mL)
	2	Reflux at 150 °C for 2 hours
	3	Transfer to 50 mL centrifuge tube
	4	Add 2 drops of concentrated $FeCl_2$ solution
	5	Add concentrated NH_4OH solution dropwise and shake until solution changes from yellow to clear and rust precipitate forms
	7	Centrifuge for 5 to 10 minutes, decant and discard supernatant
	8	Rinse × 2 with 15 mL pH 8 Milli-Q (adjust pH by addition of NH_4OH)

Step		Procedure
	9	Transfer sample to original Teflon beaker, dissolve in minimum volume of concentrated HNO_3
	10	Dry sample down, redissolve in minimum volume of concentrated HNO_3
	11	Repeat step 10
	12	Dry sample down, redissolve in 2 M HNO_3 (2 mL)
Column chemistry	1	Fill Environmental Express R1010 columns (12.9 cm length, 9.3 mm inside diameter) with a 0.5 mL thick bed of organic anionic exchange resin (eichrom, 1x8, 100-200 mesh) topped with 2 mL thick bed of pre-filter resin (TRISKEM PF-B100-A, 100-150 μm particle size)
	2	Clean anion exchange resin: fill with 10 M HCl (TM grade), rinse × 2 with Milli-Q. Add 10 mL 10 M HCl (distilled), rinse × 2 with Milli-Q. Add 10 mL 7.5 M HNO_3 (distilled), rinse × 2 with Milli-Q
	3	Condition resin: 2 × 5 mL 7.5 M HNO_3 (distilled)
	4	Load samples
	5	Collect Nd fraction*: 2 × 4 mL 7.5 M HNO_3 (distilled)
	6	Collect Th fraction: add 10 M HCl (distilled) as: 1 × 0.5 mL, 1 × 2 mL, 1 × 4 mL
	7	Collect U fraction: add Milli-Q as: 2 × 2 mL, 2 × 4 mL
	8	Dry down samples
Measurement	1	Dissolve samples in 0.1 mL HNO_3 + 0.1 mL H_2O_2 (concentrated)
	2	Add 1 drop (~ 0.0025 g) pure ^{236}U spike to Th fraction
	3	Reflux all samples overnight, dry down
	4	Redissolve in concentrated HNO_3 (minimum volume), dry down
	5	U fraction: redissolve in 1 mL 1.2 M HNO_3
	6	Th fraction: redissolve in 0.6 mL 1.2 M HNO_3 + 0.08 M HF
	7	Reflux all samples for 2 hours

*Nd fractions collected during column chemistry but not measured.

Table 9. Procedures for U and Th separation prior to isotopic analysis.

5.2 Analytical techniques

U and Th fractions were measured separately on a Thermo Neptune Multicollector ICP-MS at the University of Bristol, following established methods (For U: Robinson et al., 2002; for Th: Burke and Robinson, 2012; Chen et al., 2015).

Samples were introduced into the instrument using a CETAC Aridus, and the instrument was tuned for maximum sensitivity by adjusting the torch position and argon (sweep) and nitrogen gas flow rates. Nitrogen gas flows were then adjusted to minimise oxide production, which was assessed by the comparison of UO at mass 254 to ^{238}U intensities, and was always < 0.005 %. Equipment and instrument settings are summarised in Table 10.

For U, intensities of [235]U, [236]U and [238]U were measured using Faraday cups with 10^{11} Ω amplifiers, while [234]U intensities were measured on a Secondary Electron Multiplier Ion Counter (SEM IC). Note that at the start of each session, the [234]U concentration of each sample was measured against a standard of known concentration, and samples diluted to ensure counts of [234]U did not exceed the ion counter limit. Blanks (1.2 M HNO_3) were measured either side of each sample, and measured sample intensities corrected accordingly. As is standard practise for U-series measurements, mass bias and detector yield (i.e. relative efficiencies of the SEM IC and Faraday cups) corrections were carried out by normalising measured sample isotope ratios to international bracketing standard U112a, measured before and after each sample (average of each U112a measurement used to derive correction factor) (e.g. see Boulyga et al., 2016). It is notable that since U112a doesn't include [236]U, the correction for [236]U isotopic ratios is based on that for [235]U/[238]U, using the ratio between measured and natural [235]U/[238]U. For Th, [232]Th intensities were measured on a Faraday cup using a 10^{11} Ω amplifier, while [229]Th and [230]Th were measured using a SEM IC by peak hopping (Burke and Robinson, 2012; see cup sub-configurations in Table 10). Intensities were again corrected for blanks (1.2 M HNO_3 + 0.08 M HF), with mass bias and detector efficiency corrections carried out by normalisation to Th standard SGS. Again, correction factors were based on the average of the Th SGS measurements made before and after each sample. The procedure of peak hopping means that [229]Th and [230]Th intensities were not measured simultaneously, leading to the possible introduction of analytical uncertainties owing to signal instability. Therefore, a pure [236]U spike was added to Th fractions after column chemistry (Table 9), and [236]U simultaneously measured on a Faraday cup (10^{11} Ω amplifier). The [229]Th/[236]U and [230]Th/[236]U ratios were then used to derive [229]Th/[230]Th ratios, normalised for signal instability (Burke and Robinson, 2012).

For both U and Th isotopic measurements, some authors have carried corrections for the effects of peak tailing using a variety of methods (e.g. Cheng et al., 2013; Kerber et al., 2023). Here, however, no tailing corrections are applied, since the effects of peak tailing on our results are likely minor. Considering U, firstly, no accurate measurements of peak tailing were made during this thesis, making quantification of the possible effects of tailing difficult. However, the abundance sensitivity of the instrument (assessed by measuring the tail of the [238]U peak at [237]U) was checked prior to each analytical session and was always < 3 ppm. By assuming an abundance sensitivity of 3 ppm at [237]U, we use previously recorded tailing patterns to estimate the magnitude of the effect of [238]U peak tailing on our measurements. Cheng et al. (2013) record a typical abundance sensitivity (also measured on a Thermo Neptune ICP-MS) of ~ 2 ppm at [237]U, ~ 0.8 ppm at [236]U and ~ 0.4 ppm at [234]U. Assuming the ratio of abundance sensitivity measured at [237]U here and in Cheng et al. (2013) remains the same across the entire mass range (i.e. that the [238]U tail is a factor 50 % larger at all masses in our study), the beam sizes typical of the samples measured in this thesis ([238]U ~ 15 V; [236]U ~ 0.05 V; [234]U ~ 0.0006 V (i.e. ~ 40,000 cps)) suggest the [238]U tail contributes 0.04 % of the total measured [236]U beam and ~ 0.7 % of the total measured [234]U beam. Therefore, the effects of peak tailing on U-series isotope measurements are apparently minor, and we note these will be further reduced for [234]U by sample-standard bracketing.

Considering Th, studies measuring Th isotopes in seawater and shallow-water corals may correct for the effects of the tail of the ^{232}Th peak on ^{229}Th and ^{230}Th (e.g. Shen et al., 2008; Auro et al., 2012). However, the ^{230}Th/^{232}Th ratios of deep-sea coral samples are generally significantly larger (e.g. Edwards et al., 2003), and U-series dating of azooxanthellate corals is routinely carried out without correcting for ^{232}Th tailing (e.g. de Carvalho Ferreira et al., 2022). Here, no measurements of abundance sensitivity were made for Th isotopes, however all measured ^{232}Th beams were < 1 V while ^{230}Th/^{232}Th ratios were generally > 10^{-4} (or close to this threshold, even for uncleaned isochron samples). The effects of ^{232}Th tailing are known to be minimal at these ^{230}Th/^{232}Th ratios (e.g. < 1 ‰ in Hoffmann et al., 2007), supporting the assumption made here that no tailing correction is required (e.g. Hoffmann et al., 2007; Cheng et al., 2013). As for U, any effects of ^{232}Th peak tailing will be further reduced by sample-standard bracketing.

Internal reproducibility was assessed using repeat measurements of reference materials during each analytical session. For the analytical sessions presented here, measurements of the ^{234}U/^{238}U ratio of the Harwell uraninite reference material (HU-1) and the ^{230}Th/^{229}Th ratio of the ThB reference material (Auro et al., 2012) yielded internal precision better than 0.14 % (RSD; 2 σ). The efficacy of the full analysis procedure (including column chemistry) was assessed using HU-1, which was processed through column chemistry with each batch of samples. The small number of repeat measurements carried out here yielded an average ^{230}Th/^{238}U activity ratio of 0.9948 ± 0.0041 (2 σ; n = 4). The small number of measurements means it is uncertain whether this slight deviation from secular equilibrium is significant, although we note that this would be consistent with other studies (Hoffmann et al., 2007; Cheng et al., 2013).

Equipment/Condition	Type/comment
Sample introduction	CETAC Aridus, 50 µL/min nebuliser
Injector	Quartz
Sampler cone	Ni – standard
Skimmer cone	Ni – X
Cup configuration	U: ^{234}U on central SEM, ^{235}U on cup H1, ^{236}U on H2, ^{238}U on H3
	Th: Sub-config. 1*: ^{230}Th on central SEM, ^{232}Th on cup H1, ^{236}U on H3
	Th: Sub-config. 2: ^{229}Th on central SEM, ^{232}Th on cup H2, ^{236}U on H4
Detectors used	^{234}U, ^{229}Th and ^{230}Th on SEM, all others Faraday Cup with 10^{11} Ω resistor
RF power	1200 W
Tuning	Parameters typically tuned for sensitivity: Aridus gas flow rates, torch position (x, y, z), sample gas, the focus, x-deflection, y-deflection and shape lenses.
	Parameters tuned for peak shape: shape lens, focus quad
Cycles per measurement	U: 100
	Th: 50 for each sub-configuration*
Integration time per cycle	4 s
Resolution	Low

| Take-up time | 70 to 90 s (variable dependent on sample gas) |
| Wash time | 240 s |

*Th isotopic analysis involved peak-hopping between two cup sub-configurations, as outlined in section 5.2.

Table 10. Equipment and instrument settings used during uranium and thorium isotopic analysis.

5.3 Calculating isotope ratios and ages

The use of a synthetic ^{236}U-^{229}Th spike with precisely determined isotope concentrations permits the calculation of the concentrations of the natural U (^{234}U, ^{235}U, ^{238}U) and Th (^{230}Th, ^{232}Th) isotopes in coral samples, corrected for the contribution from the procedural blank (which was run with every column set). Activity ratios (indicated by square brackets throughout this thesis) for the natural isotopes were then calculated using decay constants chosen to be consistent with those used to calibrate the spike solution used here ($\lambda_{230} = 9.1577 \times 10^{-6}$ a^{-1} (Cheng et al., 2000b); $\lambda_{232} = 4.947500 \times 10^{-11}$ a^{-1}; $\lambda_{234} = 2.8263 \times 10^{-6}$ a^{-1} (Cheng et al., 2000b); $\lambda_{238} = 1.5513 \pm 0.0004 \times 10^{-10}$ a^{-1} (1 σ) (Jaffey et al., 1971)). Errors in λ_{230}, λ_{232} and λ_{234} were assumed negligible, following Cheng et al. (2013).

The activity ratios [^{230}Th/^{238}U] and [^{234}U/^{238}U] can be used to solve for the U-series age equation (Edwards et al., 2003), which is given by:

$$\left[\frac{230Th}{238U}\right] - 1 = -e^{-\lambda_{230}t} + \left(\frac{\delta^{234}U_m}{1000}\right)\left(\frac{\lambda_{230}}{\lambda_{230} - \lambda_{234}}\right)(1 - e^{-(\lambda_{230} - \lambda_{234})t}) \qquad (2)$$

where t is the age since carbonate formation and δ^{234}U$_m$ is defined as the present-day deviation of the ^{234}U/^{238}U ratio from secular equilibrium, calculated as:

$$\delta^{234}U_m\ (\text{‰}) = \left(\left[\frac{234U}{238U}\right] - 1\right) \times 1000 \qquad (3)$$

Application of equation 3 relies on two assumptions. Firstly, this equation requires that all the ^{230}Th measured in the sample has come from decay of ^{238}U (i.e. initial [^{230}Th/^{238}U] = 0). For deep-sea corals, this assumption is generally not appropriate (e.g. Cheng et al., 2000a), and a modified form of the age equation uses ^{232}Th measured in the sample to estimate the initial [^{230}Th/^{238}U] (Edwards et al., 2003):

$$\left(\left[\frac{230Th}{238U}\right] - \left[\frac{232Th}{238U}\right]\left[\frac{230Th}{232Th}\right]_i\left(e^{-\lambda_{230}t}\right)\right) - 1$$

$$= -e^{-\lambda_{230}t} + \left(\frac{\delta^{234}U_m}{1000}\right)\left(\frac{\lambda_{230}}{\lambda_{230} - \lambda_{234}}\right)\left(1 - e^{-(\lambda_{230} - \lambda_{234})t}\right) \qquad (4)$$

where [^{232}Th/^{238}U] is measured and [^{230}Th/^{232}Th]$_i$ is either assumed from seawater values (e.g. Cheng et al., 2000a) or constrained by isochron techniques (e.g. Lomitschka and Mangini, 1999). The estimation of

initial [230]Th in stylasterid coral skeletons and the implications for age uncertainties is the subject of extensive discussion in chapter 5.

The second assumption implicit in the calculation of U-series ages is that the sample has remained in a closed-system state with respect to the U-series decay chain from the time of formation to the time of measurement (Edwards et al., 2003). The initial $\delta^{234}U$ ($\delta^{234}U_i$) criterion is used to test for this assumption here (e.g. Cheng et al., 2000a; Edwards et al., 2003), calculated as:

$$\delta^{234}U_i = \delta^{234}U_m e^{\lambda_{234}t} \qquad (5)$$

where $\delta^{234}U_m$ is the $\delta^{234}U$ of the measured coral sample and t is the time since carbonate formation. The $\delta^{234}U$ value of seawater is thought to vary within a relatively small range over relevant timescales (i.e. $\pm$ 15 ‰; Henderson, 2002). Therefore, samples with $\delta^{234}U_i$ more than 15 ‰ from modern seawater $\delta^{234}U$ (146.8 ‰; Andersen et al., 2010) are considered likely to have undergone open-system processes, and calculated ages are regarded with caution. Again, the susceptibility of stylasterid skeletons to diagenetic alteration and the implications for their dating are discussed in detail in chapter 5.

Equations 2, 3 and 4 were solved using Monte-Carlo approach with 100,000 iterations (e.g. Chen et al., 2015). Analytical uncertainties, uncertainties in instrumental and procedural blank contributions, uncertainties in decay constants, and uncertainties in spike concentrations and masses were propagated through calculations to the point of calculating the number of atoms of each isotope present in each sample. At this point, uncertainties were propagated into activity ratios, ages and $\delta^{234}U$ values by inclusion of error terms in the Monte Carlo simulation. Errors were assigned to quantities during each iteration by multiplying the propagated error (e.g. on the number of [238]U atoms) by a factor chosen randomly from the standard normal distribution (i.e. mean = 0, standard deviation = 1). Note that for consistency, all reported activity ratios and their uncertainties were also calculated during the same Monte Carlo simulations.

6. Radiocarbon analysis

Certain stylasterid samples were also analysed for their radiocarbon (^{14}C) content, including those used in U-series dating experiments and large corals which were subsampled to generate ^{14}C growth chronologies (see chapter 5). As for U-series analyses, coral sampling procedures were varied between specimens, however the methods of sample cleaning and analysis, as well as data processing, were common to all samples. These procedures are therefore outlined in the following sections.

6.1 Sample cleaning

For all radiocarbon analyses, approximately 20 mg of each sample (far less for small samples) was cleaned by established oxidative cleaning procedures, which are detailed in Table 8 (steps 1 to 17; Adkins et al., 2002). In brief, samples were exposed to 2×20 minute rinses in a buffered (1 M NaOH) H_2O_2 oxidising solution, with a 1 minute rinse in a solution of 1 % $HclO_4$ and 30 % H_2O_2 after each oxidative step. Each

cleaned sample was then leached with a prescribed volume of 0.1 M HCl, to remove any adsorbed modern CO_2 which may have accumulated during sample storage (Adkins et al., 2002). Generally, this leaching step removed 1 to 5 mg of each sample, and the remaining sample (between 3 and 12 mg) was sent for analysis.

6.2 Analytical techniques

All radiocarbon analyses were performed at the University of Bristol Radiocarbon Accelerator Mass Spectrometry Facility (BRAMS; Knowles et al., 2019). Carbonate samples were first converted to CO_2 by reaction with H_3PO_4, before conversion to graphite by reaction with H_2 in the presence of an Fe catalyst using an IonPlus automatic graphitization (AGE3) system (Knowles et al., 2019). The $^{14}C/^{12}C$ and $^{13}C/^{12}C$ of samples, blanks and standards were then measured using a MICADAS accelerator mass spectrometer.

The $\delta^{13}C$-normalised and blank corrected $^{14}C/^{12}C$ ratio of samples was reported relative to the $^{14}C/^{12}C$ ratio of the reference material NBS Oxalic Acid II at 1950 CE, and used to derive blank-corrected ^{14}C modern fractions (Fm; equivalent to $F^{14}C$ in Reimer et al., 2004) for each sample. Repeat measurements of Fm for a coral sample with age $\sim$ 10 kyr are shown in Table 11 and yielded an average value across 2 measurement sessions of 0.2971 ± 0.0018 (2 σ, n = 9). Repeat measurements of Fm for a radiocarbon-dead coral were used to assess the procedural blank, which averaged 0.0037 (n = 9).

Measurement	BRAMS ID#	^{14}C age (years BP)	Error ($\pm$ 1 σ)	Fm	Error ($\pm$ 1 σ)
Coral standard	4992	9706	28	0.299	0.001
Coral standard	4993	9747	28	0.297	0.001
Coral standard	4994	9736	28	0.298	0.001
Coral standard	6410	9731	35	0.298	0.001
Coral standard	6411	9761	58	0.297	0.002
Coral standard	6412	9769	34	0.296	0.001
Coral standard	6413	9748	57	0.297	0.002
Coral standard	6414	9783	34	0.296	0.001
Coral standard	6415	9772	57	0.296	0.002

Table 11. Radiocarbon standard data measured as part of this thesis. Radiocarbon dates given as conventional ^{14}C ages.

Sample Fm can be converted to $D^{14}C$ (in ‰) following the equation:

$$D^{14}C \ (‰) = 1000 \times (Fm - 1) \qquad (6)$$

where $D^{14}C$ is an expression of the isotopic composition of a sample compared with the NBS Oxalic Acid II standard. The Fm can also be converted to a radiocarbon age. The number of atoms (N) of a radioactive element remaining after a given time (t) is given by the following equation:

$$N = N_0 e^{-\lambda t} \qquad (7)$$

61

where N_0 is the number of atoms at the start of the time period and λ is the appropriate decay constant. Equation 7 can be rearranged to give:

$$t = \frac{1}{\lambda} \times \ln\left(\frac{N_0}{N}\right) \quad (8)$$

where N_0/N is equivalent to the Fm. λ can also be expressed in terms of the half-life ($t_{1/2}$) of the isotope in question:

$$\lambda = \frac{\ln(2)}{t_{1/2}} \quad (9)$$

Substituting equation 9 into equation 8, and using the Libby half-life of radiocarbon (5568 years), sample radiocarbon age (in years before present (BP), where present is defined as 1950) can be expressed as:

$$^{14}Cage = -8033 \times \ln(Fm) \quad (10)$$

Note that the Libby half-life is used here for consistency with common radiocarbon age reporting, however the half-life of radiocarbon has more accurately been determined as 5730 years (Godwin, 1962). The age calculated in equation 10 is thus often referred to as the conventional radiocarbon age.

Finally, it is worth noting that the quantity $D^{14}C$ (equation 6) is not equivalent to the commonly-reported quantity $\Delta^{14}C$ (see definitions in Stuiver and Polach, 1977). $\Delta^{14}C$ can be related to Fm by the equation:

$$\Delta^{14}C\ (‰) = 1000 \times \left(\frac{Fm}{e^{\frac{(y-1950)}{8267}}} - 1\right) \quad (11)$$

where y is the sample collection year.

Calculation and calibration of true radiocarbon ages is addressed, along with sample-specific considerations, in chapter 5.

7. Summary

In the following chapters of this thesis, I present measurements of the elemental and stable boron isotopic compositions of stylasterid coral skeletons, as well as measurements of the isotopes involved in the U-series and radiocarbon decay series. The analytical techniques employed in the generation of these data largely follow published protocols. However, trouble-shooting was required over the course of the analysis period, and the procedures and solutions presented in this chapter provide useful practical guidance for future work. Most importantly, this chapter demonstrates that the wide range of geochemical measurements presented here were generated by robust and well-documented methods, and that the data itself is both accurate and reproducible.

8. Supplementary information

8.1 Stylasterid identification

The methods and uncertainties associated with stylasterid identification were outlined in chapter 1. Here, we additionally note that, where possible, the specimens used in this study were identified by experts in stylasterid taxonomy who are credited as required at the start of each chapter. Otherwise, specimens were identified to the best of the ability of J. Kershaw, following published taxonomic guides (e.g. Cairns, 1983; Cairns, 1986; Cairns, 1991; Zibrowius and Cairns, 1992). Identification used a binocular microscope and focused on gross skeletal morphology, broadly following the keys to genera outlined in Cairns (1991). Specimens were not analysed by Secondary Electron Microscopy, which can provide additional information on skeletal architecture useful for species-level identification. Recognising this, and the inherent uncertainty in stylasterid identification, all discussion is henceforth restricted to the level of genus. Where possible, species-level identifications are provided, with indications of confidence in those identifications including whether they were made by a taxonomic expert and, if not, a qualitative assessment of our confidence in the ID.

8.2 Effects of the boron TPB correction on reference material reproducibility

As discussed in detail in section 4.2.2, the reproducibility of boron isotopic measurements derived from repeat measurements of NIST RM 8301 (Coral) exhibits 2 distinct periods. Supplementary figure 1 below shows that the distinction between these periods remains robust even after correcting for the contribution of the procedural blank to measured NIST RM 8301 (Coral) $\delta^{11}B$ values.
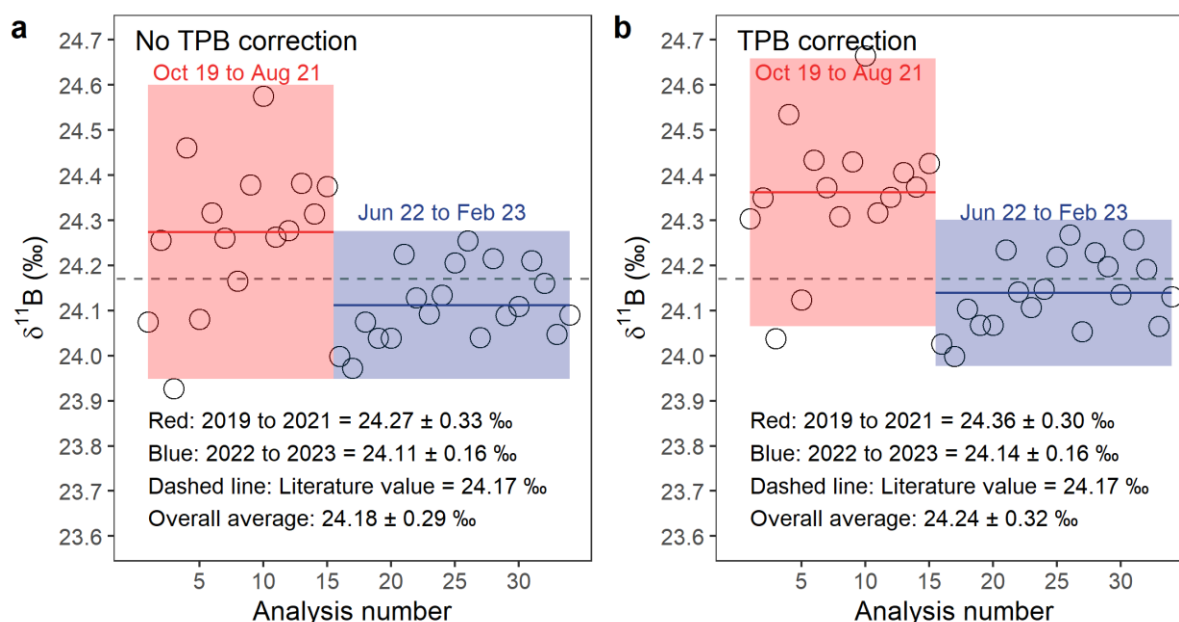
Supplementary figure 1. NIST RM 8301 (Coral) $\delta^{11}B$ values both uncorrected (a) and corrected (b) for the contribution of the total procedural blank. Note that the correction for each measurement uses the specific size and isotopic composition of the relevant blank (i.e. those in Figure 4). The difference

between the red (October 2019 – August 2021) and blue (June 2022 – February 2023) periods is robust regardless of whether or not a correction is applied.

9. References

Adkins, J.F., Griffin, S., Kashgarian, M., Cheng, H., Druffel, E.R.M., Boyle, E.A., Lawrence Edwards, R., Shen, C.-C., 2002. Radiocarbon Dating of Deep-Sea Corals. Radiocarbon 44, 567–580. https://doi.org/10.1017/S0033822200031921

Al-Ammar, A., Gupta, R.K., Barnes, R.M., 1999. Elimination of boron memory effect in inductively coupled plasma-mass spectrometry by addition of ammonia. Spectrochimica Acta Part B: Atomic Spectroscopy 54, 1077–1084. https://doi.org/10.1016/S0584-8547(99)00045-2

Al-Ammar, A.S., Gupta, R.K., Barnes, R.M., 2000. Elimination of boron memory effect in inductively coupled plasma-mass spectrometry by ammonia gas injection into the spray chamber during analysis. Spectrochimica Acta Part B: Atomic Spectroscopy 55, 629–635. https://doi.org/10.1016/S0584-8547(00)00197-X

Andersen, M.B., Stirling, C.H., Zimmermann, B., Halliday, A.N., 2010. Precise determination of the open ocean $^{234}U/^{238}U$ composition. Geochem. Geophys. Geosyst. 11 (12). https://doi.org/10.1029/2010GC003318

Auro, M.E., Robinson, L.F., Burke, A., Bradtmiller, L.I., Fleisher, M.Q., Anderson, R.F., 2012. Improvements to 232-thorium, 230-thorium, and 231-protactinium analysis in seawater arising from GEOTRACES intercalibration: Th and Pa analysis in seawater. Limnol. Oceanogr. Methods 10, 464–474. https://doi.org/10.4319/lom.2012.10.464

Barker, S., Greaves, M., Elderfield, H., 2003. A study of cleaning procedures used for foraminiferal Mg/Ca paleothermometry. Geochem. Geophys. Geosyst. 4 (9). https://doi.org/10.1029/2003GC000559

Boulyga, S.F., Koepf, A., Konegger-Kappel, S., Macsik, Z., Stadelmann, G., 2016. Uranium isotope analysis by MC-ICP-MS in sub-ng sized samples. J. Anal. At. Spectrom. 31, 2272–2284. https://doi.org/10.1039/C6JA00238B

Boyle, E.A., 1981. Cadmium, zinc, copper, and barium in foraminifera tests. Earth and Planetary Science Letters 53, 11–35. https://doi.org/10.1016/0012-821X(81)90022-4

Boyle, E.A., Keigwin, L.D., 1985. Comparison of Atlantic and Pacific paleochemical records for the last 215,000 years: changes in deep ocean circulation and chemical inventories. Earth and Planetary Science Letters 76, 135–150. https://doi.org/10.1016/0012-821X(85)90154-2

Burke, A., Robinson, L.F., 2012. The Southern Ocean's Role in Carbon Exchange During the Last Deglaciation. Science 335, 557–561. https://doi.org/10.1126/science.1208163

Cairns, S. D., 1983. Antarctic and Subantarctic Stylasterina (Coelenterata: Hydrozoa). Antarctic Research Series 38, 61–164.

Cairns, S. D., 1986. Stylasteridae (Hydrozoa: Hydroida) of the Galápagos Islands. Smithsonian Contr. Zool. 426, 1–42.

Cairns, S. D., 1991. A generic revision of the Stylasteridae (Coelenterata: Hydrozoa). Part 3. Keys to the genera. Bulletin of marine science 49(1-2), 538-545.

Cairns, S.D., 2011. Global Diversity of the Stylasteridae (Cnidaria: Hydrozoa: Athecatae). PLoS ONE 6, e21670. https://doi.org/10.1371/journal.pone.0021670

Chen, J.H., Lawrence Edwards, R., Wasserburg, G.J., 1986. ^{238}U, ^{234}U and ^{232}Th in seawater. Earth and Planetary Science Letters 80, 241–251. https://doi.org/10.1016/0012-821X(86)90108-1

Chen, T., Robinson, L.F., Burke, A., Southon, J., Spooner, P., Morris, P.J., Ng, H.C., 2015. Synchronous centennial abrupt events in the ocean and atmosphere during the last deglaciation. Science 349, 1537–1541. https://doi.org/10.1126/science.aac6159

Cheng, H., Adkins, J., Edwards, R.L., Boyle, E.A., 2000a. U-Th dating of deep-sea corals. Geochimica et Cosmochimica Acta 64, 2401–2416. https://doi.org/10.1016/S0016-7037(99)00422-6

Cheng, H., Edwards, R.L., Hoff, J., Gallup, C.D., Richards, D.A., Asmerom, Y., 2000b. The half-lives of uranium-234 and thorium-230. Chemical Geology 169, 17–33. https://doi.org/10.1016/S0009-2541(99)00157-6

Cheng, H., Lawrence Edwards, R., Shen, C.-C., Polyak, V.J., Asmerom, Y., Woodhead, J., Hellstrom, J., Wang, Y., Kong, X., Spötl, C., Wang, X., Calvin Alexander, E., 2013. Improvements in ^{230}Th dating, ^{230}Th and ^{234}U half-life values, and U–Th isotopic measurements by multi-collector inductively coupled plasma mass spectrometry. Earth and Planetary Science Letters 371–372, 82–91. https://doi.org/10.1016/j.epsl.2013.04.006

Edwards, R.L., Chen, J.H., Wasserburg, G.J., 1987. ^{238}U-^{234}U-^{230}Th-^{232}Th systematics and the precise measurement of time over the past 500,000 years. Earth and Planetary Science Letters 81, 175–192. https://doi.org/10.1016/0012-821X(87)90154-3

Edwards, R.L., Gallup, C.D., Cheng, H., 2003. Uranium-series Dating of Marine and Lacustrine Carbonates. Reviews in Mineralogy and Geochemistry 52, 363–405. https://doi.org/10.2113/0520363

Eisenhut, S., Heumann, K.G., Vengosh, A., 1996. Determination of boron isotopic variations in aquatic systems with negative thermal ionization mass spectrometry as a tracer for anthropogenic influences. Analytical and Bioanalytical Chemistry 354, 903–909. https://doi.org/10.1007/s0021663540903

Foster, G.L., 2008. Seawater pH, pCO$_2$ and [CO$^{2-}_3$] variations in the Caribbean Sea over the last 130 kyr: A boron isotope and B/Ca study of planktic foraminifera. Earth and Planetary Science Letters 271, 254–266. https://doi.org/10.1016/j.epsl.2008.04.015

Foster, G.L., Ni, Y., Haley, B., Elliott, T., 2006. Accurate and precise isotopic measurement of sub-nanogram sized samples of foraminiferal hosted boron by total evaporation NTIMS. Chemical Geology 230, 161–174. https://doi.org/10.1016/j.chemgeo.2005.12.006

Godwin, H., 1962. Radiocarbon Dating: Fifth International Conference. Nature 195, 943–945. https://doi.org/10.1038/195943a0

Guerrot, C., Millot, R., Robert, M., Négrel, P., 2011. Accurate and High-Precision Determination of Boron Isotopic Ratios at Low Concentration by MC-ICP-MS (Neptune). Geostandards and Geoanalytical Research 35, 275–284. https://doi.org/10.1111/j.1751-908X.2010.00073.x

Hathorne, E.C., Gagnon, A., Felis, T., Adkins, J., Asami, R., Boer, W., Caillon, N., Case, D., Cobb, K.M., Douville, E., deMenocal, P., Eisenhauer, A., Garbe-Schönberg, D., Geibert, W., Goldstein, S., Hughen, K., Inoue, M., Kawahata, H., Kölling, M., Cornec, F.L., Linsley, B.K., McGregor, H.V., Montagna, P., Nurhati, I.S., Quinn, T.M., Raddatz, J., Rebaubier, H., Robinson, L., Sadekov, A., Sherrell, R., Sinclair, D., Tudhope, A.W., Wei, G., Wong, H., Wu, H.C., You, C.-F., 2013. Interlaboratory study for coral Sr/Ca and other element/Ca ratio measurements. Geochem. Geophys. Geosyst. 14, 3730–3750. https://doi.org/10.1002/ggge.20230

Henderson, G.M., 2002. Seawater ($^{234}U/^{238}U$) during the last 800 thousand years. Earth and Planetary Science Letters 199, 97–110. https://doi.org/10.1016/S0012-821X(02)00556-3

Hoffmann, D.L., Prytulak, J., Richards, D.A., Elliott, T., Coath, C.D., Smart, P.L., Scholz, D., 2007. Procedures for accurate U and Th isotope measurements by high precision MC-ICPMS. International Journal of Mass Spectrometry 264, 97–109. https://doi.org/10.1016/j.ijms.2007.03.020

Jaffey, A.H., Flynn, K.F., Glendenin, L.E., Bentley, W.C., Essling, A.M., 1971. Precision Measurement of Half-Lives and Specific Activities of U^{235} and U^{238}. Phys. Rev. C 4, 1889–1906. https://doi.org/10.1103/PhysRevC.4.1889

Kasemann, S.A., Meixner, A., Erzinger, J., Viramonte, J.G., Alonso, R.N., Franz, G., 2004. Boron isotope composition of geothermal fluids and borate minerals from salar deposits (central Andes/NW Argentina). Journal of South American Earth Sciences 16, 685–697. https://doi.org/10.1016/j.jsames.2003.12.004

Kerber, I.K., Arps, J., Eichstädter, R., Kontor, F., Dornick, C., Schröder-Ritzrau, A., Babu, A., Warken, S., Frank, N., 2023. Simultaneous U and Th isotope measurements for U-series dating using MCICPMS. Nuclear Instruments and Methods in Physics Research Section B: Beam Interactions with Materials and Atoms 539, 169–178. https://doi.org/10.1016/j.nimb.2023.04.003

Knowles, T.D.J., Monaghan, P.S., Evershed, R.P., 2019. Radiocarbon Sample Preparation Procedures and the First Status Report from the Bristol Radiocarbon AMS (BRAMS) Facility. Radiocarbon 61, 1541–1550. https://doi.org/10.1017/RDC.2019.28

Lemarchand, D., Gaillardet, J., Göpel, C., Manhès, G., 2002. An optimized procedure for boron separation and mass spectrometry analysis for river samples. Chemical Geology 182, 323–334. https://doi.org/10.1016/S0009-2541(01)00329-1

Lomitschka, M., Mangini, A., 1999. Precise Th/U-dating of small and heavily coated samples of deep sea corals. Earth and Planetary Science Letters 170, 391–401. https://doi.org/10.1016/S0012-821X(99)00117-X

Misra, S., Owen, R., Kerr, J., Greaves, M., Elderfield, H., 2014. Determination of $\delta^{11}B$ by HR-ICP-MS from mass limited samples: Application to natural carbonates and water samples. Geochimica et Cosmochimica Acta 140, 531–552. https://doi.org/10.1016/j.gca.2014.05.047

Ni, Y., Foster, G.L., Bailey, T., Elliott, T., Schmidt, D.N., Pearson, P., Haley, B., Coath, C., 2007. A core top assessment of proxies for the ocean carbonate system in surface-dwelling foraminifers. Paleoceanography 22 (3). https://doi.org/10.1029/2006PA001337

Rae, J.W.B., Burke, A., Robinson, L.F., Adkins, J.F., Chen, T., Cole, C., Greenop, R., Li, T., Littley, E.F.M., Nita, D.C., Stewart, J.A., Taylor, B.J., 2018. CO_2 storage and release in the deep Southern Ocean on millennial to centennial timescales. Nature 562, 569–573. https://doi.org/10.1038/s41586-018-0614-0

Reimer, P.J., Brown, T.A., Reimer, R.W., 2004. Discussion: Reporting and Calibration of Post-Bomb [14]C Data. Radiocarbon 46, 1299–1304. https://doi.org/10.1017/S0033822200033154

Robinson, L.F., Henderson, G.M., Slowey, N.C., 2002. U–Th dating of marine isotope stage 7 in Bahamas slope sediments. Earth and Planetary Science Letters 196, 175–187. https://doi.org/10.1016/S0012-821X(01)00610-0

Shen, G.T., Boyle, E.A., 1988. Determination of lead, cadmium and other trace metals in annually-banded corals. Chemical Geology 67, 47–62. https://doi.org/10.1016/0009-2541(88)90005-8

Stewart, J.A., Christopher, S.J., Kucklick, J.R., Bordier, L., Chalk, T.B., Dapoigny, A., Douville, E., Foster, G.L., Gray, W.R., Greenop, R., Gutjahr, M., Hemsing, F., Henehan, M.J., Holdship, P., Hsieh, Y., Kolevica, A., Lin, Y., Mawbey, E.M., Rae, J.W.B., Robinson, L.F., Shuttleworth, R., You, C., Zhang, S., Day, R.D., 2020. NIST RM 8301 Boron Isotopes in Marine Carbonate (Simulated Coral and Foraminifera Solutions): Inter-laboratory $\delta^{11}B$ and Trace Element Ratio Value Assignment. Geostand Geoanal Res 45, 77–96. https://doi.org/10.1111/ggr.12363

Stewart, J.A., Strawson, I., Kershaw, J., Robinson, L.F., 2022. Stylasterid corals build aragonite skeletons in undersaturated water despite low pH at the site of calcification. Sci Rep 12, 13105. https://doi.org/10.1038/s41598-022-16787-y

Stuiver, M., Polach, H.A., 1977. Discussion Reporting of [14]C Data. Radiocarbon 19, 355–363. https://doi.org/10.1017/S0033822200003672

Vogl, J., Rosner, M., 2012. Production and Certification of a Unique Set of Isotope and Delta Reference Materials for Boron Isotope Determination in Geochemical, Environmental and Industrial Materials. Geostandards and Geoanalytical Research 36, 161–175. https://doi.org/10.1111/j.1751-908X.2011.00136.x

Yu, J., Day, J., Greaves, M., Elderfield, H., 2005. Determination of multiple element/calcium ratios in foraminiferal calcite by quadrupole ICP-MS. Geochem. Geophys. Geosyst. 6 (8). https://doi.org/10.1029/2005GC000964

Zeebe, R.E., Rae, J.W.B., 2020. Equilibria, kinetics, and boron isotope partitioning in the aqueous boric acid–hydrofluoric acid system. Chemical Geology 550, 119693. https://doi.org/10.1016/j.chemgeo.2020.119693

Zibrowius, H. and Cairns, S. D., 1992. Revision of the northeast Atlantic and Mediterranean Stylasteridae (Cnidaria: Hydrozoa). Mémoires du Muséum national d'Histoire naturelle, Paris, Séries A – Zoologie 153, 1–136.

Chapter 3: Ba/Ca of stylasterid coral skeletons records dissolved seawater barium concentrations

Contributions and acknowledgements

Summary: This chapter was published in Chemical Geology in April 2023 (Kershaw et al., 2023; https://doi.org/10.1016/j.chemgeo.2023.121355). Coauthors on this paper were Joseph A. Stewart (University of Bristol & National Institute of Standards and Technology), Ivo Strawson (University of Bristol & University of Cambridge), Maria Luiza de Carvalho Ferreira (University of Bristol & University of Chicago), Laura F. Robinson (University of Bristol), Katharine R. Hendry (University of Bristol & British Antarctic Survey), Ana Samperiz (University of Bristol & Cardiff University), Andrea Burke (University of St Andrews), James W. B. Rae (University of St Andrews), Russell D. Day (National Institute of Standards and Technology & Marine Science and Nautical Training Academy), Peter J. Etnoyer (NOAA National Centers for Coastal Ocean Science), Branwen Williams (Claremont McKenna-Pitzer-Scripps Colleges) and Vreni Häussermann (Pontificia Universidad Católica de Valparaíso).

In this paper, we present new measurements of stylasterid and scleractinian skeletal Ba/Ca and Sr/Ca ratios, and pair these with measurements of the dissolved concentration of Ba in seawater ($[Ba]_{SW}$) taken from published literature. By also compiling scleractinian Ba/Ca data from other published sources, we present new stylasterid and scleractinian Ba/Ca vs $[Ba]_{SW}$ calibrations.

I compiled [Ba]$_{SW}$ data for all samples and ancillary hydrographic variables for 21 stylasterid and 17 scleractinian samples, while Joseph A. Stewart and Ivo Strawson compiled ancillary hydrographic variables for all remaining samples. I compiled previously published scleractinian Ba/Ca data, interpreted the data and wrote the manuscript. Laura F. Robinson, Joseph A. Stewart and Katharine R. Hendry contributed to interpretations and provided comments on the manuscript. Comments on the manuscript were also provided by James W. B. Rae and Andrea Burke.

Russell D. Day, Peter J. Etnoyer, Branwen Williams and Vreni Häussermann provided samples and/or analytical support.

Data availability: All data used in this study are included in the supplementary data tables published with this paper. These data tables are freely available online, and are not reproduced in full here (https://doi.org/10.1016/j.chemgeo.2023.121355). Instead, a summary of the new coral Ba/Ca and paired [Ba]$_{SW}$ data is given as an appendix (section 7; Supplementary table 6), which also indicates which author(s) performed each measurement.

Updates in this thesis: To maintain consistency with other chapters in this thesis, I make a small number of alterations/additions to the originally published paper. These comprise additional prediction interval calculations (text added in section 2.6 and the supplementary information (section 6.4)) and an assessment of the subjective nature of the choice of ancillary hydrographic variables (supplementary information, section 6.9).

Additional acknowledgements: I would also like to thank the crew and researchers on board the research vessels which obtained the samples for this study, and Veerle Huvenne for access to the sample from cruise CE14001. Chris Coath, Carolyn Taylor, and Emily Ciscato are also thanked for their help with laboratory work at the University of Bristol. Tristan Horner and 2 anonymous reviewers provided valuable comments and suggestions during the peer review process.

1. Introduction

The dissolved concentration of barium in seawater ($[Ba]_{SW}$) has a nutrient-like profile with depth (Chan et al., 1977; Jeandel et al., 1996). Scavenging by sinking particles and the formation of barite associated with aggregated organic matter largely removes dissolved Ba from the shallow ocean, while the subsequent regeneration of barite below its saturation horizon results in increasing $[Ba]_{SW}$ with depth (e.g. Dehairs et al., 1980; Collier and Edmond, 1984; Bishop, 1988; Dymond et al., 1992; Ganeshram et al., 2003; Sternberg et al., 2005; Tang and Morel, 2006; Griffith and Paytan, 2012). The coupling between the cycling of barite and organic matter results in a link between $[Ba]_{SW}$ at shallow depths and regional primary productivity (Horner et al., 2015; Bates et al., 2017). Additionally, surface ocean $[Ba]_{SW}$ is sensitive to the position of oceanic fronts, perhaps in response to differing phytoplankton assemblages (Pyle et al., 2018). In high-latitude regions, shallow waters sink to form the major deep-water masses which fill the interior ocean basins. Below the depths of barite formation, $[Ba]_{SW}$ is primarily controlled by conservative mixing of these deep-water masses, combined with non-conservative addition and/or removal of Ba along the water-mass flow path (Horner et al., 2015; Bates et al., 2017). Reconstructing past changes in subsurface $[Ba]_{SW}$ therefore has the potential to constrain past variations in these important oceanographic processes.

The skeletal Ba/Ca ratio of marine biogenic carbonates including foraminifera , bivalves and both shallow- and deep-water corals has been shown to covary with $[Ba]_{SW}$, facilitating the use of these ratios in palaeoceanography (e.g. Lea et al., 1989; Lea and Spero, 1994; Anagnostou et al., 2011; Hönisch et al., 2011; LaVigne et al., 2011; Poulain et al., 2015; LaVigne et al., 2016; Spooner et al., 2018). In subsurface environments, Ba/Ca ratios of azooxanthellate coral groups are of particular interest, with linear relationships established between $[Ba]_{SW}$ and skeletal Ba/Ca of azooxanthellate scleractinian (Anagnostou et al., 2011; Spooner et al., 2018) and bamboo corals (LaVigne et al., 2011; Thresher et al., 2016).

However, there remain unexplained aspects of Ba-incorporation into azooxanthellate corals. For instance, azooxanthellate scleractinian Ba partition coefficients ($D_{Ba} = Ba/Ca_{coral} / Ba/Ca_{seawater}$) vary systematically with $[Ba]_{SW}$ (Spooner et al., 2018), while scleractinian corals collected from the Rekyjanes Ridge (south of Iceland) have lower D_{Ba} values than those from other locations (Hemsing et al., 2018; Spooner et al., 2018). Additionally, bamboo corals display a negative relationship between coral D_{Ba} and water depth (Geyman et al., 2019). This suggests that Ba-incorporation into azooxanthellate coral skeletons may be influenced by biological mediation of the coral calcification process (Spooner et al., 2018; Geyman et al., 2019).

Scleractinian corals calcify from a partially-enclosed calcification fluid, whose carbonate chemistry is modified by Ca-ATPase pumping to promote mineralisation (Al-Horani et al., 2003; Sinclair and Risk, 2006). The balance between coral growth rate, replenishment of the calcifying fluid with external seawater, and ion pumping, can alter the composition of the coral skeleton by Rayleigh fractionation processes (e.g. Gaetani and Cohen, 2006; Gagnon et al., 2007), which may explain variations in Ba/Ca ratios in zooxanthellate scleractinian (Gaetani and Cohen, 2006; Reed et al., 2021) and azooxanthellate bamboo corals (Geyman et al., 2019). Additionally, coprecipitation of witherite ($BaCO_3$) within the domains of aragonite may also occur due to high degrees of carbonate oversaturation in the scleractinian calcifying fluid, leading to elevated Ba-incorporation into coral aragonite (Mavromatis et al., 2018; Liu et al., 2019). These biocalcification-related effects on coral Ba/Ca ratios have the potential to introduce uncertainty into reconstructions of past $[Ba]_{SW}$, and therefore require characterisation. Discussion of these themes has thus far been limited to anthozoan coral groups (including Scleractinia and bamboo corals), while Ba/Ca ratios of hydrozoan corals remain entirely unexplored.

Stylasteridae (Class Hydrozoa: Order Anthoathecata) are the second most diverse group of hard corals and are found across a wide bathymetric and geographic range (Cairns, 2007; Cairns, 2011). The vast majority of stylasterid species form calcium carbonate skeletons, constituting an important, substrate-forming component of shallow and deep marine ecosystems (Cairns, 2011). Despite their widespread abundance and ecological importance, studies of stylasterids remain few, and their skeletal geochemistry is largely unknown.

Stylasterids can build their skeletons from aragonite, high-Mg calcite or a mixture of both polymorphs, with this suite of mineralogical variability found within individual stylasterid genera (Cairns and Macintyre, 1992; Samperiz et al., 2020). Stylasterid geochemistry can therefore be compared to both azooxanthellate scleractinian (aragonitic) and bamboo (high-Mg calcitic) corals, while controlling for their differing mineralogies. This also permits phylogenetically-controlled investigation of the role of mineralogy in determining coral geochemistry.

Recent studies reveal important distinctions between the geochemical composition of stylasterid and scleractinian skeletons. Stylasterid skeletal $\delta^{18}O$ and $\delta^{13}C$ are closer to equilibrium with seawater (Samperiz et al., 2020), while $\delta^{11}B$, U/Ca and B/Ca measurements suggest that Stylasterids calcify from a fluid with pH and $[CO_3]^{2-}$ closer to seawater than Scleractinia (Stewart et al., 2022). Furthermore, stylasterid Li/Mg and Sr/Ca correlate more strongly with seawater temperature and appear less impacted by biological mediation of the calcification process (Stewart et al., 2020a). This combined evidence for reduced modification of the stylasterid calcifying fluid suggests that stylasterid skeletons may be particularly useful

palaeoceanographic archives. In the case of Ba, other aspects of stylasterid skeletal geochemistry also suggest that the biologically mediated vital-effects impacting Ba-incorporation into scleractinian (Spooner et al., 2018) and bamboo (Geyman et al., 2019) corals, may be less pronounced in stylasterids.

Here we present the first measurements of stylasterid skeletal Ba/Ca, supplemented by new measurements of Ba/Ca from azooxanthellate Scleractinia. All Ba/Ca data are presented with paired Sr/Ca values (this study; Stewart et al., 2020a). Through inclusion of aragonitic, high-Mg calcitic and mixed mineralogy stylasterids, our data facilitate investigation of the biogenic and abiotic controls on Ba-incorporation into azooxanthellate stylasterid and scleractinian coral skeletons. By pairing Ba/Ca measurements with proximal [Ba]$_{SW}$ data (Figure 1) we assess both the biomineralisation mechanisms and palaeoceanographic utility of these different coral groups.

2.   Methods

2.1   Coral samples

We present new data from stylasterid (n = 41) and scleractinian (n = 88) coral skeletons. All corals were either collected alive (with associated organic tissue) or were preserved in "pristine" condition (i.e. no visible mineral or biological overgrowths or borings). Samples were collected from the Labrador Sea (LS; RRS *Discovery* DY081), the northeast Atlantic (NE Atl.; RRS *James Cook* JC136; R/V *Celtic Explorer* CE14001), the equatorial Atlantic (Eq. Atl.; RRS *James Cook* JC094), the Californian Channel Islands in the northeast Pacific (NE Pac.; NOAA ship *Bell M. Shimada* SH-15-03), the Drake Passage region of the Southern Ocean (SO; R/V *Nathaniel B. Palmer* 1103 and 0805; R/V *Laurence M. Gould* 0802) and the South Orkney Islands (SO (Ork); RRS *James Clark Ross* JR15005) (see Figure 1).

We organise our sample set by both taxonomic affiliation and skeletal mineralogy (see section 2.3), and stylasterid samples include aragonitic (*Adelopora, Conopora, Errina, Errinopsis, Inferiolabiata and Stylaster*), high-Mg calcitic (*Cheiloporidion, Errina and Errinopsis*) and mixed mineralogy (*Errina*) corals. Nine scleractinian genera are included in this study (*Balanophyllia, Caryophyllia, Desmophyllum, Enallopsammia, Flabellum, Lophelia, Paraconotrochus, Solenosmilia* and *Vaughanella*). Our new scleractinian data were combined with previous work to create a compiled scleractinian dataset, spanning a range of locations (Figure 1; Hemsing et al., 2018; Spooner et al., 2018). All relevant data (including sample metadata, paired hydrographic data and analytical data) are included in the online supplementary data tables.
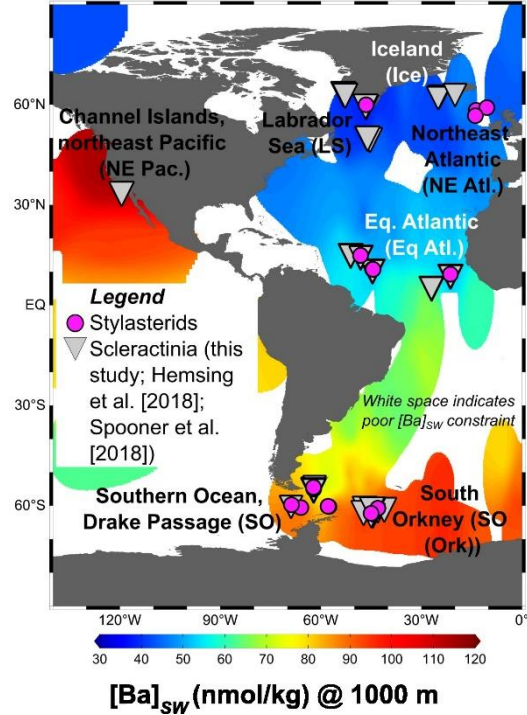
Figure 1. Map showing coral locations overlain on [Ba]$_{SW}$ at 1000 m water depth. All stylasterids were measured in this study, Scleractinia include samples measured here and by previous work (Hemsing et al., 2018; Spooner et al., 2018). Location codes used throughout are shown in brackets. [Ba]$_{SW}$ data taken from sources listed in section 2.2, in addition to Falkner et al. (1994), Smetacek et al. (1997) and Hsieh and Henderson (2017). Figure made using Ocean Data View software (Schlitzer, 2022).

2.2 Hydrographic data

Proximal [Ba]$_{SW}$ data were compiled from published sources (GEOSECS data (corals paired with stations discussed or presented in Chan et al. (1977) and Östlund et al. (1987)); Hoppema et al., 2010; Roeske and Rutgers van der Loeff, 2012; Bates et al., 2017; Serrato Marks et al., 2017; Hemsing et al., 2018; Le Roy et al., 2018; Pyle et al., 2018; Geyman et al., 2019; GEOTRACES Intermediate Data Product Group, 2021). Where necessary, data reported in units of nM were converted to nmol/kg by assuming a seawater density of 1025 kg/m³ (i.e. assuming measurements were made at atmospheric pressure and ambient room temperature). For each coral sample, the geographically closest [Ba]$_{SW}$ profile was identified, before a representative [Ba]$_{SW}$ value was calculated by linearly interpolating between the nearest two measurement depths. [Ba]$_{SW}$ measurements in the modern ocean remain sparse, and some coral samples are more proximal to [Ba]$_{SW}$ measurements than others. The average distance between coral locations and the nearest [Ba]$_{SW}$ profile was less than 350 km (all distances reported in online supplementary data tables).

Uncertainty on matched [Ba]$_{SW}$ values was estimated using the largest of either the variability in values from the three most proximal measurements to each coral location (± 2 SD), or an analytical uncertainty of ± 3 nmol/kg (calculated by applying a representative, high-end analytical uncertainty from the [Ba]$_{SW}$ datasets used (± 3 %; e.g. Hemsing et al., 2018) to the highest [Ba]$_{SW}$ value in our dataset (100 nmol/kg)). [Ba]$_{SW}$ was converted to seawater Ba/Ca ratios (μmol/mol) using a seawater [Ca] value of 10.3 mmol/kg (Nozaki, 1997). Seawater [Ca] was assigned an error of ± 5 % to account for variations in salinity.

Coral samples were also paired with ancillary hydrographic data (temperature, salinity, concentrations of phosphate, dissolved silica and oxygen, alkalinity and dissolved inorganic carbon (DIC)). Data were taken from co-located CTD or ROV measurements where possible, or extracted from the GLODAP bottle database (Lauvset et al., 2021). Temperature uncertainties were estimated from the variability between the three most proximal measurements. Hydrographic data were used to calculate carbonate system parameters including pH (total scale) and aragonite saturation state ($\Omega_{\mathrm{arag.}} = \frac{[Ca^{2+}] \times [CO_3^{2-}]}{K_{sp}^*}$) using the seacarb package in R (Gattuso et al., 2021). Input parameters were alkalinity and DIC, with dissociation constants of carbonate (K_1 and K_2) taken from Lueker et al. (2000), dissociation constants of HSO_4^- from Dickson (1990) and the boron/salinity ratio from Lee et al. (2010). All pressure corrections follow methods outlined in detail in the seacarb documentation (Gattuso et al., 2021). More information on the choice of hydrographic data and a comparison of the ancillary hydrographic data used here and in chapter 4 is included in the supplementary information (section 6.9). All relevant hydrographic variables (including all data required for carbonate system parameters) can be found in the online supplementary data tables which accompany the published version of this chapter.

2.3 Specimen mineralogy

The skeletal mineralogy of four stylasterid samples (*Errina sp.* (species: *Errina gracilis*), n = 2; *Errinopsis sp.* (species: *Errinopsis reticulum*), n = 2) was measured using x-ray diffraction techniques (e.g. Kontoyannis and Vagenas, 2000; Dickinson and McGrath, 2001). Samples of 0.2 to 0.5 mg were cut using a diamond-coated rotary blade and ground to a fine powder using a pestle and mortar. X-ray diffraction measurements were made using a Bruker D8Advance diffractometer at the University of Manchester and the University of Bristol. Instrument settings used at the University of Manchester were wavelength (λ) = 1.54060 Å and 2θ ranging from 5 to 70, while at the University of Bristol, λ = 1.54056 Å and 2θ ranged from 10 to 55. The two samples of *Errina gracilis* are composed dominantly of aragonite, with minor calcite (5.5 to 7.0 %). One sample of *Errinopsis reticulum* is composed entirely of aragonite, while the other is formed dominantly from calcite with minor (1 %) aragonite.

The mineralogy of other stylasterid samples has either been directly measured previously (n = 17; Samperiz et al., 2020) or was inferred based on published data for that species (n = 20; Cairns and Macintyre, 1992; Samperiz et al., 2020). High-Mg calcitic stylasterid corals have Sr/Ca ratios ~ 4 times lower than aragonitic specimens (Stewart et al., 2020a), and these ratios were also used to check specimen mineralogy. All scleractinian samples were assumed to be aragonitic besides one sample from the genus *Paraconotrocus*, which contains both aragonite and high-Mg calcite (Stolarski et al., 2021).

2.4   Element/Ca measurements: sample preparation

Coral samples were air dried and organic matter removed by physical scraping and treatment in dilute NaClO$_4$. A diamond-coated rotary blade was used to cut pieces of each coral for analysis. Large (e.g. 0.1 to 1 g; ~ 0.5 cm × 0.5 cm) pieces of coral were sampled to reduce the effect of intra-skeletal variability (e.g. Gagnon et al., 2007). The apical tips of stylasterid branches were also avoided, since these may be further from equilibrium with seawater than the rest of the stylasterid skeleton (Samperiz et al., 2020). Photos showing examples of sampling are included in the supplementary information (section 6.1). Samples were ground to a fine powder using a pestle and mortar, and ~ 5 mg aliquots of each powder taken for analysis. Two replicate samples were taken for each coral, with each replicate cut, cleaned, dissolved and analysed separately. Additional samples of two *Errina sp. (mixed)* corals were taken for cleaning experiments.

Most samples were cleaned following the oxidative cleaning procedures outlined in detail in chapter 2. A warm 1 % H$_2$O$_2$ (80 °C; buffered in NH$_4$OH) oxidative leach was used to remove organic matter (adapted from Boyle, 1981; Barker et al., 2003; Rae et al., 2011). At this stage, three samples of mixed mineralogy stylasterids from the genus *Errina* (JR15005-113-2421-Egr2421 (1 set of replicates) and JR15005-113-2426-Egr2426 (2 sets of replicates)) were dried, and half of each transferred to a new acid cleaned vial for additional cleaning. These new aliquots were treated with a warm, 0.002 M diethylene-triaminepentaacetic acid (DTPA) solution buffered to approximately neutral pH by 0.2 M NaOH (Lea and Boyle, 1991; Lea and Boyle, 1993; Bates, 2016). DTPA is a chelating agent, capable of dissolving contaminant barite (barium sulphate) by complexing Ba. After treatment, these samples were thoroughly rinsed using concentrated ammonia solution followed by Milli-Q (Lea and Boyle, 1993). All samples (both oxidatively cleaned and those with additional DTPA treatment) were then transferred to new acid-leached vials and subjected to a weak acid leach (0.0005 M HNO$_3$) before dissolution in distilled 0.5 M HNO$_3$.

2.5   Element/Ca measurements: analytical techniques

Element/Ca analyses were carried out using similar techniques (outlined in detail in chapter 2) at the University of Bristol (including all samples measured by J.K. in this thesis) and the National Institute of

Standards and Technology (NIST; Hollings Marine Lab; measured by Joseph A. Stewart) using a Thermo Element ICP-MS, or at the University of St Andrews (measured by Joseph A. Stewart) using an Agilent 7500 ICP-MS. Intensities of ^{138}Ba, ^{86}Sr and ^{43}Ca were measured in coral samples, blanks and well-characterised, synthetic calibrating standards to derive Ba/Ca and Sr/Ca ratios for coral samples.

Analytical reproducibility (RSD; 2s) and accuracy were assessed using repeat measurements of NIST RM 8301 (Coral) (Stewart et al., 2020b) and (uncleaned) coral reference material JCp-1 (Hathorne et al., 2013). Long-term reproducibility on both materials was better than 2 % (RSD; 2s) for Ba/Ca and Sr/Ca. Small systematic analytical offsets (< 5 %) between the labs and different calibrating standards used were quantified and corrected using NIST RM 8301 (Coral) results. To bring values into line with interlaboratory consensus values (Stewart et al., 2020b), Ba/Ca ratios measured at Bristol (BME bracketing standard), St Andrews, and at both NIST and Bristol (NBF bracketing standard) were adjusted by factors of 0.97, 1.03 and 0.95 respectively (see chapter 2 for discussion of correction factors and reporting of Bristol measurements). Sr/Ca measurements from most samples used here have been published previously (using the same dissolved solutions, Stewart et al., 2020a). To facilitate comparison, all new Sr/Ca data were normalised to NIST RM 8301 (Coral) (Stewart et al., 2020b), using a small correction factor of 0.98 (see chapter 2). Reference material mean values, reproducibility and correction factors for all labs are summarised in the online supplementary data tables.

Fe/Ca and Mn/Ca ratios were also measured to screen for the influence of non-carbonate phases including iron oxyhydroxides (e.g. Boyle, 1981). The effects of such phases on our coral Ba/Ca data are detailed in the supplementary information (section 6.2). In short, sample replicates with Fe/Ca ratios > 40 mmol/mol were excluded, following the protocol in Spooner et al. (2018). This resulted in 12 measurements from eight corals being removed from our dataset, which in practise had no effect on the principal findings of this study.

Our scleractinian Ba/Ca vs [Ba]$_{SW}$ relationship includes data from two previous studies (Spooner et al., 2018; Hemsing et al., 2018). These data were previously compiled with interlaboratory offsets accounted for using coral reference material JCp-1 (Spooner et al., 2018; see supplementary information, section 6.3 for details). We find no clear analytical offsets between these previously published data (adjusted to JCp-1) and our own, justifying direct comparison of these datasets (supplementary information, section 6.3). Seven scleractinian samples measured in our study were replicates (different cut pieces) of corals analysed previously by Spooner et al. (2018) and/or Hemsing et al. (2018). Results from each study were averaged.

2.6   Statistical analyses

For all relationships and regressions in this study, we use the Pearson correlation coefficient (*r*) to assess the degree of linear relationship between the two variables. *p*-values < 0.05 were considered significant. We report the results of both Type I (Ordinary Least Squares; OLS) and Type II (Deming) regression analyses for both our Ba/Ca vs [Ba]$_{SW}$ and Sr/Ca vs temperature calibrations. OLS regression minimises the sum of the squared residuals in the y-variable (Ba/Ca or Sr/Ca) and assumes no uncertainty on the x variable ([Ba]$_{SW}$ or temperature). Conversely, unweighted Deming regression minimises the sum of the squared residuals orthogonal to the line of best fit, recognising that both the x and y regression variables have uncertainty. Deming regressions were performed using the deming package in R (Therneau, 2018), using an unweighted approach (i.e. assuming all x and y variables have equal error).

For OLS regressions, the uncertainties associated with prediction of [Ba]$_{SW}$ from coral Ba/Ca and seawater temperature from coral Sr/Ca are also estimated. Calculating these uncertainties is far from straightforward (McClelland et al., 2021), and often calibration studies either do not include these uncertainties or do not give details of the methods used to derive them. In an addition to the published version of this chapter (Kershaw et al., 2023), I here provide additional discussion of this theme.

It is straightforward to calculate prediction intervals associated with an OLS regression line (in this case a particular Ba/Ca vs [Ba]$_{SW}$ or Sr/Ca vs temperature relationship; henceforth referred to as calibration prediction intervals), and standard statistical packages can be used to perform such calculations (e.g. the predict function in R, as used here). In this case, prediction intervals represent the range of Ba/Ca (or Sr/Ca) that a future measurement can be expected to fall within (at a particular significance level, generally 95 %), given the coral grew at a given ambient [Ba]$_{SW}$ (or seawater temperature). Complexity then arises because the desired prediction uncertainty is actually that associated with prediction of [Ba]$_{SW}$ (temperature) from a measured coral Ba/Ca (Sr/Ca) value, which represents the inverse of the calibration situation (see McClelland et al., 2021).

One intuitive approach for estimating these inverse prediction uncertainties involves reading the width or height of the calibration prediction intervals, with the latter used in the published version of this chapter (Table 1). However, in chapter 4 of this thesis, I employ a more mathematically rigorous approach, following McClelland et al. (2021). This simple method takes the y-axis scatter about the calibration line (expressed as the standard deviation of the calibration residuals; RMSE) and translates this onto the x-axis by dividing by the calibration gradient (McClelland et al., 2021). This "Simple Inverse Prediction Interval" (Simple IPI)

approach gives a single estimate of the uncertainty associated with future predictions, which depends only on the y-axis scatter about the calibration line and its gradient (McClelland et al., 2021).

For consistency across this thesis I here add these calculations to Table 1, and investigate the implications of different estimation methods in the supplementary information (section 6.4). Similar additions are made for Sr/Ca vs temperature calibrations, outlined in the supplementary information (section 6.5; Supplementary table 2).

3. Results

3.1 Coral Ba/Ca

Ba/Ca values of aragonitic stylasterid skeletons range from 7 to 19 μmol/mol, and samples span $[Ba]_{SW}$ from 40 to 100 nmol/kg. Ba partition coefficients (D_{Ba}) for stylasterid aragonite range from 1.5 to 2.3, with a mean value of 1.9 ($\pm$ 0.4, 2SD). Calcitic stylasterid Ba/Ca is lower for a given $[Ba]_{SW}$, ranging from 8 to 15 μmol/mol and covering $[Ba]_{SW}$ from 60 to 100 nmol/kg. D_{Ba} values for stylasterid calcite range from 1.3 to 1.6, with a lower mean value of 1.4 ($\pm$ 0.2, 2SD).

Scleractinian Ba/Ca data presented here were combined with existing data from Spooner et al. (2018) and Hemsing et al. (2018) to create a full scleractinian dataset consisting of 156 individual corals, 78 of which were measured for the first time in this study. Ba/Ca values of the compiled dataset range from 7 to 24 μmol/mol, spanning $[Ba]_{SW}$ from 40 to 100 nmol/kg. Aragonitic scleractinian D_{Ba} values range from 1.4 to 3.0, with a mean value of 2.0 ($\pm$ 0.6, 2SD).

Four mixed mineralogy stylasterids have Ba/Ca values which are around 1 μmol/mol higher than entirely aragonitic stylasterids living in similar $[Ba]_{SW}$ conditions (Figure 2a), corresponding to D_{Ba} values of 2.2 to 2.3 (Figure 3a). The mixed mineralogy scleractinian coral *Paraconotrochus* has a similar D_{Ba} value of 2.3. Three additional replicate pairs of mixed mineralogy stylasterids were selected for further analysis to test for the presence of barium sulphate contaminant phases, as outlined in section 2.4. The choice of cleaning procedure had no effect on Ba/Ca ratios in these samples (supplementary information, section 6.6).

3.2 Coral Ba/Ca vs $[Ba]_{SW}$ calibrations

Stylasterid (aragonitic and high-Mg calcitic) and scleractinian (aragonite only) Ba/Ca ratios are linearly related to $[Ba]_{SW}$ (Figure 2) by the regression relationships shown in Table 1. Mixed mineralogy corals were not used in regression analyses. For all taxa, OLS and Deming regressions produced gradients and intercepts within error of one another (Table 1). For the sake of simplicity and comparability with previous studies, we recommend using OLS regression calibrations for palaeoceanographic purposes. In practise, the choice of

regression method makes no difference to our interpretations. Aragonitic stylasterids are more sensitive to changes in $[Ba]_{SW}$ than high-Mg calcitic stylasterids. For Scleractinia, our new relationship between Ba/Ca and $[Ba]_{SW}$ is significantly steeper than that reported previously by Spooner et al. (2018) (Table 1). $[Ba]_{SW}$ prediction intervals (95 %) were narrowest for aragonitic stylasterids, and imply $[Ba]_{SW}$ can be reconstructed to better than 16 nmol/kg for all three coral taxa (Table 1).
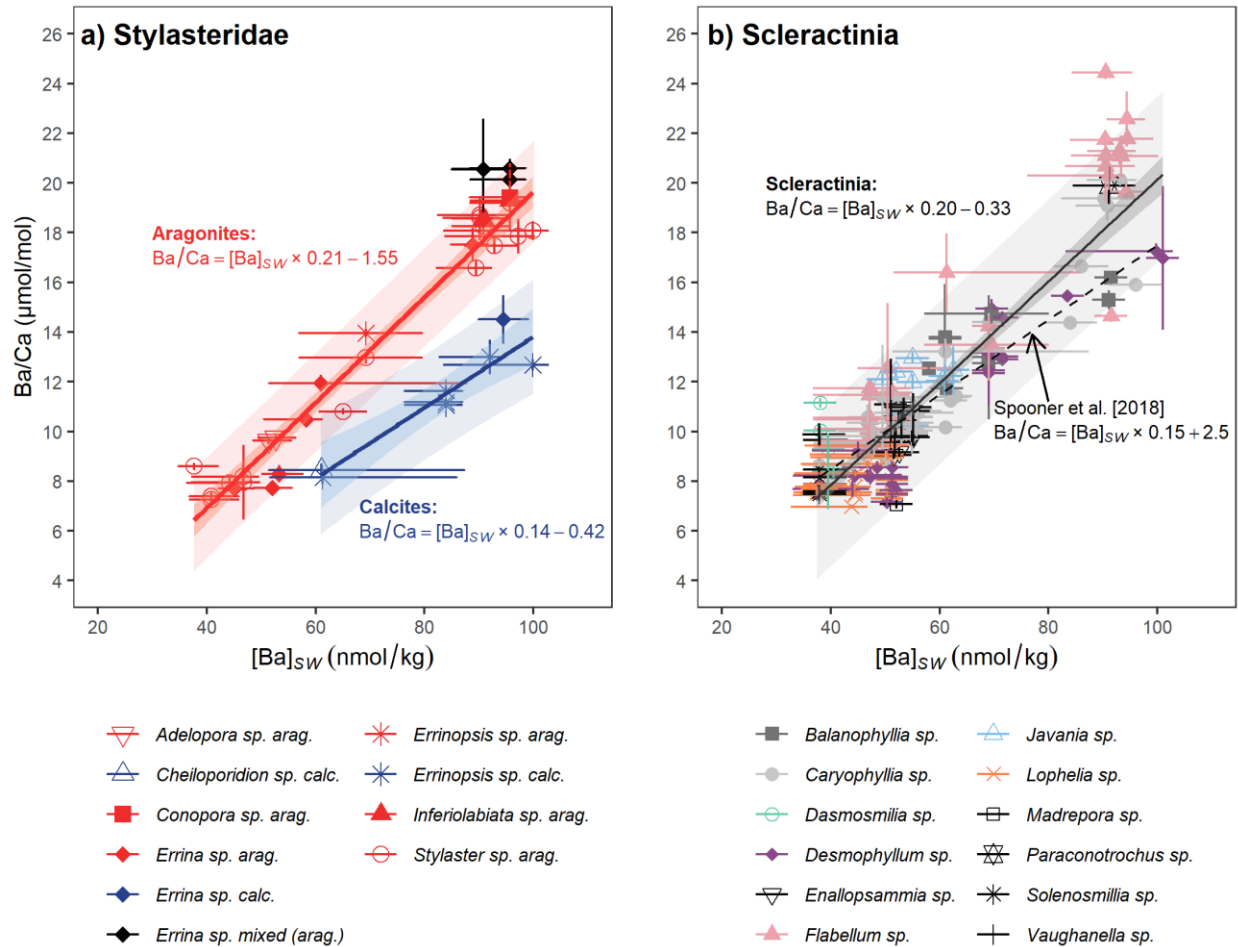
Figure 2. a) Stylasterid Ba/Ca ratios plotted as a function of $[Ba]_{SW}$. b) Compiled scleractinian Ba/Ca ratios including samples from this study, Spooner et al. (2018) and Hemsing et al. (2018) plotted as a function of $[Ba]_{SW}$. Previous calibration from Spooner et al. (2018) is shown (black dashed line). Lines of best fit were calculated using Ordinary Least Squares regression, and exclude mixed mineralogy corals. Dark shading represents 95 % confidence intervals, lighter shading represents 95% prediction intervals. Horizontal error bars on data from this study show range of $[Ba]_{SW}$ measurements from the three closest profiles ± estimated

analytical uncertainty. Vertical error bars are the largest of the analytical uncertainty or ± 2SD of replicate samples.

Taxon	Source	r	p	Regression type	Gradient, m	(± 2SE)	Intercept, c	(± 2SE)	R^2	95% prediction interval*
Stylasterids (arag. all)	This study	0.98	< 0.05	OLS	0.21	0.02	− 1.55	1.20	0.96	± 9.3 (8.8)
				Deming	0.21	0.02	− 1.57	1.38	-	
Errina sp. (arag.)	This study	0.98	< 0.05	OLS	0.24	0.05	− 3.83	3.20	0.96	
Stylaster sp. (arag.)	This study	0.98	< 0.05	OLS	0.20	0.02	− 0.72	1.56	0.96	
Stylasterids (calc. all)	This study	0.94	< 0.05	OLS	0.14	0.04	− 0.42	3.56	0.88	± 14.8 (11.4)
				Deming	0.14	0.05	− 0.45	3.75	-	
Errinopsis sp. (calc.)	This study	0.96	< 0.05	OLS	0.13	0.04	0.45	3.10	0.93	
Scleractinia (all)	This study; S18; H18	0.90	< 0.05	OLS	0.20	0.02	− 0.33	0.96	0.81	± 16.0 (15.8)
				Deming	0.21	0.02	− 0.44	1.31	-	
Caryophyllia sp.	This study; S18; H18	0.92	< 0.05	OLS	0.18	0.02	1.02	1.51	0.85	
Desmophyllum sp.	This study; S18; H18	0.95	< 0.05	OLS	0.18	0.03	0.03	1.56	0.89	
Flabellum sp.	This study; S18; H18	0.93	< 0.05	OLS	0.23	0.04	− 0.24	2.74	0.87	
Scleractinia	S18; H18	-	-	OLS	0.15	0.02	2.5	1.4	0.7	± ~ 14
Bamboo coral	L11	-	-	OLS	0.079	0.008	4.205	0.870	0.77	

Table 1. Relationships between azooxanthellate coral Ba/Ca and [Ba]$_{SW}$ in the general form: Ba/Ca = m (± 2SE) × [Ba]$_{sw}$ + c (± 2SE). Results of both Ordinary Least Squares (OLS) and unweighted (orthogonal) Deming regression shown (see section 2.6). Published data compiled from LaVigne et al. (2011) (L11), Hemsing et al. (2018) (H18) and Spooner et al. (2018) (S18). For stylasterids and Scleractinia, we recommend use of bold highlighted relationships when reconstructing past changes in [Ba]$_{SW}$. For details of regression types used and the meaning of statistical indicators, see section 2.6.

3.3 Coral Sr/Ca

Sr/Ca data for most samples in this study have previously been published (Stewart et al., 2020a), and are in good agreement with the new stylasterid (n = 20) and scleractinian (n = 17) measurements. Aragonitic corals have higher Sr/Ca (average 10.7 mmol/mol) than corals formed from high-Mg calcite (average 3.0 mmol/mol). Previously reported relationships between seawater temperature and coral Sr/Ca (Stewart et al., 2020a) are within error of those including our new samples (supplementary information, section 6.5), and aragonitic stylasterid Sr/Ca retains a stronger correlation with temperature ($r = -0.80$) than Scleractinia ($r = -0.58$) (supplementary information, section 6.5). Subsample Sr/Ca and Ba/Ca ratios of mixed mineralogy corals are negatively correlated in three out of four cases (supplementary information, section 6.5).

4. Discussion

4.1 [Ba]$_{SW}$ and sample mineralogy controls on stylasterid Ba/Ca

When split by mineralogy, stylasterid Ba/Ca ratios correlate strongly with [Ba]$_{SW}$ (Figure 2a), suggesting that [Ba]$_{SW}$ exerts a dominant control on stylasterid Ba/Ca ratios. This result is not unexpected, given stylasterids calcify from a fluid derived directly from seawater (Stewart et al., 2022). As reflected in stylasterid D$_{Ba}$ values (Figure 3a), high-Mg calcitic stylasterids contain less Ba than their aragonitic counterparts, and their Ba/Ca ratios are less sensitive (shallower slope) to changes in [Ba]$_{SW}$ (Table 1). This difference is observed when comparing samples from the same genus (*Errina sp.* and *Errinopsis sp.*; Figure 2a), and, crucially, those from the same collection locations and depths (e.g. compare aragonitic sample NBP1103-DH22-Stc1-01-Sde22aw (D$_{Ba}$ = 1.9) and calcitic sample NBP1103-DH22-Stc1-01-Efe22ax (D$_{Ba}$ = 1.3)). This strongly suggests these differences have a mineralogical origin, rather than being attributable to taxa- or location-specific variations in the calcification process (e.g. Mavromatis et al., 2018; Ulrich et al.,

2021). Although mixed mineralogy stylasterids from the genus *Errina* have higher Ba/Ca than co-located, entirely aragonitic stylasterids (Figure 3a), the reasons for this are likely specific to the species in question (supplementary information, section 6.6).

Mineralogical controls on D_{Ba} of carbonate (bio)minerals are widely acknowledged (e.g. Mavromatis et al., 2018; Ulrich et al., 2021) and may also be reflected in other azooxanthellate coral taxa. This control is demonstrated by the similar D_{Ba} values of aragonitic stylasterid and scleractinian corals, and of high-Mg calcitic stylasterid and bamboo corals, respectively (Figure 3a). This similarity provides further support for a common process of Ba-incorporation into coral carbonate via cationic substitution (e.g. Anagnostou et al., 2011; LaVigne et al., 2011; 2016; Serrato-Marks et al., 2017), and therefore suggests that Ba^{2+} substitutes more easily into coralline aragonite than high-Mg calcite. Indeed, abiogenic precipitation experiments have shown that Ba incorporates more easily into aragonite than low-Mg calcite, due to the differing crystal structures of these two minerals (e.g. Mavromatis et al., 2018; Figure 3b). However, high-Mg calcitic corals (Geyman et al., 2019; this study) have higher D_{Ba} than low-Mg calcite produced by molluscs, planktonic foraminifera and in abiogenic precipitation experiments (e.g. Lea and Spero, 1994; Gillikin et al., 2006; Gillikin et al., 2008; Hönisch et al., 2011; Mavromatis et al., 2018; Ulrich et al., 2021; Figure 3b). This could suggest that Ba-incorporation increases with Mg-content, due to increasing levels of lattice distortion (e.g. Mucci and Morse, 1983; Geyman et al., 2019).

An additional explanation for the difference between coral high-Mg calcite and low-Mg calcite is that Ba-incorporation is influenced by taxa-specific effects related to the calcification process (e.g. Mavromatis et al., 2018; Ulrich et al., 2021). Aragonitic coral (stylasterid and scleractinian) D_{Ba} values are also elevated in comparison to aragonite produced by bivalves (Gillikin et al., 2008; Figure 3b), fish (otoliths; Bath et al., 2000) and in some precipitation experiments (Mavromatis et al., 2018; Figure 3b). This has led to suggestions that Ba-incorporation into coral carbonate is elevated by the coral calcification process (Mavromatis et al., 2018), and this hypothesis is explored in more detail in section 4.6. Identifying mineralogical controls on Ba-incorporation into marine carbonates by comparison of disparate calcifying taxa (e.g. Figure 3b) is therefore difficult. Stylasterids, however, provide a phylogenetically-controlled natural mineralogical experiment, and our finding that mineralogy influences azooxanthellate coral Ba/Ca is robust. More broadly, this approach illustrates the utility of stylasterid skeletal geochemistry to deconvolve the environmental, mineralogical, and biological controls on the geochemistry of marine calcifiers (e.g. Ulrich et al., 2021).
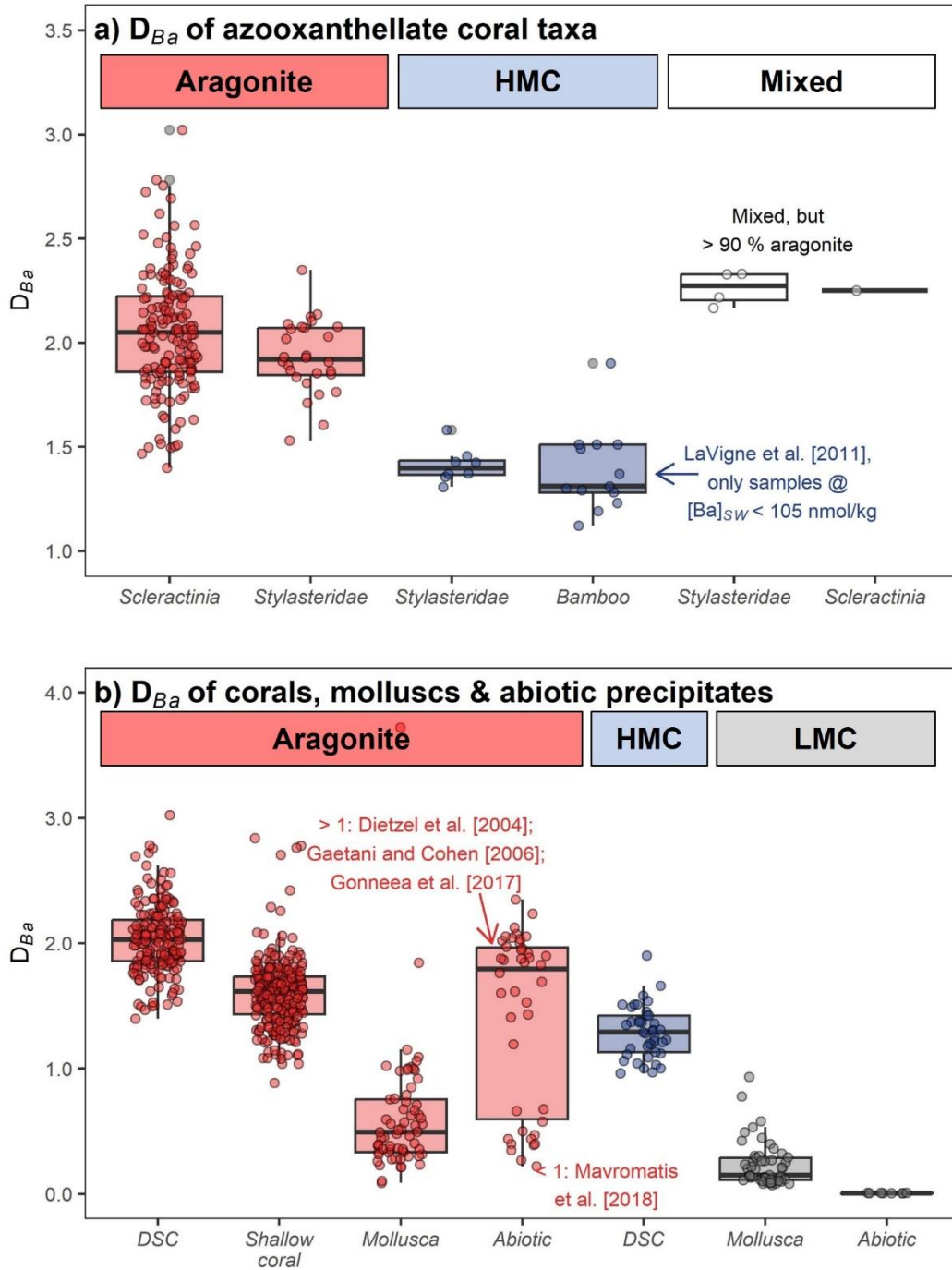
Figure 3. Boxplots showing D_{Ba} values of a) azooxanthellate coral taxa (this study; LaVigne et al., 2011; Hemsing et al., 2018; Spooner et al., 2018), and b) a wider range of marine calcifiers and abiotic precipitates, grouped by mineralogy (Dietzel et al., 2004; Gaetani and Cohen, 2006; Gonneea et al., 2017; Mavromatis et al., 2018; Ulrich et al., 2021). HMC = high-Mg calcite, LMC = low-Mg calcite.

4.2 Comparing azooxanthellate coral Ba/Ca vs [Ba]$_{SW}$ relationships

Ba/Ca vs [Ba]$_{SW}$ relationships have now been established for a range of azooxanthellate coral taxa. Comparing these reveals the dominant [Ba]$_{SW}$ and mineralogical controls on coral Ba/Ca (Figure 4).

Our new high-Mg calcitic stylasterid relationship has a steeper gradient than the bamboo coral calibration published by LaVigne et al., 2011 (Table 1). This difference is driven by bamboo coral samples paired with higher [Ba]$_{SW}$ than represented in our high-Mg calcitic stylasterid sample set (LaVigne et al., 2011; supplementary information, section 6.7). These bamboo corals from deeper, Ba-enriched waters are impacted by decreasing D$_{Ba}$ with increasing water depth (Geyman et al., 2019). While we find no such relationship between our high-Mg calcitic stylasterid D$_{Ba}$ values and depth (supplementary information, section 6.8), our samples are generally from shallower depths, with only one sample from > 1000 m. Directly comparing these datasets is therefore difficult, and considering data from the range of [Ba]$_{SW}$ represented in both studies (i.e. [Ba]$_{SW}$ < 105 nmol/kg only) reveals good agreement between the D$_{Ba}$ values and Ba/Ca vs [Ba]$_{SW}$ relationships of these two coral taxa (Figure 3; Figure 4).

Similarly, aragonitic stylasterid and scleractinian Ba/Ca ratios are strongly related to [Ba]$_{SW}$, with similar slopes and similar average D$_{Ba}$ values (Figure 4; Table 1; sections 3 and 3.2). While this suggests that [Ba]$_{SW}$ exerts a primary control on Ba/Ca ratios of both these coral taxa, more detailed comparison reveals important differences between them. Ba-incorporation into aragonitic stylasterid skeletons is less variable than into scleractinian skeletons, illustrated by the improved fit and narrower prediction interval of the regression between [Ba]$_{SW}$ and stylasterid Ba/Ca (Figure 2; Table 1), the smaller variability of stylasterid D$_{Ba}$ values (mean 1.9 ± 0.4, 2SD) compared with Scleractinia (mean 2.0 ± 0.6, 2SD; Figure 3a), and the smaller average difference between stylasterid sample replicates (Table 2). Additionally, our updated scleractinian Ba/Ca vs [Ba]$_{SW}$ relationship is significantly steeper than that reported previously (Spooner et al., 2018; Figure 4), indicating that the addition of new samples has had a significant impact on the calibration.

These robust differences between stylasterid and scleractinian Ba/Ca ratios strongly suggest that contrasting secondary processes impact Ba-incorporation into their skeletons. In the following sections, we therefore examine the nature of these putative secondary controls, focusing firstly on stylasterids, then Scleractinia, before addressing the causes of the differences in Ba-incorporation between these two coral groups.
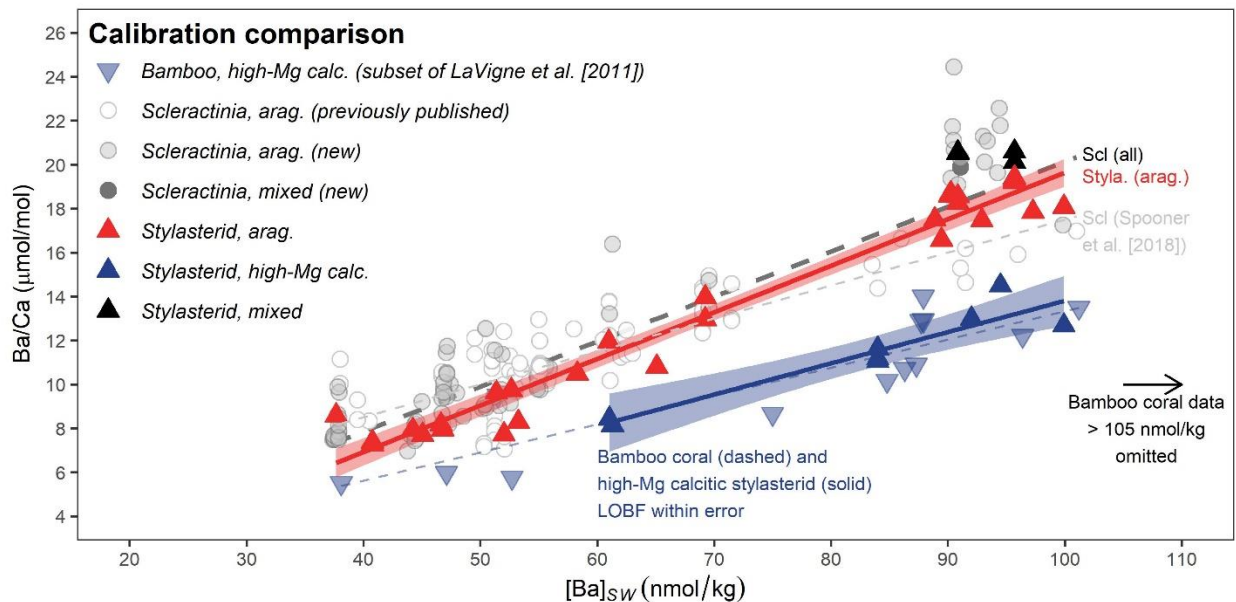
Figure 4. Comparison of Ba/Ca vs [Ba]$_{SW}$ calibrations (Ordinary Least Squares) for different azooxanthellate coral groups, including Scleractinia (this study; Hemsing et al., 2018; Spooner et al., 2018), stylasterids (this study) and bamboo corals (LaVigne et al., 2011). Data from LaVigne et al. (2011) include only data points at [Ba]$_{SW}$ < 105 nmol/kg. Error bars removed for clarity. Shading shows 95 % confidence intervals.

4.3   Assessing the robustness of the stylasterid [Ba]$_{SW}$ proxy

[Ba]$_{SW}$ and sample mineralogy exert primary controls on stylasterid Ba/Ca, suggesting this ratio may be a powerful archive of past [Ba]$_{SW}$. However, the possible influence of additional factors necessitates assessment of the reliability of stylasterids as archives of [Ba]$_{SW}$. In the following section, we investigate potential further influences on their Ba/Ca ratios, including genus-specific effects, a suite of additional hydrographic parameters, depth and location. Of these, only seawater temperature appears to influence stylasterid Ba/Ca, and the magnitude of this effect is small compared with the overriding [Ba]$_{SW}$ and mineralogical controls.

Our stylasterid sample set includes a range of genera, which could exhibit contrasting geochemical behaviour and influence our results. However, genus-specific relationships between Ba/Ca and [Ba]$_{SW}$ which span a substantial range in [Ba]$_{SW}$ are within error of the relationship for the full sample set (Table 1). This result suggests that our stylasterid relationships are not significantly biased by individual coral genera. We also find that most stylasterid genera display low variability between Ba/Ca of replicate samples (Table 2). *Conopora sp.* and *Errina sp. (calc.)* have relatively high variability, but these are based on one pair of replicates, while higher variability for mixed mineralogy stylasterids likely results from replicates incorporating variable amounts of each carbonate polymorph. This suggests that no single stylasterid genus measured here is significantly

impacted by intra-skeletal variability in Ba/Ca, and all are suitable targets for use in reconstructing [Ba]$_{SW}$ using the bulk sampling methods employed here.

Taxon	Genus	No. pairs	Mean difference Ba/Ca (µmol/mol)
Scleractinia (all)	-	79	0.39
	Balanophyllia sp.	1	0.28
	Caryophyllia sp.	20	0.22
	Desmophyllum sp.	10	0.17
	Enallopsammia sp.	8	0.25
	Flabellum sp.	21	0.45
	Lophelia sp.(bulk calyx)	12	0.99
	Solenosmillia sp.	4	0.13
	Vaughanella sp.	3	0.17
Scleractinia (mixed)	*Paraconotrochus sp. (mixed)*	1	0.53
Stylasterid arag. (all)	-	28	0.26
	Adelopora sp.	2	0.05
	Conopora sp.	1	0.97
	Errina sp.	6	0.20
	Errinopsis sp.	1	0.04
	Inferiolabiata sp.	2	0.35
	Stylaster sp.	16	0.27
Stylasterid high-Mg calc. (all)	-	8	0.24
	Cheiloporidion sp.	1	0.20
	Errina sp.	1	0.68
	Errinopsis sp.	6	0.18
Stylasterid (mixed, arag.)	*Errina sp.*	3 corals	1.42

Table 2. Mean difference between Ba/Ca of replicates (different cut pieces) of corals analysed in this study. Averages for each taxon are also shown. Values > 0.50 µmol/mol are shown in bold. For mixed mineralogy

Errina sp. samples, between 2 and 6 replicates were measured on 3 corals, difference between maximum and minimum Ba/Ca values shown.

Secondly, we examine the residuals of our stylasterid Ba/Ca vs [Ba]$_{SW}$ relationships (i.e. Ba/Ca$_{measured}$ − Ba/Ca$_{relationship}$) and stylasterid D$_{Ba}$ values to explore the influence of secondary environmental controls. These do not correlate with salinity, pH, $\Omega_{arag.}$, and dissolved phosphate concentrations ($p > 0.05$, − $0.28 < r < 0.35$; supplementary information, section 6.8). Additionally, while the residuals of the aragonitic calibration are significantly – but weakly – correlated with depth ($p = 0.02$, $r = − 0.45$), similar correlations are not observed between depth and either the residuals of the calcitic calibration, or stylasterid D$_{Ba}$ ($p > 0.05$, $0 < r < 0.32$; supplementary information, section 6.8). Furthermore, although aragonitic stylasterid D$_{Ba}$ values are significantly correlated with dissolved oxygen concentrations ($p = 0.04$, $r = 0.39$), a similar correlation is not observed for calcitic stylasterid D$_{Ba}$ values ($r = 0.08$) or for the residuals of the aragonitic or calcitic stylasterid calibrations ($p > 0.05$, $0 < r < 0.29$; supplementary information, section 6.8). Together, these results suggest that these parameters do not significantly influence Ba-incorporation into stylasterid skeletons. The strongest, consistent correlations for both aragonitic and calcitic stylasterid D$_{Ba}$ values are with temperature and dissolved silica concentrations (Figure 5; supplementary information, section 6.8). Although neither temperature nor dissolved silica concentrations are significantly correlated with regression residuals (supplementary information, section 6.8), this does not preclude their influence on stylasterid Ba-incorporation. Both temperature and dissolved silica concentrations are strongly correlated with [Ba]$_{SW}$ in our dataset. This correlation with the x variable ([Ba]$_{SW}$) means that regression residuals will not reflect their possible influence in a straightforward manner. Instead, D$_{Ba}$ values are a better indicator of their possible effects, and the observed correlations suggest that one - or both - of these parameters may exert a secondary control on stylasterid skeletal Ba/Ca.

The tight negative correlation between temperature and dissolved silica concentration in our stylasterid sample set ($r = − 0.87$) makes it difficult to isolate the effects of each variable. However, to our knowledge there is no published work examining the effects of dissolved silica concentration on Ba-incorporation into marine carbonates. Conversely, multiple experimental studies have shown that aragonite D$_{Ba}$ values are negatively correlated with ambient temperature (e.g. Dietzel et al., 2004; Gaetani and Cohen, 2006; Gonneea et al., 2017). Therefore, while we cannot discount that dissolved silica concentrations impact stylasterid D$_{Ba}$, we suggest that temperature is more likely the controlling variable. The strong correlation between temperature and dissolved silica concentration in our sample set could then lead to associated correlations between stylasterid D$_{Ba}$ and dissolved silica concentration.

Considering our stylasterid dataset more broadly, we find strong support for the role of temperature in Ba-incorporation into stylasterid skeletons. The D_{Ba} of aragonite produced by abiotic precipitation experiments is also negatively correlated with temperature (Dietzel et al., 2004; Gaetani and Cohen, 2006; Gonneea et al., 2017), and the gradients of the lines of best fit between stylasterid D_{Ba} and temperature reported here are subparallel to that reported by Dietzel et al. (2004) for abiotic aragonite (Figure 5a). Furthermore, a temperature effect can explain why aragonitic stylasterids collected from the cold waters of the Drake Passage and South Orkney regions have mean D_{Ba} values of 1.96 ($\pm$ 0.19, 2SD) and 2.09 ($\pm$ 0.05, 2SD) respectively, higher than those from the comparatively warm equatorial (1.77 ($\pm$ 0.29, 2SD)) and northeast (1.80 ($\pm$ 0.10, 2SD)) Atlantic (Figure 6b). Finally, a temperature influence can also explain the positive correlation between aragonitic stylasterid D_{Ba} values and $[Ba]_{SW}$ (Figure 6b). The negative covariation of temperature and $[Ba]_{SW}$ in the modern ocean means that colder waters tend to have higher $[Ba]_{SW}$ than warmer waters. Although we find no correlation between high-Mg calcitic stylasterid D_{Ba} values and $[Ba]_{SW}$ (gradient = 0.001, r = 0.14), this may be attributable to the smaller temperature and $[Ba]_{SW}$ range represented in this dataset.

The mechanism by which temperature impacts stylasterid D_{Ba} could relate to surface entrapment, whereby the temperature-dependent balance between crystal growth rate and element diffusivity impacts Ba-incorporation (e.g. Watson, 2004; Gaetani and Cohen, 2006). Alternatively, the biological response of the stylasterid calcification process to ambient temperature could lead to variations in Ba-incorporation due to kinetic effects or Rayleigh fractionation (Gaetani and Cohen, 2006). As discussed in section 4.5, variations in Rayleigh fractionation appear to have a relatively small influence on stylasterid D_{Ba}. This may suggest that the surface entrapment model is the more likely cause, however, this remains uncertain.

To constrain the magnitude of the temperature effect, we consider our aragonitic stylasterid sample set. Based on the correlation between aragonitic stylasterid D_{Ba} and $[Ba]_{SW}$ in our sample set, D_{Ba} increases by 11 % as $[Ba]_{SW}$ increases from 40 to 100 nmol/kg (Figure 6). Stylasterid Ba/Ca at the high (100 nmol/kg) $[Ba]_{SW}$ end of the relationship is therefore ~ 2 μmol/mol higher than the theoretical case in which D_{Ba} remains constant at the value which characterises stylasterids at low (40 nmol/kg) $[Ba]_{SW}$. Assuming this variation in D_{Ba} is driven entirely by temperature, this suggests that temperature is responsible for ~ 16 % of the overall variability in aragonitic stylasterid Ba/Ca. Therefore, while temperature does exert an influence on stylasterid Ba/Ca, these effects are minor compared with those caused by changes in $[Ba]_{SW}$, and are also smaller than those associated with sample mineralogy (average calcitic stylasterid D_{Ba} 27 % lower than aragonitic stylasterids). The small magnitude and uncertain nature of the temperature influence on stylasterid Ba/Ca (Figure 5), coupled with the uncertainties in stylasterid temperature reconstruction (Stewart et al., 2020a; $\pm$ 2.3 °C for aragonitic stylasterids at average ocean temperatures) mean that quantitatively correcting for this

effect in palaeoceanographic contexts is unlikely to lead to more accurate estimates of past $[Ba]_{SW}$. Indeed, stylasterid Ba/Ca ratios are dominantly controlled by $[Ba]_{SW}$ and sample mineralogy, and provide a useful record of $[Ba]_{SW}$. Temporal records of stylasterid Ba/Ca should, however, ideally be presented alongside corresponding records of temperature-sensitive ratios (either Li/Mg, Sr/Ca or $\delta^{18}O$ (Samperiz et al., 2020; Stewart et al., 2020a)), allowing for qualitative assessment of whether changes in temperature might contribute to fluctuations in stylasterid Ba/Ca.
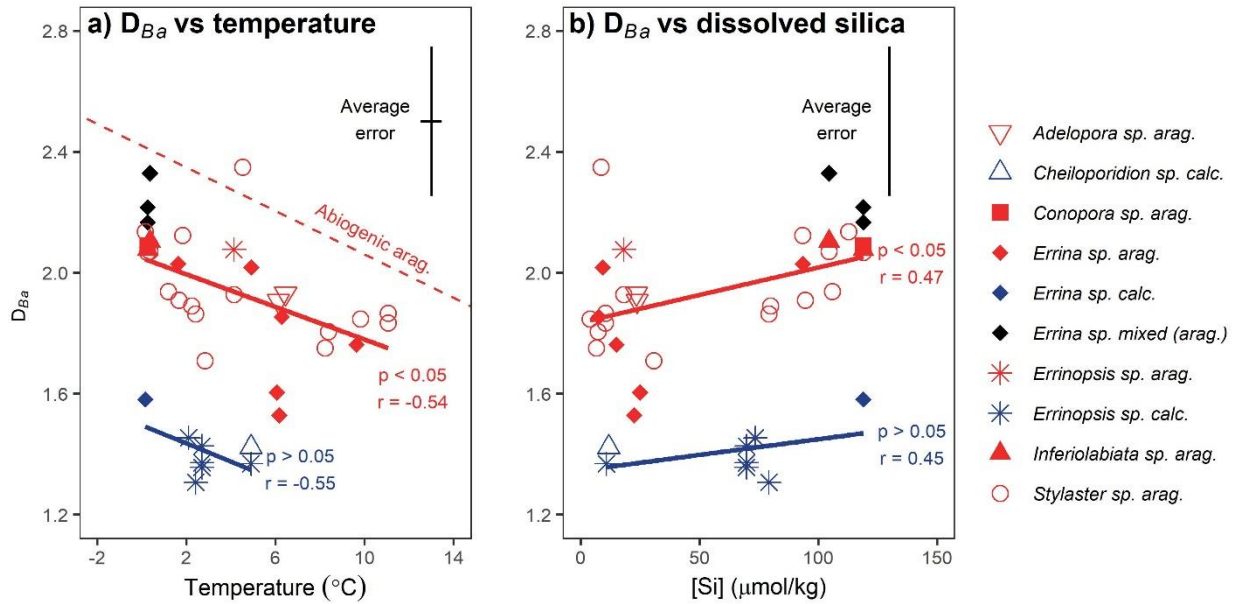
Figure 5. Stylasterid D_{Ba} values as a function of temperature (a) and dissolved silica concentration (b). Abiogenic aragonite vs temperature (dashed line) from Dietzel et al. (2004) also shown. Pearson *r* and *p*-values are shown for both aragonitic and calcitic stylasterids. Average error bars shown for data in this study, paucity of dissolved silica concentration data precludes x-error bar estimation in panel b.
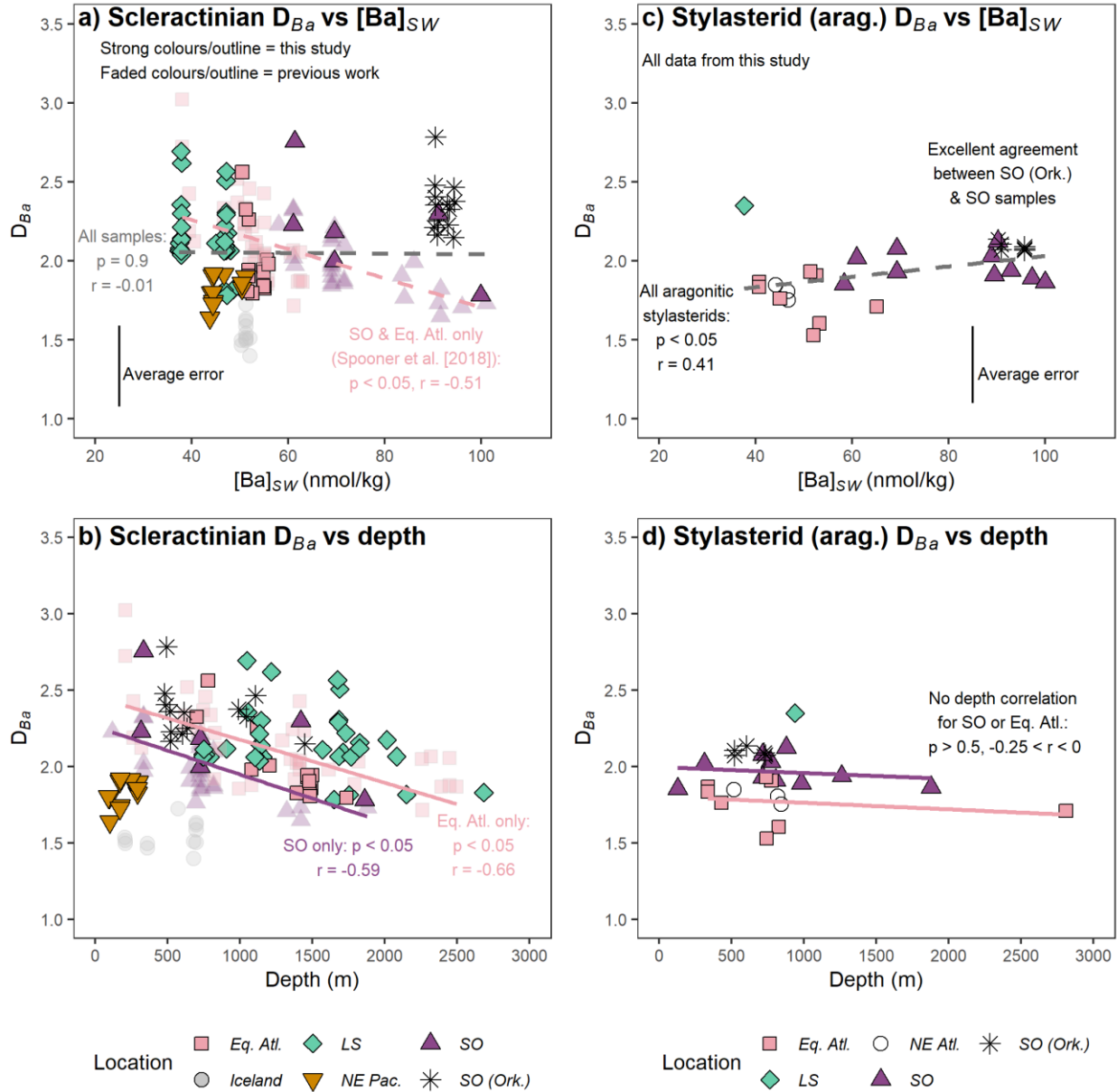
Figure 6. Scleractinian (a and c) and aragonitic stylasterid (b and d) D_{Ba} values as a function of $[Ba]_{SW}$ and depth, by location. Location codes follow Figure 1. Average vertical error bars shown in panels a and c.

4.4 Secondary controls on scleractinian Ba/Ca

Previous work found that the secondary influences on scleractinian Ba/Ca ratios were minor (Spooner et al., 2018). However, as outlined in section 4.2, comparison of our expanded scleractinian dataset with aragonitic stylasterids reveals that scleractinian Ba/Ca ratios are characterised by as-yet-unexplained

93

variability. We therefore reassess the potential influence of genus-specific effects, additional hydrographic parameters and location and depth on scleractinian Ba/Ca.

Our new scleractinian Ba/Ca vs [Ba]$_{SW}$ relationship includes samples from multiple genera, and relevant genus-specific relationships are within error of the full calibration (Table 1). However, the larger mean difference between scleractinian sample replicates - compared with aragonitic stylasterids – is driven mostly by two genera: *Lophelia* and *Flabellum* (Table 2). Considering *Lophelia*, our results are unsurprising given other heterogeneous aspects of their skeletal geochemistry (Raddatz et al., 2013; Montagna et al., 2014; Jurikova et al., 2019; Stewart et al., 2020a). The replicates measured here are samples of the entire *Lophelia* calyx, meaning Ba/Ca variability may be attributable to incorporation of skeletal centres of calcification (COCs) (Stewart et al., 2020a). To test this hypothesis, we also measured *Lophelia* samples taken only from theca walls, whose Li/Ca, Mg/Ca and Sr/Ca show smaller COC influence (see Stewart et al., 2020a, samples are same measured solutions). Theca-only subsamples have systematically lower Ba/Ca than bulk calyx samples by around 10 % (supplementary information, section 6.8). In zooxanthellate Scleractinia, COCs have elevated Ba/Ca compared to the rest of the skeleton (Holcomb et al., 2009), therefore our result may be consistent with decreased incorporation of COC material into theca-only subsamples, compared with the bulk calyx. Careful sampling of *Lophelia* theca apparently mitigates some of the effects of COC incorporation, and we use these theca-only subsamples in our Ba/Ca vs [Ba]$_{SW}$ relationship where available.

Equally, *Flabellum sp.* is prone to particularly high and variable Ba/Ca (Figure 2b). Previous studies have concluded that other aspects of the skeletal geochemistry of *Flabellum sp.*, including Li/Mg (Case et al., 2010; Cuny-Guirrec et al., 2019; Stewart et al., 2020a), Sr/Ca, $\delta^{18}O$ and $\delta^{13}C$ (Stewart et al., 2020a), are not unusual in comparison to other azooxanthellate scleractinian genera. However, multiple studies have recorded *Flabellum* from substrates dominated by fine muds and sands (e.g. Buhl-Mortensen et al., 2007; Hamel et al., 2010; Mercier et al., 2011), and some *Flabellum* species are also free-living, lying sideways in direct contact with sediment (Hamel et al., 2010; Mercier et al., 2011). This habitat may result in *Flabellum* samples experiencing higher [Ba]$_{SW}$ due to barium efflux from sediments into the water column (e.g. McManus et al., 1994; Hoppema et al., 2010; Bates et al., 2017). Additionally, this proximity to sediment may mean that *Flabellum* is particularly susceptible to contamination by Ba-bearing phases such as barite and/or Fe-Mn oxyhydroxides. Indeed, three of the six scleractinian corals which had Ba/Ca data excluded due to high Fe/Ca were *Flabellum* (supplementary information, section 6.2). However, Ba-incorporation into *Flabellum* does not differ significantly from other scleractinian genera or our overall Ba/Ca vs [Ba]$_{SW}$

relationship (Table 1). Therefore, we retain this genus in our Ba/Ca vs $[Ba]_{SW}$ relationship, but emphasise the importance of screening samples for contaminant phases.

Although genus-specific effects may account for the larger average difference between Ba/Ca of scleractinian coral replicates compared with aragonitic stylasterids, they cannot explain the overall higher variability in scleractinian D_{Ba}, or worse fit of the scleractinian Ba/Ca vs $[Ba]_{SW}$ relationship. Instead, we suggest that Ba-incorporation in scleractinian corals varies between locations, and across depth gradients. Previous work has shown that Icelandic Scleractinia have lower D_{Ba} values than those collected from the equatorial Atlantic and Southern Ocean (Hemsing et al., 2018; Spooner et al., 2018; Figure 6a). Our new data show that Scleractinia from the northeast Pacific (NE Pac.) region also have low D_{Ba}, while those from South Orkney (SO Ork) and Labrador Sea (LS) sites have high D_{Ba} (Figure 6a). These samples steepen the gradient of our scleractinian Ba/Ca vs $[Ba]_{SW}$ relationship relative to that published previously, and erode the relationship between scleractinian D_{Ba} and $[Ba]_{SW}$ (Spooner et al., 2018, their figure 10). Locational differences become increasingly apparent when D_{Ba} values are considered as a function of water depth: Scleractinia from the Drake Passage and equatorial Atlantic regions show sub-parallel, negative correlations between D_{Ba} and water depth ($r = -0.59$ and -0.66, respectively, $p < 0.05$; Figure 6b). Because $[Ba]_{SW}$ increases with increasing water depth in the modern ocean, a depth control on scleractinian D_{Ba} in these two regions may explain the correlation observed between scleractinian D_{Ba} and $[Ba]_{SW}$ when considering these two regions in isolation (Figure 6; Spooner et al., 2018, their figure 10).

No single variable can explain both the location and depth-related variability in scleractinian D_{Ba} values. While the decrease in scleractinian D_{Ba} values with increasing water depth may be explained by partition coefficients approaching unity as pressure increases (McCorkle et al., 1995), this cannot explain locational differences. We also find no strong correlations between any of the ancillary hydrographic variables considered here and either scleractinian D_{Ba} values or residuals of the Ba/Ca vs $[Ba]_{SW}$ relationship ($-0.20 < r < 0.20$; supplementary information, section 6.8). The only significant correlation found is between scleractinian calibration residuals and temperature ($p = 0.03$, $r = -0.17$). However, this correlation is weak, and temperature crucially does not correlate significantly with scleractinian D_{Ba} values ($p > 0.05$, $r = -0.15$). This strongly suggests that any influence of temperature on scleractinian Ba/Ca is either substantially weaker than that observed for stylasterids, or – perhaps more likely - is overprinted by other processes. More broadly, our results suggest that none of the additional hydrographic properties considered here exert a dominant influence on scleractinian Ba-incorporation, in agreement with previous work (Anagnostou et al., 2011; Hemsing et al., 2018; Spooner et al., 2018). Crucially, aragonitic stylasterids from the same sites show less locational variability and no correlations with water depth (Figure 6). This

suggests the driver of the variability in scleractinian D_{Ba} is specific to Scleractinia, and affects stylasterid Ba/Ca to a lesser degree.

Therefore, we suggest that depth trends and geographic differences result from the scleractinian calcification process (Spooner et al., 2018). In the following section, we consider two main mechanisms which could cause calcification-related variability in scleractinian Ba/Ca: variations in the degree of Rayleigh fractionation (i.e., the relative rates of coral growth and calcifying fluid replenishment; Gaetani and Cohen, 2006; Pretet et al., 2015; Geyman et al., 2019; Reed et al., 2021), and the precipitation of witherite ($BaCO_3$) within the domains of aragonite (Mavromatis et al., 2018; Liu et al., 2019).

4.5   Comparing scleractinian and stylasterid calcification processes

Comparing Ba/Ca and Sr/Ca ratios of stylasterid and scleractinian corals suggests that variations in the degree of Rayleigh fractionation is the most likely cause of the increased variability in scleractinian D_{Ba}. The (partial) isolation of the scleractinian calcifying fluid means that Rayleigh fractionation processes can affect the composition of the coral skeleton (e.g. Gaetani and Cohen, 2006; Gagnon et al., 2007). Because coral $D_{Ba} > 1$, barium is preferentially incorporated into the skeleton during growth, and becomes progressively depleted in the calcifying fluid. The rate of skeletal growth relative to the timescale of calcifying fluid replenishment – precipitation efficiency – thus affects how much Ba is ultimately incorporated into the coral skeleton. Indeed, Rayleigh fractionation has been suggested to affect Ba-incorporation into zooxanthellate Scleractinia (Gaetani and Cohen, 2006; Pretet et al., 2015; Reed et al., 2021) and azooxanthellate bamboo corals (Geyman et al., 2019). In this framework, decreasing D_{Ba} with increasing depth suggests that Scleractinia calcify more efficiently in deeper waters, and most efficiently in Icelandic waters, compared to other locations.

To test this hypothesis, we compare Ba/Ca data with Sr/Ca ratios measured on the same samples (same solutions; Figure 7). Stylasterid Sr/Ca ratios are sensitive to temperature, while scleractinian Sr/Ca ratios show the combined influence of temperature and Rayleigh fractionation (Gagnon et al., 2007; Ross et al., 2019; Stewart et al., 2020a; supplementary information, section 6.5). The effects of Rayleigh fractionation should in turn be reflected in the residuals of the scleractinian Sr/Ca – temperature relationship (Ross et al., 2019; Stewart et al., 2020a), and should result in a positive correlation between Sr/Ca-temperature residuals and D_{Ba} because both D_{Sr} and D_{Ba} of coral aragonite are greater than 1 (Gaetani and Cohen, 2006).

Although both aragonitic stylasterid and scleractinian D_{Ba} values are positively correlated with Sr/Ca ratios ($p < 0.05$, $r > 0.61$; Figure 7), we find an insignificant and comparatively weak correlation between

aragonitic stylasterid D_{Ba} and Sr/Ca-temperature residuals ($p = 0.07$, $r = 0.35$; Figure 7c). This strongly suggests that temperature is driving the covariance between stylasterid D_{Ba} and Sr/Ca (see section 4.3), and that variations in the degree of Rayleigh fractionation between stylasterid coral samples are small. Conversely, our scleractinian D_{Ba} values retain a significant, positive correlation with Sr/Ca-temperature residuals ($p < 0.05$, $r = 0.57$; Figure 7b), supporting the hypothesis that Rayleigh fractionation impacts Sr- and Ba-incorporation into scleractinian skeletons.

Variations in the degree of Rayleigh fractionation may explain variability in scleractinian D_{Ba} between locations and across depth gradients, as well as the absence of a dominant environmental control on scleractinian D_{Ba} (section 4.4). This is because scleractinian growth rates and the degree of isolation of the calcifying fluid are likely to be affected by a range of variables including food supply (e.g. Crook et al., 2013; Büscher et al., 2017), oxygen concentrations, carbonate system parameters and temperature (e.g. Büscher et al., 2017; Gómez et al., 2018), which in turn vary between locations and with depth. For example, decreasing D_{Ba} with increasing depth suggests that Scleractinia calcify more efficiently in deeper waters, either growing more quickly or employing greater isolation of their calcifying fluid, as previously suggested for bamboo corals (Geyman et al., 2019). Given that pH, oxygen concentration and food supply all tend to decrease with increasing depth in the ocean, it seems unlikely that coral growth rate would increase with increasing depth, and instead more efficient calcification with depth may result from increasing isolation of the scleractinian calcifying fluid (e.g. Geyman et al., 2019). Equally, Scleractinia from Iceland and the northeast Pacific apparently calcify more efficiently than those from other regions, perhaps due to high growth rates during intense seasonal peaks in primary productivity (and thus food supply) in these regions (e.g. see data in Sathyendranath et al., 2019; Sathyendranath et al., 2021). Although we cannot isolate the controlling variable(s), Rayleigh fractionation provides a plausible explanation for the variability in scleractinian D_{Ba}.

A second hypothesis for the cause of variability in scleractinian D_{Ba} is the incorporation of witherite ($BaCO_3$) into the coral skeleton during growth (Mavromatis et al., 2018), which may affect Ba/Ca ratios of zooxanthellate Scleractinia (Liu et al., 2019). It is well-established that scleractinian corals heavily modify their calcifying fluid, increasing pH and $[CO_3]^{2-}$ (and therefore $\Omega_{arag.}$) to promote calcification (Al-Horani et al., 2003; Sinclair and Risk, 2006). At high degrees of carbonate oversaturation, coprecipitation of witherite ($BaCO_3$) within the domain of aragonite is likely, but is supressed at lower degrees of oversaturation (Mavromatis et al., 2018). Therefore, variations in the carbonate chemistry of the scleractinian calcifying fluid could lead to variations in witherite formation and, consequently, coral D_{Ba}.

However, Sr/Ca ratios should be unaffected by witherite precipitation, meaning this hypothesis cannot explain the observed correlation between scleractinian Sr/Ca-temperature residuals and D_{Ba} (Figure 7b). Additionally, comparing stylasterids and Scleractinia challenges the notion that the amount of witherite precipitation is particularly sensitive to fluctuations in the carbonate chemistry of the coral calcifying fluid. Stylasterid skeletal $\delta^{11}B$, U/Ca and B/Ca suggest that stylasterids calcify from a fluid with significantly lower pH, $[CO_3]^{2-}$ and $\Omega_{arag.}$ than Scleractinia (Stewart et al., 2022). Therefore, if witherite precipitation were responding to variations in calcifying fluid carbonate chemistry, we would expect stylasterids to have consistently lower D_{Ba} values than Scleractinia. Yet, the average D_{Ba} values of these coral taxa are very similar (Figure 3a), implying that comparatively small variations in the carbonate chemistry of the scleractinian calcifying fluid are unlikely to lead to substantial differences in witherite precipitation.

Therefore, we suggest that varying degrees of Rayleigh fractionation, perhaps in response to environmental conditions, are the most likely cause of variability in scleractinian Ba/Ca ratios. Conversely, stylasterid Ba/Ca ratios are less variable, suggesting either they are not affected by Rayleigh fractionation, or that the relative rates of stylasterid growth and calcifying fluid isolation are comparatively invariant across a range of ocean conditions. This adds to the growing evidence for contrasting biomineralisation mechanisms in stylasterid and scleractinian corals, with recent work showing that stylasterid Li/Mg, Sr/Ca, $\delta^{18}O$, $\delta^{13}C$ and $\delta^{11}B$ are also less impacted by calcification-related effects than these same ratios in Scleractinia (Samperiz et al., 2020; Stewart et al., 2020a; Stewart et al., 2022).
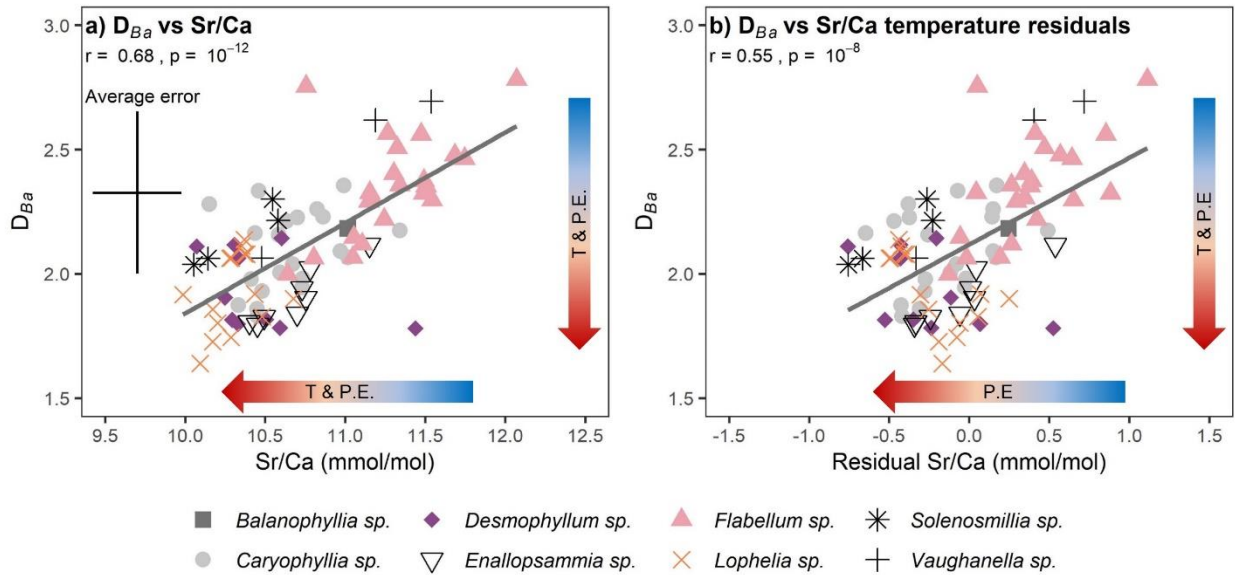
Scleractinia

Aragonitic Stylasteridae
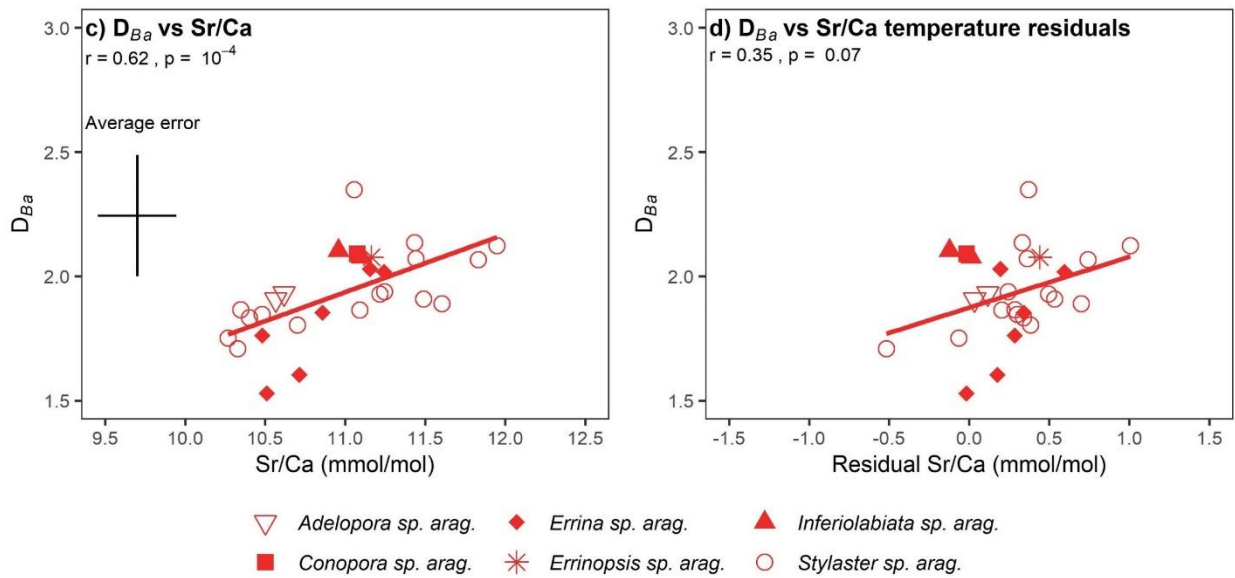
Figure 7. Scleractinian (top) and aragonitic stylasterid (bottom) D_{Ba} values as a function of Sr/Ca (a & c) and Sr/Ca temperature residuals (b & d). Effect of increasing temperature (T) and precipitation efficiency (P.E.) on Sr/Ca and D_{Ba} indicated in a and b. Average error bars shown in panels a and c. Sr/Ca error bars are the largest of the analytical uncertainty or $\pm$ 2SD of replicate samples. The mixed mineralogy scleractinian *Paraconotrochus sp.* was not included in these plots.

4.6   Implications for elevated coral D_{Ba}

The differences between stylasterid and scleractinian coral calcification may have important implications for understanding why D_{Ba} values of a range of coral taxa are - for a given mineralogy - both similar to one another, and elevated compared to other marine calcifiers and experimentally-produced carbonates (section 4.1; Figure 3).

While abiogenic aragonite with $D_{Ba} > 1$ has been produced by some precipitation experiments (Dietzel et al., 2004; Gaetani and Cohen, 2006; Gonneea et al., 2017; Figure 3b), this has recently been attributed to the influence of witherite at high aragonite saturation states, and pure aragonite produced at lower degrees of carbonate saturation ($\Omega_{arag.} < 2$) has D_{Ba} less than 1 (Mavromatis et al., 2018; Figure 3b). Therefore, it has been suggested that witherite precipitation in the domains of aragonite could also be responsible for elevated coral D_{Ba} compared with other marine calcifiers (Mavromatis et al., 2018). However, the similarity of stylasterid and scleractinian D_{Ba} values challenges this idea. As outlined above, while Scleractinia are known to calcify from a fluid which is highly oversaturated with respect to carbonate (Al-Horani et al., 2003; Sinclair and Risk, 2006), stylasterids are thought to calcify from a fluid with $\Omega_{arag.} \sim 1.5$ (Stewart et al., 2022). Therefore, although stylasterid and scleractinian corals share similar average D_{Ba}, they likely form their skeletons from fluids with very different degrees of carbonate oversaturation. In turn, this may indicate that elevated coral D_{Ba} does not result from witherite precipitation triggered by high degrees of carbonate oversaturation in the coral calcifying fluid.

These estimates of stylasterid calcifying fluid $\Omega_{arag.}$ are minimum estimates, and it is possible that a small degree of additional pH and $\Omega_{arag.}$ upregulation occurs (Stewart et al., 2022), which may exceed the threshold for witherite precipitation. In this sense, consistent amounts of witherite precipitation above its saturation threshold could cause consistent elevation in stylasterid and scleractinian coral D_{Ba}. Alternatively, enrichment in coral Ba/Ca may instead result from precipitation of amorphous carbonate phases (Mavromatis et al., 2018), or the presence of organic molecules which act as templates for calcification (e.g. Drake et al., 2021) and can influence skeletal composition (e.g. Mavromatis et al., 2017; 2018). Although we cannot constrain the reasons for the enrichment in coral D_{Ba} here, our data clearly illustrate that explanations for elevated Ba-incorporation into coral carbonate need to consider the diversity of coral calcification mechanisms.

5.   Conclusions

We present the first measurements of stylasterid skeletal Ba/Ca ratios. Mineralogy exerts a strong control on stylasterid Ba/Ca, with aragonitic samples having higher Ba/Ca than their high-Mg calcitic

counterparts. However, when each mineralogy is considered separately, stylasterid skeletal Ba/Ca ratios are strongly, linearly correlated with [Ba]$_{SW}$. We find that temperature exerts a secondary control on Ba-incorporation into stylasterid skeletons, consistent with abiogenic precipitation experiments. Simultaneous measurement of temperature sensitive Li/Mg and/or Sr/Ca ratios in stylasterid samples provides a means to qualitatively assess the possible role of temperature in palaeoceanographic [Ba]$_{SW}$ records.

Azooxanthellate scleractinian Ba/Ca ratios are more sensitive to changes in [Ba]$_{SW}$ than previously thought (Spooner et al., 2018), driven by differences in Ba-incorporation between locations and across depth gradients. Paired Ba/Ca and Sr/Ca values are consistent with the influence of Rayleigh fractionation related to the coral calcification process. The driver(s) of this process remains unclear, likely due to the competing influence of multiple oceanographic parameters on the scleractinian calcification process. Crucially, stylasterid skeletal Ba/Ca ratios are impacted less by calcification processes, and with robust [Ba]$_{SW}$ and temperature proxies now established (Samperiz et al., 2020; Stewart et al., 2020a), stylasterid corals are a valuable multi-proxy palaeoceanographic archive.

6. Supplementary information

6.1 Coral sampling strategy

As outlined in the main text, large chunks of coral samples were taken and, where possible, two samples were taken from each coral. Visually pristine areas of material were targeted, and any remaining discoloured or altered material was removed using a hand-held Dremel tool. For stylasterid corals, the apical tips of branches were avoided, since it has been shown their oxygen and carbon stable isotopic composition is further from equilibrium than bulk skeletal samples (Samperiz et al., 2020). Examples of sampling of three stylasterid specimens used in this study is shown below (Supplementary figure 1).
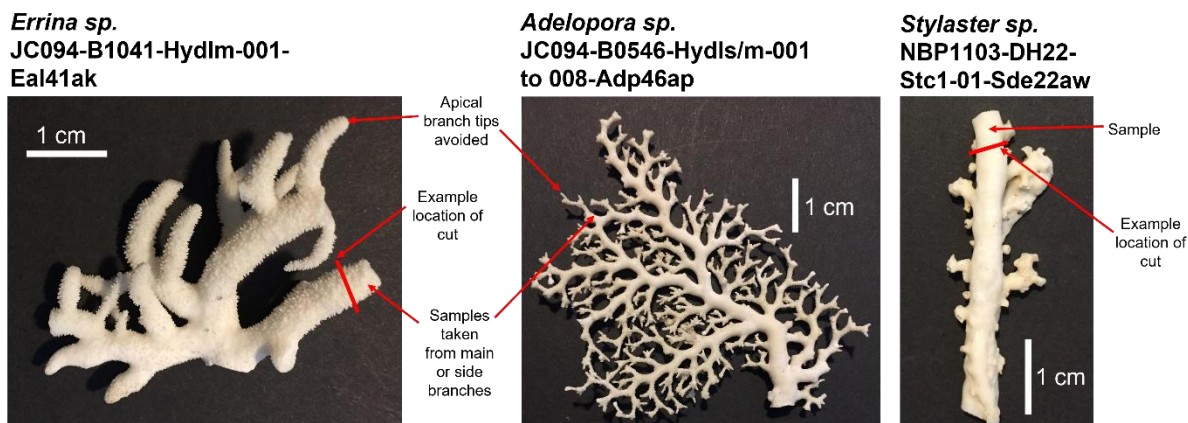
Supplementary figure 1. Photos of three stylasterid specimens used in this study. Red lines show examples of where specimens were cut to obtain samples.

6.2 Fe/Ca and Mn/Ca ratios: contamination screening

Iron oxyhydroxides are common contaminant phases which can impact element/Ca ratios in marine biogenic carbonates (e.g. Boyle, 1981). Here, we test for their influence in our dataset by measuring the Fe/Ca and Mn/Ca of sample replicates, and reporting correlations with both coral Ba/Ca and residuals of the Ba/Ca vs [Ba]$_{SW}$ relationships (Ba/Ca$_{residual}$ = Ba/Ca$_{coral}$ – Ba/Ca$_{calibration}$) (Supplementary figure 2; Supplementary figure 3).

No significant correlation is found between Ba/Ca and either Fe/Ca or Mn/Ca values for aragonitic stylasterids, or between scleractinian Ba/Ca and Fe/Ca ($p > 0.05$). However, high-Mg calcitic stylasterids show a significant ($p < 0.05$) positive correlation between these variables ($r_{Fe-Ba} = 0.69$; $r_{Mn-Ba} = 0.69$), while scleractinian Ba/Ca ratios also correlate significantly with Mn/Ca ($p < 0.05$, $r = 0.21$). Furthermore, both Fe/Ca and Mn/Ca correlate significantly and positively with residuals of the Ba/Ca vs [Ba]$_{SW}$ relationships

for both high-Mg calcitic stylasterids ($r_{\text{Fe-resid}} = 0.90$; $r_{\text{Mn-resid}} = 0.89$) and Scleractinia ($r_{\text{Fe-resid}} = 0.40$; $r_{\text{Mn-resid}} = 0.40$) (Supplementary figure 2; Supplementary figure 3).

Sample ID	No. reps excluded	Type	Taxon	Location
NBP1103-DH07-Bp-0	2	Scleractinia	*Balanophyllia sp.*	Drake Passage
NBP1103-DH14-Fpalive-8	2	Scleractinia	*Flabellum sp.*	Drake Passage
NBP1103-DH14-Fpalive-1	2	Scleractinia	*Flabellum sp.*	Drake Passage
DY081-008-ROV329-Ev024-453Flab	1	Scleractinia	*Flabellum sp.*	Labrador Sea
JC094-21-EBB-ROV228-SLP44-B1584-Carls-001	1	Scleractinia	*Caryophyllia sp.*	Equatorial Atlantic
DY081-031-ROV333-Ev037-201-590-Loph	1	Scleractinia	*Lophelia sp.*	Labrador Sea
JR15005-40-832-Egr832	1	Stylasterid, mixed	*Errina sp., mixed (arag.)*	S. Orkney
JR15005-44-907-mn-1-Ela907	2	Stylasterid, high-Mg calc.	*Errina sp., calc.*	S. Orkney

Supplementary table 1. Samples measured in this study which are excluded from calibrations due to contamination inferred from Fe/Ca ratios. Where only one replicate was removed, the remaining replicate was retained in the calibration.
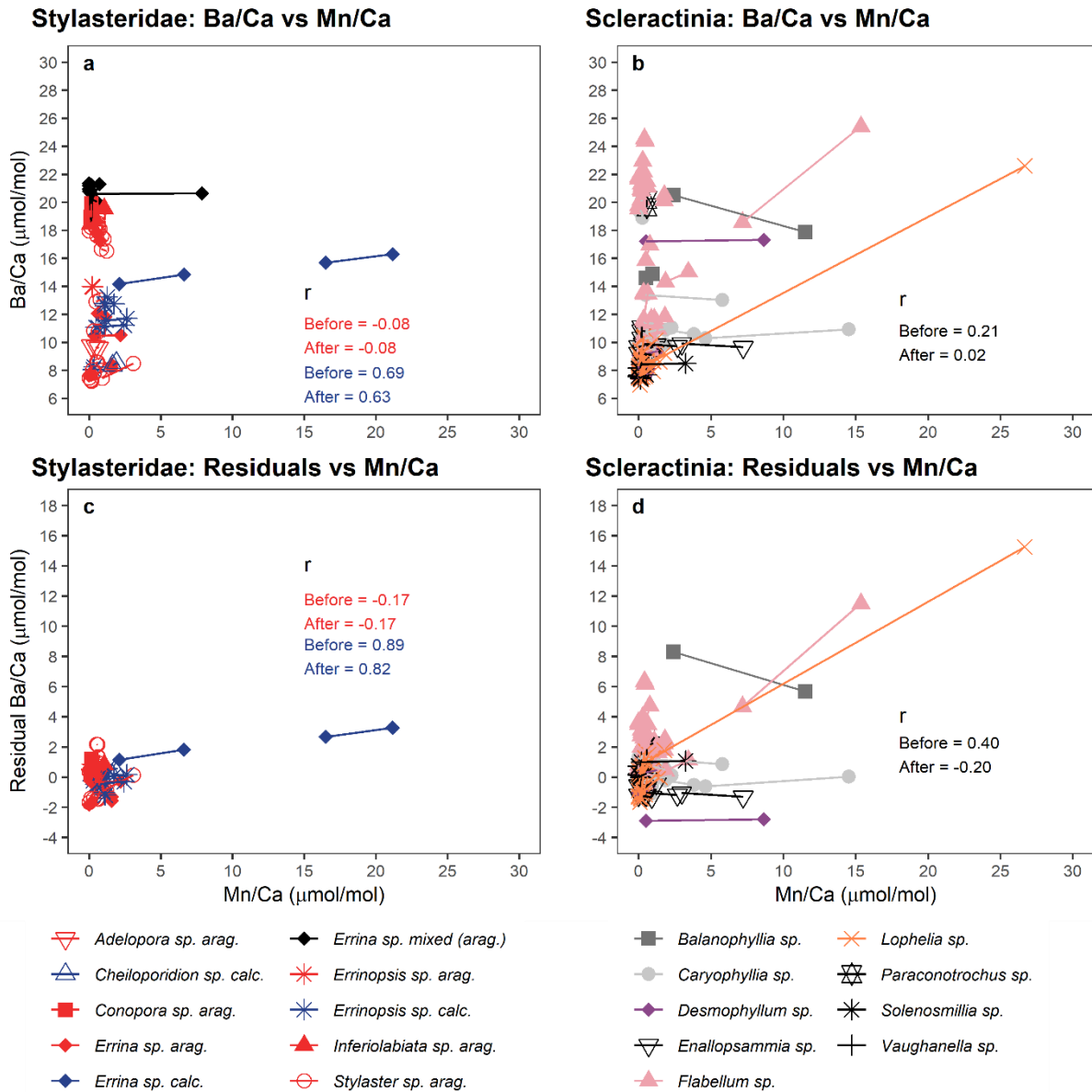
Supplementary figure 2. Correlations between Ba/Ca and Mn/Ca (a and b) and residual Ba/Ca and Mn/Ca (c and d) for corals measured in this study. Straight lines join replicates of the same coral. Pearson *r* values before and after screening are shown. All *r* values calculated using average values for each coral to avoid pseudoreplication. All *Lophelia sp.* replicates used to calculate sample averages at this stage (i.e. both bulk calyx and theca wall replicates; see main text section 4.4). Mixed mineralogy corals not included in goodness-of-fit calculations. Where Mn/Ca values were less than detection limits, values were set to 0 μmol/mol.
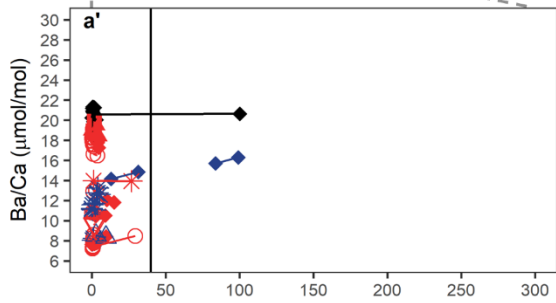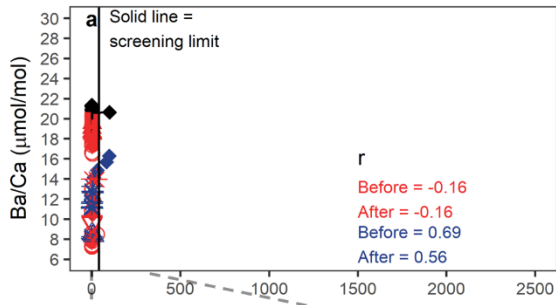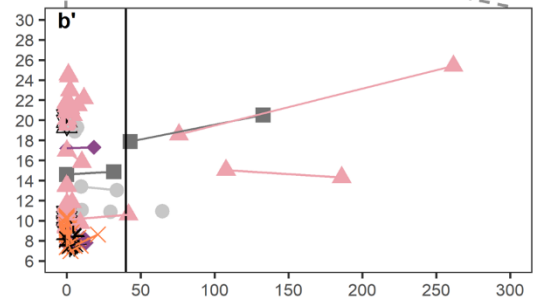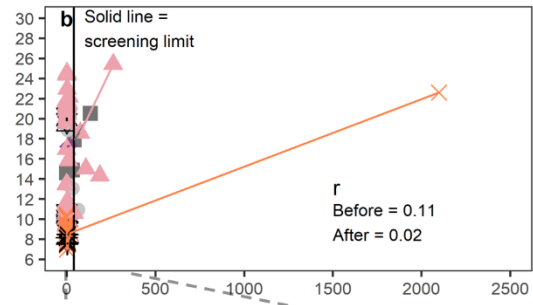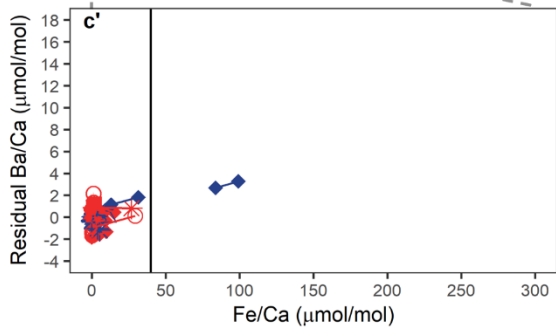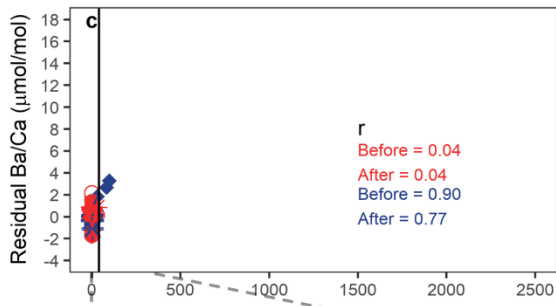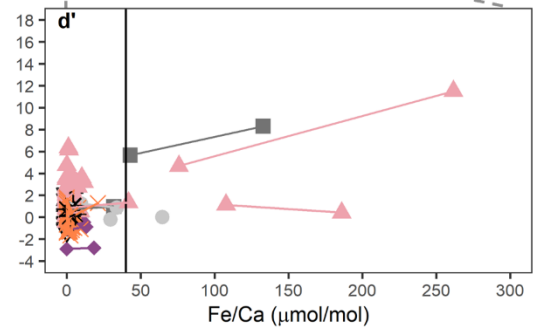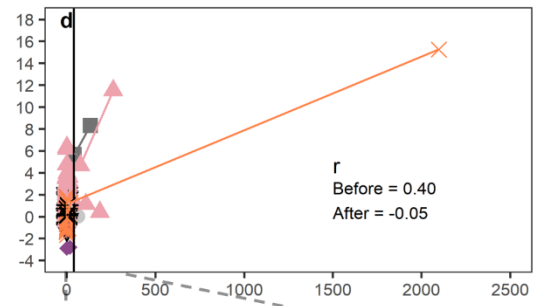
Supplementary figure 3. As Supplementary figure 2, with Mn/Ca replaced with Fe/Ca. For clarity, panels a', b', c' and d' show data from panels a, b, c and d in the Fe/Ca range 0 to 300 µmol/mol. When Fe/Ca values

were less than detection limits, values were set to 0 µmol/mol. Symbols and colours follow Supplementary figure 2.

We therefore exclude sample replicates which have Fe/Ca > 40 mmol/mol, following Spooner et al. (2018). This results in 12 measurements from eight corals being removed from our dataset, with four corals having both of their replicate analyses removed (Supplementary table 1). When these replicates are excluded, the correlations between scleractinian Ba/Ca and Mn/Ca, and scleractinian calibration residuals and Fe/Ca and Mn/Ca, become insignificant ($p > 0.05$, $-0.20 < r < 0.20$; Supplementary figure 2; Supplementary figure 3). For high-Mg calcitic stylasterids, correlations are reduced by this screening, but not removed ($r_{Fe-Ba} = 0.56$; $r_{Mn-Ba} = 0.63$; $r_{Fe-resid} = 0.77$; $r_{Mn-resid} = 0.82$; Supplementary figure 2; Supplementary figure 3). These correlations are driven almost entirely by two replicates of one *Errina sp.* sample which both have relatively high Ba/Ca residuals and slightly elevated Fe/Ca and Mn/Ca. Owing to the small magnitude of Fe/Ca and Mn/Ca enrichment in this sample, we choose to retain it in our calibration.

6.3   Scleractinian compilation: analytical offsets and uncertainties

Ba/Ca data require correction for analytical offsets which can occur between laboratories (e.g. Stewart et al., 2020b). For data measured in our study, we normalised Ba/Ca values measured in Bristol, NIST and St Andrews to the relatively homogenous NIST RM 8301 (Coral) solution (interlaboratory reproducibility for Ba/Ca 2.7 % (RSD; 1s) (Stewart et al., 2020b)).

Our new scleractinian Ba/Ca data were combined with those published in previous studies (Hemsing et al., 2018; Spooner et al., 2018) to create a compiled dataset. Laser ablation data (Anagnostou et al., 2011) were not used due to apparent analytical differences between solution and laser-ablation techniques (see Spooner et al., 2018).

NIST RM 8301 (Coral) was not available for previous studies, and instead, Ba/Ca data from these two studies was previously normalised based on measurements of the coral reference material JCp-1 (see Spooner et al., 2018). We use these JCp-1 corrected ratios in our compilation. JCp-1 Ba/Ca ratios are known to be significantly more heterogenous than NIST RM 8301 (Coral), with an interlaboratory reproducibility of ~ 9 % (RSD; 1s) (Hathorne et al., 2013). Therefore, while we did measure JCp-1 as part of our study, we chose not to use this reference material for normalisation. By instead normalising our data to NIST RM 8301 (Coral), we ensure that our dataset is compatible with future projects which may use this more homogenous reference material (Stewart et al., 2020b).

Use of different reference materials to correct for interlaboratory offsets raises the possibility of analytical differences between our data and previous work. To test for this, we measured additional replicates of 7

corals which were also measured by Spooner et al. (2018) and/or Hemsing et al. (2018). We find good agreement between coral subsamples measured in each study, and importantly find no systematic offset between data measured in our study and these studies (Supplementary figure 4). Furthermore, our long-term laboratory average values for JCp-1 – once corrected to NIST RM 8301 (Coral) - differed from the published interlaboratory value by < 4 %, meaning any additional correction would have a minor impact on our results. Therefore, direct comparison of ours and previously published datasets is justified, and in practise, any remaining analytical offsets between laboratories are unlikely to influence our findings.
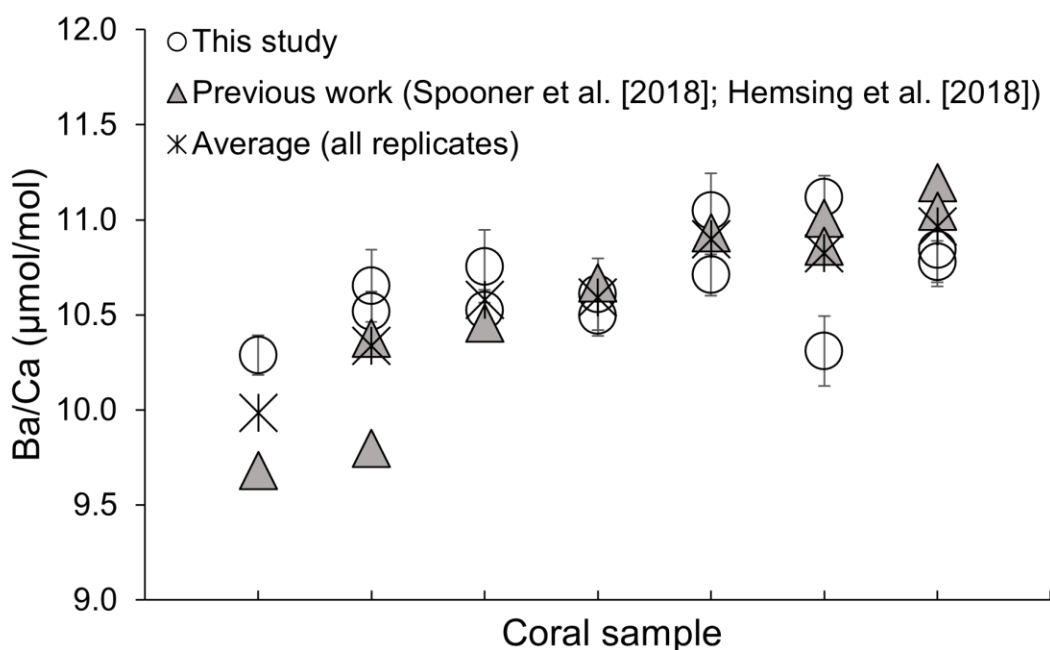
Supplementary figure 4. Replicate subsamples of corals measured in this study and by previous authors show good agreement, after correction for analytical offsets. Analytical error bars (RSD; 2s) on individual replicates from this study are shown.

6.4   Comparing prediction interval calculations

As outlined in section 2.6, the uncertainties associated with [Ba]$_{SW}$ predictions from coral Ba/Ca (and temperature predictions from coral Sr/Ca) were calculated by two methods, and these are briefly compared here. Firstly, the choice of method has no effect on prediction uncertainties associated with either the aragonitic stylasterid or scleractinian calibrations (Table 1; Supplementary table 2). Aragonitic stylasterid Ba/Ca can be used to constrain [Ba]$_{SW}$ to within ~ ± 9 nmol/kg (same uncertainty using either method), representing a clear improvement on scleractinian Ba/Ca (~ ± 16 nmol/kg; again same uncertainty using

either method) (Table 1). Meanwhile, aragonitic stylasterid Sr/Ca ratios can be used to reconstruct temperature to within ~ ± 6.5 ⁰C, again representing a clear improvement on scleractinian Sr/Ca (~ ± 9 ⁰C) (Supplementary table 2).

For high-Mg calcitic stylasterids (considering Ba/Ca only, Sr/Ca vs temperature calibration not discussed here), the difference between the two methods is more pronounced, and the Simple IPI method gives narrower prediction intervals than the original approach (Table 1). This likely results from the fact that the simple IPI approach does not incorporate any uncertainty in the calibration line itself (e.g. uncertainties in the calibration gradient or intercept), but instead assumes that all the uncertainty is derived from scatter about the calibration line (McClelland et al., 2021).

The robust mathematical framework associated with the Simple IPI method means this is the preferred method of prediction uncertainty estimation, and is used in isolation in chapter 4. Encouragingly, the choice of method makes no difference to the conclusions of this study.

6.5 Sr/Ca vs temperature correlations

Sr/Ca values for most samples used here were reported and analysed previously (Stewart et al., 2020a), and the reader is directed to this work for a detailed discussion of Sr-incorporation into azooxanthellate stylasterids and Scleractinia. These authors found a strong correlation between aragonitic stylasterid Sr/Ca and seawater temperature, and a weaker relationship for Scleractinia. Addition of new samples reported here (20 stylasterid and 17 scleractinian samples) results in relationships between coral Sr/Ca and temperature which have intercepts and gradients within error of those reported previously (Supplementary figure 5; Supplementary table 2; Stewart et al., 2020a). Compared to this previous work, the R^2 of the aragonitic stylasterid calibration is reduced slightly, and the prediction interval made wider. However, the observation that aragonitic stylasterid Sr/Ca more reliably records seawater temperature than scleractinian Sr/Ca remains robust (compare R^2 and prediction intervals in Supplementary table 2), consistent with biologically-mediated "vital effects" impacting scleractinian Sr/Ca more than stylasterid Sr/Ca (Stewart et al., 2020a).

Sr/Ca values of a number of high-Mg calcitic stylasterids were also measured in this study. However, these samples span a small temperature range, precluding assessment of whether their Sr/Ca values also correlate with seawater temperature.
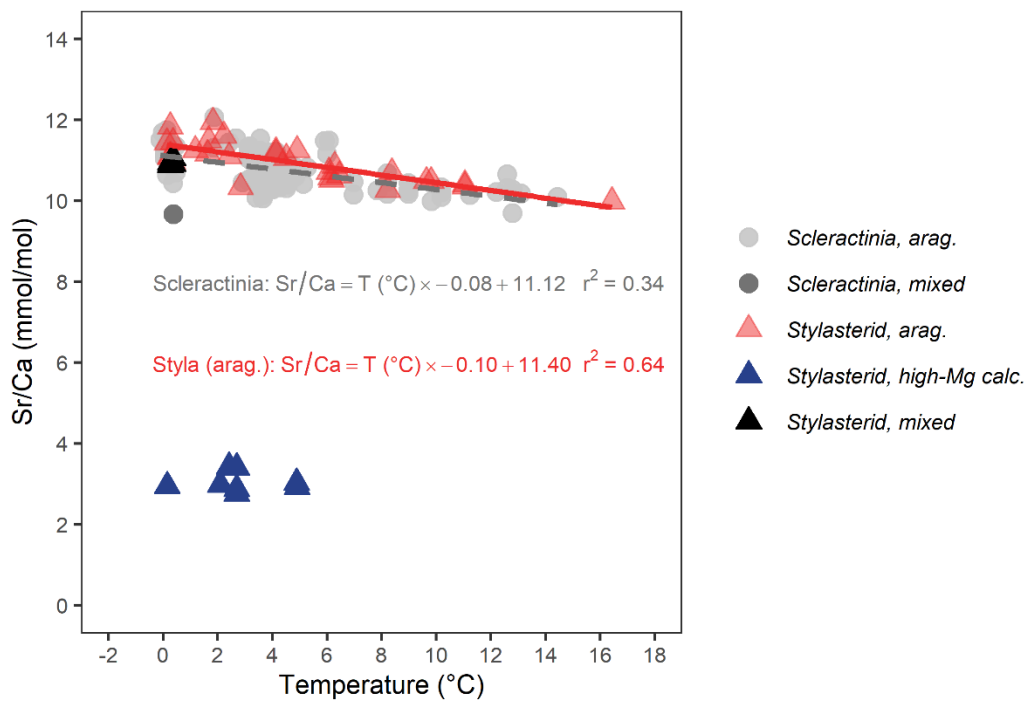
Supplementary figure 5. Relationships between Sr/Ca and seawater temperature for corals used in this study. Data are measured here, or are from Stewart et al. (2020a). Lines of best fit (Ordinary Least Squares) shown for aragonitic stylasterids (solid, red) and Scleractinia (dashed, grey).

Taxon	Source	*r*	*p*	Regression type	Gradient, m	(± 2SE)	Intercept, c	± 2SE	R²	Prediction interval (°C)*
Stylasterid, arag.	Stewart et al., (2020a)		< 0.05	OLS	−0.11		11.61		0.79	± 5.3
Stylasterid, arag.	Stewart et al. (2020a) & this study	−0.80	< 0.05	OLS	−0.10	0.03	11.40	0.17	0.64	± 6.7 (6.3)
				Deming (unweighted, orthogonal)	−0.10	0.02	11.40	0.20		
Scleractinia	Stewart et al. (2020a)		< 0.05	OLS	−0.08		11.06		0.31	> ± 7.7
Scleractinia	Stewart et al. (2020a) & this study	−0.59	< 0.05	OLS	−0.08	0.02	11.12	0.14	0.34	± 9.2 (9.1)
				Deming (unweighted, orthogonal)	−0.08	0.02	11.11	0.16		

*95 % prediction intervals in original publication calculated at the mean aragonite Sr/Ca value (~ 11 mmol/mol). For consistency with chapter 4, prediction intervals in brackets show those calculated by the Simple IPI method in McClelland et al. (2021). Comparison of prediction uncertainty estimates can be found in section 6.4.

Supplementary table 2. Summary of relationships between Sr/Ca and seawater temperature. Results of Ordinary Least Squares (OLS) and Deming (unweighted, i.e. orthogonal) regressions shown, for simplicity we recommend use of OLS regressions in palaeoceanographic contexts.

Subsample Sr/Ca and Ba/Ca ratios of mixed mineralogy corals are positively correlated in three out of four cases, indicating a shared mineralogical control on the incorporation of each element (Supplementary figure 6).
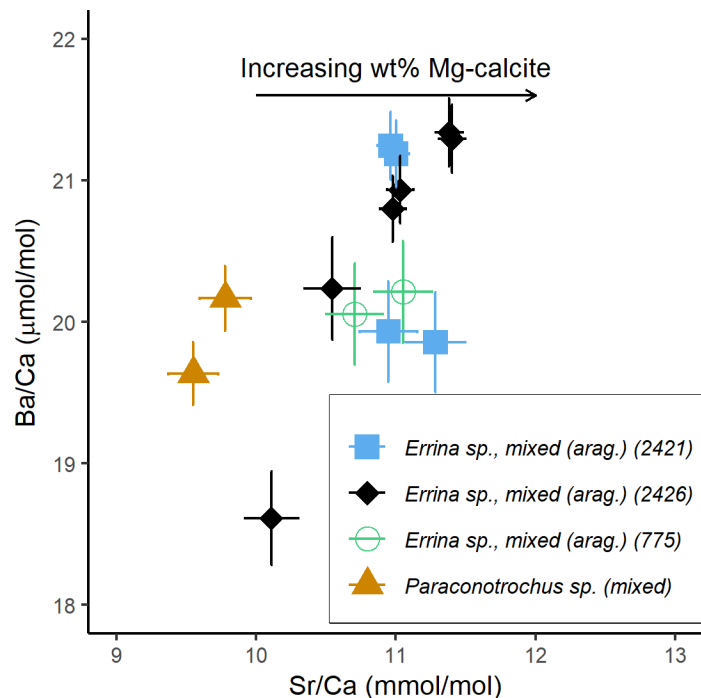
Supplementary figure 6. Ba/Ca vs Sr/Ca of mixed mineralogy coral subsamples. Colours and symbols represent different corals. One *Errina sp.* sample had only one replicate after filtering for contaminant phases, and so is not included in this plot. *Errina sp.* samples are identified by the final numbers in their sample codes. Error bars represent analytical errors (RSD; 2s).

6.6   Origin of elevated Ba/Ca in mixed mineralogy stylasterids

The four mixed mineralogy stylasterids (genus: *Errina sp.*, mixed (arag.); species: *Errina gracilis*) measured in this study have higher Ba/Ca than co-located entirely aragonitic stylasterids, despite the robust mineralogical control on stylasterid Ba/Ca outlined in section 4.1 of the main text. This elevated Ba/Ca signature is apparently specific to Ba; Sr/Ca, Li/Ca and Mg/Ca ratios measured in the same samples (same dissolved solutions) fall between entirely aragonitic and high-Mg calcitic stylasterids (Stewart et al., 2020a).

This Ba-specific signature could be caused by contamination by barite ($BaSO_4$) crystals, which are a common Ba-bearing particulate phase at mesopelagic depths (Dehairs et al., 1980). However, treatment with DTPA – a cleaning procedure designed to remove barite from marine carbonates - had no distinguishable effect on *Errina gracilis* Ba/Ca ratios, compared to standard oxidative cleaning procedures (Supplementary figure 7). Secondly, any effect of regional hydrographic conditions (e.g. temperature, see main text section 4.3) cannot explain our observations, because this should also impact on co-located aragonitic samples.

Instead, we suggest two possible alternatives. Firstly, the mixed mineralogy of this species suggests it calcifies in a different manner to other, mono-mineralic stylasterids. Variations in growth rates and/or modification of the coral calcifying fluid could lead to high and variable Ba/Ca ratios via Rayleigh fractionation processes (e.g. Gaetani and Cohen, 2006; main text section 4.5). Alternatively, other phases such as witherite ($BaCO_3$) may be present in the coral skeleton, leading to Ba-enrichment (e.g. Mavromatis et al., 2018; main text section 4.6). As noted above, Ba-incorporation in *Errina gracilis* is the exception to mineralogical rule, and the skeletal $\delta^{18}O$ and $\delta^{13}C$ of these samples are close to equilibrium with seawater (Samperiz et al., 2020; Stewart et al., 2020a). This could indicate that calcification-related effects are unlikely the cause of Ba-enrichment. However, the (relatively) similar partition coefficients of Ba into aragonite and high-Mg calcite mean that calcification-related effects discernible in Ba/Ca data could be overprinted by more extreme mineralogical controls on other elements (e.g. Mg, Li and Sr).

Alternatively, anomalously high Ba/Ca ratios may be caused by small-scale spatial and/or temporal variability in [Ba]$_{SW}$. All *Errina gracilis* samples were collected from the South Orkney region, where seasonal fluctuations in primary productivity (e.g. Jennings et al., 1984; Clarke and Leakey, 1996), phytoplankton community structure (Kang et al., 2002), sea ice extent (e.g. Murphy et al., 1995) and upwelling of Ba-rich deep waters all influence Ba cycling (Hoppema et al., 2010; Pyle et al., 2017; 2018) and could plausibly generate spatial and temporal heterogeneity in [Ba]$_{SW}$. Whether *Errina gracilis* calcifies at a different time of year to other stylasterid species is unknown, meaning we cannot assess whether temporal variations in [Ba]$_{SW}$ are responsible for their elevated Ba/Ca. However, *Errina gracilis* does form part of a group of four "field-forming" stylasterid species which are commonly found together in dense aggregations, sustained by waters rich in organic carbon, focused by local bathymetry (Post et al., 2010; Bax and Cairns, 2014). The remineralisation of barite associated with this organic carbon may result in *Errina gracilis* experiencing systematically higher [Ba]$_{SW}$ than other stylasterid species, although one sample of the entirely aragonitic species *Inferiolabiata labiata* has lower Ba/Ca than *Errina gracilis*, despite being collected from the same locality and also being a member of this "field-forming" group (Bax and Cairns, 2014).

Whether the elevated and variable Ba/Ca of *Errina gracilis* results from a calcification-related effect or is due to its specific habitat is unknown. However, the uncertainty regarding Ba-incorporation into this species, combined with its mixed mineralogy, means it is unsuitable for use in palaeoceanographic contexts.
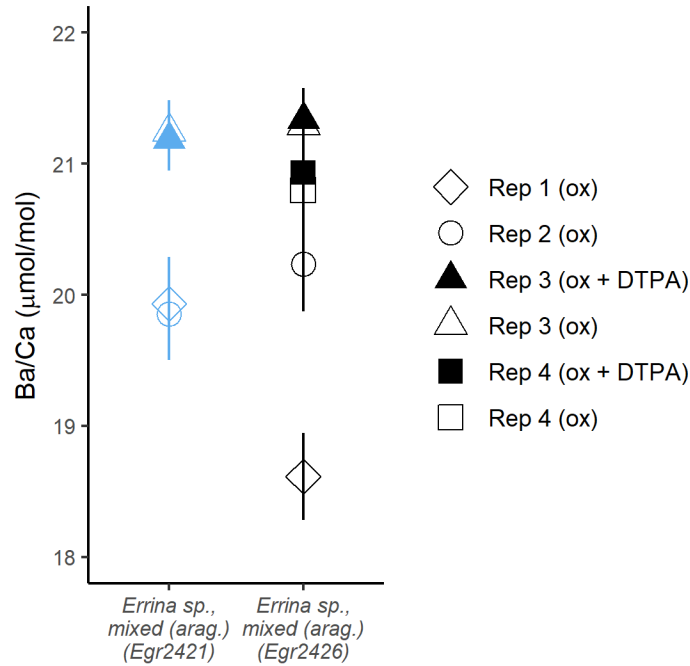
Supplementary figure 7. Cleaning experiments carried out on two mixed mineralogy *Errina sp.* corals. Symbols represent different replicates of the same powders. The two corals used were JR15005-113-2421-Egr2421 (Egr2421) and JR15005-113-2426-Egr2426 (Egr2426). Open symbols were cleaned by standard oxidative techniques (ox), filled symbols were additionally treated with DTPA (ox + DTPA). Error bars represent analytical errors (RSD; 2s).

6.7 Bamboo coral Ba/Ca

Bamboo coral Ba/Ca has previously been shown to correlate with [Ba]$_{SW}$ (LaVigne et al., 2011). Our high-Mg calcitic stylasterid Ba/Ca vs [Ba]$_{SW}$ relationship is steeper than that found for bamboo corals (LaVigne et al., 2011; red line in Supplementary figure 8). However, closer inspection of the bamboo coral data reveals a reduction in Ba-incorporation at high [Ba]$_{SW}$ (compare grey and red lines in Supplementary figure 8), likely driven by decreasing bamboo coral D$_{Ba}$ with increasing water depth (Geyman et al., 2019). When bamboo coral samples from the range of [Ba]$_{SW}$ represented in our stylasterid study (i.e. [Ba]$_{SW}$ < 105 nmol/kg) are considered, the bamboo coral Ba/Ca vs [Ba]$_{SW}$ relationship is steeper (compare grey and red lines in Supplementary figure 8) and agrees well with our high-Mg calcitic stylasterid relationship (main text, Figure 4). However, we note that the lack of a comparable interlaboratory standard may complicate direct comparison of these datasets. Finally, we also note that one bamboo coral sample is plotted differently here

to Figure 2 in LaVigne et al. (2011). Here, we are plotting this data point as it is provided in their Table 1 and supplement. In practise, the position of this sample does not change our conclusions.
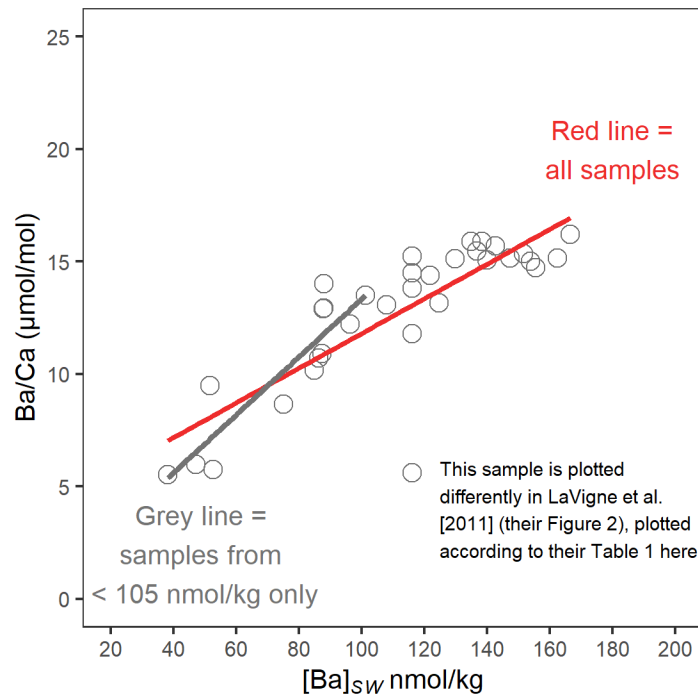
Supplementary figure 8. Bamboo coral Ba/Ca vs [Ba]$_{SW}$ from LaVigne et al. (2011). Note the reduction in gradient when including samples from higher [Ba]$_{SW}$, shown by comparison of grey and red lines. For comparability with our data set, samples from [Ba]$_{SW}$ > 105 nmol/kg are not used in Figure 3 and Figure 4 in the main text.

6.8   Additional controls on stylasterid and scleractinian Ba-incorporation

Correlations between hydrographic variables and stylasterid and scleractinian D$_{Ba}$ and Ba/Ca vs [Ba]$_{SW}$ residuals are summarised in Supplementary table 3. As outlined in the main text (sections 4.3 and 4.4), the strongest observed correlations are found for stylasterids, with both temperature and dissolved silica concentrations. We find no significant correlations between scleractinian D$_{Ba}$ values and any hydrographic parameter).

	Aragonitic stylasterids		High-Mg calcitic stylasterids		Scleractinia (compiled dataset)	
	D_{Ba}	Ba/Ca vs $[Ba]_{SW}$ residuals	D_{Ba}	Ba/Ca vs $[Ba]_{SW}$ residuals	D_{Ba}	Ba/Ca vs $[Ba]_{SW}$ residuals
Temperature (°C)	**$r = -0.54$** **$p < 0.05$**	$r = -0.16$ $p > 0.05$	**$r = -0.55$** **$p > 0.05$**	**$r = -0.4$** **$p > 0.05$**	$r = -0.15$ $p > 0.05$	**$r = -0.1$** **$p < 0.05$**
Dissolved silica (µmol/kg)	**$r = 0.47$** **$p < 0.05$**	$r = 0.14$ $p > 0.05$	**$r = 0.45$** **$p > 0.05$**	$r = 0.33$ $p > 0.05$	$r = -0.01$ $p > 0.05$	$r = 0.07$ $p > 0.05$
Depth (m)	$r = -0.18$ $p > 0.05$	**$r = -0.45$** **$p < 0.05$**	$r = -0.18$ $p > 0.05$	$r = -0.31$ $p > 0.05$	$r = -0.06$ $p > 0.05$	$r = -0.11$ $p > 0.05$
pH (total scale)	$r = 0.33$ $p > 0.05$	$r = 0.24$ $p > 0.05$	$r = 0.15$ $p > 0.05$	$r = 0.27$ $p > 0.05$	$r = 0.01$ $p > 0.05$	$r = 0.03$ $p > 0.05$
Salinity (psu)	$r = -0.28$ $p > 0.05$	$r = -0.06$ $p > 0.05$	$r = 0.34$ $p > 0.05$	$r = 0.21$ $p > 0.05$	$r = 0.03$ $p > 0.05$	$r = 0.00$ $p > 0.05$
Oxygen (µmol/kg)	**$r = 0.39$** **$p < 0.05$**	$r = 0.27$ $p > 0.05$	$r = 0.08$ $p > 0.05$	$r = 0.20$ $p > 0.05$	$r = 0.07$ $p > 0.05$	$r = 0.09$ $p > 0.05$
Phosphate (µmol/kg)	$r = 0.10$ $p > 0.05$	$r = -0.11$ $p > 0.05$	$r = 0.12$ $p > 0.05$	$r = 0.00$ $p > 0.05$	$r = 0.01$ $p > 0.05$	$r = 0.09$ $p > 0.05$
$\Omega_{arag.}$	$r = 0.02$ $p > 0.05$	$r = 0.23$ $p > 0.05$	$r = 0.00$ $p > 0.05$	$r = 0.13$ $p > 0.05$	$r = 0.19$ $p > 0.05$	$r = 0.13$ $p > 0.05$

Supplementary table 3. Correlations between coral D_{Ba}, and Ba/Ca vs $[Ba]_{SW}$ residuals, and various hydrographic parameters. Relationships with p values < 0.05 and/or r values > 0.4 or < -0.4 are shown in bold. For Scleractinia, the entire compiled dataset (this study, Spooner et al., 2018; Hemsing et al., 2018) is included in this analysis, where relevant hydrographic data were previously published. Note that some samples from Hemsing et al. (2018) were not published with associated concentrations of dissolved oxygen, phosphate or silica. Samples from Spooner et al. (2018) and Hemsing et al. (2018) were not published with associated $\Omega_{arag.}$, or carbonate system parameters to facilitate $\Omega_{arag.}$ calculation.
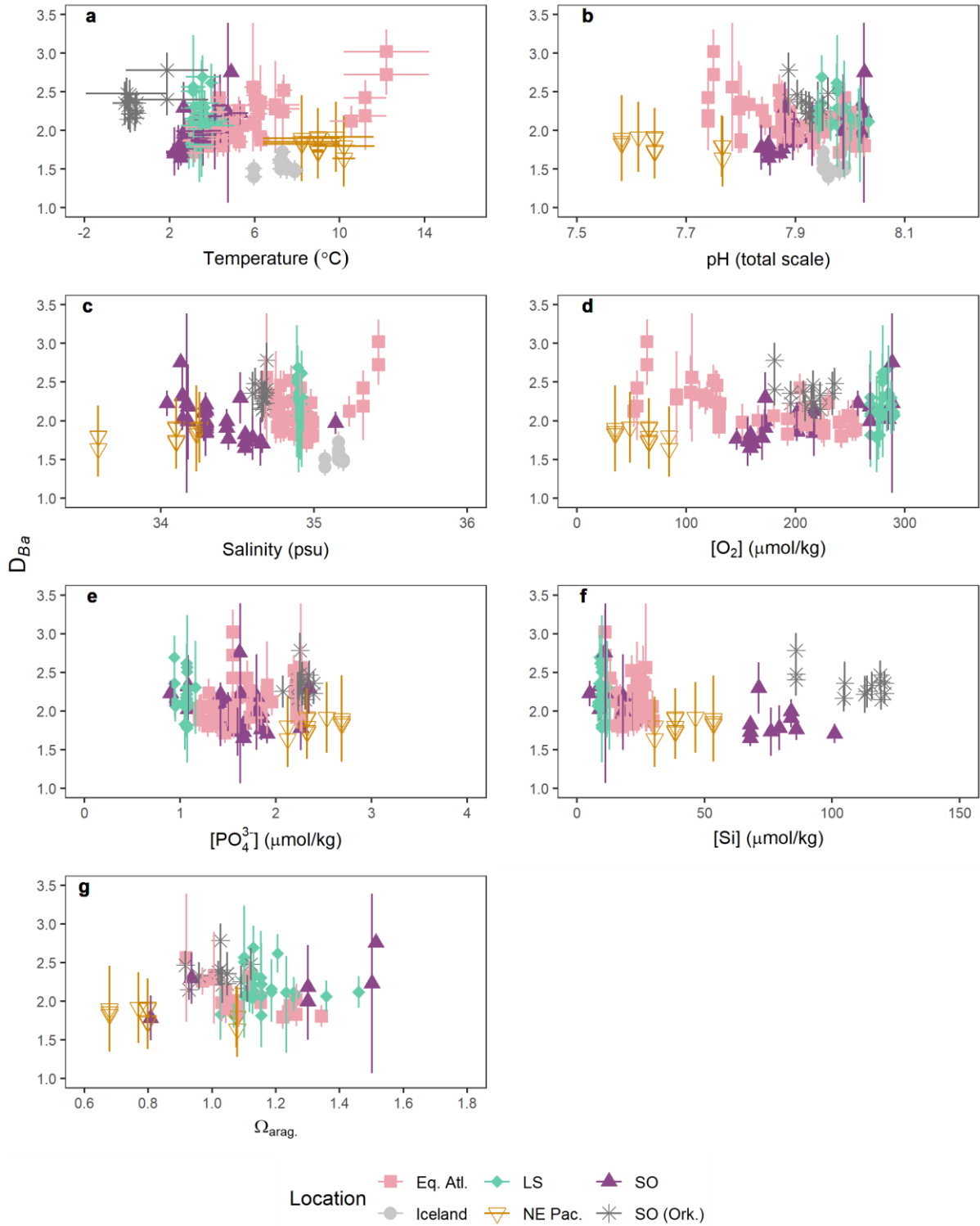
Supplementary figure 9. Scleractinian D_{Ba} values as a function of various seawater parameters. Colours and symbols represent locations. Icelandic samples from Hemsing et al. (2018) were not published with

associated concentrations of dissolved oxygen, phosphate or silica. Samples from Spooner et al. (2018) and Hemsing et al. (2018) were not published with associated $\Omega_{arag.}$, or carbonate system parameters to facilitate $\Omega_{arag.}$ calculation.

Finally, while genus-specific effects on Ba-incorporation into stylasterid and scleractinian corals appear to be minimal, we find that sampling approach is an important consideration when analysing Ba/Ca ratios of the scleractinian coral *Lophelia sp.*, owing to the systematic offset between Ba/Ca of bulk calyx and theca only subsamples (Supplementary figure 10; main text section 4.4).
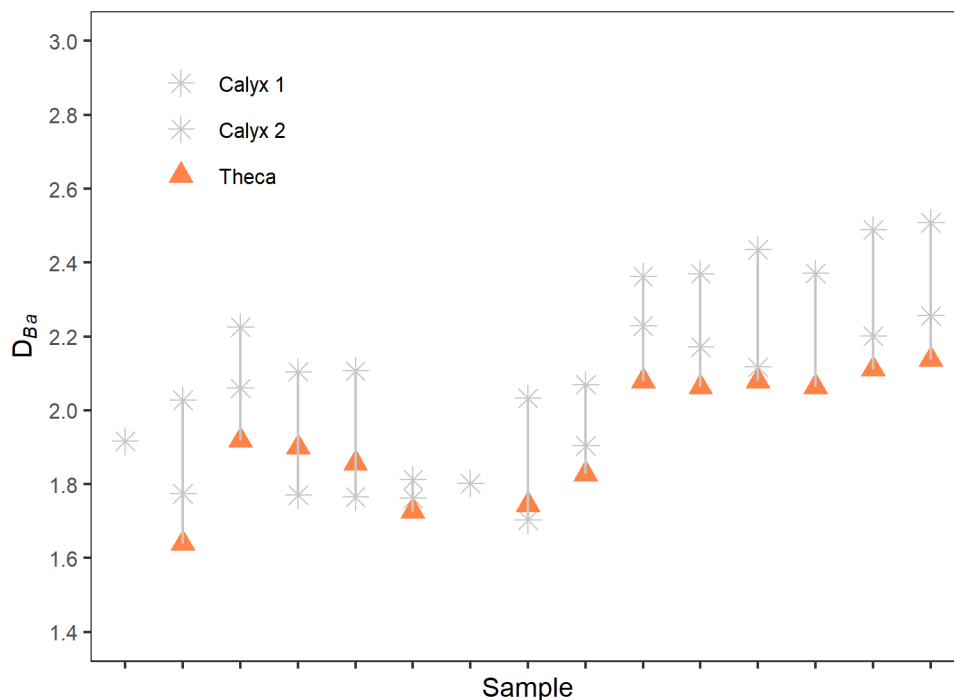
Supplementary figure 10. Effect of sampling on *Lophelia* D_{Ba}. Whole calyx samples are thought to incorporate centres of calcification (COCs), which results in increased Ba-incorporation compared to theca samples. For description of sampling, see Stewart et al. (2020a).

6.9   Effects of hydrographic data choice

As outlined in chapter 4, the method by which ancillary hydrographic variables (e.g. temperature, dissolved nutrient concentrations, alkalinity and DIC) are estimated in this chapter differs to that used in chapter 4, owing to the contrasting aims and priorities of these studies. In this section, I add to the published version of this chapter by considering the origin and implications of these methodological differences.

The differing methodologies arise because the choice of paired ancillary hydrographic data is inherently subjective (see Supplementary figure 11). For the majority of samples, there is an inevitable degree of mismatch between the coral collection location, depth and time, compared with that of a nearby hydrographic measurement. Further, the "best" choice hydrographic station for a given sample is generally unclear, with some stations closer in location to the sample, some closer in depth and others more suited in terms of their oceanographic setting. Additionally, the closest hydrographic station may, for example, have been collected many years prior to the coral collection event, while a hydrographic station further away could be a better temporal match. To add further complication, not all hydrographic variables will be measured at all stations. In particular, measurements of carbonate system parameters (i.e. alkalinity and DIC) are more rare than measurements of dissolved nutrient concentrations, which in turn are more rare than temperature and salinity measurements. This means that the "best" temperature measurement is often not associated with the "best" carbonate system measurement.
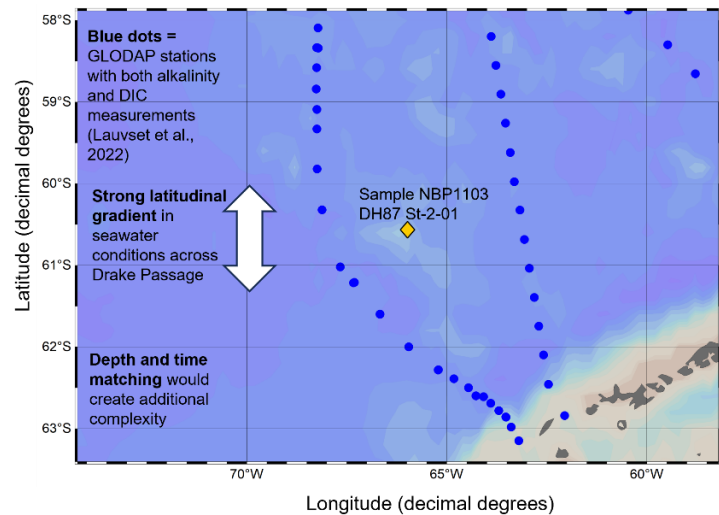
Supplementary figure 11. Example of difficulty in choosing paired hydrographic data. Map shows Drake Passage region of the Southern Ocean. Blue dots show all stations in the GLODAP bottle database with alkalinity and DIC data (Lauvset et al., 2022).

In this chapter, the ancillary hydrographic variable of most interest was seawater temperature. Thus, the first hydrographic station chosen was that with the best available temperature measurement, and the second and third options were chosen to characterise regional variability in ambient seawater temperature, and to ensure constraint on all other hydrographic variables (dissolved oxygen and nutrient concentrations, alkalinity and DIC). Conversely, chapter 4 of this thesis is concerned primarily with pairing coral geochemistry with carbonate system parameters. Therefore, the hydrographic data chosen in that chapter are the three nearest stations which include both alkalinity and DIC measurements.

Fortunately, comparing the results of these two approaches reveals the effect of choosing one over the other are generally negligible. Focusing for example on temperature, pH and $\Omega_{arag.}$ values, these differ between the two chapters by on average < 0.1 ^{o}C, < 0.02 pH units (total scale) and < 0.05 (note $\Omega_{arag.}$ is unitless), respectively. Maximum (absolute) differences between the two chapters are larger, at 0.9 ^{o}C, 0.13 pH units and 0.3, respectively. However, in all instances (aside from one sample for temperature), the temperature, pH and $\Omega_{arag.}$ estimates used in this chapter are within error of those used in chapter 4. Further, the effect of this choice has no impact on the conclusions of this study. Firstly, the Sr/Ca vs temperature calibration presented in section 6.5 is unchanged by the choice of temperature measurement (Supplementary table 4).

Temperature data used	Gradient, m	± 2 SE	Intercept, c	± 2 SE	r	p	R^2
This study (chapter 3) and Stewart et al. (2020a)	— 0.10	0.03	11.40	0.17	— 0.80	< 0.05	0.64
Chapter 4 and Stewart et al. (2020a)	— 0.10	0.03	11.42	0.19	— 0.77	< 0.05	0.59

Supplementary table 4. Comparing the results of Sr/Ca vs temperature regressions (OLS) using temperature estimates in this chapter and updated estimates in chapter 4 of this thesis. Note there is no significant difference between the two methods.

Secondly, the choice of hydrographic variables also has a negligible impact on the correlations between ancillary hydrographic variables and both D_{Ba} and Ba/Ca vs $[Ba]_{SW}$ calibration residuals (Supplementary table 5). For all variables apart from seawater pH, there is no substantial change in r values or to correlation significance, and importantly the observation that stylasterid D_{Ba} values are most strongly correlated with

temperature and dissolved silica concentrations is robust (and actually strengthened when using the alternative, chapter 4 choice) (Supplementary table 5).

The only substantial difference between the two datasets is that, when using chapter 4 pH values, aragonitic stylasterid D_{Ba} values correlate significantly with seawater pH (Supplementary table 5). Inspecting this change in more detail reveals that this correlation is close to significance whichever set of hydrographic data is used. Using chapter 3 pH values results in a correlation significant at the 90 % level ($r = 0.33$, $p = 0.09$), while using chapter 4 values results in a correlation which is (just) significant at the 95 % level ($r = 0.38$, $p = 0.05$). The actual magnitude of the effect of hydrographic data choice is thus small. Further, were chapter 4 hydrographic data to be used here, this would have minimal impact on the findings of this chapter. High-Mg calcitic stylasterid D_{Ba} values and both high-Mg calcitic and aragonitic stylasterid calibration residuals do not correlate strongly or significantly with chapter 4 seawater pH values ($-0.4 < r < 0.4$; $p > 0.05$), and temperature and dissolved silica concentrations remain the parameters which correlate most strongly with Ba incorporation into stylasterid skeletons (Supplementary table 5).

The findings of this chapter are therefore robust to the choice of ancillary hydrographic variables. More broadly, this analysis displays that while choosing paired hydrographic data is inherently subjective, the approach adopted in this thesis is robust. Since the hydrographic data used in chapter 4 is the most recently compiled (e.g. uses the most recent GLODAP bottle database (Lauvset et al., 2022)), I recommend use of this data for any future work.

Variable	Hydrographic dataset	Aragonitic stylasterids		High-Mg calcitic stylasterids	
		D_{Ba}	Ba/Ca vs $[Ba]_{SW}$ residuals	D_{Ba}	Ba/Ca vs $[Ba]_{SW}$ residuals
Temperature (^{0}C)	Chapter 3	$r = -0.54$ $p < 0.05$	$r = -0.16$ $p > 0.05$	$r = -0.55$ $p > 0.05$	$r = -0.4$ $p > 0.05$
	Chapter 4	$r = -0.56$ $p < 0.05$	$r = -0.17$ $p > 0.05$	$r = -0.55$ $p > 0.05$	$r = -0.44$ $p > 0.05$
Dissolved silica (μmol/kg)	Chapter 3	$r = 0.47$ $p < 0.05$	$r = 0.14$ $p > 0.05$	$r = 0.45$ $p > 0.05$	$r = 0.33$ $p > 0.05$
	Chapter 4	$r = 0.47$ $p < 0.05$	$r = 0.15$ $p > 0.05$	$r = 0.47$ $p > 0.05$	$r = 0.35$ $p > 0.05$
pH (total scale)	Chapter 3	$r = 0.33$ $p > 0.05$	$r = 0.24$ $p > 0.05$	$r = 0.15$ $p > 0.05$	$r = 0.27$ $p > 0.05$
	Chapter 4	$r = 0.38$ $p < 0.05$	$r = 0.35$ $p > 0.05$	$r = -0.10$ $p > 0.05$	$r = 0.03$ $p > 0.05$
Salinity (psu)	Chapter 3	$r = -0.28$ $p > 0.05$	$r = -0.06$ $p > 0.05$	$r = 0.34$ $p > 0.05$	$r = 0.21$ $p > 0.05$
	Chapter 4	$r = -0.28$ $p > 0.05$	$r = -0.07$ $p > 0.05$	$r = 0.34$ $p > 0.05$	$r = 0.21$ $p > 0.05$
Phosphate (μmol/kg)	Chapter 3	$r = 0.10$ $p > 0.05$	$r = -0.11$ $p > 0.05$	$r = 0.12$ $p > 0.05$	$r = 0.00$ $p > 0.05$
	Chapter 4	$r = 0.13$ $p > 0.05$	$r = -0.12$ $p > 0.05$	$r = 0.33$ $p > 0.05$	$r = 0.20$ $p > 0.05$
$\Omega_{arag.}$	Chapter 3	$r = 0.02$ $p > 0.05$	$r = 0.23$ $p > 0.05$	$r = 0.00$ $p > 0.05$	$r = 0.13$ $p > 0.05$
	Chapter 4	$r = 0.00$ $p > 0.05$	$r = 0.27$ $p > 0.05$	$r = -0.16$ $p > 0.05$	$r = -0.03$ $p > 0.05$

Supplementary table 5. The effect of using hydrographic data in chapter 4 of this thesis on correlations between coral D_{Ba} and Ba/Ca vs $[Ba]_{SW}$ residuals with various hydrographic parameters. Chapter 3 values taken from Supplementary table 3. Relationships with p values < 0.05 and/or r values > 0.4 or < -0.4 are

shown in bold. Note oxygen values not used in chapter 4, while depth values did not change, so these variables are not included here.

7.   Appendix: New coral Ba/Ca data used in this chapter

Source of geochemical data	Sample ID	Type	[Ba]$_{sw}$ (nmol/kg)	± 2 σ	Ba/Ca (μmol/mol)	± 2 σ
This thesis	NBP1103-DH87-St-2-01-Erfe87aa	Stylasterid, high-Mg calc.	92	6	12.99	0.70
This thesis	NBP1103-TO104-St-4-1-Erfe04ac	Stylasterid, high-Mg calc.	84	5	11.06	0.12
This thesis	NBP1103-DH07-St-01-01-Erre07ad	Stylasterid, high-Mg calc.	61	30	8.14	0.26
This thesis	NBP0805-TB04-Stps-A-01-Erre04ae	Stylasterid, arag.	69	17	13.96	0.16
This thesis	CE14011-03-08-Sge08aj	Stylasterid, arag.	44	5	7.93	0.32
This thesis	JC094-B0109-Hydls-001-Sty09am	Stylasterid, arag.	41	3	7.38	0.22
This thesis	JC094-B0480-Hydls(f)-001-Sty80an	Stylasterid, arag.	41	3	7.26	0.08
This thesis	NBP1103-TO104-St-9-6-Erfe4as	Stylasterid, high-Mg calc.	84	5	11.63	0.20
This thesis	NBP1103-DH22-Stc1-01-Sde22aw	Stylasterid, arag.	100	15	18.08	0.38
This thesis	JC094-B1041-Hydlm-001-Eal41ak	Stylasterid, arag.	52	3	7.72	0.22
This thesis	JC094-B0548-Hydls/m-001 to 019-Eal48aq	Stylasterid, arag.	45	3	7.71	0.09
This thesis	JC094-B0546-Hydls/m-001 to 008-Adp46ap	Stylasterid, arag.	53	3	9.75	0.11
This thesis	JC094-B0541-Hydlm-001-Seb41ay	Stylasterid, arag.	65	3	10.80	0.12
This thesis	NBP1103-DH22-Stc1-01-Efe22ax	Stylasterid, high-Mg calc.	100	15	12.68	0.23
This thesis	NBP1103-TB02-St-01-Chpo02av	Stylasterid, high-Mg calc.	61	32	8.43	0.28

Source of geochemical data	Sample ID	Type	[Ba]$_{SW}$ (nmol/kg)	± 2 σ	Ba/Ca (µmol/mol)	± 2 σ
This thesis	NBP1103-TO104-St-4-2W-Erfe4ar	Stylasterid, high-Mg calc.	84	5	11.18	0.13
This thesis	JC094-B0519-Hydlm-001 to 027-Adp19ao	Stylasterid, arag.	51	3	9.63	0.15
This thesis	JR15005-Ev113-2429-Il29bd	Stylasterid, arag.	91	5	18.56	0.26
This thesis	JR15005-Ev39-784-Il39be	Stylasterid, arag.	96	4	19.29	0.72
This thesis	JR15005-Ev40-831-CoV831bf	Stylasterid, arag.	96	4	19.41	1.37
IS and JS	NBP0805-TB01-EanC1	Stylasterid, arag.	61	32	11.95	0.34
IS and JS	STY-1-Ean1	Stylasterid, arag.	58	5	10.49	0.19
IS and JS	NBP1103-DH39-St-2-02-Ebo02	Stylasterid, arag.	89	3	17.51	0.68
IS and JS	JC094-F0184-Hydlm-001-Eal001	Stylasterid, arag.	53	3	8.29	0.35
IS and JS	JR15005-38-775-Egr775	Stylasterid, mixed	96	4	20.13	0.36
IS and JS	JR15005-40-832-Egr832	Stylasterid, mixed	96	4	20.59	0.37
IS, JS and this thesis	JR15005-113-2421-Egr2421	Stylasterid, mixed	91	5	20.55	1.53
IS, JS and this thesis	JR15005-113-2426-Egr2426	Stylasterid, mixed	91	5	20.54	2.05
IS and JS	JR15005-43-844-Ela844	Stylasterid, high-Mg calc.	94	3	14.51	0.97
IS and JS	JR15005-113-2427-Sro2427	Stylasterid, arag.	91	5	18.26	0.33
IS and JS	JR15005-114-2453-Sro2453	Stylasterid, arag.	90	9	18.71	0.53
IS and JS	JR15005-40-835-Sro835	Stylasterid, arag.	96	4	19.20	0.34
IS and JS	NBP1103-DH54-Stp-1-Sde54	Stylasterid, arag.	93	4	17.48	0.31
IS and JS	NBP1103-DH37-Stp-1-1-Sde37	Stylasterid, arag.	90	5	18.59	0.88

Source of geochemical data	Sample ID	Type	[Ba]$_{SW}$ (nmol/kg)	± 2 σ	Ba/Ca (μmol/mol)	± 2 σ
IS and JS	NBP1103-DH40-Stp-1-1-Sde40	Stylasterid, arag.	89	5	16.58	0.30
IS and JS	NBP1103-DH88-Stp-1-1-Sde88	Stylasterid, arag.	97	11	17.85	0.70
IS and JS	NBP0805-TB04-Dp-A-001-Sde001	Stylasterid, arag.	69	17	12.96	0.23
IS and JS	DY081-52-339-26-1141-Sgr1141	Stylasterid, arag.	38	3	8.59	0.15
IS and JS	JC136-1901-sp-1Sbr1901	Stylasterid, arag.	47	7	8.17	0.47
IS and JS	JC136-3712-sp-1-Sib3712	Stylasterid, arag.	47	7	7.95	1.50
This thesis	DY081 STN36 ROV335 EV53-985	Scleractinia, arag.	38	3	7.49	0.27
This thesis	DY081 STN36 ROV335-EV33-0948	Scleractinia, arag.	38	3	8.46	0.11
This thesis	DY081 STN36 ROV335 EV72-612	Scleractinia, arag.	38	3	7.57	0.27
This thesis	DY081 STN36 ROV335 EV53-0917	Scleractinia, arag.	38	3	8.14	0.09
JS	NBP1103-DH14-Bpalive-1	Scleractinia, arag.	70	17	14.74	0.39
JS	DY081-005-ROV327-Ev051-190-97-Car	Scleractinia, arag.	50	9	8.91	0.30
JS	DY081-005-ROV327-Ev072-190-6-Car	Scleractinia, arag.	48	3	9.62	0.56
JS	DY081-005-ROV327-Ev074-190-85-Car	Scleractinia, arag.	47	3	10.01	0.38
JS	DY081-013-ROV331-Ev011-193-469Car	Scleractinia, arag.	47	11	9.54	0.53
JS	DY081-036-ROV335-Ev017-202-988Car	Scleractinia, arag.	38	3	9.64	0.17
JS	DY081-052-ROV339-Ev015-210-1103Car	Scleractinia, arag.	38	3	8.65	0.20

Source of geochemical data	Sample ID	Type	[Ba]$_{SW}$ (nmol/kg)	± 2 σ	Ba/Ca (µmol/mol)	± 2 σ
JS	DY081-052-ROV339-Ev017-210-1135Car	Scleractinia, arag.	38	3	9.88	0.45
JS	DY081-013-ROV331-Ev005-193-471Car	Scleractinia, arag.	47	8	9.81	0.17
JS	DY081-036-ROV335-Ev045-202-921Car	Scleractinia, arag.	38	3	7.59	0.17
JS	JC094-15-EBA-ROV227-SLP46-B0018-Carlm-001	Scleractinia, arag.	56	4	10.82	0.34
JS	JC094-21-EBB-ROV228-SLP28-B1206-Carlm-001	Scleractinia, arag.	55	3	10.35	0.18
JS	JC094-21-EBB-ROV228-SLP30-B1256-Carls-001	Scleractinia, arag.	55	3	9.90	0.37
JS	JC094-21-EBB-ROV228-SLP34-B1264-Carlm-001	Scleractinia, arag.	55	3	10.29	0.18
JS & Hemsing et al. (2018)	JC094-21-EBB-ROV228-SLP44-B1584-Carls-001	Scleractinia, arag.	55	3	9.98	0.86
JS	JC094-33-VEM-ROV231-SLP67-B1010-Carlm-001	Scleractinia, arag.	52	3	11.37	0.20
JS	JC094-4-EBA-ROV222-SLP-SCP-NET2-F0001-Carlm-001	Scleractinia, arag.	56	6	10.74	0.41
JS & Hemsing et al. (2018) & Spooner et al. (2018)	JC094-5-EBA-ROV223-SLP9-B0244-Carls-001	Scleractinia, arag.	47	11	10.34	0.75
JS & Spooner et al. (2018)	JC094-5-EBA-ROV223-SLP9-B0245-Carls-001	Scleractinia, arag.	47	11	10.58	0.31
JS & Spooner et al. (2018)	JC094-7-EBA-ROV224-SLP48-B0561-Carlm-001	Scleractinia, arag.	55	3	10.59	0.18

Source of geochemical data	Sample ID	Type	[Ba]$_{SW}$ (nmol/kg)	± 2 σ	Ba/Ca (µmol/mol)	± 2 σ
JS & Spooner et al. (2018)	JC094-7-EBA-ROV224-SCP49-B0579-Carlm-001	Scleractinia, arag.	55	3	10.90	0.35
JS	NBP1103-TB02-Cp-1	Scleractinia, arag.	61	32	13.21	0.51
MLCF	JR15005-Ev114R-2911	Scleractinia, arag.	90	9	19.37	0.22
MLCF	JR15005-Ev32-606	Scleractinia, arag.	93	3	20.13	0.23
MLCF	JR15005-Ev113-2428-2	Scleractinia, arag.	91	5	19.08	0.60
JS	DY081-036-ROV335-Ev052-202-914DD-Lrg	Scleractinia, arag.	38	3	7.88	0.57
JS	DY081-005-ROV327-Ev066-190-39Dia	Scleractinia, arag.	49	3	8.56	0.15
JS	DY081-007-ROV328-Ev006-191-139Dia	Scleractinia, arag.	47	10	8.23	0.15
JS	DY081-050-ROV338-Ev014-208-1182Dia	Scleractinia, arag.	38	3	7.73	0.14
JS	DY081-050-ROV338-Ev018-209-1228Dia	Scleractinia, arag.	37	3	7.48	0.18
JS	DY081-008-ROV329-Ev061-192-445Dia	Scleractinia, arag.	47	12	8.19	0.32
JS	DY081-013-ROV331-Ev023-194-473Dia	Scleractinia, arag.	45	10	9.22	0.36
JS	NBP1103-DH17-Dpalive-fragments	Scleractinia, arag.	100	15	17.26	0.31
JS	CINMSDesmo-019.1	Scleractinia, arag.	44	9	8.21	0.23
JS	CINMSDesmo-026.1	Scleractinia, arag.	44	9	7.68	0.33
JS & Spooner et al. (2018)	JC094-15-EBA-ROV227-ARM38-B0141-Enall-001	Scleractinia, arag.	55	3	10.82	0.72
JS	JC094-15-EBA-ROV227-ARM38-B1585-Enals-002	Scleractinia, arag.	55	3	9.77	0.36
JS	JC094-21-EBB-ROV228-ARM33-B0027-Enall-001	Scleractinia, arag.	55	3	9.80	0.24
JS	JC094-33-VEM-ROV231-ARM21-B0510-Enall-001	Scleractinia, arag.	52	3	9.76	0.18

Source of geochemical data	Sample ID	Type	[Ba]$_{SW}$ (nmol/kg)	± 2 σ	Ba/Ca (µmol/mol)	± 2 σ
JS	JC094-33-VEM-ROV231-SLP9-B1004-Enals-001	Scleractinia, arag.	52	3	9.57	0.61
JS	JC094-42-VEM-ROV233-ARM79-B0089-Enall-001	Scleractinia, arag.	53	3	9.16	0.19
JS & Spooner et al. (2018)	JC094-48-VAY-ROV236-SLP11-B1044-Enalm-001	Scleractinia, arag.	53	3	10.96	0.38
JS	JC094-56-GRM-ROV239-SLP10-B1492-Enall-001	Scleractinia, arag.	52	3	9.04	0.16
JS	DY081-007-ROV328-Ev015-116Flab	Scleractinia, arag.	47	12	11.46	0.25
JS	DY081-007-ROV328-Ev017-138Flab	Scleractinia, arag.	47	12	9.45	0.17
JS	DY081-008-ROV329-Ev011-422Flab	Scleractinia, arag.	47	10	9.36	0.17
JS	DY081-008-ROV329-Ev024-453Flab	Scleractinia, arag.	47	11	10.10	0.18
JS	DY081-008-ROV329-Ev043-406Flab	Scleractinia, arag.	47	12	10.54	0.25
JS	DY081-008-ROV329-Ev047-426Flab	Scleractinia, arag.	47	12	10.49	1.33
JS	DY081-008-ROV329-Ev056-386Flab	Scleractinia, arag.	47	12	11.75	0.21
JS	DY081-013-ROV331-Ev004-539Flab	Scleractinia, arag.	47	8	9.64	0.35
JS	JC094-15-EBA-ROV227-SLP59-B0020-Flall-001	Scleractinia, arag.	50	12	12.55	2.62
JS	JC094-48-VAY-ROV236-SLP51-B1042-Flalm-001	Scleractinia, arag.	51	3	11.57	0.30
JS	NBP1103-DH07-Flab-0	Scleractinia, arag.	61	30	16.39	1.58

Source of geochemical data	Sample ID	Type	[Ba]$_{SW}$ (nmol/kg)	± 2 σ	Ba/Ca (µmol/mol)	± 2 σ
JS	NBP1103-DH14-Fpalive-5	Scleractinia, arag.	70	17	13.48	0.24
JS	NBP1103-DH16-Fpalive-2	Scleractinia, arag.	91	12	20.30	0.56
MLCF	JR15005-Ev80-1662	Scleractinia, arag.	90	6	21.74	0.24
MLCF	JR15005-Ev44-901	Scleractinia, arag.	94	3	21.78	0.25
MLCF	JR15005-Ev63-1221	Scleractinia, arag.	91	6	24.45	0.28
MLCF	JR15005-Ev91-1875	Scleractinia, arag.	91	8	20.68	1.41
MLCF	JR15005-Ev79-1593	Scleractinia, arag.	90	6	21.10	0.57
MLCF	JR15005-Ev105-2205	Scleractinia, arag.	94	3	19.64	0.31
MLCF	JR15005-Ev33-674	Scleractinia, arag.	93	3	21.29	0.55
MLCF	JR15005-Ev23-451	Scleractinia, arag.	93	4	21.08	0.83
MLCF	JR15005-Ev95-2080	Scleractinia, arag.	94	3	22.57	1.12
JS	DY081-031-ROV333-Ev032-201-583-Loph	Scleractinia, arag.	37	3	7.57	0.09
JS	DY081-031-ROV333-Ev033-201-570-Loph	Scleractinia, arag.	37	3	7.51	0.08
JS	DY081-031-ROV333-Ev035-201-630-Loph	Scleractinia, arag.	37	3	7.56	0.09
JS	DY081-031-ROV333-Ev037-201-590-Loph	Scleractinia, arag.	37	3	7.51	0.08
JS	DY081-034-ROV334-Ev004-202-678-Loph	Scleractinia, arag.	37	3	7.68	0.09
JS	DY081-036-ROV335-Ev030-202-933-Loph	Scleractinia, arag.	38	3	7.86	0.09
JS	CINMSLoph-005	Scleractinia, arag.	51	15	9.43	0.11
JS	CINMSLoph-043	Scleractinia, arag.	45	8	7.54	0.08
JS	CINMSLoph-045	Scleractinia, arag.	50	13	8.95	0.10
JS	CINMSLoph-001	Scleractinia, arag.	47	11	8.69	0.15
JS	CINMSLoph-002	Scleractinia, arag.	44	9	6.97	0.08
JS	CINMSLoph-004	Scleractinia, arag.	45	8	8.30	0.09
JS	CINMSLoph-014	Scleractinia, arag.	50	13	9.08	0.10
JS	CINMSLoph-024	Scleractinia, arag.	44	9	7.76	0.14

Source of geochemical data	Sample ID	Type	[Ba]$_{SW}$ (nmol/kg)	± 2 σ	Ba/Ca (μmol/mol)	± 2 σ
JS	CINMSLoph-018	Scleractinia, arag.	44	9	7.44	0.08
MLCF	JR15005-Ev142-2965	Scleractinia, mixed	91	6	19.90	0.75

Supplementary table 6. New coral Ba/Ca data used in this chapter. Ba/Ca given as the average of all replicates with Fe/Ca < 40 μmol/mol, corrected for analytical offsets. Corals which had no replicates with Fe/Ca < 40 μmol/mol are not included here. For full geochemical data and metadata of all samples – including those compiled from published sources - the reader is referred to the published version of this chapter, where all data is freely available online (Kershaw et al., 2023; https://doi.org/10.1016/j.chemgeo.2023.121355). As outlined in the Contributions and acknowledgements at the start of this chapter, multiple coauthors contributed geochemical data to this thesis. These contributions are listed here, using the following abbreviations: JS (Joseph A. Stewart), IS (Ivo Strawson) and MLCF (Maria Luiza de Carvalho Ferreira). The 7 samples also measured by Hemsing et al. (2018) and Spooner et al. (2018) are also indicated, coral Ba/Ca quoted here as the average of all available replicates, corrected for analytical offsets (see section 2.5 and supplementary information (section 6.3) for details). I was responsible for compilation of all [Ba]$_{SW}$ data. Errors in [Ba]$_{SW}$ represent the larger of either a representative analytical uncertainty (± 3 nmol/kg) or variability between 3 nearest measurements (2 standard deviations). Errors in Ba/Ca represent the larger of the analytical uncertainty or variability between sample replicate analyses (2 standard deviations).

8.   References

Al-Horani, F.A., Al-Moghrabi, S.M., de Beer, D., 2003. Microsensor study of photosynthesis and calcification in the scleractinian coral, Galaxea fascicularis: active internal carbon cycle. Journal of Experimental Marine Biology and Ecology 288, 1–15. https://doi.org/10.1016/S0022-0981(02)00578-6

Anagnostou, E., Sherrell, R.M., Gagnon, A., LaVigne, M., Field, M.P., McDonough, W.F., 2011. Seawater nutrient and carbonate ion concentrations recorded as P/Ca, Ba/Ca, and U/Ca in the deep-sea coral Desmophyllum dianthus. Geochimica et Cosmochimica Acta 75, 2529–2543. https://doi.org/10.1016/j.gca.2011.02.019

Barker, S., Greaves, M., Elderfield, H., 2003. A study of cleaning procedures used for foraminiferal Mg/Ca paleothermometry. Geochemistry, Geophysics, Geosystems, 4.(9). https://doi.org/10.1029/2003GC000559

Bates, S., 2016. Barium uptake by foraminifera: understanding past and present ocean processes. Doctoral dissertation, University of Bristol.

Bates, S.L., Hendry, K.R., Pryer, H.V., Kinsley, C.W., Pyle, K.M., Woodward, E.M.S., Horner, T.J., 2017. Barium isotopes reveal role of ocean circulation on barium cycling in the Atlantic. Geochimica et Cosmochimica Acta 204, 286–299. https://doi.org/10.1016/j.gca.2017.01.043

Bath, G.E., Thorrold, S.R., Jones, C.M., Campana, S.E., McLaren, J.W., Lam, J.W.H., 2000. Strontium and barium uptake in aragonitic otoliths of marine fish. Geochimica et Cosmochimica Acta 64, 1705–1714. https://doi.org/10.1016/S0016-7037(99)00419-6

Bax, N., Cairns, S.D., 2014. Chapter 5.7. Stylasteridae (Cnidaria: Hydrozoa). In: De Broyer C., Koubbi P., Griffiths H.J., Raymond B., Udekem d'Acoz C. d', et al. (eds.). Biogeographic Atlas of the Southern Ocean. Scientific Committee on Antarctic Research, Cambridge, pp. 107-112

Bishop, J.K.B., 1988. The barite-opal-organic carbon association in oceanic particulate matter. Nature 332, 341–343. https://doi.org/10.1038/332341a0

Boyle, E.A., 1981. Cadmium, zinc, copper, and barium in foraminifera tests. Earth and Planetary Science Letters 53, 11–35. https://doi.org/10.1016/0012-821X(81)90022-4

Buhl-Mortensen, L., Mortensen, P.B., Armsworthy, S., Jackson, D., 2007. Field observations of Flabellum spp. and laboratory study of the behavior and respiration of Flabellum alabastrum. Bulletin of Marine Science 81, 543–552.

Büscher, J.V., Form, A.U., Riebesell, U., 2017. Interactive Effects of Ocean Acidification and Warming on Growth, Fitness and Survival of the Cold-Water Coral Lophelia pertusa under Different Food Availabilities. Frontiers in Marine Science 4, 101. https://doi.org/10.3389/fmars.2017.00101

Cairns, S.D., 2011. Global Diversity of the Stylasteridae (Cnidaria: Hydrozoa: Athecatae). PLoS ONE 6, e21670. https://doi.org/10.1371/journal.pone.0021670

Cairns, S.D., 2007. Deep-water corals: an overview with special reference to diversity and distribution of deep-water scleractinian corals. Bulletin of Marine Science 81, 311–322.

Cairns, S.D., Macintyre, I.G., 1992. Phylogenetic Implications of Calcium Carbonate Mineralogy in the Stylasteridae (Cnidaria: Hydrozoa). PALAIOS 7, 96. https://doi.org/10.2307/3514799

Case, D.H., Robinson, L.F., Auro, M.E., Gagnon, A.C., 2010. Environmental and biological controls on Mg and Li in deep-sea scleractinian corals. Earth and Planetary Science Letters 300, 215–225. https://doi.org/10.1016/j.epsl.2010.09.029

Chan, L.H., Drummond, D., Edmond, J.M., Grant, B., 1977. On the barium data from the Atlantic GEOSECS expedition. Deep Sea Research 24, 613–649. https://doi.org/10.1016/0146-6291(77)90505-7

Clarke, A., Leakey, R.J.G., 1996. The seasonal cycle of phytoplankton, macronutrients, and the microbial community in a nearshore antarctic marine ecosystem. Limnology and Oceanography 41, 1281–1294. https://doi.org/10.4319/lo.1996.41.6.1281

Collier, R., Edmond, J., 1984. The trace element geochemistry of marine biogenic particulate matter. Progress in Oceanography 13, 113–199. https://doi.org/10.1016/0079-6611(84)90008-9

Crook, E.D., Cooper, H., Potts, D.C., Lambert, T., Paytan, A., 2013. Impacts of food availability and pCO_2 on planulation, juvenile survival, and calcification of the azooxanthellate scleractinian coral Balanophyllia elegans. Biogeosciences 10, 7599–7608. https://doi.org/10.5194/bg-10-7599-2013

Cuny-Guirriec, K., Douville, E., Reynaud, S., Allemand, D., Bordier, L., Canesi, M., Mazzoli, C., Taviani, M., Canese, S., McCulloch, M., Trotter, J., Rico-Esenaro, S.D., Sanchez-Cabeza, J.-A., Ruiz-Fernández, A.C., Carricart-Ganivet, J.P., Scott, P.M., Sadekov, A., Montagna, P., 2019. Coral Li/Mg thermometry: Caveats and constraints. Chemical Geology 523, 162–178. https://doi.org/10.1016/j.chemgeo.2019.03.038

Dehairs, F., Chesselet, R., Jedwab, J., 1980. Discrete suspended particles of barite and the barium cycle in the open ocean. Earth and Planetary Science Letters 49, 528–550. https://doi.org/10.1016/0012-821X(80)90094-1

Dickinson, S.R., McGrath, K.M., 2001. Quantitative determination of binary and tertiary calcium carbonate mixtures using powder X-ray diffraction. Analyst 126, 1118–1121. https://doi.org/10.1039/b103004n

Dietzel, M., Gussone, N., Eisenhauer, A., 2004. Co-precipitation of Sr^{2+} and Ba^{2+} with aragonite by membrane diffusion of CO_2 between 10 and 50 °C. Chemical Geology 203, 139–151. https://doi.org/10.1016/j.chemgeo.2003.09.008

Drake, J.L., Varsano, N., Mass, T., 2021. Genetic basis of stony coral biomineralization: History, trends and future prospects. Journal of Structural Biology 213, 107782. https://doi.org/10.1016/j.jsb.2021.107782

Dymond, J., Suess, E., Lyle, M., 1992. Barium in Deep-Sea Sediment: A Geochemical Proxy for Paleoproductivity. Paleoceanography 7, 163–181. https://doi.org/10.1029/92PA00181

Falkner, K. K., Macdonald, R. W., Carmack, E. C., Weingartner, T., 1994. Barium in seawater and sediments from the Artic Ocean. PANGAEA, https://doi.org/10.1594/PANGAEA.734072

Gaetani, G.A., Cohen, A.L., 2006. Element partitioning during precipitation of aragonite from seawater: A framework for understanding paleoproxies. Geochimica et Cosmochimica Acta 70, 4617–4634. https://doi.org/10.1016/j.gca.2006.07.008

Gagnon, A.C., Adkins, J.F., Fernandez, D.P., Robinson, L.F., 2007. Sr/Ca and Mg/Ca vital effects correlated with skeletal architecture in a scleractinian deep-sea coral and the role of Rayleigh fractionation. Earth and Planetary Science Letters 261, 280–295. https://doi.org/10.1016/j.epsl.2007.07.013

Ganeshram, R.S., François, R., Commeau, J., Brown-Leger, S.L., 2003. An experimental investigation of barite formation in seawater. Geochimica et Cosmochimica Acta 67, 2599–2605. https://doi.org/10.1016/S0016-7037(03)00164-9

Gattuso J.-P., Epitalon J.-M., Lavigne H., Orr J., 2021. seacarb: seawater carbonate chemistry. R package version 3.3.0. http://CRAN.R-project.org/package=seacarb

GEOTRACES Intermediate Data Product Group (2021). The GEOTRACES Intermediate Data Product 2021 (IDP2021). NERC EDS British Oceanographic Data Centre NOC. https://doi.org/10.5285/cf2d9ba9-d51d-3b7c-e053-8486abc0f5fd.

Geyman, B.M., Ptacek, J.L., LaVigne, M., Horner, T.J., 2019. Barium in deep-sea bamboo corals: Phase associations, barium stable isotopes, & prospects for paleoceanography. Earth and Planetary Science Letters 525, 115751. https://doi.org/10.1016/j.epsl.2019.115751

Gillikin, D.P., Dehairs, F., Lorrain, A., Steenmans, D., Baeyens, W., André, L., 2006. Barium uptake into the shells of the common mussel (Mytilus edulis) and the potential for estuarine paleo-chemistry reconstruction. Geochimica et Cosmochimica Acta 70, 395–407. https://doi.org/10.1016/j.gca.2005.09.015

Gillikin, D.P., Lorrain, A., Paulet, Y.-M., André, L., Dehairs, F., 2008. Synchronous barium peaks in high-resolution profiles of calcite and aragonite marine bivalve shells. Geo-Marine Letters 28, 351–358. https://doi.org/10.1007/s00367-008-0111-9

Gómez, C.E., Wickes, L., Deegan, D., Etnoyer, P.J., Cordes, E.E., 2018. Growth and feeding of deep-sea coral Lophelia pertusa from the California margin under simulated ocean acidification conditions. PeerJ 6:e5671. https://doi.org/10.7717/peerj.5671

Gonneea, M.E., Cohen, A.L., DeCarlo, T.M., Charette, M.A., 2017. Relationship between water and aragonite barium concentrations in aquaria reared juvenile corals. Geochimica et Cosmochimica Acta 209, 123–134. https://doi.org/10.1016/j.gca.2017.04.006

Griffith, E.M., Paytan, A., 2012. Barite in the ocean - occurrence, geochemistry and palaeoceanographic applications. Sedimentology 59, 1817–1835. https://doi.org/10.1111/j.1365-3091.2012.01327.x

Hamel, J.-F., Sun, Z., Mercier, A., 2010. Influence of size and seasonal factors on the growth of the deep-sea coral Flabellum alabastrum in mesocosm. Coral Reefs 29, 521–525. https://doi.org/10.1007/s00338-010-0590-9

Hathorne, E.C., Gagnon, A., Felis, T., Adkins, J., Asami, R., Boer, W., Caillon, N., Case, D., Cobb, K.M., Douville, E., deMenocal, P., Eisenhauer, A., Garbe-Schönberg, D., Geibert, W., Goldstein, S., Hughen, K., Inoue, M., Kawahata, H., Kölling, M., Cornec, F.L., Linsley, B.K., McGregor, H.V., Montagna, P., Nurhati, I.S., Quinn, T.M., Raddatz, J., Rebaubier, H., Robinson, L., Sadekov, A., Sherrell, R., Sinclair, D., Tudhope, A.W., Wei, G., Wong, H., Wu, H.C., You, C.-F., 2013. Interlaboratory study for coral Sr/Ca and other element/Ca ratio measurements. Geochemistry, Geophysics, Geosystems 14, 3730–3750. https://doi.org/10.1002/ggge.20230

Hemsing, F., Hsieh, Y.-T., Bridgestock, L., Spooner, P.T., Robinson, L.F., Frank, N., Henderson, G.M., 2018. Barium isotopes in cold-water corals. Earth and Planetary Science Letters 491, 183–192. https://doi.org/10.1016/j.epsl.2018.03.040

Holcomb, M., Cohen, A.L., Gabitov, R.I., Hutter, J.L., 2009. Compositional and morphological features of aragonite precipitated experimentally from seawater and biogenically by corals. Geochimica et Cosmochimica Acta 73, 4166–4179. https://doi.org/10.1016/j.gca.2009.04.015

Hönisch, B., Allen, K.A., Russell, A.D., Eggins, S.M., Bijma, J., Spero, H.J., Lea, D.W., Yu, J., 2011. Planktic foraminifers as recorders of seawater Ba/Ca. Marine Micropaleontology 79, 52–57. https://doi.org/10.1016/j.marmicro.2011.01.003

Hoppema, M., Dehairs, F., Navez, J., Monnin, C., Jeandel, C., Fahrbach, E., de Baar, H.J.W., 2010. Distribution of barium in the Weddell Gyre: Impact of circulation and biogeochemical processes. Marine Chemistry 122, 118–129. https://doi.org/10.1016/j.marchem.2010.07.005

Horner, T.J., Kinsley, C.W., Nielsen, S.G., 2015. Barium-isotopic fractionation in seawater mediated by barite cycling and oceanic circulation. Earth and Planetary Science Letters 430, 511–522. https://doi.org/10.1016/j.epsl.2015.07.027

Hsieh, Y.-T., Henderson, G.M., 2017. Barium stable isotopes in the global ocean: Tracer of Ba inputs and utilization. Earth and Planetary Science Letters 473, 269–278. https://doi.org/10.1016/j.epsl.2017.06.024

Jeandel, C., Dupré, B., Lebaron, G., Monnin, C., Minster, J.-F., 1996. Longitudinal distributions of dissolved barium, silica and alkalinity in the western and southern Indian Ocean. Deep Sea Research Part I: Oceanographic Research Papers 43, 1–31. https://doi.org/10.1016/0967-0637(95)00098-4

Jennings, J.C., Gordon, L.I., Nelson, D.M., 1984. Nutrient depletion indicates high primary productivity in the Weddell Sea. Nature 309, 51–54. https://doi.org/10.1038/309051a0

Jurikova, H., Liebetrau, V., Raddatz, J., Fietzke, J., Trotter, J., Rocholl, A., Krause, S., McCulloch, M., Rüggeberg, A., Eisenhauer, A., 2019. Boron isotope composition of the cold-water coral Lophelia pertusa along the Norwegian margin: Zooming into a potential pH-proxy by combining bulk and high-resolution approaches. Chemical Geology 513, 143–152. https://doi.org/10.1016/j.chemgeo.2019.01.005

Kang, J., Kang, S., Lee, J., Lee, S., 2002. Seasonal variation of microalgal assemblages at a fixed station in King George Island, Antarctica, 1996. Marine Ecology Progress Series 229, 19–32. https://doi.org/10.3354/meps229019

Kershaw, J., Stewart, J.A., Strawson, I., De Carvalho Ferreira, M.L., Robinson, L.F., Hendry, K.R., Samperiz, A., Burke, A., Rae, J.W.B., Day, R.D., Etnoyer, P.J., Williams, B., Häussermann, V., 2023. Ba/Ca of stylasterid coral skeletons records dissolved seawater barium concentrations. Chemical Geology 622, 121355. https://doi.org/10.1016/j.chemgeo.2023.121355

Kontoyannis, C.G., Vagenas, N.V., 2000. Calcium carbonate phase analysis using XRD and FT-Raman spectroscopy. Analyst 125, 251–255. https://doi.org/10.1039/a908609i

Lauvset, S.K., Lange, N., Tanhua, T., Bittig, H.C., Olsen, A., Kozyr, A., Álvarez, M., Becker, S., Brown, P.J., Carter, B.R., Cotrim da Cunha, L., Feely, R.A., van Heuven, S., Hoppema, M., Ishii, M., Jeansson, E., Jutterström, S., Jones, S.D., Karlsen, M.K., Lo Monaco, C., Michaelis, P., Murata, A., Pérez, F.F., Pfeil, B., Schirnick, C., Steinfeldt, R., Suzuki, T., Tilbrook, B., Velo, A., Wanninkhof, R., Woosley, R.J., Key, R.M., 2021. An updated version of the global interior ocean biogeochemical data product, GLODAPv2.2021. Earth Syst. Sci. Data 13, 5565–5589. https://doi.org/10.5194/essd-13-5565-2021

Lauvset, S.K., Lange, N., Tanhua, T., Bittig, H.C., Olsen, A., Kozyr, A., Alin, S., Álvarez, M., Azetsu-Scott, K., Barbero, L., Becker, S., Brown, P.J., Carter, B.R., Da Cunha, L.C., Feely, R.A., Hoppema, M., Humphreys, M.P., Ishii, M., Jeansson, E., Jiang, L.-Q., Jones, S.D., Lo Monaco, C., Murata, A., Müller, J.D., Pérez, F.F., Pfeil, B., Schirnick, C., Steinfeldt, R., Suzuki, T., Tilbrook, B., Ulfsbo, A., Velo, A., Woosley, R.J., Key, R.M., 2022. GLODAPv2.2022: the latest version of the global interior ocean biogeochemical data product. Earth Syst. Sci. Data 14, 5543–5572. https://doi.org/10.5194/essd-14-5543-2022

LaVigne, M., Grottoli, A.G., Palardy, J.E., Sherrell, R.M., 2016. Multi-colony calibrations of coral Ba/Ca with a contemporaneous in situ seawater barium record. Geochimica et Cosmochimica Acta 179, 203–216. https://doi.org/10.1016/j.gca.2015.12.038

LaVigne, M., Hill, T.M., Spero, H.J., Guilderson, T.P., 2011. Bamboo coral Ba/Ca: Calibration of a new deep ocean refractory nutrient proxy. Earth and Planetary Science Letters 312, 506–515. https://doi.org/10.1016/j.epsl.2011.10.013

Le Roy, E., Sanial, V., Charette, M.A., van Beek, P., Lacan, F., Jacquet, S.H.M., Henderson, P.B., Souhaut, M., García-Ibáñez, M.I., Jeandel, C., Pérez, F.F., Sarthou, G., 2018. The [226]Ra–Ba relationship in the North Atlantic during GEOTRACES-GA01. Biogeosciences 15, 3027–3048. https://doi.org/10.5194/bg-15-3027-2018

Lea, D.W., Boyle, E.A., 1993. Determination of carbonate-bound barium in foraminifera and corals by isotope dilution plasma-mass spectrometry. Chemical Geology 103, 73–84. https://doi.org/10.1016/0009-2541(93)90292-Q

Lea, D.W., Boyle, E.A., 1991. Barium in planktonic foraminifera. Geochimica et Cosmochimica Acta 55, 3321–3331. https://doi.org/10.1016/0016-7037(91)90491-M

Lea, D.W., Shen, G.T., Boyle, E.A., 1989. Coralline barium records temporal variability in equatorial Pacific upwelling. Nature 340, 373–376. https://doi.org/10.1038/340373a0

Lea, D.W., Spero, H.J., 1994. Assessing the reliability of paleochemical tracers: Barium uptake in the shells of planktonic foraminifera. Paleoceanography and Paleoclimatology 9, 445–452. https://doi.org/10.1029/94PA00151

Liu, Y., Li, X., Zeng, Z., Yu, H.-M., Huang, F., Felis, T., Shen, C.-C., 2019. Annually-resolved coral skeletal $\delta^{138/134}$Ba records: A new proxy for oceanic Ba cycling. Geochimica et Cosmochimica Acta 247, 27–39. https://doi.org/10.1016/j.gca.2018.12.022

Lueker, T.J., Dickson, A.G., Keeling, C.D., 2000. Ocean pCO_2 calculated from dissolved inorganic carbon, alkalinity, and equations for K_1 and K_2: validation based on laboratory measurements of CO_2 in gas and seawater at equilibrium. Marine Chemistry 70, 105–119. https://doi.org/10.1016/S0304-4203(00)00022-0

Mavromatis, V., Immenhauser, A., Buhl, D., Purgstaller, B., Baldermann, A., Dietzel, M., 2017. Effect of organic ligands on Mg partitioning and Mg isotope fractionation during low-temperature precipitation of calcite in the absence of growth rate effects. Geochimica et Cosmochimica Acta 207, 139–153. https://doi.org/10.1016/j.gca.2017.03.020

Mavromatis, V., Goetschl, K.E., Grengg, C., Konrad, F., Purgstaller, B., Dietzel, M., 2018. Barium partitioning in calcite and aragonite as a function of growth rate. Geochimica et Cosmochimica Acta 237, 65–78. https://doi.org/10.1016/j.gca.2018.06.018

McClelland, H.L.O., Halevy, I., Wolf-Gladrow, D.A., Evans, D., Bradley, A.S., 2021. Statistical Uncertainty in Paleoclimate Proxy Reconstructions. Geophysical Research Letters 48. https://doi.org/10.1029/2021GL092773

McCorkle, D.C., Martin, P.A., Lea, D.W., Klinkhammer, G.P., 1995. Evidence of a dissolution effect on benthic foraminiferal shell chemistry: δ^{13}C, Cd/Ca, Ba/Ca, and Sr/Ca results from the Ontong Java Plateau. Paleoceanography and Paleoclimatology 10, 699–714. https://doi.org/10.1029/95PA01427

McManus, J., Berelson, W.M., Klinkhammer, G.P., Kilgore, T.E., Hammond, D.E., 1994. Remobilization of barium in continental margin sediments. Geochimica et Cosmochimica Acta 58, 4899–4907. https://doi.org/10.1016/0016-7037(94)90220-8

Mercier, A., Sun, Z., Hamel, J.-F., 2011. Reproductive periodicity, spawning and development of the deep-sea scleractinian coral Flabellum angulare. Marine Biology 158, 371–380. https://doi.org/10.1007/s00227-010-1565-7

Montagna, P., McCulloch, M., Douville, E., López Correa, M., Trotter, J., Rodolfo-Metalpa, R., Dissard, D., Ferrier-Pagès, C., Frank, N., Freiwald, A., Goldstein, S., Mazzoli, C., Reynaud, S., Rüggeberg, A., Russo, S.,

Taviani, M., 2014. Li/Mg systematics in scleractinian corals: Calibration of the thermometer. Geochimica et Cosmochimica Acta 132, 288–310. https://doi.org/10.1016/j.gca.2014.02.005

Mucci, A., Morse, J.W., 1983. The incorporation of Mg^{2+} and Sr^{2+} into calcite overgrowths: influences of growth rate and solution composition. Geochimica et Cosmochimica Acta 47, 217–233. https://doi.org/10.1016/0016-7037(83)90135-7

Murphy, E.J., Clarke, A., Symon, C., Priddle, J., 1995. Temporal variation in Antarctic sea-ice: analysis of a long term fast-ice record from the South Orkney Islands. Deep Sea Research Part I: Oceanographic Research Papers 42, 1045–1062. https://doi.org/10.1016/0967-0637(95)00057-D

Nozaki, Y., 1997. A fresh look at element distribution in the North Pacific Ocean. Eos Trans. AGU 78, 221–221. https://doi.org/10.1029/97EO00148

Östlund, H Gote, Craig, Harmon C, Broecker, Wallace S, Spencer, Derek W, GEOSECS, 1987. Shorebased measurements during the GEOSECS Pacific expedition. https://doi.org/10.1594/PANGAEA.743238

Post, A.L., O'Brien, P.E., Beaman, R.J., Riddle, M.J., De Santis, L., 2010. Physical controls on deep water coral communities on the George V Land slope, East Antarctica. Antarctic Science 22, 371–378. https://doi.org/10.1017/S0954102010000180

Poulain, C., Gillikin, D.P., Thébault, J., Munaron, J.M., Bohn, M., Robert, R., Paulet, Y.-M., Lorrain, A., 2015. An evaluation of Mg/Ca, Sr/Ca, and Ba/Ca ratios as environmental proxies in aragonite bivalve shells. Chemical Geology 396, 42–50. https://doi.org/10.1016/j.chemgeo.2014.12.019

Pretet, C., Zuilen, K., Nägler, T.F., Reynaud, S., Böttcher, M.E., Samankassou, E., 2015. Constraints on barium isotope fractionation during aragonite precipitation by corals. The Depositional Record 1, 118–129. https://doi.org/10.1002/dep2.8

Pyle, K.M., Hendry, K.R., Sherrell, R.M., Meredith, M.P., Venables, H., Lagerström, M., Morte-Ródenas, A., 2017. Coastal barium cycling at the West Antarctic Peninsula. Deep Sea Research Part II: Topical Studies in Oceanography 139, 120–131. https://doi.org/10.1016/j.dsr2.2016.11.010

Pyle, K.M., Hendry, K.R., Sherrell, R.M., Legge, O., Hind, A.J., Bakker, D., Venables, H., Meredith, M.P., 2018. Oceanic fronts control the distribution of dissolved barium in the Southern Ocean. Marine Chemistry 204, 95–106. https://doi.org/10.1016/j.marchem.2018.07.002

Raddatz, J., Liebetrau, V., Rüggeberg, A., Hathorne, E., Krabbenhöft, A., Eisenhauer, A., Böhm, F., Vollstaedt, H., Fietzke, J., López Correa, M., Freiwald, A., Dullo, W.-Chr., 2013. Stable Sr-isotope, Sr/Ca,

Mg/Ca, Li/Ca and Mg/Li ratios in the scleractinian cold-water coral Lophelia pertusa. Chemical Geology 352, 143–152. https://doi.org/10.1016/j.chemgeo.2013.06.013

Rae, J.W.B., Foster, G.L., Schmidt, D.N., Elliott, T., 2011. Boron isotopes and B/Ca in benthic foraminifera: Proxies for the deep ocean carbonate system. Earth and Planetary Science Letters 302, 403–413. https://doi.org/10.1016/j.epsl.2010.12.034

Reed, E.V., Thompson, D.M., Cole, J.E., Lough, J.M., Cantin, N.E., Cheung, A.H., Tudhope, A., Vetter, L., Jimenez, G., Edwards, R.L., 2021. Impacts of Coral Growth on Geochemistry: Lessons From the Galápagos Islands. Paleoceanography and Paleoclimatology 36. https://doi.org/10.1029/2020PA004051

Roeske, T., Rutgers van der Loeff, M. M., 2012. Barium measured on water bottle samples during POLARSTERN cruise ANT-XXIV/3. PANGAEA, https://doi.org/10.1594/PANGAEA.786619

Ross, C.L., DeCarlo, T.M., McCulloch, M.T., 2019. Calibration of Sr/Ca, Li/Mg and Sr-U Paleothermometry in Branching and Foliose Corals. Paleoceanography and Paleoclimatology 34, 1271–1291. https://doi.org/10.1029/2018PA003426

Samperiz, A., Robinson, L.F., Stewart, J.A., Strawson, I., Leng, M.J., Rosenheim, B.E., Ciscato, E.R., Hendry, K.R., Santodomingo, N., 2020. Stylasterid corals: A new paleotemperature archive. Earth and Planetary Science Letters 545, 116407. https://doi.org/10.1016/j.epsl.2020.116407

Sathyendranath, S., Brewin, R., Brockmann, C., Brotas, V., Calton, B., Chuprin, A., Cipollini, P., Couto, A., Dingle, J., Doerffer, R., Donlon, C., Dowell, M., Farman, A., Grant, M., Groom, S., Horseman, A., Jackson, T., Krasemann, H., Lavender, S., Martinez-Vicente, V., Mazeran, C., Mélin, F., Moore, T., Müller, D., Regner, P., Roy, S., Steele, C., Steinmetz, F., Swinton, J., Taberner, M., Thompson, A., Valente, A., Zühlke, M., Brando, V., Feng, H., Feldman, G., Franz, B., Frouin, R., Gould, R., Hooker, S., Kahru, M., Kratzer, S., Mitchell, B., Muller-Karger, F., Sosik, H., Voss, K., Werdell, J., Platt, T., 2019. An Ocean-Colour Time Series for Use in Climate Studies: The Experience of the Ocean-Colour Climate Change Initiative (OC-CCI). Sensors 19, 4285. https://doi.org/10.3390/s19194285

Sathyendranath, S., Jackson, T., Brockmann, C., Brotas, V., Calton, B., Chuprin, A., Clements, O., Cipollini, P., Danne, O., Dingle, J., Donlon, C., Grant, M., Groom, S., Krasemann, H., Lavender, S., Mazeran, C., Mélin, F., Müller, D., Steinmetz, F., Valente, A., Zühlke, M., Feldman, G., Franz, B., Frouin, R., Werdell, J., Platt, T., 2021. ESA Ocean Colour Climate Change Initiative (Ocean_Colour_cci): Version 5.0 Data. https://doi.org/10.5285/1DBE7A109C0244AAAD713E078FD3059A

Serrato Marks, G., LaVigne, M., Hill, T.M., Sauthoff, W., Guilderson, T.P., Roark, E.B., Dunbar, R.B., Horner, T.J., 2017. Reproducibility of Ba/Ca variations recorded by northeast Pacific bamboo corals. Paleoceanography and Paleoclimatology 32, 966–979. https://doi.org/10.1002/2017PA003178

Schlitzer, R., 2022. Ocean Data View, https://odv.awi.de

Sinclair, D.J., Risk, M.J., 2006. A numerical model of trace-element coprecipitation in a physicochemical calcification system: Application to coral biomineralization and trace-element 'vital effects.' Geochimica et Cosmochimica Acta 70, 3855–3868. https://doi.org/10.1016/j.gca.2006.05.019

Smetacek, V., de Baar, H. J. W., Bathmann, U., Lochte, K., Rutgers van der Loeff, M. M., 1997. Biogeochemistry of barium measured on water bottle samples during POLARSTERN cruise ANT-X/6. PANGAEA, https://doi.org/10.1594/PANGAEA.88250

Spooner, P.T., Robinson, L.F., Hemsing, F., Morris, P., Stewart, J.A., 2018. Extended calibration of cold-water coral Ba/Ca using multiple genera and co-located measurements of dissolved barium concentration. Chemical Geology 499, 100–110. https://doi.org/10.1016/j.chemgeo.2018.09.012

Sternberg, E., Tang, D., Ho, T.-Y., Jeandel, C., Morel, F.M.M., 2005. Barium uptake and adsorption in diatoms. Geochimica et Cosmochimica Acta 69, 2745–2752. https://doi.org/10.1016/j.gca.2004.11.026

Stewart, J.A., Robinson, L.F., Day, R.D., Strawson, I., Burke, A., Rae, J.W.B., Spooner, P.T., Samperiz, A., Etnoyer, P.J., Williams, B., Paytan, A., Leng, M.J., Häussermann, V., Wickes, L.N., Bratt, R., Pryer, H., 2020a. Refining trace metal temperature proxies in cold-water scleractinian and stylasterid corals. Earth and Planetary Science Letters 545, 116412. https://doi.org/10.1016/j.epsl.2020.116412

Stewart, J.A., Christopher, S.J., Kucklick, J.R., Bordier, L., Chalk, T.B., Dapoigny, A., Douville, E., Foster, G.L., Gray, W.R., Greenop, R., Gutjahr, M., Hemsing, F., Henehan, M.J., Holdship, P., Hsieh, Y., Kolevica, A., Lin, Y., Mawbey, E.M., Rae, J.W.B., Robinson, L.F., Shuttleworth, R., You, C., Zhang, S., Day, R.D., 2020b. NIST RM 8301 Boron Isotopes in Marine Carbonate (Simulated Coral and Foraminifera Solutions): Inter-laboratory δ11B and Trace Element Ratio Value Assignment. Geostandards and Geoanalytical Research 45, 77–96. https://doi.org/10.1111/ggr.12363

Stewart, J.A., Strawson, I., Kershaw, J., Robinson, L.F., 2022. Stylasterid corals build aragonite skeletons in undersaturated water despite low pH at the site of calcification. Scientific Reports 12, 13105. https://doi.org/10.1038/s41598-022-16787-y

Stolarski, J., Coronado, I., Murphy, J.G., Kitahara, M.V., Janiszewska, K., Mazur, M., Gothmann, A.M., Bouvier, A.-S., Marin-Carbonne, J., Taylor, M.L., Quattrini, A.M., McFadden, C.S., Higgins, J.A., Robinson,

L.F., Meibom, A., 2021. A modern scleractinian coral with a two-component calcite–aragonite skeleton. Proc. Natl. Acad. Sci. U.S.A. 118, e2013316117. https://doi.org/10.1073/pnas.2013316117

Tang, D., Morel, F.M.M., 2006. Distinguishing between cellular and Fe-oxide-associated trace elements in phytoplankton. Marine Chemistry 98, 18–30. https://doi.org/10.1016/j.marchem.2005.06.003

Therneau, T., 2018. deming: Deming, Theil-Sen, Passing-Bablock and Total Least Squares Regression. R package version 1.4. https://CRAN.R-project.org/package=deming

Thresher, R.E., Fallon, S.J., Townsend, A.T., 2016. A "core-top" screen for trace element proxies of environmental conditions and growth rates in the calcite skeletons of bamboo corals (Isididae). Geochimica et Cosmochimica Acta 193, 75–99. https://doi.org/10.1016/j.gca.2016.07.033

Ulrich, R.N., Guillermic, M., Campbell, J., Hakim, A., Han, R., Singh, S., Stewart, J.D., Román-Palacios, C., Carroll, H.M., De Corte, I., Gilmore, R.E., Doss, W., Tripati, A., Ries, J.B., Eagle, R.A., 2021. Patterns of Element Incorporation in Calcium Carbonate Biominerals Recapitulate Phylogeny for a Diverse Range of Marine Calcifiers. Frontiers in Earth Science 9, 641760. https://doi.org/10.3389/feart.2021.641760

van Dijk, I., de Nooijer, L.J., Reichart, G.-J., 2017. Trends in element incorporation in hyaline and porcelaneous foraminifera as a function of pCO_2. Biogeosciences 14, 497–510. https://doi.org/10.5194/bg-14-497-2017

Watson, E.B., 2004. A conceptual model for near-surface kinetic controls on the trace-element and stable isotope composition of abiogenic calcite crystals. Geochimica et Cosmochimica Acta 68, 1473–1488. https://doi.org/10.1016/j.gca.2003.10.003

Yamazaki, A., Yano, M., Harii, S., Watanabe, T., 2021. Effects of light on the Ba/Ca ratios in coral skeletons. Chemical Geology 559, 119911. https://doi.org/10.1016/j.chemgeo.2020.119911

Chapter 4: Stylasterid boron isotopes as a novel archive of seawater pH

Contributions and acknowledgements

1   Introduction

Subsurface ocean pH varies as a function of a number of climatically-relevant parameters, including biological productivity, carbon remineralisation, ocean circulation patterns and ocean-atmosphere gas exchange (e.g. Feely et al., 2004; Lauvset et al., 2020). Reconstructing changes in ocean pH throughout Earth's history can therefore provide valuable constraints on the causes of coeval shifts in Earth's climate, and contribute to our understanding of links between the global ocean and the wider earth system. To this end, the boron isotopic composition of marine biogenic carbonates has been developed as a tool for reconstructing ocean pH, and applied in a variety of contexts (e.g. Hemming and Hanson, 1992; Sanyal et al., 1995; Hönisch et al., 2008; Rae et al., 2014; Martínez-Botí et al., 2015; Sosdian et al., 2018; Rae et al., 2018; Shao et al., 2019; Shuttleworth et al., 2021).

The premise of the boron isotope-pH proxy has been widely discussed elsewhere (e.g. Hemming and Hanson, 1992; Foster and Rae, 2016). Briefly, the boron isotopic composition of a given material can be defined as the ratio of the two stable boron isotopes ([11]B, 80 % abundance, and [10]B, 20 % abundance) in the material, compared with the standard reference material NIST SRM 951 (Foster, 2008):

$$\delta^{11}B_x \ (‰) = \frac{\left(\frac{^{11}B}{^{10}B}\right)_x - \left(\frac{^{11}B}{^{10}B}\right)_{NIST951}}{\left(\frac{^{11}B}{^{10}B}\right)_{NIST951}} \times 1000 \qquad (1)$$

In seawater, boron occurs in two dominant forms: boric acid ($B(OH)_3$) and the borate anion ($B(OH)_4^-$). The relative concentration of these two species depends on the pH-dependent equilibrium (Figure 1):

$$B(OH)_3 + 2H_2O \ \rightleftharpoons B(OH)_4^- + H_3O^+ \qquad (2)$$
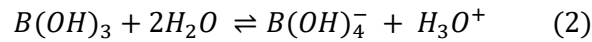
There is also a substantial boron isotopic fractionation between $B(OH)_3$ and $B(OH)_4^-$, resulting in [11]B being more abundant in $B(OH)_3$ (Figure 1; Klochko et al., 2006). Together, the pH-dependence of boron speciation and isotopic offset between the major boron species results in the $\delta^{11}B$ of both $B(OH)_3$ and $B(OH)_4^-$ (hereafter $\delta^{11}B_{boric}$ and $\delta^{11}B_{borate}$, respectively) exhibiting a strong dependence on seawater pH (Figure 1). For $B(OH)_4^-$, this pH-dependence is given by the following equation:

$$\delta^{11}B_{borate} = \frac{\delta^{11}B_{SW} + 10^{pK_B^* - pH} \times \left(\delta^{11}B_{SW} - 10^3 \times (\alpha_B - 1)\right)}{1 + \alpha_B \times 10^{pK_B^* - pH}} \qquad (3)$$

(following Zeebe and Wolf-Gladrow, 2001, where: $\delta^{11}B_{SW}$ = boron isotopic composition of seawater (39.61 ‰; Foster et al., 2010); α_B = fractionation factor between the borate anion and boric acid (1.0272; Klochko et al., 2006); pK_B^* = pressure, temperature and salinity-specific equilibrium constant).
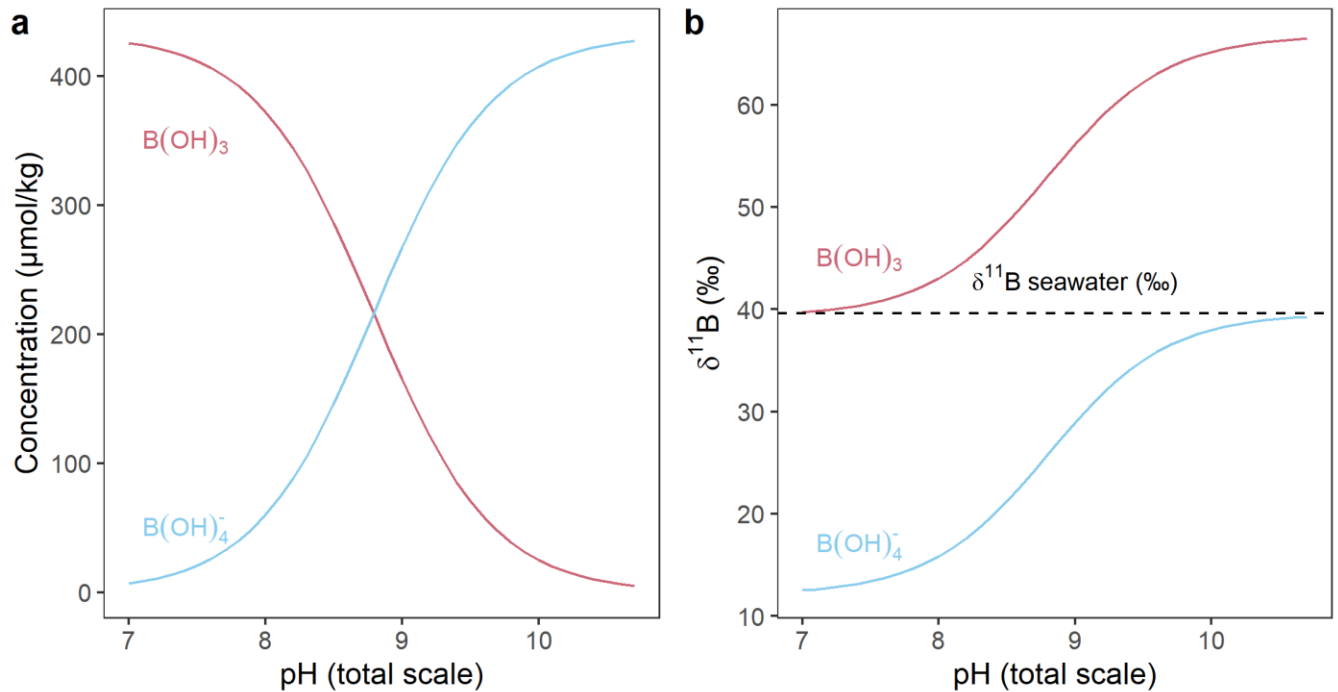
Figure 1. a. Concentration and b. $\delta^{11}B$ of $B(OH)_3$ and $B(OH)_4^-$, both as a function of seawater pH. Calculations follow Zeebe and Wolf-Gladrow (2001), using $\delta^{11}B_{SW}$ and α_B as outlined in the text, with pK_B^* = 8.79 (average paired with corals in this study).

When marine calcifying organisms (e.g. foraminifera and corals) build carbonate skeletons, the elements present in seawater can be incorporated into the carbonate lattice, with their concentration and isotopic signature controlled by seawater composition, environmental conditions, the principles of crystal formation, and biological mediation of the calcification process (e.g. Gaetani and Cohen, 2006; Gagnon et al., 2007; Anagnostou et al., 2012; Marchitto et al., 2018). In the case of boron, it is thought that the charged $B(OH)_4^-$ is dominantly incorporated into the carbonate lattice in the place of the CO_3^{2-} ion (e.g. Hemming and Hanson, 1992; Sen et al., 1994; Hemming et al., 1995, although see Rollion-Bard et al., 2011; Noireaux et al., 2015; Branson, 2018; Farmer et al., 2019 for possible exceptions). Thus, marine carbonate $\delta^{11}B$ should reflect the $\delta^{11}B_{borate}$ in the fluid from which that carbonate formed, allowing the pH of this fluid to be inferred. Since calcification fluids are derived from seawater, this in turn permits the use of marine biogenic carbonate $\delta^{11}B$ to reconstruct past changes in ocean carbonate chemistry.

A variety of marine calcifying organisms have been studied as archives of seawater pH, including foraminifera (e.g. Spivack et al., 1993; Sanyal et al., 1995; Sanyal et al., 1996; Rae et al., 2011; Henehan et al., 2013), surface corals (e.g. Hönisch et al., 2004; Pelejero et al., 2005; Wei et al., 2009; Trotter et al., 2011) and azooxanthellate

144

(also referred to as *deep sea* or *cold water*) corals (e.g. Anagnostou et al., 2012; McCulloch et al., 2012; Stewart et al., 2016; Rae et al., 2018). Here, I focus on azooxanthellate corals, with their wide-ranging depth habitat and geographic distribution making them ideal targets for reconstructing changes in the pH of the ocean's interior. Most previous work has focused on applying boron isotopic techniques to azooxanthellate scleractinian corals, based on the observation that their skeletal $\delta^{11}B$ varies linearly with $\delta^{11}B_{borate}$ (e.g. Anagnostou et al., 2012; McCulloch et al., 2012; Stewart et al., 2016). Importantly, scleractinian coral skeletons can be accurately and precisely dated by U-series techniques, allowing temporal reconstruction of ocean pH through time (e.g. Cheng et al., 2000; Rae et al., 2018). Furthermore, other aspects of scleractinian skeletal geochemistry can be utilised to develop an holistic understanding of changes in ocean conditions/processes, including seawater temperature, primary productivity, and ocean circulation patterns (e.g. Van De Flierdt et al., 2010; Anagnostou et al., 2011; Hemsing et al., 2018; Spooner et al., 2018; Stewart et al., 2020b; chapter 3).

Despite the success of using scleractinian coral $\delta^{11}B$ to reconstruct changes in ocean pH, studies measuring $\delta^{11}B$ of other azooxanthellate coral skeletons are rare. While boron isotopic data has been published for some octocorals (e.g. *Corallium* in McCulloch et al. (2012) and bamboo corals in Farmer et al. (2015)), the boron isotopic composition of stylasterid coral skeletons has remained – until recently – entirely unexplored. However, in a preliminary study, it was recently shown that stylasterid skeletal $\delta^{11}B$ falls close to equilibrium with $\delta^{11}B_{borate}$, raising the possibility that stylasterids could be utilised as a new archive of past ocean pH (Stewart et al., 2022). Stylasterid $\delta^{11}B$ could be a particularly powerful tool when combined with other aspects of stylasterid geochemistry, given that stylasterid Li/Mg and $\delta^{18}O$ record ocean temperature (Samperiz et al., 2020; Stewart et al., 2020b), stylasterid Ba/Ca correlates with the circulation and productivity-sensitive $[Ba]_{SW}$ (chapter 3), and stylasterid $\Delta^{14}C$ can record changes in seawater radiocarbon age (King et al., 2018). However, the small range of $\delta^{11}B_{borate}$ (i.e. seawater pH conditions) and limited number of stylasterid taxa represented by the sample set in Stewart et al. (2022) currently preclude quantitative assessment of their potential utility in this regard.

This initial study of stylasterid $\delta^{11}B$ also provided valuable insight into coral calcification mechanisms, and the controls on the boron isotopic composition of coral carbonate (Stewart et al., 2022). Scleractinian corals calcify from a partially-enclosed calcifying fluid, the pH of which is increased by the coral to promote biomineralisation (e.g. Al-Horani et al., 2003). Azooxanthellate scleractinian coral $\delta^{11}B$ records the signature of this biologically-mediated pH upregulation, and is significantly heavier (i.e. more positive) than $\delta^{11}B_{borate}$ (McCulloch et al., 2012; Anagnostou et al., 2012). Further, intra-skeletal variations in scleractinian $\delta^{11}B$ have contributed to the identification of discrete skeletal elements, including rapidly precipitated Centres of Calcification (CoCs) (e.g. Blamart et al., 2007; Stewart et al., 2016; Jurikova et al., 2019).

Conversely, the finding that stylasterids have $\delta^{11}B$ in equilibrium with $\delta^{11}B_{borate}$ suggests either that stylasterid corals do not employ a pH upregulation strategy to the same degree as that in scleractinian corals, or that the boron isotopic composition of stylasterid carbonate is decoupled from calcifying fluid pH (Stewart et al., 2022). If the former is true, stylasterids must rely on alternative means to build their skeletons, perhaps using organic molecules to catalyse carbonate mineralisation (e.g. Drake et al., 2013; Mass et al., 2013; Von Euw et al., 2017). Alternatively, a coupled modelling and geochemical approach has shown that, in the presence of pH upregulation in the calcifying fluid, boric acid diffusion across calcifying fluid membranes can equilibrate calcifying fluid $\delta^{11}B_{borate}$ with seawater $\delta^{11}B_{borate}$, partially or wholly masking the signature of pH upregulation in coral $\delta^{11}B$ (Gagnon et al., 2021). This provides a potential mechanism by which stylasterids could employ some form of pH upregulation, and may be supported by correlated variability in stylasterid subsample B/Ca, U/Ca and $\delta^{11}B$ (Stewart et al., 2022). However, the existence and magnitude of stylasterid pH upregulation remains an open question, with important implications for the energetic cost of stylasterid calcification, and their resilience to future changes in ocean conditions (Guinotte et al., 2006; McCulloch et al., 2012; Gagnon et al., 2021). The vulnerability of deep-sea corals such as stylasterids is of particular concern, since these organisms form vital components of marine ecosystems by providing habitats for a wider range of species (e.g. Roberts and Cairns, 2014).

Comparing stylasterid and scleractinian coral $\delta^{11}B$ suggests marked differences in the calcification strategies of these two coral groups. This notion is supported by the fact that stylasterids can calcify from aragonite, high-Mg calcite or a mixture of both carbonate polymorphs (Cairns and Macintyre, 1992; Samperiz et al., 2020). This feature of their biomineralisation strategy is thought to be unique amongst coral groups, with scleractinian corals calcifying almost exclusively from aragonite (a notable exception to the rule being the mixed mineralogy *Paraconotrochus sp.* (Stolarski et al., 2021)). The variability in stylasterid skeletal mineralogy is not only of interest in biomineralisation contexts, but can also be utilised to study the mineralogical controls on elemental and isotopic incorporation into biogenic carbonates (e.g. chapter 3). In the case of $\delta^{11}B$, a number of abiogenic laboratory experiments have found differences between the $\delta^{11}B$ composition of synthetic aragonite and calcite, with calcite often found to have heavier $\delta^{11}B$ than $\delta^{11}B_{borate}$ (e.g. Noireaux et al., 2015; Farmer et al., 2019; Henehan et al., 2022). The origin of these differences remains contentious (e.g. compare Farmer et al., 2019 and Henehan et al., 2022), and may be difficult to identify in natural carbonates because abiogenic mineralogical effects can be overprinted by between-taxa variability in the degree of biologically-mediated pH upregulation (e.g. see comparison of Scleractinia and *Corallium* in McCulloch et al., 2012). Conversely, intra-genus variability in stylasterid mineralogy provides a unique opportunity to perform a phylogenetically-controlled study on boron incorporation mechanisms into biogenic aragonite and high-Mg calcite.

Stylasterid δ^{11}B thus has potential to inform on the development of δ^{11}B-pH proxies, coral biomineralisation mechanisms and the mineralogical controls on boron incorporation into marine carbonates. As outlined above, our current understanding of stylasterid δ^{11}B is based on a relatively small number of samples from a narrow range of ocean conditions (n = 17; $14.7 < \delta^{11}B_{borate}$ (‰) < 16.4; $0.9 < \Omega_{arag.} < 2.0$; Stewart et al., 2022), inhibiting complete assessment of some of these themes. To address this knowledge gap, I present a significantly expanded dataset of aragonitic (n = 40 new samples) and calcitic (n = 8 new samples) stylasterid δ^{11}B measurements, paired with trace elemental ratios (Li/Ca, Mg/Ca, Li/Mg, B/Ca, Na/Ca, Sr/Ca, Ba/Ca and U/Ca). I explore the differences between aragonitic and high-Mg calcitic stylasterid δ^{11}B, and use stylasterid samples from a wide range of locations, species and ocean conditions ($13.3 < \delta^{11}B_{borate}$ (‰) < 18.6; $0.5 < \Omega_{arag.} < 3.7$) to investigate their utility as archives of seawater δ^{11}B$_{borate}$, as well as providing new insights into their biocalcification mechanism.
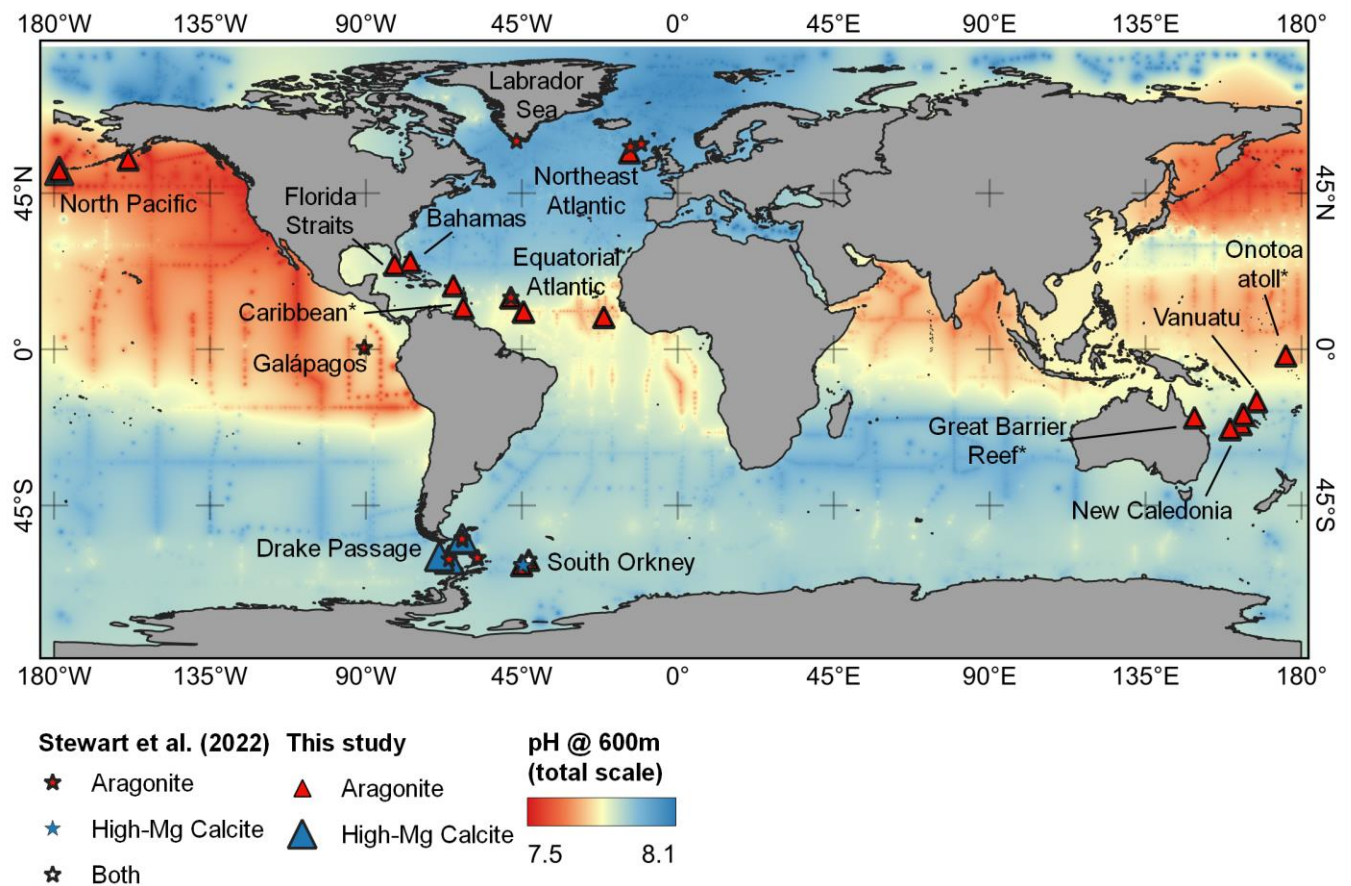
Figure 2. Map showing coral locations from this study (triangles) and Stewart et al. (2022) (stars) overlain on pH at 600 m water depth (average depth of coral collection sites in the compiled dataset). pH was calculated in Ocean Data View software (Schlitzer, 2023) using alkalinity and DIC pairs from the GLODAP bottle

database (Lauvset et al., 2022). *Samples from starred locations not included in $\delta^{11}B$ vs $\delta^{11}B_{borate}$ calibrations owing to lack of proximal carbonate system data. Map created using QGIS, pH surface generated using IDW interpolation.

2 Methodology

2.1 Coral samples

Forty-eight stylasterid corals were collected alive (with associated organic tissue) or in pristine condition from the locations shown in Figure 2. Samples were collected during expeditions to the Drake Passage region of the Southern Ocean (R/V *Nathaniel B. Palmer* 0805 and 1103), the South Orkney Islands (RRS *James Clark Ross* 15005), the equatorial Atlantic (RRS *James Cook* 094), New Caledonia (R/V *Alis* KANADEEP 1 and SPANBIOS 2021; accessed via le Muséum national d'Histoire naturelle in Paris), the northeast Atlantic (R/V *Celtic Explorer* 14011), the Florida Straits (R/V *Seward Johnson* 2007) and the north Pacific (F/V *Alaska Provider* 201601; *F/V Alaskan Leader* 202001; accessed via the NOAA Alaska Deep-Sea Coral and Sponge Initiative). Additional samples were provided from a range of low latitude locations (between 30 °N and 30 °S; Great Barrier Reef, Vanuatu, Caribbean Sea, Onotoa Atoll, Bahamas) by the Smithsonian National Museum of Natural History.

Samples include both aragonitic (n = 40 individuals; *Adelopora sp., Conopora sp., Cyclohelia sp., Errina sp., Errinopsis sp., Inferiolabiata sp., Stephanohelia sp., Stylaster sp.*) and high-Mg calcitic (n = 8 individuals; *Cheiloporidion sp., Errinopora sp., Errinopsis sp.*) stylasterid genera. Sample mineralogy was either directly measured or inferred using a combination of x-ray diffraction, trace element geochemistry and published records (following procedure in chapter 3; Cairns and Macintyre, 1992; Samperiz et al., 2020).

2.2 Combination with previous work and additional measurements

The 48 coral samples measured for the first time in this work were combined with an initial dataset based on 17 stylasterid samples (Strawson, 2019; Stewart et al., 2020b; Stewart et al., 2022). Li/Ca, Mg/Ca and Sr/Ca ratios for this initial sample set were published in Stewart et al. (2020b), B/Ca, U/Ca and $\delta^{11}B$ in Stewart et al. (2022), and Ba/Ca ratios in Strawson (2019) and chapter 3 of this thesis. For 7 corals in this initial dataset, stylasterid apical tips (see section 2.3) were previously measured for their element/Ca ratios, although these data are as yet unpublished and were not discussed in Strawson (2019) or subsequent publications (Stewart et al., 2020b; Stewart et al., 2022). These data are included here, along with paired boron isotopic values for these tip samples, which were measured as part of this thesis. The origin of apical tip data is included in the appendix (section 7; Supplementary table 3).

2.3   Sample preparation

Samples were air dried immediately after collection (or after accessing from ethanol storage in museum collections), and remaining organic material removed by physical scraping. Bulk skeletal samples were obtained for all corals, taken in duplicate where the sample was sufficiently large (n = 43 corals sampled in duplicate; n = 5 corals represented by 1 bulk sample only). Pieces of coral were cut using a handheld dremmel tool from the primary branch of each specimen where possible (following Samperiz et al., 2020; Stewart et al., 2020b). Large (i.e. 50 to 500 mg) pieces were taken to reduce the effects of intraskeletal variability, which has been shown to influence deep-sea coral element/Ca ratios (e.g. Gagnon et al., 2007) and boron isotopic values (e.g. Stewart et al., 2016; Fietzke and Wall, 2022). Furthermore, apical branch tips were avoided when taking bulk samples, since their $\delta^{18}O$ and $\delta^{13}C$ composition suggests they are geochemically distinct from bulk samples, likely owing to faster growth rates at branch tips than the rest of the stylasterid skeleton (Samperiz et al., 2020). Instead, these apical tips were sampled separately where possible, again using a handheld dremmel tool (n = 19 corals). Sampling methods are summarised in Figure 3.

After cutting, visual contaminant phases were removed by physical abrasion, and samples crushed to small grains using a pestle and mortar. An ~ 5 mg aliquot of each powdered sample (for smaller tip samples, amount was often < 2 mg) was cleaned using standard oxidative cleaning techniques for boron isotope analysis (adapted from Barker et al., 2003; Ni et al., 2007). The full cleaning procedure is outlined in chapter 2. Briefly, samples were treated with a warm (80 ^{0}C) oxidising solution consisting of 1 % H_2O_2 buffered by 0.1 M NH_4OH for 15 minutes. Samples were then rinsed, transferred to an acid-cleaned plastic vial, and subjected to a weak acid leach (0.0005 M HNO_3) before dissolution in distilled 0.5 M HNO_3.
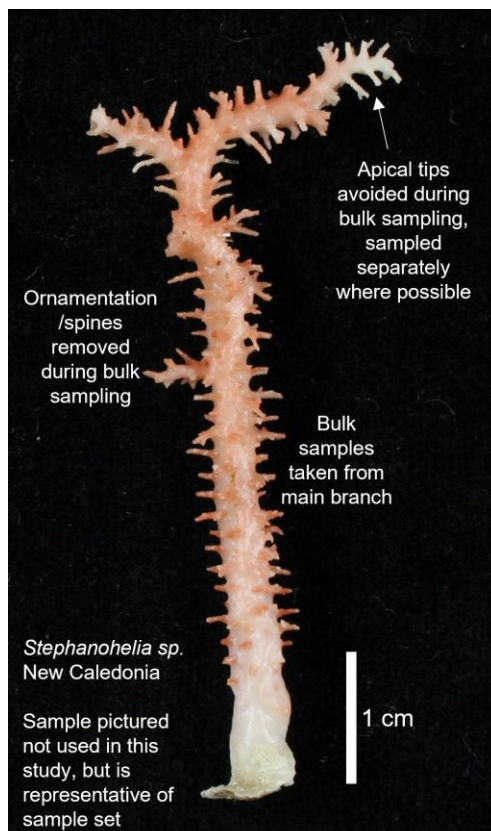
Figure 3. Example of live *Stephanohelia sp.* sample showing sampling strategy, including separate sampling of apical branch tips. Note this sample was not used directly in this study, but is extremely similar (same species, collection location, collection depth and gross morphology) to sample MNHN-IK-2015-3403.

2.4   Analytical techniques

Element/Ca ratios and boron isotopic values were measured following the analytical procedures outlined in detail in chapter 2. Briefly, Li/Ca, B/Ca, Na/Ca, Mg/Ca, Sr/Ca, Ba/Ca and U/Ca ratios were measured at the University of Bristol using a Thermo-Element ICP-MS. Intensities of [7]Li, [11]B, [23]Na, [26]Mg, [43]Ca, [86]Sr, [138]Ba and [238]U were measured in samples, blanks and a well-characterised gravimetric bracketing standard to derive element/Ca ratios for each coral sample. Na/Ca ratios were not measured for all samples and so are not discussed in detail here, but are included for brief discussion in section 4.1.3. Analytical reproducibility was assessed using repeat measurements of reference materials NIST RM 8301 (Coral) (Stewart et al., 2020a) and JCp-1 (Hathorne et al., 2013) and was better than 2 % (RSD; 2 σ) for all ratios (chapter 2). Accuracy was assessed using NIST RM 8301 (Coral), and long-term average values for all elements differed from published

values by < 3 %. Values were adjusted by the correction factors outlined in chapter 2 to facilitate direct comparison with previous work (Strawson, 2019; Stewart et al., 2020b; Stewart et al., 2022).

Boron isotope values were derived by first passing a small aliquot of each dissolved sample through microcolumns containing Amberlite IRA 743 anionic exchange resin to separate boron from the carbonate matrix (Foster, 2008). Boron isotope values were then measured on this purified fraction using established Multi-Collector ICP-MS techniques at the University of Bristol, reported relative to NIST SRM 951 (chapter 2; Foster, 2008; Rae et al., 2018). Analytical reproducibility and accuracy were assessed by repeat measurements of NIST RM 8301 (Coral). Reproducibility was assessed separately for the each of 2 measurement periods represented here, with measurements between October 2019 and August 2021 yielding an average value of 24.27 ± 0.33 ‰ (n = 15; 2 σ) and measurements between June 2022 and February 2023 an average value of 24.11 ± 0.16 ‰ (n = 19; 2 σ) (see Chapter 2, section 4.2.2 for detailed discussion). Coral samples were assigned the relevant analytical uncertainty for the period they were measured in. Measurements in both periods are in good agreement with both the interlaboratory consensus value (Stewart et al., 2020a) and the value reported for the previously published stylasterid dataset used in this compilation (24.27 ± 0.16 ‰; Stewart et al., 2022). Procedural blanks were also monitored, and were typically small (average 47 pg, n = 20). Implied blank corrections using the long term average procedural blank $\delta^{11}B$ (— 8 ± 31 ‰; 2 σ) were ≤ 0.12 ‰ for all samples aside from one replicate of calcitic sample Erfe04ac (implied correction + 0.28 ‰). Owing to the small magnitude of blank correction and large uncertainty in procedural blank isotope ratios, I chose not to correct sample $\delta^{11}B$ for this effect, which in practise has no impact on the conclusions of this study.

2.5 Hydrographic data

Ambient seawater temperature, salinity, nutrient concentrations (dissolved phosphate and silica), alkalinity and dissolved inorganic carbon (DIC) were estimated at coral collection sites using co-located Remotely Operated Vehicle (ROV) or Conductivity, Temperature and Depth (CTD) cast measurements if available, or GLODAP bottle data (Lauvset et al., 2021; Lauvset et al., 2022; tabulated in Supplementary table 4). Coral samples from sites represented in Stewart et al. (2022) were paired with the same hydrographic data as that study, to ensure consistency. Each coral sample from a new site was matched with the closest available hydrographic station at which alkalinity and DIC were both measured, with two further stations containing alkalinity and DIC measurements used to characterise variability in local seawater conditions. Where nutrient measurements were reported in units of µmol/L, an appropriate seawater density (based on measured salinity and assuming a 20 ⁰C laboratory temperature) was used to convert to units of µmol/kg. Hydrographic data for 20 samples were published previously (chapter 3; Kershaw et al., 2023), without the requirement that all three stations had independent alkalinity and DIC measurements. Therefore, paired hydrographic data presented here differ for

some samples. Encouragingly, using the new hydrographic data compiled here does not change the interpretations in the previous study (see chapter 3).

Finally, 4 corals were not paired with the full range of hydrographic conditions, because these samples were taken from shallow (< 25 m), carbonate reef environments, which can experience high-amplitude, daily and seasonal fluctuations in environmental conditions including pH and $\Omega_{arag.}$ (e.g. Kline et al., 2015; DeCarlo et al., 2017). Including these samples in the $\delta^{11}B_{coral}$ vs $\delta^{11}B_{borate}$ calibration was therefore considered to be too uncertain, however these samples are used in all plots or calculations presented here which do not require estimation of ambient seawater conditions, and are discussed in more detail in section 3.1 and the supplementary information (section 6.1).

2.6   Calculating carbonate system parameters

Hydrographic data were then used to calculate carbonate system parameters including pH (total scale) and aragonite saturation state ($\Omega_{arag.} = \frac{[Ca^{2+}] \times [CO_3^{2-}]}{K_{sp}^*}$) using the seacarb package in R (Gattuso et al., 2022). Input parameters were alkalinity and DIC, with dissociation constants of carbonate (K_1 and K_2) taken from Lueker et al. (2000), dissociation constants of HSO_4^- from Dickson (1990) and the boron/salinity ratio from Lee et al. (2010). Variability in pH at coral collection sites averaged $\pm$ 0.06 pH units (2 σ of three nearest estimates) with a maximum variability of $\pm$ 0.14 pH units.

The boron isotopic composition of the borate anion in seawater was calculated using equation 3, following Zeebe and Wolf-Gladrow (2001), using a boron isotopic composition of seawater ($\delta^{11}B_{SW}$) = 39.61 ‰ (Foster et al., 2010), and a fractionation factor between borate ion and boric acid (α_B) = 1.0272 (Klochko et al., 2006). Some recent studies have advocated for the use of α_B = 1.026 (e.g. Nir et al., 2015; Henehan et al., 2022). The effects of the choice of α_B value are outlined in the supplementary information (see section 6.2). Temperature, salinity and pressure-dependent values of pK_B^* were calculated in seacarb. Uncertainty in $\delta^{11}B_{borate}$ was assessed using variability between the three nearest hydrographic stations for each coral and averaged $\pm$ < 0.5 ‰ (2 σ) with a maximum value of $\pm$ 1.9 ‰ (2 σ) for corals collected from the site in the Florida Straits.

K_1 and K_2 values from Lueker et al. (2000) are strictly only valid at temperatures > 2 ⁰C. Therefore, for the small number of samples from temperatures < 2 ⁰C in this dataset, the chosen formulation for calculating the carbonate system is technically invalid. In particular, the approach used here could be modified to use K_1 and K_2 values which are valid at temperatures < 2 ⁰C (Papadimitriou et al., 2018; Sulpis et al., 2020). Indeed, a vast array of possible combinations of acid dissociation constants exist, each with its own merits, with little consensus as to which combination is most appropriate (Woosley, 2021). For instance, while the constants in

Papadimitriou et al. (2018) are valid at temperatures < 2 °C, these constants were designed for use on sea-ice brines, which likely differ significantly in their composition and salinity to seawater. To test for the implications of using different acid dissociation constants in this study, I compare $\delta^{11}B_{borate}$ values calculated using K_1 and K_2 values from Lueker et al. (2000) (L2000 in Figure 4) and Sulpis et al. (2020) (S2020 in Figure 4). The two methods of estimation diverge as temperature decreases, reaching at most 0.16 ‰ difference, and using constants from Lueker et al. (2000) results in lower $\delta^{11}B_{borate}$ than using constants from Sulpis et al. (2020) (Figure 4). These differences are not insignificant and indeed exceed estimates of regional variability for some samples. However, for all samples the difference between the two approaches is far smaller than the average regional variability in $\delta^{11}B_{borate}$, and small enough that in practise, the choice of dissociation constants makes no difference to the conclusions of this study. Therefore, I use constants from Lueker et al. (2000), which is consistent with current suggestions for best practise (e.g. Dickson et al., 2007; Woosley, 2021) and also with previous work (e.g. Stewart et al., 2022).
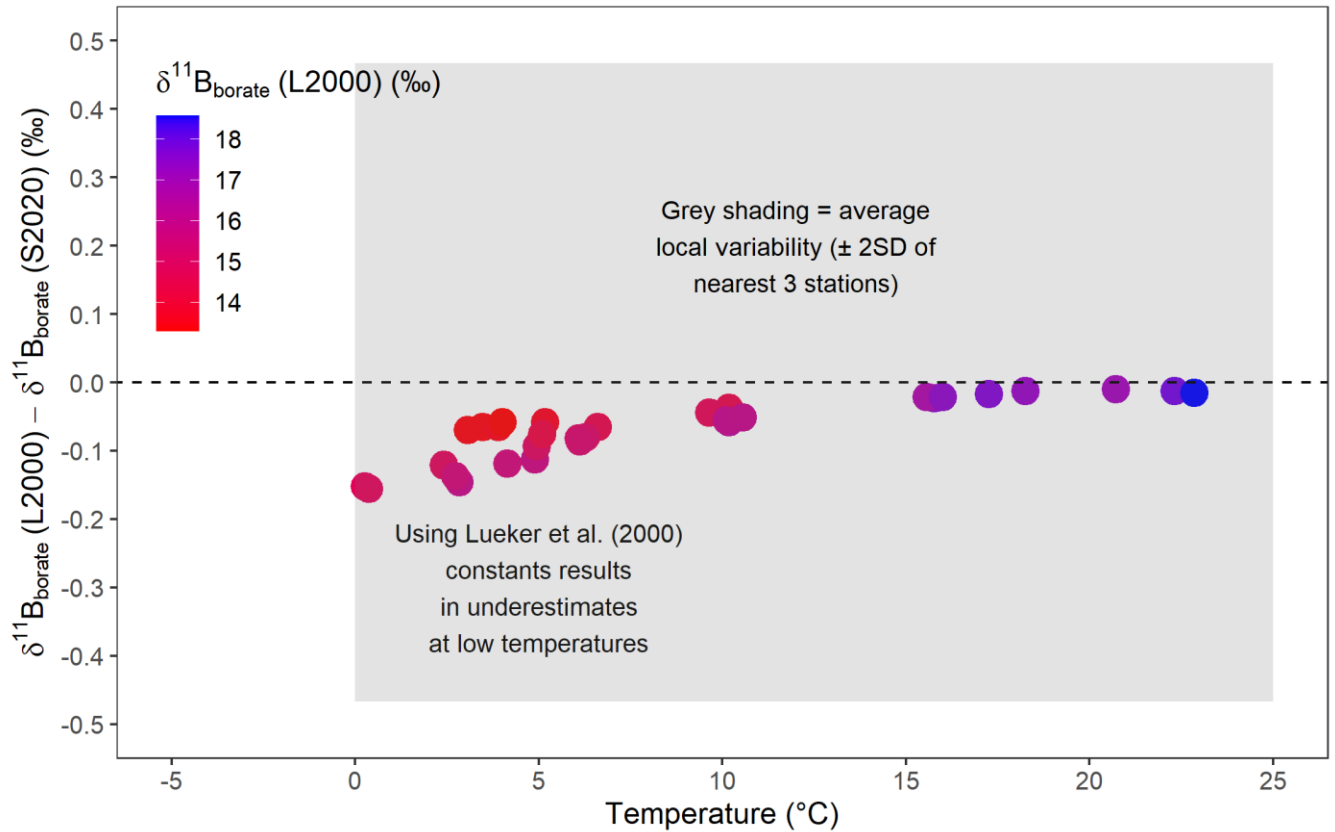
Figure 4. Difference between $\delta^{11}B_{borate}$ paired with each coral sample, calculated using dissociation constants K_1 and K_2 from Lueker et al. (2000) (L2000) and Sulpis et al. (2020) (S2020), plotted as a function of

temperature. Colour of points shows $\delta^{11}B_{borate}$ calculated using dissociation constants of Lueker et al. (2000). Grey shaded region shows average variability in $\delta^{11}B_{borate}$ from three nearest available measurements (2 σ).

3 Results

3.1 Stylasterid skeletal $\delta^{11}B$

Bulk aragonitic stylasterid $\delta^{11}B$ (herein $\delta^{11}B_{Sty.arag.}$) falls close to paired estimates of seawater $\delta^{11}B_{borate}$, varying from 13.2 to 18.8 ‰ across a $\delta^{11}B_{borate}$ range from 13.3 ‰ to 18.6 ‰ (Figure 5). Bulk-sampled high-Mg calcitic stylasterid $\delta^{11}B$ (herein $\delta^{11}B_{Sty.calc.}$) is higher for a given $\delta^{11}B_{borate}$, varying from 15.2 ‰ to 18.0 ‰ across a $\delta^{11}B_{borate}$ range of 14.2 ‰ to 15.7 ‰ (Figure 5; Figure 6). Samples measured in this study were combined with those in Stewart et al. (2022) to form a compiled dataset. The difference between $\delta^{11}B_{Sty.arag.}$ and $\delta^{11}B_{Sty.calc.}$ in this dataset is reflected in the higher $\Delta\delta^{11}B_{coral}$ (i.e. $\delta^{11}B_{coral} - \delta^{11}B_{borate}$) of high-Mg calcitic stylasterids (1.6 ± 0.5 ‰ (1 σ)) compared to aragonitic stylasterids (0.2 ± 0.8 ‰ (1 σ)) (Figure 6). The results of a 2-sample t-test confirm that this difference is statistically significant ($p < 10^{-6}$; testing the alternative hypothesis that the mean $\Delta\delta^{11}B$ for high-Mg calcitic stylasterids is greater than that for aragonitic stylasterids).

Both $\delta^{11}B_{Sty.arag.}$ and $\delta^{11}B_{Sty.calc.}$ are strongly and linearly correlated with $\delta^{11}B_{borate}$ (Table 1; Figure 5). Ordinary least squares and unweighted deming (equivalent to orthogonal least squares, calculated using the deming package in R (Therneau, 2018)) regression analyses produce very similar results (Table 1). The gradients and intercepts of the two high-Mg calcitic stylasterid relationships are within error of one another, while for aragonitic stylasterids the error margins of each overlap significantly (Table 1). In the interests of simplicity and comparability with previous work, the following discussion focuses on ordinary least squares regressions, which are recommended for use in palaeoceanographic reconstructions.

The $\delta^{11}B_{Sty.arag.}$ and $\delta^{11}B_{Sty.calc.}$ vs $\delta^{11}B_{borate}$ relationships have gradients close to 1 (Table 1). One genus-specific relationship was calculated for the aragonitic genus *Stylaster sp.*, and was found to be indistinguishable from the full aragonitic stylasterid calibration, albeit with a slightly improved goodness-of-fit (Table 1). The use of these relationships in palaeoceanographic contexts, and comparison with the other azooxanthellate coral taxa included in Table 1 is discussed in section 4.2.

As outlined in section 2.5, 4 stylasterid samples measured here were not paired with the ambient hydrographic parameters needed to calculate $\delta^{11}B_{borate}$. These samples were taken from tropical carbonate reef environments at latitudes between − 20 and + 20 ⁰N and depths between 2.5 and 25 m, and are discussed in more detail in the supplementary information (section 6.1). Briefly, their $\delta^{11}B$ values fall between 16.6 and 18.8 ‰, which agree well with the global average $\delta^{11}B_{borate}$ calculated from all available GLODAP data in this latitude and depth range (Supplementary figure 1, Supplementary figure 2). While these samples are not used in the

calibration of stylasterid $\delta^{11}B$ with $\delta^{11}B_{borate}$ or in plots which involve carbonate system parameters (e.g. $\Omega_{arag.}$ in Figure 13), these data are used in other calculations, wherever possible.

The boron isotopic data presented here is tabulated in the appendix (section 7; Supplementary table 1).

Taxon	Regression type	Source	Gradient ± 2 SE	Intercept ± 2 SE	r	p	R^2	95 % prediction (‰)*
Aragonitic Stylasteridae	Ordinary least squares	This study & S22	0.95 ± 0.17	0.90 ± 2.70	0.84	< 0.05	0.71	± 1.6
Aragonitic Stylasteridae	Unweighted deming (i.e. orthogonal)	This study & S22	1.16 ± 0.20	− 2.31 ± 2.96	0.84	< 0.05	N/A	N/A
Stylaster sp. arag.	Ordinary least squares	This study & S22	0.99 ± 0.20	0.38 ± 3.11	0.88	< 0.05	0.77	± 1.6
High-Mg calcitic Stylasteridae	Ordinary least squares	This study & S22	1.19 ± 0.72	− 1.34 ± 10.94	0.76	< 0.05	0.58	± 0.9
High-Mg calcitic Stylasteridae	Unweighted deming (i.e. orthogonal)	This study & S22	1.79 ± 0.54	− 10.37 ± 8.01	0.76	< 0.05	N/A	N/A
High-Mg calcitic bamboo coral	Ordinary least squares	F15	0.42 ± 0.25	9.28 ± 3.8	0.81	< 0.05	0.66	± 1.7
Desmophyllum dianthus (lowest Mg/Ca fibre only)	Ordinary least squares	S16	0.93 ± 0.34	12.02 ± 5.26	0.91	<0.05	0.83	± 1.0
Desmophyllum dianthus (bulk)	Ordinary least squares	A12, M12, S16, R18	0.57 ± 0.32	17.42 ± 4.99	0.66	< 0.05	0.44	± 2.7

Table 1. Summary of $\delta^{11}B_{coral}$ vs $\delta^{11}B_{borate}$ regressions for a range of azooxanthellate coral taxa. Data from this study, A12 (Anagnostou et al., 2012), M12 (McCulloch et al., 2012), F15 (Farmer et al., 2015), S16 (Stewart et al., 2016), R18 (Rae et al., 2018) and S22 (Stewart et al., 2022). *95 % prediction intervals calculated using Simple IPI approach in McClelland et al. (2021) (see section 4.2 for details).
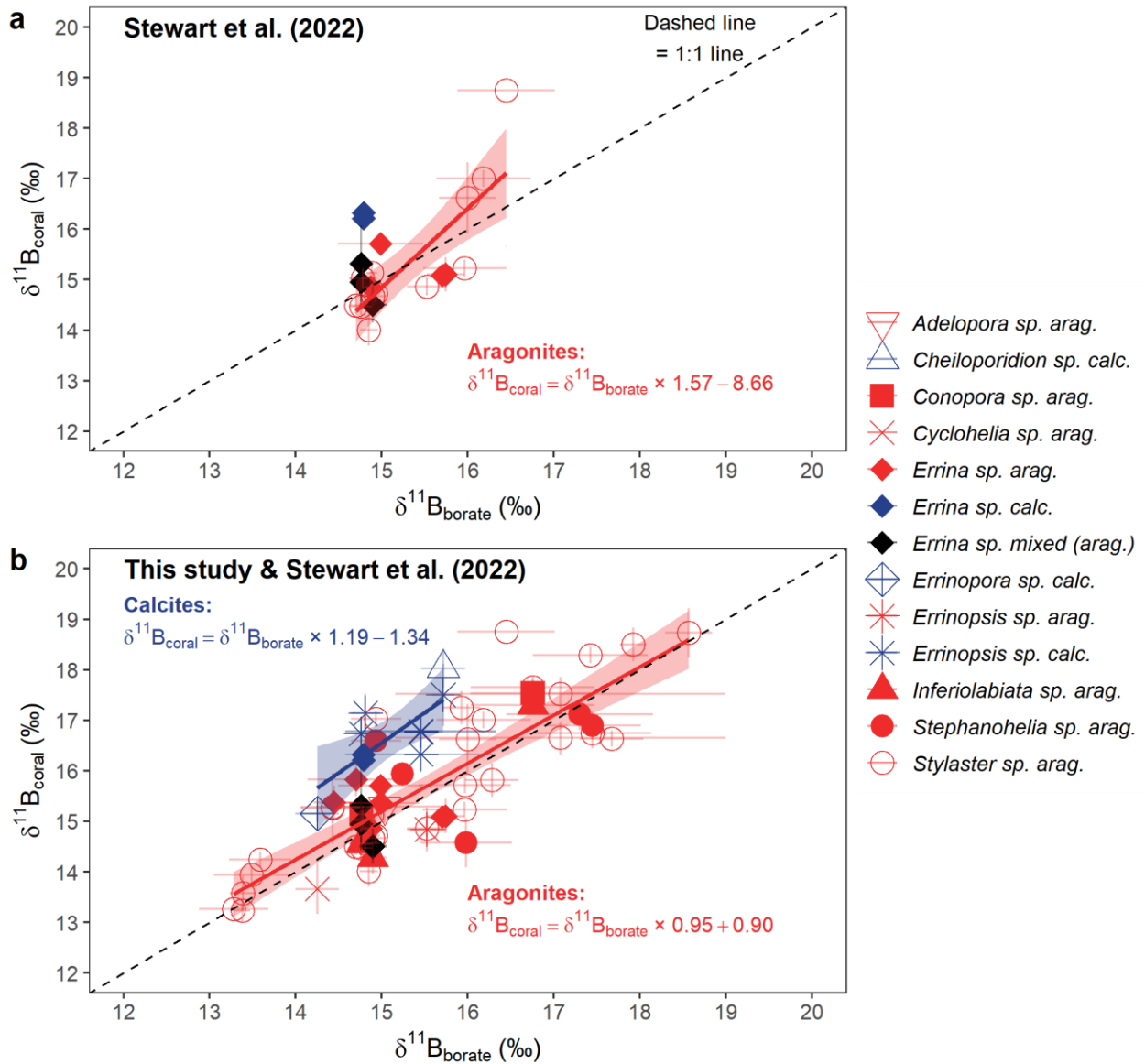
Figure 5. Stylasterid coral δ^{11}B as a function of the boron isotopic composition of the borate anion in seawater ($\delta^{11}B_{borate}$). a. Data from Stewart et al. (2022) only. b. Data from Stewart et al. (2022) and new data from this study. In both panels, vertical error bars use the larger of either the long-term analytical reproducibility or the variability between sample replicates ($\pm$ 2 σ). Horizontal error bars calculated from the variability between the nearest 3 seawater measurements ($\pm$ 2 σ). Lines of best fit calculated by ordinary least squares regression, shading indicates 95 % confidence intervals. Note samples labelled as *Errina sp. mixed (arag.)* are the mixed mineralogy (but > 90 % aragonite) samples in Stewart et al. (2022), which are not included in either regression. 4 aragonitic stylasterid samples were not paired with ambient $\delta^{11}B_{borate}$ so are not included in this plot (see sections 2.5 and 3.1).
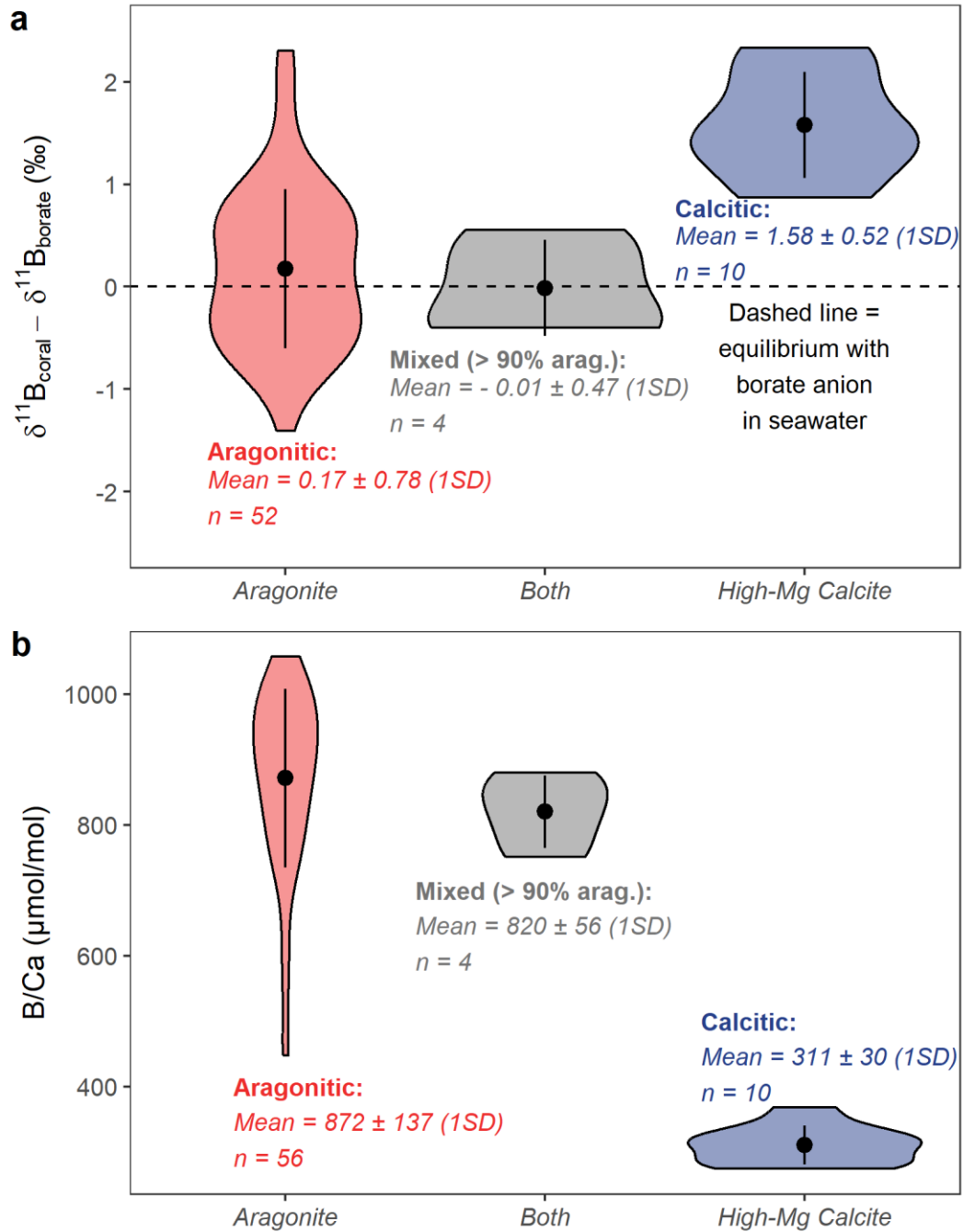
Figure 6. Violin plot showing difference between a. $\delta^{11}B_{coral} - \delta^{11}B_{borate}$ (i.e. $\Delta\delta^{11}B$) and b. B/Ca (bottom) for stylasterids grouped by mineralogy. Data include samples in this study and Stewart et al. (2022). Black points and bars show mean values and variability respectively ($\pm$ 1 σ). 4 aragonitic samples were not paired with ambient $\delta^{11}B_{borate}$ so are not included in plot a, but are used plot b (see sections 2.5 and 3.1).

3.2　Bulk sample element/Ca ratios

Bulk stylasterid Li/Ca, B/Ca, Mg/Ca, Sr/Ca, Ba/Ca, U/Ca and calculated Li/Mg ratios are presented here to complement paired $\delta^{11}B_{coral}$ measurements and inform on stylasterid biocalcification mechanisms (all data tabulated in the appendix; section 7; Supplementary table 2). In agreement with previous work, bulk stylasterid B/Ca and U/Ca ratios are shown to be influenced by sample mineralogy, with aragonitic stylasterids having higher B/Ca and U/Ca (B/Ca average: 872 µmol/mol; U/Ca average: 288 nmol/mol; n = 56) than high-Mg calcitic stylasterids (B/Ca average: 311 µmol/mol; U/Ca average: 133 nmol/mol; n = 10) (Stewart et al., 2022; Figure 6). Additionally, I confirm the finding that aragonitic stylasterids have higher B/Ca and lower U/Ca than aragonitic azooxanthellate scleractinian corals (Stewart et al., 2022; Supplementary figure 4). For further discussion of the controls on bulk stylasterid elemental compositions, the reader is referred to Stewart et al. (2020b) (Li/Ca, Mg/Ca and Sr/Ca (and Li/Mg)), Stewart et al. (2022) (B/Ca and U/Ca) and chapter 3 of this thesis (Sr/Ca & Ba/Ca).

Here, I focus on the variability in stylasterid element/Ca ratios and $\delta^{11}B_{coral}$ within individual coral specimens. By calculating the difference between replicate analyses (separate solid coral pieces) for each sample and each geochemical indicator (i.e. replicate 1 − replicate 2, for a given geochemical measurement), the correlations between these differences can be quantified (Figure 7). For aragonitic stylasterids, significant positive correlations (i.e. $p < 0.05$) are observed between $\delta^{11}B_{coral}$ and both Ba/Ca and U/Ca, while U/Ca also correlates negatively with B/Ca and positively with Ba/Ca. Further, Mg/Ca is correlated positively with Li/Ca and B/Ca, and negatively with Li/Mg, which is also correlated negatively with B/Ca. For calcitic stylasterids, U/Ca is again correlated negatively with B/Ca, with further significant correlations between Sr/Ca and U/Ca, Mg/Ca and $\delta^{11}B_{coral}$, and finally Li/Mg and both Li/Ca and B/Ca (Figure 7).
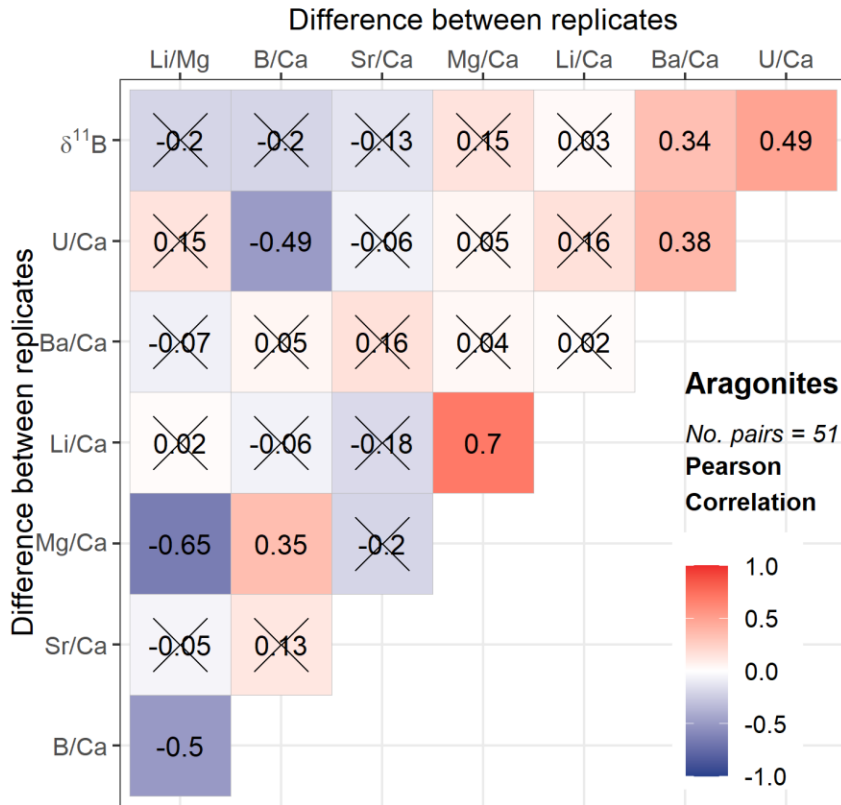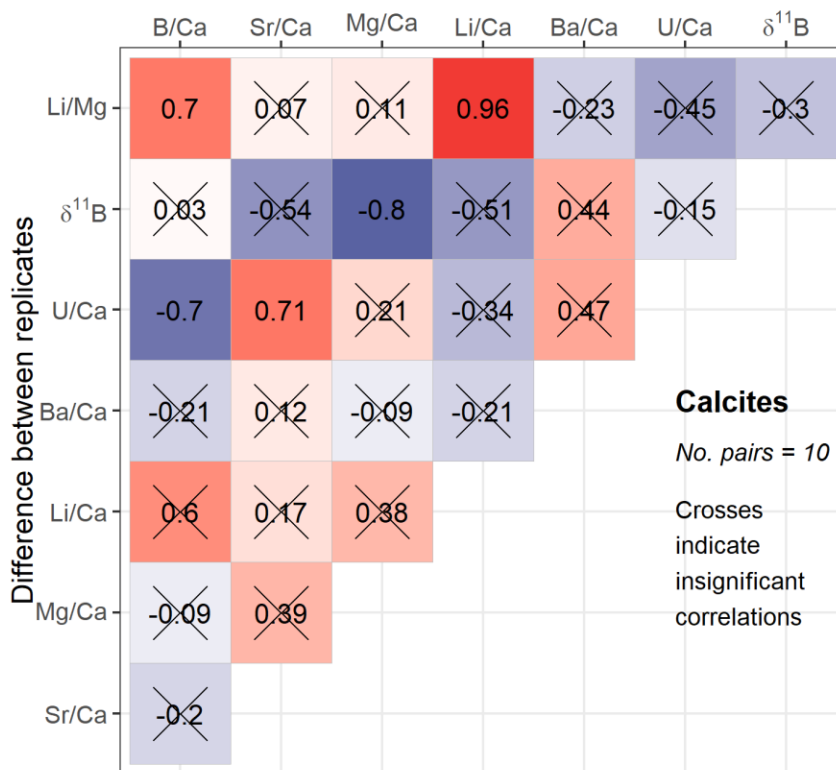
Figure 7. Correlation matrix showing how the difference between sample replicate analyses (i.e. replicate 1 − replicate 2) correlates for each geochemical indicator. For example, the negative correlation between B/Ca and U/Ca indicates that when replicate 1 of a given sample has higher B/Ca than replicate 2, replicate 1 likely also has lower U/Ca. Numbers in each square show the Pearson correlation coefficient (r). Red colours and coefficients > 1 represent positive correlations, blue colours and coefficients < 1 indicate negative correlations. Crosses show that a given correlation is not significant at the 95 % level (i.e. $p > 0.05$).

3.3   Apical tips

As outlined in section 2.3, stylasterid apical tips were also sampled and analysed for the full suite of geochemical parameters assessed here (data tabulated in the appendix; section 7; Supplementary table 3). Fifteen aragonitic and 4 mixed mineralogy stylasterids were sampled in this way. Considering aragonitic stylasterids, apical tips are significantly enriched in Li/Ca, and depleted in Sr/Ca, compared to bulk skeletal samples (Table 2; significance assessed using a one-sample *t*-test, 95 % significance level). Mg/Ca, Li/Mg, Ba/Ca, U/Ca and $\delta^{11}B_{coral}$ show no significant difference between apical tips and bulk skeletal samples, however, U/Ca is extremely variable (Figure 8). For mixed mineralogy stylasterids, tips are significantly depleted in Sr/Ca, and have heavier $\delta^{11}B$, than bulk average samples (Table 2).

For aragonitic stylasterids, the significant number of samples allows investigation of the correlations between geochemical parameters when considering the difference between apical tips and bulk skeletal samples (average of both bulk sample replicates where applicable). Almost all the geochemical parameters considered show strong and significant correlations with one another (Figure 9). Overall, Mg/Ca, Li/Ca and B/Ca are negatively correlated with Sr/Ca, U/Ca and $\delta^{11}B_{coral}$, with positive correlations between the constituent members of those two groupings (Figure 9). Ba/Ca does not correlate significantly with any other parameter, however these correlations are likely impacted by two outliers (Figure 8). Indeed, when these two samples are removed, Ba/Ca shows significant correlations with all of the other geochemical indicators considered apart from Li/Mg, correlating positively with Sr/Ca, U/Ca and $\delta^{11}B_{coral}$, and negatively with Mg/Ca, Li/Ca and B/Ca. Li/Mg is not significantly correlated with Li/Ca, Sr/Ca, U/Ca or Ba/Ca (whether considering the full dataset or that with Ba/Ca outliers removed), but exhibits significant correlations with B/Ca, Mg/Ca and $\delta^{11}B_{coral}$. More generally, correlations between Li/Mg and other parameters are reduced in significance and strength compared with Mg/Ca and Li/Ca.

Mineralogy	Li/Ca (µmol/mol)	B/Ca (µmol/mol)	Mg/Ca (mmol/mol)	Li/Mg (mmol/mol)	Sr/Ca (mmol/mol)	Ba/Ca (µmol/mol)	U/Ca (nmol/mol)	$\delta^{11}B$ (‰)
Aragonitic (n = 15)	**+ 0.39**	+ 15.8	+ 0.16 (p = 0.06)	− 0.03	**− 0.15**	+ 0.28	+ 10.6	+ 0.01
Mixed (n = 4)	+ 3.10 (p = 0.055)	− 54.6 (p = 0.08)	+ 3.22 (p = 0.06)	− 0.24	**− 0.43**	+ 0.91 (p = 0.06)	+ 150 (p = 0.06)	**+ 0.31**

Table 2. Mean difference between apical tip and bulk average stylasterid geochemistry. Values in bold are significantly different from 0 (one sample t-test, 95 % significance level, i.e. $p < 0.05$).
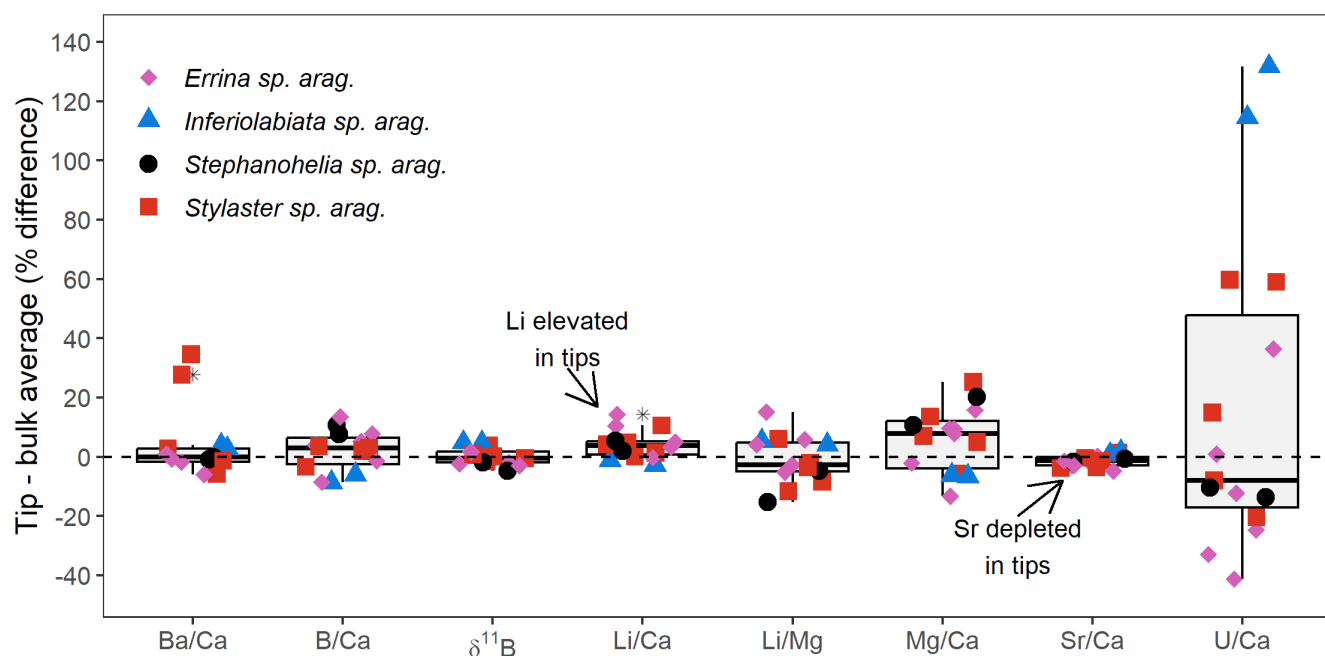
Figure 8. Percentage difference between apical tip and bulk average aragonitic stylasterid subsamples. Individual data points in red circles, statistical outliers (i.e. greater than 1.5 × interquartile range from the median) additionally indicated by grey asterisks. Data from this study, Stewart et al. (2020b) and Stewart et al. (2022).

162
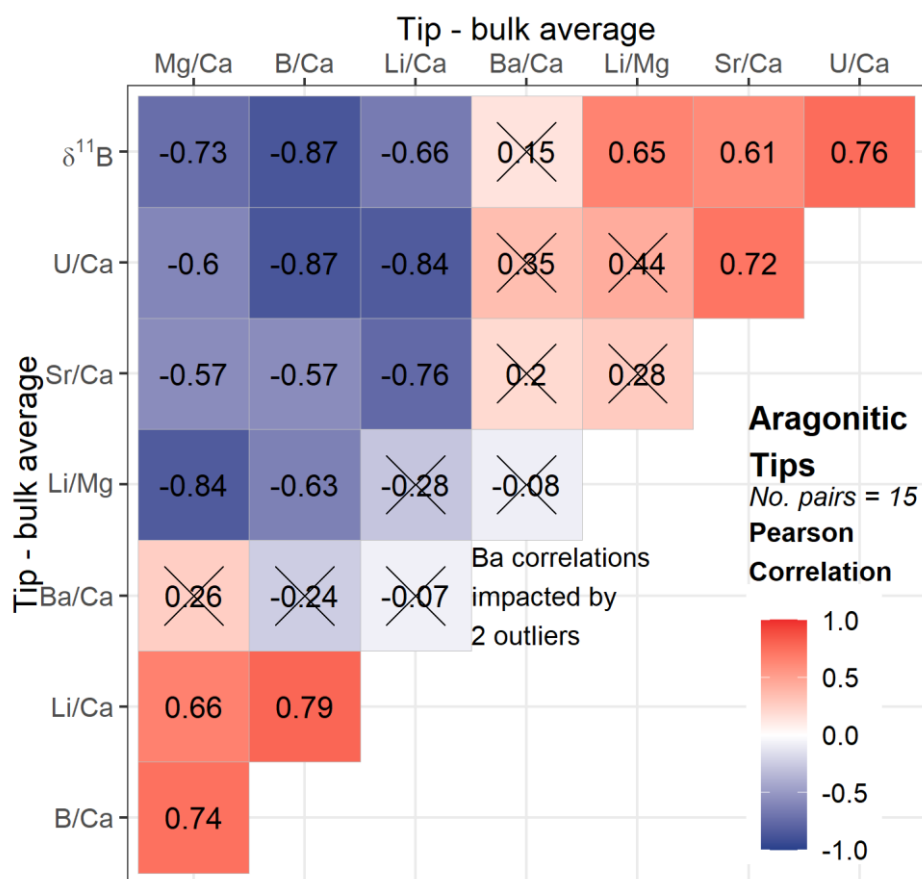
Figure 9. Correlation matrix showing how the difference between apical tip and bulk average (i.e. average of replicates 1 and 2, where 2 replicates were measured) stylasterid geochemistry correlates for each geochemical indicator (following Figure 7). Data includes aragonitic stylasterids only, $\delta^{11}B$ values not corrected for TPB contribution. Data from this study, Stewart et al. (2020b) and Stewart et al. (2022). Ba/Ca correlations likely impacted by outliers (section 3.3).

4   Discussion

4.1   Boron incorporation into stylasterid skeletons

Both $\delta^{11}B_{Sty.arag.}$ and $\delta^{11}B_{Sty.calc.}$ are linearly correlated with ambient $\delta^{11}B_{borate}$ (Figure 5). However, high-Mg calcitic stylasterids have significantly heavier $\delta^{11}B$ for a given $\delta^{11}B_{borate}$ than aragonitic stylasterids, by ~ 1.5 ‰ (Figure 6; section 3.1). When coupled with the observation that high-Mg calcitic stylasterids also have lower skeletal B/Ca (Stewart et al., 2022; Figure 6), this suggests that boron incorporation into stylasterid skeletons differs between mineralogies. The details of these incorporation mechanisms need to be explored before stylasterid $\delta^{11}B$ can be considered as an archive of past ocean pH.

4.1.1 Boron incorporation into stylasterid aragonite

Boron occurs in seawater in two forms: boric acid ($B(OH)_3$) and the borate anion ($B(OH)_4^-$). The premise of the boron isotope-pH proxy is that boron in marine carbonates is derived from only one of these sources, which is generally assumed to be the borate anion (e.g. Hemming and Hanson, 1992). Indeed, the relationship between $\delta^{11}B_{Sty.arag.}$ and $\delta^{11}B_{borate}$ has a gradient close to 1 and an intercept within error of 0 (Table 1). The good agreement between $\delta^{11}B_{Sty.arag.}$ and $\delta^{11}B_{borate}$ is further illustrated by the fact that aragonitic stylasterids have an average $\Delta\delta^{11}B$ which is also within error (1 σ) of 0 (Figure 6). This strongly supports the notion that boron incorporated into stylasterid aragonite is derived dominantly from $B(OH)_4^-$, in agreement with previous studies which focused on other biogenic and synthetic aragonites (e.g. Hemming and Hanson, 1992; Sen et al., 1994; Hemming et al., 1995; Mavromatis et al., 2015; Noireaux et al., 2015; Balan et al., 2016; Henehan et al., 2022; Chen et al., 2023). Additionally, we observe significant, positive correlations between B/Ca and Mg/Ca ratios when considering both the difference between aragonitic stylasterid bulk sample replicates (Figure 7) and the difference between bulk samples and stylasterid apical tips (Figure 8). The origin of these correlations is explored in more detail in section 4.3. Here, it is sufficient to note that similar correlations have been observed for the aragonitic scleractinian coral *D. dianthus* (Chen et al., 2023). These authors used a modelling framework to argue that the positive slope of this correlation was best supported by the sole incorporation of $B(OH)_4^-$ into coral aragonite (Chen et al., 2023). The existence of similar correlations here may, therefore, provide further support for the notion that boron incorporation into aragonitic stylasterid skeletons is dominated by $B(OH)_4^-$ (see section 4.3 for more detailed discussion). Despite this, some scatter does exist in the $\delta^{11}B_{Sty.arag.}$ vs $\delta^{11}B_{borate}$ calibration (Figure 5). This suggests that additional factors may influence $\delta^{11}B_{Sty.arag.}$ (e.g. Blamart et al., 2007; Rollion-Bard et al., 2010; Rollion-Bard et al, 2011; Anagnostou et al., 2012; McCulloch et al., 2012). These factors are explored in more detail in section 4.3.

4.1.2 Boron incorporation into stylasterid high-Mg calcite

By contrast, $\delta^{11}B_{Sty.calc.}$ is elevated by ~ 1 to 2 ‰ compared with ambient $\delta^{11}B_{Sty.arag.}$ (and equivalently $\delta^{11}B_{borate}$), and this isotopic elevation is coupled with lower skeletal B/Ca than found in aragonitic stylasterids (Stewart et al., 2022; Figure 6). These observations cannot be readily explained by simple incorporation of $B(OH)_4^-$ derived from an unmodified seawater source. Crucially, calcite $\delta^{11}B$ elevated above $\delta^{11}B_{borate}$ has also been observed for other biogenic marine calcifiers (e.g. bamboo corals: Farmer et al., 2015), and by studies investigating synthetic calcite (Noireaux et al., 2015; Farmer et al., 2019; Henehan et al., 2022). Similarly, synthetic calcites have generally lower B/Ca than synthetic aragonites (e.g. Kitano et al., 1978; Hemming et al., 1995; Mavromatis et al., 2015).

The similar trends in B-incorporation into high-Mg calcitic stylasterids and other biogenic and synthetic calcites are striking, and suggestive of a shared origin, for which various mineralogical hypotheses have been proposed. Firstly, the large isotopic fractionation between $B(OH)_3$ and $B(OH)_4^-$ (Figure 1) means that incorporation of small amounts of $B(OH)_3$ could result in calcite having higher $\delta^{11}B$ than aragonite (Noireaux et al., 2015; Branson, 2018; Farmer et al., 2019). This mechanism can be understood by appeal to the differing crystal structures of aragonite and calcite, as well as the surface kinetics of mineral growth (e.g. Branson, 2018; Farmer et al., 2019). In this framework, as crystals grow, ions both attach and detach from the crystal surface, with the relative rates of attachment, detachment and crystal growth determining the overall crystal composition. In the aragonite lattice, tetrahedrally-coordinated $B(OH)_4^-$ is more stable than $B(OH)_3$, while in calcite, the opposite is true. This means that $B(OH)_4^-$ both attaches more readily and detaches less often than $B(OH)_3$ in aragonite, meaning the majority of boron is derived from $B(OH)_4^-$. Conversely, in calcite, $B(OH)_4^-$ detaches more readily from the growing crystal surface than $B(OH)_3$, resulting in an increased proportional contribution to total boron from $B(OH)_3$ (Noireaux et al., 2015; Uchikawa et al., 2015; Balan et al., 2016; Branson, 2018; Farmer et al., 2019). In both aragonite and calcite, the assumed positive charge of the crystal surface (in this model) results in increased initial attachment of $B(OH)_4^-$, rather than $B(OH)_3$, with the increased stability of $B(OH)_4^-$ in the aragonite lattice also accounting for higher aragonitic B/Ca ratios, compared with calcite.

Alternatively, differences between $\delta^{11}B_{Sty.calc.}$ and $\delta^{11}B_{borate}$ may result from isotopic fractionation induced by electrostatic effects during boron adsorption and/or detachment, which have been suggested to influence boron isotopic incorporation into synthetic calcites (e.g. Saldi et al., 2018; Henehan et al., 2022; although see Branson, 2018). Whether these effects occur in natural systems is uncertain, and it is likely that boron isotopic fractionations are heavily suppressed under natural conditions, compared with those utilised in the laboratory (e.g. Farmer et al., 2019; Henehan et al., 2022). Here, I consider one model which suggests that isotopic fractionation occurs during detachment of $B(OH)_4^-$ from the growing crystal surface (Henehan et al., 2022). Under this model, boron incorporation into both synthetic aragonites and calcites is dominated by $B(OH)_4^-$, readily explaining the higher B/Ca of aragonites owing to the crystal structure considerations outlined above. Henehan et al. (2022) propose that the electrostatic potential toward which ions are initially attracted is not that which exists at the crystal surface, but that at the surface at which ions are first held in fixed positions. This potential is referred to as the ζ-potential, and is negative in most natural calcites (e.g. Al Mahrouqi et al., 2017). In turn, this suggests that $B(OH)_4^-$ ions must be initially attracted toward the growing mineral as positively charged ion pairs, in association with Ca^{2+} or Mg^{2+} (Henehan et al., 2022). The eventual incorporation of Mg^{2+}/Ca^{2+} into the $CaCO_3$ lattice then involves either the breaking of the association between these positive ions and $B(OH)_4^-$, or charge balance being achieved by association with a monovalent cation, such Na^+. Isotopic fractionations could reasonably occur during these processes, and differences in the boron isotopic

composition of synthetic aragonite and calcite could in turn result from their differing ζ-potentials and/or lattice structures (Henehan et al., 2022).

Although B-incorporation into aragonitic and high-Mg calcitic stylasterids displays strong similarities to synthetic studies, a final hypothesis which may explain the offset between $\delta^{11}B_{Sty.calc.}$ and $\delta^{11}B_{borate}$ is that calcitic stylasterids employ a small amount of biologically-mediated pH upregulation, in contrast to their aragonitic counterparts. This hypothesis is discussed in more detail in section 4.1.3, and has been implicated as the cause of elevations in scleractinian and bamboo coral $\delta^{11}B$ compared with $\delta^{11}B_{borate}$, owing to the pH sensitivity of the $\delta^{11}B$ signature of marine carbonates (e.g. McCulloch et al., 2012; Farmer et al., 2015).

4.1.3 Stylasterid $\delta^{11}B$ is consistent with mineralogical controls on boron incorporation

While all the mechanisms outlined above can explain the heavier $\delta^{11}B_{Sty.calc.}$ compared with $\delta^{11}B_{Sty.arag.}$, I suggest that mineralogical considerations – rather than biologically-mediated pH upregulation – provide the most parsimonious explanation. Firstly, at the Mg/Ca ratios which characterise high-Mg calcitic stylasterids (80 to 120 mmol/mol; Stewart et al., 2020b; this study), high-Mg calcite is equivalently or less soluble than aragonite (Ries, 2011). Therefore, it is unclear why high-Mg calcitic stylasterids would employ additional pH upregulation compared to their equally or more soluble aragonitic counterparts. Secondly, $\delta^{11}B$ of coral carbonate may not record pH upregulation in a straightforward manner, with the diffusion of boric acid possibly playing an important role in final $\delta^{11}B$, complicating the traditional interpretation of this geochemical signature (Gagnon et al., 2021; Stewart et al., 2022; section 4.3). Finally, if pH upregulation in calcitic stylasterids were the cause of the observed offset, one might expect that the magnitude of this offset would depend on calcification-relevant seawater conditions (e.g. nutrient concentrations, pH, $\Omega_{arag.}$) as suggested for bamboo corals (Farmer et al., 2015). However, the magnitude of the offset between $\delta^{11}B_{Sty.calc.}$ and $\delta^{11}B_{borate}$ is not significantly correlated with any hydrographic variable considered here (temperature, salinity, phosphate, dissolved silica, alkalinity, DIC, pH or $\Omega_{arag.}$).

Considering instead abiogenic, mineralogical origins, the data presented here do not provide unequivocal support for either of the two proposed abiogenic, mineralogical mechanisms by which boron is incorporated into calcite (compare Farmer et al., 2019; Henehan et al., 2022). For example, if boric acid incorporation were important, one would expect that lighter $\delta^{11}B_{Sty.calc.}$ signatures (i.e. more $B(OH)_4^-$ detachment) would be accompanied by lower B/Ca. However, I find no correlation between high-Mg calcitic stylasterid $\Delta\delta^{11}B$ and B/Ca ($r = 0.25$, $p > 0.05$), and no significant correlation between the differences between calcitic stylasterid sample replicate B/Ca and $\delta^{11}B$ (Figure 7). As part of their study, Henehan et al. (2022) found a strong, positive correlation between the concentrations of Na and B in synthetic carbonates. Na/Ca ratios were not measured

for all samples presented here and so are not included in Figure 7. However, for the 7 calcitic samples for which Na/Ca ratios were measured, I find no significant correlation of variations in Na/Ca and B/Ca between sample replicates ($p > 0.05$).

Despite this, the agreement between $\delta^{11}B_{Sty.arag.}$ with $\delta^{11}B_{borate}$, and the offset between $\delta^{11}B_{Sty.calc.}$ and $\delta^{11}B_{borate}$, are strikingly similar to observations made on synthetic carbonates. This strongly suggests that this difference is most likely the result of mineralogical influences on boron isotope incorporation into marine carbonates, and provides novel evidence for the occurrence of this effect in a natural system. This conclusion has important implications for the use of stylasterids as archives of seawater pH, which are addressed in the following section.

4.2   Stylasterids as archives of seawater pH

The key finding of the present work is the new observation that, when calibrated across a wide range of pH environments, stylasterid $\delta^{11}B$ correlates strongly and linearly with $\delta^{11}B_{borate}$. In turn, this suggests that stylasterid corals may be a new archive of past ocean pH (see section 1 for an explanation of the boron isotope-pH proxy in marine carbonates). In the following sections, I discuss the use of stylasterid $\delta^{11}B$ as an archive of past ocean pH, considering aragonitic and high-Mg calcitic stylasterids separately, given the robust evidence for differences between their boron incorporation mechanisms (section 4.1).

4.2.1   Aragonitic stylasterid $\delta^{11}B$ vs $\delta^{11}B_{borate}$

The first key observation is that aragonitic stylasterids have $\delta^{11}B$ in equilibrium with $\delta^{11}B_{borate}$, in contrast to azooxanthellate scleractinian corals (e.g. McCulloch et al., 2012; Anagnostou et al., 2012; Stewart et al., 2016; Figure 10). The comparatively low $\delta^{11}B$ signature of stylasterid coral skeletons is instead more similar to calcitic and aragonitic foraminifera (e.g. Rae et al., 2011; Henehan et al., 2013; Stewart et al., 2022; Figure 10). Indeed, scleractinian corals generally exhibit skeletal $\delta^{11}B$ offset to far higher values than $\delta^{11}B_{borate}$, interpreted as the signature of pH upregulation (Anagnostou et al., 2012; McCulloch et al., 2012). This is clearly illustrated by comparison of the intercepts of the aragonitic stylasterid $\delta^{11}B$ vs $\delta^{11}B_{borate}$ calibration (within error of 0 ‰) compared with that of various *D. dianthus* calibrations (Table 1; Figure 10; Anagnostou et al., 2012; McCulloch et al., 2012; Stewart et al., 2016; Rae et al., 2018).

Importantly, the potentially variable magnitude of the $\delta^{11}B$ to $\delta^{11}B_{borate}$ offset in scleractinian corals means that species-specific, empirical calibrations need to be derived (e.g. McCulloch et al., 2012). Conversely, $\delta^{11}B_{Styla.arag.}$ from a range of locations and genera is in equilibrium with $\delta^{11}B_{borate}$. It is possible that some of the scatter in the aragonitic stylasterid calibration may result from genus-specific effects. However, considering samples from only *Stylaster sp. (arag.)* – the genus present in this sample set across the widest range of $\delta^{11}B_{borate}$ – results in a

calibration within error of the full calibration, albeit with a slightly improved r and R^2 (Table 1). The magnitude of inter-species $\delta^{11}B$ offsets is thus demonstrably smaller than observed for scleractinian corals (McCulloch et al., 2012), providing strong evidence that the suite of aragonitic stylasterid taxa represented here can be considered as directly comparable archives of $\delta^{11}B_{borate}$.

A further advantage of using $\delta^{11}B_{Styla.arag.}$ to reconstruct $\delta^{11}B_{borate}$ is the low level of intra-skeletal variability, compared with scleractinian $\delta^{11}B$. It has been widely reported that scleractinian coral skeletons can be extremely heterogeneous in their $\delta^{11}B$ composition (e.g. variations up to 8 ‰), owing to incorporation of skeletal elements including CoCs (e.g. Blamart et al., 2007; Stewart et al., 2016; Jurikova et al., 2019). While the dataset presented here cannot constrain the magnitude of micro-scale variability in stylasterid $\delta^{11}B$, comparing the bulk aragonitic stylasterid calibration found here with a bulk-sample *Desmophyllum dianthus* calibration (including data from Anagnostou et al., 2012; McCulloch et al., 2012; Stewart et al., 2016; compiled in Rae et al., 2018) reveals that the aragonitic stylasterid calibration exhibits far less scatter, reflected in its higher r and R^2 values (Table 1; Figure 10). Indeed, the goodness-of-fit (and 95 % prediction uncertainty, see below) of the bulk aragonitic stylasterid calibration presented here is more similar to that of the microsampled *D. dianthus* calibration in Stewart et al. (2016) (Table 1). This *D. dianthus* calibration employed a microsampling approach to minimise incorporation of CoCs, coupled with monitoring of Mg/Ca to specifically choose the subsample with the lowest degree of CoC incorporation from each coral (Stewart et al., 2016). This approach is both time-consuming and is limited to large samples in which skeletal morphology is clear. By contrast, the bulk stylasterid sampling approach employed here is simple, user-friendly and non-selective, making the goodness-of-fit of the $\delta^{11}B_{Styla.arag.}$ vs $\delta^{11}B_{borate}$ relationship particularly striking.

Despite relatively small intra-coral variability, significant scatter does exist between stylasterid specimens and thus in the $\delta^{11}B_{Styla.arag.}$ vs $\delta^{11}B_{borate}$ calibration. Much of this variability may be attributable to estimates of $\delta^{11}B_{borate}$, which in some locations (e.g. the Florida Straits) can be highly uncertain (Figure 5). However, the significant, negative covariation between $\delta^{11}B_{Styla.arag.}$ and U/Ca between bulk sample replicates suggests that some of this scatter is correlated with elemental variability, and in turn may result from intra-skeletal variability in stylasterid $\delta^{11}B$ (Figure 7). This possibility is addressed further in section 4.3, and suggests that stylasterid biomineralisation processes exerts some influence on stylasterid skeletal $\delta^{11}B$. Encouragingly, the influence of these processes appears to be effectively minimised by using large, bulk skeletal samples, and avoiding the apical tips of growing branches (sections 4.3 and 4.4).

To quantify the uncertainty associated with $\delta^{11}B_{borate}$ reconstruction using $\delta^{11}B_{Styla.arag.}$, I estimate 95 % prediction uncertainties associated with the calibration (Table 1). Deriving prediction uncertainties associated with calibration-based reconstructions is non-trivial, and a variety of possible approaches have been proposed

(McClelland et al., 2021). Here, I use the "Simple Inverse Prediction Interval" (Simple IPI) approach outlined by McClelland et al. (2021) to provide estimates of the uncertainty associated with $\delta^{11}B_{borate}$ estimation using azooxanthellate coral $\delta^{11}B$. The same calculations were also carried out for previously published *D. dianthus* and bamboo coral calibrations to provide direct comparability.

The results of the Simple IPI approach demonstrate that the new $\delta^{11}B_{Styla.arag.}$ calibration facilitates more precise prediction of $\delta^{11}B_{borate}$ than the commonly-used bulk *D. dianthus* (Table 1). The width of the 95 % prediction interval ($\sim \pm 1.6$ ‰) for aragonitic stylasterids implies that, at a typical $\delta^{11}B_{borate}$ of 15.5 ‰, ocean pH can be reconstructed to $\sim \pm 0.20$ pH units (assuming $pK_B^* = 8.79$ (average from this study)). This uncertainty is significantly larger than those reported for *D. dianthus* (Anagnostou et al., 2012; Stewart et al., 2016), which were based on 95 % confidence intervals – rather than prediction intervals. Recalculating pH bounds using the prediction interval calculated here reveals that pH reconstruction using aragonitic stylasterids is more precise than using bulk *D. dianthus* (± 0.30 pH units), illustrating the comparative potential of aragonitic stylasterids as palaeo-pH archives.

In combination with stylasterid $\delta^{18}O$, Li/Mg, Ba/Ca and $\Delta^{14}C$, the $\delta^{11}B_{Styla.arag.}$ vs pH proxy developed here may be used to provide holistic constraint on shifts in ocean temperatures, radiocarbon content, carbonate system parameters and $[Ba]_{SW}$ through time, in turn facilitating the reconstruction of the temporal evolution of a range of oceanographically and climatically-relevant processes (King et al., 2018; Samperiz et al., 2020; Stewart et al., 2020b; chapter 3).

4.2.2 High-Mg calcitic stylasterid $\delta^{11}B$ vs $\delta^{11}B_{borate}$

$\delta^{11}B_{Styla.calc.}$ also correlates with $\delta^{11}B_{borate}$ (Table 1; Figure 5), suggesting that $\delta^{11}B_{Styla.calc.}$ may also be a promising archive of ocean pH. As outlined in section 4.1, it is possible that high-Mg calcitic stylasterids incorporate boron from either a boric acid source, or experience boron isotopic fractionation during mineralisation. Both processes could conceivably be sensitive to multiple factors (e.g. instantaneous rate of crystal growth) which may vary through time, presenting some challenges to the application of $\delta^{11}B_{Styla.calc.}$ in palaeoceanographic contexts.

Despite this, the empirical calibration between $\delta^{11}B_{Styla.calc.}$ and $\delta^{11}B_{borate}$ presented here is robust, and intriguingly has narrower prediction intervals (considering the graphical range constrained by data) than the aragonitic stylasterid calibration (Figure 10). Such improved prediction contrasts with the worse R-squared, wider confidence intervals and more uncertain gradient and intercept of the $\delta^{11}B_{Styla.calc.}$ vs $\delta^{11}B_{borate}$ relationship compared with the $\delta^{11}B_{Styla.arag.}$ vs $\delta^{11}B_{borate}$ relationship. These statistical differences likely result in part from the steeper gradient of the $\delta^{11}B_{Styla.calc.}$ vs $\delta^{11}B_{borate}$ relationship, since in the Simple IPI approach prediction

interval width is inversely proportional to the calibration gradient (McClelland et al., 2021). Crucially, consideration of prediction intervals suggests that the current $\delta^{11}B_{Styla.calc.}$ vs $\delta^{11}B_{borate}$ calibration is robust, and this promising observation could be confirmed by calibrating $\delta^{11}B_{Styla.calc.}$ across a wider pH range.
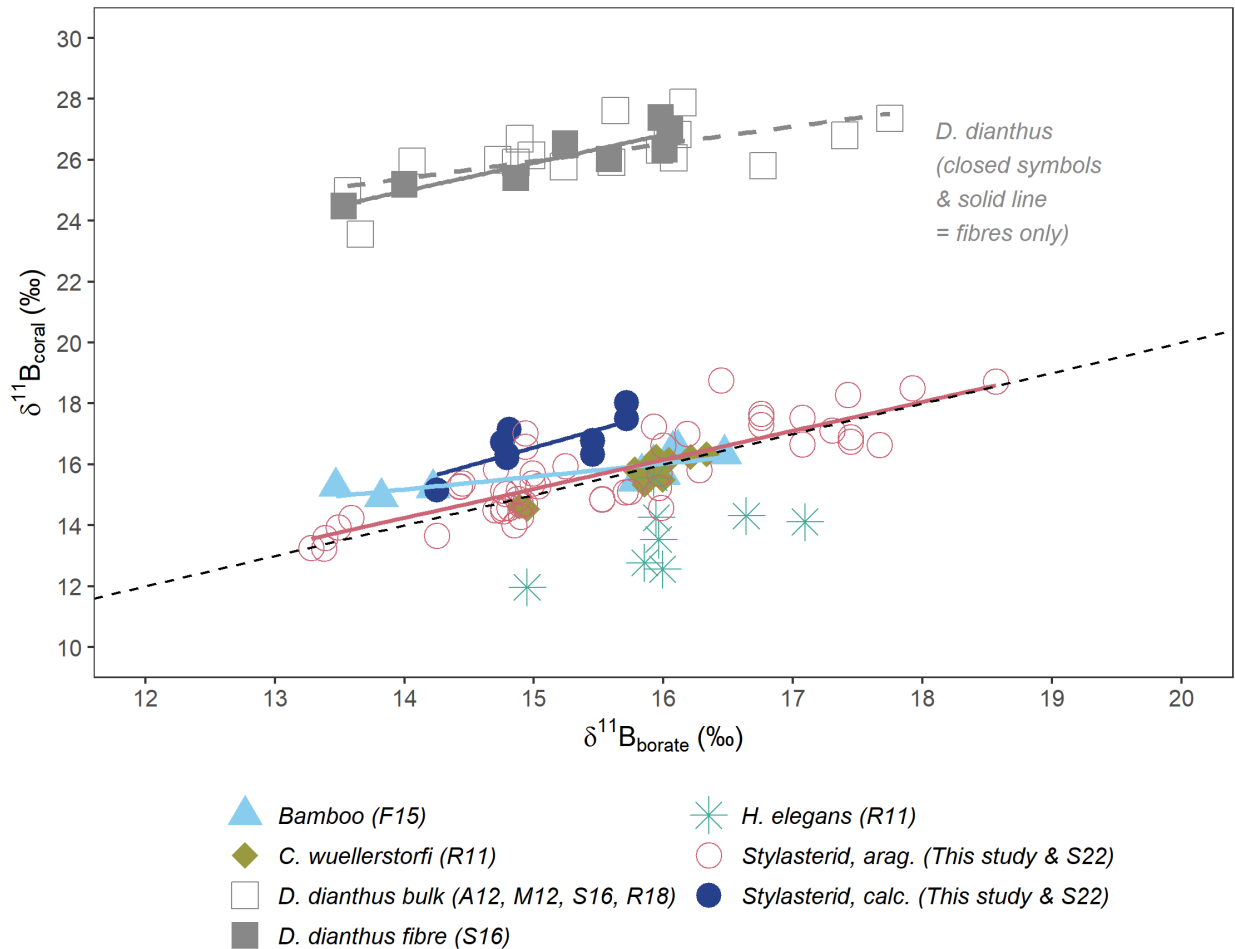
Figure 10. Comparison of azooxanthellate coral and benthic foraminiferal $\delta^{11}B$ vs $\delta^{11}B_{borate}$ relationships. Dashed line is 1:1 line. Data from R11 (Rae et al., 2011), A12 (Anagnostou et al., 2012), M12 (McCulloch et al., 2012), F15 (Farmer et al., 2015), S16 (Stewart et al., 2016), R18 (Rae et al., 2018; used for compiled bulk *D. dianthus* calibration), S22 (Stewart et al., 2022) and this study.

4.3   Evidence for biological mediation of the stylasterid calcifying fluid

Having addressed boron incorporation mechanisms into stylasterid skeletons, and their utility as sensors of ocean pH, I now consider whether the data presented here can provide novel insights into stylasterid coral

calcification mechanisms. The only other study of stylasterid $\delta^{11}B$ values reported the surprising observation that stylasterid $\delta^{11}B$ is close to $\delta^{11}B_{borate}$, in stark contrast to scleractinian corals (Stewart et al., 2022). Previously, coral $\delta^{11}B$ values have been used to infer coral calcifying fluid pH, a line of reasoning which relies on the pH-dependence of the boron isotopic signature of $B(OH)_4^-$ and the assumption that boron in aragonite is derived dominantly from $B(OH)_4^-$ (e.g. McCulloch et al., 2012; Figure 1). In the case of azooxanthellate scleractinian corals, their boron isotopic composition is significantly heavier than $\delta^{11}B_{borate}$, consistent with biologically-mediated upregulation of pH in the scleractinian calcifying fluid (e.g. Anagnostou et al., 2012; McCulloch et al., 2012; Gagnon et al., 2021). Applying this understanding to the low $\delta^{11}B$ values of aragonitic stylasterids suggests that they employ little or no pH upregulation (Stewart et al., 2022).

The sample set measured by Stewart et al. (2022) included stylasterids from a relatively small range of environments and hydrographic conditions ($\Omega_{arag.}$ from 0.9 to 2.0). Here, I show that aragonitic stylasterid samples collected from an extremely wide range of ocean conditions ($\Omega_{arag.}$ from 0.5 to 3.7) all show $\delta^{11}B$ close to $\delta^{11}B_{borate}$ (Figure 13). This finding is particularly important when considering stylasterids from the North Pacific, which grew in waters with extremely low saturation states with respect to aragonite ($\Omega_{arag.} \sim 0.5$; Figure 13). This presents `challenges to the notions that pH upregulation is required for azooxanthellate coral calcification, and/or that the $\delta^{11}B$ of coral skeletons records pH at the site of calcification.

As outlined by Stewart et al. (2022), low stylasterid $\delta^{11}B$ suggests that either the boron isotopic composition of stylasterid skeletons does not record the pH of their calcifying fluid, or that stylasterids do not employ pH upregulation during calcification, instead relying on alternative biomineralisation pathways, such as using organic molecules to catalyse calcification (e.g. Drake et al., 2013; Mass et al., 2013; Von Euw et al., 2017; reviews in Tambutté et al., 2011; Falini et al., 2015). These two possible interpretations cannot easily be distinguished. However, the expanded stylasterid dataset and consideration of a wide range of element/Ca ratios presented here provides important new evidence which is discussed in the following sections. I restrict focus to aragonitic stylasterids, as the possibility that calcitic stylasterids incorporate boron from either a boric acid source, or are impacted by isotope fractionation during boron incorporation, further complicates interpretation of their $\delta^{11}B$ signature (section 4.1).

4.3.1 Is aragonitic stylasterid $\delta^{11}B$ decoupled from calcifying fluid pH?

Broadly, two mechanisms have been proposed to decouple coral calcifying fluid pH from the boron isotopic composition of the calcifying fluid. Firstly, active transport of bicarbonate ion with associated co-transport of $B(OH)_4^-$ has been linked to low skeletal $\delta^{11}B$ of some skeletal elements in the scleractinian coral *Lophelia pertusa* (Fietzke and Wall, 2022). In the case of stylasterids, this process was ruled out owing to the negative covariation

of B/Ca and $\delta^{11}B$ when comparing between stylasterid and scleractinian corals (Stewart et al., 2022). Since the expanded sample set presented here supports this observation (Supplementary figure 4), I do not discuss this mechanism further, and the reader is referred to Stewart et al. (2022) for further details.

Alternatively, recent work has shown that boric acid diffusion across calcifying fluid membranes is another plausible mechanism by which the boron isotopic composition of the coral calcifying fluid can be decoupled from calcifying fluid pH (Gagnon et al., 2021). In this model, the boron isotopic composition of the coral calcifying fluid is controlled by the balance between the pH of the fluid, the rate of boric acid diffusion between the calcifying fluid and seawater (D_B), and the timescale of seawater flushing of the coral calcifying fluid (kz; Gagnon et al., 2021; higher kz represents more frequent flushing; Figure 11). Diffusion of boric acid occurs owing to the pH dependence of boron speciation, which means that pH upregulation in the coral calcifying fluid leads to lower $[B(OH)_3]$ in the calcifying fluid, compared with external seawater. The resulting $B(OH)_3$ concentration gradient promotes diffusion of boric acid into the calcifying fluid. When the rate of diffusion is fast compared with the rate of seawater flushing of the calcifying fluid (i.e. high D_B/kz), boric acid diffusion simultaneously increases total boron concentrations in the calcifying fluid, and equilibrates the boron isotopic signature of the calcifying fluid with that of seawater, effectively decoupling $\delta^{11}B_{CF}$ from calcifying fluid pH. Conversely, when kz is rapid compared with D_B (low D_B/kz), the boron isotopic signature of the calcifying fluid retains sensitivity to calcifying fluid pH, because there is insufficient time for significant boric acid diffusion to occur. In this framework, the boron isotopic composition of stylasterid carbonate may not record calcifying fluid pH in a straightforward manner, and the evidence of any pH upregulation could be masked by high stylasterid D_B/kz (Gagnon et al., 2021; Stewart et al., 2022).

Figure 11. Reproduced from Gagnon et al. (2021). Schematic of key fluxes into and out of the calcifying fluid (CF). Note that kz and D_B are in units of ms^{-1}, k = inverse of time taken to replenish CF, z = volume:area

ratio of the CF. Fluxes in red show those directly related to pH upregulation, which will also impact diffusion of other species (e.g. CO_2).

High D_B/kz (either fast rates of boric acid diffusion, or slow flushing of the calcifying fluid with seawater) may explain why aragonitic stylasterids have lower $\delta^{11}B$ and U/Ca, but higher B/Ca than azooxanthellate scleractinian corals (discussed in detail in Stewart et al., 2022; Supplementary figure 4). Of interest here is that this model can also explain broader aspects of stylasterid geochemistry, which are apparent in the new data presented here.

Firstly, bulk aragonitic stylasterid $\delta^{11}B$ was previously found to be positively correlated with U/Ca and negatively correlated with B/Ca, while U/Ca and B/Ca were negatively correlated (Stewart et al., 2022). Similar trends were observed for the difference between stylasterid sample replicates, although the significance of these trends was not quantified (Stewart et al., 2022). In the expanded dataset presented here, bulk aragonitic stylasterid $\delta^{11}B$, U/Ca and B/Ca are not significantly correlated (Supplementary figure 4). Further, our significantly larger dataset reveals that B/Ca and $\delta^{11}B$ are not significantly correlated when considering the differences between bulk sample replicates (Figure 7). However, intra-skeletal variability is significantly correlated between U/Ca and both B/Ca (negative) and $\delta^{11}B$ (positive) (Figure 7).

Additional insight can also be gained by considering the sub-sampling carried out in this study. The bulk sampling approach employed by Stewart et al. (2022) (and in this study) is specifically designed to minimise the impact of calcification-related effects on stylasterid geochemistry (e.g. Gagnon et al., 2007; Samperiz et al., 2020; Stewart et al., 2020b; Stewart et al., 2022; section 2.3). Importantly, this approach also avoids the growing tips of stylasterid branches, which have been shown to have stable oxygen and carbon isotopic signatures further from equilibrium with seawater and are thus inferred to be most impacted by calcification-related effects (Samperiz et al., 2020). While avoidance of apical tips has proved highly effective in developing stylasterids as archives of seawater conditions (e.g. Samperiz et al., 2020; Stewart et al., 2020b; chapter 3; section 4.2), it may not be the most suitable for studying the very effects it is designed to minimise. Therefore, I additionally compare stylasterid apical tips with bulk skeletal samples, in an attempt to better elucidate the mechanisms which cause intra-skeletal variability in stylasterid geochemistry.

The results of this experiment are striking. Of most importance is the observation that the geochemical differences between apical tips and bulk skeletal samples are highly and significantly correlated for almost all elements (Figure 9; Figure 12) (note that a correlation between two geochemical indicators in Figure 9 means that, in a cross plot of those two indicators as in Figure 12 (panels a, c, e and g), the lines joining tip samples to the corresponding bulk average value from the same coral have similar gradients). B/Ca correlates negatively and significantly with U/Ca and $\delta^{11}B$, and U/Ca and $\delta^{11}B$ are significantly, positively correlated (Figure 9;

Figure 12). The new data presented here thus provide strong and statistically-significant evidence in favour of correlated variability in stylasterid δ^{11}B, U/Ca and B/Ca, which can be explained by the paired influence of boric acid diffusion and variations in seawater flushing of the stylasterid calcifying fluid (Stewart et al., 2022; summarised in Figure 12). The negative covariation of δ^{11}B and B/Ca is predicted because at higher D_B/kz, boric acid diffusion increases total boron concentrations in the calcifying fluid, as well as driving δ^{11}B lower (Stewart et al., 2022). Similarly, variations in kz have been inferred to impact coral U/Ca ratios, with slow rates of seawater flushing (i.e. high D_B/kz, assuming constant D_B) resulting in lower U/Ca (Gothmann and Gagnon, 2021).

Further support for this model may also come from the observation that stylasterids from the North Pacific have, on average, lower B/Ca than stylasterids from other locations (Figure 13). These corals grew in waters which are heavily undersaturated with respect to aragonite (Figure 13), and also have generally higher [DIC] than elsewhere (Supplementary figure 5). In the model of Gagnon et al. (2021), the pH of the coral calcifying fluid is thought to be held constant between samples. Since corals derive DIC from seawater, and the ratio of [DIC]/[CO_3^{2-}] depends primarily on pH, at constant pH, higher DIC leads to higher [CO_3^{2-}] and thus lower [B(OH)$_4^-$]/[CO_3^{2-}] (Gagnon et al., 2021). This process can explain why scleractinian coral B/Ca decreases linearly with increasing [DIC], and may also explain why stylasterids from the North Pacific have generally lower B/Ca than those collected from other regions. I note, however, that more generally the correlation between aragonitic stylasterid B/Ca and [DIC] is insignificant (Supplementary figure 5).

Considering a wider range of stylasterid geochemistry reveals that this model can also explain trends in the other aspects of stylasterid geochemistry presented here. Almost all of the elements considered show significant covariation when considering the difference between apical tips and the bulk skeleton, characterised by Li/Ca, Mg/Ca and B/Ca correlating negatively with U/Ca, Sr/Ca and δ^{11}B (and Ba/Ca, when outliers are removed), and positive correlations between the constituents of those two groupings (Figure 9; Figure 12; note that Li/Mg ratios will be addressed in section 4.4). To what extent can these correlations be explained by variations in D_B/kz? Assuming that boric acid diffusion does not impact on other elements, variations in seawater flushing rate (kz) are consistent with Rayleigh fractionation impacting the incorporation of elements into stylasterid carbonate. The incorporation of elements including Li, Mg and Sr can be understood by reference to partition

coefficients (D_X; where $D_X = \dfrac{\frac{X}{Ca}_{coral}}{\frac{X}{Ca}_{fluid}}$ e.g. Gaetani and Cohen, 2006). Li and Mg have partition

coefficients into aragonite << 1, meaning they are preferentially excluded from the aragonite lattice during crystallisation (e.g. Marriott et al., 2004; Gabitov et al., 2008; Mavromatis et al., 2022). Meanwhile, Sr has an aragonite partition coefficient > 1 (Gaetani and Cohen, 2006). When calcification proceeds from a closed fluid

reservoir, elements with $D_X \ll 1$ are initially excluded from the lattice and become enriched in the fluid. As more of the fluid is used up, these elements are incorporated in greater proportions into the solid phase. Conversely, elements with $D_X > 1$ are initially enriched in the solid phase, but as more of the fluid is used they become progressively depleted. The extent to which Rayleigh fractionation occurs depends on how much of the fluid reservoir is used before it is refreshed. In the context of coral calcification, this depends on the balance between coral growth rate and the rate of flushing of the calcifying fluid (i.e. kz above). This balance can be conceptualised as the precipitation efficiency of coral calcification (e.g. Gaetani and Cohen, 2006).

Variations in coral growth rate and and/or timescales of seawater flushing (i.e. kz) can therefore cause correlated variations in Rayleigh-sensitive elements, which would lead to correlations consistent with those observed between all aspects of stylasterid geochemistry considered here (Figure 9). For example, stylasterid Li/Ca and Mg/Ca are strongly, positively correlated with one another, and are both negatively correlated with $\delta^{11}B$ (Figure 9; Figure 12). This is consistent (for instance) with increased Mg and Li incorporation during times of increased precipitation efficiency. If this were achieved by slower replenishment of the stylasterid calcifying fluid (i.e. lower kz), lower $\delta^{11}B$ would result from the corresponding increase in D_B/kz. More broadly, a recent study showed that Rayleigh fractionation processes can explain the positive correlation between Mg/Ca and Li/Ca, and the negative correlation between Mg/Ca and Sr/Ca, in the aragonitic coral *D. dianthus* (Chen et al., 2023). Our results are consistent with this framework, providing further indication that Rayleigh fractionation processes impact aragonitic stylasterid geochemistry.

Finally, the significant, positive correlations we observe between stylasterid subsample Mg/Ca and B/Ca (whether considering the difference between bulk sample replicates, or the difference between bulk samples and apical tip subsamples) is worthy of additional discussion (Figure 7; Figure 8). This correlation is strikingly similar to that recently observed in the scleractinian coral *D. dianthus* (Figure 7; Figure 8; Chen et al., 2023). These authors use a calcification model to argue that this correlation cannot be explained by boric acid diffusion, and instead suggest that Mg and B incorporation share sensitivity to the degree of alkalinity pumping employed during coral calcification (Chen et al., 2023). At higher rates of alkalinity pumping (which in this model is assumed to be dominated by H^+ removal, rather than Ca^{2+} influx), Mg and B incorporation increase, with the observed relationship best explained when B incorporation is dominated by $B(OH)_4^-$ substituting for CO_3^{2-}, following the rule $[B(OH)_4^-]/[CO_3^{2-}]^{0.5}$ (Chen et al., 2023). Absent the application of a similar calcification model here, it remains uncertain whether this mechanism is responsible for the correlation observed between B/Ca and Mg/Ca in aragonitic stylasterids. However, should this process impact on aragonitic stylasterid geochemistry, it would not only provide further support for boron incorporation into stylasterid aragonite being dominated by $B(OH)_4^-$ (see section 4.1.1), it would also suggest that aragonitic stylasterids employ some

form of alkalinity pumping (i.e. pH upregulation), in turn providing a means by which boric acid diffusion could occur (Chen et al., 2023).
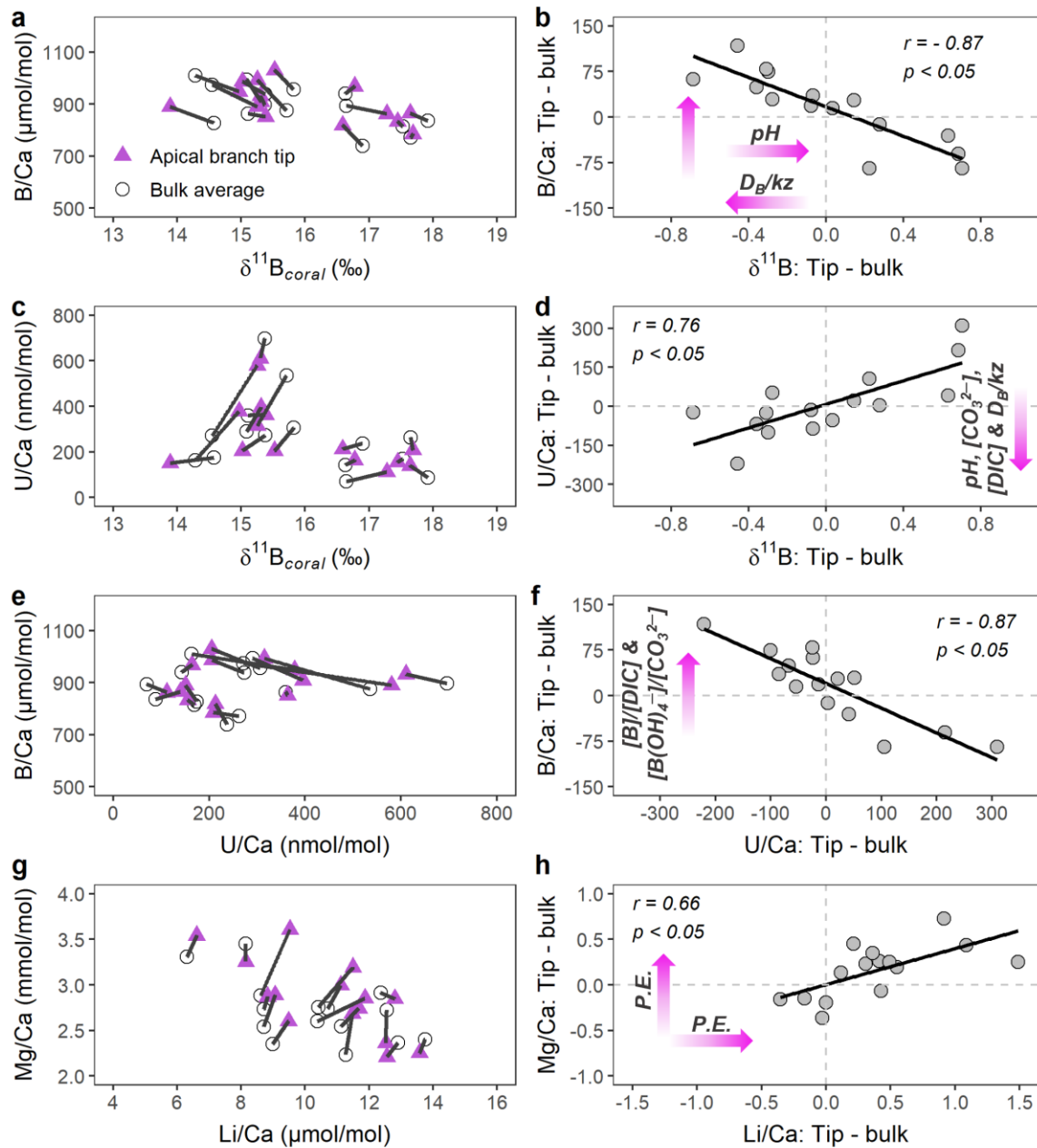
Figure 12. a, c, e and g: comparing stylasterid apical tip (purple triangles) and bulk average (open circles) geochemistry, solid lines join measurements from the same coral. b, d, f and h: correlations between differences in tip and bulk average geochemistry, where each point represents one line from panels a, c, e and g, respectively. Each plot is a graphical representation of the corresponding correlation in Figure 9, solid line in each panel shows linear least squares regression. Purple arrows show theoretical effects of processes

and parameters described in the main text. P.E. indicates precipitation efficiency. Data from this study, Stewart et al. (2020b) and Stewart et al. (2022).

Overall, the range of stylasterid geochemical parameters considered here thus provide evidence in support of the boric acid diffusion model of Gagnon et al. (2021). The role of boric acid diffusion in turn requires that stylasterids employ some amount of pH upregulation, necessary to permit boric acid diffusion into their calcifying fluid and thus leading to covariation between stylasterid δ^{11}B and B/Ca. The signature of this pH upregulation could be overprinted by high D_B/kz, either due to fast diffusion of boric acid or slow rates of calcifying fluid replenishment (Stewart et al., 2022). Further, the existence of a positive correlation between stylasterid Mg/Ca and B/Ca may provide evidence for pH upregulation in the stylasterid calcifying fluid (Chen et al., 2023). The magnitude of stylasterid calcifying fluid pH upregulation remains an outstanding question, although the absence of a correlation between stylasterid δ^{18}O and U/Ca suggests it is small compared with Scleractinia (Stewart et al., 2022).

4.3.2 Can variability in stylasterid geochemistry be explained without pH upregulation?

Despite the explanatory power of the boric acid diffusion model outlined above, there are mechanisms by which corals can calcify without the need for pH upregulation, with organic molecules known to play an important role in coral calcification (e.g. Drake et al., 2013; Mass et al., 2013; Von Euw et al., 2017; reviews in Tambutté et al., 2011; Falini et al., 2015). It is worth considering, therefore, whether the geochemical data presented here can rule out a model of stylasterid calcification which employs no pH upregulation at all.

Firstly, covariation in Rayleigh-sensitive elements including Mg/Ca, Li/Ca and Sr/Ca can be explained without the need for pH upregulation, as Rayleigh fractionation implies the sole requirement that stylasterid calcification proceeds from a closed fluid reservoir. Similarly, stylasterid δ^{11}B close to δ^{11}B$_{borate}$ could simply indicate that the pH of the stylasterid calcifying fluid is equivalent to that of seawater. However, the existence of covariation between stylasterid δ^{11}B and the full suite of element/Ca ratios is difficult to explain without pH upregulation. Variations in kz provide a convenient link in this regard between Rayleigh fractionation (impacting the incorporation of various elements) and the degree of boron isotopic equilibrium reached with external seawater, in the case that boric acid diffuses between seawater and the calcifying fluid. Implicit in this link is the elevation of stylasterid calcifying fluid pH, which is required to facilitate boric acid diffusion. It is difficult to conceive of other processes which could cause such covariation of boron isotopic and elemental compositions. One possibility is the influence of isotopic fractionation during boron attachment and detachment (Henehan et al., 2022). Variations in coral growth rate could conceivably provide a link between boron isotopic fractionation and trace element compositions, the latter either via associated kinetic effects or variations in precipitation efficiency (e.g. Gaetani and Cohen, 2006; Gagnon et al., 2007). However, the mechanisms by which these could

lead to such strong and consistent correlations is entirely unclear. Finally, the observed positive correlation between subsample B/Ca and Mg/Ca is conveniently explained by a model in which each ratio is controlled by alkalinity pumping (Chen et al., 2023). Whether this process affects aragonitic stylasterids remains uncertain, however this model is presently the best available explanation for this observation, in turn providing additional support for pH upregulation in aragonitic stylasterids.

Overall, the existence of strong correlations between stylasterid $\delta^{11}B$ and various element/Ca ratios is best explained by variations in $D_B/k\chi$. Indeed, the framework of Gagnon et al. (2021) provides a holistic explanation for a variety of trends in stylasterid skeletal geochemistry. This suggests that stylasterids likely employ an amount of calcifying fluid pH upregulation, although the magnitude of that upregulation remains an open question, as does the role of organic molecules in facilitating stylasterid calcification.
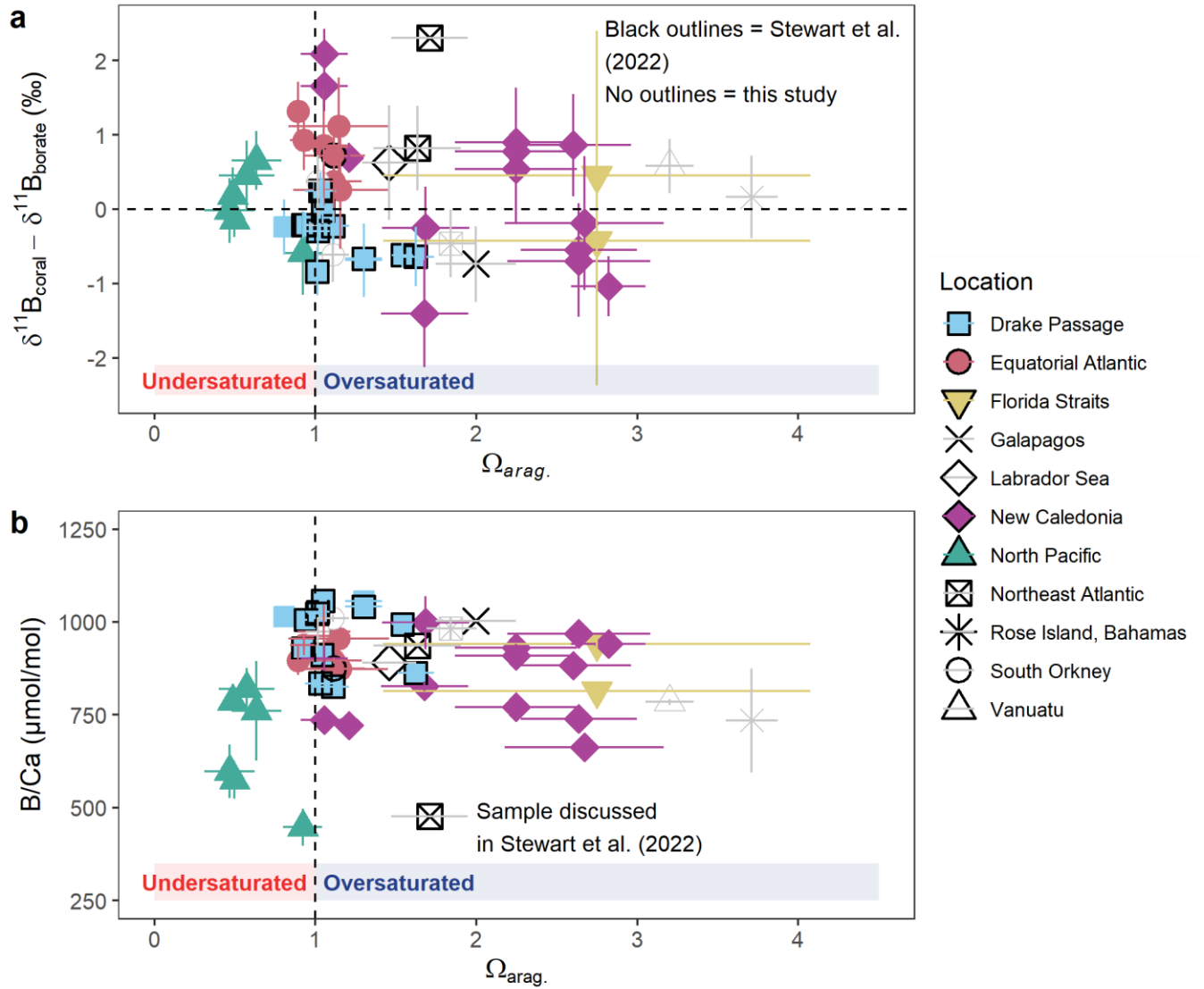
Figure 13. Aragonitic stylasterid a. $\delta^{11}B_{coral} - \delta^{11}B_{borate}$ (i.e. $\Delta\delta^{11}B$) and b. B/Ca (bottom) as a function of seawater aragonite saturation state ($\Omega_{arag.}$). Coral data include samples from Stewart et al. (2022) (distinguished with black outlines in both panels) and this study. $\delta^{11}B_{borate}$ and $\Omega_{arag.}$ were estimated as outlined in section 2.5. Vertical error bars are largest of analytical reproducibility or variability between sample replicates (2 σ). Horizontal error bars estimated using variability between 3 closest hydrographic stations (2 σ). Colours and symbols represent the broad regions from which samples were collected. Four samples measured here were not paired with ambient seawater carbonate parameters so are not included here (see section 2.5).

4.4 Wider implications of apical tip geochemistry

Consideration of the geochemistry of the growing tips of stylasterid branches (Figure 3) also has implications for models of their growth. Stylasterid apical tips have δ^{18}O and δ^{13}C further from equilibrium than bulk skeletal samples (Samperiz et al., 2020). This observation was interpreted as evidence that stylasterid branch tips are influenced by "vital effects" during calcification, and attributed to increased pH upregulation and/or kinetic isotope fractionation owing to faster rates of precipitation at branch tips (Samperiz et al., 2020). Further, the δ^{18}O and δ^{13}C composition of the core of stylasterid branches similarly has a more negative isotopic signature (i.e. further from equilibrium) than bulk skeletal samples (Wisshak et al., 2009; Samperiz et al., 2020). This could reflect the incorporation of the isotopic signature from apical tips into branch cores, as the coral grows.

The cause of intra-skeletal heterogeneity in stylasterid δ^{18}O and δ^{13}C remains enigmatic (Samperiz et al., 2020). Indeed, subsequent studies have sought to avoid sampling the apical tips of stylasterid branches to minimise the influence of these calcification-related effects, leading to a paucity of other geochemical data against which to assess models of stylasterid calcification (Stewart et al., 2020b; Stewart et al., 2022; chapter 3). The boron isotopic and elemental composition dataset presented here thus provides valuable constraint in this regard.

Firstly, the apical tips of 4 mixed mineralogy (dominantly aragonitic) stylasterids are significantly depleted in Sr/Ca and have heavier δ^{11}B, compared with bulk skeletal samples (Student's t-test; 95 % significance level; Table 2). Apical tips of these samples are also enriched in Li/Ca, Mg/Ca, U/Ca and Ba/Ca, and depleted in B/Ca and Li/Mg at slightly lower significance levels ($0.05 < p < 0.12$). These variations could result from calcification-related processes, as discussed below. However, the magnitude of enrichments in Mg/Ca, Li/Ca and δ^{11}B, in particular, suggests that these signals may at least have a partly mineralogical origin, and imply that high-Mg calcite may be concentrated in branch tips (Table 2). Unfortunately, the small number of samples, low statistical significance of observed differences and the absence of detailed intra-sample mineralogical analyses means this remains highly speculative.

Considering secondly aragonitic stylasterids – for which a significant number of samples were measured – I find that some of the geochemical parameters considered here show significant offsets between apical tips and bulk skeletal samples (Table 2; Figure 8). Li/Ca is elevated while Sr/Ca is depleted in apical branch tips. Mg/Ca is also elevated in branch tips, with lower statistical significance ($p = 0.06$). Importantly, apical tip and bulk skeletal δ^{11}B, B/Ca, and U/Ca are not significantly different, with U/Ca in particular showing a large degree of variability but no consistent offset (Table 2; Figure 8).

These data are consistent with the notion that stylasterid apical tips grow on average faster than the bulk stylasterid skeleton. Elevation of Li/Ca (and Mg/Ca) and depletion of Sr/Ca in branch tips is consistent with

more complete "precipitation efficiency" in a Rayleigh fractionation framework. This suggests either faster growth or less frequent replenishment of the stylasterid calcifying fluid in branch tips compared with the bulk skeleton. Of these two mechanisms by which to alter precipitation efficiency, faster growth rates seem more likely, especially when considering the more negative $\delta^{18}O$ and $\delta^{13}C$ values in branch tips, which may be partly explained by increased kinetic isotope fractionation (Samperiz et al., 2020).

Whether additional pH upregulation at branch tips is the mechanism by which faster growth is achieved is uncertain. The boron isotopic signature of any additional pH upregulation may be overprinted by boric acid diffusion, as outlined in section 4.3.1, which would be faster owing to the higher concentration gradient between the stylasterid calcifying fluid and seawater. However, apical tip B/Ca and U/Ca could conceivably record the signal of increased pH upregulation. Faster diffusion of boric acid should lead to elevated tip B/Ca, while higher pH could also lead to lower U/Ca, owing to the proposed sensitivity of U speciation and incorporation to pH (e.g. Inoue et al., 2011; Chen et al., 2021). While B/Ca is on average elevated in the tips of both aragonitic and high-Mg calcitic stylasterids, these elevations have low statistical significance ($p > 0.2$). Meanwhile, U/Ca values are highly variable, being both elevated and depleted in tips, compared with the bulk skeleton (Figure 8). The data presented here thus do not provide strong support for additional pH upregulation at stylasterid apical tips. While this may be the best explanation for apical tip depletions in $\delta^{18}O$ and $\delta^{13}C$ compared with the bulk skeleton (Samperiz et al., 2020), it is worth noting that faster growth rates may also be achieved by other means, for example by concentration of organic material at fast-growing sites, which has been observed for scleractinian Centres of Calcification (Benzerara et al., 2011; Von Euw et al., 2017).

Overall, while the mechanism remains uncertain, the data presented here support the notion that the apical tips of stylasterid branches grow faster than the rest of the skeleton, furthering evidence in favour of a two-stage model of stylasterid growth (Wisshak et al., 2009; Samperiz et al., 2020). This model postulates that stylasterids rapidly precipitate an initial skeletal framework, before branch thickening – perhaps accompanied by some skeletal dissolution – occurs more slowly. This multi-stage growth may explain why the highly correlated differences in the geochemistry of stylasterid apical tips and bulk skeletal samples are reduced in their significance and strength when considering the differences between bulk sample replicates (compare Figure 7 and Figure 9). If bulk samples are comprised dominantly of slowly precipitated, secondary material, any Rayleigh fractionation or kinetic effects would be significantly reduced.

More broadly, these data have implications for using stylasterids as palaeoceanographic archives. Branch tips are the youngest part of stylasterid skeletons, which form by vertical extension on decadal to centennial timescales (King et al., 2018; chapter 5). Previous work has advocated for sampling along the branch of a single stylasterid skeleton from base to tip, creating a record of ocean conditions which can span 10's to 100's of years

(King et al., 2018; explored further in chapter 5). The correlated variability between the geochemical indicators presented here, coupled with previous work (Samperiz et al., 2020), demonstrates that some palaeoceanographically-relevant ratios, including Sr/Ca, $\delta^{11}B$ and $\delta^{18}O$ (and Ba/Ca), are likely affected by calcification-related processes in stylasterid apical tips, which may complicate their application in palaeoceanographic reconstructions. Encouragingly, apical tip Ba/Ca and $\delta^{11}B$ are not significantly different from bulk samples, suggesting that the impacts of calcification-related processes are relatively minor in magnitude. Further, I recommend that when records are generated from live-collected stylasterids where the apical tip represents the actively-growing part of the skeleton, apical tip geochemistry should be compared with modern seawater conditions to assess proxy performance.

An exception to these potential complications is stylasterid Li/Mg ratios, which are a potentially powerful archive of seawater temperature (Stewart et al., 2020b). Differences between apical tip and bulk stylasterid Li/Mg ratios are not significantly correlated with Sr/Ca, U/Ca or Ba/Ca ratios (either with or without outliers) (Figure 9). Further, Li/Mg is not significantly elevated in apical tips, in contrast to Li/Ca and Mg/Ca as discussed above (Table 2; Figure 8). This supports the notion that taking the ratio of Li/Ca and Mg/Ca effectively cancels out some of the calcification-related effects on those ratios (e.g. Case et al., 2010; Montagna et al., 2014; Stewart et al., 2020b). Apical tip Li/Mg ratios may therefore be used as robust archives of seawater temperature.

Finally, a bulk sampling approach such as that employed here and in previous studies apparently homogenises many of the geochemical variations outlined above, reaffirming the finding that bulk stylasterid geochemistry has high potential as a palaeoceanographic tool (Samperiz et al., 2020; Stewart et al, 2020b; Stewart et al., 2022).

5   Conclusions

By significantly expanding the available dataset of stylasterid $\delta^{11}B$ measurements, this chapter provides important insights into boron partitioning into these marine carbonates, the utility of stylasterids as pH archives and stylasterid biomineralisation mechanisms.

$\delta^{11}B_{Sty.calc.}$ is 1 to 2 ‰ higher than $\delta^{11}B_{Sty.arag.}$, for a given $\delta^{11}B_{borate}$. This finding bears striking resemblance to comparisons of synthetic aragonite and calcite produced in laboratory settings. The differences in boron partitioning into stylasterid aragonite and high-Mg calcite are, therefore, most consistent with an abiogenic, mineralogical control on boron incorporation. While aragonitic stylasterids apparently incorporate boron from a $B(OH)_4^-$ source, high-Mg calcitic stylasterids may incorporate small amounts of $B(OH)_3$, or are affected by isotopic fractionation during $B(OH)_4^-$ incorporation. While the mechanistic origin of the offset between

$\delta^{11}B_{Sty.calc.}$ and $\delta^{11}B_{Sty.arag.}$ remains uncertain, our data provide an important demonstration of this effect in a natural setting, setting key limits on the conditions which could be targeted by future experimental work.

The similarity of $\delta^{11}B_{Sty.arag.}$ with $\delta^{11}B_{borate}$ raises the possibility that $\delta^{11}B_{Sty.arag.}$ records variations in seawater pH. I show that $\delta^{11}B_{Sty.arag.}$ can be used to reconstruct seawater pH to within a 95 % prediction interval of $\pm$ 0.2 pH units, representing a significant improvement on the commonly-used bulk-sampled scleractinian *D. dianthus*. I also report a robust empirical relationship between $\delta^{11}B_{Sty.calc.}$ and $\delta^{11}B_{borate}$, albeit across a smaller range of $\delta^{11}B_{borate}$. Future work could aim to calibrate this promising proxy across a wider range of pH conditions, which in turn may provide constraint on the mechanisms of B-incorporation into stylasterid high-Mg calcite.

More broadly, stylasterid geochemistry has now been shown to reliably record seawater temperature (Samperiz et al., 2020; Stewart et al., 2020b), $[Ba]_{SW}$ (chapter 3) and seawater radiocarbon content (King et al., 2018). The addition of a stylasterid $\delta^{11}B$-pH relationship contributes to a now wide and varied stylasterid geochemical toolbox, which is ready to be applied in the pursuit of palaeoceanographic reconstruction.

Finally, I confirm the finding that intra-sample covariation exists between stylasterid $\delta^{11}B$, B/Ca and U/Ca (Stewart et al., 2022), show that these trends are statistically significant, and show that they can be best explained by variations in D_B/k_χ. This model requires that stylasterids employ some amount of pH upregulation in their calcification fluid. The magnitude of this upregulation remains an open question, with important implications for the energetic burden of stylasterid calcification and thus their resilience in a changing ocean.

6 Supplementary information

6.1 Tropical, shallow water samples

Four samples measured here were taken from shallow, tropical reef/atoll environments, in which uncertainty on carbonate system parameters was considered too large to permit pairing these samples with the full range of hydrographic variables considered in this study (section 2.5). Despite this, it is still instructive to consider whether the $\delta^{11}B$ of these samples is consistent with the other stylasterid samples measured in this study.

All 4 samples are aragonitic in mineralogy, and from the genus *Stylaster*. To explore the context of their $\delta^{11}B$ signatures, I compare coral $\delta^{11}B$ with the possible ambient $\delta^{11}B_{borate}$ at these sites using all available hydrographic data from the GLODAP bottle database which fall within 10 ⁰N/S and 10 ⁰E/W of each sample, at depths of < 25 m (Supplementary figure 1; Supplementary figure 2; Lauvset et al., 2022). The distribution of this hydrographic data is shown in Supplementary figure 2, with the data used for each sample shown within the black square outlines. The GLODAP database was filtered for the above locational constraints, and only stations with the full suite of hydrographic variables required for $\delta^{11}B_{borate}$ calculation (temperature, salinity, dissolved phosphate and silicate, DIC and alkalinity) were used. $\delta^{11}B_{borate}$ was calculated as in section 2.6, with the average value for the appropriate area assigned to each coral sample.

As shown in Supplementary figure 1, 3 of the 4 coral $\delta^{11}B$ values are well within 2 standard deviations of the average $\delta^{11}B_{borate}$ calculated for that sample. Since all these samples are aragonitic, this suggests their $\delta^{11}B$ is in equilibrium with $\delta^{11}B_{borate}$, which is more broadly consistent with the wider range of aragonitic samples in this study. 1 sample (USNM85791) falls below the estimated average $\delta^{11}B_{borate}$. However, this is likely because this sample was collected from the Great Barrier Reef, from which there is very little proximal hydrographic data available for the calculation of $\delta^{11}B_{borate}$ (Supplementary figure 2). Additionally, measurements in the GLODAP database are more likely to be from open ocean sites than directly above carbonate reef environments. Thus, the implied variability in $\delta^{11}B_{borate}$ is likely a minimum estimate, and larger variations – particularly in waters directly overlying carbonate reef environments - are eminently plausible. Overall, these shallow water stylasterid samples provide compelling additional evidence that aragonitic stylasterids from the full range of ocean conditions have $\delta^{11}B$ in equilibrium with $\delta^{11}B_{borate}$.
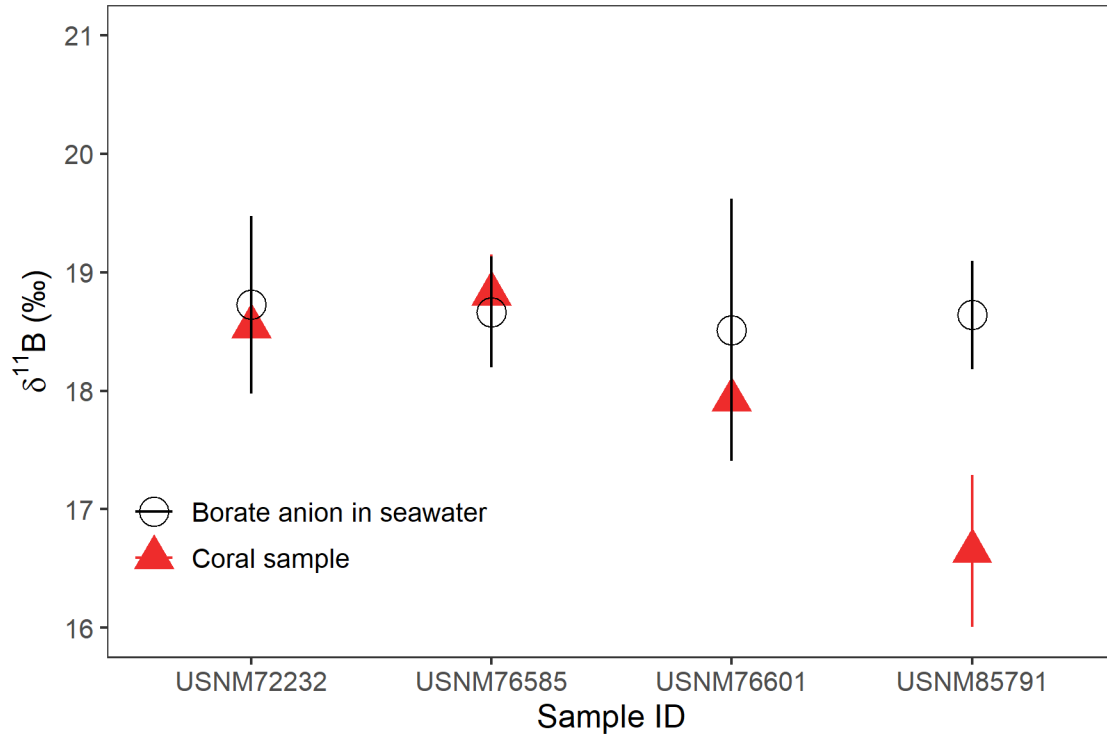
Supplementary figure 1. $\delta^{11}B$ of shallow water, tropical stylasterid samples (red triangles) compared with estimated $\delta^{11}B_{borate}$ calculated as in section 6.1 (black circles). Error bars on $\delta^{11}B_{borate}$ are calculated from the variability in all data from the appropriate sampled region ($\pm$ 2 σ). Error bars on coral $\delta^{11}B$ values are the largest of either analytical reproducibility or variability between sample replicates ($\pm$ 2 σ).
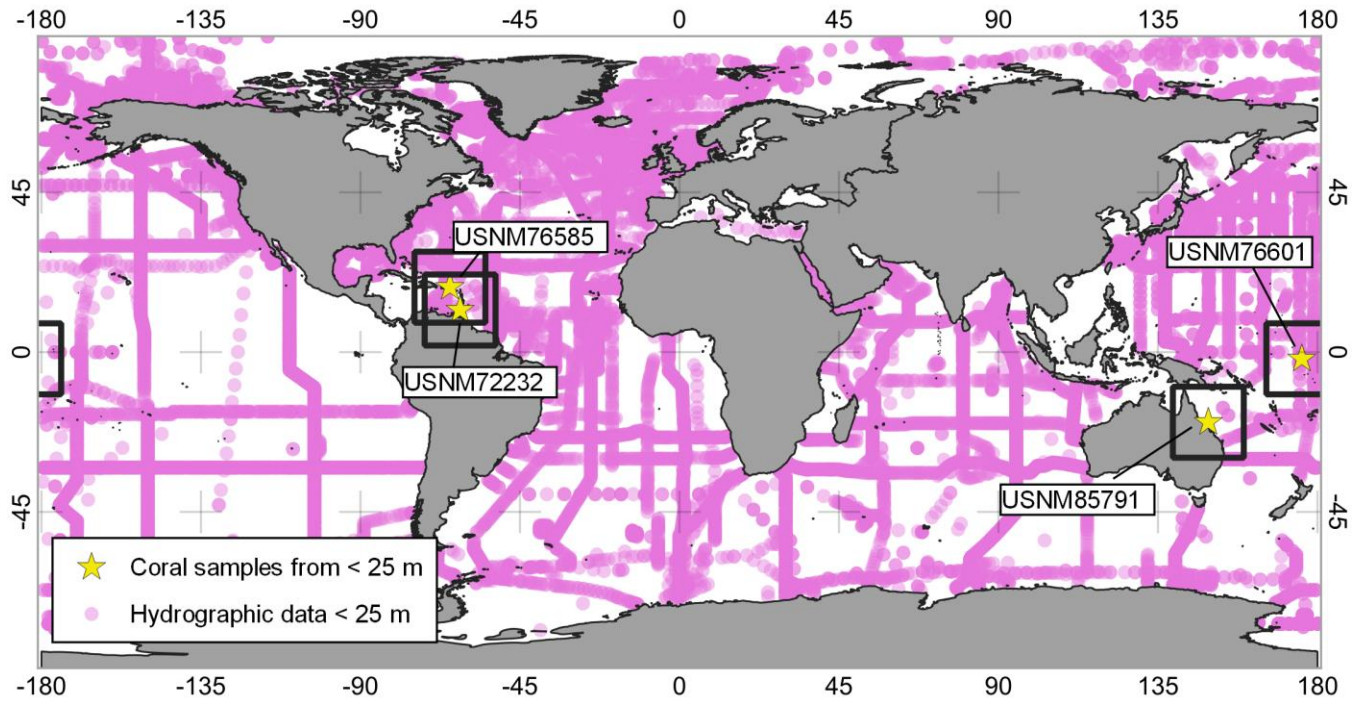
Supplementary figure 2. Map showing locations of coral samples and hydrographic data (from the GLODAP bottle database; Lauvset et al., 2022) used to estimate average $\delta^{11}B_{borate}$ for shallow, tropical waters. Hydrographic data used for each sample were taken from within the appropriate outlined region, note that the region for sample USNM76601 straddles 180 °E/W. Map produced using QGIS.

6.2   Effect of α_B

As outlined in section 2.6, the value of the fractionation factor between borate ion and boric acid (α_B) is uncertain. Generally, most recent studies (e.g. Rae et al., 2011; Anagnostou et al., 2012; McCulloch et al., 2012; Farmer et al., 2015; Stewart et al., 2022) have used a value of 1.0272, which was proposed by Klochko et al. (2006). However, Nir et al. (2015) suggested that a value of 1.026 may be more appropriate, which was later supported by the findings of Henehan et al. (2022).

The effect of the choice of α_B in this dataset is shown in Supplementary figure 3 below. While using a value of 1.0272 implies excellent agreement between aragonitic stylasterid $\delta^{11}B$ and $\delta^{11}B_{borate}$, using a value of 1.026 suggests that aragonitic stylasterids have a $\delta^{11}B$ signature which is systematically ~ 1 ‰ lighter than $\delta^{11}B_{borate}$.

It is difficult to conceive of mechanisms to explain why stylasterid $\delta^{11}B$ would be lighter than ambient $\delta^{11}B_{borate}$, and to do so would likely involve stylasterids inhabiting a low-pH microenvironment. For example, similar signatures have been observed for infaunal foraminifera, and attributed to sediment pore waters having a lower pH than the overlying seawater (Rae et al., 2011). Given that stylasterids live well clear of the sediment-water interface, these considerations should not be relevant to stylasterids. More broadly, it is unclear why stylasterids would inhabit low-pH environments and indeed what such an environment would constitute, especially given the global coverage of our sample set.

Overall, the excellent agreement between aragonitic stylasterid $\delta^{11}B$ and $\delta^{11}B_{borate}$ calculated using a fractionation factor of 1.0272 suggests that this fractionation factor is most appropriate for the sample set presented here, and this value is used throughout this chapter. However, the results of this α_B comparison exercise illustrate the critical importance of accurately constraining the value of α_B for the interpretation of boron isotopic data.
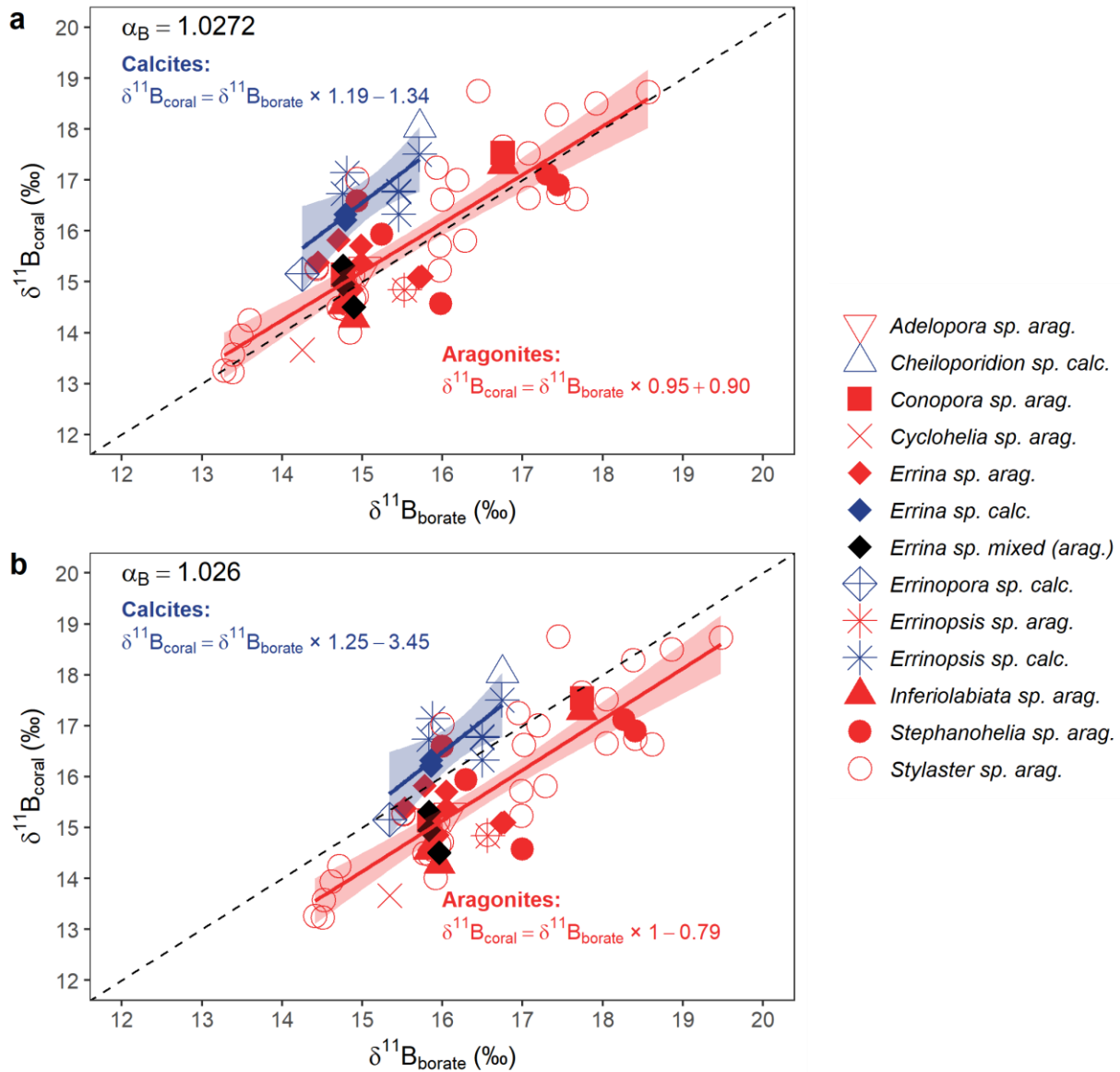
Supplementary figure 3. Effect of the choice of borate anion-boric acid fractionation factor (α_B) on the results of this study. Panel a shows $\delta^{11}B_{borate}$ values calculated using $\alpha_B = 1.0272$ (Klochko et al., 2006). Panel b shows calculations using $\alpha_B = 1.026$ (Nir et al., 2015). Annotations show the results of linear least squares regression analyses. Shading around lines shows 95 % confidence intervals. Note that error bars have been removed for clarity.

6.3   Correlations between bulk stylasterid B/Ca, U/Ca and δ¹¹B
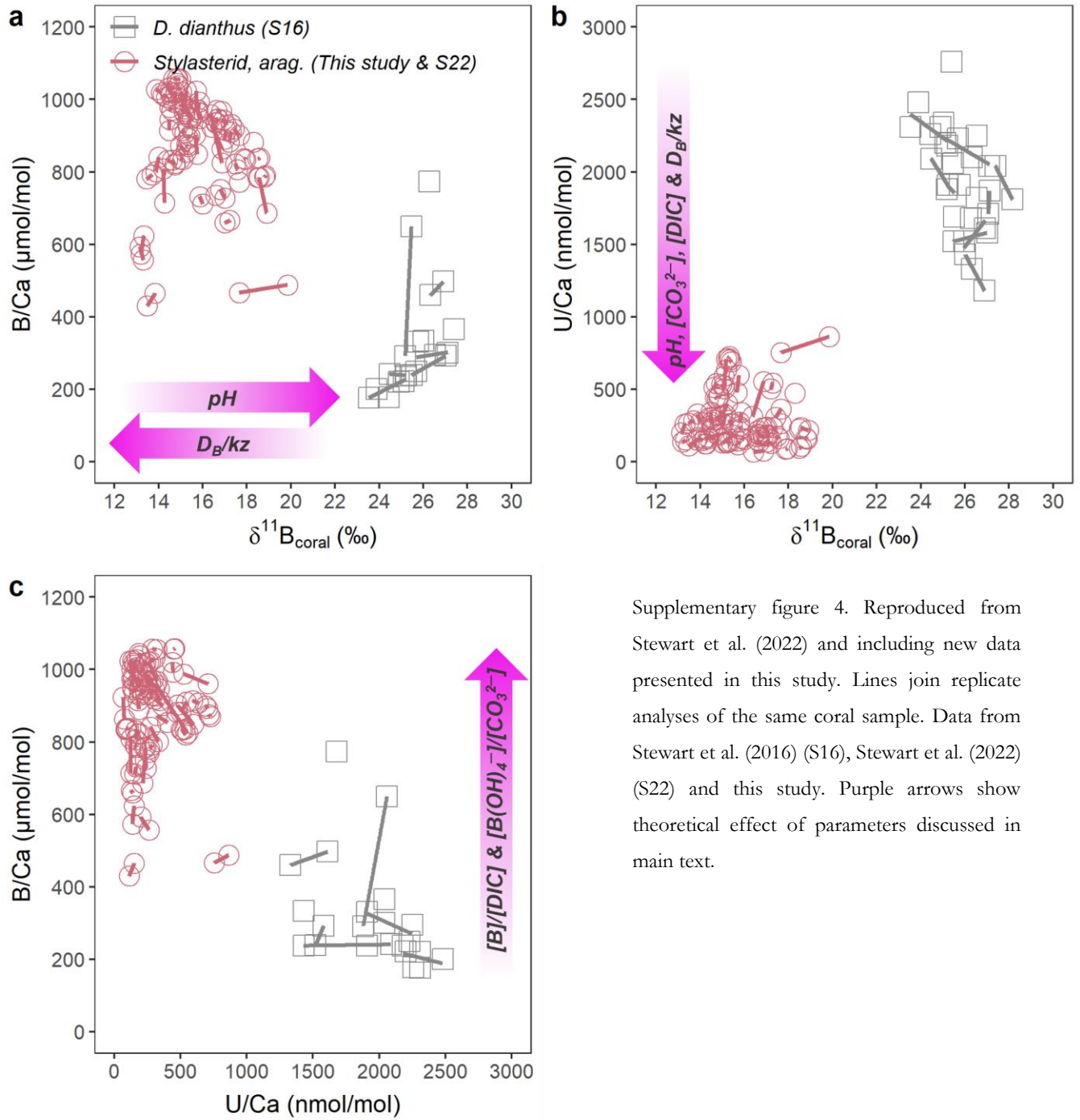
Supplementary figure 4. Reproduced from Stewart et al. (2022) and including new data presented in this study. Lines join replicate analyses of the same coral sample. Data from Stewart et al. (2016) (S16), Stewart et al. (2022) (S22) and this study. Purple arrows show theoretical effect of parameters discussed in main text.

6.4 Aragonitic stylasterid B/Ca as a function of seawater [DIC]
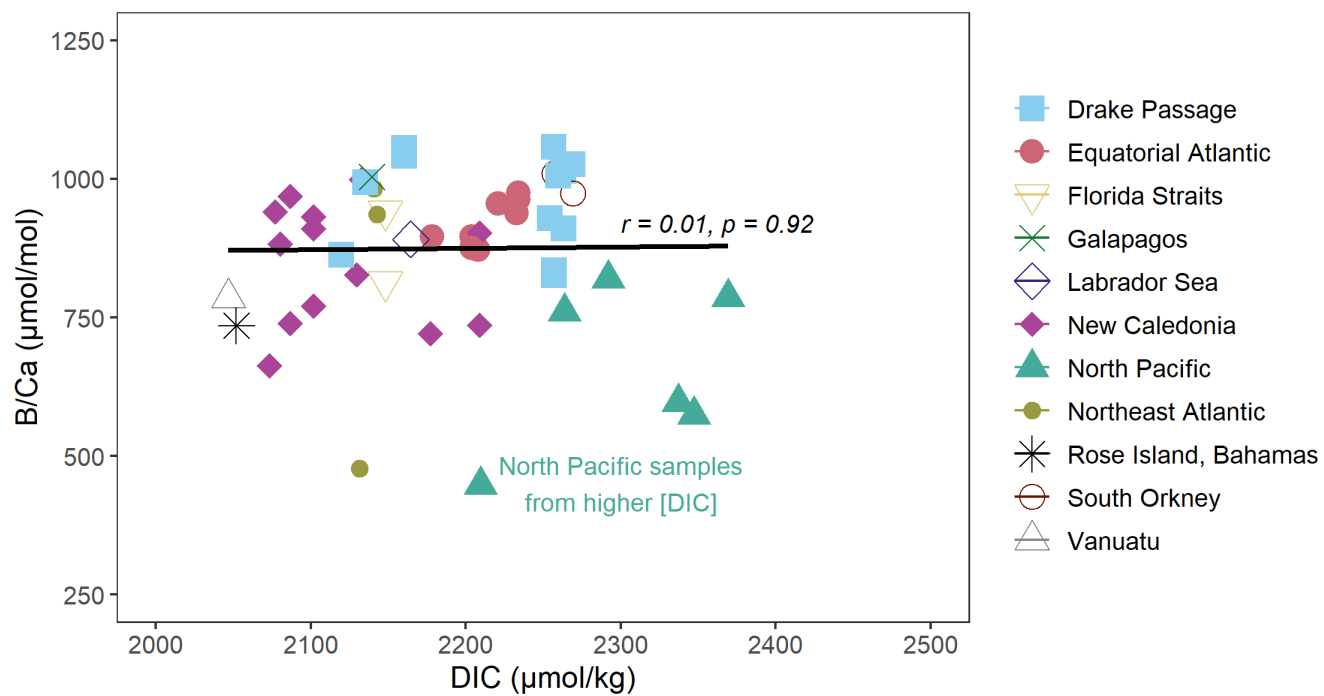
Supplementary figure 5. Aragonitic stylasterid B/Ca ratios plotted as a function of seawater [DIC]. Symbols and colours relate to different sample regions. Note North Pacific samples are from higher [DIC]. Linear fit through all data shown in solid line, with Pearson's correlation coefficient showing no significant overall trend.

7 Appendix: Summary of data generated in this thesis

Source	Sample ID	Taxon	Latitude (^{0}N)	Longitude (^{0}E)	Depth (m)	$\delta^{11}B_{borate}$ (‰)	Error $\delta^{11}B_{borate}$ (± 2 SD; ‰)*	$\delta^{11}B_{coral}$ (‰)	Error $\delta^{11}B_{coral}$ (± 2 SD; ‰)**
This study	NBP1103 DH87 St-2-01	*Errinopsis sp. calc.*	-60.57	-65.98	904	14.76	0.09	16.73	0.33
This study	NBP1103 TO104 St-4-1	*Errinopsis sp. calc.*	-59.72	-68.79	692	15.45	0.88	16.32	0.33
This study	NBP1103 DH07 St-01-01	*Errinopsis sp. calc.*	-54.51	-62.23	334	15.71	0.13	17.50	0.62
This study	NBP0805 TB04 Stps-A-01	*Errinopsis sp. arag.*	-54.73	-62.26	715	15.53	0.23	14.84	0.44
This study	CE14011-03-08	*Stylaster sp. arag.*	56.68	-13.90	517	16.28	0.31	15.82	0.33
This study	JC094-B0109-Hydls-001	*Stylaster sp. arag.*	9.24	-21.32	339	14.43	0.37	15.26	0.70
This study	JC094-B0480-Hydls(f)-001	*Stylaster sp. arag.*	9.24	-21.32	339	14.43	0.37	15.29	0.33
This study	NBP1103 TO104 St-9-6	*Errinopsis sp. calc.*	-59.72	-68.79	692	15.45	0.88	16.78	0.33
This study	NBP1103 DH22 Stc1-01	*Stylaster sp. arag.*	-54.84	-62.13	1879	14.81	0.17	14.57	0.33
This study	JC094-B1041-Hydlm-001	*Errina sp. arag.*	14.89	-48.16	743	14.45	0.24	15.38	0.33
This study	JC094-B0548-Hydls/m-001 to 019	*Errina sp. arag.*	14.88	-48.15	431	14.70	0.56	15.82	0.33
This study	JC094-B0546-Hydls/m-001 to 008	*Errina sp. arag.*	14.89	-48.15	776	14.99	0.45	15.37	0.33
This study	JC094-B0541-Hydlm-001	*Stylaster sp. arag.*	10.78	-44.60	2809	15.93	0.22	17.24	0.33

Source	Sample ID	Taxon	Latitude (°N)	Longitude (°E)	Depth (m)	$\delta^{11}B_{borate}$ (‰)	Error $\delta^{11}B_{borate}$ (± 2 SD; ‰)*	$\delta^{11}B_{coral}$ (‰)	Error $\delta^{11}B_{coral}$ (± 2 SD; ‰)**
This study	NBP1103 DH22 Stc1-01	*Errinopsis sp. calc.*	-54.84	-62.13	1879	14.81	0.17	17.14	0.38
This study	NBP1103-TB02-St-01	*Cheiloporidion sp. calc.*	-54.49	-62.19	316	15.71	0.26	18.03	0.39
This study	NBP1103 TO104 St-4-2W	*Errinopsis sp. calc.*	-59.72	-68.79	692	15.45	0.88	16.76	0.33
This study	USNM85791	*Stylaster sp. arag.*	-19.72	149.20	8	No data	No data	16.65	0.64
This study	USNM1248338	*Stylaster sp. arag.*	-15.07	167.15	209	17.92	0.16	18.50	0.33
This study	USNM76585	*Stylaster sp. arag.*	18.32	-64.75	24	No data	No data	18.82	0.33
This study	USNM72232	*Stylaster sp. arag.*	11.88	-61.89	13	No data	No data	18.54	0.33
This study	USNM76601	*Stylaster sp. arag.*	-1.87	175.57	3	No data	No data	17.92	0.33
This study	USNM93950	*Stylaster sp. arag.*	25.13	-77.18	91	18.57	0.27	18.73	0.48
This study	JC094-B0519-Hydlm-001 to 027	*Adelopora sp. arag.*	10.72	-44.42	739	15.03	0.72	15.29	0.33
This study	JR15005-Ev113-2429	*Inferiolabiata sp. arag.*	-60.76	-42.98	522	14.90	0.16	14.28	0.33
This study	JR15005-Ev39-784	*Inferiolabiata sp. arag.*	-62.28	-45.01	735	14.76	0.13	14.55	0.33
This study	JR15005-Ev40-831	*Conopora sp. arag.*	-62.28	-45.00	726	14.76	0.13	15.14	0.33
This study	Sty09	*Stylaster sp. arag.*	24.33	-81.68	192	17.07	1.92	17.53	0.33
This study	Sty10-sp-1	*Stylaster sp. arag.*	24.33	-81.68	192	17.07	1.92	16.65	0.33

Source	Sample ID	Taxon	Latitude (°N)	Longitude (°E)	Depth (m)	$\delta^{11}B_{borate}$ (‰)	Error $\delta^{11}B_{borate}$ (± 2 SD; ‰)*	$\delta^{11}B_{coral}$ (‰)	Error $\delta^{11}B_{coral}$ (± 2 SD; ‰)**
This study	MNHN-IK-2014-3455	*Stephanohelia sp. arag.*	-21.65	162.70	787	15.24	0.08	15.93	0.19
This study	MNHN-IK-2014-3554	*Stylaster sp. arag.*	-23.07	159.45	356	17.42	0.67	18.29	0.16
This study	MNHN-IK-2014-3610	*Conopora sp. arag.*	-23.03	159.47	365	16.75	0.72	17.53	0.33
This study	MNHN-IK-2014-3612	*Stylaster sp. arag.*	-23.03	159.47	365	16.75	0.72	17.66	0.16
This study	MNHN-IK-2014-3613	*Inferiolabiata sp. arag.*	-23.03	159.47	365	16.75	0.72	17.30	0.16
This study	MNHN-IK-2015-3483	*Stephanohelia sp. arag.*	-18.69	163.39	239	17.30	0.85	17.11	0.30
This study	MNHN-IK-2015-3444	*Stephanohelia sp. arag.*	-18.87	163.34	512	15.98	0.53	14.57	0.48
This study	MNHN-IK-2015-3557	*Stephanohelia sp. arag.*	-18.98	163.32	366	17.45	0.57	16.90	0.27
This study	MNHN-IK-2015-3597	*Stephanohelia sp. arag.*	-18.82	163.12	850	14.94	0.30	16.59	0.16
This study	MNHN-IK-2015-3593	*Stylaster sp. arag.*	-18.98	163.41	309	17.67	0.37	16.63	0.16
This study	MNHN-IK-2015-3595	*Stylaster sp. arag.*	-18.92	163.26	489	15.97	0.53	15.71	0.16
This study	MNHN-IK-2015-3596	*Stylaster sp. arag.*	-18.82	163.12	850	14.94	0.30	17.03	0.16
This study	MNHN-IK-2015-3430	*Stylaster sp. arag.*	-18.96	163.39	331	17.45	0.68	16.75	0.31
This study	NOAA_202001_2	*Stylaster sp. arag.*	54.60	-158.62	249	13.59	0.36	14.24	0.16
This study	NOAA_906022	*Errinopora sp. calc.*	51.49	-178.50	204	14.25	0.25	15.15	0.16

Source	Sample ID	Taxon	Latitude (°N)	Longitude (°E)	Depth (m)	$\delta^{11}B_{borate}$ (‰)	Error $\delta^{11}B_{borate}$ (± 2 SD; ‰)*	$\delta^{11}B_{coral}$ (‰)	Error $\delta^{11}B_{coral}$ (± 2 SD; ‰)**
This study	NOAA_906402	*Cyclohelia sp. arag.*	51.49	-178.50	204	14.25	0.25	13.66	0.50
This study	NOAA_202001_1	*Stylaster sp. arag.*	51.67	-178.84	667	13.38	0.09	13.23	0.21
This study	NOAA_202001_3	*Stylaster sp. arag.*	51.75	-178.33	804	13.39	0.15	13.58	0.34
This study	NOAA_202001_10	*Stylaster sp. arag.*	51.75	-178.92	370	13.49	0.44	13.94	0.17
This study	NOAA_202001_16	*Stylaster sp. arag.*	51.36	-178.50	590	13.28	0.40	13.26	0.16
Stewart et al. (2022)	NBP0805-TB01-EanC1	*Errina sp. arag.*	-54.47	-62.19	312	15.70	0.06	15.09	0.16
Stewart et al. (2022)	STY-1-Ean1	*Errina sp. arag.*	-55.05	-62.11	130	15.74	0.22	15.10	0.34
Stewart et al. (2022)	NBP1103-DH39-St-2-02-Ebo02	*Errina sp. arag.*	-60.17	-57.85	770	14.87	0.07	14.85	0.16
Stewart et al. (2022)	JC094-F0184-Hydlm-001-Eal001	*Errina sp. arag.*	14.89	-48.15	826	14.99	0.49	15.71	0.16
Stewart et al. (2022)	JR15005-113-2427-Sro2427	*Stylaster sp. arag.*	-60.76	-42.98	522	14.90	0.16	14.67	0.17
Stewart et al. (2022)	JR15005-114-2453-Sro2453	*Stylaster sp. arag.*	-60.75	-42.97	605	14.78	0.16	15.03	0.19
Stewart et al. (2022)	JR15005-40-835-Sro835	*Stylaster sp. arag.*	-62.28	-45.00	726	14.76	0.13	14.47	0.16

Source	Sample ID	Taxon	Latitude (°N)	Longitude (°E)	Depth (m)	$\delta^{11}B_{borate}$ (‰)	Error $\delta^{11}B_{borate}$ (± 2 SD; ‰)*	$\delta^{11}B_{coral}$ (‰)	Error $\delta^{11}B_{coral}$ (± 2 SD; ‰)**
Stewart et al. (2022)	NBP1103-DH54-Stp-1-Sde54	*Stylaster sp. arag.*	-60.25	-57.60	1262	14.93	0.05	14.72	0.16
Stewart et al. (2022)	NBP1103-DH37-Stp-1-1-Sde37	*Stylaster sp. arag.*	-60.17	-57.88	878	14.85	0.11	14.01	0.30
Stewart et al. (2022)	NBP1103-DH40-Stp-1-1-Sde40	*Stylaster sp. arag.*	-60.18	-57.84	806	14.88	0.06	15.13	0.16
Stewart et al. (2022)	NBP1103-DH88-Stp-1-1-Sde88	*Stylaster sp. arag.*	-60.56	-65.96	982	14.70	0.08	14.49	0.16
Stewart et al. (2022)	NBP0805-TB04-Dp-A-001-Sde001	*Stylaster sp. arag.*	-54.73	-62.26	715	15.53	0.23	14.86	0.16
Stewart et al. (2022)	DY081-52-339-26-1141-Sgr1141	*Stylaster sp. arag.*	59.93	-46.50	939	16.00	0.33	16.62	0.70
Stewart et al. (2022)	JC136-1901-sp-1Sbr1901	*Stylaster sp. arag.*	58.29	-13.64	820	16.18	0.55	17.00	0.16
Stewart et al. (2022)	JC136-3712-sp-1-Sib3712	*Stylaster sp. arag.*	59.10	-10.48	845	16.45	0.57	18.75	3.09
Stewart et al. (2022)	AL1508 02-013-01-D-Sma013	*Stylaster sp. arag.*	0.38	-90.44	63	15.96	0.48	15.23	0.16
Stewart et al. (2022)	JR15005-38-775-Egr775	*Errina sp. mixed (arag.)*	-62.28	-45.00	727	14.76	0.13	14.95	0.53

Source	Sample ID	Taxon	Latitude (^{0}N)	Longitude (^{0}E)	Depth (m)	$\delta^{11}B_{borate}$ (‰)	Error $\delta^{11}B_{borate}$ (± 2 SD; ‰)*	$\delta^{11}B_{coral}$ (‰)	Error $\delta^{11}B_{coral}$ (± 2 SD; ‰)**
Stewart et al. (2022)	JR15005-40-832-Egr832	*Errina sp. mixed (arag.)*	-62.28	-45.00	726	14.76	0.13	15.32	0.74
Stewart et al. (2022)	JR15005-113-2421-Egr2421	*Errina sp. mixed (arag.)*	-60.76	-42.98	522	14.90	0.16	14.50	0.16
Stewart et al. (2022)	JR15005-113-2426-Egr2426	*Errina sp. mixed (arag.)*	-60.76	-42.98	522	14.90	0.16	14.51	0.35
Stewart et al. (2022)	JR15005-43-844-Ela844	*Errina sp. calc.*	-62.33	-44.54	1000	14.79	0.08	16.21	0.16
Stewart et al. (2022)	JR15005-44-907-mn-1-Ela907	*Errina sp. calc.*	-62.33	-44.55	991	14.79	0.08	16.32	0.16

*Error represents variability between 3 nearest hydrographic stations (2 σ)

**Error represents larger of either analytical reproducibility or variation between sample replicates (2 σ)

Supplementary table 1. Summary of $\delta^{11}B_{coral}$ vs $\delta^{11}B_{borate}$ data used in this chapter.

Sample ID	Li/Ca (μmol/mol)		B/Ca (μmol/mol)		Mg/Ca (mmol/mol)		Sr/Ca (mmol/mol)		Ba/Ca (μmol/mol)		U/Ca (nmol/mol)		$\delta^{11}B$ (‰)	
	R1	R2	R1	R2	R1	R2	R1	R2	R1	R2	R1	R2	R1	R2
NBP1103 DH87 St-2-01	50.90	50.24	280.74	286.34	86.60	86.95	2.97	2.99	12.74	13.24	181.13	199.68	16.68	16.79
NBP1103 TO104 St-4-1	49.32	49.88	279.47	280.36	81.50	81.55	3.36	3.45	11.06	11.06	193.64	228.32	16.33	16.32
NBP1103 DH07 St-01-01	58.63	64.25	335.18	345.17	93.12	95.25	3.01	3.04	8.24	8.05	94.56	81.30	17.72	17.28
NBP0805 TB04 Stps-A-01	13.02	12.86	1056.12	1055.43	2.64	2.63	11.17	11.16	13.94	13.98	284.99	319.65	14.68	14.99
CE14011-03-08	12.19	11.82	971.61	992.76	3.07	2.94	10.39	10.58	7.82	8.04	241.25	225.51	15.79	15.84
JC094-B0109-Hydls-001	11.05	11.32	948.90	1000.00	3.11	3.12	10.30	10.39	7.31	7.46	183.46	129.63	15.51	15.01
JC094-B0480-Hydls(f)-001	10.85	10.78	951.46	974.45	3.13	3.08	10.41	10.39	7.23	7.28	138.23	130.88	15.37	15.20
NBP1103 TO104 St-9-6	47.55	47.60	292.07	288.59	84.54	84.47	2.77	2.74	11.56	11.70	106.39	99.64	16.71	16.86
NBP1103 DH22 Stc1-01	12.25	12.80	1011.46	1017.52	2.30	2.38	11.02	11.16	17.95	18.22	225.07	237.06	14.56	14.58

Sample ID	Li/Ca (μmol/mol)		B/Ca (μmol/mol)		Mg/Ca (mmol/mol)		Sr/Ca (mmol/mol)		Ba/Ca (μmol/mol)		U/Ca (nmol/mol)		$\delta^{11}B$ (‰)	
	R1	R2	R1	R2	R1	R2	R1	R2	R1	R2	R1	R2	R1	R2
JC094-B1041-Hydlm-001	10.66	10.75	947.07	928.17	2.77	2.70	10.50	10.52	7.80	7.64	260.13	285.41	15.44	15.31
JC094-B0548-Hydls/m-001 to 019	10.47	10.36	964.00	947.00	2.79	2.72	10.45	10.51	7.70	7.72	272.85	338.46	15.78	15.86
JC094-B0546-Hydls/m-001 to 008	11.11	11.15	893.23	899.54	2.50	2.59	10.56	10.57	9.75	9.74	703.58	689.17	15.34	15.40
JC094-B0541-Hydlm-001	10.03	10.02	910.21	882.51	1.93	1.91	10.32	10.33	10.82	10.78	541.99	503.78	17.28	17.21
NBP1103 DH22 Stc1-01	41.96	40.87	280.56	267.69	80.29	82.00	3.40	3.45	12.76	12.60	242.70	278.80	17.27	17.01
NBP1103-TB02-St-01	59.63	59.14	366.12	370.83	91.21	90.47	2.93	2.92	8.34	8.53	106.03	93.49	17.89	18.17
NBP1103 TO104 St-4-2W	40.20	39.47	317.09	314.79	85.97	85.93	2.84	2.91	11.22	11.14	139.18	156.32	16.86	16.67
USNM85791	7.98	8.31	863.46	923.75	3.35	3.54	9.95	9.79	5.01	5.02	74.16	65.66	16.87	16.42
USNM1248338	7.63		785.12		2.95		9.98		4.96		225.59		18.50	

Sample ID	Li/Ca (µmol/mol)		B/Ca (µmol/mol)		Mg/Ca (mmol/mol)		Sr/Ca (mmol/mol)		Ba/Ca (µmol/mol)		U/Ca (nmol/mol)		δ^{11}B (‰)	
	R1	R2	R1	R2	R1	R2	R1	R2	R1	R2	R1	R2	R1	R2
USNM76585	5.97	6.02	789.67	786.41	3.07	3.13	9.00	9.04	29.23	27.54	155.95	163.85	18.84	18.80
USNM72232	6.23	6.18	837.90	836.18	3.33	3.24	9.05	9.07	5.46	5.38	104.98	92.03	18.59	18.50
USNM76601	6.34	6.27	834.63	836.91	3.29	3.33	9.37	9.34	5.61	6.12	87.92	87.63	17.96	17.89
USNM93950	7.64	7.42	784.51	685.71	2.92	2.57	10.04	10.30	6.34	6.49	237.04	214.67	18.56	18.90
JC094-B0519-Hydlm-001 to 027	11.19	11.41	869.92	875.22	2.54	2.61	10.63	10.60	9.58	9.68	724.79	712.62	15.31	15.27
JR15005-Ev113-2429	12.90	12.93	1005.87	1012.97	2.37	2.36	10.94	10.98	18.47	18.65	170.05	156.16	14.37	14.20
JR15005-Ev39-784	13.73	13.78	969.76	978.44	2.39	2.42	11.15	11.06	19.55	19.04	290.18	251.08	14.59	14.51
JR15005-Ev40-831	13.60	13.49	987.65	960.27	2.47	2.48	10.97	11.18	18.93	19.90	525.51	708.21	15.09	15.18
Sty09	8.93	8.28	822.66	805.39	3.00	2.76	9.83	9.88	6.67	6.68	176.57	161.00	17.48	17.57
Sty10-sp-1	9.19	9.52	946.51	936.55	3.08	3.18	10.06	10.05	7.54	7.62	186.88	212.84	16.69	16.61
MNHN-IK-2014-3455	9.77	9.71	731.16	711.24	2.45	2.37	11.26	11.24	6.95	6.70	163.17	151.85	15.87	16.00
MNHN-IK-2014-3554	7.87		882.58		2.72		9.95		5.12		471.96		18.29	

Sample ID	Li/Ca (µmol/mol)		B/Ca (µmol/mol)		Mg/Ca (mmol/mol)		Sr/Ca (mmol/mol)		Ba/Ca (µmol/mol)		U/Ca (nmol/mol)		δ^{11}B (‰)	
	R1	R2	R1	R2	R1	R2	R1	R2	R1	R2	R1	R2	R1	R2
MNHN-IK-2014-3610	8.11	8.24	918.44	900.83	2.66	2.62	9.89	10.01	5.61	5.70	305.33	361.93	17.42	17.65
MNHN-IK-2014-3612	8.70		770.87		2.54		10.39		5.73		262.02		17.66	
MNHN-IK-2014-3613	9.41		931.50		3.05		9.94		6.07		235.70		17.30	
MNHN-IK-2015-3483	8.26	8.23	659.75	665.61	2.21	2.15	11.21	11.20	5.66	5.61	136.44	126.80	17.01	17.22
MNHN-IK-2015-3444	11.28	11.26	822.77	831.71	2.18	2.28	11.94	11.71	9.60	9.41	187.77	160.62	14.75	14.40
MNHN-IK-2015-3557	8.87	9.11	727.65	751.56	2.29	2.42	11.30	11.32	6.50	6.49	241.08	233.35	17.00	16.80
MNHN-IK-2015-3597	9.16		736.01		2.36		11.27		6.70		171.64		16.59	
MNHN-IK-2015-3593	8.62	8.80	934.96	946.19	2.70	2.77	10.36	10.28	5.76	5.72	149.13	136.12	16.59	16.67
MNHN-IK-2015-3595	10.29	10.14	1023.37	973.11	2.68	2.59	10.73	10.72	7.67	7.56	115.77	141.39	15.71	15.72

Sample ID	Li/Ca (μmol/mol)		B/Ca (μmol/mol)		Mg/Ca (mmol/mol)		Sr/Ca (mmol/mol)		Ba/Ca (μmol/mol)		U/Ca (nmol/mol)		δ^{11}B (‰)	
	R1	R2	R1	R2	R1	R2	R1	R2	R1	R2	R1	R2	R1	R2
MNHN-IK-2015-3596	8.68	8.64	913.64	890.53	2.80	2.77	10.19	10.22	5.62	5.63	176.79	184.43	17.06	16.99
MNHN-IK-2015-3430	9.34	9.26	970.20	967.24	2.94	2.93	10.20	10.18	5.91	5.90	188.24	177.75	16.64	16.86
NOAA_202001_2	13.65	13.51	808.39	713.46	2.82	2.76	10.37	10.25	9.83	9.49	122.70	121.30	14.22	14.27
NOAA_906022	83.42	84.69	313.80	309.30	119.43	118.40	3.29	3.30	7.80	7.98	25.34	48.29	15.13	15.18
NOAA_906402	13.51	14.14	465.01	430.08	3.08	3.20	9.55	9.53	10.42	10.49	148.65	110.53	13.84	13.48
NOAA_202001_1	12.53	12.33	592.23	556.75	2.17	2.15	10.47	10.62	16.51	16.96	197.99	260.90	13.16	13.30
NOAA_202001_3	13.27	13.25	780.15	791.98	2.50	2.51	10.70	10.74	16.84	17.04	264.73	284.33	13.46	13.70
NOAA_202001_10	12.59	12.93	800.35	840.18	2.51	2.63	10.95	10.94	13.33	13.45	329.39	273.01	13.88	14.00
NOAA_202001_16	14.25	14.26	572.17	622.97	2.77	2.79	10.14	10.33	12.37	12.79	135.76	148.12	13.21	13.32

Supplementary table 2. Geochemistry of sample replicates (R1 and R2) measured as part of this thesis. Ba/Ca and Sr/Ca ratios for some samples are presented in chapter 3. All element/Ca ratios corrected for analytical offsets (section 2.4). For relevant analytical errors, the reader is referred to section 2.4 and chapter 2 of this thesis. Blank cells indicate that no second replicate was measured. Sample Li/Mg ratios were calculated directly from Li/Ca and Mg/Ca values shown here.

Sample ID	Source of El/Ca ratios	Li/Ca (µmol/mol)	B/Ca (µmol/mol)	Mg/Ca (mmol/mol)	Sr/Ca (mmol/mol)	Ba/Ca (µmol/mol)	U/Ca (nmol/mol)	δ¹¹B (‰)
JC094-B1041-Hydlm-001	This study	11.12	987.04	3.00	10.26	7.58	205.44	15.02
JC094-B0548-Hydls/m-001 to 019	This study	11.50	1030.00	3.19	10.17	7.57	205.17	15.52
JC094-B0546-Hydls/m-001 to 008	This study	11.68	931.97	2.74	10.59	9.75	611.05	15.30
USNM85791	This study	8.15	862.74	3.26	10.00	5.15	111.62	17.28
USNM76601	This study	6.61	865.13	3.54	9.32	7.49	139.58	17.64
JR15005-Ev113-2429	This study	12.56	948.49	2.21	11.14	19.29	377.96	14.97
JR15005-Ev39-784	This study	13.59	890.06	2.25	11.19	19.84	580.40	15.25
Sty09	This study	9.52	832.67	3.61	9.50	8.99	155.22	17.45
MNHN-IK-2014-3612	This study	9.06	785.21	2.89	9.99	5.40	208.42	17.69
MNHN-IK-2015-3444	This study	11.48	889.68	2.68	11.63	9.43	150.35	13.89
MNHN-IK-2015-3557	This study	9.48	818.53	2.60	11.23	6.49	212.65	16.59
MNHN-IK-2015-3593	This study	8.83	968.53	2.87	10.18	5.66	163.87	16.78
NBP0805-TB01-EanC1	I.S. and J.S.*	12.53	909.29	2.36	11.09	11.87	395.59	15.31
STY-1-Ean1	I.S. and J.S.	12.80	851.18	2.85	10.54	10.59	363.22	15.38
JC094-F0184-Hydlm-001-Eal001	I.S. and J.S.	11.87	993.13	2.85	10.20	7.79	314.97	15.25
JR15005-38-775-Egr775	I.S. and J.S.	22.56	751.14	14.69	10.25	21.31	621.85	15.11
JR15005-40-832-Egr832	I.S. and J.S.	22.67	729.78	14.62	10.37	20.88	1041.60	15.64
JR15005-113-2421-Egr2421	I.S. and J.S.	16.87	826.92	7.82	11.03	21.51	558.95	15.01
JR15005-113-2426-Egr2426	I.S. and J.S.	24.40	755.40	15.07	9.91	19.97	346.07	14.75

*I.S. and J.S. refers to unpublished data generated by Ivo Strawson and Joseph Stewart as part of Strawson (2019), see section 2.2 for details.

Supplementary table 3. Apical tip geochemistry of stylasterid samples. All element/Ca ratios corrected for analytical offsets (section 2.4). For relevant analytical errors, the reader is referred to section 2.4 and chapter 2 of this thesis. Li/Mg ratios were calculated directly from Li/Ca and Mg/Ca values shown here.

Some element/Ca ratio data were generated as part of a previous study and are as-yet-unpublished (Strawson, 2019). All boron isotopic data for these samples were generated as part of this thesis.

Sample ID	Option	Cruise	Station	Year	Depth (m)	Temp. (°C)	Sal. (psu)	Phos. (μmol/ kg)	Sil. (μmol/ kg)	Alk. (μmol/ kg)	DIC (μmol/ kg)	$\Omega_{arag.}$	pH (total scale)	$\delta^{11}B_{borate}$ (‰)
NBP1103 DH87 St-2-01	1	740H20090203	24	2009	878	2.4	34.6	2.3	73.5	2343	2251	0.98	7.88	14.76
	2	33LG20060321	17	2006	999	1.5	34.7	2.3	75.5	2356	2262	0.96	7.89	14.81
	3	740H20090203	22	2009	876	2.3	34.6	2.4	77.6	2342	2253	0.96	7.87	14.72
NBP1103 TO104 St-4-1	1	NBP1103	CTD100	2011	651	2.7	34.4	1.8	63.8	2311	2181	1.29	8.00	15.45
	2	740H20090203	22	2009	751	2.4	34.6	2.4	73.9	2337	2251	0.97	7.87	14.67
	3	740H20090203	24	2009	627	2.5	34.4	2.3	62.0	2329	2238	1.02	7.89	14.73
NBP1103 DH07 St-01-01	1	NBP1103	TowCam5	2011	337	4.9	34.1	1.6	10.9	2281	2135	1.51	8.03	15.71
	2	740H20090203	72	2009	373	4.7	34.2	1.6	11.1	2285	2139	1.50	8.03	15.71
	3	740H20090203	78	2009	376	4.8	34.2	1.6	10.6	2286	2134	1.55	8.04	15.83
NBP0805 TB04 Stps-A-01	1	740H20090203	78	2009	735	4.1	34.2	1.8	18.1	2294	2160	1.30	7.99	15.53
	2	740H20090203	78	2009	684	4.2	34.2	1.8	17.3	2293	2156	1.34	8.00	15.59
	3	740H20090203	72	2009	747	3.8	34.2	1.9	21.5	2291	2166	1.23	7.97	15.37
CE14011-03-08	1	64PE20070830	46	2007	500	10.2	35.4	0.8	4.8	2326	2141	1.84	8.02	16.28
	2	74DI20120731	30	2012	504	9.8	35.4	0.7	4.0	2323	2150	1.73	7.99	16.06
	3	64PE20070830	43	2007	522	9.4	35.3	1.0	8.6	2326	2158	1.68	7.99	15.98

Sample ID	Option	Cruise	Station	Year	Depth (m)	Temp. (°C)	Sal. (psu)	Phos. (µmol/kg)	Sil. (µmol/kg)	Alk. (µmol/kg)	DIC (µmol/kg)	$\Omega_{arag.}$	pH (total scale)	$\delta^{11}B_{borate}$ (‰)
JC094-B0109-Hydls-001	1	JC094	ROV5	2013	333	10.2	35.1	1.6	14.9	2312	2234	1.05	7.74	14.43
	2	06M320150501	533	2015	322	10.8	35.1	2.0	13.6	2302	2246	0.92	7.66	14.11
	3	06M320150501	532	2015	347	10.6	35.1	2.0	13.8	2301	2245	0.91	7.67	14.11
JC094-B0480-Hydls(f)-001	1	JC094	ROV5	2013	333	10.2	35.1	1.6	14.9	2312	2234	1.05	7.74	14.43
	2	06M320150501	533	2015	322	10.8	35.1	2.0	13.6	2302	2246	0.92	7.66	14.11
	3	06M320150501	532	2015	347	10.6	35.1	2.0	13.8	2301	2245	0.91	7.67	14.11
NBP1103 TO104 St-9-6	1	NBP1103	CTD100	2011	651	2.7	34.4	1.8	63.8	2311	2181	1.29	8.00	15.45
	2	740H20090203	22	2009	751	2.4	34.6	2.4	73.9	2337	2251	0.97	7.87	14.67
	3	740H20090203	24	2009	627	2.5	34.4	2.3	62.0	2329	2238	1.02	7.89	14.73
NBP1103 DH22 Stc1-01	1	740H20090203	74	2009	1753	2.4	34.6	2.3	79.3	2354	2263	0.81	7.84	14.81
	2	740H20090203	72	2009	1750	2.4	34.6	2.4	80.4	2354	2261	0.82	7.84	14.84
	3	06AQ20080210	249	2008	1998	1.8	34.7	2.2	96.4	2362	2263	0.80	7.86	14.97
JC094-B1041-Hydlm-001	1	316N19821201	20	1982	717	6.6	34.8	2.2	23.6	2308	2233	0.93	7.77	14.45
	2	316N20030922	54	2003	744	6.2	34.7	2.2	24.5	2308	2221	0.99	7.81	14.64
	3	33AT20120419	34	2012	764	7.0	34.9	2.1	21.5	2308	2219	1.01	7.80	14.67
JC094-B0548-Hydls/m-001 to 019	1	316N19821201	19	1982	448	9.6	35.1	1.9	15.1	2316	2221	1.14	7.79	14.70
	2	316N19821201	18	1982	492	10.1	35.2	1.7	14.1	2313	2198	1.28	7.84	15.03
	3	316N19821201	18	1982	398	12.1	35.5	1.4	10.0	2323	2191	1.46	7.86	15.27

Sample ID	Option	Cruise	Station	Year	Depth (m)	Temp. (°C)	Sal. (psu)	Phos. (μmol/kg)	Sil. (μmol/kg)	Alk. (μmol/kg)	DIC (μmol/kg)	$\Omega_{arag.}$	pH (total scale)	$\delta^{11}B_{borate}$ (‰)
JC094-B0546-Hydls/m-001 to 008	1	JC094	CTD44	2013	804	6.1	34.8	2.2	24.4	2311	2204	1.12	7.87	14.99
	2	316N19821201	19	1982	791	5.9	34.7	2.2	26.1	2307	2226	0.95	7.80	14.56
	3	33AT20120419	31	2012	764	6.4	34.7	2.2	23.5	2308	2219	1.01	7.82	14.68
JC094-B0541-Hydlm-001	1	JC094	CTD32	2013	2805	2.8	34.9	1.3	30.1	2323	2178	0.89	7.94	15.93
	2	JC094	CTD39	2013	2800	2.8	34.9	1.4	32.4	2320	2173	0.90	7.95	15.98
	3	323019940104	218	1994	2766	2.9	34.9	1.4	30.3	2331	2175	0.95	7.97	16.14
NBP1103 DH22 Stc1-01	1	740H20090203	74	2009	1753	2.4	34.6	2.3	79.3	2354	2263	0.81	7.84	14.81
	2	740H20090203	72	2009	1750	2.4	34.6	2.4	80.4	2354	2261	0.82	7.84	14.84
	3	06AQ20080210	249	2008	1998	1.8	34.7	2.2	96.4	2362	2263	0.80	7.86	14.97
NBP1103-TB02-St-01	1	NBP1103	TowCam5	2011	337	4.9	34.1	1.6	9.4	2281	2135	1.51	8.03	15.71
	2	740H20090203	78	2009	376	4.8	34.2	1.6	10.6	2286	2134	1.55	8.04	15.83
	3	74JC20181103	8	2018	255	4.7	34.2	1.6	8.3	2274	2136	1.47	8.01	15.57
NBP1103 TO104 St-4-2W	1	NBP1103	CTD100	2011	651	2.7	34.4	1.8	63.8	2311	2181	1.29	8.00	15.45
	2	740H20090203	22	2009	751	2.4	34.6	2.4	73.9	2337	2251	0.97	7.87	14.67
	3	740H20090203	24	2009	627	2.5	34.4	2.3	62.0	2329	2238	1.02	7.89	14.73
USNM85791	N/A													
	N/A													
	N/A													

Sample ID	Option	Cruise	Station	Year	Depth (m)	Temp. (°C)	Sal. (psu)	Phos. (µmol/ kg)	Sil. (µmol/ kg)	Alk. (µmol/ kg)	DIC (µmol/ kg)	$\Omega_{arag.}$	pH (total scale)	$\delta^{11}B_{borate}$ (‰)
USNM1 248338	1*	35A319940923	1	1994	183	22.3	35.8	0.6	1.0	2348	2047	3.20	8.06	17.92
	2*	35A319940923	2	1994	179	23.1	35.9	0.6	1.0	2365	2052	3.34	8.06	18.08
	3*	35A319940923	1	1994	163	23.1	35.8	0.6	1.0	2355	2046	3.31	8.06	18.02
USNM7 6585	N/A													
	N/A													
	N/A													
USNM7 2232	N/A													
	N/A													
	N/A													
USNM7 6601	N/A													
	N/A													
	N/A													
USNM9 3950	1	33RO19980123	116	1998	91	22.8	36.7	0.0	0.9	2399	2052	3.71	8.11	18.57
	2	74DI20100106	17	2010	79	23.6	36.7	0.0	0.9	2391	2054	3.62	8.08	18.36
	3	29HE19920714	101	1992	101	23.9	36.7	0.0	0.7	2399	2046	3.79	8.10	18.62
JC094-B0519-Hydlm-001 to 027	1	JC094	ROV41	2013	737	6.3	34.7	2.2	24.4	2319	2208	1.16	7.88	15.03
	2	06M320150501	478	2015	742	6.4	34.7	2.2	23.5	2300	2222	0.94	7.78	14.50
	3	06M320150501	481	2015	746	6.4	34.7	2.3	24.7	2295	2227	0.88	7.75	14.35

Sample ID	Option	Cruise	Station	Year	Depth (m)	Temp. (°C)	Sal. (psu)	Phos. (μmol/kg)	Sil. (μmol/kg)	Alk. (μmol/kg)	DIC (μmol/kg)	$\Omega_{arag.}$	pH (total scale)	$\delta^{11}B_{borate}$ (‰)
JR15005-Ev113-2429	1	74JC20100319	930	2010	505	0.4	34.7	2.2	104.6	2358	2257	1.11	7.95	14.90
	2	74JC20100319	30	2010	601	0.4	34.7	2.2	108.4	2352	2260	1.02	7.92	14.75
	3	74JC20100319	26	2010	603	0.1	34.7	2.3	112.8	2351	2257	1.03	7.93	14.78
JR15005-Ev39-784	1	316N19831007	128	1984	662	0.3	34.7	2.3	119.0	2362	2269	1.02	7.92	14.76
	2	06AQ20060825	565	2006	800	0.4	34.7	2.3	119.0	2360	2263	1.01	7.92	14.85
	3	74JC20071231	12	2008	593	0.2	34.7	2.3	119.0	2359	2259	1.08	7.94	14.89
JR15005-Ev40-831	1	316N19831007	128	1984	662	0.3	34.7	2.3	119.0	2362	2269	1.02	7.92	14.76
	2	06AQ20060825	565	2006	800	0.4	34.7	2.3	119.0	2360	2263	1.01	7.92	14.85
	3	74JC20071231	12	2008	593	0.2	34.7	2.3	119.0	2359	2259	1.08	7.94	14.89
Sty09	1	33RO20170718	91	2017	200	20.7	36.8	0.3	2.0	2406	2148	2.75	7.99	17.07
	2	33RO20170718	93	2017	202	11.7	35.5	1.5	11.8	2333	2196	1.55	7.88	15.33
	3	33RO20170718	92	2017	172	20.2	36.7	0.4	2.3	2398	2152	2.64	7.97	16.90
Sty10-sp-1	1	33RO20170718	91	2017	200	20.7	36.8	0.3	2.0	2406	2148	2.75	7.99	17.07
	2	33RO20170718	93	2017	202	11.7	35.5	1.5	11.8	2333	2196	1.55	7.88	15.33
	3	33RO20170718	92	2017	172	20.2	36.7	0.4	2.3	2398	2152	2.64	7.97	16.90
MNHN-IK-2014-3455	1	318M19940327	267	1994	792	6.1	34.5	1.9	26.1	2298	2177	1.21	7.91	15.24
	2	318M19940327	263	1994	798	5.7	34.4	2.0	30.5	2302	2184	1.18	7.91	15.19
	3	49NZ20090410	221	2009	755	5.9	34.4	2.0	27.2	2300	2184	1.19	7.91	15.16

Sample ID	Option	Cruise	Station	Year	Depth (m)	Temp. (°C)	Sal. (psu)	Phos. (μmol/kg)	Sil. (μmol/kg)	Alk. (μmol/kg)	DIC (μmol/kg)	$\Omega_{arag.}$	pH (total scale)	$\delta^{11}B_{borate}$ (‰)
MNHN-IK-2014-3554	1	318M19940327	269	1994	353	15.8	35.4	0.7	2.5	2338	2080	2.60	8.08	17.42
	2	49NZ20090410	229	2009	367	15.6	35.4	0.7	2.8	2321	2102	2.25	8.01	16.75
	3	318M19940327	273	1994	342	16.6	35.4	0.7	2.4	2320	2080	2.46	8.04	17.11
MNHN-IK-2014-3610	1	49NZ20090410	229	2009	367	15.6	35.4	0.7	2.8	2321	2102	2.25	8.01	16.75
	2	49NZ20090410	226	2009	368	16.0	35.4	0.7	2.3	2322	2096	2.31	8.02	16.86
	3	318M19940327	269	1994	353	15.8	35.4	0.7	2.5	2338	2080	2.60	8.08	17.42
MNHN-IK-2014-3612	1	49NZ20090410	229	2009	367	15.6	35.4	0.7	2.8	2321	2102	2.25	8.01	16.75
	2	49NZ20090410	226	2009	368	16.0	35.4	0.7	2.3	2322	2096	2.31	8.02	16.86
	3	318M19940327	269	1994	353	15.8	35.4	0.7	2.5	2338	2080	2.60	8.08	17.42
MNHN-IK-2014-3613	1	49NZ20090410	229	2009	367	15.6	35.4	0.7	2.8	2321	2102	2.25	8.01	16.75
	2	49NZ20090410	226	2009	368	16.0	35.4	0.7	2.3	2322	2096	2.31	8.02	16.86
	3	318M19940327	269	1994	353	15.8	35.4	0.7	2.5	2338	2080	2.60	8.08	17.42
MNHN-IK-2015-3483	1	318M19940327	256	1994	241	18.2	35.6	0.5	1.9	2329	2073	2.67	8.04	17.30
	2	318M19940327	259	1994	247	18.5	35.6	0.5	1.9	2367	2063	3.14	8.12	18.10
	3	318M19940327	257	1994	250	18.6	35.6	0.5	1.6	2330	2065	2.76	8.05	17.46
MNHN-IK-2015-3444	1	318M19940327	259	1994	503	10.1	34.8	1.3	7.3	2296	2130	1.68	7.98	15.98
	2	318M19940327	257	1994	501	10.6	34.8	1.3	7.7	2299	2133	1.69	7.97	15.97
	3	35A320120628	3	2012	532	9.1	34.6	1.3	11.4	2299	2160	1.45	7.93	15.51

Sample ID	Option	Cruise	Station	Year	Depth (m)	Temp. (°C)	Sal. (psu)	Phos. (µmol/kg)	Sil. (µmol/kg)	Alk. (µmol/kg)	DIC (µmol/kg)	$\Omega_{arag.}$	pH (total scale)	$\delta^{11}B_{borate}$ (‰)
MNHN-IK-2015-3557	1	318M19940327	257	1994	346	16.0	35.4	0.7	2.9	2347	2087	2.64	8.08	17.45
	2	318M19940327	259	1994	346	15.7	35.4	0.7	3.0	2320	2087	2.38	8.04	17.00
	3	318M19940327	257	1994	396	14.5	35.2	0.9	3.9	2327	2100	2.29	8.04	16.92
MNHN-IK-2015-3597	1	318M19940327	256	1994	893	4.9	34.4	2.1	42.0	2311	2209	1.06	7.87	14.94
	2	318M19940327	259	1994	791	5.7	34.4	2.0	26.8	2296	2177	1.20	7.92	15.23
	3	318M19940327	259	1994	899	4.8	34.4	2.1	42.0	2312	2203	1.10	7.89	15.05
MNHN-IK-2015-3593	1	318M19940327	257	1994	300	17.2	35.5	0.6	2.1	2353	2077	2.82	8.09	17.67
	2	318M19940327	259	1994	298	17.3	35.5	0.6	2.3	2325	2072	2.61	8.05	17.30
	3	318M19940327	257	1994	346	16.0	35.4	0.7	2.9	2347	2087	2.64	8.08	17.45
MNHN-IK-2015-3595	1	318M19940327	257	1994	501	10.6	34.8	1.3	7.7	2299	2133	1.69	7.97	15.97
	2	318M19940327	259	1994	503	10.1	34.8	1.3	7.3	2296	2130	1.68	7.98	15.98
	3	35A320120628	3	2012	532	9.1	34.6	1.3	11.4	2299	2160	1.45	7.93	15.51
MNHN-IK-2015-3596	1	318M19940327	256	1994	893	4.9	34.4	2.1	42.0	2311	2209	1.06	7.87	14.94
	2	318M19940327	259	1994	791	5.7	34.4	2.0	26.8	2296	2177	1.20	7.92	15.23
	3	318M19940327	259	1994	899	4.8	34.4	2.1	42.0	2312	2203	1.10	7.89	15.05
MNHN-IK-2015-3430	1	318M19940327	257	1994	346	16.0	35.4	0.7	2.9	2347	2087	2.64	8.08	17.45
	2	318M19940327	259	1994	346	15.7	35.4	0.7	3.0	2320	2087	2.38	8.04	17.00
	3	318M19940327	257	1994	300	17.2	35.5	0.6	2.1	2353	2077	2.82	8.09	17.67

Sample ID	Option	Cruise	Station	Year	Depth (m)	Temp. (°C)	Sal. (psu)	Phos. (µmol/kg)	Sil. (µmol/kg)	Alk. (µmol/kg)	DIC (µmol/kg)	$\Omega_{arag.}$	pH (total scale)	$\delta^{11}B_{borate}$ (‰)
NOAA _202001 _2	1	49NZ20010723	98	2001	251	5.2	33.9	2.6	66.8	2276	2264	0.63	7.61	13.59
	2	49NZ20010723	94	2001	251	4.1	33.9	3.1	87.5	2302	2317	0.51	7.53	13.30
	3	325019930515	92	1993	254	3.9	33.9	3.1	92.5	2298	2319	0.49	7.51	13.25
NOAA _906022	1	49NZ20071008	19	2007	199	5.1	33.5	2.4	67.0	2271	2210	0.92	7.78	14.25
	2	49NZ20071008	20	2007	199	4.7	33.5	2.5	71.0	2276	2226	0.84	7.75	14.07
	3	318M19730822	218	1973	200	3.3	33.7	2.6	75.8	2264	2220	0.80	7.75	14.01
NOAA _906402	1	49NZ20071008	19	2007	199	5.1	33.5	2.4	67.0	2271	2210	0.92	7.78	14.25
	2	49NZ20071008	20	2007	199	4.7	33.5	2.5	71.0	2276	2226	0.84	7.75	14.07
	3	318M19730822	218	1973	200	3.3	33.7	2.6	75.8	2264	2220	0.80	7.75	14.01
NOAA _202001 _1	1	49NZ20071008	15	2007	663	3.5	34.1	3.1	119.8	2338	2347	0.50	7.54	13.38
	2	49NZ20071008	17	2007	625	3.5	34.1	3.1	120.1	2337	2343	0.52	7.55	13.41
	3	49NZ20071008	19	2007	694	3.7	34.2	3.2	114.7	2337	2352	0.47	7.51	13.32
NOAA _202001 _3	1	325019930705	17	1993	804	3.1	34.3	3.1	136.3	2360	2369	0.49	7.54	13.39
	2	49NZ20071008	13	2007	792	3.4	34.2	3.2	125.5	2346	2368	0.44	7.49	13.26
	3	49NZ20071008	17	2007	823	3.2	34.2	3.2	134.2	2357	2365	0.49	7.54	13.40
NOAA _202001 _10	1	49NZ20071008	15	2007	366	3.9	33.8	2.9	89.9	2295	2292	0.57	7.59	13.49
	2	325019930705	17	1993	354	3.5	34.0	3.0	105.5	2310	2317	0.54	7.56	13.39
	3	49NZ20071008	19	2007	397	4.6	33.7	2.7	79.0	2286	2256	0.70	7.67	13.81

Sample ID	Option	Cruise	Station	Year	Depth (m)	Temp. (°C)	Sal. (psu)	Phos. (µmol/ kg)	Sil. (µmol/ kg)	Alk. (µmol/ kg)	DIC (µmol/ kg)	$\Omega_{arag.}$	pH (total scale)	$\delta^{11}B_{borate}$ (‰)
NOAA _202001 _16	1	49NZ20071008	19	2007	596	4.0	34.1	3.1	101.2	2318	2337	0.47	7.50	13.28
	2	318M19730822	218	1973	596	3.3	34.2	3.0	127.0	2332	2316	0.61	7.63	13.65
	3	325019930705	17	1993	604	3.3	34.2	3.1	125.0	2344	2359	0.48	7.52	13.32

*Dissolved phosphate and silica estimated from cruise 31OC19870606, station 68, 203 m depth

Supplementary table 4. Summary of hydrographic data paired with corals measured in this thesis. All corals were paired with the nearest 3 hydrographic stations. Option 1 data were paired with the coral, and options 2 and 3 used to characterise variability. Data taken from bottles collected during co-located ROV or CTD deployments during cruises NBP1103 and JC094, or the GLODAP bottle database (Lauvset et al., 2022). All temperature, salinity, alkalinity and DIC measurements are unique. Phosphate and silicate data were not included for all bottles, and in these instances use measurements from the other bottles matched with that sample. $\Omega_{arag.}$, pH and $\delta^{11}B$ values calculated as outlined in section 2.6.

8   References

Al Mahrouqi, D., Vinogradov, J., Jackson, M.D., 2017. Zeta potential of artificial and natural calcite in aqueous solution. Advances in Colloid and Interface Science 240, 60–76. https://doi.org/10.1016/j.cis.2016.12.006

Al-Horani, F.A., Al-Moghrabi, S.M., de Beer, D., 2003. Microsensor study of photosynthesis and calcification in the scleractinian coral, *Galaxea fascicularis*: active internal carbon cycle. Journal of Experimental Marine Biology and Ecology 288, 1–15. https://doi.org/10.1016/S0022-0981(02)00578-6

Anagnostou, E., Huang, K.-F., You, C.-F., Sikes, E.L., Sherrell, R.M., 2012. Evaluation of boron isotope ratio as a pH proxy in the deep sea coral *Desmophyllum dianthus*: Evidence of physiological pH adjustment. Earth and Planetary Science Letters 349–350, 251–260. https://doi.org/10.1016/j.epsl.2012.07.006

Anagnostou, E., Sherrell, R.M., Gagnon, A., LaVigne, M., Field, M.P., McDonough, W.F., 2011. Seawater nutrient and carbonate ion concentrations recorded as P/Ca, Ba/Ca, and U/Ca in the deep-sea coral *Desmophyllum dianthus*. Geochimica et Cosmochimica Acta 75, 2529–2543. https://doi.org/10.1016/j.gca.2011.02.019

Balan, E., Pietrucci, F., Gervais, C., Blanchard, M., Schott, J., Gaillardet, J., 2016. First-principles study of boron speciation in calcite and aragonite. Geochimica et Cosmochimica Acta 193, 119–131. https://doi.org/10.1016/j.gca.2016.07.026

Barker, S., Greaves, M., Elderfield, H., 2003. A study of cleaning procedures used for foraminiferal Mg/Ca paleothermometry. Geochem. Geophys. Geosyst. 4 (9). https://doi.org/10.1029/2003GC000559

Benzerara, K., Menguy, N., Obst, M., Stolarski, J., Mazur, M., Tylisczak, T., Brown, G.E., Meibom, A., 2011. Study of the crystallographic architecture of corals at the nanoscale by scanning transmission X-ray microscopy and transmission electron microscopy. Ultramicroscopy 111, 1268–1275. https://doi.org/10.1016/j.ultramic.2011.03.023

Blamart, D., Rollion-Bard, C., Meibom, A., Cuif, J.-P., Juillet-Leclerc, A., Dauphin, Y., 2007. Correlation of boron isotopic composition with ultrastructure in the deep-sea coral *Lophelia pertusa*: Implications for biomineralization and paleo-pH. Geochem. Geophys. Geosyst. 8 (12). https://doi.org/10.1029/2007GC001686

Branson, O., 2018. Boron Incorporation into Marine $CaCO_3$, in: Marschall, H., Foster, G. (Eds.), Boron Isotopes, Advances in Isotope Geochemistry. Springer International Publishing, Cham, pp. 71–105. https://doi.org/10.1007/978-3-319-64666-4_4

Cairns, S.D., Macintyre, I.G., 1992. Phylogenetic Implications of Calcium Carbonate Mineralogy in the Stylasteridae (Cnidaria: Hydrozoa). PALAIOS 7, 96–107. https://doi.org/10.2307/3514799

Case, D.H., Robinson, L.F., Auro, M.E., Gagnon, A.C., 2010. Environmental and biological controls on Mg and Li in deep-sea scleractinian corals. Earth and Planetary Science Letters 300, 215–225. https://doi.org/10.1016/j.epsl.2010.09.029

Chen, S., Littley, E.F.M., Rae, J.W.B., Charles, C.D., Adkins, J.F., 2021. Uranium Distribution and Incorporation Mechanism in Deep-Sea Corals: Implications for Seawater [CO_3^{2-}] Proxies. Front. Earth Sci. 9, 641327. https://doi.org/10.3389/feart.2021.641327

Chen, S., Littley, E.F.M., Rae, J.W.B., Charles, C.D., Guan, Y., Adkins, J.F., 2023. Coherent tracer correlations in deep-sea corals and implications for biomineralization mechanisms underlying vital effects. Geochimica et Cosmochimica Acta 343, 304–322. https://doi.org/10.1016/j.gca.2022.12.006

Cheng, H., Adkins, J., Edwards, R.L., Boyle, E.A., 2000. U-Th dating of deep-sea corals. Geochimica et Cosmochimica Acta 64, 2401–2416. https://doi.org/10.1016/S0016-7037(99)00422-6

DeCarlo, T.M., Cohen, A.L., Wong, G.T.F., Shiah, F., Lentz, S.J., Davis, K.A., Shamberger, K.E.F., Lohmann, P., 2017. Community production modulates coral reef pH and the sensitivity of ecosystem calcification to ocean acidification. J. Geophys. Res. Oceans 122, 745–761. https://doi.org/10.1002/2016JC012326

Dickson, A.G., 1990. Standard potential of the reaction: AgCl(s) + 12H$_2$(g) = Ag(s) + HCl(aq), and and the standard acidity constant of the ion HSO$_4^-$ in synthetic sea water from 273.15 to 318.15 K. The Journal of Chemical Thermodynamics 22, 113–127. https://doi.org/10.1016/0021-9614(90)90074-Z

Dickson, A.G., Sabine, C.L., Christian, J.R., Bargeron, C.P., North Pacific Marine Science Organization (Eds.), 2007. Guide to best practices for ocean CO$_2$ measurements, PICES special publication. North Pacific Marine Science Organization, Sidney, BC.

Drake, J.L., Mass, T., Haramaty, L., Zelzion, E., Bhattacharya, D., Falkowski, P.G., 2013. Proteomic analysis of skeletal organic matrix from the stony coral *Stylophora pistillata*. Proc. Natl. Acad. Sci. U.S.A. 110, 3788–3793. https://doi.org/10.1073/pnas.1301419110

Falini, G., Fermani, S., Goffredo, S., 2015. Coral biomineralization: A focus on intra-skeletal organic matrix and calcification. Seminars in Cell & Developmental Biology 46, 17–26. https://doi.org/10.1016/j.semcdb.2015.09.005

Farmer, J.R., Branson, O., Uchikawa, J., Penman, D.E., Hönisch, B., Zeebe, R.E., 2019. Boric acid and borate incorporation in inorganic calcite inferred from B/Ca, boron isotopes and surface kinetic modeling. Geochimica et Cosmochimica Acta 244, 229–247. https://doi.org/10.1016/j.gca.2018.10.008

Farmer, J.R., Hönisch, B., Robinson, L.F., Hill, T.M., 2015. Effects of seawater-pH and biomineralization on the boron isotopic composition of deep-sea bamboo corals. Geochimica et Cosmochimica Acta 155, 86–106. https://doi.org/10.1016/j.gca.2015.01.018

Feely, R.A., Sabine, C.L., Lee, K., Berelson, W., Kleypas, J., Fabry, V.J., Millero, F.J., 2004. Impact of Anthropogenic CO_2 on the $CaCO_3$ System in the Oceans. Science 305, 362–366. https://doi.org/10.1126/science.1097329

Fietzke, J., Wall, M., 2022. Distinct fine-scale variations in calcification control revealed by high-resolution 2D boron laser images in the cold-water coral *Lophelia pertusa*. Sci. Adv. 8, eabj4172. https://doi.org/10.1126/sciadv.abj4172

Foster, G.L., 2008. Seawater pH, pCO_2 and $[CO_3^{2-}]$ variations in the Caribbean Sea over the last 130 kyr: A boron isotope and B/Ca study of planktic foraminifera. Earth and Planetary Science Letters 271, 254–266. https://doi.org/10.1016/j.epsl.2008.04.015

Foster, G.L., Pogge Von Strandmann, P.A.E., Rae, J.W.B., 2010. Boron and magnesium isotopic composition of seawater. Geochem. Geophys. Geosyst. 11 (8). https://doi.org/10.1029/2010GC003201

Foster, G.L., Rae, J.W.B., 2016. Reconstructing Ocean pH with Boron Isotopes in Foraminifera. Annu. Rev. Earth Planet. Sci. 44, 207–237. https://doi.org/10.1146/annurev-earth-060115-012226

Gabitov, R.I., Gaetani, G.A., Watson, E.B., Cohen, A.L., Ehrlich, H.L., 2008. Experimental determination of growth rate effect on U^{6+} and Mg^{2+} partitioning between aragonite and fluid at elevated U^{6+} concentration. Geochimica et Cosmochimica Acta 72, 4058–4068. https://doi.org/10.1016/j.gca.2008.05.047

Gaetani, G.A., Cohen, A.L., 2006. Element partitioning during precipitation of aragonite from seawater: A framework for understanding paleoproxies. Geochimica et Cosmochimica Acta 70, 4617–4634. https://doi.org/10.1016/j.gca.2006.07.008

Gagnon, A.C., Adkins, J.F., Fernandez, D.P., Robinson, L.F., 2007. Sr/Ca and Mg/Ca vital effects correlated with skeletal architecture in a scleractinian deep-sea coral and the role of Rayleigh fractionation. Earth and Planetary Science Letters 261, 280–295. https://doi.org/10.1016/j.epsl.2007.07.013

Gagnon, A.C., Gothmann, A.M., Branson, O., Rae, J.W.B., Stewart, J.A., 2021. Controls on boron isotopes in a cold-water coral and the cost of resilience to ocean acidification. Earth and Planetary Science Letters 554, 116662. https://doi.org/10.1016/j.epsl.2020.116662

Gattuso J., Epitalon J., Lavigne H., Orr J., 2022. seacarb: Seawater Carbonate Chemistry. R package version 3.3.1. https://CRAN.R-project.org/package=seacarb

Gothmann, A.M., Gagnon, A.C., 2021. The primary controls on U/Ca and minor element proxies in a cold-water coral cultured under decoupled carbonate chemistry conditions. Geochimica et Cosmochimica Acta 315, 38–60. https://doi.org/10.1016/j.gca.2021.09.020

Guinotte, J.M., Orr, J., Cairns, S., Freiwald, A., Morgan, L., George, R., 2006. Will human-induced changes in seawater chemistry alter the distribution of deep-sea scleractinian corals? Frontiers in Ecology and the Environment 4, 141–146. https://doi.org/10.1890/1540-9295(2006)004[0141:WHCISC]2.0.CO;2

Hathorne, E.C., Gagnon, A., Felis, T., Adkins, J., Asami, R., Boer, W., Caillon, N., Case, D., Cobb, K.M., Douville, E., deMenocal, P., Eisenhauer, A., Garbe-Schönberg, D., Geibert, W., Goldstein, S., Hughen, K., Inoue, M., Kawahata, H., Kölling, M., Cornec, F.L., Linsley, B.K., McGregor, H.V., Montagna, P., Nurhati, I.S., Quinn, T.M., Raddatz, J., Rebaubier, H., Robinson, L., Sadekov, A., Sherrell, R., Sinclair, D., Tudhope, A.W., Wei, G., Wong, H., Wu, H.C., You, C.-F., 2013. Interlaboratory study for coral Sr/Ca and other element/Ca ratio measurements. Geochem. Geophys. Geosyst. 14, 3730–3750. https://doi.org/10.1002/ggge.20230

Hemming, N.G., Hanson, G.N., 1992. Boron isotopic composition and concentration in modern marine carbonates. Geochimica et Cosmochimica Acta 56, 537–543. https://doi.org/10.1016/0016-7037(92)90151-8

Hemming, N.G., Reeder, R.J., Hanson, G.N., 1995. Mineral-fluid partitioning and isotopic fractionation of boron in synthetic calcium carbonate. Geochimica et Cosmochimica Acta 59, 371–379. https://doi.org/10.1016/0016-7037(95)00288-B

Hemsing, F., Hsieh, Y.-T., Bridgestock, L., Spooner, P.T., Robinson, L.F., Frank, N., Henderson, G.M., 2018. Barium isotopes in cold-water corals. Earth and Planetary Science Letters 491, 183–192. https://doi.org/10.1016/j.epsl.2018.03.040

Henehan, M.J., Klein Gebbinck, C.D., Wyman, J.V.B., Hain, M.P., Rae, J.W.B., Hönisch, B., Foster, G.L., Kim, S.-T., 2022. No ion is an island: Multiple ions influence boron incorporation into $CaCO_3$. Geochimica et Cosmochimica Acta 318, 510–530. https://doi.org/10.1016/j.gca.2021.12.011

Henehan, M.J., Rae, J.W.B., Foster, G.L., Erez, J., Prentice, K.C., Kucera, M., Bostock, H.C., Martínez-Botí, M.A., Milton, J.A., Wilson, P.A., Marshall, B.J., Elliott, T., 2013. Calibration of the boron isotope proxy in the planktonic foraminifera *Globigerinoides ruber* for use in palaeo-CO$_2$ reconstruction. Earth and Planetary Science Letters 364, 111–122. https://doi.org/10.1016/j.epsl.2012.12.029

Hönisch, B., Bickert, T., Hemming, N.G., 2008. Modern and Pleistocene boron isotope composition of the benthic foraminifer *Cibicidoides wuellerstorfi*. Earth and Planetary Science Letters 272, 309–318. https://doi.org/10.1016/j.epsl.2008.04.047

Hönisch, B., Hemming, N.G., Grottoli, A.G., Amat, A., Hanson, G.N., Bijma, J., 2004. Assessing scleractinian corals as recorders for paleo-pH: Empirical calibration and vital effects. Geochimica et Cosmochimica Acta 68, 3675–3685. https://doi.org/10.1016/j.gca.2004.03.002

Inoue, M., Suwa, R., Suzuki, A., Sakai, K., Kawahata, H., 2011. Effects of seawater pH on growth and skeletal U/Ca ratios of *Acropora digitifera* coral polyps. Geophys. Res. Lett. 38, L12809. https://doi.org/10.1029/2011GL047786

Jurikova, H., Liebetrau, V., Raddatz, J., Fietzke, J., Trotter, J., Rocholl, A., Krause, S., McCulloch, M., Rüggeberg, A., Eisenhauer, A., 2019. Boron isotope composition of the cold-water coral *Lophelia pertusa* along the Norwegian margin: Zooming into a potential pH-proxy by combining bulk and high-resolution approaches. Chemical Geology 513, 143–152. https://doi.org/10.1016/j.chemgeo.2019.01.005

Kershaw, J., Stewart, J.A., Strawson, I., De Carvalho Ferreira, M.L., Robinson, L.F., Hendry, K.R., Samperiz, A., Burke, A., Rae, J.W.B., Day, R.D., Etnoyer, P.J., Williams, B., Häussermann, V., 2023. Ba/Ca of stylasterid coral skeletons records dissolved seawater barium concentrations. Chemical Geology 622, 121355. https://doi.org/10.1016/j.chemgeo.2023.121355

King, T.M., Rosenheim, B.E., Post, A.L., Gabris, T., Burt, T., Domack, E.W., 2018. Large-Scale Intrusion of Circumpolar Deep Water on Antarctic Margin Recorded by Stylasterid Corals. Paleoceanography and Paleoclimatology 33, 1306–1321. https://doi.org/10.1029/2018PA003439

Kitano, Y., Okumura, M., Idogaki, M., 1978. Coprecipitation of borate-boron with calcium carbonate. Geochem. J. 12, 183–189. https://doi.org/10.2343/geochemj.12.183

Kline, D.I., Teneva, L., Hauri, C., Schneider, K., Miard, T., Chai, A., Marker, M., Dunbar, R., Caldeira, K., Lazar, B., Rivlin, T., Mitchell, B.G., Dove, S., Hoegh-Guldberg, O., 2015. Six Month In Situ High-Resolution Carbonate Chemistry and Temperature Study on a Coral Reef Flat Reveals Asynchronous pH and Temperature Anomalies. PLoS ONE 10, e0127648. https://doi.org/10.1371/journal.pone.0127648

Klochko, K., Kaufman, A.J., Yao, W., Byrne, R.H., Tossell, J.A., 2006. Experimental measurement of boron isotope fractionation in seawater. Earth and Planetary Science Letters 248, 276–285. https://doi.org/10.1016/j.epsl.2006.05.034

Lauvset, S.K., Carter, B.R., Pèrez, F.F., Jiang, L. -Q., Feely, R.A., Velo, A., Olsen, A., 2020. Processes Driving Global Interior Ocean pH Distribution. Global Biogeochem. Cycles 34. https://doi.org/10.1029/2019GB006229

Lauvset, S.K., Lange, N., Tanhua, T., Bittig, H.C., Olsen, A., Kozyr, A., Alin, S., Álvarez, M., Azetsu-Scott, K., Barbero, L., Becker, S., Brown, P.J., Carter, B.R., Da Cunha, L.C., Feely, R.A., Hoppema, M., Humphreys, M.P., Ishii, M., Jeansson, E., Jiang, L.-Q., Jones, S.D., Lo Monaco, C., Murata, A., Müller, J.D., Pérez, F.F., Pfeil, B., Schirnick, C., Steinfeldt, R., Suzuki, T., Tilbrook, B., Ulfsbo, A., Velo, A., Woosley, R.J., Key, R.M., 2022. GLODAPv2.2022: the latest version of the global interior ocean biogeochemical data product. Earth Syst. Sci. Data 14, 5543–5572. https://doi.org/10.5194/essd-14-5543-2022

Lauvset, S.K., Lange, N., Tanhua, T., Bittig, H.C., Olsen, A., Kozyr, A., Álvarez, M., Becker, S., Brown, P.J., Carter, B.R., Cotrim da Cunha, L., Feely, R.A., van Heuven, S., Hoppema, M., Ishii, M., Jeansson, E., Jutterström, S., Jones, S.D., Karlsen, M.K., Lo Monaco, C., Michaelis, P., Murata, A., Pérez, F.F., Pfeil, B., Schirnick, C., Steinfeldt, R., Suzuki, T., Tilbrook, B., Velo, A., Wanninkhof, R., Woosley, R.J., Key, R.M., 2021. An updated version of the global interior ocean biogeochemical data product, GLODAPv2.2021. Earth Syst. Sci. Data 13, 5565–5589. https://doi.org/10.5194/essd-13-5565-2021

Lee, K., Kim, T.-W., Byrne, R.H., Millero, F.J., Feely, R.A., Liu, Y.-M., 2010. The universal ratio of boron to chlorinity for the North Pacific and North Atlantic oceans. Geochimica et Cosmochimica Acta 74, 1801–1811. https://doi.org/10.1016/j.gca.2009.12.027

Lueker, T.J., Dickson, A.G., Keeling, C.D., 2000. Ocean pCO$_2$ calculated from dissolved inorganic carbon, alkalinity, and equations for K_1 and K_2: validation based on laboratory measurements of CO$_2$ in gas and seawater at equilibrium. Marine Chemistry 70, 105–119. https://doi.org/10.1016/S0304-4203(00)00022-0

Marchitto, T.M., Bryan, S.P., Doss, W., McCulloch, M.T., Montagna, P., 2018. A simple biomineralization model to explain Li, Mg, and Sr incorporation into aragonitic foraminifera and corals. Earth and Planetary Science Letters 481, 20–29. https://doi.org/10.1016/j.epsl.2017.10.022

Marriott, C.S., Henderson, G.M., Crompton, R., Staubwasser, M., Shaw, S., 2004. Effect of mineralogy, salinity, and temperature on Li/Ca and Li isotope composition of calcium carbonate. Chemical Geology 212, 5–15. https://doi.org/10.1016/j.chemgeo.2004.08.002

Martínez-Botí, M.A., Marino, G., Foster, G.L., Ziveri, P., Henehan, M.J., Rae, J.W.B., Mortyn, P.G., Vance, D., 2015. Boron isotope evidence for oceanic carbon dioxide leakage during the last deglaciation. Nature 518, 219–222. https://doi.org/10.1038/nature14155

Mass, T., Drake, J.L., Haramaty, L., Kim, J.D., Zelzion, E., Bhattacharya, D., Falkowski, P.G., 2013. Cloning and Characterization of Four Novel Coral Acid-Rich Proteins that Precipitate Carbonates In Vitro. Current Biology 23, 1126–1131. https://doi.org/10.1016/j.cub.2013.05.007

Mavromatis, V., Brazier, J.-M., Goetschl, K.E., 2022. Controls of temperature and mineral growth rate on Mg incorporation in aragonite. Geochimica et Cosmochimica Acta 317, 53–64. https://doi.org/10.1016/j.gca.2021.10.015

Mavromatis, V., Montouillout, V., Noireaux, J., Gaillardet, J., Schott, J., 2015. Characterization of boron incorporation and speciation in calcite and aragonite from co-precipitation experiments under controlled pH, temperature and precipitation rate. Geochimica et Cosmochimica Acta 150, 299–313. https://doi.org/10.1016/j.gca.2014.10.024

McClelland, H.L.O., Halevy, I., Wolf-Gladrow, D.A., Evans, D., Bradley, A.S., 2021. Statistical Uncertainty in Paleoclimate Proxy Reconstructions. Geophysical Research Letters 48. https://doi.org/10.1029/2021GL092773

McCulloch, M., Trotter, J., Montagna, P., Falter, J., Dunbar, R., Freiwald, A., Försterra, G., López Correa, M., Maier, C., Rüggeberg, A., Taviani, M., 2012. Resilience of cold-water scleractinian corals to ocean acidification: Boron isotopic systematics of pH and saturation state up-regulation. Geochimica et Cosmochimica Acta 87, 21–34. https://doi.org/10.1016/j.gca.2012.03.027

Montagna, P., McCulloch, M., Douville, E., López Correa, M., Trotter, J., Rodolfo-Metalpa, R., Dissard, D., Ferrier-Pagès, C., Frank, N., Freiwald, A., Goldstein, S., Mazzoli, C., Reynaud, S., Rüggeberg, A., Russo, S., Taviani, M., 2014. Li/Mg systematics in scleractinian corals: Calibration of the thermometer. Geochimica et Cosmochimica Acta 132, 288–310. https://doi.org/10.1016/j.gca.2014.02.005

Ni, Y., Foster, G.L., Bailey, T., Elliott, T., Schmidt, D.N., Pearson, P., Haley, B., Coath, C., 2007. A core top assessment of proxies for the ocean carbonate system in surface-dwelling foraminifers. Paleoceanography 22 (3). https://doi.org/10.1029/2006PA001337

Nir, O., Vengosh, A., Harkness, J.S., Dwyer, G.S., Lahav, O., 2015. Direct measurement of the boron isotope fractionation factor: Reducing the uncertainty in reconstructing ocean paleo-pH. Earth and Planetary Science Letters 414, 1–5. https://doi.org/10.1016/j.epsl.2015.01.006

Noireaux, J., Mavromatis, V., Gaillardet, J., Schott, J., Montouillout, V., Louvat, P., Rollion-Bard, C., Neuville, D.R., 2015. Crystallographic control on the boron isotope paleo-pH proxy. Earth and Planetary Science Letters 430, 398–407. https://doi.org/10.1016/j.epsl.2015.07.063

Papadimitriou, S., Loucaides, S., Rérolle, V.M.C., Kennedy, P., Achterberg, E.P., Dickson, A.G., Mowlem, M., Kennedy, H., 2018. The stoichiometric dissociation constants of carbonic acid in seawater brines from 298 to 267 K. Geochimica et Cosmochimica Acta 220, 55–70. https://doi.org/10.1016/j.gca.2017.09.037

Pelejero, C., Calvo, E., McCulloch, M.T., Marshall, J.F., Gagan, M.K., Lough, J.M., Opdyke, B.N., 2005. Preindustrial to Modern Interdecadal Variability in Coral Reef pH. Science 309, 2204–2207. https://doi.org/10.1126/science.1113692

Rae, J.W.B., Burke, A., Robinson, L.F., Adkins, J.F., Chen, T., Cole, C., Greenop, R., Li, T., Littley, E.F.M., Nita, D.C., Stewart, J.A., Taylor, B.J., 2018. CO_2 storage and release in the deep Southern Ocean on millennial to centennial timescales. Nature 562, 569–573. https://doi.org/10.1038/s41586-018-0614-0

Rae, J.W.B., Foster, G.L., Schmidt, D.N., Elliott, T., 2011. Boron isotopes and B/Ca in benthic foraminifera: Proxies for the deep ocean carbonate system. Earth and Planetary Science Letters 302, 403–413. https://doi.org/10.1016/j.epsl.2010.12.034

Rae, J.W.B., Sarnthein, M., Foster, G.L., Ridgwell, A., Grootes, P.M., Elliott, T., 2014. Deep water formation in the North Pacific and deglacial CO_2 rise. Paleoceanography 29, 645–667. https://doi.org/10.1002/2013PA002570

Ries, J.B., 2011. Skeletal mineralogy in a high-CO_2 world. Journal of Experimental Marine Biology and Ecology 403, 54–64. https://doi.org/10.1016/j.jembe.2011.04.006

Roberts, J.M., Cairns, S.D., 2014. Cold-water corals in a changing ocean. Current Opinion in Environmental Sustainability 7, 118–126. https://doi.org/10.1016/j.cosust.2014.01.004

Rollion-Bard, C., Blamart, D., Cuif, J.-P., Dauphin, Y., 2010. *In situ* measurements of oxygen isotopic composition in deep-sea coral, *Lophelia pertusa*: Re-examination of the current geochemical models of biomineralization. Geochimica et Cosmochimica Acta 74, 1338–1349. https://doi.org/10.1016/j.gca.2009.11.011

Rollion-Bard, C., Blamart, D., Trebosc, J., Tricot, G., Mussi, A., Cuif, J.-P., 2011. Boron isotopes as pH proxy: A new look at boron speciation in deep-sea corals using ^{11}B MAS NMR and EELS. Geochimica et Cosmochimica Acta 75, 1003–1012. https://doi.org/10.1016/j.gca.2010.11.023

Saldi, G.D., Noireaux, J., Louvat, P., Faure, L., Balan, E., Schott, J., Gaillardet, J., 2018. Boron isotopic fractionation during adsorption by calcite – Implication for the seawater pH proxy. Geochimica et Cosmochimica Acta 240, 255–273. https://doi.org/10.1016/j.gca.2018.08.025

Samperiz, A., Robinson, L.F., Stewart, J.A., Strawson, I., Leng, M.J., Rosenheim, B.E., Ciscato, E.R., Hendry, K.R., Santodomingo, N., 2020. Stylasterid corals: A new paleotemperature archive. Earth and Planetary Science Letters 545, 116407. https://doi.org/10.1016/j.epsl.2020.116407

Sanyal, A., Hemming, N.G., Broecker, W.S., Lea, D.W., Spero, H.J., Hanson, G.N., 1996. Oceanic *p*H control on the boron isotopic composition of foraminifera: Evidence from culture experiments. Paleoceanography 11, 513–517. https://doi.org/10.1029/96PA01858

Sanyal, A., Hemming, N.G., Hanson, G.N., Broecker, W.S., 1995. Evidence for a higher pH in the glacial ocean from boron isotopes in foraminifera. Nature 373, 234–236. https://doi.org/10.1038/373234a0

Schlitzer, R., 2023. Ocean Data View, https://odv.awi.de.

Sen, S., Stebbins, J.F., Hemming, N.G., Ghosh, B., 1994. Coordination environments of B impurities in calcite and aragonite polymorphs: A ^{11}B MAS NMR study. American Mineralogist 79, 819–825.

Shao, J., Stott, L.D., Gray, W.R., Greenop, R., Pecher, I., Neil, H.L., Coffin, R.B., Davy, B., Rae, J.W.B., 2019. Atmosphere-Ocean CO_2 Exchange Across the Last Deglaciation From the Boron Isotope Proxy. Paleoceanography and Paleoclimatology 34, 1650–1670. https://doi.org/10.1029/2018PA003498

Shuttleworth, R., Bostock, H.C., Chalk, T.B., Calvo, E., Jaccard, S.L., Pelejero, C., Martínez-García, A., Foster, G.L., 2021. Early deglacial CO_2 release from the Sub-Antarctic Atlantic and Pacific oceans. Earth and Planetary Science Letters 554, 116649. https://doi.org/10.1016/j.epsl.2020.116649

Sosdian, S.M., Greenop, R., Hain, M.P., Foster, G.L., Pearson, P.N., Lear, C.H., 2018. Constraining the evolution of Neogene ocean carbonate chemistry using the boron isotope pH proxy. Earth and Planetary Science Letters 498, 362–376. https://doi.org/10.1016/j.epsl.2018.06.017

Spivack, A.J., You, C.-F., Smith, H.J., 1993. Foraminiferal boron isotope ratios as a proxy for surface ocean pH over the past 21 Myr. Nature 363, 149–151. https://doi.org/10.1038/363149a0

Spooner, P.T., Robinson, L.F., Hemsing, F., Morris, P., Stewart, J.A., 2018. Extended calibration of cold-water coral Ba/Ca using multiple genera and co-located measurements of dissolved barium concentration. Chemical Geology 499, 100–110. https://doi.org/10.1016/j.chemgeo.2018.09.012

Stewart, J.A., Anagnostou, E., Foster, G.L., 2016. An improved boron isotope pH proxy calibration for the deep-sea coral *Desmophyllum dianthus* through sub-sampling of fibrous aragonite. Chemical Geology 447, 148–160. https://doi.org/10.1016/j.chemgeo.2016.10.029

Stewart, J.A., Christopher, S.J., Kucklick, J.R., Bordier, L., Chalk, T.B., Dapoigny, A., Douville, E., Foster, G.L., Gray, W.R., Greenop, R., Gutjahr, M., Hemsing, F., Henehan, M.J., Holdship, P., Hsieh, Y., Kolevica, A., Lin, Y., Mawbey, E.M., Rae, J.W.B., Robinson, L.F., Shuttleworth, R., You, C., Zhang, S., Day, R.D., 2020a. NIST RM 8301 Boron Isotopes in Marine Carbonate (Simulated Coral and Foraminifera Solutions): Inter-laboratory $\delta^{11}B$ and Trace Element Ratio Value Assignment. Geostand Geoanal Res 45, 77–96. https://doi.org/10.1111/ggr.12363

Stewart, J.A., Robinson, L.F., Day, R.D., Strawson, I., Burke, A., Rae, J.W.B., Spooner, P.T., Samperiz, A., Etnoyer, P.J., Williams, B., Paytan, A., Leng, M.J., Häussermann, V., Wickes, L.N., Bratt, R., Pryer, H., 2020b. Refining trace metal temperature proxies in cold-water scleractinian and stylasterid corals. Earth and Planetary Science Letters 545, 116412. https://doi.org/10.1016/j.epsl.2020.116412

Stewart, J.A., Strawson, I., Kershaw, J., Robinson, L.F., 2022. Stylasterid corals build aragonite skeletons in undersaturated water despite low pH at the site of calcification. Sci Rep 12, 13105. https://doi.org/10.1038/s41598-022-16787-y

Stolarski, J., Coronado, I., Murphy, J.G., Kitahara, M.V., Janiszewska, K., Mazur, M., Gothmann, A.M., Bouvier, A.-S., Marin-Carbonne, J., Taylor, M.L., Quattrini, A.M., McFadden, C.S., Higgins, J.A., Robinson, L.F., Meibom, A., 2021. A modern scleractinian coral with a two-component calcite–aragonite skeleton. Proc. Natl. Acad. Sci. U.S.A. 118, e2013316117. https://doi.org/10.1073/pnas.2013316117

Strawson, I., 2019. Paleoceanographic utility and calcification mechanisms of Stylasterid corals. University of Bristol, Master's thesis.

Sulpis, O., Lauvset, S.K., Hagens, M., 2020. Current estimates of K_1^* and K_2^* appear inconsistent with measured CO_2 system parameters in cold oceanic regions. Ocean Sci. 16, 847–862. https://doi.org/10.5194/os-16-847-2020

Tambutté, S., Holcomb, M., Ferrier-Pagès, C., Reynaud, S., Tambutté, É., Zoccola, D., Allemand, D., 2011. Coral biomineralization: From the gene to the environment. Journal of Experimental Marine Biology and Ecology 408, 58–78. https://doi.org/10.1016/j.jembe.2011.07.026

Therneau, T., 2018. deming: Deming, Theil-Sen, Passing-Bablock and Total Least Squares Regression. R package version 1.4. https://CRAN.R-project.org/package=deming

Trotter, J., Montagna, P., McCulloch, M., Silenzi, S., Reynaud, S., Mortimer, G., Martin, S., Ferrier-Pagès, C., Gattuso, J.-P., Rodolfo-Metalpa, R., 2011. Quantifying the pH 'vital effect' in the temperate zooxanthellate coral *Cladocora caespitosa*: Validation of the boron seawater pH proxy. Earth and Planetary Science Letters 303, 163–173. https://doi.org/10.1016/j.epsl.2011.01.030

Uchikawa, J., Penman, D.E., Zachos, J.C., Zeebe, R.E., 2015. Experimental evidence for kinetic effects on B/Ca in synthetic calcite: Implications for potential $B(OH)_4^-$ and $B(OH)_3$ incorporation. Geochimica et Cosmochimica Acta 150, 171–191. https://doi.org/10.1016/j.gca.2014.11.022

Van De Flierdt, T., Robinson, L.F., Adkins, J.F., 2010. Deep-sea coral aragonite as a recorder for the neodymium isotopic composition of seawater. Geochimica et Cosmochimica Acta 74, 6014–6032. https://doi.org/10.1016/j.gca.2010.08.001

Von Euw, S., Zhang, Q., Manichev, V., Murali, N., Gross, J., Feldman, L.C., Gustafsson, T., Flach, C., Mendelsohn, R., Falkowski, P.G., 2017. Biological control of aragonite formation in stony corals. Science 356, 933–938. https://doi.org/10.1126/science.aam6371

Wei, G., McCulloch, M.T., Mortimer, G., Deng, W., Xie, L., 2009. Evidence for ocean acidification in the Great Barrier Reef of Australia. Geochimica et Cosmochimica Acta 73, 2332–2346. https://doi.org/10.1016/j.gca.2009.02.009

Wisshak, M., López Correa, M., Zibrowius, H., Jakobsen, J., Freiwald, A., 2009. Skeletal reorganisation affects geochemical signals, exemplified in the stylasterid hydrocoral *Errina dabneyi* (Azores Archipelago). Mar. Ecol. Prog. Ser. 397, 197–208. https://doi.org/10.3354/meps08165

Woosley, R.J., 2021. Evaluation of the temperature dependence of dissociation constants for the marine carbon system using pH and certified reference materials. Marine Chemistry 229, 103914. https://doi.org/10.1016/j.marchem.2020.103914

Zeebe, R.E., Wolf-Gladrow, D.A., 2001. CO_2 in seawater: equilibrium, kinetics, isotopes, Elsevier oceanography series. Elsevier, Amsterdam ; New York.

Chapter 5: It's not U, it's Th(em): dating stylasterid corals is complicated

Contributions and acknowledgements

1.   Introduction

The global ocean plays a crucial role in regulating Earth's climate by distributing heat, carbon and nutrients around the planet, and exchanging these with the atmosphere (e.g. Macdonald and Wunsch, 1996; Ganachaud and Wunsch, 2000; Rahmstorf, 2002; Bigg et al., 2003; Reid et al., 2009; chapter 1). Changes in past ocean conditions provide valuable "natural experiments", which we can use to interrogate the links between Earth's ocean and climate. These can both inform our understanding of the processes linking these two components of the Earth system, as well as aiding prediction of future changes due to anthropogenic greenhouse gas emissions. The limited spatial and temporal extent of direct ocean observation hampers its use on timescales longer than a few decades. Studying longer-term processes, and setting modern trends in proper context, requires the use of indirect proxies (e.g. chapter 1).

The carbonate skeletons of organisms including foraminifera, molluscs and zooxanthellate and azooxanthellate corals have been developed as valuable archives of past changes in ocean conditions (e.g. reviews in Druffel, 1997; Kucera, 2007; Robinson et al., 2014; Immenhauser et al., 2016). Azooxanthellate corals in particular have emerged as a key tool for the reconstruction of subsurface ocean conditions on centennial to millennial timescales, owing in part to their occurrence in deep waters beyond the influence of daily or seasonal fluctuations in ocean conditions (e.g. Robinson et al., 2014; Rae et al., 2018; Chen et al., 2020; Stewart et al., 2021).

Much previous work developing azooxanthellate corals as an archive of past ocean conditions has focused on azooxanthellate scleractinian corals, as well as octocorals (e.g. chapter 1; review in Robinson et al., 2014). This thesis has instead focused on a comparatively poorly-studied group of azooxanthellate hydrozoan coral, the stylasterids, with an emphasis thus far on elucidating the relationships between the inorganic geochemistry of their skeletons and ambient seawater conditions. Stylasterid inorganic geochemistry correlates with numerous oceanographic parameters including temperature (Samperiz et al., 2020; Stewart et al., 2020b), barium seawater concentrations ([Ba]$_{SW}$; chapter 3), Δ^{14}C (King et al., 2018) and pH (chapter 4; Stewart et al., 2022). Importantly, stylasterid geochemistry appears to be, in many respects, a higher fidelity record of seawater conditions compared with scleractinian coral geochemistry, likely owing to the differing calcification mechanisms of these two coral groups (Samperiz et al., 2020; Stewart et al., 2020b; Stewart et al., 2022; chapter 3; chapter 4).

This suggests that stylasterids may be a powerful and under-explored archive of past ocean conditions, particularly when considering their widespread distribution in the modern ocean (e.g. Cairns, 1992; 2011). However, before stylasterids can be considered a go-to palaeoceanographic archive, it is necessary to develop tools by which we can accurately and precisely date their skeletons, so that geochemical proxy measurements can be placed into robust chronological frameworks (see chapter 1). Previous work has successfully developed these frameworks for anthozoan coral groups, broadly following two lines of inquiry. Firstly, the ages of individual, sub-fossil (i.e. dead on collection) corals can be constrained, and

multiple corals of differing ages used to build up a record of changes in ocean conditions through time (e.g. Chen et al., 2015; Rae et al., 2018; Stewart et al., 2021; Chen et al., 2023). Alternatively, many corals (including the stylasterids; King et al., 2018) grow on decadal to centennial timescales (e.g. Robinson et al., 2014). By subsampling individual specimens, one can constrain coral lifespans and growth chronologies, and intra-skeletal variations in geochemistry can be used to reconstruct changes in ocean conditions during the period of coral growth (e.g. Montero-Serrano et al., 2013; King et al., 2018).

In both of these pursuits (i.e. measuring individual dates on sub-fossil coral specimens and constructing coral growth chronologies), radiometric isotope systems have emerged as a key tool. Here, I explore the application of two of these systems – U-series and radiocarbon - to stylasterid coral skeletons.

1.1   U-series dating

U-series techniques have been widely employed to date sub-fossil azooxanthellate scleractinian corals (e.g. Cheng et al., 2000a; Burke and Robinson, 2012; Chen et al., 2015), and have also been used to generate growth chronologies of individual azooxanthellate scleractinian specimens (e.g. Montero-Serrano et al., 2013). This technique exploits the U-series decay chain, in which ^{238}U decays by alpha emission to ^{234}Th with a half-life of 4.51 Ga, before a series of rapid (assumed inconsequential owing to the short half-lives of the isotopes involved) β decay steps form ^{234}U, which subsequently decays to ^{230}Th by α emission with a half-life of $\sim$ 247 ka (Figure 1). ^{230}Th ultimately undergoes radioactive decay by α emission to form the rest of the U-series decay chain, which terminates with the stable isotope ^{206}Pb. By measuring the isotopic ratios of ^{238}U, ^{234}U and ^{230}Th, one can calculate a sample age, t, by the equation (following Edwards et al., 2003; Figure 1):

$$\left[\frac{^{230}Th}{^{238}U}\right] - 1 = -e^{-\lambda_{230}t} + \left(\frac{\delta^{234}U_m}{1000}\right)\left(\frac{\lambda_{230}}{\lambda_{230} - \lambda_{234}}\right)\left(1 - e^{-(\lambda_{230} - \lambda_{234})t}\right) \qquad (1)$$

where square brackets indicate activity ratios, λ values are isotopic decay constants and $\delta^{234}U_m$ is defined as the present-day deviation of the $^{234}U/^{238}U$ ratio from secular equilibrium, calculated as:

$$\delta^{234}U_m \ (\text{‰}) = \left(\left[\frac{^{234}U}{^{238}U}\right] - 1\right) \times 1000 \qquad (2)$$

The above equation assumes that all measured ^{230}Th is derived from the radioactive decay of U in the coral skeleton (herein referred to as the radiogenic component; solid black line in Figure 1). For zooxanthellate scleractinian corals living at shallow depths, the validity of this assumption derives from the observation that surface ocean $[^{230}Th]$ is extremely low, due primarily to the high particle reactivity of Th, which is readily removed from the surface ocean in a matter of years by scavenging onto sinking particles (e.g. Moore, 1981; Bacon and Anderson, 1982). However, this assumption cannot be made for deep-sea – or azooxanthellate – corals. Profiles of oceanic $[^{230}Th]$ reveal that its concentration increases with depth, owing to continuous exchange of ^{230}Th between the dissolved (seawater) and scavenged

phases (e.g. Moore, 1981; Bacon and Anderson, 1982). As a consequence, some [230]Th will be incorporated into the skeletons of azooxanthellate corals at the time of skeletal formation. Additionally, [230]Th can be added by accumulation of Th-bearing, non-carbonate phases in the time from growth to collection, which can include organic and Fe-Mn coatings, as well as silicate sediment phases (e.g. Cheng et al., 2000a). Although cleaning procedures have been designed to remove these phases, cleaning rarely removes all trace residual contaminant phases, and these represent a possible source of added [230]Th which also needs to be accounted for (e.g. Lomitschka and Mangini, 1999; Cheng et al., 2000a). The effects of initial/added [230]Th are illustrated in Figure 1.

To correct for this initial/added [230]Th component, a modified form of the age equation utilises the activity of the extremely long-lived isotope [232]Th measured in the sample (expressed as [$^{232}Th/^{238}U$]), coupled with an assumed initial [$^{230}Th/^{232}Th$]$_i$, to derive a correction term for initial/added sample [$^{230}Th/^{238}U$] (Edwards et al., 2003; black dashed line in Figure 1):

$$\left(\left[\frac{^{230}Th}{^{238}U} \right] - \left[\frac{^{232}Th}{^{238}U} \right] \left[\frac{^{230}Th}{^{232}Th} \right]_i \left(e^{-\lambda_{230}t} \right) \right) - 1$$

$$= -e^{-\lambda_{230}t} + \left(\frac{\delta^{234}U_m}{1000} \right) \left(\frac{\lambda_{230}}{\lambda_{230} - \lambda_{234}} \right) \left(1 - e^{-(\lambda_{230} - \lambda_{234})t} \right) \quad (3)$$

In the dating of azooxanthellate scleractinian corals, [$^{230}Th/^{232}Th$]$_i$ is normally estimated based on seawater or modern coral values (e.g. Burke and Robinson, 2012; Rae et al., 2018; Chen et al., 2020; de Carvalho Ferreira et al., 2022; Chen et al., 2023). These [$^{230}Th/^{232}Th$]$_i$ estimates are uncertain further back in time, and the general procedure has been to assign this value an error of up to ± 100 % (2 σ), and to propagate this through age calculations (e.g. Burke and Robinson, 2012; de Carvalho Ferreira et al., 2022; Chen et al., 2023). For a cleaned azooxanthellate scleractinian coral with high [U], the proportion of radiogenic [230]Th far outweighs that from initial/added sources. Thus, even with the uncertainty in the estimate of [$^{230}Th/^{232}Th$]$_i$, it is possible to date scleractinian corals to a precision suitable for studying centennial and millennial shifts in ocean conditions (e.g. Chen et al., 2015; Rae et al., 2018; Stewart et al., 2021; Chen et al., 2023).

Despite the success of applying U-series techniques to scleractinian corals, attempts to apply U-series techniques to other azooxanthellate coral groups have been less successful. For instance, low skeletal [U] and susceptibility to diagenetic alteration complicates U-series dating of calcitic octocorals (e.g. Robinson et al., 2007; Gutjahr et al., 2013). Stylasterid corals, on the other hand, remain entirely unexplored in this regard. The small amount of available stylasterid U/Ca data suggests that aragonitic stylasterids have higher U/Ca than high-Mg calcitic stylasterids, and that stylasterids of both mineralogies have lower U/Ca than scleractinian corals (chapter 4; Stewart et al., 2022). The implications of this low U/Ca for the application of U-series techniques is yet to be explored.
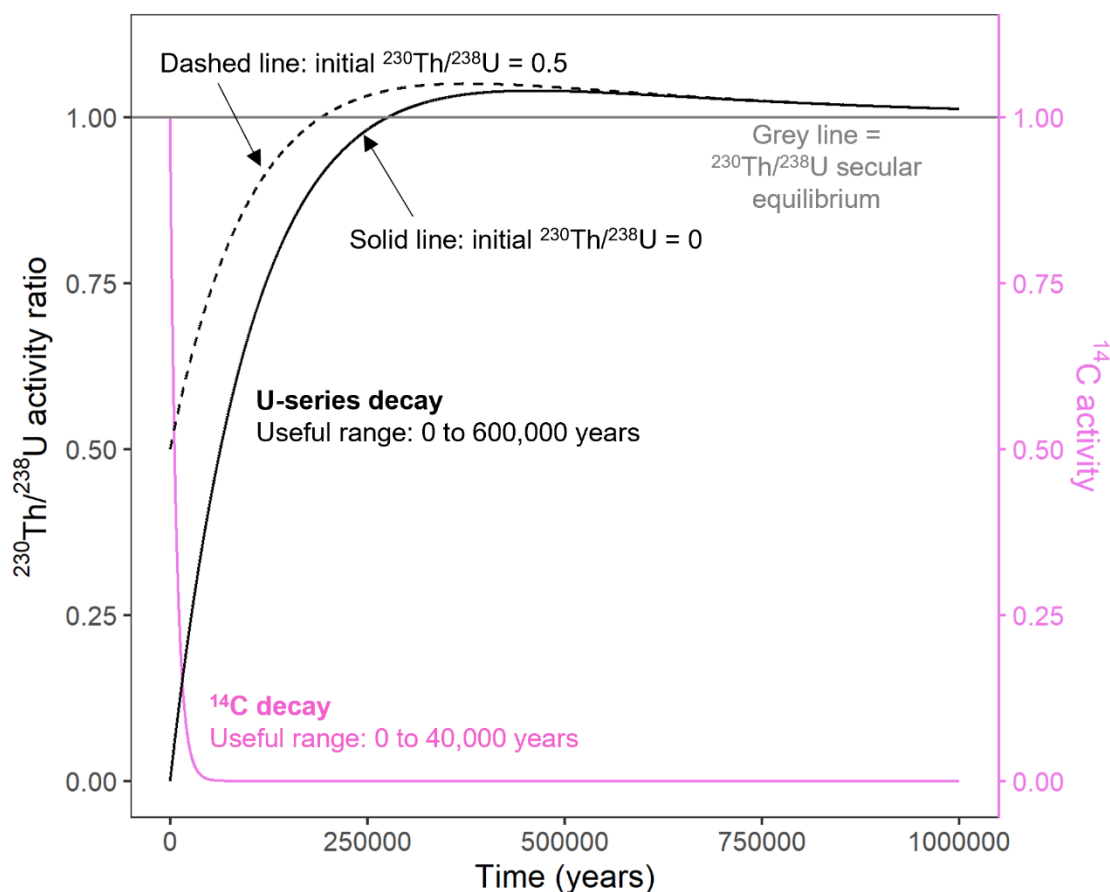
Figure 1. Example U-series (black lines) and ^{14}C (purple line) decay curves plotted as a function of time. ^{14}C calculations assume half-life = 5730 years (Godwin, 1962). U-series lines show solutions to equation 3, with initial ^{230}Th/^{238}U activity = 0 (solid line; equivalent to the solution to equation 1) and initial ^{230}Th/^{238}U activity = 0.5 (dashed line). Note that an initial ^{230}Th/^{238}U activity = 0.5 is highly unrealistic but is chosen here to clearly display the effect of increasing the initial ^{230}Th/^{238}U activity ratio on U-series decay. U-series calculations use the decay constants in section 2.4, and assume an initial δ^{234}U equal to modern seawater (146.8 ‰; Andersen et al., 2010).

1.2   Radiocarbon dating techniques

The radiocarbon content of azooxanthellate corals has also been used to constrain coral ages and growth chronologies, as well as information on changes in ocean circulation (e.g. Adkins et al., 1998; Adkins et al., 2002; Farmer et al., 2015; Chen et al., 2020; Chen et al., 2023). Natural radiocarbon (^{14}C) is produced in the upper atmosphere, and decays with a half-life of ~ 5730 years (Godwin, 1962; Figure 1). The shorter half-life of ^{14}C compared with relevant U-series isotopes (section 1.1) means that the geochronological and palaeoceanographic uses of ^{14}C dating are restricted to ~ the last 40,000 years (Figure 1). ^{14}C is transferred into the ocean by air-sea gas exchange, the timescale of which results in ^{14}C in the surface ocean being hundreds of ^{14}C years older than that found in the atmosphere. This time lag is referred to as the surface ocean reservoir age (e.g. Reimer and Reimer, 2001; Heaton et al., 2020).

When a parcel of surface seawater sinks, it is isolated from the atmosphere, and its ^{14}C signature will continue to decay. The ^{14}C signature of an azooxanthellate coral thus includes both the component of decay relevant to the age of the coral, as well as the initial radiocarbon age of the water the coral grew from. Subsurface seawater radiocarbon ages can vary spatially and temporally, meaning that absolute ages of sub-fossil scleractinian corals measured by radiocarbon techniques are generally more uncertain than those derived from U-series methods. In the case of dating individual sub-fossil scleractinian coral specimens, this has led to the development of radiocarbon techniques as a reconnaissance dating tool, used to guide selection of samples for more labour-intensive and time-consuming U-series techniques (e.g. Burke et al., 2010). In turn, paired radiocarbon and U-series dates measured on individual corals can permit the estimation of subsurface seawater radiocarbon age and its variation through time. The combination of these two techniques has been widely applied to scleractinian corals, with temporal variations in seawater radiocarbon age used to provide important constraint on variations in ocean ventilation on a variety of timescales (e.g. Goldstein et al., 2001; Chen et al., 2015; Chen et al., 2020; Chen et al., 2023).

In addition, radiocarbon dating subsamples of individual azooxanthellate corals has emerged as a powerful tool by which to study growth chronologies and rates of live-collected or close to modern samples (e.g. Farmer et al., 2015; King et al., 2018). In addition to natural ^{14}C, radiocarbon was also produced by the testing of atomic weapons in the late 1950's. The invasion of, peak in, and subsequent decay of bomb-radiocarbon in the ocean can be used to provide information on modern sample growth chronologies (e.g. Roark et al., 2006; Farmer et al., 2015; Frenkel et al., 2017), while tracking the incursion of bomb-radiocarbon into the deep ocean can also provide valuable information on the rate and patterns of ocean circulation (e.g. Broecker et al., 1978).

Only one previous study has analysed the ^{14}C content of stylasterid coral skeletons (King et al., 2018). This work demonstrated that stylasterid skeletons reliably record the radiocarbon content of the waters they grow in, and that individual stylasterids can grow on 10 to 100-year timescales (King et al., 2018). This suggests that, if combined with other established stylasterid proxies, radiocarbon-dated stylasterid skeletons could be valuable archives of recent, decadal-centennial changes in ocean conditions.

1.3   This study

Here, I explore the application of U-series and radiocarbon dating techniques to stylasterid skeletons. I investigate both the dating of individual, sub-fossil stylasterid specimens (n = 8 corals measured by U-series, including 3 corals with paired ^{14}C dates) and the generation of stylasterid growth chronologies using radiocarbon techniques (n = 4 corals). The results indicate that U-series dating stylasterid coral skeletons is complicated by their low U-content, which limits the precision of obtained ages. While this does not eliminate all utility of dating stylasterids by U-series methods, they are instead more likely to be of most use as high-resolution archives of recent oceanographic change. Stylasterid growth chronologies measured here suggest growth timescales consistent with previous work (King et al., 2018), and – for one

sample – permit the production of a coherent growth chronology which can be converted to calendar years. Finally, I use this sample to demonstrate the first application of the stylasterid Li/Mg-temperature, Ba/Ca-[Ba]$_{SW}$ and δ^{11}B-pH proxies developed both by previous work (Stewart et al., 2020b) and in this thesis (chapters 3 and 4). This multi-proxy record provides constraint on the 20th century evolution of ocean conditions in the mid-depth equatorial Atlantic.
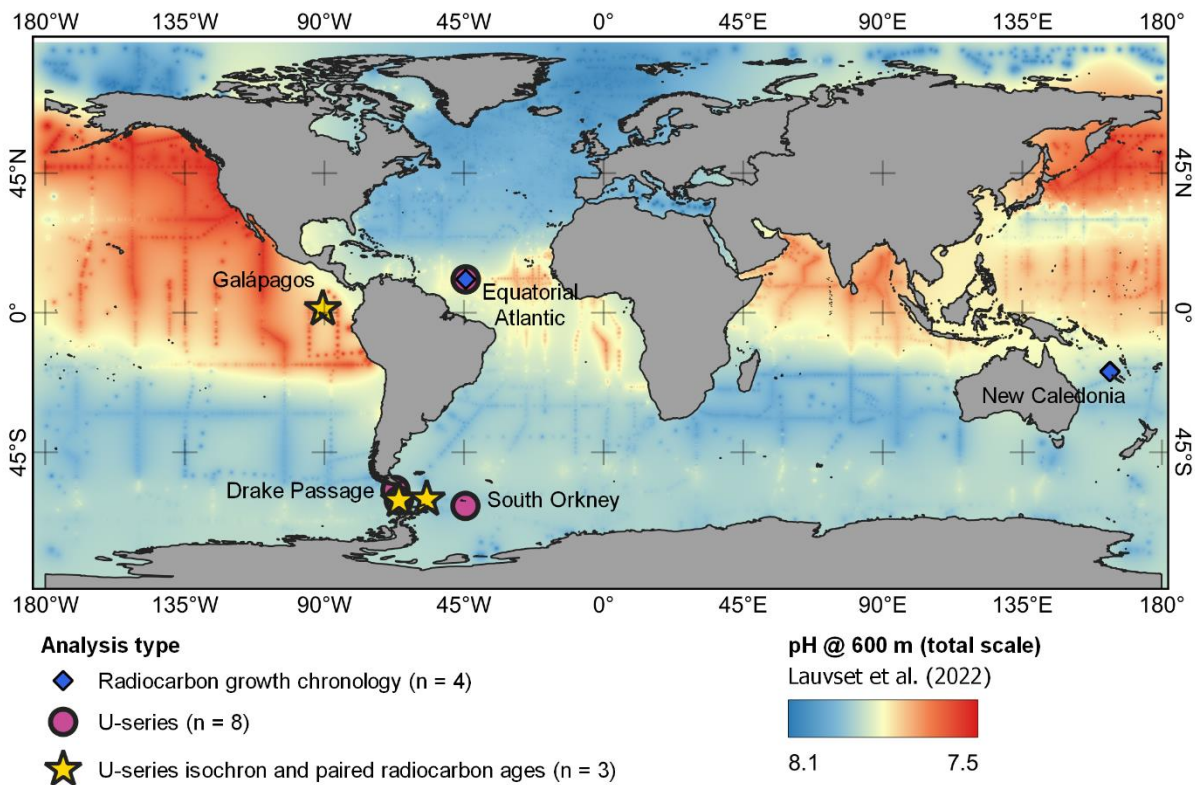
Figure 2. Locations of samples used in this study, overlain on pH (total scale) at 600 m water depth. pH calculated in Ocean Data View software (Schlitzer, 2023) using alkalinity and DIC pairs in the GLODAP bottle database (Lauvset et al., 2022) (see full calculation details in chapter 4). For 3 of the 8 corals measured by U-series techniques (purple circles), ages were also derived by U-series isochron and radiocarbon techniques (yellow stars).

2. Materials and methods

2.1 Coral samples

I analysed 12 individual stylasterid corals, which were collected during expeditions to the Drake Passage region of the Southern Ocean (R/V *Nathaniel B. Palmer* 1103), the South Orkney Islands (RRS *James Clark Ross* 15005), the equatorial Atlantic (RRS *James Cook* 094), the Galápagos Platform (M/V *Alucia* 1508) and New Caledonia (R/V *Alis* SPANBIOS 2021; accessed via le Muséum national d'Histoire naturelle in Paris (MNHN)) (Figure 2).

Sample ID	Short ID	Latitude (°N)	Longitude (°E)	Depth (m)	Location	Species	Live?	Mg/Ca (mmol/ mol)**
					U-series experiments			
AL1508-02-040-03-C-A	Sma04zx*	1.20	−90.52	176	Galápagos	*Stylaster marenzelli[a]*	No	3.00
NBP1103-DH134-St-3	Sde134zv	−57.17	−67.10	1012	Drake Passage	*Stylaster densicaulis[b]*	No	2.56
NBP1103-DH75-Stc-1	Sde75zz	−60.61	−66.00	1196	Drake Passage	*Stylaster densicaulis[b]*	No	2.30
NBP1103-DH88-Stp-1	Sde88zl*	−60.56	−65.96	982	Drake Passage	*Stylaster densicaulis[a]*	No	2.38
NBP1103-DH43-St-01	Sde43zg*	−60.18	−57.00	823	Drake Passage	*Stylaster densicaulis[c]*	No	2.29
JC094-BO519-Hydlm-001 thru 027	Adp519zw	10.72	−44.42	739	Equatorial Atlantic	*Adelopora sp.[c]*	No	2.69
JC094-041-VEM-ROV-232-SLP-041-FO130 Hyd c-s/m-001	Adp130zt	10.71	−44.42	727	Equatorial Atlantic	*Adelopora pseudothyron[b]*	No	No data
JR15005-Ev45-941	Sde45zy	−62.33	−44.53	1013	South Orkney	*Stylaster densicaulis[b]*	No	2.42
					Radiocarbon subsampling experiments			
MNHN-IK-2015-3403a	3403a	−18.92	163.35	425	New Caledonia	*Stephanohelia cf. gracilis[a]*	Yes - 2021	2.31
MNHN-IK-2015-3403b	3403b	−18.92	163.35	425	New Caledonia	*Stephanohelia cf. gracilis[a]*	Yes - 2021	2.26

Sample ID	Short ID	Latitude (°N)	Longitude (°E)	Depth (m)	Location	Species	Live?	Mg/Ca (mmol/ mol)**
MNHN-IK-2015-3225	PS3225	−19.10	163.32	201	New Caledonia	*Stylaster cf. biflabellum Cairns, 2015[a]*	No	2.88
JC094-B0088-Hydlm-001	Adp88	10.73	−44.42	1175	Equatorial Atlantic	*Adelopora pseudothyron[b]*	Yes - 2013	2.64

[a] High degree of confidence in taxonomic ID – ID by taxonomic expert

[b] Medium degree of confidence in taxonomic ID – ID by J. Kershaw

[c] Low degree of confidence in taxonomic ID – ID by J. Kershaw

* Samples used for U-series isochron experiments

** For U-series isochron samples, Mg/Ca ratios were measured on the Crush-clean sample aliquot (see section 2.2.1). For radiocarbon sub-sampling experiments, Mg/Ca ratios are average of all subsamples

Table 1. Summary of metadata for samples used in this study. Note that coral samples are referred to by their short sample IDs throughout this chapter.

Immediately after collection (or storage in ethanol at the MNHN), samples were air dried and organic matter removed by physical scraping and/or treatment in dilute NaClO. The specimens used represent 3 stylasterid genera: *Stylaster sp.*, *Adelopora sp.* and *Stephanohelia sp.*. The identification of corroded and/or coated stylasterids is fraught with uncertainty, and I therefore provide a qualitative assessment of the degree of confidence in taxonomic identifications (Table 1). All sample metadata are summarised in Table 1.

All samples were assumed to be aragonitic based on inference from published records where possible (Cairns and Macintyre, 1992; Samperiz et al., 2020), and supported for all but one specimen (Adp130zt) by measured Mg/Ca ratios (Table 1; section 3.1). I have reasonable confidence in my identification of specimen Adp130zt, and it is extremely similar in both gross morphology and collection location to specimen Adp519zw, supporting the validity of the aragonite assumption for this specimen.

2.2 Coral subsampling and cleaning
2.2.1 U-series experiments

Eight individual stylasterid corals were selected for U-series analysis (Table 1). The first measurement made for all corals is henceforth referred to as the Clean aliquot (Table 2). Approximately 150 to 200 mg of each sample was cut using a diamond-coated rotary blade and split into multiple chunks of carbonate. Areas of visible alteration and contamination were removed using a handheld rotary cutting tool, prior to chemical cleaning (see section 2.3). For corals not used in isochron experiments (see below), one chunk of each coral subsample (aside from Adp130zt; see section 2.1) was separated and crushed to small grains

using a pestle and mortar. Approximately 5 mg of this homogenised powder was taken for analysis of element/Ca ratios.

For 3 of the 8 corals sampled for U-series experiments (Sde88zl, Sma04zx and Sde43zg; Table 1), 4 additional subsamples were taken for isochron experiments (Table 2; Supplementary figure 1). Each isochron is thus defined by 5 distinct aliquots, henceforth referred to as the Crush-clean, Clean, Mechanical, Unclean and Coating aliquots (Table 2). The first four of these comprise 150 to 200 mg carbonate samples subjected to varying degrees of mechanical and chemical cleaning (Table 2; chemical cleaning procedures outlined in section 2.3). For the Crush-clean aliquot, samples were crushed to a fine powder which was homogenised and split into paired U-series (~ 150 mg), radiocarbon (~ 20 mg) and element/Ca ratio (~ 5 mg) subsamples. The fifth and final Coating aliquot was taken by scraping visible coatings (~ 5 mg) from the outermost surface of each coral using a diamond-coated drill bit (Table 2). The appearance of each coral sample and the aliquots taken from them are shown in Supplementary figure 1.

Subsample name	Brief description	Mechanically cleaned?	Chemically cleaned?	Crushed prior to chemical cleaning?
Crush-clean	Bulk carbonate sample with outer coatings and corroded regions removed, sample then crushed and cleaned by standard oxidative and reductive methods.	Yes	Yes	Yes
Clean	Bulk carbonate sample with outer coatings and corroded regions removed, cleaned by standard oxidative and reductive methods.	Yes	Yes	No
Mechanical	Bulk carbonate sample with outer coatings and corroded regions removed	Yes	No	No
Unclean	Bulk carbonate sample including outer coatings and corroded regions	No	No	No
Coating	Outer surface of sample	No	No	No

Progressive cleaning

Table 2. Description of subsamples used in U-series isochrons. Photos are shown in Supplementary figure 1.

2.2.2 Radiocarbon subsampling experiments

I also subsampled 4 corals to construct radiocarbon growth chronologies (Table 1). All 4 corals comprised branches with a clear axis of preferential growth, and each coral was thus sampled multiple times along a single branch from base to tip (Figure 3). Approximately 2 mm thick strips of tape were stuck perpendicular to the axis of growth at intervals along each branch, samples photographed, and the taped intervals cut using a handheld rotary cutting tool. This resulted in a series of 2 mm thick, radial branch cross sections. Note that the tip samples of corals Adp88, 3403A and 3403B were 5 mm thick.

Skeletal ornamentation and the presumed-modern outer surface of each section were removed (amount removed varied for each sample, but was generally 10 to 20 % of the sector diameter), along with any further visible contamination or alteration. Samples were crushed using a pestle and mortar, with a 5 mg aliquot taken for paired element/Ca and boron isotopic analyses, and the remaining material (between 5 and 20 mg) used for radiocarbon analysis.

The distance of each subsample from the branch tip was measured along the central branch axis using the Ruler tool in Inkscape, based on photographs taken prior to subsampling (see procedure above). Sample Adp88 was significantly non-planar, complicating measurement by this technique. Therefore, distances for this sample were also measured using a piece of string, with the two measurement methods yielding total branch lengths within 1 mm of each other (~ 5.20 cm). Systematic errors of ± 0.05 cm were assigned to each length measurement.
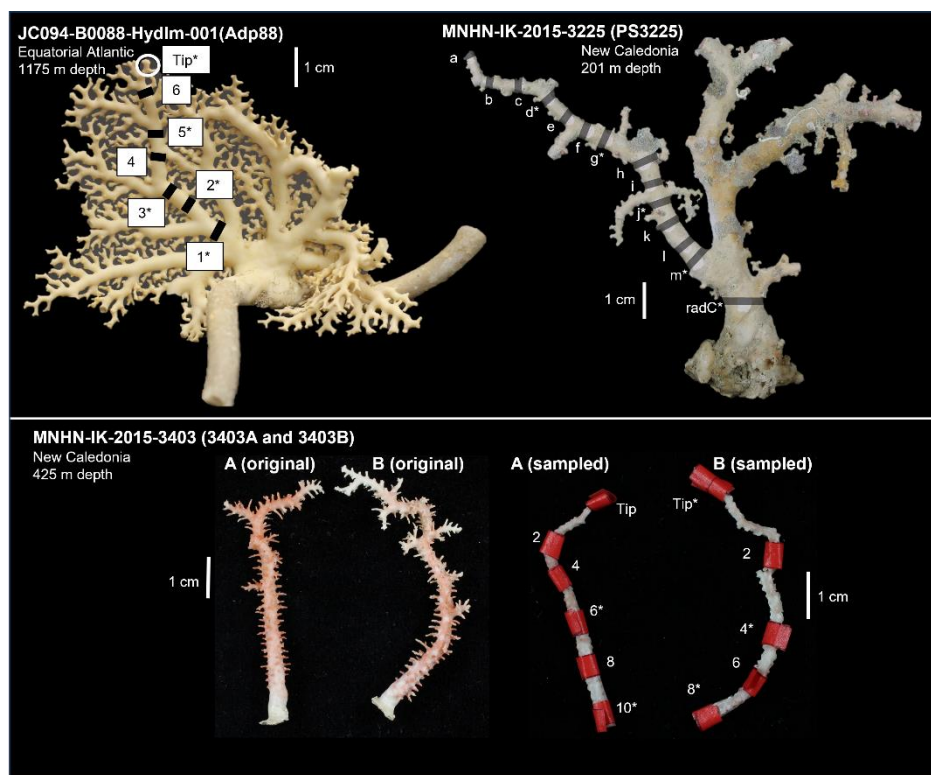
Figure 3. Summary of radiocarbon subsampling experiments. Subsamples with an asterisk were sampled for radiocarbon, element/Ca and $\delta^{11}B$ ratios were measured for all other subsamples. For samples 3403A and 3403B, original samples are shown on the left of the panel, and samples with ornamentation removed are shown on the right including (red) taped-off sampling regions.

2.3 U-series: analytical techniques

Clean and Crush-clean aliquots were subjected to the oxidative and reductive cleaning methods outlined in detail in chapter 2 (Shen and Boyle, 1988; Cheng et al., 2000a). All samples were then dissolved in 7.5 M HNO_3. This was sufficient to completely dissolve samples cleaned at least mechanically (i.e. all Mechanical, Clean and Crush-clean aliquots). Unclean and Coating aliquots clearly contained residual

material which was not dissolved by this initial step. This residue was thus separated, dissolved in mixed HNO_3/HF and dried down, before being redissolved in 7.5 M HNO_3 and combined with the rest of the sample. By initially dissolving most of the carbonate phase in 7.5 M HNO_3, the formation of solid Ca-fluoride phases was effectively avoided.

The separation and measurement of U-series isotopes followed the methods outlined in chapter 2. Briefly, a mixed ^{229}Th-^{236}U spike was added to each sample gravimetrically, U and Th coprecipitated with Fe-hydroxides, and separated by established column chemistry procedures (Edwards et al., 1987; Burke and Robinson, 2012; Chen et al., 2015). U and Th fractions were then measured separately on a Thermo Neptune MC-ICP-MS, following established methods (for U: Robinson et al., 2002; for Th: Burke and Robinson, 2012; Chen et al., 2015). Isotope ratios were derived by bracketing to standards U112a (U) and ThSGS (Th). Analytical reproducibility was assessed by repeat measurements of the $^{234}U/^{238}U$ ratio of the Harwell uraninite reference material (HU-1) and the $^{230}Th/^{229}Th$ ratio of the ThB reference material (Auro et al., 2012), which yielded internal precision better than 0.14 % (RSD; 2 σ). The efficacy of the full analysis procedure (including column chemistry) was assessed using the secular-equilibrium reference material HU-1, which was processed through column chemistry with each batch of samples. The small number of repeat measurements carried out here yielded an average $^{230}Th/^{238}U$ activity ratio of 0.9948 ± 0.0041 (2 σ; n = 4).

2.4   U-series: calculations

U-series activity ratios were derived for all aliquots using a Monte-Carlo approach with 100,000 iterations (modified from Chen et al., 2015). Note that activity ratios and their uncertainties could be derived analytically. In practise, both approaches yield identical results. Decay constants were chosen to be consistent with those used to calibrate the spike solution used here ($\lambda^{230} = 9.1577 \times 10^{-6}$ a^{-1} (Cheng et al., 2000b); $\lambda^{232} = 4.947500 \times 10^{-11}$ a^{-1}; $\lambda^{234} = 2.8263 \times 10^{-6}$ a^{-1} (Cheng et al., 2000b); $\lambda^{238} = 1.5513 \pm 0.0004 \times 10^{-10}$ (1 σ) a^{-1} (Jaffey et al., 1971)). Analytical uncertainties, uncertainties in instrumental and procedural blank contributions, uncertainties in decay constants, and uncertainties in spike concentrations and masses were propagated through calculations and into the Monte Carlo simulation. Errors in λ^{230}, λ^{232} and λ^{234} were assumed negligible, following Cheng et al. (2013).

For all Clean aliquots, the same Monte Carlo simulation was used to solve the U-series decay equation (equation 3; Edwards et al., 2003) and derive U-series ages and $\delta^{234}U$ values. To facilitate comparison with radiocarbon measurements, all ages are reported in years before present (BP), where present is defined as the calendar year 1950. Ages derived ignoring the contribution of initial ^{230}Th are referred to as uncorrected. I also calculate ages which account for initial ^{230}Th, using $[^{230}Th/^{232}Th]_i$ values which have been commonly applied when correcting scleractinian U-series ages from the same regions: 14.8 ± 14.8 (2 σ) for the Atlantic (e.g. Robinson et al., 2005; de Carvalho Ferreira et al., 2022), 37 ± 37 (2 σ) for the Southern Ocean (e.g. Chen et al., 2023) and 91.4 ± 91.4 (2 σ) for the Galápagos (e.g. Chen et al., 2020).

U-series isochrons were constructed for 3 corals using IsoplotR software (Vermeesch, 2018; implemented in R version 4.2.2). [^{238}U/^{232}Th], [^{234}U/^{232}Th] and [^{230}Th/^{232}Th] were used to form Rosholt-type A and B isochrons. Isochrons were first calculated using the three-dimensional Maximum Likelihood formulation from Ludwig and Titterington (1994). Although Ludwig and Titterington (1994) recommend the use of Osmond-type isochrons for visualisation of U-series data, Rosholt-type isochrons are preferred here to more clearly illustrate the variability in [^{230}Th/^{232}Th] between sample aliquots. The degree of overdispersion in each dataset was assessed using the Mean Squared Weighted Deviation (MSWD). Where MSWD >> 1, scatter in the data exceed that expected from analytical uncertainties. I attribute this overdispersion to isotopic variability in detrital [^{230}Th/^{232}Th], and use a dispersion model associated with this activity ratio to reduce the MSWD to 1 (IsoplotR model 3; Vermeesch, 2018). As for the singular ages calculated from Clean aliquots, isochron ages are reported in calendar years BP.

2.5   Radiocarbon: analytical techniques

~ 20 mg (minimum 5 mg) of selected samples was taken for radiocarbon analysis. All samples were cleaned and analysed following established protocols detailed in chapter 2. Briefly, samples were first oxidatively cleaned and then reacted with 0.1 M HCl to remove any adsorbed modern CO_2 which may have accumulated during sample storage (chapter 2; Adkins et al., 2002). All radiocarbon analyses were then performed at the University of Bristol Radiocarbon Accelerator Mass Spectrometry Facility (BRAMS; Knowles et al., 2019). Carbonate samples were graphitised using an IonPlus automatic graphitization (AGE3) system (Knowles et al., 2019), before the ^{14}C/^{12}C and ^{13}C/^{12}C of samples, blanks and standards were measured using a MICADAS accelerator mass spectrometer.

The blank corrected ^{14}C/^{12}C ratio of samples relative to the reference material NBS Oxalic Acid II at 1950 CE was used to calculate sample ^{14}C modern fractions (Fm; see definition in chapter 2). Sample Fm was then converted to conventional radiocarbon ages (i.e. using the Libby half-life, reported in years BP where present refers to the calendar year 1950). Repeat measurements of Fm for a coral sample with age ~ 10 kyr yielded an average value of 0.2971 ± 0.0018 (2 σ, n = 9). Repeat measurements of Fm for a radiocarbon-dead coral were used to assess the procedural blank, which averaged 0.0037 (n = 9).

2.6   Radiocarbon: age calculations and paired seawater data

For samples used in isochron experiments (Sde43zg, Sde88zl and Sma04zx), I estimate true radiocarbon ages by first correcting coral ages for seawater radiocarbon age (i.e. a "reservoir age" correction, using a ΔR value), before calibrating corrected coral ages against the Marine20 curve (Heaton et al., 2020).

For Drake Passage samples Sde43zg and Sde88zl (800 to 1000 m depth), I estimate site-specific seawater conventional radiocarbon ages using the closest (in depth and geographic location) seawater Δ^{14}C values taken from the GLODAP bottle database (Lauvset et al., 2022) (Figure 4). Following definitions in Stuiver and Polach (1977), Δ^{14}C values can be converted to conventional ^{14}C ages using the equation:

$$^{14}Cage = -8033 \times \ln\left(\left(\frac{\Delta^{14}C}{1000} + 1\right) \times e^{\frac{y-1950}{8267}}\right) \qquad (4)$$

where y is the sample collection year. Note that in my calculations I use y values rounded to the whole year in which the sample was collected. Uncertainty in seawater radiocarbon age was estimated using the variation between the three nearest available measurements ($\pm$ 2 standard deviations). For these samples, I convert modern seawater ages to ΔR values (summarised in Figure 4) and use these to correct measured coral ages. Implicit in this calculation is the assumption that seawater radiocarbon age has not changed substantially between the time the samples were alive and the modern day (i.e. the past 5000 years). The validity of this assumption is supported by the relatively constant reservoir age observed at relevant depths in the Drake Passage across the Holocene (Chen et al., 2023).

For sample Sma04zx, modern seawater at the coral collection site (Galápagos Islands, 176 m) is clearly influenced by bomb-derived ^{14}C (Figure 4), while this sample evidently grew prior to bomb-radiocarbon release (see ages in Table 5). To estimate the pre-bomb seawater radiocarbon age at this site, I interpolate between surface ocean reservoir age prior to bomb-radiocarbon release (weighted mean of 4 closest measurements used from Taylor and Berger, 1967; accessed via Reimer and Reimer, 2001) and a nearby subsurface, pre-bomb seawater radiocarbon age derived from paired U-Th and ^{14}C measurements on an azooxanthellate scleractinian coral from 627 m (U-series age 145 years BP; Chen et al., 2020) (Figure 4).

After correction by the ΔR values summarised in Figure 4, coral ages were calibrated against the Marine20 curve (Heaton et al., 2020). Calibration was performed using BChron software in R (Haslett and Parnell, 2008). Ages are given as the median of a random sampling of the probability distribution, and uncertainties quoted as the 95 % confidence interval (i.e. $\pm$ 2 σ). Final quoted errors include propagated analytical, seawater radiocarbon age and calibration uncertainties.

I do not perform the same conversion to true radiocarbon ages for samples used in radiocarbon subsampling experiments (Adp88, 3403A, 3403B and PS3225) (see section 5 for detailed discussion). However, to aid interpretations, I do estimate modern seawater radiocarbon ages at the coral collection sites, with seawater data taken from CTD and ROV deployments during cruise JC094 in the equatorial Atlantic (Chen et al., 2015; for sample Adp88) and the GLODAP database (Lauvset et al., 2022; for samples PS3225, 3403A and 3403B). The conversion to seawater radiocarbon age (and estimation of uncertainties) follows the procedures outlined above. For sample PS3225, I additionally estimate the pre-bomb surface reservoir age using the weighted average of all measurements within 2000 km of the coral collection location (Toggweiler et al., 1991; Burr et al., 1998; Druffel and Griffin, 1999; Ulm, 2002; Guilderson et al., 2004; Petchey et al., 2004; Petchey et al., 2008a and 2008b; Burr et al., 2009; Ulm et al., 2009; Petchey et al., 2013; Komugabe et al., 2014; Hua et al., 2015; Wu et al., 2021; accessed via Reimer and Reimer, 2001).

a. Sde43zg (Drake Passage, 823 m)

Seawater ^{14}C age taken from nearest GLODAP measurement:

Seawater age = 1318 years BP
ΔR = 714 ± 21 (2σ)

○ GLODAP
● GLODAP - matched

Conventional ^{14}C age (years BP)

Dashed lines = coral collection depths
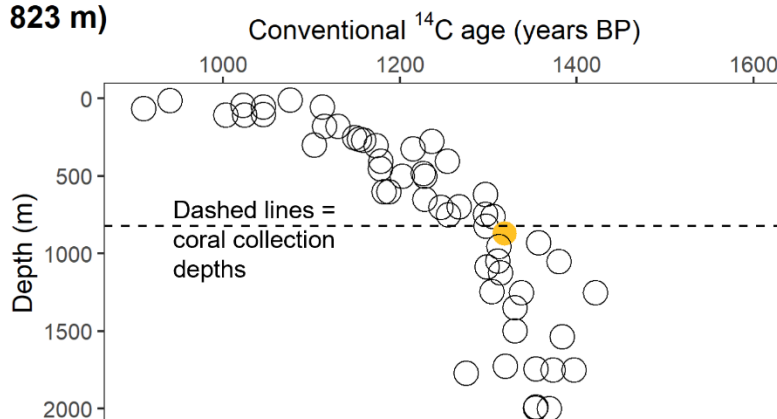
b. Sde88zl (Drake Passage, 982 m)

Seawater ^{14}C age taken from nearest GLODAP measurement:

Seawater age = 1307 years BP
ΔR = 703 ± 108 (2σ)

○ GLODAP
● GLODAP - matched

Conventional ^{14}C age (years BP)
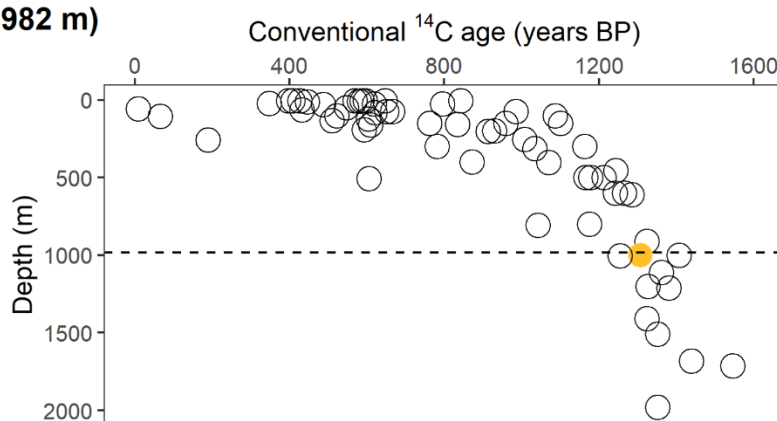
c. Sma04zx (Galápagos, 176 m)

Seawater ^{14}C age interpolated between pre-1950 surface ocean and depth:

Seawater age = 587 years BP
ΔR = − 17 ± 214 (2σ)

○ GLODAP
● Interpolated value
◆ Pre-bomb age @ 627 m (C20)
■ Pre-bomb surface R (T&B67)

Conventional ^{14}C age (years BP)

Modern seawater influenced by bomb-derived ^{14}C at coral collection depth

Paired coral U-series and ^{14}C measurements give pre-bomb R @ 627 m depth (coral U-series age = 145 years BP) (C20)
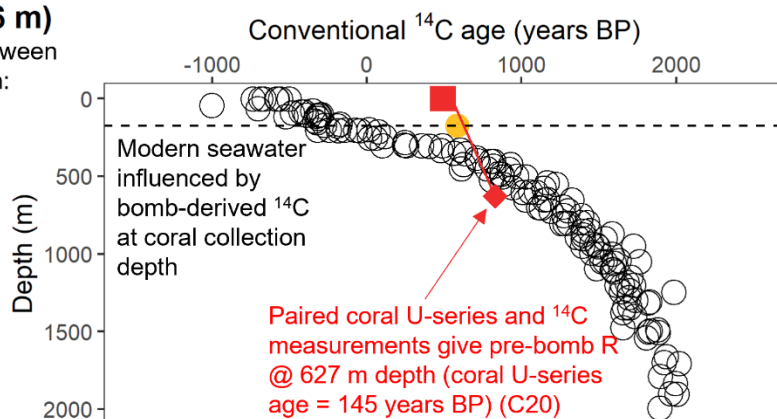
Figure 4. Seawater data used to correct coral radiocarbon ages. ΔR values used to correct each sample are shown in bold. ΔR values for samples Sde43zg and Sde88zl based on nearest GLODAP Δ^{14}C value, converted to conventional radiocarbon ages following equation 4 (Lauvset et al., 2022; section 2.6). Uncertainty based on variability between 3 nearest ages. ΔR value for Sma04zx based on interpolation between pre-bomb surface ocean reservoir age (taken from Taylor and Berger, 1967 (T&B67)) and an estimate of pre-bomb subsurface seawater radiocarbon age based on a pair of coral U-series and ^{14}C dates (Chen et al., 2020 (C20); see section 2.6).

2.7   Element/Ca and boron isotopic ratios: analytical techniques

Element/Ca ratios and – for samples used in radiocarbon subsampling experiments - paired boron isotopic values were measured following the analytical procedures outlined in detail in chapter 2. Briefly,

samples were first cleaned using standard oxidative cleaning techniques for boron isotope analysis (adapted from Barker et al., 2003; Ni et al., 2007). Samples were treated with a warm (80 °C) oxidising solution consisting of 1 % H_2O_2 buffered by 0.1 M NH_4OH for 15 minutes. Samples were then rinsed, transferred to an acid-cleaned plastic vial, and subjected to a weak acid leach (0.0005 M HNO_3) before dissolution in distilled 0.5 M HNO_3.

Li/Ca, Mg/Ca, Ba/Ca and U/Ca ratios were then measured at the University of Bristol using a Thermo-Element2 ICP-MS. Fe/Ca and Mn/Ca ratios were also measured to screen for the influence of non-carbonate phases. Intensities of ^7Li, ^{26}Mg, ^{43}Ca, ^{55}Mn, ^{56}Fe, ^{138}Ba and ^{238}U were measured in samples, blanks and a well-characterised bracketing standard to derive element/Ca ratios for each coral sample. Analytical reproducibility was assessed for Li/Ca, Mg/Ca, Ba/Ca and U/Ca using repeat measurements of reference materials NIST RM 8301 (Coral) (Stewart et al., 2020a) and JCp-1 (Hathorne et al., 2013) and was better than 2 % (RSD; 2 σ) for all ratios (chapter 2). Accuracy was assessed using NIST RM 8301 (Coral), and long-term average values for all elements differed from published values by < 3 %. Values were adjusted by the correction factors outlined in chapter 2.

Boron isotope values were derived by first passing a small aliquot of each dissolved sample through microcolumns containing Amberlite IRA 743 anionic exchange resin, to separate boron from the carbonate matrix (Foster, 2008). Boron isotope values were then measured on this purified fraction using established Multi-Collector ICP-MS techniques at the University of Bristol, reported relative to NIST SRM 951 (chapter 2; Foster, 2008; Rae et al., 2018). Analytical reproducibility and accuracy were assessed by repeat measurements of NIST RM 8301 (Coral). Reproducibility was assessed separately for the each of 2 measurement periods represented here, with measurements between October 2019 and August 2021 yielding an average value of 24.27 ± 0.33 ‰ (n = 15; 2 σ) and measurements between June 2022 and February 2023 an average value of 24.11 ± 0.16 ‰ (n = 19; 2 σ) (see Chapter 2, section 4.2.2 for detailed discussion). Coral samples were assigned the relevant analytical uncertainty for the period they were measured in. Measurements in both periods are in excellent agreement with both the interlaboratory consensus value (Stewart et al., 2020a). Procedural blanks were also monitored and were typically small (average 47 pg, n = 20). Implied blank corrections using the long term average procedural blank $\delta^{11}B$ (− 8 ± 31 ‰; 2 σ) were ≤ 0.05 ‰ for all samples, and I thus chose not to correct for this effect.

Coral Li/Mg, Ba/Ca and $\delta^{11}B$ were converted to palaeo-seawater temperature, $[Ba]_{SW}$ and $\delta^{11}B_{borate}$ using the aragonitic stylasterid calibrations presented in Stewart et al. (2020b) (stylasterid specific), chapter 3 and chapter 4, respectively. Palaeo-seawater pH was calculated using the rearranged form of the equation (following Zeebe and Wolf-Gladrow, 2001):

$$\delta^{11}B_{borate} = \frac{\delta^{11}B_{SW} + 10^{pK_B^* - pH} \times \left(\delta^{11}B_{SW} - 10^3 \times (\alpha_B - 1)\right)}{1 + \alpha_B \times 10^{pK_B^* - pH}} \qquad (5)$$

where: palaeo-$\delta^{11}B_{borate}$ values were estimated from coral $\delta^{11}B$ (chapter 4); palaeo-seawater pK_B^* values were calculated in the seacarb package in R (Gattuso et al., 2022) using coral Li/Mg-derived palaeo-seawater temperatures and a location and depth specific modern day salinity (see section 2.8); $\delta^{11}B_{SW}$ = boron isotopic composition of seawater (39.61 ‰; Foster et al., 2010); α_B = fractionation factor between the borate anion and boric acid (1.0272; Klochko et al., 2006).

2.8   Estimating additional hydrographic parameters

I also report ambient seawater temperature and the boron isotopic composition of the borate anion in seawater ($\delta^{11}B_{borate}$) for sample Adp88. Seawater temperature, salinity, nutrient concentrations (dissolved phosphate and silica), alkalinity and dissolved inorganic carbon (DIC) were estimated at the coral collection site using co-located bottle measurements taken during CTD deployment on cruise JC094. Hydrographic data were then used to calculate carbonate system parameters (e.g. pH) using the seacarb package in R (Gattuso et al., 2022). Input parameters were alkalinity and DIC, with dissociation constants of carbonate (K_1 and K_2) taken from Lueker et al. (2000), dissociation constants of HSO_4^- from Dickson (1990) and the boron/salinity ratio from Lee et al. (2010). The boron isotopic composition of the borate anion in seawater ($\delta^{11}B_{borate}$) was then calculated in seacarb as outlined in chapter 4. Uncertainty in temperature and $\delta^{11}B_{borate}$ are reported as ± 2 σ, and were estimated as the variation of the JC094 data and the nearest 2 GLODAP stations which contained alkalinity and DIC measurements (Lauvset et al., 2022).

$[Ba]_{SW}$ was also estimated using a nearby published profile also collected during cruise JC094 (Bates et al., 2017). Depth interpolation and unit conversions follow those outlined in chapter 3. A representative analytical uncertainty is applied to these values (± 3 nmol/kg; Bates et al., 2017; see chapter 3).

3.   Results

3.1   Specimen Mg/Ca and mineralogy

The mineralogy of the stylasterid specimens analysed here was inferred from previous mineralogical determinations (Cairns and Macintyre, 1992; Samperiz et al., 2020), and confirmed using Mg/Ca ratios as outlined in section 2.1. Mg/Ca ratios of all samples measured ranged from 2.3 to 3.0 mmol/mol (Table 1). When compared with published Mg/Ca ratios for aragonitic and high-Mg calcitic stylasterids (~3 and 80 mmol/mol, respectively; Stewart et al., 2020b), these values are consistent with all specimens in this study being composed predominantly of aragonite.

3.2   U-series results

3.2.1   Clean aliquot ages

The Clean aliquots of the 8 stylasterid corals dated by U-series techniques here have skeletal $[^{238}U]$ ranging from 0.8 to 1.6 ppm (mean 1.2 ± 0.5 ppm; 2 σ) (Figure 5; Table 3). The U/Ca ratios of these corals average 550 ± 180 nmol/mol (2 σ; n = 7 as U/Ca ratios not measured for sample Adp130zt), and are comparable to, but at the high end of, previously published modern stylasterid U/Ca ratios (Figure 5;

Stewart et al., 2022; chapter 4). Concentrations of the 2 isotopes of Th considered here - ^{230}Th and ^{232}Th – average 2.0 ± 5.8 ppt (2 σ) and 5600 ±11000 ppt (2 σ), respectively (Figure 5; Table 3).

Measured isotope ratios were used to calculate coral ages and both measured and initial δ^{234}U (δ^{234}U$_m$ and δ^{234}U$_i$, respectively), which are summarised in Table 3 and Figure 6. Two sets of calculations were made for each coral, one assuming no contribution of initial ^{230}Th, and the other correcting for the contribution of initial ^{230}Th (section 2.4). Uncorrected coral ages ranged from 100 to 60,000 years BP (Figure 6; Table 3). For the 5 samples with uncorrected ages > 1000 years, correction for initial ^{230}Th substantially reduced the inferred coral ages by between 3000 and 10000 years (Figure 6; Table 3). Correction for initial ^{230}Th also significantly increased the errors on calculated ages, compared with the analytical uncertainties associated with uncorrected ages (Figure 6; Table 3).

For the three corals with uncorrected ages < 1000 years, two have corrected ages with errors < 100 % of the coral age (samples Sde88zl and Sde134zv; Table 3). However, for sample Sma04zx, correction for initial ^{230}Th results in an age < 0 years BP, with a substantial (± 250 years, 2 σ) error.

δ^{234}U$_i$ values (both corrected for initial ^{230}Th and not) for all but one sample are within 6 ‰ of the modern seawater value (Figure 6). The exception is sample Sde75zz, which shows significantly elevated δ^{234}U$_i$ (Table 3; Figure 6). The δ^{234}U$_m$ of this sample is close to the modern seawater value (Figure 6).
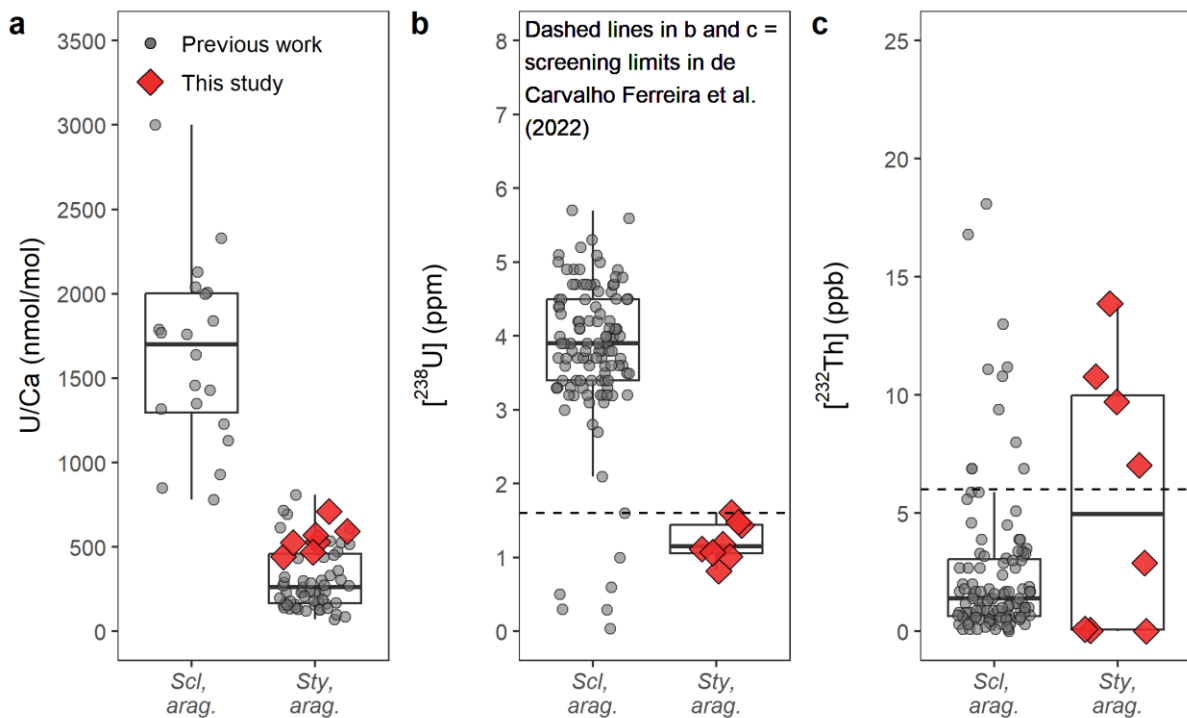
Figure 5. a) U/Ca values for modern Scleractinia (Anagnostou et al., 2011) and both modern (Stewart et al., 2022; chapter 4; grey circles) and sub-fossil (this study; red diamonds) stylasterids. Stylasterid samples in panel a were cleaned oxidatively and analysed by solution ICP-MS (see full procedure in section 2.7; Stewart et al., 2022), while scleractinian samples in panel a were not oxidatively cleaned and were

analysed by laser ablation techniques (Anagnostou et al., 2011). b) Skeletal [^{238}U] for Scleractinia (de Carvalho Ferreira et al., 2022) and aragonitic stylasterids (this study). c) [^{232}Th] for Scleractinia (de Carvalho Ferreira et al., 2022) and aragonitic stylasterids (this study). All corals in panel b and c were analysed using the U-series cleaning and measurement procedures outlined here (sections 2.3 and 2.4; de Carvalho Ferreira et al., 2022). Dashed lines in b and c show limits below ([^{238}U]) and above ([^{232}Th]) which coral ages were excluded from further analysis in de Carvalho Ferreira et al. (2022).
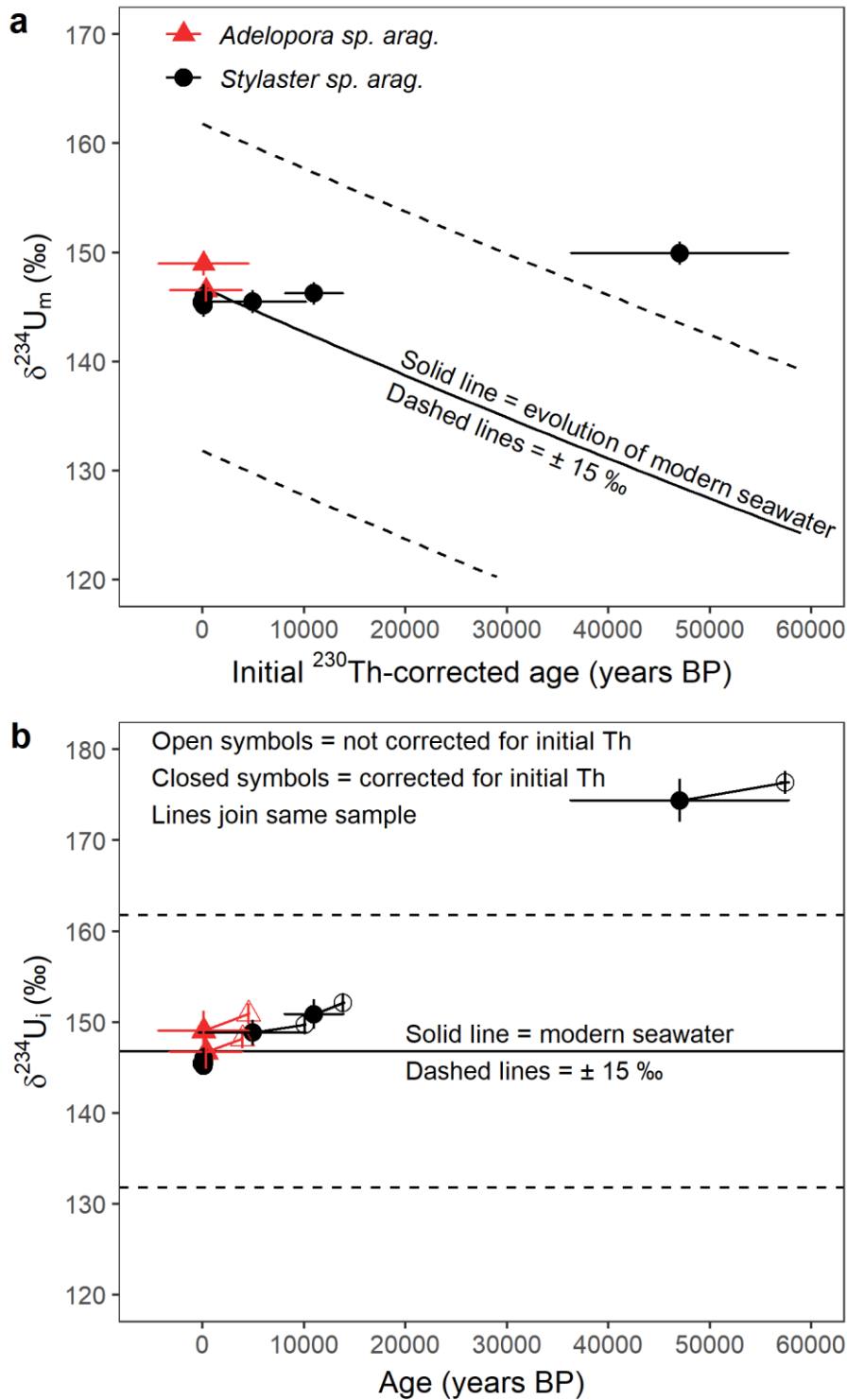
Figure 6. a. Measured $\delta^{234}U$ ($\delta^{234}U_m$) against U-series ages corrected for the contribution of initial ^{230}Th using assumed $[^{230}Th/^{232}Th]_i$ values (see section 2.4). Solid line shows the expected evolution of the modern seawater $\delta^{234}U$ value (146.8 ‰; Andersen et al., 2010) through time, dashed lines show ± 15 ‰ variability (Henderson, 2002). b. Initial $\delta^{234}U$ ($\delta^{234}U_i$) against sample ages, both uncorrected (open symbols) and corrected (filled symbols; as in plot a) for the contribution of initial ^{230}Th. All error bars are ± 2 σ.

Sample ID	Age (unc.) (years BP)	± 2 σ	Age (cor.) (years BP)	± 2 σ	$\delta^{234}U_m$ (‰)	± 2 σ	$\delta^{234}U_i$ (cor.) (‰)	± 2 σ	[238U] (ppm)	± 2 σ	[232Th] (ppb)	± 2 σ	[230Th/238U]	± 2 σ
Sde88z1[a]	112	7	98	16	146.0	1.1	146.0	1.1	0.822	0.002	0.0101	0.0003	0.00192	0.00007
Sde43zg[a]	13855	88	10986	2909	146.2	1.0	150.9	1.6	1.179	0.003	2.8969	0.0129	0.13759	0.00080
Sde134zv[a]	124	7	76	49	145.1	1.0	145.2	1.0	1.021	0.002	0.0429	0.0008	0.00204	0.00008
Sde75zz[a]	57393	380	47035	10816	149.9	1.1	171.3	5.4	1.120	0.003	9.7189	0.0417	0.47530	0.00238
Sde45zy[a]	10154	57	4896	5285	145.5	1.1	147.5	2.5	1.606	0.004	7.0253	0.0304	0.10189	0.00054
Adp130zt[b]	3901	28	357	3592	146.5	1.1	146.7	1.8	1.429	0.003	10.7746	0.0465	0.04098	0.00028
Adp519zw[b]	4524	30	106	4505	149.0	1.1	149.0	2.2	1.484	0.003	13.8742	0.0599	0.04738	0.00030
Sma04zx[c]	163	3	−78	241	145.4	1.1	145.4	1.1	1.072	0.003	0.0905	0.0005	0.00246	0.00004

$[^{230}Th/^{232}Th]_i$ used for age correction:

[a]37 ± 37 (2 σ)

[b]14.8 ± 14.8 (2 σ)

[c]91.4 ± 91.4 (2 σ)

Table 3. Results of U-series dating experiments on Clean aliquots (see section 2.2.1). Ages were corrected using $[^{230}Th/^{232}Th]_i$; values commonly applied when dating scleractinian corals (see section 2.4).

3.2.2 Isochron experiments and radiocarbon ages

Rosholt-type isochrons were constructed for 3 corals, with radiocarbon ages also measured for each of these samples (Table 4; Table 5). Considering isochron results, firstly, the 5 aliquots measured for each sample spanned a range of isotopic concentrations and activity ratios, which are tabulated in the supplementary information (section 7.1; Supplementary table 1). Mechanical and chemical sample cleaning reduced measured [^{232}Th] for all 3 corals (Figure 7). The strategy of crushing samples prior to chemical cleaning (the Crush-clean aliquot) resulted in only a small reduction in [^{232}Th] for sample Sde43zg, compared with the Clean aliquot, while for samples Sma04zx and Sde88zl, the Crush-clean aliquot had slightly higher [^{232}Th] than the Clean aliquot (Figure 7). Mechanical and chemical cleaning had no effect on [^{238}U] for samples Sma04zx and Sde88zl, while for sample Sde43zg, mechanically cleaned aliquots had [^{238}U] ~ 1 ppm lower than uncleaned aliquots (Figure 7).

3-dimensional maximum likelihood regression analyses were first performed on 3-aliquot datasets including the Crush-clean, Clean and Mechanical aliquots, before 5-aliquot regressions were performed which additionally used the Unclean and Coating aliquots (Figure 8). The results of 3-dimensional maximum likelihood regression revealed that all isochrons were significantly overdispersed (8 < MSWD < 3500; Table 4; see section 2.4 for explanation of MSWD).

Sample	3-aliquot isochron			5-aliquot isochron		
	Age (± 2 σ)	[^{230}Th/^{232}Th]$_i$	MSWD	Age (± 2 σ)	[^{230}Th/^{232}Th]$_i$	MSWD
Sde43zg	4332 ± 2902	103 ± 38	437	3680 ± 1232	112 ± 13	400
Sma04zx	96 ± 14	27 ± 3	8	72 ± 21	34 ± 4	243
Sde88zl	97 ± 6	4 ± 1	14	N/A	N/A	3500

Table 4. Results of 3- and 5-aliquot isochron analyses. All ages given as years BP. Over-dispersion is attributed to [^{230}Th/^{232}Th]$_i$. For details of calculations and the meaning of statistical indicators, see section 2.4.

Radiocarbon ages were also measured for samples Sde43zg, Sde88zl and Sma04zx. Full results are summarised in Table 5, including coral ages which have been corrected for seawater radiocarbon age and calibrated to the Marine20 curve (Heaton et al., 2020; see section 2.6 for full details). These corrected, calibrated ages are henceforth referred to as corrected radiocarbon ages.

Sample	Conventional ^{14}C age (uncorrected, uncalibrated) (years BP)	Error (± 1 σ)	Fm	Error (± 1 σ)	ΔR value used (years)	Error (± 1 σ)	Corrected and calibrated ^{14}C age (years BP)	Final error (± 2σ)
Sde43zg	4451	26	0.575	0.002	714	11	3492	162
Sma04zx	646	25	0.923	0.003	− 17	112	149	243
Sde88zl	1411	25	0.839	0.003	703	54	166	186

Table 5. Radiocarbon ages and modern fractions (Fm) for samples used in U-series isochron experiments. Radiocarbon analyses were performed on Crush-clean aliquots. All ages given as years BP, where present is defined as 1950. Age correction and calibration follows procedures outlined in section 2.6, using ΔR values shown in table. Note that errors on uncorrected ^{14}C ages and Fm are given as ± 1 σ, as is convention, but final errors on corrected and calibrated ages are given as ± 2 σ. Final uncertainties include propagated analytical, seawater radiocarbon age and calibration uncertainties.

When accounting for overdispersion as outlined in section 2.4, 3-aliquot and 5-aliquot isochrons yield broadly consistent ages and $[^{230}Th/^{232}Th]_i$ for samples Sma04zx and Sde43zg (Table 4; Figure 8). For both samples, the 5-aliquot approach gives a younger age and higher $[^{230}Th/^{232}Th]_i$ than the 3-aliquot approach (Table 4; Figure 8). Isochron $[^{230}Th/^{232}Th]_i$ differs substantially from the values assumed when making the Clean aliquot age calculations in section 3.2.1. The isochron ages of sample Sde43zg differ significantly from the U-series age of the Clean aliquot, and were closer to - and within error of - the corrected ^{14}C age (Figure 8; Figure 9). For sample Sma04zx, isochron ages are again within error of the corrected ^{14}C age (Figure 8; Figure 9), and are substantially better constrained than the Clean aliquot U-series age (Figure 9).

For sample Sde88zl, the 3-aliquot approach yielded ages within error of the uncorrected and corrected Clean aliquot U-series ages, and the corrected ^{14}C age (Figure 8; Figure 9). However, the 5-aliquot approach failed to produce a meaningful age. Inspection of the Rosholt-type A isochron plot ($[^{230}Th/^{232}Th]$ vs $[^{238}U/^{232}Th]$) for this coral reveals the 5-aliquot regression has a negative line of best fit (Figure 8).
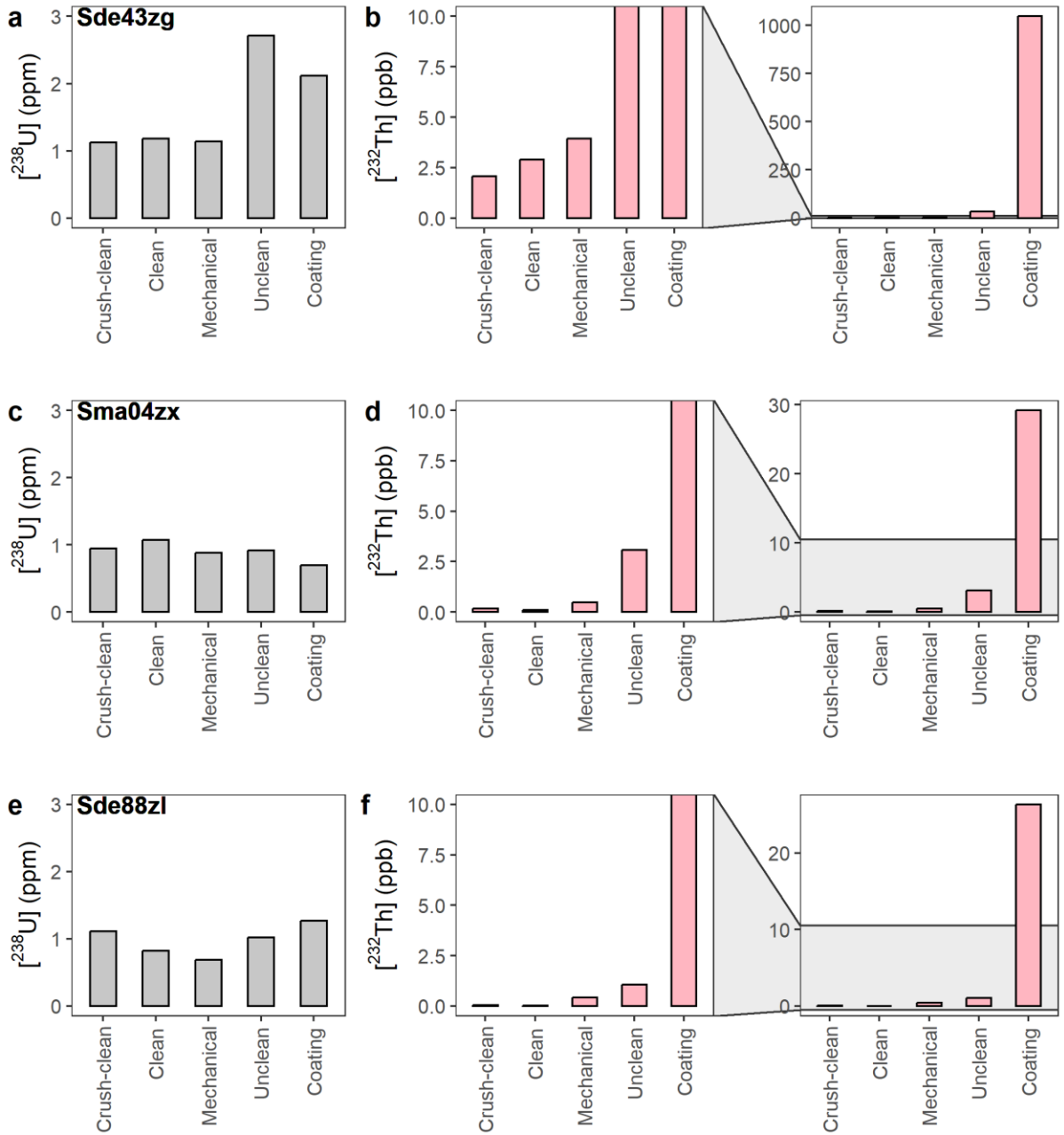
Figure 7. Measured [238U] (a, c and e; grey) and [232Th] (b, d and f; pink) for isochron subsamples. Subsamples are described in section 2.2.1 and Table 2. Owing to the wide range of [232Th] between coral subsamples, two scales are shown for each plot.
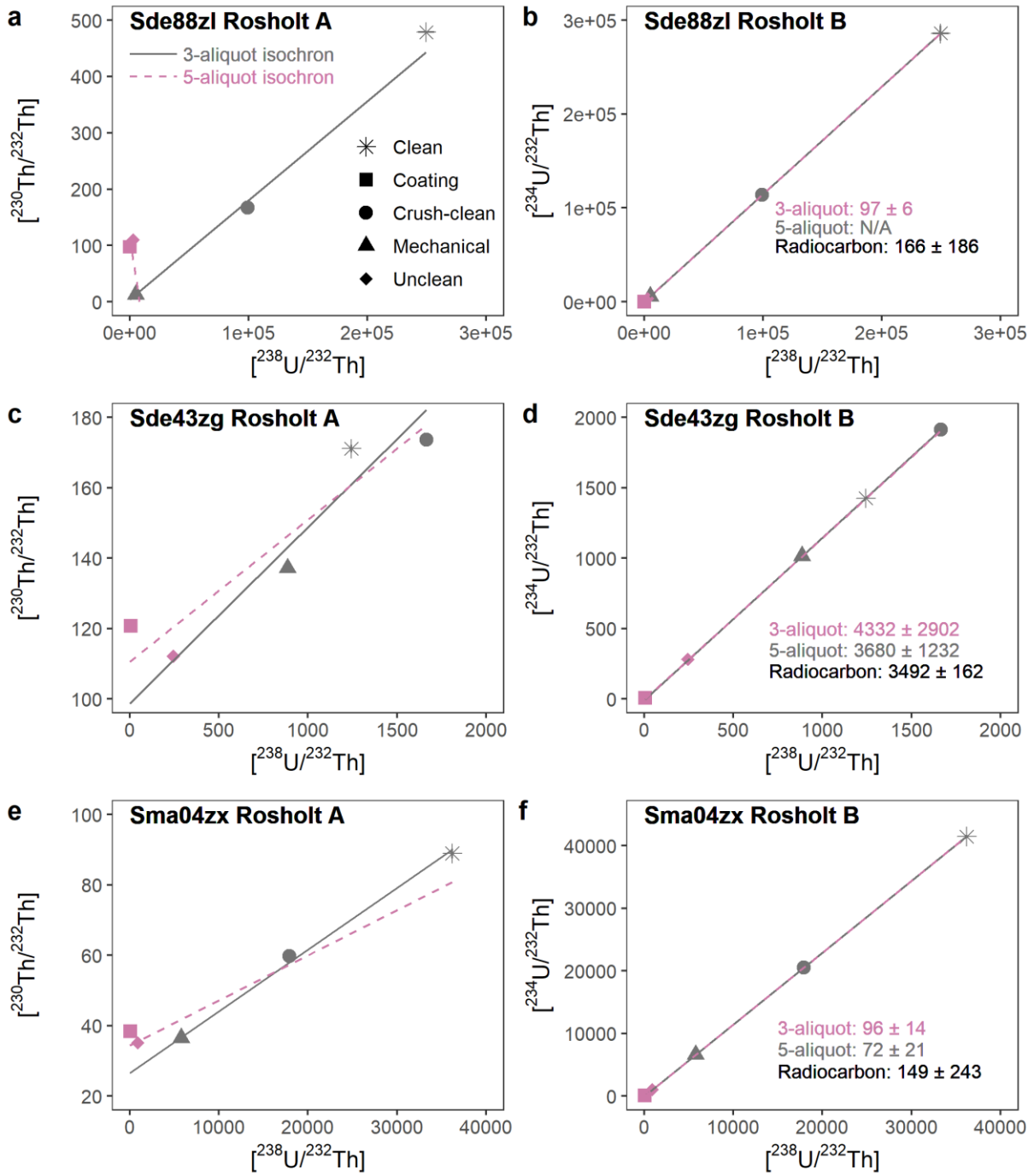
Figure 8. Rosholt-type A (a, c and e) and B (b, d and f) isochrons for corals Sde88zl, Sde43zg and Sma04zx. Colours and symbols in all plots follow the legend in panel a. Regression lines calculated by the 3-dimensional, analytical error-weighted Maximum Likelihood Technique (Ludwig and Titterington, 1994; see section 2.4). Errorbars (± 2 σ) are shown but are generally smaller than data points. Isochron ages are shown in panels b, d and f, along with corrected and calibrated radiocarbon ages (see section 2.6). All ages given in years BP, errors are ± 2 σ.
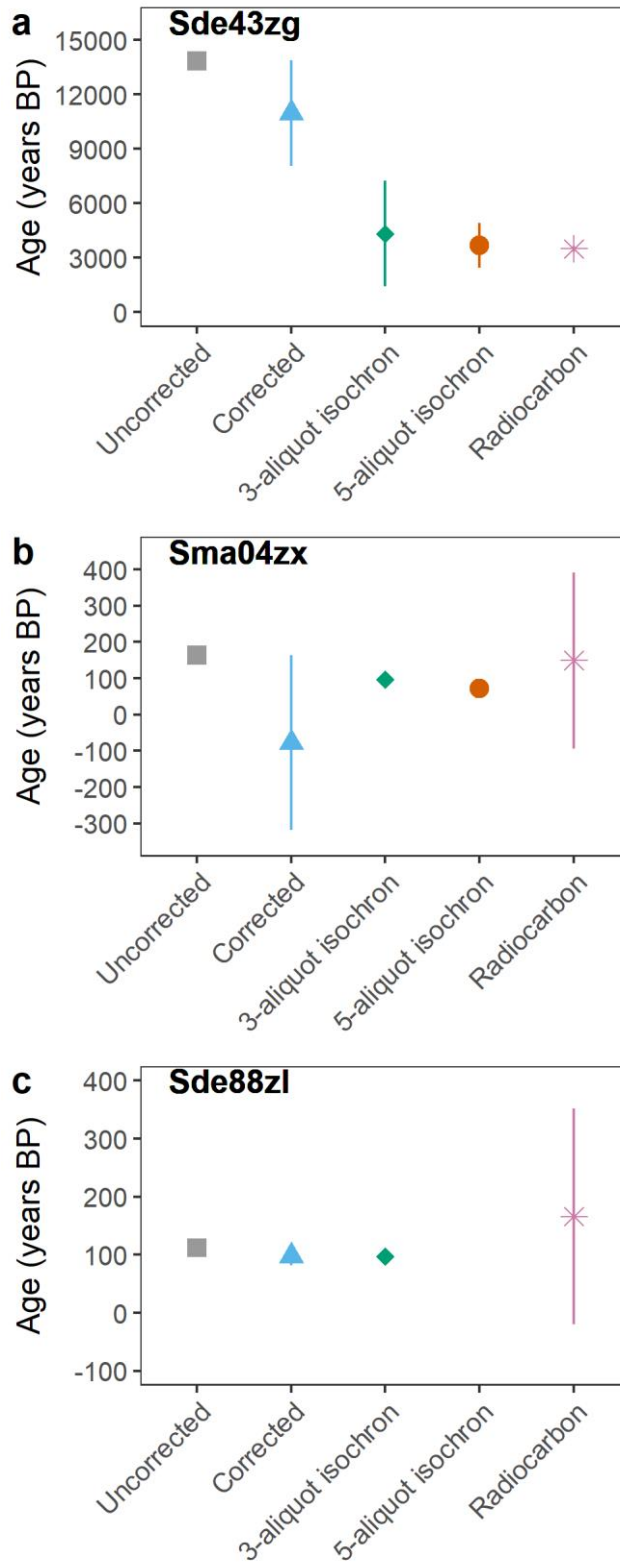
Figure 9. Comparison of radiometric dating techniques applied to samples Sde43zg, Sma04zx and Sde88zl. Uncorrected = U-series age of the Clean aliquot uncorrected for initial ^{230}Th. Corrected = U-series age of the Clean aliquot corrected for initial ^{230}Th assuming commonly applied $[^{230}\text{Th}/^{232}\text{Th}]_i$ ratios (see section 2.4). Radiocarbon ages have been corrected and calibrated (see section 2.6). No 5-aliquot isochron age was obtained for sample Sde88zl (see section 3.2.2). All error bars are ± 2 σ.

3.3 Radiocarbon subsampling experiments

In addition to U-series experiments, I also subsampled 4 corals to study variations in subsample geochemistry including radiocarbon content, Li/Mg, Ba/Ca and $\delta^{11}B$. I present these results in the following sections, before the development of radiocarbon age models is discussed for each sample in turn in section 5.1. The conversion of coral geochemistry to reconstructed hydrographic parameters is discussed for sample Adp88 in section 5.3 (Figure 16).

3.3.1 Coral subsampling: radiocarbon

Subsample conventional ^{14}C ages for each of the four corals analysed for ^{14}C growth chronologies are shown in Figure 10, and tabulated in the supplementary information (section 7.2; Supplementary table 2). For sample Adp88, conventional ^{14}C ages are strongly, linearly correlated with distance along the branch, with ages decreasing toward the branch tip (Figure 10; $R^2 = 0.82$; $p = 0.03$; Table 6). Excluding the tip sample from the regression analysis improves model fit slightly, although at the cost of some significance ($R^2 = 0.86$; $p = 0.07$; Table 6). Calculating growth rate using all samples yields a slightly faster growth rate (0.58 mm/year) than when excluding the tip sample from regression (0.42 mm/year; Table 6). The ^{14}C ages of the tip subsample (738 ± 25 years) and subsample taken furthest from the tip (796 ± 25 years) are within error of one another at the 2 σ level. Calculating the rate of branch extension using these two subsamples in isolation suggests a faster growth rate (0.85 mm/year) than implied by the fit through all measured subsamples. The maximum possible growth rate calculated using the bounds of the 1 σ error envelopes of the base and tip subsamples suggests a growth rate > 6 mm/year. The ^{14}C age of the branch tip is older than, but within error of, that of modern seawater (Figure 10; Table 6).

For sample PS3225, conventional ^{14}C ages are again linearly correlated with distance along the branch, although with more scatter and lower significance (Figure 10; $R^2 = 0.61$; $p = 0.12$; Table 6). One sample (at ~ 9 cm from the branch end) is responsible for much of the scatter about this line, and removing this sample from the regression analysis results in an extremely strong and more significant fit (Figure 10; $R^2 = 0.98$; $p = 0.01$; Table 6). All ^{14}C subsample ages are significantly older than the modern, depth-matched seawater radiocarbon age (Table 6). However, all but one subsamples have ^{14}C ages which are younger than the range of nearby estimates of pre-bomb surface ocean reservoir ages (Figure 10). Interpretation of growth rate in this sample – and subsequent construction of a growth chronology – is likely to be complicated (section 5.1.2).

All subsamples of the 2 live-collected *Stephanohelia sp.* samples from New Caledonia have conventional ^{14}C ages < − 200 years BP (Figure 10). The ^{14}C age of the tip subsample from coral 3403B is significantly less negative than ambient seawater (Figure 10). Growth chronologies are not presented here for these samples, and their ^{14}C ages are discussed in more detail in section 5.1.3.

Sample	Regression model	Growth rate ± 2 SE (mm/year)	¹⁴C branch end age ± 2 SE (years BP)	Calendar year at branch end	R²	p	Modern seawater ¹⁴C age ± 2 σ (years BP)
Adp88	All samples	0.58 ± 0.31	716 ± 562	2013	0.82	0.03	685 ± 196
	Excluding tip	0.42 ± 0.24	686 ± 586		0.86	0.07	
PS3225	All samples	0.43 ± 0.40	155 ± 332	Unknown	0.61	0.12	− 720 ± 67
	Excluding sample @ ~ 9 cm along branch	0.53 ± 0.11	203 ± 83		0.98	0.01	

Table 6. Summary of linear regression (distance along branch vs conventional ¹⁴C age) for samples Adp88 and PS3225. Modern seawater ¹⁴C ages estimated as outlined in section 2.6.
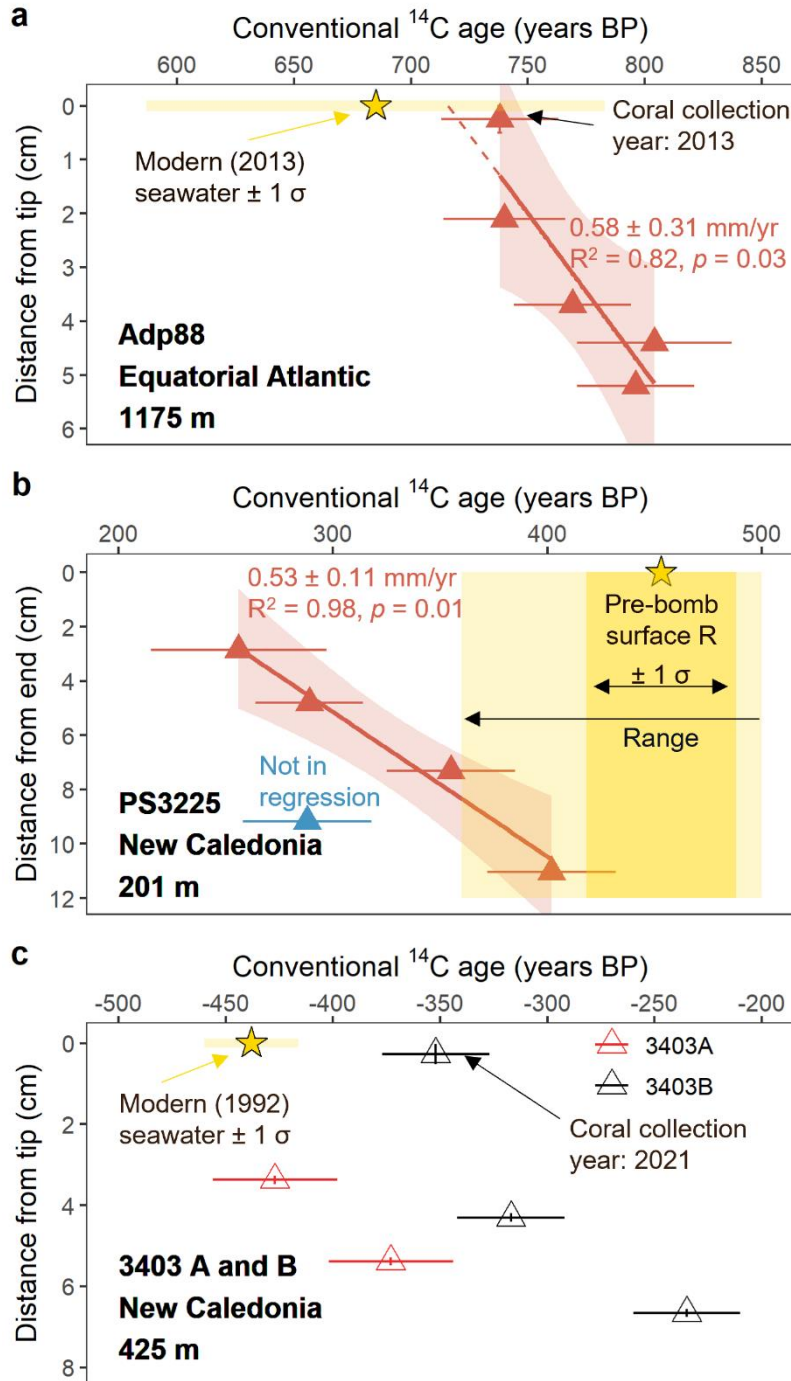
Figure 10. Distance along branch (measured from the youngest end) as a function of conventional ^{14}C age for samples Adp88 (a), PS3225 (b) and 3403A and 3403B (c; same panel, note these represent 2 corals collected from the same location (see Figure 3)). Note that the tip of the branch used for sample PS3225 was not present (see Figure 3). Error bars on ^{14}C ages are ± 1 σ, distance error bars show sample thickness (2 mm except for tip subsamples which are 5 mm). Gold stars represent best-estimate seawater ^{14}C ages for panels a (Chen et al., 2015) and c (GLODAP: Lauvset et al., 2022), shaded bar represents variability (± 1 σ) assessed from nearby GLODAP stations (Lauvset et al., 2022; section 2.6). Pre-bomb surface reservoir age shown for panel b with variability shown as ± 1 σ (dark shading) and range (light

shading) (see section 2.6 for data sources and calculation details). Ordinary least squares regression lines shown for panels a and b, shading denotes 95 % confidence interval.

3.3.2   Coral subsampling: Li/Mg, Ba/Ca and δ^{11}B

I also present variations in subsample Li/Mg, Ba/Ca and δ^{11}B ratios for coral Adp88 (Equatorial Atlantic, 1175 m depth), with the aim of reconstructing seawater temperature, [Ba]$_{sw}$ and pH, respectively. Subsample Li/Mg, Ba/Ca and δ^{11}B ratios were also measured on corals PS3225, 3403A and 3403B (tabulated in the supplementary information; section 7.2; Supplementary table 2), however these ratios are not discussed further for reasons outlined in the discussion (see section 5).

Focusing on sample Adp88, subsample Li/Mg, Ba/Ca and δ^{11}B ratios are presented in Figure 11. Coral Li/Mg decreases by ~ 0.4 mmol/mol from the oldest to youngest subsample, and is correlated with distance from the branch tip at the 90 % significance level ($r = 0.73$, $p = 0.06$; Figure 11). Most of the change in Li/Mg occurs in the interval between the tip and next youngest subsample. Subsample Ba/Ca exhibits no significant trend along the branch length ($r = 0.21$, $p = 0.65$). Finally, coral δ^{11}B decreases slightly from the oldest sample to the youngest by ~ 0.2 ‰. However, the δ^{11}B of these samples are within error of one another, and the correlation between coral δ^{11}B and distance along the branch measured from the growing tip is insignificant at the 90 % level ($r = 0.65$, $p = 0.12$; Figure 11).

Apical tip Li/Mg and δ^{11}B are within error of the values expected based on modern ambient seawater temperature and δ^{11}B$_{borate}$, when established calibrations are applied (see section 2.7) (Figure 11). However, apical tip Ba/Ca is significantly elevated compared with the value expected from ambient [Ba]$_{sw}$ (Figure 11).
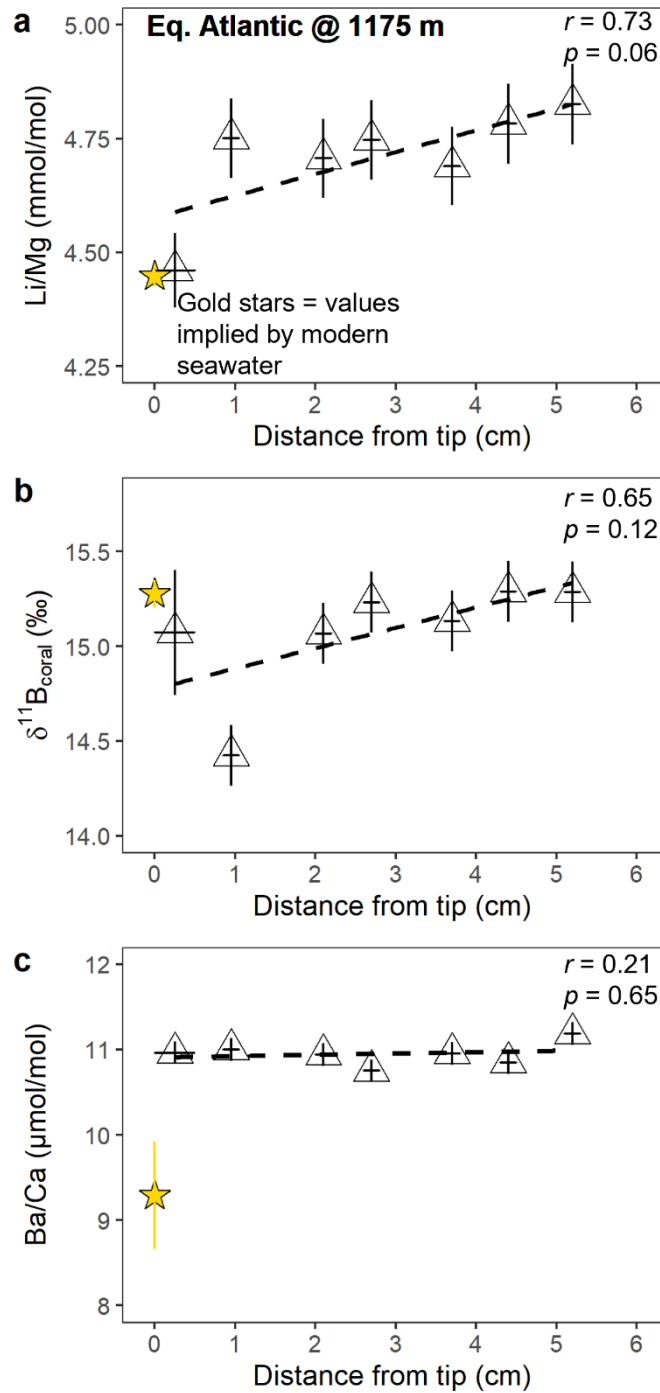
Figure 11. Coral Li/Mg (a), δ^{11}B (b) and Ba/Ca (c) as a function of distance from branch tip for sample Adp88 (Equatorial Atlantic, 1175 m depth). Dashed lines show results of Ordinary Least Squares regressions. Vertical error bars are analytical uncertainties on coral geochemistry ($\pm$ 2 σ), horizontal error bars are along-branch subsample thickness (5 mm for apical tip sub sample, 2 mm for all others). Yellow stars in a, b and c show values of coral geochemistry expected from modern ambient seawater temperature, seawater $\delta^{11}B_{borate}$ and $[Ba]_{SW}$, respectively, using the calibrations outlined in section 2.7 ($\pm$ 2 σ). Seawater temperature and $\delta^{11}B_{borate}$ taken from the GLODAP bottle database (Lauvset et al., 2022), $[Ba]_{SW}$ from Bates et al. (2017). See section 2.8 for full details of hydrographic variable estimation and error estimation.

4. Discussion: Challenges of U-series dating of stylasterids

Application of established U-series techniques to stylasterids yields ages which have, in some instances, uncertainties far exceeding 100 % of the coral age (Table 3; Figure 6). Additionally, ages derived by this approach can differ significantly from those calculated by radiocarbon and isochron methods (Table 4; Figure 9). The following section addresses the reasons for these observations. In short, the precision and accuracy of stylasterid U-series dates are limited by low skeletal [U], which results in small amounts of radiogenic ^{230}Th production. This is coupled with the generally porous nature of stylasterid skeletons, which results in an inherent susceptibility to contamination by Th-bearing phases. Together, these two factors mean that accurate correction for initial/added ^{230}Th has a far greater impact when dating stylasterid corals, compared with scleractinian corals.

4.1 Stylasterid skeletal [U] and [^{232}Th]

One of the primary controls on the accuracy and precision of azooxanthellate coral U-series ages is the relative proportions of radiogenic (the fraction of interest) and added/initial ^{230}Th, which together form the total measured ^{230}Th (e.g. Cheng et al., 2000a). It has long been recognised that in many carbonate materials, initial/added ^{230}Th is non-negligible, and needs to be accounted for (e.g. Bischoff and Fitzpatrick, 1991; Cheng et al., 2000a; Edwards et al., 2003; Richards and Dorale, 2003; see equation 3). When dating azooxanthellate corals, the uncertainty in this correction contributes substantially to the error in final calculated ages.

Inspection of equation 3 illustrates that as measured coral [^{232}Th/^{238}U] increases, so does the impact of correction for initial/added ^{230}Th, and thus the precision of the calculated age decreases. For this reason, high skeletal [^{238}U] and low [^{232}Th] are commonly used as quality control indicators when dating scleractinian corals (e.g. de Carvalho Ferreira et al., 2022; Figure 5).

In these respects, stylasterids are poorly suited to U-series dating compared with scleractinian corals (Figure 5). Stylasterid skeletal [^{238}U], firstly, is significantly lower than azooxanthellate scleractinian [^{238}U] (Figure 5). The samples used in this study also have relatively high [U] compared with most aragonitic stylasterids, illustrated by comparison of their U/Ca ratios with previously measured live stylasterids (Stewart et al., 2022; chapter 4) (Figure 5). The samples used here thus likely represent something of a best-case scenario in this context. The origin of low stylasterid skeletal U/Ca compared with azooxanthellate Scleractinia has been attributed to differences in their calcification mechanisms, with stylasterids employing little pH-upregulation during calcification (see Stewart et al., 2022; chapter 4). It is notable that aragonitic stylasterid [^{238}U] is still around an order of magnitude higher than that reported for calcitic octocorals (e.g. Gutjahr et al., 2013), suggesting that aragonitic stylasterids may be better suited to U-series dating than calcitic coral taxa. Although I did not measure any high-Mg calcitic stylasterids here, their low U/Ca compared with their aragonitic counterparts suggest they would be more poorly suited to application of U-series techniques (Stewart et al., 2022; chapter 4).

In addition to low [^{238}U], the data suggest that stylasterid skeletons are particularly susceptible to contamination by Th-bearing phases. 4 of the 8 stylasterid samples measured here have [^{232}Th] which exceeds 3 ppb, and the average stylasterid [^{232}Th] presented here is higher than that generally reported for scleractinian datasets (e.g. de Carvalho Ferreira et al., 2022) (Figure 5). The small number of samples prevents statistically robust quantification of this observation. However, I suggest that the architecture of stylasterid skeletons means it is likely they are more susceptible to contamination than scleractinian corals.

Stylasterid skeletons can be extremely porous, being composed of a number of channels which connect the skeleton interior to the surface (e.g. Moseley, 1878). When the coral is alive, these channels are filled with organic coral tissue, which will decay postmortem. This decay could lead to U and Th being complexed from the surrounding fluids, and has been linked to elevated skeletal ^{232}Th in shallow water scleractinian corals (e.g. Tomiak et al., 2016; supplementary information, section 7.4). Additionally, the flushing of seawater through these channels after death may lead to addition of Th-bearing phases such as clays. Cross sections of stylasterid skeletons reveal clear evidence of contaminant phases embedded within the skeletal framework (supplementary information, section 7.4) which are difficult to clean mechanically. This is important because the mechanical cleaning step appears to be the most important, resulting in the largest decrease in [^{232}Th] of all the cleaning steps employed (Figure 7), a finding which agrees well with previous work (van de Flierdt et al., 2010). The position of these contaminant phases within the skeleton also means that the standard approach of chemically cleaning chunks of coral (i.e. the Clean aliquot; see section 2.2.1) does not guarantee exposure to chemical cleaning reagents. Crushing samples prior to chemical cleaning may increase exposure to cleaning reagents, although the efficacy of this technique in our sample set is not seen in every sample. For sample Sde43zg, the Crush-clean aliquot exhibited a substantial reduction in [^{232}Th] compared with the Clean aliquot (~ 2 ppb compared with ~ 3 ppb) (Figure 7). For the other 2 corals, Crush-clean aliquots showed higher [^{232}Th] than the Clean aliquots, although all aliquots had low [^{232}Th] (< 1 ppb) (Figure 7; Supplementary table 1).

Stylasterid species evidently vary in their macroscale porosity, meaning some species may be less susceptible to post-mortem contamination by Th-bearing phases than others. Is notable that I here targeted specimens which did not display significant macroscale porosity (e.g. Supplementary figure 1), and yet still observe evidence for increased susceptibility to contamination in comparison to scleractinian corals. Microscale porosity is likely the more relevant consideration here, as contamination on smaller spatial scales is the most difficult to remove mechanically. Unfortunately, the small number of species represented in our sample set precludes an assessment of which species are most suitable for U-series dating. However, it is likely that some species will be more suitable than others, and assessing sample porosity prior to analysis may represent a method by which to select the most promising samples.

Thus, in comparison to scleractinian corals, stylasterids have lower skeletal [^{238}U], and may be more susceptible to contamination by Th-bearing phases. Together, these two factors result in stylasterid [^{232}Th/^{238}U] being – in general - higher than scleractinian [^{232}Th/^{238}U]. This increases the importance of

the correction for initial/added ^{230}Th, and in turn decreases the achievable precision of stylasterid U-series ages. Despite this, accurate correction for initial/added ^{230}Th may still yield ages with precision sufficient to be useful in certain palaeoceanographic contexts. In the following sections, I explore two possible correction methods, before making recommendations for best practise when dating stylasterids by U-series methods.

4.2   Correction for [^{230}Th/^{232}Th]$_i$

The commonly-applied method for correcting for initial/added ^{230}Th in azooxanthellate scleractinian corals relies on subtracting an initial [^{230}Th/^{238}U]$_i$ term from that measured on the sample. [^{230}Th/^{238}U]$_i$ is estimated by multiplying measured sample [^{232}Th/^{238}U] by an assumed [^{230}Th/^{232}Th]$_i$ value (equation 3). As outlined in section 1.1, these [^{230}Th/^{232}Th]$_i$ estimates are highly uncertain, but for scleractinian corals with high [U] and low [^{232}Th], the magnitude of the correction is small enough to permit dating to a precision suitable for studying centennial and millennial shifts in ocean conditions (e.g. Chen et al., 2015; Rae et al., 2018; Stewart et al., 2021; Chen et al., 2023).

However, application of this method to stylasterids illustrates the complications imposed by low stylasterid skeletal [U] and high [^{232}Th]. The correction for initial ^{230}Th results in a substantial reduction in calculated age and increase in age uncertainty for almost all of the stylasterid samples considered here (Table 3; Figure 6). For 4 of the 8 samples, the substantial effect of the ^{230}Th correction may be partly explained by high levels of initial/added Th, reflected in their elevated [^{232}Th] (Figure 5). Considering the 4 samples with [^{232}Th] less than the screening limit used in de Carvalho Ferreira et al. (2022), the corrected age for one sample (Sma04zx) is a negative age, 2 samples have ages ~ 100 years BP with uncertainties of between 20 and 50 years (Sde88zl and Sde134zv), while another (Sde43zg) has an age of ~ 10,000 ± 3000 years BP (Table 3).

The age precision of these low ^{232}Th stylasterid samples suggests that application of U-series dating techniques to stylasterids could have use in a variety of palaeoceanographic contexts. However, precision is no guarantee of accuracy. To test whether the above approach yields accurate ages, I performed additional isochron and radiocarbon measurements on three corals (Figure 9). An isochron approach permits sample-specific estimates of [^{230}Th/^{232}Th]$_i$, allowing assessment of whether commonly-assumed values are appropriate for our samples, and thus whether the traditionally-applied approach yields accurate ages. The details of the isochron approach are discussed further in section 4.3, and I here focus solely on comparison of ages derived by these different approaches.

The 3 methods (traditional [^{230}Th/^{232}Th]$_i$ correction, isochron and radiocarbon) yield consistent ages for sample Sde88zl (Figure 9). Despite this, the [^{230}Th/^{232}Th]$_i$ of the 3-aliquot isochron approach differs markedly from that commonly assumed (4 and 37, respectively; Table 4). However, this sample has extremely low [^{232}Th], meaning the effect of correction for [^{230}Th/^{232}Th]$_i$ is small, thus demonstrating that extremely clean stylasterid samples can be accurately dated without sample-specific constraint on

$[^{230}Th/^{232}Th]_i$. This is not true, however, for samples Sma04zx and Sde43zg. For both samples, an isochron approach provides sample-specific estimates of $[^{230}Th/^{232}Th]_i$ (~ 30 and ~ 100, respectively; Table 4) which differ substantially from the commonly-applied regional estimates used in the calculation of corrected ages of the Clean aliquots (91.4 and 37, respectively; see section 2.4). As a result of the correction for initial ^{230}Th in these samples, the ages derived from the isochron approach also differ substantially from the corrected Clean aliquot ages. For sample Sde43zg, the magnitude of the difference is > 6000 years, and concerningly far exceeds the error estimate on the corrected Clean aliquot age (Figure 9). Crucially, independent radiocarbon constraint on sample ages suggests that the isochron ages are the more accurate estimate of the two (Figure 9). Both of these samples therefore indicate that even for stylasterid samples with relatively high [U] (compared with other stylasterids) and which have been effectively cleaned (giving low $[^{232}Th]$), it is still critically important to accurately constrain sample-specific $[^{230}Th/^{232}Th]_i$. Using regional estimates of this value holds no guarantee of accuracy, as reflected in the large uncertainties commonly associated with these values, and the large range in $[^{230}Th/^{232}Th]_i$ reported by previous azooxanthellate coral studies (e.g. Cheng et al., 2000a; Gutjahr et al., 2013).

4.3   Challenges with the isochron approach

Any approach to stylasterid dating must therefore consider methods to more accurately estimate $[^{230}Th/^{232}Th]_i$. As alluded to above, isochrons provide one method by which this constraint can be achieved. Isochron methods have previously been applied to estimate $[^{230}Th/^{232}Th]_i$ and derive sample ages for a variety of carbonate materials (e.g. Luo and Ku, 1991; Lomitschka and Mangini, 1999; Cheng et al., 2000a; Shen et al., 2008; Obert et al., 2016; Wang et al., 2022). While an isochron approach may hold promise when dating stylasterids, the observations made here suggest that its application is challenging.

The most widely applied regression tool for generating U-series isochrons is the analytical error-weighted, 3-dimensional maximum likelihood technique (Ludwig and Titterington, 1994). Application of this method to our data yields lines of best fit which are significantly overdispersed (MSWD >> 1; see section 2.4; Table 4). An MSWD > 1 indicates that the scatter about an isochron line of best fit cannot be accounted for by analytical uncertainties alone. Although this overdispersion could be caused by underestimation of analytical uncertainties, I am confident in the uncertainty estimates made and thus discount this possibility. Alternatively, a high MSWD indicates the influence of factors not accounted for in the isochron model.

U-series isochrons are formulated on the assumption that each aliquot contains varying proportions of two components with distinct $[^{232}Th/^{238}U]$, but the same $[^{230}Th/^{232}Th]_i$ (e.g. Ludwig and Titterington, 1994; Edwards et al., 2003). Introduction of a third (or more) isotopically-distinct component violates the isochron assumption, and has been proposed to explain isochron scatter for a variety of sample types (e.g. Lin et al., 1996; Henderson et al., 2001; Richards and Dorale, 2003; Shen et al., 2008).

Evidence for more than 2 isotopically-distinct components in our samples comes from comparing the results of the 3- and 5-aliquot datasets. The 3-aliquot approach includes samples subjected to at least mechanical cleaning, while the 5-aliquot approach additionally includes the entirely uncleaned and outer coating sample. For the two corals for which both approaches yielded reasonable results (Sma04zx and Sde43zg), the 5-aliquot approach gives younger ages, and a higher implied $[^{230}Th/^{232}Th]_i$ (Table 4). The consistency of the observed offsets for both samples is striking, and suggests that a component with increased $[^{230}Th/^{232}Th]$ is contributing to the coating and uncleaned samples, compared with those samples cleaned at least mechanically. This is supported by sample Sde88, for which the $[^{230}Th/^{232}Th]$ of the uncleaned and outer coating samples is significantly higher than the $[^{230}Th/^{232}Th]_i$ expected from extrapolation of the 3-aliquot isochron line of best fit (Figure 8). For the 5-aliquot approach, this ultimately results in a negative relationship between $[^{230}Th/^{232}Th]$ and $[^{238}U/^{232}Th]$, thus preventing calculation of a reasonable age (Figure 8; Table 4).

The outer coatings of all samples measured here are thus enriched in ^{232}Th compared with bulk skeletal material. Together, these represent 2 isotopically-distinct components. I suggest that organic matter may represent a third source of U-series isotopes. As outlined in section 4.1, organic matter is more likely to be trapped in spaces within the stylasterid skeleton, given their porosity. This organic matter likely represents a source of Th, evidenced by the reduction in $[^{232}Th]$ following chemical cleaning which was observed for all samples (Figure 7). It is entirely plausible that the isotopic composition of this organic matter differs to that of the outer coatings and initial Th incorporated into the coral skeleton (supplementary information, section 7.4). Indeed, Th-isotopic heterogeneity has been noted between a wide range of particle sources, including clays, organic matter and Fe-Mn oxyhydroxides (e.g. Richards and Dorale, 2003).

The origin of overdispersion in our stylasterid isochrons thus appears to be the contribution of three or more isotopically-distinct sources of U-series isotopes. Isochron techniques can be adapted to account for this overdispersion, and here I calculate isochron ages and their uncertainties by adding an additional dispersion term to analytical uncertainties, with dispersion attributed entirely to the $[^{230}Th/^{232}Th]$ of added/initial Th (IsoplotR, model 3; Vermeesch, 2018). In this manner, meaningful isochron ages and uncertainties can be generated for stylasterid coral samples. More broadly, an isochron approach allows for sample-specific constraint on $[^{230}Th/^{232}Th]_i$, removing the need to assume this value and providing some assurance of the accuracy of calculated ages.

4.4 $\delta^{234}U_i$ and susceptibility to alteration

An aspect of U-series dating yet to be discussed is the requirement that the system remains closed with respect to U from the time of coral death to measurement (e.g. Edwards et al., 2003). Indeed, the porous nature of stylasterid skeletons discussed above may act to increase the likelihood of post-mortem carbonate alteration and thus open-system U behaviour, which apparently complicates U-series dating of octocoral taxa (e.g. Robinson et al., 2007; Gutjahr et al., 2013; see supplementary information, section

7.4). As outlined in chapter 2, a common test for open-system behaviour is whether sample $\delta^{234}U_i$ falls within the bounds of modern seawater (e.g. Cheng et al., 2000a; Edwards et al., 2003; see chapter 2). Encouragingly, $\delta^{234}U_i$ for 7 of the 8 stylasterid samples measured was within 6 ‰ of the modern seawater value (146.8 ‰; Andersen et al., 2010; Figure 6). However, the oldest sample measured had significantly higher $\delta^{234}U_i$ than expected (Figure 6). The measured $\delta^{234}U_m$ of this sample was close to modern seawater, consistent with addition of U with a modern isotopic signature and providing strong evidence for open-system behaviour in this sample. With only one sample of significant age (i.e. > 10,000 years) in our dataset, the susceptibility of stylasterids to post-mortem diagenesis and open-system U behaviour remains an open question. However, their porosity and evidence for increased susceptibility to contamination (section 4.1; supplementary information, section 7.4) suggests this may represent an additional limiting factor in our ability to date these corals by U-series methods.

4.5   A practical U-series dating outlook

Low stylasterid [U] – coupled with their susceptibility to contamination by Th-bearing phases – means the achievable precision of stylasterid U-series dates is not as good as for scleractinian corals. That their low [U] in comparison to Scleractinia arises from the differing calcification mechanisms of these two groups is somewhat ironic, given those same differences in biomineralisation apparently make stylasterids comparatively reliable recorders of past ocean conditions (Samperiz et al., 2020; Stewart et al., 2020b; Stewart et al., 2022; chapter 3; chapter 4). Determination of sample-specific $[^{230}Th/^{232}Th]_i$ can aid the measurement of accurate stylasterid U-series ages, and isochron approaches provide a potential – if time consuming – means to achieve this. In practical terms, however, the attractiveness and applicability of isochron dating may be limited by small sample sizes, the large time burden associated with making multiple measurements, and significant overdispersion. Without determination of sample-specific $[^{230}Th/^{232}Th]_i$, accuracy of ages is dependent on achieving a small magnitude of initial ^{230}Th correction, which may be achieved through careful sample selection and cleaning.

In many cases, however, it will be necessary to accept that stylasterid U-series ages are inherently uncertain. I suggest that stylasterid dates presented without qualification of sample-specific $[^{230}Th/^{232}Th]_i$ should consider the potential effect of a wide range of possible $[^{230}Th/^{232}Th]_i$, and could present a range of possible ages in addition to a best-estimate. In this way, stylasterid U-series ages could be used in a robust manner to investigate scientific questions which do not require great age precision, such as shifts in stylasterid distribution or changes in ocean conditions on long (e.g. glacial-interglacial) timescales (e.g. following themes in Frank et al., 2011; Corbera et al., 2021; de Carvalho Ferreira et al., 2022).

5   Discussion: Radiocarbon growth chronologies

Given the difficulties associated with U-series dating stylasterid skeletons, I also explore the possible use of stylasterids as high-resolution archives of recent oceanographic change. This exploration is primarily motivated by previous work which demonstrated that ^{14}C dating multiple subsamples from the same

specimen can produce coherent stylasterid growth chronologies spanning centennial timescales (King et al., 2018). I explore this theme further here, coupled with the application of recent proxy developments (Stewart et al., 2020b; chapter 3; chapter 4).

5.1   Stylasterid [14]C: growth chronologies

The following sections outline and interpret the ^{14}C-based growth chronologies of samples Adp88, PS3225, 3403A and 3403B. At the start of each section, the relevant distance vs ^{14}C age plot is reproduced from Figure 10 for ease of reference, together with an additional plot showing contextual seawater data (Figure 12; Figure 13; Figure 14).

5.1.1   Sample Adp88 (Equatorial Atlantic, 1175 m)
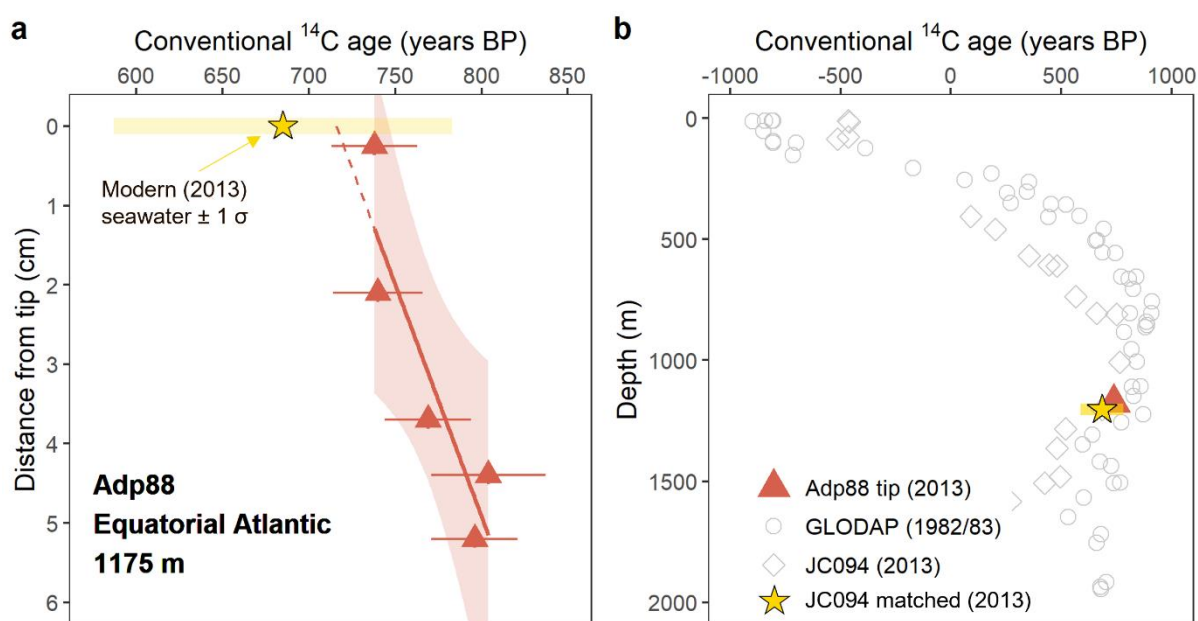
Figure 12. a. Distance along branch vs conventional ^{14}C age for sample Adp88, reproduced from Figure 10. b. Comparing Adp88 apical tip ^{14}C age (red triangle) to seawater conventional ^{14}C ages calculated from nearby GLODAP Δ^{14}C measurements (grey circles; Lauvset et al., 2022) and taken from published bottle data collected during CTD and ROV deployments during cruise JC094 (grey diamonds; Chen et al., 2015; note sample Adp88 was also collected during cruise JC094). The chosen paired seawater value is shown by the gold star in both panels ($\pm$ 1 σ). Error bars on ^{14}C ages are $\pm$ 1 σ, and are smaller than the symbol in panel b.

For sample Adp88, firstly, the linear correlation between conventional ^{14}C age and distance along the branch suggests a broadly constant rate of vertical extension of between 0.4 and 0.6 mm/year, dependent on whether the apical tip subsample is included in the regression (Figure 10; Figure 12; Table 6).

The apical tip subsample has a conventional ^{14}C age which is slightly older than that estimated for ambient seawater (Figure 10; Figure 12). This may be explained by a combination of the sampling strategy and recent trends in ambient seawater conditions at this site. At a coral growth rate of 0.5 mm/year, the 5

mm along-branch thickness of the tip subsample (note all other subsamples were 2 mm thick; section 2.2.2) represents ~ 10 years of coral growth, meaning much of the subsample grew prior to the coral collection year (2013). This temporal integration acts to make the tip subsample ^{14}C age older than seawater at the time of collection. This evidently cannot explain the full ~ 50 year difference between tip subsample age and seawater. However, this trend may be compounded by recent changes in the ^{14}C content of seawater at this site. It has been shown that the ^{14}C age of seawater at this depth in the equatorial Atlantic has become younger over the past 30 years, likely due to the very recent first incursion of bomb-derived ^{14}C at intermediate depths in this region (Liu, 2022). This observation may be seen by comparison of seawater data from the GLODAP database (sampled in 1982 and 1983; Lauvset et al., 2022) and that collected during cruise JC094 in 2013 (Chen et al., 2015) (Figure 12). Thus, not only does the tip subsample incorporate carbonate material which is older than the coral collection year, but ambient seawater ^{14}C age may also have been older at this time. Together, these factors provide a likely explanation as to why the tip subsample ^{14}C age is older than that expected from modern ambient seawater.

An alternative possibility which could explain the faster inferred growth rate when including the apical tip sample in regression analysis (Table 6) is that specimen growth rate increased toward the branch tip. However, this interpretation would require an increase from 0.42 mm/year to almost 1 cm/year. A growth rate of 1 cm/year exceeds the maximum range of previously published stylasterid growth rates (see section 5.2; Table 7), and it also seems unlikely that such a vast change in growth rate would occur within a single coral.

The tip subsample ^{14}C age falls within the estimated variability in ambient seawater ^{14}C values (at the 1 σ level) and overall appears to faithfully record the ^{14}C signature of ambient seawater (Figure 10; Figure 12). Further, while I find a faster inferred growth rate when the tip sample is included in the regression than when it is excluded (0.58 mm/year vs 0.42 mm/year; Table 6), these estimates are again within error of one another (at the 2 σ significance level; Table 6). The choice of whether to include the tip subsample in calculations is therefore inconsequential to the conclusions of this study.

The above discussion also highlights some of the uncertainties implicit in the sampling methodology employed here. As outlined in section 3.3.1, calculating a growth rate using only the ^{14}C ages of the branch tip and the subsample furthest from the tip suggests a faster growth rate (0.85 mm/year) than that calculated using all subsamples. Additionally, the ^{14}C ages of the branch tip and subsample furthest from the tip are within error of one another at the 2 σ level. This suggests that the coral growth rate calculated here is poorly constrained and may underestimate the true rate of vertical branch extension. However, as discussed above, individual subsample ^{14}C ages may be affected by incorporation of material of varying ages, changes in ambient seawater ^{14}C age and temporal changes in coral growth rate, as well as analytical uncertainties (generally ± 25 years on all samples). By using multiple subsamples to calculate the average coral growth rate, the effects of analytical uncertainties and incorporation of material of varying ages can

be somewhat reduced, since these factors should affect all subsamples in a similar manner. Thus, while it is possible that coral Adp88 grew faster than 0.58 mm/year, the strength and significance of the correlation between all subsample ^{14}C ages suggests that this remains the best, and most robust, estimate of coral growth rate for this sample.

I therefore assume that coral Adp88 grew linearly and at a constant growth rate constrained by all 5 measured subsamples. With knowledge that the sample was collected alive in the year 2013, I use the inferred coral growth rate to assign a calendar age to each subsample (note that ages are assigned at the midpoint of each subsample), and construct an absolute age model for this specimen (Figure 16; full data tabulated in the supplementary information, Supplementary table 2). This methodology suggests the subsamples measured here grew across the period 1924 to 2013, and thus that this coral may represent a valuable record of changes in intermediate-depth (1175 m) equatorial Atlantic conditions across much of the 20th century. This possibility is explored in section 5.3.

5.1.2 Sample PS3225 (New Caledonia, 201 m)

Turning to sample PS3225, I again find a linear correlation between conventional ^{14}C age and distance along the branch (Figure 10; Figure 13; Table 6). One sample falls off the trend of decreasing age with decreasing distance from the branch end (Figure 10; Figure 13). Removing this sample from the regression results in an extremely strong linear correlation with high significance ($R^2 = 0.98$, $p = 0.01$; Table 6). The interpretation of these results is, however, complicated.
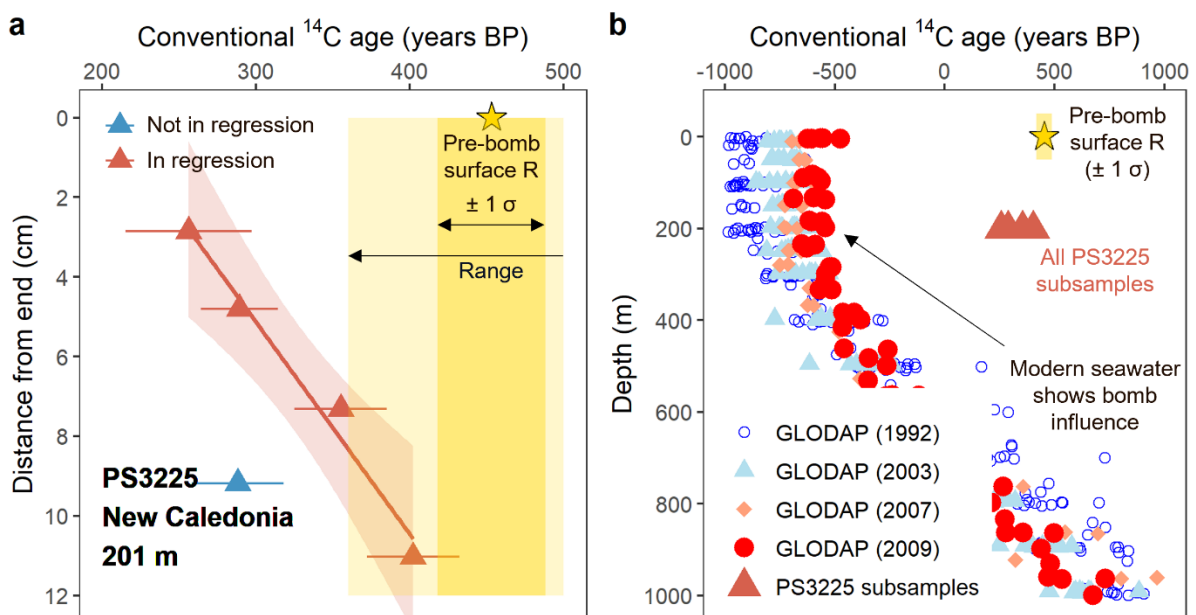
Figure 13. a. Distance along branch vs conventional ^{14}C age for sample PS3225, reproduced from Figure 10. b. Comparing PS3225 subsample ^{14}C ages (red triangles) to seawater conventional ^{14}C ages calculated from nearby GLODAP Δ^{14}C measurements (Lauvset et al., 2022). Note seawater measurements are distinguished by collection year, discussed in section 5.1.3. The chosen paired seawater value is shown by the gold star in both panels (± 1 σ). Pre-bomb surface reservoir age shown in both panels, with

Firstly, this coral was dead on collection, meaning that – in contrast to sample Adp88 - I do not have independent age control on any part of the skeleton. An alternative approach to converting ^{14}C ages to absolute calendar ages is to estimate a seawater radiocarbon age for the collection location, and subsequently calibrate these ages against the Marine20 curve (Heaton et al., 2020; see section 2.5).

Modern depth-matched seawater conventional ^{14}C age is estimated from the GLODAP database to be − 720 ± 67 (2 σ) years BP (Figure 13; Table 6; Lauvset et al., 2022), reflecting the clear influence of bomb-derived radiocarbon at this site. Subsample radiocarbon ages are significantly older than this, suggesting this sample grew before the influence of substantial incursion of bomb-derived [14]C (Figure 10; Figure 13). Deriving estimates of pre-bomb seawater radiocarbon ages is complicated by a paucity of data at depth. However, surface ocean pre-bomb reservoir ages are more abundant, and - assuming that seawater radiocarbon ages increase with depth - can be used to estimate a minimum pre-bomb seawater radiocarbon age for this sample. The pre-bomb surface ocean reservoir age for this region averages 453 ± 35 years BP (1 σ; n = 33), with individual values ranging from 360 to 680 years BP (Figure 10; Figure 13). The geographically closest measurements (from New Caledonia) suggest a reservoir age of ~ 485 years BP, although this study emphasises the large regional variability caused by seasonal variations in upwelling (Petchey et al., 2004).

Subsample ^{14}C ages from coral PS3225 are in the most part younger than pre-bomb surface reservoir age values (Figure 10; Figure 13). The most likely explanation for these young ^{14}C ages is the influence of bomb-derived [14]C. Additional evidence for the contribution of bomb-derived ^{14}C comes from measurements on an outer portion of the radial section from which the oldest subsample (PS3225.radC) was taken (see supplementary information, section 7.5). This outer rim subsample has a conventional ^{14}C age of 83 years BP (Supplementary figure 5; Supplementary table 2), significantly younger than any reasonable marine reservoir age, thus strongly implying some influence of bomb-derived [14]C (see supplementary information, section 7.5).

The interpretation of a ^{14}C chronology for sample PS3225 depends on the mechanism by which bomb-derived ^{14}C contributes to measured ages. One option is that this coral records the gradual incursion of bomb radiocarbon at this site. Inspection of Figure 10 (and excluding the outlier subsample) reveals that the range of pre-bomb surface reservoir ages was first exceeded at 7.2 cm from the branch end, with the last measured subsample being at 2.8 cm. This model therefore requires that this coral grew at least 4.4 cm in the time after the initial incursion of bomb-^{14}C at this site, but before seawater Δ^{14}C became negative. An estimate of bomb-derived radiocarbon incursion in New Caledonian waters at ~ 200 m depth suggests that Δ^{14}C signatures (and thus, conventional ^{14}C ages) became significantly negative within 10 years of the first detected incursion (Landman et al., 1988). This rapid change in seawater Δ^{14}C is supported by a deeper time series from 400 to 500 m in the Tasman Sea, recorded by fish otoliths, which

suggested a first incursion of bomb-derived ^{14}C in the early 1960's, and a peak at negative Δ^{14}C values within ~ 20 years (Grammer et al., 2015; Figure 15). This would therefore require growth rates for this specimen to be at least 4.4 mm/year. In reality, coral growth rate would likely have to far exceed this, given that the outer rim sample introduced above also has a non-negative ^{14}C age. If this outer rim sample represents the youngest part of this coral, this suggests that entire 7.2 cm of branch grew in ~ 10 years. Although within the range of published values (section 5.2; Table 7), growth rates > 4 mm/year are significantly larger than those inferred for other samples in this study, and those found for Southern Ocean stylasterids by King et al. (2018) (Table 7).

Alternatively, subsamples of this coral may include a mixture of pre-bomb carbon and younger bomb-derived carbon, the latter of which could be derived from either post-mortem alteration or from the younger, outer surface of the coral. The sampling technique of cutting discs perpendicular to each branch likely results in integration of material which grew at different times. Although branch growth is clearly fastest parallel to the branch, slower branch thickening in a radial direction must occur (e.g. King et al., 2018). Although care was taken to remove the outer surface of each subsample, it is possible that some younger material was incorporated into each subsample. If this material had the extremely young ^{14}C signature characteristic of modern seawater at this site (Figure 13), only a small amount would be required to substantially alter pre-bomb coral ages.

Alternatively, post-mortem precipitation of secondary carbonate with the signature of modern seawater could have an equivalent effect. The porous nature of stylasterid skeletons and their susceptibility to alteration has already been discussed in section 4.1. It is notable that all branch cross sections showed consistent evidence for pink colouration in branch centres with whiter colouration toward outer rims, in addition to numerous pore spaces which were variably filled with contaminant phases and/or appear white in colour (see supplementary information, section 7.5). This may indicate potential evidence of secondary carbonate precipitation, which could have inherited a modern, post-bomb ^{14}C signature. This process has been shown to impact ^{14}C dates in shallow-water corals (e.g. Zaunbrecher et al., 2010; Druffel-Rodriguez et al., 2012)

Evidence in favour of the hypothesis of added, bomb-derived ^{14}C is provided by subsample PS3225.m (at ~ 9 cm from the branch end), which has a younger ^{14}C age than expected from the rest of the coral chronology. This could be explained by a greater influence of bomb-derived ^{14}C for this sample. Whether this added, young ^{14}C is derived from the youngest part of the coral growing after the addition of bomb-^{14}C at this site, or from the contribution of secondary carbonate is uncertain, however the visual evidence for post-mortem alteration suggests this is the more likely hypothesis.

Interpretation of subsample ^{14}C ages in sample PS3225 is thus highly uncertain. Despite this, the strong, linear correlation between subsample ^{14}C age and distance along the branch (when excluding sample PS3225.m) is striking. It may be that pervasive alteration of this sample caused addition of a relatively constant (proportionally) amount of bomb-derived ^{14}C to each subsample, thus offsetting each by a

constant amount and maintaining the linear relationship shown in Figure 10 (reproduced in Figure 13). The calculated growth rate is consistent with those calculated for specimen Adp88 and for samples in King et al. (2018), and suggests that the 11 cm length of this branch represents ~ 206 years of growth (Table 7). However, owing to the substantial uncertainties present, I do not attempt to convert conventional ^{14}C ages into calendar years for this sample. More broadly, this sample illustrates that the susceptibility of stylasterids to contamination has implications for dating these corals by radiocarbon techniques, and that live-collected, pristine specimens are likely the best targets for this technique.

5.1.3 Samples 3403A and B (New Caledonia, 425 m)

Finally, ^{14}C ages for samples 3403A and 3403B are significantly negative (Figure 10; Figure 14). This is consistent with all subsamples showing the signature of bomb-derived ^{14}C, in agreement with ambient seawater (Figure 10; Figure 14). The apical tip ^{14}C age from sample 3403B is less negative than the paired ambient seawater value (Figure 10; Figure 14). However, the seawater sample is not from the same site as the coral collection location owing to the sparse regional data coverage, and was collected in 1992, some 30 years prior to the coral sample (coral collection in 2021). In the period between 1992 and 2009, GLODAP bottle data reveal that the signature of bomb-derived ^{14}C in this region has started to decay, and ambient seawater ^{14}C ages are becoming less negative (Figure 14). Thus, the mismatch in collection location and time of the coral and seawater samples may well explain the difference in their ^{14}C signatures.

Turning now to the growth chronologies of samples 3403A and 3403B, low sampling resolution precludes identification of key features including the first incursion of, and peak in, bomb ^{14}C at this site, which have been used to provide valuable chronological constraint in some previous studies (e.g. Roark et al., 2006; Sherwood and Edinger, 2009). However, the fact that all subsamples measured here show clear evidence for bomb ^{14}C does allow us to place minimum bounds on the vertical growth rates of these samples.
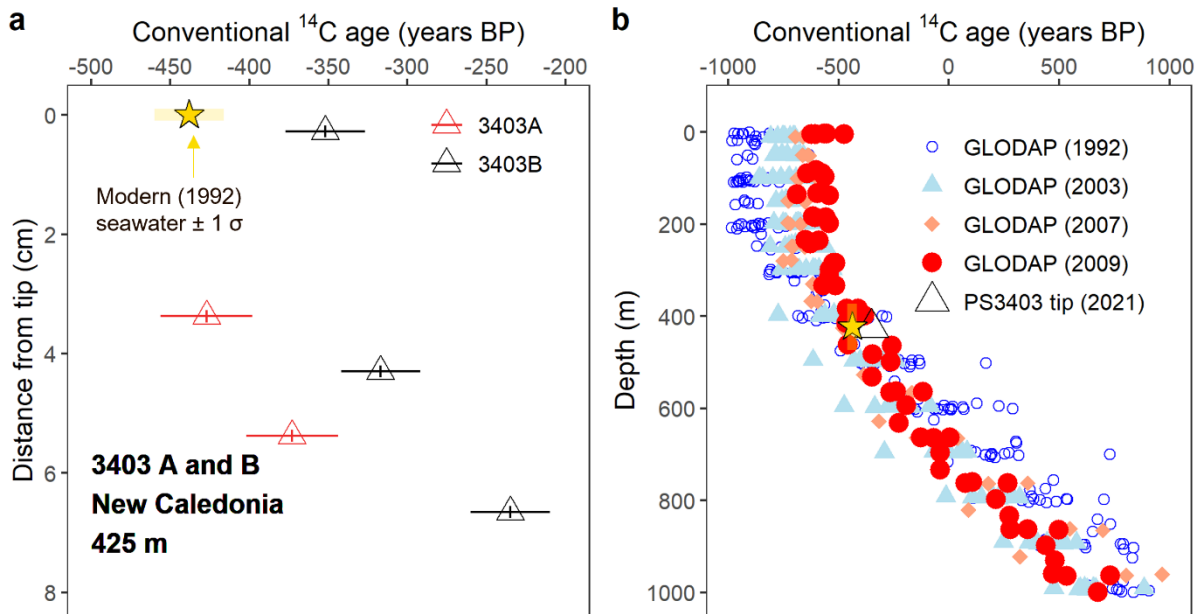
Figure 14. a. Distance along branch vs conventional ^{14}C age for samples 3403A and 3403B, reproduced from Figure 10. b. Comparing PS3403B apical tip subsample ^{14}C age (black triangle) to seawater conventional ^{14}C ages calculated from nearby GLODAP Δ^{14}C measurements (Lauvset et al., 2022). Note seawater measurements are distinguished by collection year. The chosen paired seawater value is shown by the gold star in both panels ($\pm$ 1 σ).

As outlined in section 5.1.2, the first marine signature of bomb radiocarbon in the New Caledonian region was in the late 1950's, and estimates suggest this signal may have penetrated to 400 m water depth by ~ 1965 (Landman et al., 1988). This is supported by fish otoliths from 400 to 500 m in the Tasman Sea, which record the first incursion of bomb radiocarbon in 1963 (Grammer et al., 2015; Figure 15). Given all subsamples from corals 3403A and 3403B are influenced by bomb ^{14}C, this suggests that these corals were at most 58 years old at the time of collection in 2021, implying minimum growth rates of 0.9 and 1.1 mm/year for 3043A and 3403B, respectively.

Further constraint can be placed on the growth rate of sample 3403B. ^{14}C ages for this sample become significantly more negative toward the branch tip (Figure 10; Figure 14; Figure 15). This indicates that sample 3403B started growing before the peak in bomb-^{14}C occurred at this site, a suggestion further supported by the more negative subsample ages of the co-located specimen 3403A. Previous work suggests that the bomb-^{14}C signature at 400 to 500 m in the Tasman Sea peaked in the early 1980's (Grammer et al., 2015; Figure 15). Assuming a similar timescale for the New Caledonian region suggests that sample 3403B started growing prior to this date. Overall, this implies that sample 3403B was at most 58 years old and at least 41 years old at the time of collection in 2021, and in turn suggests a growth rate of between 1.1 and 1.6 mm/year (Table 7).
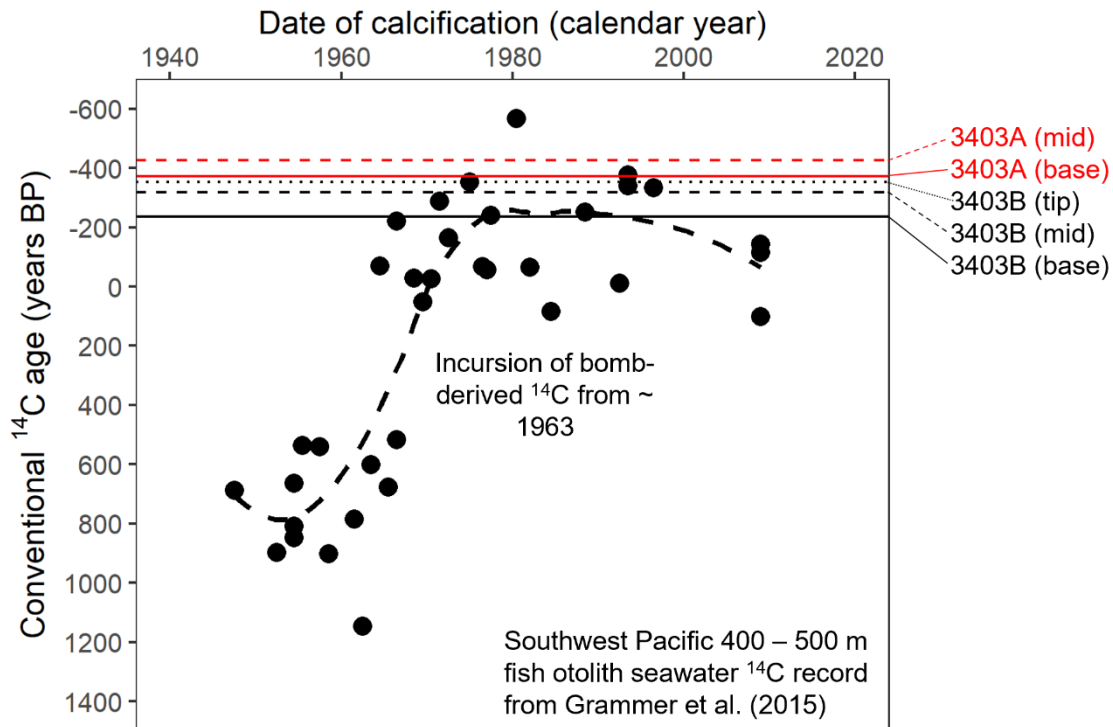
Figure 15. Record of seawater ^{14}C age at 400 to 500 m depth in the Southwest Pacific, derived from fish otoliths (Grammer et al., 2015). Note y axis inversion. Conventional ^{14}C ages were calculated from published Fm values in Grammer et al. (2015), using the equation ^{14}Cage $= -8033 \times \ln(Fm)$. Dashed line through data shows a LOESS fit. Also shown as horizontal lines are the ^{14}C ages of subsamples from corals 3403A and 3403B. Note there is a large location difference between fish and coral collection sites, likely leading to differences in absolute ^{14}C ages. However, the timescales of bomb-radiocarbon mixing and decay may be more comparable between the two sites.

5.2   Stylasterid coral growth rates

The growth rates of stylasterid corals measured here are compared with previously published growth rate estimates in Table 7. Estimates for samples Adp88 and PS3225 agree well with those of King et al. (2018), the only other study to estimate stylasterid growth rates by radiometric techniques. Sample 3403B suggests faster, but still comparable, growth rates of 1.1 to 1.6 mm/year. Together, these data provide strong evidence for slower rates of stylasterid growth than suggested by photographic studies (Chong and Stratford, 2002; Miller et al., 2004; Wisshak et al., 2009). This conclusion remains robust for sample Adp88 when using the faster growth rate calculated from the difference in age of the branch tip and subsample furthest from the tip (0.85 mm/year; see section 3.3.1 and discussion in section 5.1.1).

Whether growth rates determined by radiometric techniques and photographic methods are directly comparable is unclear. For instance, studies based on photography span time periods of at most 3 years (Miller et al., 2004), and may struggle to resolve slower rates of growth (King et al., 2018). Additionally, short term stylasterid growth rates likely far exceed net skeletal growth rates over a prolonged period of time, for instance due to growth hiatuses or branch damage.

More broadly, I suggest that the view of stylasterids as fast-growing corals may falsely imply their resilience to disturbances, for instance by bottom trawling. Radiometrically-derived growth rates < 2 mm/year have now been reported for a range of specimens from the Southern Ocean (King et al., 2018), southwest Pacific (this study) and equatorial Atlantic (this study) (Table 7). The destruction of large stylasterid specimens and the ecosystems they support by activities such as bottom trawling may therefore represent the destruction of skeletons which took decades or even centuries to form, and may take equally significant periods of time to recover.

5.3   Applying the stylasterid skeletal Li/Mg, Ba/Ca and δ^{11}B palaeo-ocean proxies

The primary objective of this study was to develop geochronological tools which would allow the application of stylasterid geochemical proxies in palaeoceanographic contexts. Although dating stylasterid corals by U-series techniques is challenging, construction of radiocarbon growth chronologies of live-collected stylasterids exhibited greater promise as a palaeoceanographic tool. Indeed, sample Adp88 (from 1175 m in the equatorial Atlantic) apparently grew over a period spanning much of the 20th century (calendar years 1924 to 2013; section 5.1.1). In the following section, I use Li/Mg, Ba/Ca and δ^{11}B ratios measured on this sample to provide constraint on variations in mid-depth equatorial Atlantic temperature, $[Ba]_{SW}$ and pH across this time period, which are summarised in Figure 16. This figure directly follows Figure 11, with the x-axis converted to time using the age model in section 5.1.1 and coral geochemistry converted to seawater parameters using the calibrations and calculations outlined in section 2.7.

Considering firstly the fidelity of the proxies used here, the Li/Mg and δ^{11}B ratios of the (assumed modern) branch tip subsample imply temperature and pH values within error of modern seawater (Figure 11; Figure 16). Importantly, this suggests that apical tip geochemistry is faithfully recording seawater parameters, despite evidence that δ^{11}B of stylasterid apical tips can be influenced by calcification-related effects (chapter 4; note also that apical tip Li/Mg ratios are impacted by these effects to a lesser degree). This reaffirms our confidence in the use of both these ratios to reconstruct variations in seawater conditions. Conversely, $[Ba]_{SW}$ implied by subsample Ba/Ca is elevated above the modern seawater value by ~ 10 nmol/kg (Figure 11; Figure 16). This offset is within the range of the 95 % prediction interval of the stylasterid Ba/Ca vs $[Ba]_{SW}$ calibration (chapter 3) and is broadly consistent across all subsamples. I therefore choose to interpret subsample Ba/Ca as a record of $[Ba]_{SW}$, but focus on relative changes between subsamples, rather than absolute reconstructed $[Ba]_{SW}$ values. Finally, the objectively low Fe/Ca values of our subsamples (<0.8 μmol/mol) suggest that contaminant phases do not influence our observations (discussed in detail in the supplementary information, section 7.3).

Study	Genus	Growth rate (mm/year)*	Basis	Location and depth	Notes
This study	*Adelopora sp.* (Adp88)	0.58	Radiocarbon	Equatorial Atlantic, 1175 m	Single branch extension rate
	Stylaster sp. (PS3225)	0.53	Radiocarbon	New Caledonia, 201 m	Highly uncertain. Single branch extension rate
	Stephanohelia sp. (3403A)	> 0.9	Radiocarbon	New Caledonia, 425 m	Minimum estimate, single branch extension rate
	Stephanohelia sp. (3403B)	1.1 - 1.6	Radiocarbon	New Caledonia, 425 m	Single branch extension rate
Chong and Stratford (2002)	*Errina novaezelandiae*	2.7	Stereo photogrammetry	Doubtful Sound, New Zealand (fjord), 16 to 18 m	Branch extension rate. 62 branches from 7 colonies
Miller et al. (2004)	*Errina novaezelandiae*	7	Photography	Doubtful Sound, New Zealand (fjord), < 40 m	Average of 27 colonies observed over 3 years. Measurement is change in colony width, therefore not directly comparable with branch extension rates
Wisshak et al. (2009)	*Errina dabneyi*	4 - 6	Photography	Azores, ~ 500 m	Branch extension rate, 1 colony
King et al. (2018)	*Errina sp.*	0.24 – 0.51	Radiocarbon	Wilkes Land/Ross Sea, 500 to 1700 m	Branch extension rate, 4 measurements in this range

Table 7. Growth rates of stylasterids in this study and published previously. Note that where growth rates were inferred from radiocarbon methods, growth rates are given in mm/^{14}C year. Our growth rate estimate for sample PS3225 is considered highly uncertain, as addressed in section 5.1.2.

Having established the robustness of the proxies used, the most striking palaeoceanographic observation I make is a significant (at the 90 % level) trend of decreasing coral Li/Mg toward the branch tip ($r = 0.7$, $p = 0.06$; Figure 11). When distance along the branch is converted to calendar age and Li/Mg to temperature, this trend represents an increase in seawater temperature of ~ 1.7 ^{0}C over the 90 year timespan of the record, with the majority of this change occurring in the last 15 years of coral growth (between ~ 1997 and 2013) (Figure 16). I note that although Li/Mg ratios of the base and tip subsamples are significantly different from one another (i.e. differ by more than the analytical error; Figure 11), the implied temperature change between the base and tip is within the 95 % prediction uncertainty associated with temperature reconstruction using stylasterid Li/Mg ratios ($\pm$ 1.7 ^{0}C; Stewart et al., 2020b; Figure 16).

However, much of the scatter in the Li/Mg vs temperature calibration likely results from using different coral species from different locations, and this source of variability would be removed when comparing subsamples from a single coral, as in this study. Overall, the excellent agreement between the apical tip subsample and modern seawater (Figure 11; Figure 16), coupled with the statistically significant trend in coral Li/Mg along the branch (Figure 11), suggests that the reconstructed temperature increase is robust.
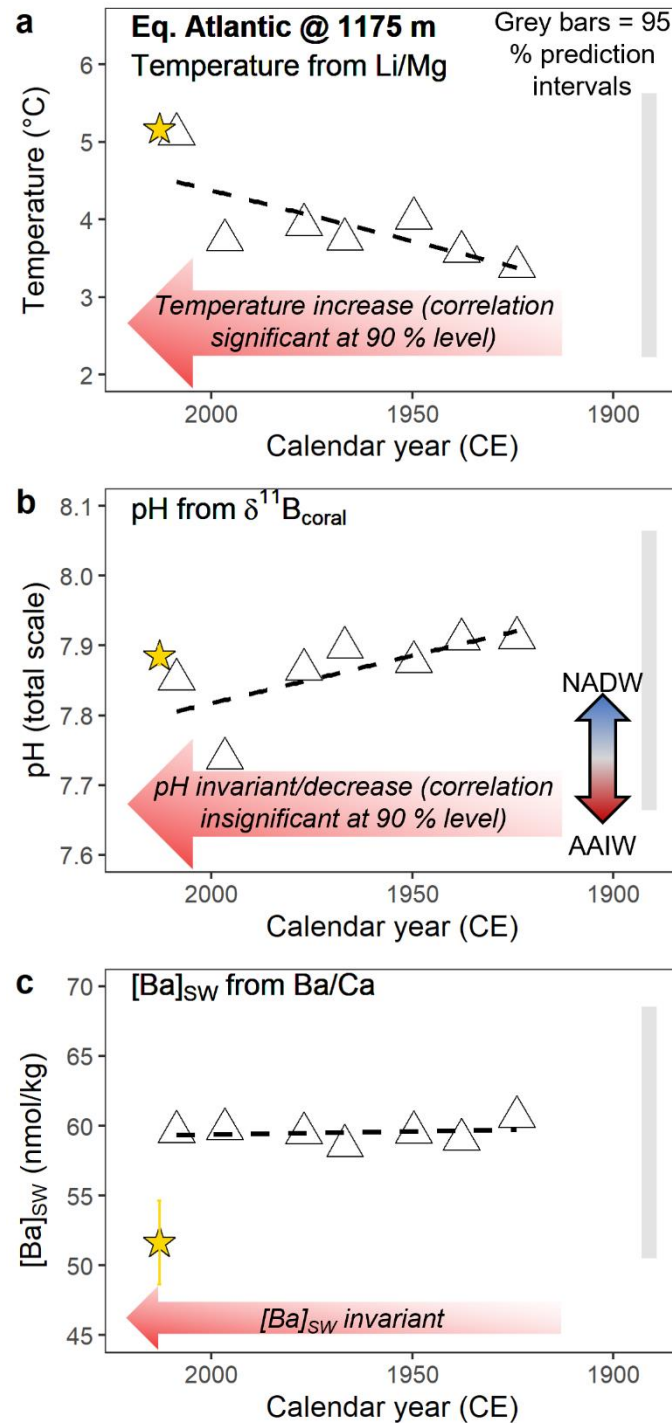

Figure 16. Reconstructed seawater temperature (a), seawater pH (b) and [Ba]$_{SW}$ (c) as a function of time, from coral Adp88 (Equatorial Atlantic, 1175 m depth). Age model follows results in section 5.1.1.

Hydrographic parameters calculated based on coral geochemistry, using calibrations and calculations outlined in section 2.7. Grey bars show the 95 % prediction uncertainty for each calibration, centred on the mean of the reconstructed values ($\pm$ 1.7 °C (Stewart et al., 2020b), $\pm$ 0.2 pH units (chapter 4) and $\pm$ 9 nmol/kg (chapter 3), respectively). In panel b, double-headed arrow shows theoretical effect of increased contributions of North Atlantic Deep Water (NADW) and Antarctic Intermediate Water (AAIW) at this site.
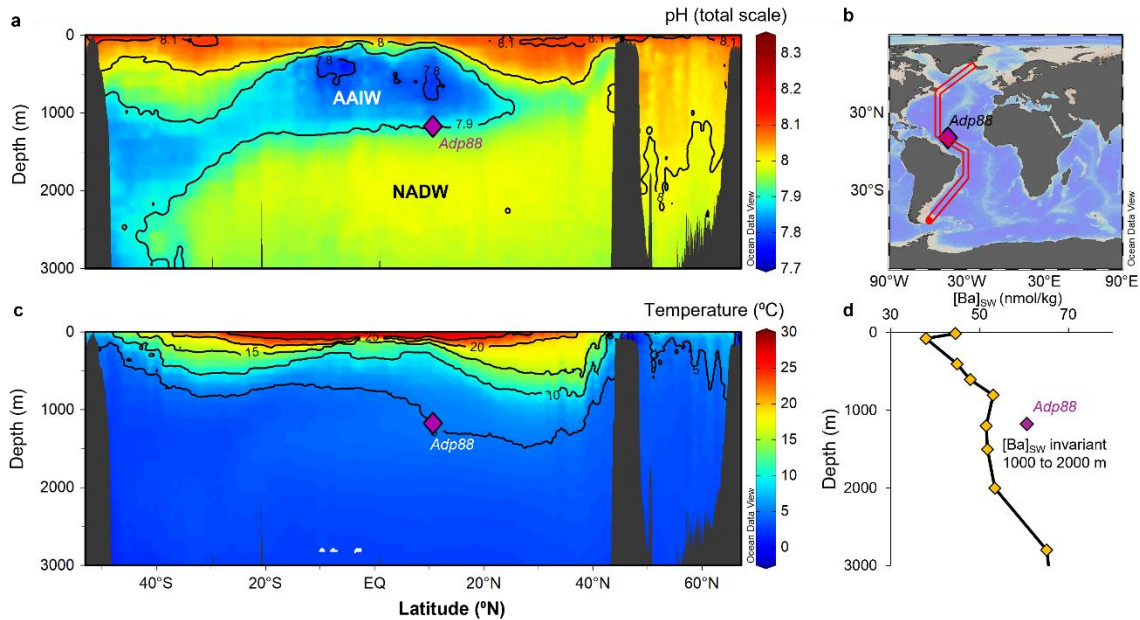
Figure 17. Modern hydrographic setting for sample Adp88, with pH (a), temperature (c) and [Ba]$_{SW}$ (d) shown. Temperature and pH data taken from the GLODAP bottle database (Lauvset et al., 2022). pH calculated in Ocean Data View software (Schlitzer, 2023) using alkalinity and DIC pairs. [Ba]$_{SW}$ data taken from the co-located profile in Bates et al. (2017). Figure produced in Ocean Data View software (Schlitzer, 2023).

The warming trend observed is consistent with a range of direct observational and modelling based studies, which suggest that intermediate depth (i.e. ~ upper 2000 m) north Atlantic warming has occurred across the late 20th and early 21st centuries (e.g. Arbic and Owens, 2001; Lozier et al., 2008; Häkkinen et al., 2015; Desbruyères et al., 2017). On longer timescales, comparison of data from the *Challenger* expeditions (1872 to 1876) with those from Argo deployments (2004 to 2010) reveals a global warming trend at ~ 900 m (Roemmich et al., 2012). A major advantage of our approach is the continuous and somewhat temporally-averaged nature of the coral subsamples. Given a growth rate of 0.6 mm/year (section 5.1.1; Table 7), the 2 mm branch slices taken here represent 3 to 4 years of coral growth. This time integration mitigates for the influence of monthly to decadal variability which can complicate the comparison of temperature measurements made at single points in time (e.g. Bryden et al., 2003; Wunsch and Heimbach, 2006; Lozier et al., 2008).

There are a number of plausible mechanisms by which seawater temperature may have increased at this site over the 20th century. Observational and modelling-based studies have broadly attributed warming

trends to: (i) vertical displacement of isopycnals bringing warmer waters to greater depth ("heave"; e.g. Arbic and Owens, 2001; Häkkinen et al., 2015) and (ii) warming along isopycnals ("spiciness"; e.g. Lozier et al., 2008; Desbruyères et al., 2017). The relative contributions of these components to the overall warming trend at a given location are depth, time, location and model dependent (e.g. Häkkinen et al., 2015; Desbruyères et al., 2017).

Here, I suggest that the multi-proxy approach employed helps to deconvolve the possible sources of warming at this site, which is close to the modern-day boundary between Antarctic Intermediate Water (AAIW) and North Atlantic Deep Water (NADW) (Figure 17). Since NADW is warmer than AAIW, one possibility which would result in warming is an increased relative contribution of NADW at this site, either by a shoaling of the boundary between these two water masses (a "heave" component), or by a reduction in the northward penetration of AAIW into the Atlantic. Reconstruction of seawater pH from stylasterid δ^{11}B allows a test of this hypothesis. An increase in the relative contribution of NADW through time should lead to a corresponding increase in seawater pH, since NADW has generally higher pH than carbon-rich AAIW (Figure 17). However, coral δ^{11}B exhibits no statistically-significant trend along the length of the branch ($r = 0.65$, $p = 0.12$; Figure 11), and if anything decreases toward the branch tip (Figure 16). This suggests either an invariance of, or decrease in, ambient seawater pH at this site through time, inconsistent with an increased influence of NADW (Figure 16; Figure 17).

Alternatively, an increase in the depth of the thermocline in this region could lead to warming by increased diffusive or advective heat transfer to the coral collection site, in turn helping to explain the relative invariance of seawater pH and [Ba]$_{SW}$ (Figure 16). It is possible that a deepening of the thermocline in the equatorial Atlantic might also result in a corresponding deepening of the boundary between AAIW and NADW, which is also consistent with our observations. Owing to the weak regional depth gradient in seawater pH, a deepening of the AAIW/NADW boundary would result in a slight decrease in seawater pH at the coral collection site of no more than 0.1 pH units (Figure 17). As noted above, the relationship between stylasterid δ^{11}B and distance along the branch suggests a statistically insignificant decrease in seawater pH (Figure 16). This is consistent with a deepening of the AAIW/NADW boundary, which would result in small changes in ambient seawater pH (< 0.1 pH units) compared with the prediction uncertainty associated with this proxy (~ 0.2 pH units; see chapter 4). Further, the absence of a depth gradient in [Ba]$_{SW}$ at these depths (Figure 17) means that a deflection of the AAIW/NADW boundary is also consistent with the invariance of reconstructed [Ba]$_{SW}$ (Figure 16). As outlined above, this downward heave of isopycnals has been linked to recent intermediate-depth warming in various locations across the north Atlantic (e.g. Arbic and Owens, 2001; Lozier et al., 2008; Häkkinen et al., 2015; Desbruyères et al., 2017). Further, modelling and proxy-based studies have inferred a deepening of the Atlantic thermocline during periods in Earth's past, including during Heinrich Stadials and the Younger Dryas (e.g. Rühlemann et al., 2004; Hain et al., 2014; Pedro et al., 2018) and at the termination of the Little Ice Age (Liu, 2022).

The multi-proxy approach employed here suggests this is the most likely explanation for the warming trend I observe at this site. A deepening of the thermocline and associated subsurface warming across the late 20th and early 21st centuries may be linked with a reduction in the strength of the Atlantic Meridional Overturning Circulation (AMOC) (e.g. Arbic and Owens, 2001; Rühlemann et al., 2004). Indeed, subsurface tropical and north Atlantic warming has been linked to periods of weakened AMOC strength in Earth's past (e.g. Rühlemann et al., 2004; Marcott et al., 2011; Galbraith et al., 2016; Pedro et al., 2018; Oppo et al., 2023). However, the significance of recent variations in the strength of AMOC remain highly uncertain (e.g. compare Caesar et al., 2021 and Kilbourne et al., 2022).

Overall, these data provide evidence for intermediate-depth, tropical north Atlantic warming across the 20th century, which agrees with direct observational records and model outputs. Most of the implied warming occurs in the period 1997 to 2013. By employing a multi-proxy approach, I suggest this warming is most likely linked to a deepening of the thermocline. Importantly, these data represent only the second use of stylasterid corals in a palaeoceanographic context (see King et al. (2018) for the first), and are the first application of the recently developed stylasterid temperature, pH and [Ba]$_{SW}$ proxies. This analysis illustrates the power of employing a multiproxy approach, which here permits the distinction of two plausible explanations for the changes observed. More broadly, the robust geochemical proxies developed in this thesis, coupled with a simple yet effective sampling procedure, provide a blueprint for the use of large, live-collected stylasterid skeletons to reconstruct past variations in ocean conditions.

6   Conclusions

In this study, I demonstrate the utility of stylasterid corals as palaeoceanographic archives, as well as the challenges of employing them as such. U-series dating stylasterid corals is complicated by their low skeletal [U] and susceptibility to contamination by Th-bearing phases. These characteristics mean that, in general, accurately correcting for the contribution of initial/added ^{230}Th is crucial to obtaining accurate ages. The procedure commonly-applied to scleractinian corals – in which a regional [^{230}Th/^{232}Th]$_i$ value is assumed and assigned a 100 % 2 σ uncertainty – produces ages which are imprecise and, owing to the large variability in sample-specific [^{230}Th/^{232}Th]$_i$, may be highly inaccurate. I demonstrate that an isochron approach – while complicated by the likely presence of three or more isotopically-distinct U-Th sources - provides one means to achieve sample-specific [^{230}Th/^{232}Th]$_i$, which in turns provides some assurance of age accuracy and improved precision. In practise, however, the construction of isochrons is unlikely to be attractive in palaeoceanographic contexts, owing to the time-consuming and sample-intensive nature of this technique.

Stylasterids dated by U-series techniques are, therefore, unlikely to be useful as archives of centennial to millennial changes in ocean conditions in the manner that scleractinian corals have been so successfully employed. However, U-series approaches applied to stylasterids may still be useful for studies of longer timescales and which can tolerate age imprecision. For example, it may be possible to explore multi-millennial shifts in stylasterid distributions and ocean conditions (e.g. following de Carvalho Ferreira et al.,

2022). In these instances, I recommend careful sample selection and rigorous cleaning to reduce [^{232}Th] as far as is practical, coupled with consideration of the full range of possible [^{230}Th/^{232}Th]$_i$ values. In this way, one can provide upper and lower age bounds for each sample – in addition to a best estimate – thus ensuring the robustness of any conclusions.

Stylasterid radiocarbon growth chronologies, on the other hand, exhibit far greater promise as a palaeoceanographic tool. Our data confirm the finding that large stylasterid skeletons grow on decadal to centennial timescales (King et al., 2018), and that coherent growth chronologies can be constructed for pristine, live-collected samples. Using a coral dated as such, I demonstrate the first application of stylasterid Li/Mg-temperature, δ^{11}B-pH and Ba/Ca-[Ba]$_{SW}$ proxies in a palaeoceanographic context. This multi-proxy approach illustrates a warming trend in the intermediate-depth north Atlantic since the early 1900's, coupled with minimal variability in pH and [Ba]$_{SW}$. I suggest that these observations are most consistent with a deepening of the thermocline, which may be linked with variations in AMOC strength. Overall, the approach employed here demonstrates that, by application of a simple sampling strategy, coupled with robust proxy calibrations, large, live-collected stylasterids can be used to provide powerful palaeoceanographic constraint on decadal to centennial timescales, representing a clear target for future work.

Finally, the stylasterid radiocarbon growth chronologies presented here imply skeletal growth rates in agreement with the only other existing study of this kind (King et al., 2018). These growth rates (≤ 1.6 mm/year) are significantly slower than those suggested by photogrammetric studies, and a stylasterid colony with branches 10 cm long can be expected to be on the order of 100 years old. This emerging picture contrasts with a view of stylasterids as fast growing corals, and suggests that the recovery of ecosystems containing stylasterid colonies from destructive activities such as bottom trawling - if indeed the ecosystem is able to recover - could take hundreds of years. The data presented here and by King et al. (2018) provide a clear illustration of the long-lived nature of stylasterid corals, strengthening the case for protection of these corals and the ecosystems they support.

7   Supplementary information

7.1   Isochron aliquots and their activity ratios

Aliquots used in isochrons (Table 2; section 2.2.1) are photographed below, along with the full coral specimen prior to sampling (Supplementary figure 1). Coating aliquots are not pictured, but appeared as labelled in the "Unclean" aliquot. Isochron aliquot activity ratios, errors and error correlations are shown in Supplementary table 1.
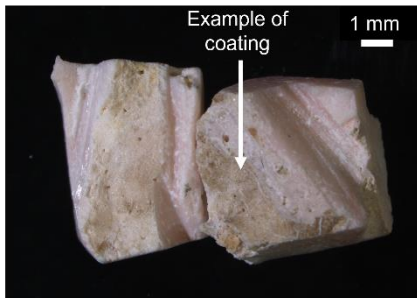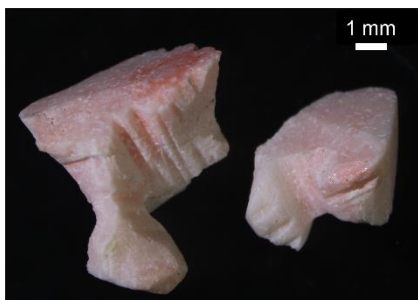
Sma04zx

Stylaster marenzelli

Galápagos Islands
176 m depth
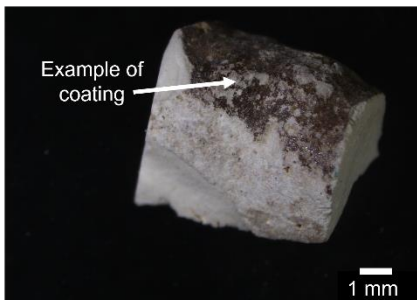
Sde43zg

Stylaster densicaulis

Shackleton Fracture Zone,
Drake Passage
856 m depth

A. Unclean

Example of coating

1 mm

B. Mechanical

1 mm

C. Clean

1 mm

D. Crush-clean

5 mm
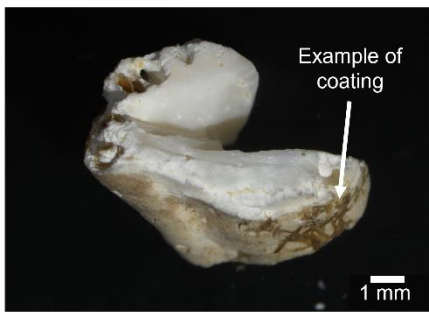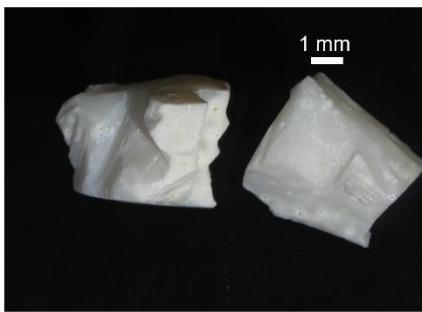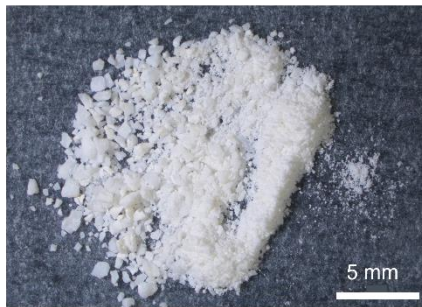
Sde88zl

Stylaster densicaulis

**Interim Seamount, Drake Passage
982 m depth**

2 cm

Supplementary figure 1. Isochron aliquots used in this study. Labels in each panel refer to the aliquots defined in Table 2. Note all pictures were taken prior to chemical cleaning steps. Coating aliquots were not pictured, annotations in panel a for each coral show the appearance of coatings for each sample.

Sample	Aliquot	[^{238}U] (ppm)	± 2 σ	[^{232}Th] (ppb)	± 2 σ	[^{238}U/^{232}Th]	± 2 σ	[^{234}U/^{232}Th]	± 2 σ	[^{230}Th/^{232}Th]	± 2 σ	rho84	rho80	rho40
Sde88zl	Crush-clean	1.112	0.003	0.0342	0.0009	99267.87	2516.67	113759.14	2881.71	166.78	7.80	0.999	0.541	0.541
	Clean	0.822	0.002	0.0101	0.0003	249627.80	6859.09	286065.58	7860.80	478.59	22.42	0.999	0.581	0.583
	Mechanical	0.688	0.003	0.4130	0.0057	5095.39	70.74	5835.48	80.98	12.83	0.41	0.998	0.402	0.403
	Unclean	1.020	0.002	1.0727	0.0044	2905.55	13.02	3327.83	14.95	109.93	0.79	0.977	0.504	0.500
	Coating	1.269	0.018	26.3386	0.3910	147.20	0.75	168.99	0.93	97.33	0.68	0.918	0.534	0.500
Sma04zx	Crush-clean	0.948	0.003	0.1617	0.0010	17918.38	122.09	20527.00	140.42	59.80	1.10	0.989	0.267	0.266
	Clean	1.072	0.003	0.0905	0.0005	36191.91	210.54	41455.05	241.49	88.91	1.38	0.986	0.307	0.305
	Mechanical	0.884	0.002	0.4672	0.0022	5783.61	30.25	6639.24	34.92	36.56	0.40	0.982	0.354	0.355
	Unclean	0.913	0.002	3.0880	0.0135	903.49	4.40	1034.64	5.04	35.17	0.28	0.983	0.471	0.468
	Coating	0.695	0.011	29.1783	0.4998	72.83	0.42	83.39	0.52	38.35	0.34	0.914	0.442	0.409
Sde43zg	Crush-clean	1.122	0.003	2.0579	0.0092	1665.98	8.24	1913.22	9.50	173.63	1.19	0.982	0.546	0.544
	Clean	1.179	0.003	2.8969	0.0129	1243.47	6.23	1425.31	7.15	171.09	1.16	0.984	0.542	0.542
	Mechanical	1.140	0.003	3.9299	0.0172	886.62	4.33	1016.19	4.98	137.18	0.88	0.982	0.569	0.567
	Unclean	2.714	0.006	33.7414	0.1466	245.79	1.17	281.76	1.35	112.10	0.71	0.982	0.576	0.578
	Coating	2.116	0.083	1046.2662	42.1423	6.18	0.03	7.07	0.04	120.77	0.79	0.918	0.570	0.527

Supplementary table 1. Isochron aliquot U and Th concentrations, activity ratios and error correlations (rhoXY values) required to generate all plots and calculations in this thesis. Note that activity ratios and their errors were generated by Monte Carlo simulation, and will thus differ slightly from those calculated from the isotope concentrations recorded here.

7.2 Geochemical data for radiocarbon subsampling experiments

Subsample ^{14}C ages, Li/Mg, Ba/Ca and δ^{11}B used in this study are shown in Supplementary table 2.

| Sample	Subsample	Distance from branch end (cm)	Fm	Error (± 1 σ)	^{14}C age (years BP)	Error (± 1 σ)	Calendar year (CE)	Li/Mg (mmol/mol)	Ba/Ca (µmol/mol)	δ^{11}B (‰)
PS3403A	3403A.T	0.2						3.82	7.80	14.60
(live-	3403A.2	1.6						4.50	7.78	15.46
collected in	3403A.4	2.3						4.67	7.73	15.71
2021)	3403A.6	3.4	1.055	0.004	− 427	29		4.66	7.81	16.04
	3403A.8	4.3						4.80	7.87	16.00
	3403A.10	5.4	1.047	0.004	− 373	29		4.71	7.89	15.99
PS3403B	3403B.T	0.3	1.045	0.003	− 352	25		4.19	8.25	15.33
(live-	3403B.2	2.5						4.54	7.86	15.88
collected in	3403B.4	4.3	1.040	0.003	− 317	25		4.74	7.96	16.17
2021)	3403B.6	5.4						4.66	7.72	15.92
	3403B.8	6.7	1.030	0.003	− 235	25		4.71	7.73	16.13
PS3225	PS3225.a	0.1						2.63	5.56	18.97
(dead-	PS3225.b	1.1						2.67	5.50	18.68
collected in	PS3225.c	1.9						2.65	5.55	18.78
2021)	PS3225.d	2.9	0.969	0.005	256	41		2.64	5.52	18.60
	PS3225.e	3.6						2.64	5.55	18.71
	PS3225.f	4.2						2.70	5.45	18.87
	PS3225.g	4.8	0.965	0.003	289	25		2.65	5.47	18.89
	PS3225.h	6.1						2.66	5.50	18.76

Sample	Subsample	Distance from branch end (cm)	Fm	Error (± 1 σ)	^{14}C age (years BP)	Error (± 1 σ)	Calendar year (CE)	Li/Mg (mmol/mol)	Ba/Ca (µmol/mol)	δ^{11}B (‰)
	PS3225.i	6.7						2.71	5.44	18.99
	PS3225.j	7.3	0.957	0.004	355	30		2.66	5.43	18.90
	PS3225.k	7.9						2.69	5.39	19.09
	PS3225.l	8.7						2.71	5.37	19.01
	PS3225.m	9.2	0.965	0.004	288	30		2.73	5.43	18.99
	PS3225.radC	11.0	0.951	0.004	402	30		2.70	5.32	18.86
	PS3225.radInt		0.953	0.004	384	31		2.64	5.51	18.10
	PS3225.radOut		0.990	0.004	83	30		2.73	5.54	18.07
Adp88 (live-collected in 2013)	Adp88ca.1	5.2	0.906	0.003	796	25	1924	4.83	11.19	15.29
	Adp88ca.2	4.4	0.905	0.004	804	33	1938	4.78	10.85	15.29
	Adp88ca.3	3.7	0.909	0.003	769	25	1950	4.69	10.95	15.13
	Adp88ca.4	2.7					1967	4.75	10.75	15.23
	Adp88ca.5	2.1	0.912	0.003	740	26	1977	4.71	10.94	15.07
	Adp88ca.6	1.0					1997	4.75	11.00	14.42
	Adp88.T	0.3	0.912	0.003	738	25	2009	4.46	10.96	15.07

Supplementary table 2. Geochemical measurements for subsamples used in radiocarbon subsampling experiments. Radiocarbon dates given as conventional ^{14}C ages. Note Li/Mg, Ba/Ca and δ^{11}B were not discussed for samples PS3403A, PS3403B and PS3225, but are included here for completion. Subsample labels follow Figure 3 (where T refers to Tip). Analytical errors on Li/Mg, Ba/Ca and δ^{11}B measurements were ± 2 %, 1 % and 0.16 ‰, respectively (aside from sample Adp88.T, for which δ^{11}B reproducibility is assigned as 0.33 ‰; see section 2.7). Li/Mg and Ba/Ca ratios corrected for analytical offsets as outlined in section 2.7. Note that subsample positions (i.e. distances from the branch end) were recorded at the midpoint of each radial subsample slice.

7.3 Adp88: Fe/Ca and Mn/Ca contamination indicators

Subsample Fe/Ca and Mn/Ca ratios were monitored to check for the influence of contaminant phases on Li/Mg, Ba/Ca and $\delta^{11}B$ proxies. Fe/Ca and Mn/Ca ratios are not correlated with either Ba/Ca or $\delta^{11}B$ ($-0.1 < r < 0.1$, $p > 0.8$). However, strong correlations were observed between subsample Li/Mg and both Fe/Ca and Mn/Ca ($r < -0.8$, $p < 0.05$). Despite this, I suggest that these correlations do not indicate the significant influence of Fe/Ca or Mn/Ca in our dataset. Firstly, these correlations result primarily from the tip subsample, which has low Li/Mg and slightly elevated Fe/Ca and Mn/Ca (Supplementary figure 2). This same tip subsample has a Li/Mg value which, when converted to seawater temperature, agrees extremely well with modern seawater (Figure 11). This suggests that the Li/Mg ratio of this subsample is faithfully recording ambient seawater parameters, and is minimally influenced by additional factors. Additionally, subsample Fe/Ca and Mn/Ca values are extremely low. For Mn/Ca, values are less than detection limits for 5 of the 7 subsamples, while for Fe/Ca, even the tip subsample (Fe/Ca = 0.8 µmol/mol) is significantly lower than all commonly applied screening limits (e.g. 40 µmol/mol in Spooner et al., 2018; chapter 3). Finally, any significant influence of contaminant phases ought also to elevate the Ba/Ca ratio of the tip subsample, however this is not observed (Supplementary figure 2). Thus, I am confident that contaminant phases are unlikely the cause of our observations.
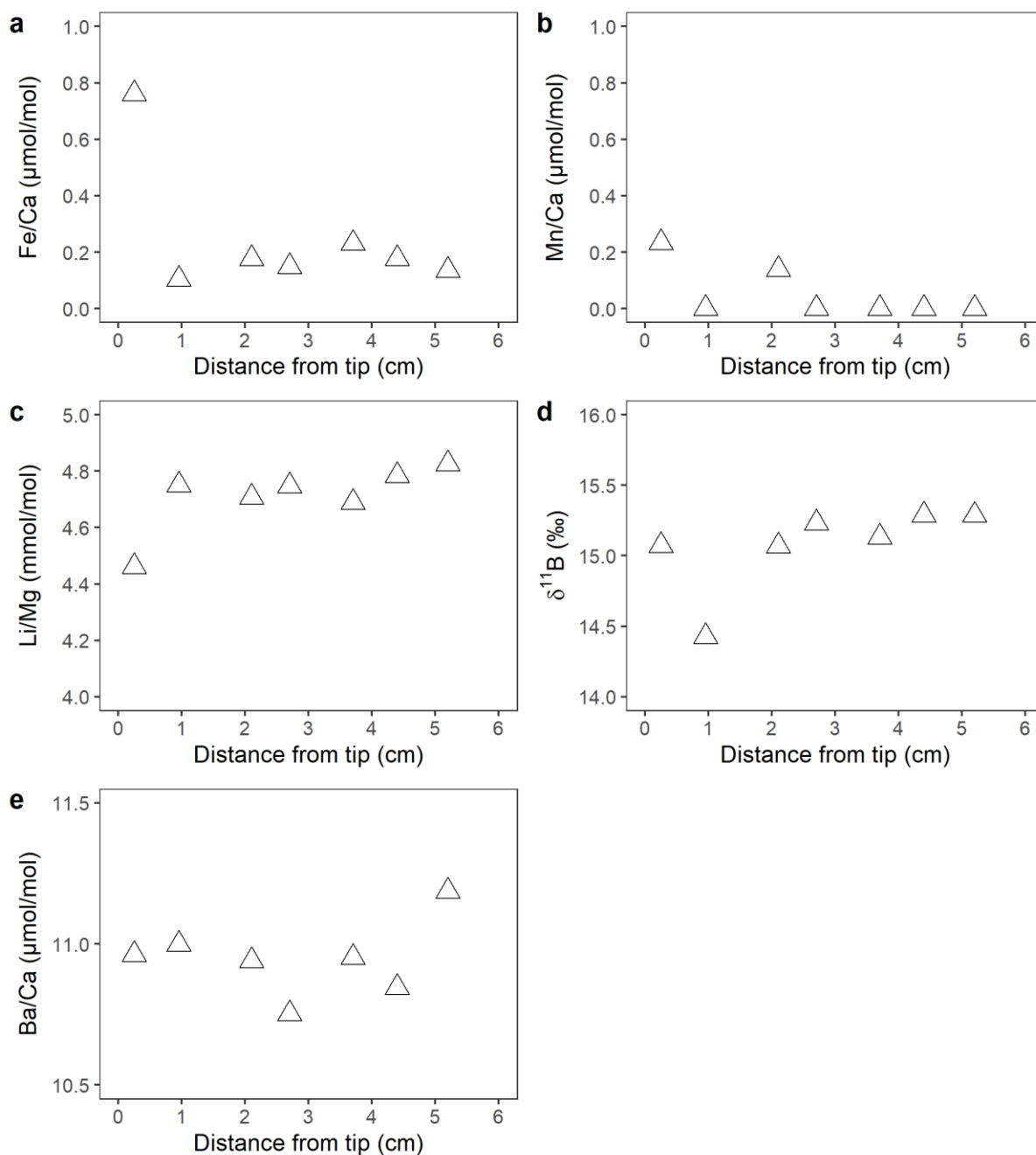
Supplementary figure 2. Variations in subsample geochemistry with distance along the branch for sample Adp88.

7.4   Stylasterid porosity: Th-bearing contaminant phases and diagenetic alteration

As outlined in the main text (section 4.1), stylasterids may be particularly susceptible to contamination by Th-bearing phases owing to the porous nature of their skeletons. Additionally, this porosity may result in multiple types of contaminant phase being deposited differentially within the skeleton, which could contribute to the observed scatter in the isochrons developed here (section 4.3). Finally, the porosity of stylasterid skeletons may lead to an increased susceptibility to diagenetic alteration, with the possibility of open-system U-series behaviour (section 4.4).

One sample from the Bristol collection (not measured here) illustrates these points well (Supplementary figure 3). The sample is evidently coated in a brown/black material, which can easily be removed mechanically. However, small, sub-mm pores are also evident at the branch exterior, which are difficult to clean mechanically. Additionally, exposing the branch interior in cross-section reveals the deposition of significant quantities of a second, lighter brown/orange material. This material is concentrated along the central branch axis. Finally, white, chalky skeletal zones provide clear visual evidence for alteration of primary carbonate, along the same central axis as the orange contaminant material. This alteration apparently propagates from a point on the branch surface.

Overall, these observations support the existence of at least two contaminant phases in stylasterid skeletons. The dark-coloured phase (Fe-Mn coating?) is concentrated on the branch exterior, while the softer, lighter-coloured material is found in the branch core (organic matter?). If these contaminant phases have different $[^{230}Th/^{232}Th]_i$, this may explain isochron overdispersion (section 4.3). This sample also illustrates how these contaminant phases are linked to stylasterid skeletal structure, and how alteration of primary carbonate may also occur in similar orientations. While only one sample is presented here, the porosity of stylasterid skeletons and presence of cyclosystems on branch surfaces are common features of a number of stylasterid genera. Thus, I suggest that these observations are likely to hold true for a wider array of stylasterid specimens, reducing the suitability of U-series dating techniques for this taxon more broadly.

Mechanically-cleaned branch exterior

Small pores evident

1 mm

Original sample

Sde23zn
Stylaster sp. (uncertain)
NBP0805-Dr23-Stns-A-JK2
Drake Passage,
Shackleton Fracture Zone
819 m

1 cm

Branch interior (cross-section)

1 mm

Contaminant phases deposited in branch interior

Whiter areas indicate carbonate alteration

Alteration propagates from branch exterior – cyclosystem?

Supplementary figure 3. Example of a stylasterid specimen exhibiting contamination and alteration features referred to in the main text. Sample was not measured in this study. Sample metadata is summarised in the figure.

7.5   Sample PS3225: additional observations

As outlined in the main text (section 5.1.2), ^{14}C ages of sample PS3225 are younger than expected, and may be influenced by bomb radiocarbon. Examples of two of the cross sections on which ^{14}C ages were measured are shown in Supplementary figure 4. These reveal that cross sections had a pink inner centre, with a whiter outer rim. This colour gradient may indicate post-mortem diagenetic alteration. I also observe significant internal porosity, which again often has a white colouration. Whether the material within these pores is primary or secondary is at this stage unknown, however the visual appearance of branch cross sections is consistent with post-mortem infilling of internal porosity with secondary carbonate. If this secondary material inherited the ^{14}C signature of modern seawater, pervasive alteration of this specimen could explain the younger-than-expected radiocarbon ages observed.
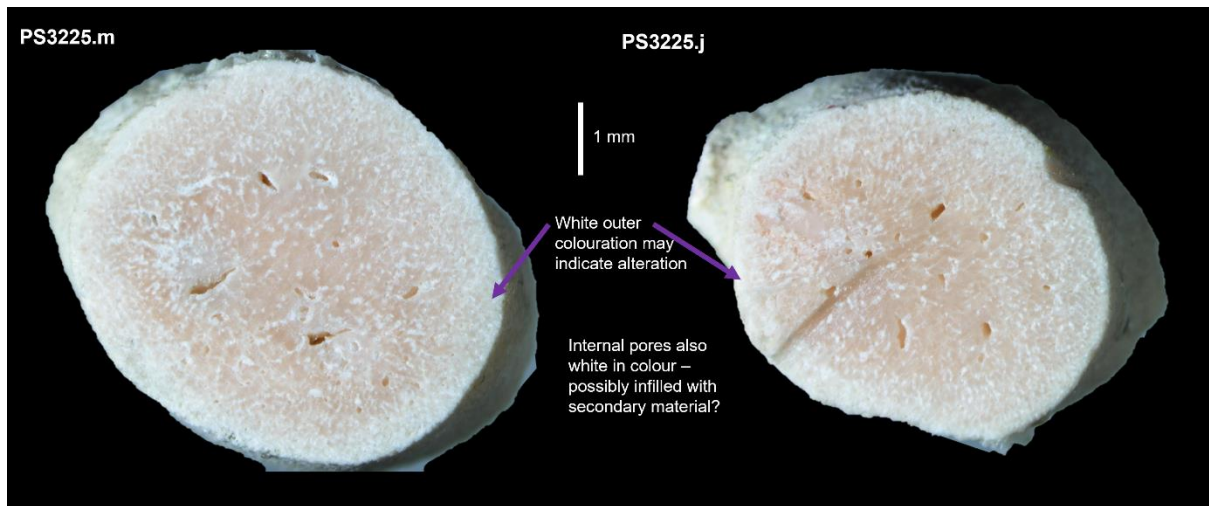
Supplementary figure 4. Photographs of two subsamples of coral PS3225 which were analysed for ^{14}C ages. Scale bar is common to each sample. Photos oriented to show branch cross sections.

Additionally, I present measurements of ^{14}C ages at 3 points along the thickest branch cross section, to investigate the possible influence of bomb radiocarbon in this sample (Supplementary figure 5). This section is that which the oldest subsample (PS3225.radC) was taken. The outermost subsample from this section shows a ^{14}C age of ~ 80 years, which is both significantly older than modern seawater, but significantly younger than pre-bomb surface ocean reservoir age (Figure 10; Figure 13). Therefore, this outermost subsample clearly shows the influence of bomb radiocarbon, which may be incorporated by the precipitation of secondary carbonate (see section 5.1.2 for detailed discussion).
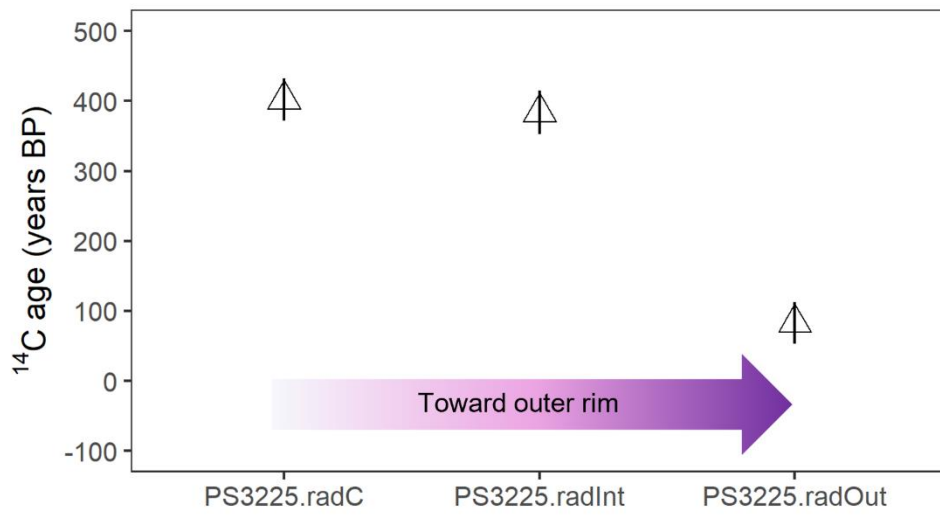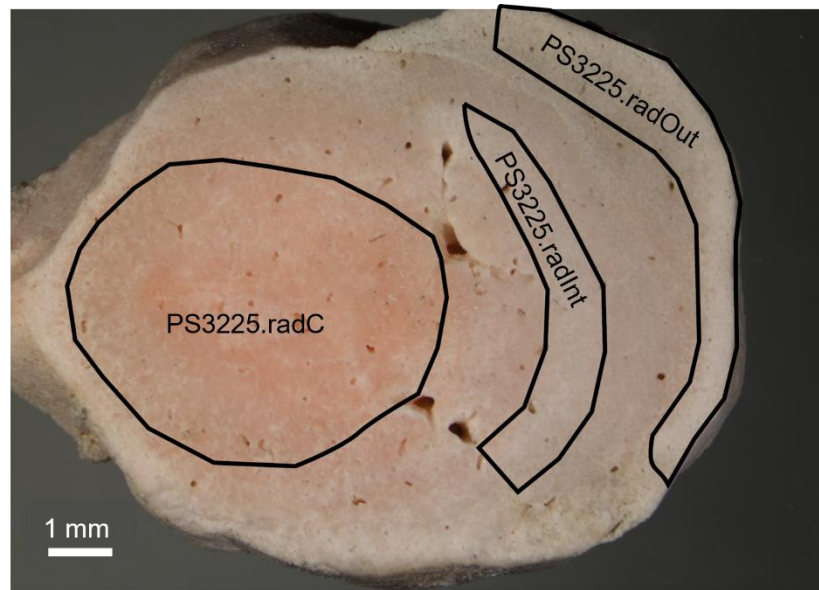
Supplementary figure 5. [14]C ages of subsamples taken from thickest branch subsection. Areas within black lines show the extent of each subsample. Subsample PS3225.radC is the oldest subsample used in the branch chronology. Ages reported as conventional ^{14}C years, analytical error bars are shown ($\pm$ 1 σ).

8   References

Adkins, J.F., Cheng, H., Boyle, E.A., Druffel, E.R.M., Edwards, R.L., 1998. Deep-Sea Coral Evidence for Rapid Change in Ventilation of the Deep North Atlantic 15,400 Years Ago. Science 280, 725–728. https://doi.org/10.1126/science.280.5364.725

Adkins, J.F., Griffin, S., Kashgarian, M., Cheng, H., Druffel, E.R.M., Boyle, E.A., Lawrence Edwards, R., Shen, C.-C., 2002. Radiocarbon Dating of Deep-Sea Corals. Radiocarbon 44, 567–580. https://doi.org/10.1017/S0033822200031921

Anagnostou, E., Sherrell, R.M., Gagnon, A., LaVigne, M., Field, M.P., McDonough, W.F., 2011. Seawater nutrient and carbonate ion concentrations recorded as P/Ca, Ba/Ca, and U/Ca in the deep-sea coral *Desmophyllum dianthus*. Geochimica et Cosmochimica Acta 75, 2529–2543. https://doi.org/10.1016/j.gca.2011.02.019

Andersen, M.B., Stirling, C.H., Zimmermann, B., Halliday, A.N., 2010. Precise determination of the open ocean $^{234}U/^{238}U$ composition. Geochem. Geophys. Geosyst. 11. https://doi.org/10.1029/2010GC003318

Arbic, B.K., Owens, W.B., 2001. Climatic Warming of Atlantic Intermediate Waters. J. Climate 14, 4091–4108. https://doi.org/10.1175/1520-0442(2001)014<4091:CWOAIW>2.0.CO;2

Auro, M.E., Robinson, L.F., Burke, A., Bradtmiller, L.I., Fleisher, M.Q., Anderson, R.F., 2012. Improvements to 232-thorium, 230-thorium, and 231-protactinium analysis in seawater arising from GEOTRACES intercalibration: Th and Pa analysis in seawater. Limnol. Oceanogr. Methods 10, 464–474. https://doi.org/10.4319/lom.2012.10.464

Bacon, M.P., Anderson, R.F., 1982. Distribution of thorium isotopes between dissolved and particulate forms in the deep sea. J. Geophys. Res. 87, 2045. https://doi.org/10.1029/JC087iC03p02045

Barker, S., Greaves, M., Elderfield, H., 2003. A study of cleaning procedures used for foraminiferal Mg/Ca paleothermometry. Geochem. Geophys. Geosyst. 4. https://doi.org/10.1029/2003GC000559

Bates, S.L., Hendry, K.R., Pryer, H.V., Kinsley, C.W., Pyle, K.M., Woodward, E.M.S., Horner, T.J., 2017. Barium isotopes reveal role of ocean circulation on barium cycling in the Atlantic. Geochimica et Cosmochimica Acta 204, 286–299. https://doi.org/10.1016/j.gca.2017.01.043

Bigg, G.R., Jickells, T.D., Liss, P.S., Osborn, T.J., 2003. The role of the oceans in climate. Int. J. Climatol. 23, 1127–1159. https://doi.org/10.1002/joc.926

Bischoff, J.L., Fitzpatrick, J.A., 1991. U-series dating of impure carbonates: An isochron technique using total-sample dissolution. Geochimica et Cosmochimica Acta 55, 543–554. https://doi.org/10.1016/0016-7037(91)90011-S

Broecker, W.S., Peng, T.-H., Stuiver, M., 1978. An estimate of the upwelling rate in the equatorial Atlantic based on the distribution of bomb radiocarbon. J. Geophys. Res. 83, 6179. https://doi.org/10.1029/JC083iC12p06179

Bryden, H.L., McDonagh, E.L., King, B.A., 2003. Changes in Ocean Water Mass Properties: Oscillations or Trends? Science 300, 2086–2088. https://doi.org/10.1126/science.1083980

Burke, A., Robinson, L.F., McNichol, A.P., Jenkins, W.J., Scanlon, K.M., Gerlach, D.S., 2010. Reconnaissance dating: A new radiocarbon method applied to assessing the temporal distribution of Southern Ocean deep-sea corals. Deep Sea Research Part I: Oceanographic Research Papers 57, 1510–1520. https://doi.org/10.1016/j.dsr.2010.07.010

Burke, A., Robinson, L.F., 2012. The Southern Ocean's Role in Carbon Exchange During the Last Deglaciation. Science 335, 557–561. https://doi.org/10.1126/science.1208163

Burr, G.S., Beck, J.W., Corrège, T., Cabioch, G., Taylor, F.W., Donahue, D.J., 2009. Modern and Pleistocene Reservoir Ages Inferred from South Pacific Corals. Radiocarbon 51, 319–335. https://doi.org/10.1017/S0033822200033853

Burr, G.S., Beck, J.W., Taylor, F.W., Récy, J., Edwards, R.L., Cabioch, G., Corrège, T., Donahue, D.J., O'malley, J.M., 1998. A High-Resolution Radiocarbon Calibration Between 11,700 and 12,400 Calendar Years Bp Derived from ^{230}Th Ages of Corals from Espiritu Santo Island, Vanuatu. Radiocarbon 40, 1093–1105. https://doi.org/10.1017/S0033822200019147

Caesar, L., McCarthy, G.D., Thornalley, D.J.R., Cahill, N., Rahmstorf, S., 2021. Current Atlantic Meridional Overturning Circulation weakest in last millennium. Nat. Geosci. 14, 118–120. https://doi.org/10.1038/s41561-021-00699-z

Cairns, S.D., 2011. Global Diversity of the Stylasteridae (Cnidaria: Hydrozoa: Athecatae). PLoS ONE 6, e21670. https://doi.org/10.1371/journal.pone.0021670

Cairns, S.D., 1992. Worldwide distribution of the Stylasteridae (Cnidaria: Hydrozoa). Sci. Mar. 56, 125–130.

Cairns, S.D., Macintyre, I.G., 1992. Phylogenetic Implications of Calcium Carbonate Mineralogy in the Stylasteridae (Cnidaria: Hydrozoa). PALAIOS 7, 96–107. https://doi.org/10.2307/3514799

Chen, T., Robinson, L.F., Burke, A., Claxton, L., Hain, M.P., Li, T., Rae, J.W.B., Stewart, J., Knowles, T.D.J., Fornari, D.J., Harpp, K.S., 2020. Persistently well-ventilated intermediate-depth ocean through the last deglaciation. Nat. Geosci. 13, 733–738. https://doi.org/10.1038/s41561-020-0638-6

Chen, T., Robinson, L.F., Burke, A., Southon, J., Spooner, P., Morris, P.J., Ng, H.C., 2015. Synchronous centennial abrupt events in the ocean and atmosphere during the last deglaciation. Science 349, 1537–1541. https://doi.org/10.1126/science.aac6159

Chen, T., Robinson, L.F., Li, T., Burke, A., Zhang, X., Stewart, J.A., White, N.J., Knowles, T.D.J., 2023. Radiocarbon evidence for the stability of polar ocean overturning during the Holocene. Nat. Geosci. 16, 631–636. https://doi.org/10.1038/s41561-023-01214-2

Cheng, H., Adkins, J., Edwards, R.L., Boyle, E.A., 2000a. U-Th dating of deep-sea corals. Geochimica et Cosmochimica Acta 64, 2401–2416. https://doi.org/10.1016/S0016-7037(99)00422-6

Cheng, H., Edwards, R.L., Hoff, J., Gallup, C.D., Richards, D.A., Asmerom, Y., 2000b. The half-lives of uranium-234 and thorium-230. Chemical Geology 169, 17–33. https://doi.org/10.1016/S0009-2541(99)00157-6

Cheng, H., Lawrence Edwards, R., Shen, C.-C., Polyak, V.J., Asmerom, Y., Woodhead, J., Hellstrom, J., Wang, Y., Kong, X., Spötl, C., Wang, X., Calvin Alexander, E., 2013. Improvements in ^{230}Th dating, ^{230}Th and ^{234}U half-life values, and U–Th isotopic measurements by multi-collector inductively coupled plasma mass spectrometry. Earth and Planetary Science Letters 371–372, 82–91. https://doi.org/10.1016/j.epsl.2013.04.006

Chong, A.K., Stratford, P., 2002. Underwater digital stereo-observation technique for red hydrocoral study. Photogrammetric Engineering & Remote Sensing 68, 745–751.

Corbera, G., Lo Iacono, C., Standish, C.D., Anagnostou, E., Titschack, J., Katsamenis, O., Cacho, I., Van Rooij, D., Huvenne, V.A.I., Foster, G.L., 2021. Glacio-eustatic variations and sapropel events as main controls on the Middle Pleistocene-Holocene evolution of the Cabliers Coral Mound Province (W Mediterranean). Quaternary Science Reviews 253, 106783. https://doi.org/10.1016/j.quascirev.2020.106783

de Carvalho Ferreira, M.L., Robinson, L.F., Stewart, J.A., Li, T., Chen, T., Burke, A., Kitahara, M.V., White, N.J., 2022. Spatial and temporal distribution of cold-water corals in the Northeast Atlantic Ocean over the last 150 thousand years. Deep Sea Research Part I: Oceanographic Research Papers 190, 103892. https://doi.org/10.1016/j.dsr.2022.103892

Desbruyères, D., McDonagh, E.L., King, B.A., Thierry, V., 2017. Global and Full-Depth Ocean Temperature Trends during the Early Twenty-First Century from Argo and Repeat Hydrography. J. Climate 30, 1985–1997. https://doi.org/10.1175/JCLI-D-16-0396.1

Dickson, A.G., 1990. Standard potential of the reaction: AgCl(s) +12H2(g) = Ag(s) + HCl(aq), and and the standard acidity constant of the ion HSO_4^- in synthetic sea water from 273.15 to 318.15 K. The Journal of Chemical Thermodynamics 22, 113–127. https://doi.org/10.1016/0021-9614(90)90074-Z

Druffel, E.R.M., 1997. Geochemistry of corals: Proxies of past ocean chemistry, ocean circulation, and climate. Proc. Natl. Acad. Sci. U.S.A. 94, 8354–8361. https://doi.org/10.1073/pnas.94.16.8354

Druffel, E.R.M., Griffin, S., 1999. Variability of surface ocean radiocarbon and stable isotopes in the southwestern Pacific. J. Geophys. Res. 104, 23607–23613. https://doi.org/10.1029/1999JC900212

Druffel-Rodriguez, K.C., Vetter, D., Griffin, S., Druffel, E.R.M., Dunbar, R.B., Mucciarone, D.A., Ziolkowski, L.A., Sanchez-Cabeza, J.-A., 2012. Radiocarbon and stable isotopes in Palmyra corals during the past century. Geochimica et Cosmochimica Acta 82, 154–162. https://doi.org/10.1016/j.gca.2010.11.028

Edwards, R.L., Chen, J.H., Wasserburg, G.J., 1987. ^{238}U-^{234}U-^{230}Th-^{232}Th systematics and the precise measurement of time over the past 500,000 years. Earth and Planetary Science Letters 81, 175–192. https://doi.org/10.1016/0012-821X(87)90154-3

Edwards, R.L., Gallup, C.D., Cheng, H., 2003. Uranium-series Dating of Marine and Lacustrine Carbonates. Reviews in Mineralogy and Geochemistry 52, 363–405. https://doi.org/10.2113/0520363

Farmer, J.R., Robinson, L.F., Hönisch, B., 2015. Growth rate determinations from radiocarbon in bamboo corals (genus *Keratoisis*). Deep Sea Research Part I: Oceanographic Research Papers 105, 26–40. https://doi.org/10.1016/j.dsr.2015.08.004

Foster, G.L., 2008. Seawater pH, pCO$_2$ and [CO$^{2-}_3$] variations in the Caribbean Sea over the last 130 kyr: A boron isotope and B/Ca study of planktic foraminifera. Earth and Planetary Science Letters 271, 254–266. https://doi.org/10.1016/j.epsl.2008.04.015

Frank, N., Freiwald, A., Correa, M.L., Wienberg, C., Eisele, M., Hebbeln, D., Van Rooij, D., Henriet, J.-P., Colin, C., Van Weering, T., De Haas, H., Buhl-Mortensen, P., Roberts, J.M., De Mol, B., Douville, E., Blamart, D., Hatte, C., 2011. Northeastern Atlantic cold-water coral reefs and climate. Geology 39, 743–746. https://doi.org/10.1130/G31825.1

Frenkel, M.M., LaVigne, M., Miller, H.R., Hill, T.M., McNichol, A., Gaylord, M.L., 2017. Quantifying bamboo coral growth rate nonlinearity with the radiocarbon bomb spike: A new model for paleoceanographic chronology development. Deep Sea Research Part I: Oceanographic Research Papers 125, 26–39. https://doi.org/10.1016/j.dsr.2017.04.006

Galbraith, E.D., Merlis, T.M., Palter, J.B., 2016. Destabilization of glacial climate by the radiative impact of Atlantic Meridional Overturning Circulation disruptions. Geophysical Research Letters 43, 8214–8221. https://doi.org/10.1002/2016GL069846

Ganachaud, A., Wunsch, C., 2000. Improved estimates of global ocean circulation, heat transport and mixing from hydrographic data. Nature 408, 453–457. https://doi.org/10.1038/35044048

Gattuso J., Epitalon J., Lavigne H., Orr J., 2022. seacarb: Seawater Carbonate Chemistry. R package version 3.3.1. https://CRAN.R-project.org/package=seacarb

Godwin, H., 1962. Radiocarbon Dating: Fifth International Conference. Nature 195, 943–945. https://doi.org/10.1038/195943a0

Goldstein, S.J., Lea, D.W., Chakraborty, S., Kashgarian, M., Murrell, M.T., 2001. Uranium-series and radiocarbon geochronology of deep-sea corals: implications for Southern Ocean ventilation rates and the oceanic carbon cycle. Earth and Planetary Science Letters 193, 167–182. https://doi.org/10.1016/S0012-821X(01)00494-0

Grammer, G.L., Fallon, S.J., Izzo, C., Wood, R., Gillanders, B.M., 2015. Investigating bomb radiocarbon transport in the southern Pacific Ocean with otolith radiocarbon. Earth and Planetary Science Letters 424, 59–68. https://doi.org/10.1016/j.epsl.2015.05.008

Guilderson, T.P., Schrag, D.P., Cane, M.A., 2004. Surface Water Mixing in the Solomon Sea as Documented by a High-Resolution Coral ^{14}C Record. J. Climate 17, 1147–1156. https://doi.org/10.1175/1520-0442(2004)017<1147:SWMITS>2.0.CO;2

Gutjahr, M., Vance, D., Hoffmann, D.L., Hillenbrand, C.-D., Foster, G.L., Rae, J.W.B., Kuhn, G., 2013. Structural limitations in deriving accurate U-series ages from calcitic cold-water corals contrast with robust coral radiocarbon and Mg/Ca systematics. Chemical Geology 355, 69–87. https://doi.org/10.1016/j.chemgeo.2013.07.002

Hain, M.P., Sigman, D.M., Haug, G.H., 2014. Distinct roles of the Southern Ocean and North Atlantic in the deglacial atmospheric radiocarbon decline. Earth and Planetary Science Letters 394, 198–208. https://doi.org/10.1016/j.epsl.2014.03.020

Häkkinen, S., Rhines, P.B., Worthen, D.L., 2015. Heat content variability in the North Atlantic Ocean in ocean reanalyses. Geophys. Res. Lett. 42, 2901–2909. https://doi.org/10.1002/2015GL063299

Haslett, J., Parnell, A., 2008. A Simple Monotone Process with Application to Radiocarbon-Dated Depth Chronologies. Journal of the Royal Statistical Society Series C: Applied Statistics 57, 399–418. https://doi.org/10.1111/j.1467-9876.2008.00623.x

Hathorne, E.C., Gagnon, A., Felis, T., Adkins, J., Asami, R., Boer, W., Caillon, N., Case, D., Cobb, K.M., Douville, E., deMenocal, P., Eisenhauer, A., Garbe-Schönberg, D., Geibert, W., Goldstein, S., Hughen, K., Inoue, M., Kawahata, H., Kölling, M., Cornec, F.L., Linsley, B.K., McGregor, H.V., Montagna, P., Nurhati, I.S., Quinn, T.M., Raddatz, J., Rebaubier, H., Robinson, L., Sadekov, A., Sherrell, R., Sinclair, D., Tudhope, A.W., Wei, G., Wong, H., Wu, H.C., You, C.-F., 2013. Interlaboratory study for coral Sr/Ca and other element/Ca ratio measurements. Geochem. Geophys. Geosyst. 14, 3730–3750. https://doi.org/10.1002/ggge.20230

Heaton, T.J., Köhler, P., Butzin, M., Bard, E., Reimer, R.W., Austin, W.E.N., Bronk Ramsey, C., Grootes, P.M., Hughen, K.A., Kromer, B., Reimer, P.J., Adkins, J., Burke, A., Cook, M.S., Olsen, J., Skinner, L.C.,

2020. Marine20—The Marine Radiocarbon Age Calibration Curve (0–55,000 cal BP). Radiocarbon 62, 779–820. https://doi.org/10.1017/RDC.2020.68

Henderson, G.M., 2002. Seawater (^{234}U/^{238}U) during the last 800 thousand years. Earth and Planetary Science Letters 199, 97–110. https://doi.org/10.1016/S0012-821X(02)00556-3

Henderson, G.M., Slowey, N.C., Fleisher, M.Q., 2001. U-Th dating of carbonate platform and slope sediments. Geochimica et Cosmochimica Acta 65, 2757–2770. https://doi.org/10.1016/S0016-7037(01)00621-4

Hua, Q., Webb, G.E., Zhao, J., Nothdurft, L.D., Lybolt, M., Price, G.J., Opdyke, B.N., 2015. Large variations in the Holocene marine radiocarbon reservoir effect reflect ocean circulation and climatic changes. Earth and Planetary Science Letters 422, 33–44. https://doi.org/10.1016/j.epsl.2015.03.049

Immenhauser, A., Schöne, B.R., Hoffmann, R., Niedermayr, A., 2016. Mollusc and brachiopod skeletal hard parts: Intricate archives of their marine environment. Sedimentology 63, 1–59. https://doi.org/10.1111/sed.12231

Jaffey, A.H., Flynn, K.F., Glendenin, L.E., Bentley, W.C., Essling, A.M., 1971. Precision Measurement of Half-Lives and Specific Activities of ^{235}U and ^{238}U. Phys. Rev. C 4, 1889–1906. https://doi.org/10.1103/PhysRevC.4.1889

Kilbourne, K.H., Wanamaker, A.D., Moffa-Sanchez, P., Reynolds, D.J., Amrhein, D.E., Butler, P.G., Gebbie, G., Goes, M., Jansen, M.F., Little, C.M., Mette, M., Moreno-Chamarro, E., Ortega, P., Otto-Bliesner, B.L., Rossby, T., Scourse, J., Whitney, N.M., 2022. Atlantic circulation change still uncertain. Nat. Geosci. 15, 165–167. https://doi.org/10.1038/s41561-022-00896-4

King, T.M., Rosenheim, B.E., Post, A.L., Gabris, T., Burt, T., Domack, E.W., 2018. Large-Scale Intrusion of Circumpolar Deep Water on Antarctic Margin Recorded by Stylasterid Corals. Paleoceanography and Paleoclimatology 33, 1306–1321. https://doi.org/10.1029/2018PA003439

Knowles, T.D.J., Monaghan, P.S., Evershed, R.P., 2019. Radiocarbon Sample Preparation Procedures and the First Status Report from the Bristol Radiocarbon AMS (BRAMS) Facility. Radiocarbon 61, 1541–1550. https://doi.org/10.1017/RDC.2019.28

Komugabe, A.F., Fallon, S.J., Thresher, R.E., Eggins, S.M., 2014. Modern Tasman Sea surface reservoir ages from deep-sea black corals. Deep Sea Research Part II: Topical Studies in Oceanography 99, 207–212. https://doi.org/10.1016/j.dsr2.2013.05.024

Kucera, M., 2007. Chapter Six Planktonic Foraminifera as Tracers of Past Oceanic Environments, in: Developments in Marine Geology. Elsevier, pp. 213–262. https://doi.org/10.1016/S1572-5480(07)01011-1

Landman, N.H., Druffel, E.R.M., Cochran, J.K., Donahue, D.J., Jull, A.J.T., 1988. Bomb-produced radiocarbon in the shell of the chambered nautilus: rate of growth and age at maturity. Earth and Planetary Science Letters 89, 28–34. https://doi.org/10.1016/0012-821X(88)90030-1

Lauvset, S.K., Lange, N., Tanhua, T., Bittig, H.C., Olsen, A., Kozyr, A., Alin, S., Álvarez, M., Azetsu-Scott, K., Barbero, L., Becker, S., Brown, P.J., Carter, B.R., Da Cunha, L.C., Feely, R.A., Hoppema, M., Humphreys, M.P., Ishii, M., Jeansson, E., Jiang, L.-Q., Jones, S.D., Lo Monaco, C., Murata, A., Müller, J.D., Pérez, F.F., Pfeil, B., Schirnick, C., Steinfeldt, R., Suzuki, T., Tilbrook, B., Ulfsbo, A., Velo, A., Woosley, R.J., Key, R.M., 2022. GLODAPv2.2022: the latest version of the global interior ocean biogeochemical data product. Earth Syst. Sci. Data 14, 5543–5572. https://doi.org/10.5194/essd-14-5543-2022

Lee, K., Kim, T.-W., Byrne, R.H., Millero, F.J., Feely, R.A., Liu, Y.-M., 2010. The universal ratio of boron to chlorinity for the North Pacific and North Atlantic oceans. Geochimica et Cosmochimica Acta 74, 1801–1811. https://doi.org/10.1016/j.gca.2009.12.027

Lin, J.C., Broecker, W.S., Anderson, R.F., Hemming, S., Rubenstone, J.L., Bonani, G., 1996. New ^{230}Th/U and ^{14}C ages from Lake Lahontan carbonates, Nevada, USA, and a discussion of the origin of initial thorium. Geochimica et Cosmochimica Acta 60, 2817–2832. https://doi.org/10.1016/0016-7037(96)00136-6

Liu, Q., 2022. Exploring recent ocean ventilation and biogeochemical variations using deep-sea corals. PhD thesis, University of Bristol.

Lomitschka, M., Mangini, A., 1999. Precise Th/U-dating of small and heavily coated samples of deep sea corals. Earth and Planetary Science Letters 170, 391–401. https://doi.org/10.1016/S0012-821X(99)00117-X

Lozier, M.S., Leadbetter, S., Williams, R.G., Roussenov, V., Reed, M.S.C., Moore, N.J., 2008. The Spatial Pattern and Mechanisms of Heat-Content Change in the North Atlantic. Science 319, 800–803. https://doi.org/10.1126/science.1146436

Ludwig, K.R., Titterington, D.M., 1994. Calculation of ^{230}ThU isochrons, ages, and errors. Geochimica et Cosmochimica Acta 58, 5031–5042. https://doi.org/10.1016/0016-7037(94)90229-1

Lueker, T.J., Dickson, A.G., Keeling, C.D., 2000. Ocean pCO$_2$ calculated from dissolved inorganic carbon, alkalinity, and equations for K_1 and K_2: validation based on laboratory measurements of CO$_2$ in gas and seawater at equilibrium. Marine Chemistry 70, 105–119. https://doi.org/10.1016/S0304-4203(00)00022-0

Luo, S., Ku, T.-L., 1991. U-series isochron dating: A generalized method employing total-sample dissolution. Geochimica et Cosmochimica Acta 55, 555–564. https://doi.org/10.1016/0016-7037(91)90012-T

Macdonald, A.M., Wunsch, C., 1996. An estimate of global ocean circulation and heat fluxes. Nature 382, 436–439. https://doi.org/10.1038/382436a0

Marcott, S.A., Clark, P.U., Padman, L., Klinkhammer, G.P., Springer, S.R., Liu, Z., Otto-Bliesner, B.L., Carlson, A.E., Ungerer, A., Padman, J., He, F., Cheng, J., Schmittner, A., 2011. Ice-shelf collapse from subsurface warming as a trigger for Heinrich events. Proc. Natl. Acad. Sci. U.S.A. 108, 13415–13419. https://doi.org/10.1073/pnas.1104772108

Miller, K.J., Mundy, C.N., Chadderton, W.L., 2004. Ecological and genetic evidence of the vulnerability of shallow-water populations of the stylasterid hydrocoral *Errina novaezelandiae* in New Zealand's fiords. Aquatic Conserv: Mar. Freshw. Ecosyst. 14, 75–94. https://doi.org/10.1002/aqc.597

Moore, W.S., 1981. The thorium isotope content of ocean water. Earth and Planetary Science Letters 53, 419–426. https://doi.org/10.1016/0012-821X(81)90046-7

Montero-Serrano, J.-C., Frank, N., Tisnérat-Laborde, N., Colin, C., Wu, C.-C., Lin, K., Shen, C.-C., Copard, K., Orejas, C., Gori, A., De Mol, L., Van Rooij, D., Reverdin, G., Douville, E., 2013. Decadal changes in the mid-depth water mass dynamic of the Northeastern Atlantic margin (Bay of Biscay). Earth and Planetary Science Letters 364, 134–144. https://doi.org/10.1016/j.epsl.2013.01.012

Moseley, H.N., 1878. The Croonian lecture: On the Structure of the Stylasteridae, a Family of the Hydroid Stony Corals. Philosophical Transactions of the Royal Society of London 169, 425-503.

Ni, Y., Foster, G.L., Bailey, T., Elliott, T., Schmidt, D.N., Pearson, P., Haley, B., Coath, C., 2007. A core top assessment of proxies for the ocean carbonate system in surface-dwelling foraminifers. Paleoceanography 22, PA3212. https://doi.org/10.1029/2006PA001337

Obert, J.C., Scholz, D., Felis, T., Brocas, W.M., Jochum, K.P., Andreae, M.O., 2016. ^{230}Th/U dating of Last Interglacial brain corals from Bonaire (southern Caribbean) using bulk and theca wall material. Geochimica et Cosmochimica Acta 178, 20–40. https://doi.org/10.1016/j.gca.2016.01.011

Oppo, D.W., Lu, W., Huang, K.-F., Umling, N.E., Guo, W., Yu, J., Curry, W.B., Marchitto, T.M., Wang, S., 2023. Deglacial Temperature and Carbonate Saturation State Variability in the Tropical Atlantic at Antarctic Intermediate Water Depths. Paleoceanog and Paleoclimatol 38, e2023PA004674. https://doi.org/10.1029/2023PA004674

Pedro, J.B., Jochum, M., Buizert, C., He, F., Barker, S., Rasmussen, S.O., 2018. Beyond the bipolar seesaw: Toward a process understanding of interhemispheric coupling. Quaternary Science Reviews 192, 27–46. https://doi.org/10.1016/j.quascirev.2018.05.005

Petchey, F., Anderson, A., Hogg, A., Zondervan, A., 2008a. The marine reservoir effect in the Southern Ocean: An evaluation of extant and new ΔR values and their application to archaeological chronologies. Journal of the Royal Society of New Zealand 38, 243–262. https://doi.org/10.1080/03014220809510559

Petchey, F., Anderson, A., Zondervan, A., Ulm, S., Hogg, A., 2008b. New Marine ΔR Values for the South Pacific Subtropical Gyre Region. Radiocarbon 50, 373–397. https://doi.org/10.1017/S0033822200053509

Petchey, F., Phelan, M., Peter White, J., 2004. New ΔR Values for the Southwest Pacific Ocean. Radiocarbon 46, 1005–1014. https://doi.org/10.1017/S0033822200036079

Petchey, F., Ulm, S., David, B., McNiven, I.J., Asmussen, B., Tomkins, H., Dolby, N., Aplin, K., Richards, T., Rowe, C., Leavesley, M., Mandui, H., 2013. High-resolution radiocarbon dating of marine materials in archaeological contexts: radiocarbon marine reservoir variability between *Anadara*, *Gafrarium*, *Batissa*, *Polymesoda* spp. and Echinoidea at Caution Bay, Southern Coastal Papua New Guinea. Archaeol Anthropol Sci 5, 69–80. https://doi.org/10.1007/s12520-012-0108-1

Rae, J.W.B., Burke, A., Robinson, L.F., Adkins, J.F., Chen, T., Cole, C., Greenop, R., Li, T., Littley, E.F.M., Nita, D.C., Stewart, J.A., Taylor, B.J., 2018. CO_2 storage and release in the deep Southern Ocean on millennial to centennial timescales. Nature 562, 569–573. https://doi.org/10.1038/s41586-018-0614-0

Rahmstorf, S., 2002. Ocean circulation and climate during the past 120,000 years. Nature 419, 207–214. https://doi.org/10.1038/nature01090

Reid, P.C., Fischer, A.C., Lewis-Brown, E., Meredith, M.P., Sparrow, M., Andersson, A.J., Antia, A., Bates, N.R., Bathmann, U., Beaugrand, G., Brix, H., Dye, S., Edwards, M., Furevik, T., Gangstø, R., Hátún, H., Hopcroft, R.R., Kendall, M., Kasten, S., Keeling, R., Le Quéré, C., Mackenzie, F.T., Malin, G., Mauritzen, C., Ólafsson, J., Paull, C., Rignot, E., Shimada, K., Vogt, M., Wallace, C., Wang, Z., Washington, R., 2009. Chapter 1 Impacts of the Oceans on Climate Change, in: Advances in Marine Biology. Elsevier, pp. 1–150. https://doi.org/10.1016/S0065-2881(09)56001-4

Reimer, P.J., Reimer, R.W., 2001. A Marine Reservoir Correction Database and On-Line Interface. Radiocarbon 43, 461–463. https://doi.org/10.1017/S0033822200038339

Richards, D.A., Dorale, J.A., 2003. Uranium-series Chronology and Environmental Applications of Speleothems. Reviews in Mineralogy and Geochemistry 52, 407–460. https://doi.org/10.2113/0520407

Roark, E., Guilderson, T., Dunbar, R., Ingram, B., 2006. Radiocarbon-based ages and growth rates of Hawaiian deep-sea corals. Mar. Ecol. Prog. Ser. 327, 1–14. https://doi.org/10.3354/meps327001

Robinson, L.F., Adkins, J.F., Frank, N., Gagnon, A.C., Prouty, N.G., Brendan Roark, E., De Flierdt, T.V., 2014. The geochemistry of deep-sea coral skeletons: A review of vital effects and applications for palaeoceanography. Deep Sea Research Part II: Topical Studies in Oceanography 99, 184–198. https://doi.org/10.1016/j.dsr2.2013.06.005

Robinson, L.F., Adkins, J.F., Keigwin, L.D., Southon, J., Fernandez, D.P., Wang, S.-L., Scheirer, D.S., 2005. Radiocarbon Variability in the Western North Atlantic During the Last Deglaciation. Science 310, 1469–1473. https://doi.org/10.1126/science.1114832

Robinson, L.F., Henderson, G.M., Slowey, N.C., 2002. U–Th dating of marine isotope stage 7 in Bahamas slope sediments. Earth and Planetary Science Letters 196, 175–187. https://doi.org/10.1016/S0012-821X(01)00610-0

Robinson, L.F., Adkins, J.F., Scheirer, D.S., Fernandez, D.P., Gagnon, A. and Waller, R.G., 2007. Deep-sea scleractinian coral age and depth distributions in the northwest Atlantic for the last 225,000 years. Bulletin of Marine Science, 81(3), 371-391.

Roemmich, D., John Gould, W., Gilson, J., 2012. 135 years of global ocean warming between the Challenger expedition and the Argo Programme. Nature Clim Change 2, 425–428. https://doi.org/10.1038/nclimate1461

Rühlemann, C., Mulitza, S., Lohmann, G., Paul, A., Prange, M., Wefer, G., 2004. Intermediate depth warming in the tropical Atlantic related to weakened thermohaline circulation: Combining paleoclimate data and modeling results for the last deglaciation. Paleoceanography 19, PA1025. https://doi.org/10.1029/2003PA000948

Samperiz, A., Robinson, L.F., Stewart, J.A., Strawson, I., Leng, M.J., Rosenheim, B.E., Ciscato, E.R., Hendry, K.R., Santodomingo, N., 2020. Stylasterid corals: A new paleotemperature archive. Earth and Planetary Science Letters 545, 116407. https://doi.org/10.1016/j.epsl.2020.116407

Schlitzer, R., 2023. Ocean Data View, odv.awi.de.

Shen, C.-C., Li, K.-S., Sieh, K., Natawidjaja, D., Cheng, H., Wang, X., Edwards, R.L., Lam, D.D., Hsieh, Y.-T., Fan, T.-Y., Meltzner, A.J., Taylor, F.W., Quinn, T.M., Chiang, H.-W., Kilbourne, K.H., 2008. Variation of initial ^{230}Th/^{232}Th and limits of high precision U–Th dating of shallow-water corals. Geochimica et Cosmochimica Acta 72, 4201–4223. https://doi.org/10.1016/j.gca.2008.06.011

Shen, G.T., Boyle, E.A., 1988. Determination of lead, cadmium and other trace metals in annually-banded corals. Chemical Geology 67, 47–62. https://doi.org/10.1016/0009-2541(88)90005-8

Sherwood, O.A., Edinger, E.N., 2009. Ages and growth rates of some deep-sea gorgonian and antipatharian corals of Newfoundland and Labrador. Can. J. Fish. Aquat. Sci. 66, 142–152. https://doi.org/10.1139/F08-195

Spooner, P.T., Robinson, L.F., Hemsing, F., Morris, P., Stewart, J.A., 2018. Extended calibration of cold-water coral Ba/Ca using multiple genera and co-located measurements of dissolved barium concentration. Chemical Geology 499, 100–110. https://doi.org/10.1016/j.chemgeo.2018.09.012

Stewart, J.A., Christopher, S.J., Kucklick, J.R., Bordier, L., Chalk, T.B., Dapoigny, A., Douville, E., Foster, G.L., Gray, W.R., Greenop, R., Gutjahr, M., Hemsing, F., Henehan, M.J., Holdship, P., Hsieh, Y., Kolevica, A., Lin, Y., Mawbey, E.M., Rae, J.W.B., Robinson, L.F., Shuttleworth, R., You, C., Zhang, S., Day, R.D., 2020a. NIST RM 8301 Boron Isotopes in Marine Carbonate (Simulated Coral and Foraminifera Solutions): Inter-laboratory δ^{11}B and Trace Element Ratio Value Assignment. Geostand Geoanal Res 45, 77–96. https://doi.org/10.1111/ggr.12363

Stewart, J.A., Li, T., Spooner, P.T., Burke, A., Chen, T., Roberts, J., Rae, J.W.B., Peck, V., Kender, S., Liu, Q., Robinson, L.F., 2021. Productivity and Dissolved Oxygen Controls on the Southern Ocean Deep-Sea Benthos During the Antarctic Cold Reversal. Paleoceanography and Paleoclimatology 36, e2021PA004288. https://doi.org/10.1029/2021PA004288

Stewart, J.A., Robinson, L.F., Day, R.D., Strawson, I., Burke, A., Rae, J.W.B., Spooner, P.T., Samperiz, A., Etnoyer, P.J., Williams, B., Paytan, A., Leng, M.J., Häussermann, V., Wickes, L.N., Bratt, R., Pryer, H., 2020b. Refining trace metal temperature proxies in cold-water scleractinian and stylasterid corals. Earth and Planetary Science Letters 545, 116412. https://doi.org/10.1016/j.epsl.2020.116412

Stewart, J.A., Strawson, I., Kershaw, J., Robinson, L.F., 2022. Stylasterid corals build aragonite skeletons in undersaturated water despite low pH at the site of calcification. Sci Rep 12, 13105. https://doi.org/10.1038/s41598-022-16787-y

Stuiver, M., Polach, H.A., 1977. Discussion Reporting of [14]C Data. Radiocarbon 19, 355–363. https://doi.org/10.1017/S0033822200003672

Taylor, R.E., Berger, R., 1967. Radiocarbon Content of Marine Shells from the Pacific Coasts of Central and South America. Science 158, 1180–1182. https://doi.org/10.1126/science.158.3805.1180.b

Toggweiler, J.R., Dixon, K., Broecker, W.S., 1991. The Peru upwelling and the ventilation of the south Pacific thermocline. J. Geophys. Res. 96, 20467. https://doi.org/10.1029/91JC02063

Tomiak, P.J., Andersen, M.B., Hendy, E.J., Potter, E.K., Johnson, K.G., Penkman, K.E.H., 2016. The role of skeletal micro-architecture in diagenesis and dating of *Acropora palmata*. Geochimica et Cosmochimica Acta 183, 153–175. https://doi.org/10.1016/j.gca.2016.03.030

Ulm, S., 2002. Marine and estuarine reservoir effects in central Queensland, Australia: Determination of ΔR values. Geoarchaeology 17, 319–348. https://doi.org/10.1002/gea.10017

Ulm, S., Petchey, F., Ross, A., 2009. Marine reservoir corrections for Moreton Bay, Australia. Archaeology in Oceania 44, 160–166. https://doi.org/10.1002/j.1834-4453.2009.tb00060.x

van de Flierdt, T., Robinson, L.F., Adkins, J.F., 2010. Deep-sea coral aragonite as a recorder for the neodymium isotopic composition of seawater. Geochimica et Cosmochimica Acta 74, 6014–6032. https://doi.org/10.1016/j.gca.2010.08.001

Vermeesch, P., 2018. IsoplotR: A free and open toolbox for geochronology. Geoscience Frontiers 9, 1479–1493. https://doi.org/10.1016/j.gsf.2018.04.001

Wang, M., Chen, T., Feng, D., Zhang, X., Li, T., Robinson, L.F., Liang, Q., Bialik, O.M., Liu, Y., Makovsky, Y., 2022. Uranium-thorium isotope systematics of cold-seep carbonate and their constraints on geological methane leakage activities. Geochimica et Cosmochimica Acta 320, 105–121. https://doi.org/10.1016/j.gca.2021.12.016

Wisshak, M., López Correa, M., Zibrowius, H., Jakobsen, J., Freiwald, A., 2009. Skeletal reorganisation affects geochemical signals, exemplified in the stylasterid hydrocoral *Errina dabneyi* (Azores Archipelago). Mar. Ecol. Prog. Ser. 397, 197–208. https://doi.org/10.3354/meps08165

Wu, Y., Fallon, S.J., Cantin, N.E., Lough, J.M., 2021. SURFACE OCEAN RADIOCARBON FROM A *PORITES* CORAL RECORD IN THE GREAT BARRIER REEF: 1945–2017. Radiocarbon 63, 1193–1203. https://doi.org/10.1017/RDC.2020.141

Wunsch, C., Heimbach, P., 2006. Estimated Decadal Changes in the North Atlantic Meridional Overturning Circulation and Heat Flux 1993–2004. Journal of Physical Oceanography 36, 2012–2024. https://doi.org/10.1175/JPO2957.1

Zaunbrecher, L.K., Cobb, K.M., Beck, J.W., Charles, C.D., Druffel, E.R.M., Fairbanks, R.G., Griffin, S., Sayani, H.R., 2010. Coral records of central tropical Pacific radiocarbon variability during the last millennium. Paleoceanography 25, PA4212. https://doi.org/10.1029/2009PA001788

Zeebe, R.E., Wolf-Gladrow, D.A., 2001. CO_2 in seawater: equilibrium, kinetics, isotopes, Elsevier oceanography series. Elsevier, Amsterdam; New York.

Chapter 6: Conclusions and perspectives

Contributions and acknowledgements

1.   Overview

This thesis presents novel inorganic geochemical data measured on stylasterid coral skeletons. The two primary aims of this thesis were to (i) develop stylasterid inorganic geochemistry as a palaeoceanographic tool and (ii) investigate stylasterid biomineralisation mechanisms to provide information on their vulnerability/resilience in a changing ocean. In the following sections, I first summarise the main conclusions as they relate to each theme, before highlighting suggested areas for future research in section 4.

2.   Palaeoceanographic potential

This thesis develops stylasterids as palaeoceanographic tools by both calibrating stylasterid inorganic geochemistry with ocean conditions, and developing tools to radiometrically date their skeletons. These are addressed in the following sections, and the current state of the stylasterid palaeoceanographic toolbox is summarised in Table 1.

2.1   Proxy development

This thesis significantly expands the stylasterid palaeoceanographic toolbox by developing stylasterid skeletal Ba/Ca and $\delta^{11}B$ as novel archives of past ocean $[Ba]_{SW}$ and pH, respectively. The calibration lines developed include a number of stylasterid genera collected from a diverse range of geographic locations, and are therefore robust and widely applicable.

In both proxy systems explored here, stylasterid inorganic geochemistry more reliably records seawater conditions than azooxanthellate scleractinian coral geochemistry, which has been widely applied in palaeoceanographic reconstruction (e.g. Rae et al., 2018; Chen et al., 2020; Stewart et al., 2021; T. Chen et al., 2023). The improved goodness-of-fit of the stylasterid calibrations suggest stronger environmental controls on stylasterid skeletal geochemistry, in agreement with conclusions drawn from previous studies of stylasterid $\delta^{18}O$ and Li/Mg (Samperiz et al., 2020; Stewart et al., 2020). The origin of the improved fit of stylasterid geochemical calibrations compared with azooxanthellate Scleractinia is almost certainly related to the disparate calcification mechanisms of these two coral groups, as discussed in section 3.

Together with established stylasterid temperature (Li/Mg and $\delta^{18}O$) proxies (Samperiz et al., 2020; Stewart et al., 2020), the stylasterid $[Ba]_{SW}$ and pH proxies developed here form a powerful set of palaeoceanographic tools with the potential to provide constraint on past variations in fundamental hydrographic variables (temperature, pH) as well as climatically-relevant oceanic processes (circulation, primary productivity and carbon storage). In combination with the global distribution of stylasterids in the modern ocean (Cairns, 2011), the strong relationships between stylasterid inorganic geochemistry and key hydrographic variables suggest they hold great promise as an archive of past ocean conditions.

Measurement	Study	Palaeoceanographic use	Comment
Ba/Ca	This thesis, chapter 3	Proxy for $[Ba]_{SW}$	All calibrations show key advantages (e.g. higher R^2, narrower prediction intervals) compared to equivalent calibrations using scleractinian corals
$\delta^{11}B$	This thesis, chapter 4 & Stewart et al. (2022)	Proxy for seawater pH	
$\delta^{18}O$	Samperiz et al. (2020)	Proxy for seawater temperature	
Li/Mg*	Stewart et al. (2020)	Proxy for seawater temperature	
Sr/Ca*	Stewart et al. (2020) and this thesis, chapter 3	Proxy for seawater temperature	
U-series	This thesis, chapter 5	Dating	Low skeletal [U] in stylasterids creates difficulties in achieving the high precision U-series dates that are typical obtained for U-rich scleractinian corals. May be useful on longer (e.g. glacial-interglacial) timescales.
^{14}C	This thesis, chapter 5 & King et al. (2018)	Dating and proxy for seawater $\Delta^{14}C$	Stylasterid $\Delta^{14}C$ reliably records seawater $\Delta^{14}C$, simple sampling strategy for generating robust ^{14}C growth chronologies established. Large, live-collected stylasterids acting as archives of recent (decadal to centennial) oceanographic change are key targets for future work

*Stylasterid Li/Mg ratios are a more robust temperature proxy than Sr/Ca ratios, and are the preferred stylasterid elemental temperature proxy (see Stewart et al., 2020)

Table 1. The stylasterid palaeoceanographic toolbox. Table summarises existing proxy calibrations (either published or developed in this thesis) and the potential applications of U-series and radiocarbon (^{14}C) radiometric dating techniques.

2.2 Radiometric dating

This promising proxy potential motivated the investigations in chapter 5 of this thesis, in which I explore the application of two radiometric dating techniques (U-series and radiocarbon) to stylasterid coral skeletons. As outlined in chapter 1, temporal constraint on the age of a palaeoceanographic archive is fundamental to its development. Despite this, prior to this thesis, only one published study had investigated the application of radiometric dating to stylasterid corals, with a focus on radiocarbon (King et al., 2018).

Considering U-series techniques, firstly, I find that low stylasterid skeletal [U] compared with azooxanthellate scleractinian corals results in smaller amounts of radiogenic ^{230}Th production, while the porous nature of stylasterid skeletons promotes accumulation of Th-bearing contaminant phases and may increase their susceptibility to diagenetic alteration. Together, these factors limit the achievable age precision when dating stylasterids by U-series techniques. The origin of low stylasterid skeletal [U] compared with azooxanthellate Scleractinia appears to be the differing calcification mechanisms of these two coral groups (Stewart et al., 2022). Somewhat ironically, then, the same calcification-related differences which make stylasterid skeletal geochemistry a more reliable record of oceanic conditions than scleractinian coral geochemistry are also those which complicate the application of U-series dating techniques to stylasterid skeletons.

Despite this, stylasterid specimens can be dated by U-series techniques, albeit to a limited degree of precision, while isochron techniques represent one possible strategy to more accurately date larger specimens. However, the difficulty associated with finding suitable samples, coupled with the time-consuming nature of isochron techniques, means that generating palaeoceanographic records at centennial/millennial resolution from stylasterid skeletons using U-series techniques is – in contrast to scleractinian corals - unlikely to be an efficient and fruitful avenue for future research. Instead, U-series dated sub-fossil stylasterids are likely better suited to investigating temporal changes in seawater conditions and coral occurrence over longer (e.g. glacial-interglacial) timescales (e.g. following themes in Frank et al., 2011; de Carvalho Ferreira et al., 2022).

Conversely, large stylasterid coral skeletons dated by radiocarbon techniques do hold significant promise as archives of recent, decadal to centennial changes in oceanographic conditions. A previous study demonstrated how along-branch sub-sampling and radiocarbon dating can be used to constrain the timescale of stylasterid skeletal growth and found that stylasterid specimens collected from the Southern Ocean grow on decadal to centennial timescales (King et al., 2018). Here, I confirm these observations using stylasterids collected in the equatorial Atlantic and southwest Pacific. These new data confirm that large stylasterid colonies exhibit integrated growth rates between 0.5 and 1.5 mm/year, far slower than those implied by photogrammetric studies (King et al., 2018). In turn, this suggests that these colonies and the ecosystems they support could take centuries to recover from disturbances or destruction (see section 3.2).

In a palaeoceanographic context, the decadal to centennial timescale of stylasterid growth, coupled with our ability to generate coherent radiocarbon growth chronologies, suggests that large, live-collected stylasterid specimens may be ideal palaeoceanographic targets. To demonstrate this, I couple the radiocarbon growth chronology for one specimen used in this thesis with the geochemical proxies outlined above to constrain variations in mid-depth (~ 1200 m) equatorial Atlantic pH, temperature and [Ba]$_{SW}$ over the period 1924 to 2013. These data reveal a robust warming trend across the 20th century,

which, when considered in combination with previously published proxy records, likely results from a deepening of the thermocline in this region.

3. Stylasterid biomineralisation and resilience

The geochemical data generated as part of this thesis also provide important insights into stylasterid biomineralisation. Broadly, these investigations fall under two themes: i) boron isotopic insights into stylasterid calcification and ii) radiocarbon constraints on stylasterid skeletal growth rates.

3.1 Boron isotopes and stylasterid calcification

In chapter 4 of this thesis, I show that stylasterids from an extremely broad range of oceanographic environments have skeletal $\delta^{11}B$ in equilibrium with seawater $\delta^{11}B_{borate}$. Crucially, this feature of stylasterid skeletal geochemistry is observed for samples collected from waters in the north Pacific, which are significantly undersaturated with respect to aragonite. This finding agrees with an initial study of the boron isotopic composition of stylasterid skeletons, which investigated a smaller number of samples from a more limited range of oceanic conditions (Stewart et al., 2022). Together, the initial data in Stewart et al. (2022) and those presented in this thesis unequivocally demonstrate that – regardless of ambient seawater conditions – stylasterid skeletal $\delta^{11}B$ is in equilibrium with seawater $\delta^{11}B_{borate}$.

This finding has important implications for physico-chemical models of coral calcification, and for interpretations of coral skeletal boron isotopic signatures. Firstly, applying the traditional interpretation of coral skeletal $\delta^{11}B$ as reflecting calcifying fluid pH, stylasterid skeletal $\delta^{11}B$ in equilibrium with $\delta^{11}B_{borate}$ suggests that stylasterids do not employ any upregulation of their calcifying fluid pH. However, a recent study showed that boric acid diffusive connectivity between the coral calcifying fluid and external seawater can decouple coral skeletal $\delta^{11}B$ from calcifying fluid pH (Gagnon et al., 2021). Indeed, the correlations between stylasterid B/Ca, U/Ca and $\delta^{11}B$ found by previous work and supported by the new data presented here can be best explained by a calcification model which invokes boric acid diffusion (Stewart et al., 2022). In particular, the comparison between apical tip and bulk skeletal geochemistry presented for the first time in chapter 4 of this thesis reveals strongly correlated variability in a wide range of geochemical parameters, which are consistent with the influence of boric acid diffusion (and Rayleigh fractionation) on stylasterid skeletal geochemistry.

If diffusion of boric acid is to explain correlations in stylasterid geochemistry, stylasterids must employ some degree of calcifying fluid pH upregulation. This is supported by deviations of stylasterid $\delta^{18}O$ and $\delta^{13}C$ from equilibrium (Samperiz et al., 2020), however these $\delta^{18}O$ and $\delta^{13}C$ deviations are smaller in magnitude than those found for scleractinian corals (Samperiz et al., 2020; Stewart et al., 2020). Furthermore, the finding that stylasterid element/Ca ratios display less variability than in Scleractinia (Stewart et al., 2020) is also reinforced by the Ba/Ca and Sr/Ca data presented in chapter 3 of this thesis.

Perhaps the most likely scenario suggested by the range of stylasterid inorganic geochemical data which now exists is one in which stylasterid corals employ some pH upregulation (required to permit diffusion of boric acid into the stylasterid calcifying fluid), but that this upregulation is muted compared with scleractinian corals (thus explaining the reduced evidence for biological modification of the stylasterid calcifying fluid and the stronger correlations between stylasterid geochemistry and environmental parameters). However, the magnitude of stylasterid pH upregulation remains an open question, which will have important implications for their resilience to future changes in seawater conditions. On the one hand, reduced reliance on pH upregulation suggests that stylasterids may be particularly susceptible to future ocean acidification (e.g. Stewart et al., 2022). However, the distribution of stylasterids in the modern ocean clearly demonstrates they are able to build skeletons in waters undersaturated with respect to aragonite (this thesis, chapter 4; Auscavitch et al., 2020; Stewart et al., 2022). Thus, a decreased reliance on pH upregulation may instead confer upon them an increased resilience, perhaps owing to the smaller energetic burden of a calcification strategy which instead relies on, for instance, organic molecules to catalyse carbonate formation (e.g. Drake et al., 2013; Mass et al., 2013; Von Euw et al., 2017; Stewart et al., 2022). Distinguishing these two hypotheses is a key target for future work, and suggested avenues of research are outlined in section 4.

3.2   Stylasterid growth rates

In addition, as outlined above, the new stylasterid radiocarbon growth chronologies presented here reveal that stylasterids from two contrasting oceanographic regions (the equatorial Atlantic and southwest Pacific) have growth rates $\leq \sim 1.5$ mm/year. These estimates agree well with a previous radiocarbon-based study on Southern Ocean stylasterids (King et al., 2018; growth rates ~ 0.5 mm/year) in that they are significantly slower than estimates derived from observational, photogrammetric studies. Discrepancies between different methods of growth-rate estimation are not unexpected, and the possible reasons for this are outlined in chapter 5. Most likely is that photogrammetric studies provide instantaneous rates of growth, while a radiometric approach provides an integrated view of skeletal growth, incorporating for instance periods of no growth or skeletal dissolution/damage.

Importantly, the consistently slow growth rates implied by radiometric techniques suggest that stylasterid colonies from a wide range of locations grow over the course of tens to hundreds of years. This finding is extremely important in conservation contexts, as it provides a minimum estimate for the recovery time of large stylasterid colonies and the ecosystems they support after damage from disturbances, such as those caused by trawling. To view stylasterids as fast-growing corals which can recover quickly from damage would be to ignore the mounting evidence which suggests that stylasterid colonies can represent decades or even centuries of growth.

4.   Summary and outlook

Overall, the data presented in this thesis significantly expand our understanding of stylasterid geochemistry as a palaeoceanographic tool and provide novel insights into stylasterid biomineralisation. Inevitably, these data have highlighted existing evidence gaps and generated new questions, thus providing clear targets for future work. The most pressing of these are shown in Figure 1.

Stylasterid sample being collected in the Galápagos Islands, 797 m depth

Aragonite saturation horizon at ~ 300 m*

How are stylasterids able to survive (thrive?) in undersaturated conditions without substantial pH upregulation?

Branches > 10 cm long = > 100 years of growth?

Centennial record of eastern equatorial Pacific deep ocean conditions?

Cruise: FKt230918
Gear: ROV SuBastian, SciCam
Depth: 797 m
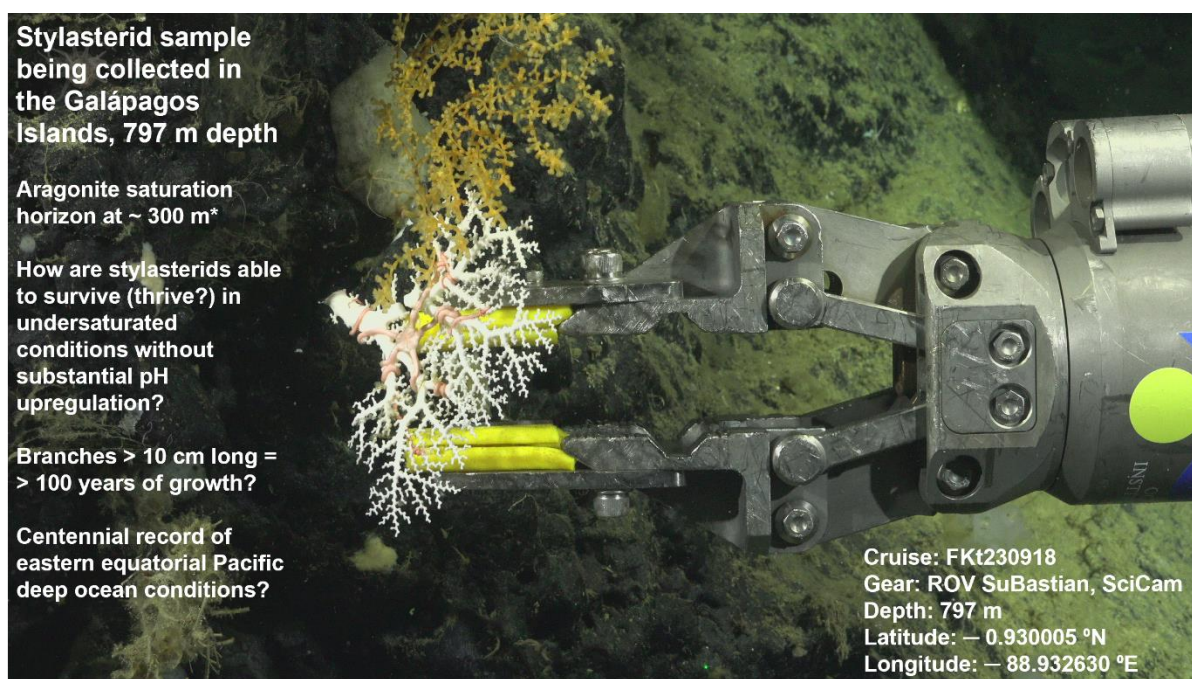Latitude: — 0.930005 ºN
Longitude: — 88.932630 ºE

Figure 1. Stylasterid sample being collected by the manipulator arm of ROV SuBastian during cruise FKt230918. Longest branch of specimen is ~ 10 cm in length. White text summarises main outstanding research questions leading from this thesis, which are exemplified by this specimen. *Aragonite saturation horizon depth estimated using nearest available GLODAP bottle alkalinity and DIC measurements (Lauvset et al., 2022), with carbonate system parameters calculated following method in chapter 4. Image acknowledgements: Schmidt Ocean Institute/Galápagos National Park Directorate/Charles Darwin Foundation/ Memorial University of Newfoundland.

Focusing firstly on stylasterid biomineralisation, constraining the degree of stylasterid calcifying fluid pH upregulation and the associated energetic burden of calcification will be key to understanding their resilience in a changing ocean. Numerical modelling perspectives may provide constraint in this regard, as illustrated by recent studies focusing on scleractinian corals (e.g. Gagnon et al., 2021; S. Chen et al., 2023). A particular target for future work regarding stylasterids is using the boron isotopic and element/Ca ratio data presented in this thesis and by previous work (Stewart et al., 2022) as inputs into a calcification model which includes the role of boric acid diffusion (Gagnon et al., 2021). Further, note that this thesis focuses entirely on the inorganic aspects of stylasterid skeletal geochemistry. Given the distinct possibility that stylasterids rely more heavily on organic molecules to promote calcification than scleractinian corals,

comparing the organic geochemical composition of stylasterid and scleractinian coral skeletons is likely to yield new and important insights.

Additionally, observational evidence and my own experiences onboard cruises AT50-09 and FKt230918 to the Galápagos Islands suggest that stylasterid corals are generally found at deeper depths and in more undersaturated waters than scleractinian corals. This observation should be interrogated statistically and at other locations: such observations will be important to our assessment of stylasterid resilience. Quantifying these observations using collected specimens or museum databases is difficult, owing to factors including sampling bias and an absence of proximal hydrographic data (specifically carbonate system data) to assess ambient seawater conditions. One powerful tool in this regard could be systematic analysis of video imagery collected during cruises AT50-09 and FKt230918, which would enable statistically-rigorous assessments of benthic community composition which could in turn be paired with proximal hydrographic data (including carbonate system parameters) collected during cruise AT50-09. Finally, to my knowledge no attempts have ever been made to culture stylasterids under prescribed conditions. The ability to do so would allow us to investigate the effects of, for instance, changing pH or food supply on their calcification, thus providing fundamental insights into their resilience.

In a palaeoceanographic context, further developmental work could of course be carried out, for instance by calibrating other aspects of stylasterid skeletal geochemistry with seawater conditions (e.g. Nd isotopes), or by investigating ^{210}Pb systematics, which could provide precise radiometric age constraint in fast growing specimens. However, an array of geochemical tools now exist which permit the application of stylasterid geochemistry in palaeoceanographic contexts. As outlined in chapter 1, observations of recent, decadal to centennial changes in deep ocean conditions are fundamental to our understanding of the impact of anthropogenic emissions on Earth's ocean, yet remain sparse. Large, live-collected stylasterid specimens represent an ideal target to address this data gap, and suitable stylasterid samples have been documented and collected from sites across the global ocean, including sites in climatically-important regions such as the Southern Ocean and north Pacific (e.g. Samperiz et al., 2020; Robson; 2023). Perhaps the most important finding of this thesis it that, with robust stylasterid temperature, $[Ba]_{SW}$ and pH proxies now established, as well as a simple method for generating coherent radiocarbon-based growth chronologies, large, live-collected stylasterids should now be considered a go-to archive of recent (i.e. decadal to centennial) change in the deep ocean.

5.　References

Auscavitch, S.R., Lunden, J.J., Barkman, A., Quattrini, A.M., Demopoulos, A.W.J., Cordes, E.E., 2020. Distribution of deep-water scleractinian and stylasterid corals across abiotic environmental gradients on three seamounts in the Anegada Passage. PeerJ 8, e9523. https://doi.org/10.7717/peerj.9523

Cairns, S.D., 2011. Global Diversity of the Stylasteridae (Cnidaria: Hydrozoa: Athecatae). PLoS ONE 6, e21670. https://doi.org/10.1371/journal.pone.0021670

Chen, T., Robinson, L.F., Burke, A., Claxton, L., Hain, M.P., Li, T., Rae, J.W.B., Stewart, J., Knowles, T.D.J., Fornari, D.J., Harpp, K.S., 2020. Persistently well-ventilated intermediate-depth ocean through the last deglaciation. Nat. Geosci. 13, 733–738. https://doi.org/10.1038/s41561-020-0638-6

Chen, S., Littley, E.F.M., Rae, J.W.B., Charles, C.D., Guan, Y., Adkins, J.F., 2023. Coherent tracer correlations in deep-sea corals and implications for biomineralization mechanisms underlying vital effects. Geochimica et Cosmochimica Acta 343, 304–322. https://doi.org/10.1016/j.gca.2022.12.006

Chen, T., Robinson, L.F., Li, T., Burke, A., Zhang, X., Stewart, J.A., White, N.J., Knowles, T.D.J., 2023. Radiocarbon evidence for the stability of polar ocean overturning during the Holocene. Nat. Geosci. 16, 631–636. https://doi.org/10.1038/s41561-023-01214-2

de Carvalho Ferreira, M.L., Robinson, L.F., Stewart, J.A., Li, T., Chen, T., Burke, A., Kitahara, M.V., White, N.J., 2022. Spatial and temporal distribution of cold-water corals in the Northeast Atlantic Ocean over the last 150 thousand years. Deep Sea Research Part I: Oceanographic Research Papers 190, 103892. https://doi.org/10.1016/j.dsr.2022.103892

Drake, J.L., Mass, T., Haramaty, L., Zelzion, E., Bhattacharya, D., Falkowski, P.G., 2013. Proteomic analysis of skeletal organic matrix from the stony coral *Stylophora pistillata*. Proc. Natl. Acad. Sci. U.S.A. 110, 3788–3793. https://doi.org/10.1073/pnas.1301419110

Frank, N., Freiwald, A., Correa, M.L., Wienberg, C., Eisele, M., Hebbeln, D., Van Rooij, D., Henriet, J.-P., Colin, C., Van Weering, T., De Haas, H., Buhl-Mortensen, P., Roberts, J.M., De Mol, B., Douville, E., Blamart, D., Hatte, C., 2011. Northeastern Atlantic cold-water coral reefs and climate. Geology 39, 743–746. https://doi.org/10.1130/G31825.1

Gagnon, A.C., Gothmann, A.M., Branson, O., Rae, J.W.B., Stewart, J.A., 2021. Controls on boron isotopes in a cold-water coral and the cost of resilience to ocean acidification. Earth and Planetary Science Letters 554, 116662. https://doi.org/10.1016/j.epsl.2020.116662

King, T.M., Rosenheim, B.E., Post, A.L., Gabris, T., Burt, T., Domack, E.W., 2018. Large-Scale Intrusion of Circumpolar Deep Water on Antarctic Margin Recorded by Stylasterid Corals. Paleoceanography and Paleoclimatology 33, 1306–1321. https://doi.org/10.1029/2018PA003439

Lauvset, S.K., Lange, N., Tanhua, T., Bittig, H.C., Olsen, A., Kozyr, A., Alin, S., Álvarez, M., Azetsu-Scott, K., Barbero, L., Becker, S., Brown, P.J., Carter, B.R., Da Cunha, L.C., Feely, R.A., Hoppema, M., Humphreys, M.P., Ishii, M., Jeansson, E., Jiang, L.-Q., Jones, S.D., Lo Monaco, C., Murata, A., Müller, J.D., Pérez, F.F., Pfeil, B., Schirnick, C., Steinfeldt, R., Suzuki, T., Tilbrook, B., Ulfsbo, A., Velo, A., Woosley, R.J., Key, R.M., 2022. GLODAPv2.2022: the latest version of the global interior ocean biogeochemical data product. Earth Syst. Sci. Data 14, 5543–5572. https://doi.org/10.5194/essd-14-5543-2022

Mass, T., Drake, J.L., Haramaty, L., Kim, J.D., Zelzion, E., Bhattacharya, D., Falkowski, P.G., 2013. Cloning and Characterization of Four Novel Coral Acid-Rich Proteins that Precipitate Carbonates In Vitro. Current Biology 23, 1126–1131. https://doi.org/10.1016/j.cub.2013.05.007

Rae, J.W.B., Burke, A., Robinson, L.F., Adkins, J.F., Chen, T., Cole, C., Greenop, R., Li, T., Littley, E.F.M., Nita, D.C., Stewart, J.A., Taylor, B.J., 2018. CO_2 storage and release in the deep Southern Ocean on millennial to centennial timescales. Nature 562, 569–573. https://doi.org/10.1038/s41586-018-0614-0

Robson, E., 2023. Stylasterid coral biocalcification and their potential as palaeoceanographic archives. Master's thesis, University of Bristol.

Samperiz, A., Robinson, L.F., Stewart, J.A., Strawson, I., Leng, M.J., Rosenheim, B.E., Ciscato, E.R., Hendry, K.R., Santodomingo, N., 2020. Stylasterid corals: A new paleotemperature archive. Earth and Planetary Science Letters 545, 116407. https://doi.org/10.1016/j.epsl.2020.116407

Stewart, J.A., Li, T., Spooner, P.T., Burke, A., Chen, T., Roberts, J., Rae, J.W.B., Peck, V., Kender, S., Liu, Q., Robinson, L.F., 2021. Productivity and Dissolved Oxygen Controls on the Southern Ocean Deep-Sea Benthos During the Antarctic Cold Reversal. Paleoceanography and Paleoclimatology 36, e2021PA004288. https://doi.org/10.1029/2021PA004288

Stewart, J.A., Robinson, L.F., Day, R.D., Strawson, I., Burke, A., Rae, J.W.B., Spooner, P.T., Samperiz, A., Etnoyer, P.J., Williams, B., Paytan, A., Leng, M.J., Häussermann, V., Wickes, L.N., Bratt, R., Pryer, H., 2020. Refining trace metal temperature proxies in cold-water scleractinian and stylasterid corals. Earth and Planetary Science Letters 545, 116412. https://doi.org/10.1016/j.epsl.2020.116412

Stewart, J.A., Strawson, I., Kershaw, J., Robinson, L.F., 2022. Stylasterid corals build aragonite skeletons in undersaturated water despite low pH at the site of calcification. Sci Rep 12, 13105. https://doi.org/10.1038/s41598-022-16787-y

Von Euw, S., Zhang, Q., Manichev, V., Murali, N., Gross, J., Feldman, L.C., Gustafsson, T., Flach, C., Mendelsohn, R., Falkowski, P.G., 2017. Biological control of aragonite formation in stony corals. Science 356, 933–938. https://doi.org/10.1126/science.aam6371